The High Level Vibration Test Program

Final Report

The High Level Vibration
Test Program

Final Report

Prepared by
Y. J. Park, J. R. Curreri, C. H. Hofmayer

Brookhaven National Laboratory
Upton, NY 11973

Prepared for
Division of Engineering
Office of Nuclear Regulatory Research
U.S. Nuclear Regulatory Commission
Washington, DC 20555
NRC FIN A3288

ABSTRACT

As part of a cooperative study between the United States and Japan, the U.S. Nuclear Regulatory Commission (USNRC) and the Ministry of International Trade and Industry (MITI) of Japan agreed to perform a test program that would subject a large scale piping model to significant plastic strains under excitation conditions greater than the design condition for nuclear power plants. The objective was to compare the results of the tests with state-of-the-art analyses. Comparisons were done at different excitation levels from elastic to elastic-plastic to levels where cracking was induced in the test model. The vibration tests and post-test examination were carried out in Japan by the Nuclear Power Engineering Test Center (NUPEC). Input motion development and pre- and post-test analysis were carried out in the United States at the Brookhaven National Laboratory (BNL) and the Electric Power Research Institute (EPRI).

This report describes the results of the cooperative studies performed both in Japan and the United States.

EXECUTIVE SUMMARY

As part of a cooperative agreement between the Agency of Natural Resource and Energy (ANRE) of the Ministry of International Trade and Industry (MITI) of Japan and the United States Nuclear Regulatory Commission (NRC), the Nuclear Power Engineering Test Center (NUPEC) and Brookhaven National Laboratory (BNL) jointly performed high level vibration tests and analyses of nuclear power piping. The purpose was to obtain test data in the elastic-plastic region of the piping, which would be compared with analytical predictions. Ten (10) electric companies and four (4) manufacturers in Japan and the Electric Power Research Institute (EPRI) in the U.S. also participated in this cooperative program.

The tests were performed on a large scale modified model of one loop of a PWR system which was previously tested by NUPEC as part of their seismic proving test program. The excitation was increased up to the limits of the vibration table. Substantial plasticity was induced in some parts of the test model.

The test plan and the preparation for the test (establishment of test procedure, preparation of instrumentation, etc.) were completed by March 1988. The vibration test was carried out in April and May 1988 and preliminary data processing was completed by the end of December 1988.

Pre-test analysis predictions were made by BNL and EPRI. BNL also performed post-test analyses and compared the analytical results with the experimental data.

The test provided extensive non-linear dynamic response data of piping in the elastic-plastic region. The test results were compared with the elastic-plastic analysis results obtained by the latest version of well known structural computer codes. The comparisons show that the vibration responses (acceleration, displacement, etc.) of elastic-plastic analysis are in good agreement with those of the tests, while strains (stresses) in the piping are generally not as good. The tests also confirmed that the present seismic design methods provide a large safety margin.

A summary of the more important conclusions, together with a general overview of the accomplishments of the entire program, is presented in Section 8.0 of this report.

ACKNOWLEDGEMENTS

Table of Contents

Table of Contents

Table of Contents

Table of Contents

List of Tables

List of Tables

List of Figures

List of Figures

List of Figures

List of Figures

List of Figures

List of Figures

List of Figures

1.0 INTRODUCTION

In Japan, proving tests are performed to demonstrate the seismic reliability of nuclear power plants using large scale models on the large vibration table at the Tadotsu Engineering Laboratory of Nuclear Power Engineering Test Center (NUPEC). The test specimens are subjected to the excitation due to design earthquakes S_1 and S_2, i.e., the maximum design earthquake and the extreme design earthquake, respectively. The test results have demonstrated that the components and equipment included in the test program were not damaged nor failed due to the design earthquake excitations. The test models suffered no significant plastic strain.

As part of a cooperative study between the United States and Japan, the U.S. Nuclear Regulatory Commission (USNRC) and the Ministry of International Trade and Industry (MITI) of Japan agreed to perform a test program that would subject a large scale piping model to significant plastic strains under excitation conditions greater than the design condition for nuclear power plants. The objective was to compare the results of the tests with state-of-the-art analyses. Comparisons were done at different excitation levels from elastic to elastic plastic to levels where cracking was induced in the test model. The vibration tests and post-test examination were carried out in Japan by NUPEC. Input motion development and pre-and post-test analysis were carried out in the United States at the Brookhaven National Laboratory (BNL) and the Electric Power Research Institute (EPRI).

The tests involved increasing the excitation up to the limits of the Tadotsu vibration table in order to induce inelastic response in a large piping model. The model was subjected to a maximum acceleration well beyond what nuclear power plants are designed to withstand. This program was called the High Level Vibration Test (HLVT).

The test model used in the HLVT program was supplied by MITI after it was tested by NUPEC as part of their seismic proving test program. It was constructed by modifying the 1/2.5 scale model of one loop of a PWR primary coolant system. The upper and middle steam generator shell supports of the model, which simulated the actual plant condition, were removed and the steam generator shell was truncated. In addition, the four lower support columns of the steam generator were replaced by a pin-type support. A modified earthquake excitation was used to drive the structure to a condition of substantial strain. Since the piping was pressurized, and the high level input motion was repeated several times, it was possible to investigate the effects of ratchetting, fatigue, crack initiation and crack propagation as well.

The entire program involving the analysis and test results for the HLVT are summarized in this report. This includes the

vibration table design characteristics, the details of the piping system that was tested, the material description, the selection and modification of the earthquake time history, the effects of detuning, the test procedure, test implementation and test results, the development and spread of plasticity, the onset and propagation of cracking, the pretest analyses and comparisons with the test results. The post-test metallurgical investigations of material appearance and mechanical properties are also discussed. Post-test analyses using various non-linear finite element models were carried out and compared with the test measurements. Finally, the failure mode is assessed and an evaluation is made of the safety margin for the HLVT model. The conclusions drawn from the program are summarized in the last section.

2.0 OVERALL PLAN

Many methods and computer codes are currently used for dynamic responses involving extensive plasticity. Large general purpose non-linear finite element codes have been used by the nuclear industry to assess and demonstrate the safety of Category 1 structures under severe seismic and accident conditions. Tests are also routinely done to show the operational and safety adequacy of nuclear structures and equipment. Ultimately, professional design codes must be satisfied to qualitatively demonstrate that there is an adequate safety margin in the structures. But comprehensive and detailed comparisons of analytical results with test measurements involving large scale complex systems excited to failure under earthquake type excitations have been lacking. The purpose to the HLVT program was to produce this type of information.

The extensive series of proving tests that were recently completed in Japan provided an opportunity to explore the possibility of conducting such a program. MITI sponsored the proving tests to confirm the safety and reliability of large components of nuclear power plants. The tests were conducted by NUPEC at the Tadotsu Engineering Laboratory.

It had been anticipated that the structural models tested at Tadotsu would respond elastically to the proving tests and would be in the undamaged state at the end of the tests. The NRC and EPRI were interested in follow-on tests to evaluate the ability of analytical methods to predict the onset of structural damage and failure due to excessive strain under very large earthquake-like excitations.

The first task of the HLVT Program was to evaluate whether the objective of inducing a failure with the tested models could be achieved. At the request of the NRC, BNL initiated a study to investigate the feasibility of using the Tadotsu facility for inducing substantial plasticity into the test models that were used in the Japanese proving tests.

2.1 Feasibility Test Model

One of the structures studied was a 1/2.5 scale test model of a primary coolant system. The system is shown in Figure 2.1. The model consists of a steam generator, a reactor coolant pump, and three sections of the primary piping system, i.e., the hot leg, the crossover leg and the cold leg. The reactor vessel itself is not included because the piping-reactor connection is assumed to be fixed or rigid. In its place is a rigid structural support. The hot leg is about 80 inches long, has an outer diameter of 13.9 inches and is 1.14 inches thick. The outer diameter and thickness of the crossover leg are 14.8 inches and 1.22 inches, respectively, and its total length is about 96 inches. The cold leg is about 92 inches long with an outer pipe diameter of 13.2 inches and a pipe

thickness of 1.10 inches. The weights of the major components of the test model including the water are; steam generator 176.4 kips, reactor coolant pump 38.6 kips and the piping system 15.2 kips.

The steam generator is laterally supported at three locations (see Figure 2.1). The top and intermediate supports provide translational restraints in the two lateral directions (i.e., x and y), whereas the bottom supports provide translational as well as rotational restraints in all three directions (x, y and z). The coolant pump, on the other hand, has one set of lateral supports with translational restraints near the top, and another set of supports at the bottom with six directional restraints similar to that of the steam generator.

The test was to be run under a constant pressure of 2.23 ksi at normal room temperature. The piping system material is SCS14A stainless steel which has a nominal yield strength of 30.0 ksi and a nominal tensile strength of 70.1 ksi. The Young's modulus of this material is 28298.0 ksi.

2.2 Test Machine Design Characteristics

The vibration table is designed to impart a particular excitation expressed in terms of the acceleration unit "g." The maximum performance of the testing machine is bounded on all sides by the various practical limitations that are built into the design. At the low frequency end, the design limitation is imposed by the physical maximum stroke of the actuators.

At a somewhat higher frequency, but still at the low frequency end, a maximum velocity is specified because of the hydraulic fluid flow capability. The hydraulic power supply has a limitation imposed primarily by the servovalve maximum flow capacity in conjunction with the magnitude of the hydraulic power source.

The machine performance characteristics are bounded on the high frequency side by the combined flexibility associated with the oil column interacting with the piping flexibility and with the masses of the moving parts of the table.

As shown in Figure 2.2 the maximum table acceleration capabilities are developed in the center frequency range. The maximum acceleration depends upon the particular table load. It is seen from the performance curve that the maximum acceleration is limited by the velocity capability from about 0.5Hz to 6Hz with a 500 metric ton inertia load. A maximum acceleration of 2.72g can be developed over the frequency range of 5Hz to 12Hz. Beyond 12Hz, the acceleration drops off due to high frequency effects.

To utilize the full capabilities of the test table, the acceleration time history was increased by appropriate multiplication factors within the design limits of the

displacement, velocity and acceleration constraints of the table. The multiplication factors are obtained from a comparison of the required motion for a specific time history with the allowable table motion. The smallest limiting factor associated with the three motion limits (i.e., displacement, velocity and acceleration) determines the actual peak excitation that can be achieved by the test table.

2.3 Test Model for High Level Vibration Tests (HLVT)

The HLVT model that was actually tested is shown in Figure 2.3. The proving test model shown in Figure 2.1 was modified to the model shown in Figure 2.3. Note that the upper and middle steam generator supports were removed from the proving test model. The steam generator shell was truncated at the tapered section. The lower support structure was also redesigned for this test model. A single vertical column was used in place of a four column support. The single column is pinned to rotate in the X-Z plane, which also contains the hot leg. This is the plane which contains the excitation and where most of the response motion will occur. Figure 2.3 shows two views of the system as it is mounted to the support structure.

To assess the feasibility of achieving plastic strains in the test, and to properly plan the test, elastic and elastic-plastic finite element analyses were performed. The finite element description for the SAP5 computer code elastic analysis of the truncated coolant loop system is shown in Figure 2.4. The single column support structure is modeled between the nodes 53 through 58. The hinge pin is located at node 56. Six degrees of freedom restraints are located at nodes 9, 40 and 53. Two snubbers are placed at node 45 in the X and Y direction on the RCP.

For elastic-plastic analysis, the MARC code was used. The finite element description for the model is much more detailed for this analysis, as shown in Figure 2.5. To identify the locations where the high strains initiate, and how the strain spreads out from these points, many elements are used.

In particular, each of the five pipe elbows is described by multiple elements. The elbow closest to the steam generator has the greatest detail. This is done because the highest strains are expected to occur at these locations. The hot leg elbow, nodes 5 through 52, is divided up into three shorter elbows along its central axis. This is shown in Figure 2.6. The circular cross sections of each of the three pieces is divided up into twelve shell elements around the circumference.

The cross-over leg contains three elbows. The elbow closest to the steam generator is divided up in the same manner as the one previously described in the hot leg, except that there are only two axial sections instead of three. The remaining two elbows are

modeled as single sections with six arc segments around the circumference, but they still have the same three integration points along the arc of each segment and eleven integration points through the thickness. The single elbow in the cold leg is modeled similar to these last two in the cross-over leg.

2.4 Analytical Approach

The analytical evaluation was aimed at maximizing the response of the test model by selectively matching the frequency characteristics of the vibration table and the major frequency components of the input excitations to the test model. The frequency characteristics of the vibration table were obtained from the design specifications which were evaluated with respect to displacement, velocity and acceleration limitations. Model characteristics (natural frequencies and mode shapes) of the test model were determined from the detailed finite element models of the test configuration. Various earthquake records were evaluated in order to select input excitations that were the most suitable for the HLVT program. Time adjustment factors were used on these input excitations to bring their frequency characteristics into the desired range.

Stresses in the test model were first obtained by response spectra and time history analysis methods using the SAP5 computer code. When these methods indicated stresses substantially above yield, a plasticity time history analysis was performed to determine the extent of the plastic deformations.

2.4.1 Results of Feasibility Analysis

The major findings of the feasibility analysis were as follows:

1. The model of the PWR primary coolant system will not undergo plastic deformation even when excited optimally and using the full capacity of the vibration table.

2. If the modified model is excited optimally, there is no doubt that substantial plasticity will occur in the piping system, even at reduced machine capacity. (Optimal excitation is described in Section 3.0.)

From the results of the feasibility study it was clear that the Tadotsu shaker facility has sufficient capacity to induce substantial plasticity and possibly even failure in a modified model when excited by an optimal earthquake-like input.
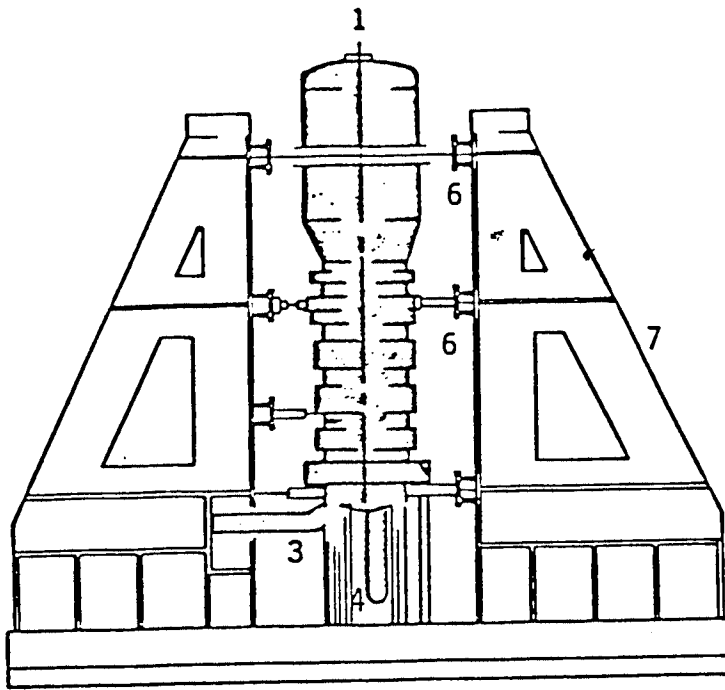
(1) Front View

LEGEND:

1 - steam generator
2 - reactor coolant pump
3 - hot leg pipe
4 - cross over leg pipe
5 - cold leg pipe
6 - lateral supports
7 - support frame
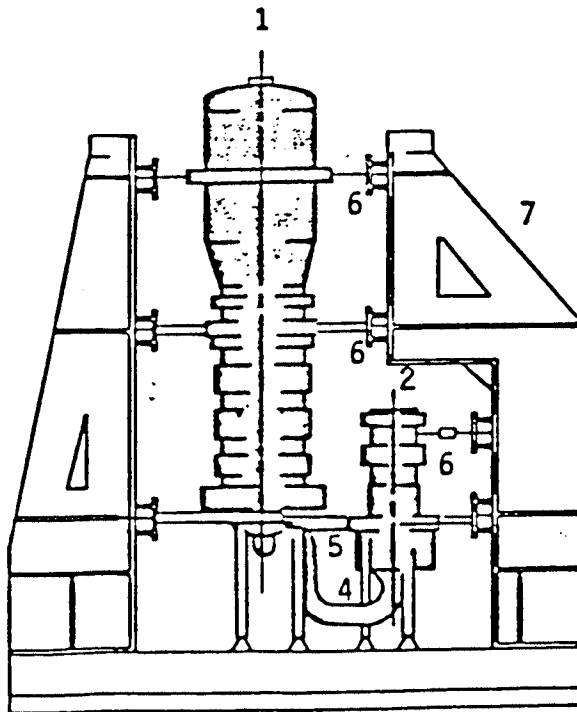
(2) Side View with
    coolant pump

Figure 2.1   Test Model of PWR Primary Coolant
              System with Support Structure
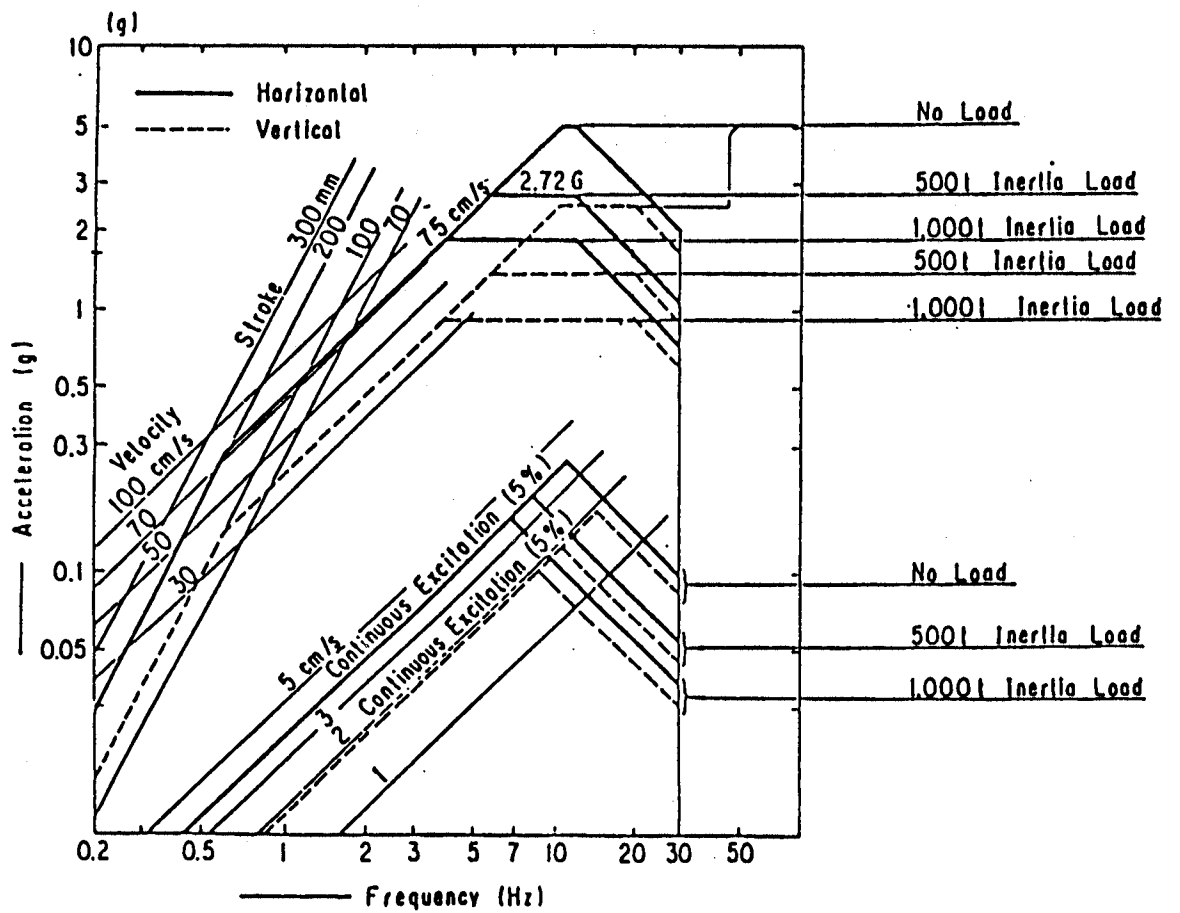
Figure 2.2   Performance Characteristics of
             Tadotsu Shake Table (Simultaneous)
             Horizontal - Vertical Excitation)
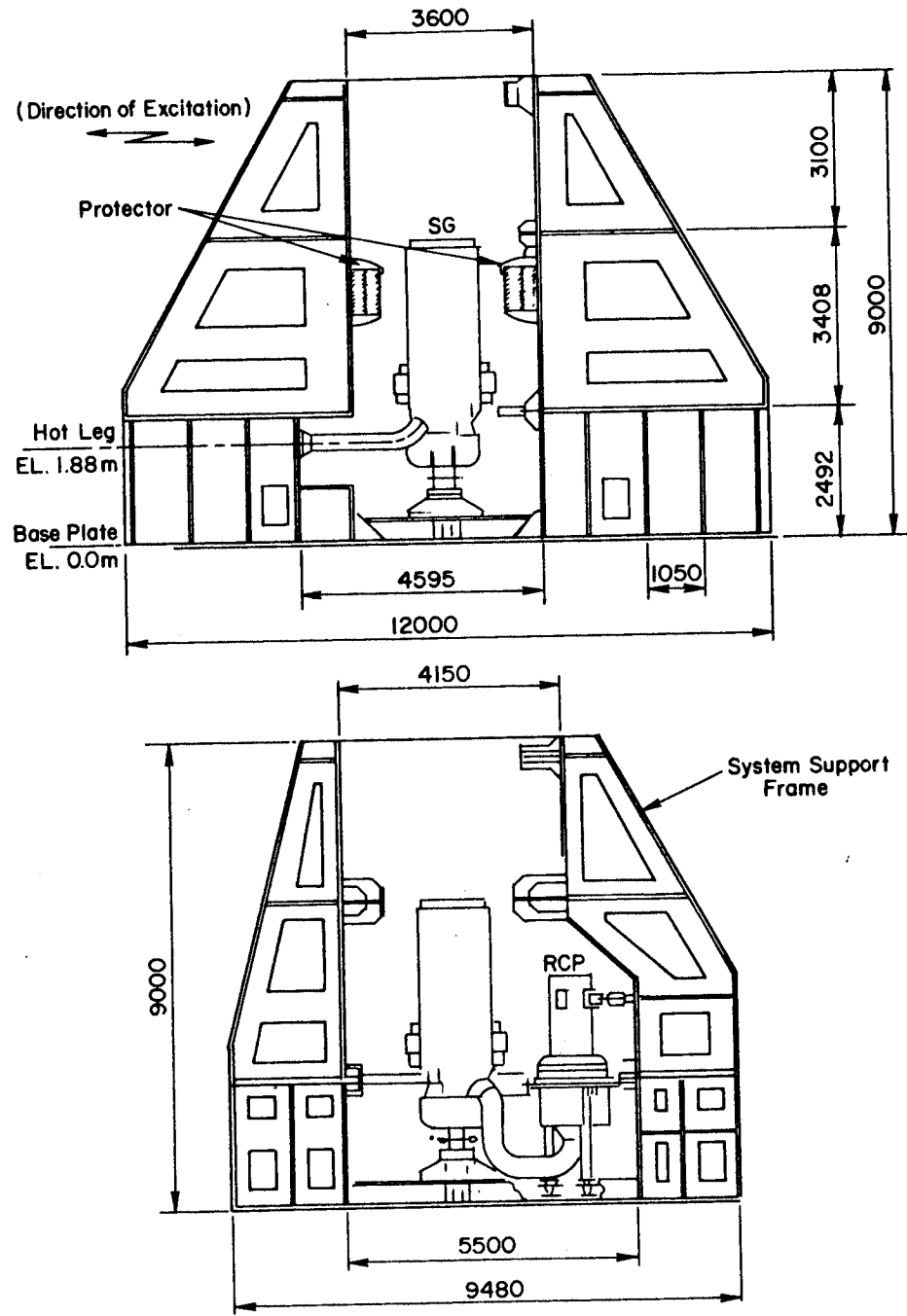
Figure 2.3 Test Model for High Level Vibration Test
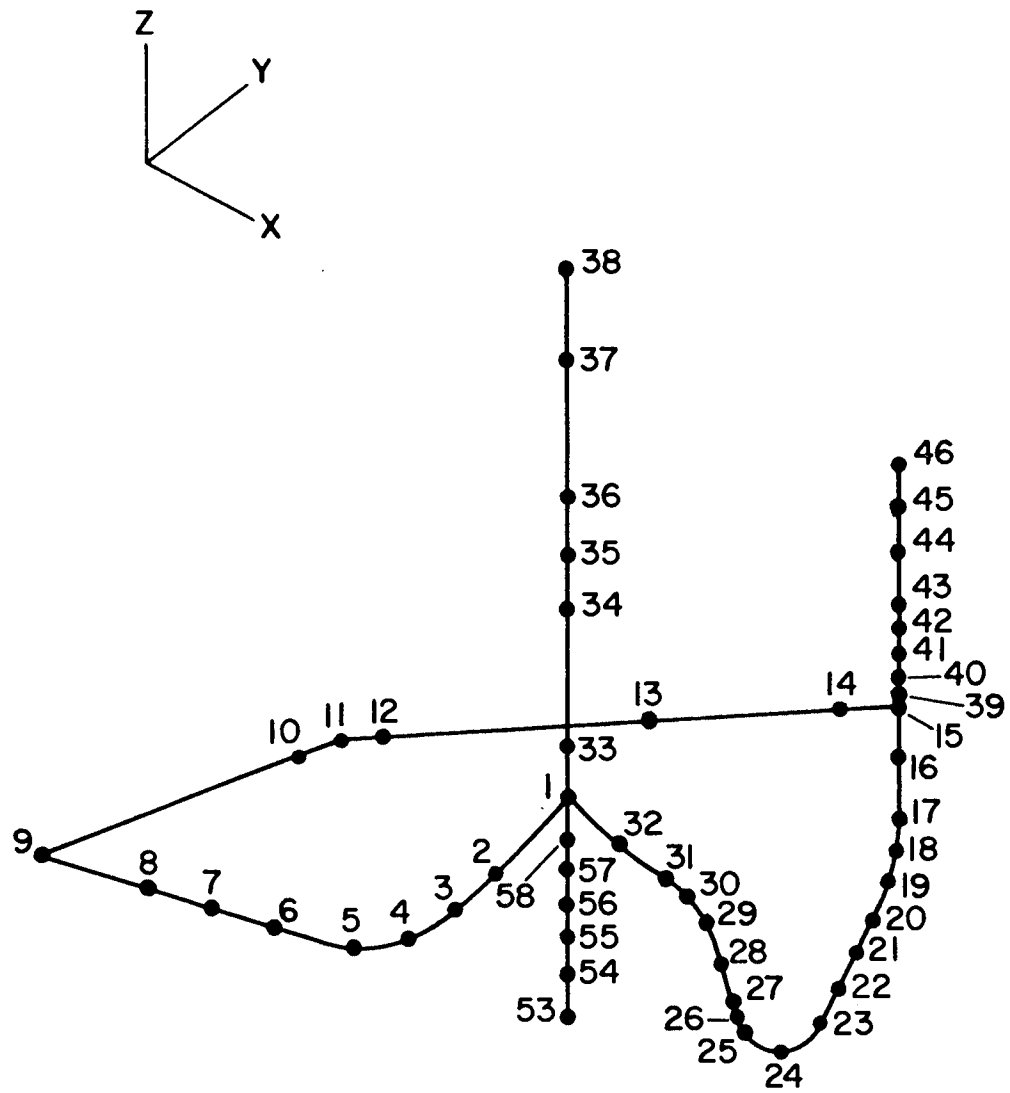
Figure 2.4   SAP 5 Finite Element Idealization
of Model C-1
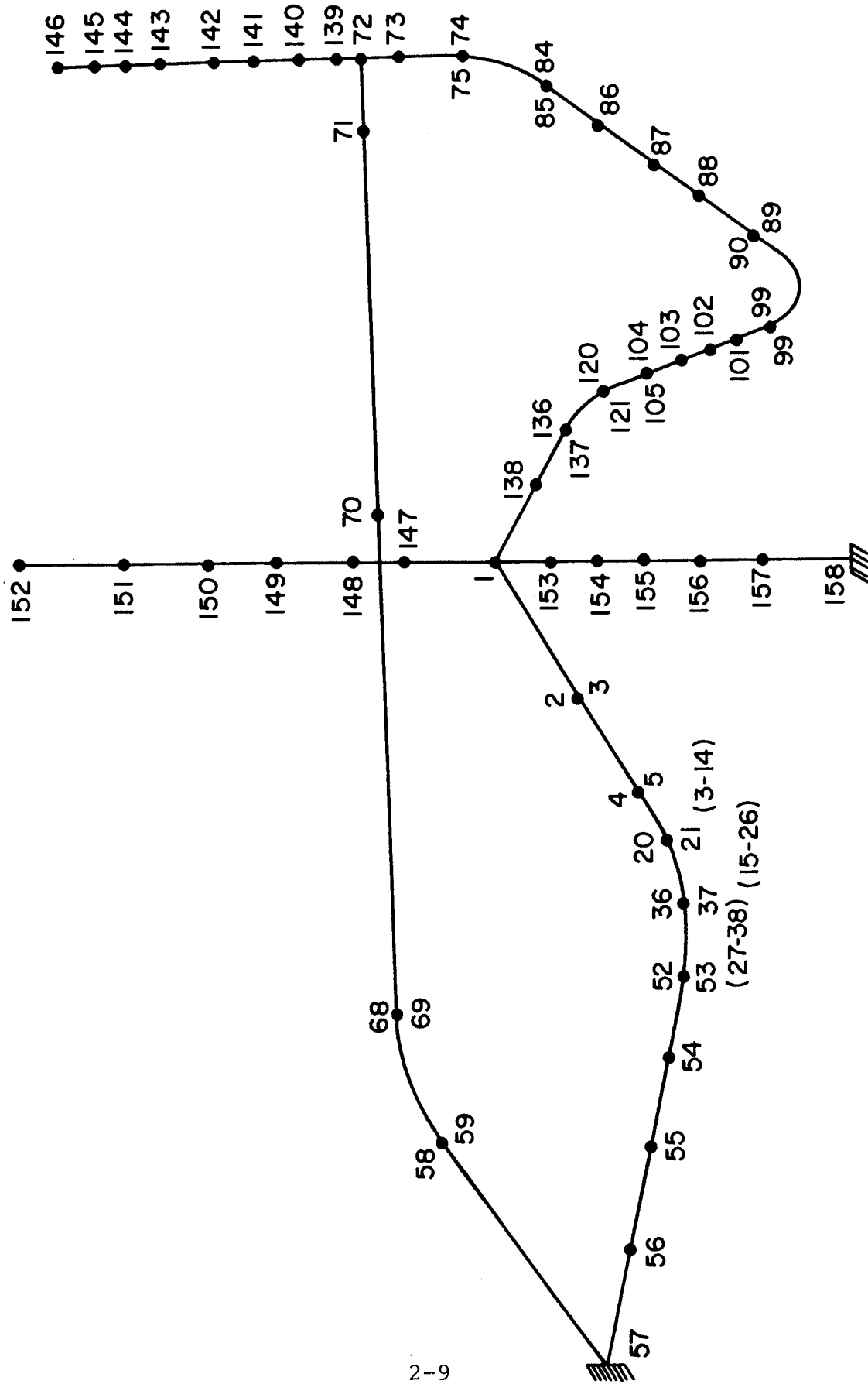
Figure 2.5 MARC Finite Element Idealization of Model C-1
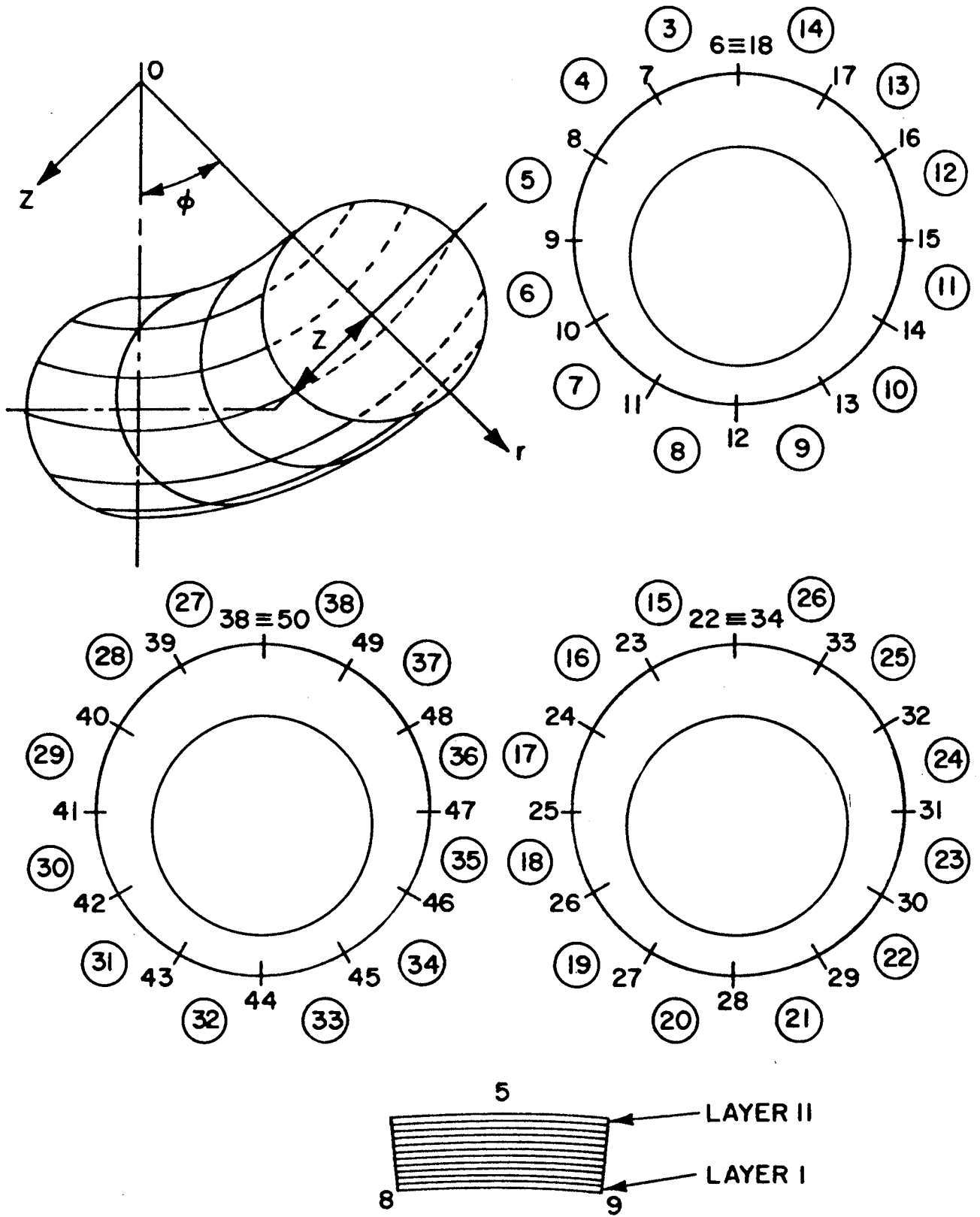
Figure 2.6   Finite Element Idealization of Hot Leg Elbow

3.0 INPUT MOTION DEVELOPMENT

3.1 Requirements for Table Motion

The selection of the excitation time history was done with three guidelines in mind; namely, the time history:

a) was deduced from an actual earthquake or had similar characteristics,
b) was compatible with the characteristics of the vibration table at Tadotsu,
c) established a peak response early in the event so that only a short portion of the time history was needed for the analysis. This was considered very important for the plasticity analysis which required short time steps for a time history solution and could, therefore, be costly.

3.2 Original El Centro Earthquake Record

Several earthquake time histories were examined. These included the N-S, E-W and an SRSS combination of El Centro, the Kern County earthquake and several locations of San Fernando. Of these different earthquake time histories, only the N-S component of El Centro peaks before 5 seconds and has what might be characterized as an exponential-like envelope on the time history portion leading up to the peak. This characteristic enhances the ability of an excitation to build-up a response quickly and with the use of minimum energy. Accordingly, the El Centro time history was selected to start the analysis.

Figures 3.1 (1), 3.1 (2) and 3.1 (3), respectively, show the El Centro acceleration time histories of the N-S component, the E-W component and the SRSS combination of the two. The peak acceleration value is 0.345g for the combination. This is also the peak value of the N-S component.

The response spectra in Figure 3.2 show that the components of El Centro produce essentially two separate peaks. On the other hand, the combined time history focuses the energy of the excitation to produce a predominant single central peak. Since the test model has a single mode that will be excited to a condition of substantial strain, and since it would be desirable to reduce the overall load on the driving vibration machine, the combined time history shown in Figure 3.1 (3) was selected for use in the analysis.

The peak acceleration of the combined El Centro earthquake occurs at 2.14 seconds. Response spectra were made for increasing time segments of the time history. These were generated for the first 2 seconds, then for the first 2.25 seconds and for the first 2.5 seconds. The intention was to examine how the various portions of the response spectra were developed with increasing time

intervals. This was considered important since some detuning action is expected to occur under large strains. To increase the response it is necessary that the development of higher peaks on the response spectrum (RS), as they are produced in time, follows the detuning of the system. Figure 3.3 shows the results for these three time intervals. The response spectrum for the first 2 seconds of El Centro is shown in Figure 3.3 (a). The corresponding RS, for the first 4 seconds is sketched in for comparison as a dotted curve. Note that the peak is not attained for the increased time intervals up to the first 2.5 seconds. But, the peak at 4Hz is being approached in the correct direction to account for detuning, that is from the right to the left (decreasing frequency). The smaller peak at 6Hz on the response spectrum is produced by the time history in the first 2 seconds.

However, as shown in Figure 3.4 (a), the largest peak is essentially attained when the time history is run for 3 seconds, with only a small difference occurring between the response spectra for 3 seconds and for 4 seconds.

Finally, Figure 3.4 (c) gives a comparison between the RS for the first 4 seconds and for the full 30 seconds of El Centro. Here it is seen that, except for some minor lower level peaks, virtually the entire RS for 30 seconds is accomplished in the first 4 seconds.

The conclusion is that only the first 4 seconds of El Centro is enough to represent the action of an actual earthquake. This fulfills criterion (a) of the desired characteristics that were sought in selecting a suitable time history. While this is not essential in carrying out our objective, it was nevertheless thought desirable for the purposes of the analysis to have this characteristic. It also satisfies criterion (c), since the peak response is established early within the time history and so helps in conserving time for the plastic analysis.

3.3 Time History Characteristics - Vibration Limits

In Section 3.1, three guidelines were listed for consideration in the determination of a suitable time history. In selecting the first four seconds of El Centro, criteria (a) and (c) have been satisfied, as previously stated. Guideline (b) says that the time history must be compatible with the characteristics of the vibration table at Tadotsu. This will now be examined.

The maximum performance of the testing machine is bounded by the various practical limitations that are built into the design. At the low frequency end, the design limitation is imposed by the maximum stroke of the actuators. The displacement limitation is 20cm. At a somewhat higher frequency, but still at the low

frequency end, a velocity limitation of 75cm/sec occurs. At the higher frequency, starting at about 5Hz, the acceleration limitation of 2.72g is stipulated for a table load of 500 metric tons.

To utilize the full capabilities of the test table, the acceleration time history can be increased by appropriate multiplication factors within the design limits of the displacement, velocity and acceleration constraints of the table. The factors are obtained from a comparison of the required motion for a specific time history with the allowable table motion. The smallest multiplication factor associated with the three motion limits (i.e, displacement, velocity and acceleration) determines the actual peak excitation that can be achieved by the test table.

For El Centro, the maximum acceleration is 0.345g, the maximum velocity is 33cm/sec and the maximum displacement is 9.5cm. As shown in Figure 3.4, the peak of the response spectrum is at 4Hz. The analysis of the test model has shown that the natural frequency of interest is 5.7Hz. If time scaling is used to shift the response spectrum peak to 5.7Hz, the maximum velocity and displacement of the time history are reduced. The peak velocity is reduced to 23cm/sec while the peak displacement becomes 4.7cm. Using this information, the limiting magnification factors are calculated. Table 3.1 shows the factors that may be applied to an excitation so that the resulting time history is compatible with the characteristics of the vibration machine. The magnification limitation is 3.3, as determined by the velocity factor shown in Table 3.1.

3.4   Time History Modification

The details of the El Centro time history were examined to determine whether an enhancement in the response behavior could be obtained by local modifications. The intention was to see whether the earthquake peak acceleration magnitude and characteristics could be maintained while, at the same time, raising and broadening the response spectrum. Only certain selected changes in the time history were introduced. The peak acceleration was not changed.

For a linearly elastic system, increasing the response spectrum produces a proportionate increase in the stress and strain that is developed. The response will increase if the input excitation has an increasing envelope on a sine wave tuned to the structure's natural frequency. Since it is intended to produce large plastic strains in the system, a non-linear response will result at some level of plastic strain. When the time history is initially scaled so that the peak of the response spectrum coincides with the natural frequency, a detuning will occur as large strains, which are in substantial excess of the yield strain, are produced. If the response spectrum is broad, and if subsequent

elements of the time history are responsible for the breath, then the large response will be maintained by the excitation. If this is not so then the system response will decrease.

Modifications to the time history were made with this understanding of the development of large motion. The time history of El Centro was divided into two time intervals. The first is the time period up to the occurrence of the peak acceleration. The second is the time period after the peak acceleration. Modifications were introduced separately into each portion of the time period.

Figure 3.5 (1) shows the first four seconds of the combined El Centro time history. Figure 3.5 (2) is the corresponding El Centro response spectrum with the single peak, as previously shown.

Some elements of the time history which occur before the peak acceleration were modified. This is the portion of the time history between 1.74 seconds and 2.09 seconds, as seen in Figure 3.5 (3). Figure 3.5 (4) shows the response spectrum (RS) due to this change. Note that the maximum value of the RS has been increased by the ratio of 1.4 divided by 1.14, or by a factor of 1.23. At the same time, the RS has been broadened (at the 1g level) by a factor of about two. All that was done to accomplish this is a local modification in the time history that raises what appears as a depressed peak at t = 1.88 seconds to a positive value. The positive value was selected to continue the exponential like envelope of the excitation.

Figure 3.6 shows the effect of some modifications to the time history after the occurrence of the peak acceleration. If the RS for El Centro , shown in Figure 3.5 (2), is to be broadened to the left (decreasing frequency), the time history should be changed to contain periodic elements at the reduced frequency. The time interval shown by "a" contains a mixture of frequencies from high (shown by spikes) to low, shown by the gap in positive acceleration values across this time period. A time history which occupies essentially a single period of about 0.5sec is placed in this gap, as shown in Figure 3.6 (1). The response spectrum in Figure 3.6 (2) shows that the width of the RS at 1g has been increased by a factor greater than 2 because of the increased response in the vicinity of 2Hz.

Figure 3.6 (3) shows the effect of a different kind of change to the local time history in this same interval. Instead of a single cycle, the time history was modified to include two cycles in the same interval "a." Since this doubles the frequency content in this interval, as compared to the previous case, the response at about 4Hz is significantly increased from the peak that was there in the original time history. Accordingly, the magnitude at 4Hz is increased by 27% without any change in the width of the RS at 1g.

The two cases are illustrative of the process for introducing changes in the time history (TH) for the purpose of increasing the width of the RS or for increasing the maximum magnitude. It is seen that to broaden the RS requires having various periods present in the TH while to raise the RS requires having more cycles of the same period in the TH. For a given limited length to the time history, both cannot be done. Even though a compromise must be made, the resulting time history can still be modified to produce an RS which exceeds the original El Centro RS both in terms of breath as well as in terms of maximum magnitude. In addition, the velocity limitation imposed by the physical requirements of the vibration machine could be improved by modifying the time history.

The Case V TH shown in Figure 3.7 combines the time histories of Cases II and IV shown in Figures 3.5 and 3.6. As was previously stated, Case II significantly broadens and increases the response spectrum while Case IV adds a peak on top. The combined RS is shown in Figure 3.7 (2).

Finally, Case VI, adds a little more time to the periods of the first few cycles of the increasing envelope excitation of El Centro, starting at about 1.4 seconds. This delays the occurrence of the peak acceleration somewhat from the original El Centro. Case VI is shown in Figures 3.7 (3) and 3.7 (4). For this case, the RS is substantially increased by a factor of 21.4/11.14, or 1.88 while still giving a modest increase in the width of the RS at the 1g level.

3.5 Time History Selection

The response spectra developed in Section 3.4 show the response of linearly elastic one degree of freedom systems. They cannot be used directly for a system where the natural frequency changes under large strains. The system under analysis will detune at some level. Our projections from the previous work that was done show that a substantial portion of an element cross section will go plastic. Because of this, the natural frequency will be reduced and, at the same time, the damping will be increased.

Considering this kind of dynamic response, the time history should have a response spectrum that is high enough to produce the condition of substantial strain and yet be broad enough to accommodate some detuning. Case VI (Figure 3.7 (4)) gives the greatest response but, Case V is wider and develops this width with subsequent elements of the time history. Furthermore, preliminary calculations showed that the magnitudes produced with Case V are sufficient to create about 3% strain. Therefore, Case V was selected to be used with the finite element model, designated as Model C-1, for pre-test linear and non-linear analysis.

3.6 Time History Scaling Used for Model C-1

The second natural frequency of Model C-1 is 5.7Hz and has the normal mode essentially in the X-direction. This is the direction of the horizontal motion when Model C-1 is mounted on the Tadotsu Vibration Table. It is the natural frequency which will be excited to a condition of large strain.

The peak of the RS of El Centro is at 4Hz. For the initial analysis using the Case V time history, the location of the peak on the frequency coordinate was raised to 5.7Hz by time scaling the input time history. This was accomplished by changing the numerical value of the 4 second duration of El Centro to 2.8 seconds, which shifts the RS peak to 5.7Hz. When the effects of detuning were evaluated, the peak of the RS was shifted somewhat to the left (at a lower frequency) of 5.7Hz.

The magnitude of the acceleration peak for El Centro is 0.345g. This was also increased to take advantage of the large capability of the Tadotsu machine.

3.7 Amplitude Multiplication for Selected Time History

The maximum velocity capability of the Tadotsu Vibration Machine is 75cm/sec. The maximum velocity of the original El Centro Earthquake is 33cm/sec. This gives a permissible multiplication factor of 2.3, as shown in Table 3.1.

The modified time history that was selected has a maximum velocity that is much less than the maximum velocity of El Centro. The maximum velocity for the selected time history (Case V shown in Figure 3.7 (1) is 24cm/sec for a response spectra peak occurring at 4Hz. In addition, Model C-1 has a natural frequency of 5.7Hz. These numerical values were used to calculate the maximum permissible factor as follows:

multiplication factor = 75/24 x 5.7/4.0 = 4.5

Modifications were made to the duration and to the magnitude of this preliminary excitation time history in accordance with the characteristics of Model C-1 and with the machine capability. The duration was reduced from 4 seconds to 2.8 seconds and the magnitude was increased by the factor 4.5 from 0.345g to 1.55g.

3.8 Detuning

It was expected that the system would detune at some level of strain. The preliminary time history was used to obtain responses in the structure. Figure 3.8 shows the hoop strain that was computed at elements 18 and 27. The results indicated that 3% strain would develop in element 27 at about 1.58 seconds (Figure 3.8 (2). It is seen that the maximum strain is the delayed effect

of the time history portion up to the peak acceleration value. But the peak of the response spectra occurs after 1.58 seconds and the largest strain should also have occurred after this time. This did not happen.

It appeared that the system's natural frequency characteristics were changed because of the large strains that had been produced in many elements. Detuning had occurred and the portion of the excitation time history after the peak had become dynamically ineffective.

To compensate for this changed condition, the detuned natural frequency was evaluated at various time locations. The times were selected to show how the natural frequency was affected by the substantial plastic strain. For example, at the time of maximum strain in element 27, the natural frequency was computed to be 4.36Hz. As compared to the elastic natural frequency of 5.7Hz, this amounts to a lower bound detuning of about 24%.

The detuning was evaluated by noting the maximum strain in each of the elements that yielded. A new modulus of elasticity for each section was calculated in accordance with the ratio of the secant modulus at the given strain, considering the extent of yield, to the elastic tangent. These properties were put into the MARC code and the natural frequencies were computed. The extent of the detuning was evaluated for five points during a full period of vibration of the system. The strain time history in element 27 was used to determine the effect of detuning over this full period.

A natural frequency of the system was calculated at each of the time points shown by A, B, C, D and E in Figure 3.9. Table 3.2 shows the results. The average natural frequency for the full period was 4.5Hz.

3.9   Second Time History Scaling

To continue to drive the system to large responses, a second time history scaling was needed. This was applied only to the time history portion after the occurrence of the peak acceleration. This is the portion of the time history which produces the sharp peak on the RS. For this portion, the scaling was done so that the peak of the response spectrum is moved to a somewhat lower frequency to coincide with the detuned natural frequency of 4.5Hz. The start of the new time scaling was selected to be 1.54 seconds. The time increments after this time were spread out (lower frequency content) to cover the detuned frequency range. An additional cycle was added to increase the time for a maximum response to occur. The final time history is shown in Figure 3.10. The 2.8 seconds duration of the original time history that was used prior to the evaluation of detuning has now been extended by the new time scaling to 3.35 seconds. Figure 3.11 shows the Response Spectrum at 5% damping. In Figure 3.11, the largest RS peak is

produced by the portion of the time history that occurs after the maximum acceleration peak of the excitation. The second RS peak at 5.7Hz is the result of the acceleration peak of this time history.

3.10 Time History for a Complete Vibration Test

The time history that was used following the analysis of Section 3.9 had a duration of 3.35 seconds, as shown in Figure 3.10. Further modifications to this time history were made as discussed in Section 4.0.

Before conducting the test, the time history was adjusted by time scaling to better correspond to the natural frequency of the actual model, as determined by preliminary HLVT test runs. The final time history that was selected is shown in Figure 3.12 and was designated the Maximum Plastic Runs (MPR) time history. The corresponding response spectra are shown in Figure 3.13. This time history has a peak acceleration of 1.82g (1785 gal) and was within the acceleration, velocity and displacement limits of the shaking table. Once again the velocity limit controlled the multiplication factor for the time history. Time scaling was used to shift the peak of the response spectrum to approximately 85 percent of the natural frequency of the test model. This was done to take into account any possible detuning that may occur as large strains are developed. Pre-test analyses indicated that this time history could produce strains in the piping system in excess of 3 percent.

Once the MPR level was achieved in the test sequence, it was desired to repeat this level of excitation a number of times to study ratchetting and fatigue effects. Since this test time history was short, it was decided to repeat the time history four times during one run. A quiet period of approximately 6 seconds was left between each time history segment to eliminate any adverse interaction effects that may occur if they were linked one right after the other. Since it was uncertain as to the amount of detuning that might occur at this test level, the time scale of each segment was changed slightly. This resulted in shifting the peak of the response spectrum for each time history segment by about 5 percent*. Thus, it broadened the response spectrum for the entire test time history and provided further assurance that the desired strains could be achieved. The complete MPR time history and corresponding response spectra are shown in Figures 3.14 and 3.15. The four segments were designated A-B-C-D as shown in Figure 3.14. Segment A corresponds to the time history shown in Figure

---

* Further adjustments to the final test input wave modified this relationship somewhat. The actual recorded time history during the tests resulted in a frequency shift of 8% from the first to the second wave segment and 7% from the second to the third wave segment and the third to the fourth wave segment.

3.12.   To establish the parameters for proper control of the shaking table, the four segment wave had to be run at the lower test levels as well.   However, in order to minimize fatigue damage until the full MPR level was reached, some intermediate level test runs were performed using only the Segment A time history.   The test procedure is fully discussed in Section 5.0.

Table 3.1   Multiplication Factors for Use of
El Centro Shake Table

	Vibration Table Limit	El Centro at 4Hz Peak	Limiting Factor	El Centro at 5.7Hz	Limiting Factor
acc	2.72g @ 5.2Hz	.35g	4.2	.35g	7.7
vel	75cm/sec	33cm/sec	2.3	23cm/sec	3.3
disp	20cm	9.5cm	2.1	4.7cm	4.3

Table 3.2   Evaluation of Detuned Natural Frequency

Time Point	Detuned Natural Frequency
A	4.89
B	4.62
C	4.36
D	4.46
E	4.41
	4.54Hz (average)
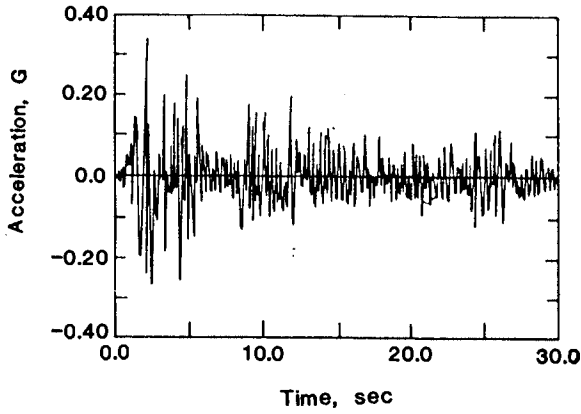
(1) N-S Component
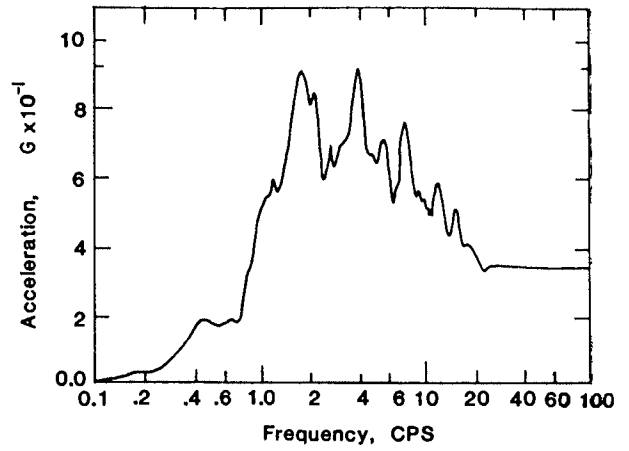
(1) N-S Component
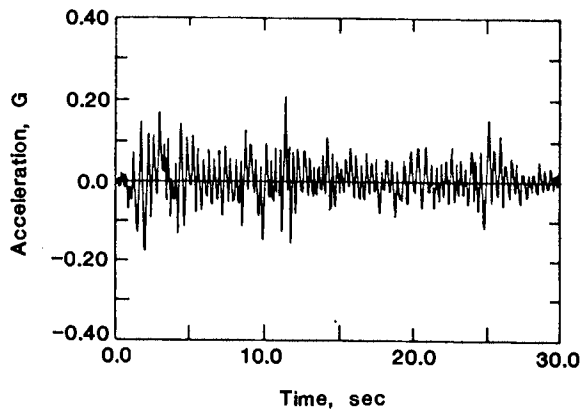
(2) E-W Component
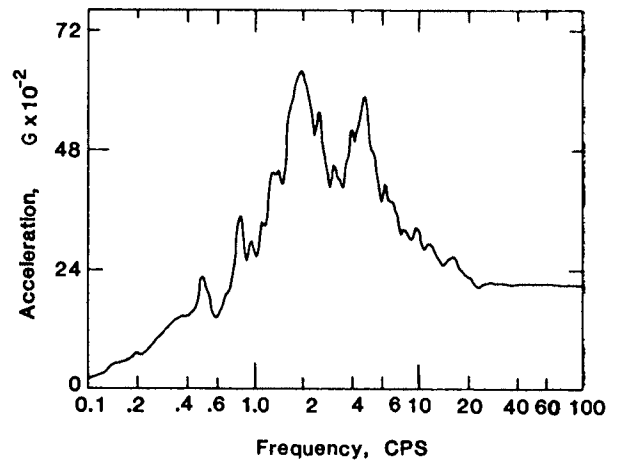
(2) E-W Component
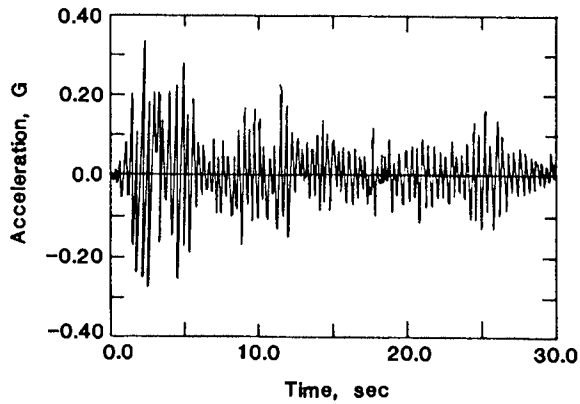
(3) SRSS Combination
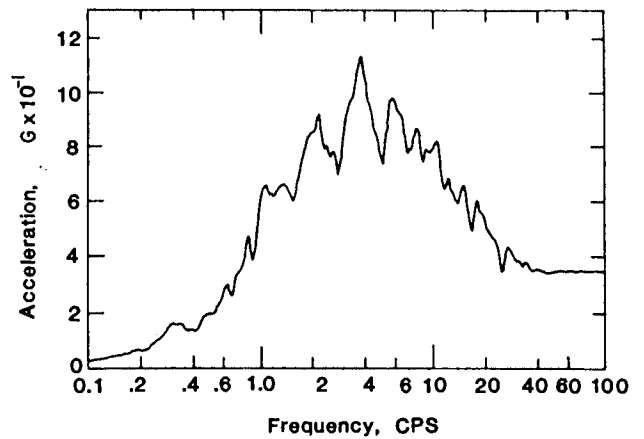
(3) SRSS Combination

Figure 3.1   Time History Record
             of the El Centro
             Earthquake

Figure 3.2   Response Spectra of
             the El Centro
             Earthquake

3-11
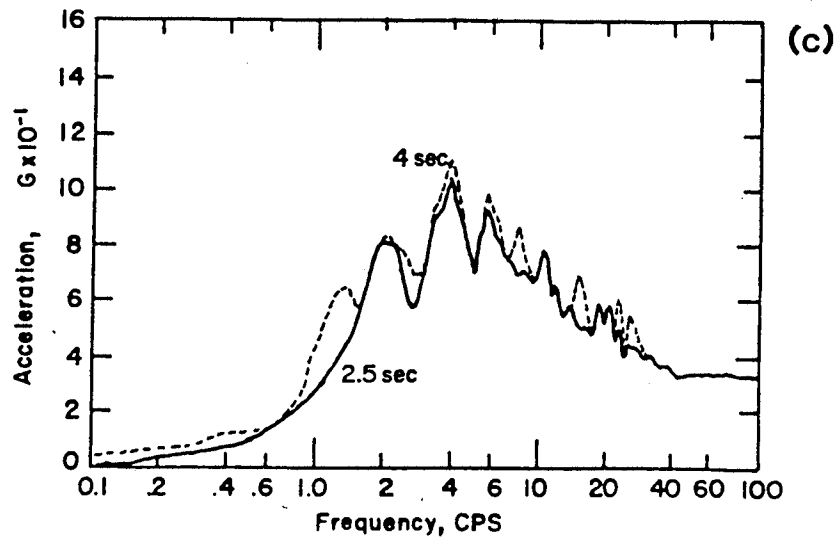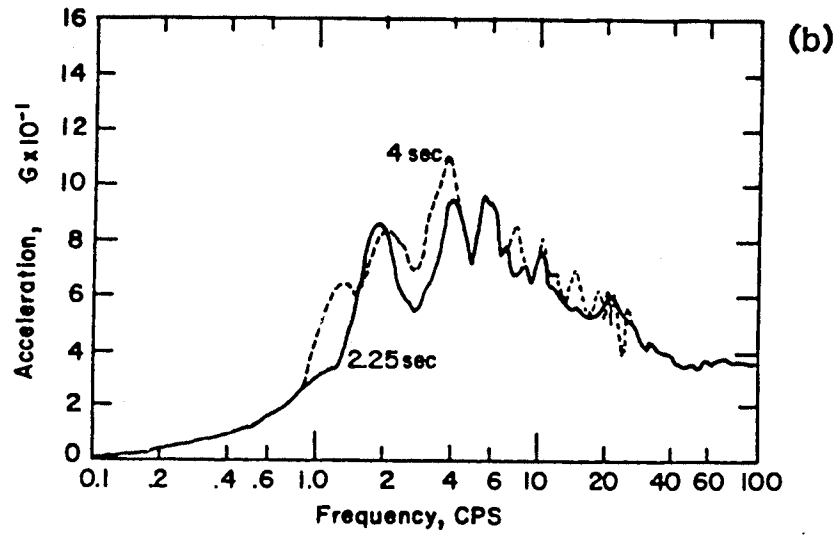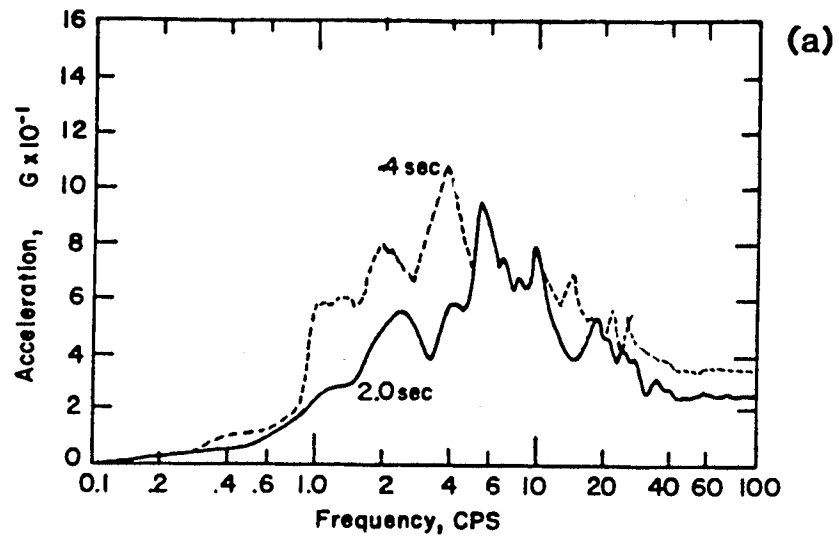
Figure 3.3   Development of Combined El Centro Response
Spectra with Increasing Time up to 2.5
Seconds
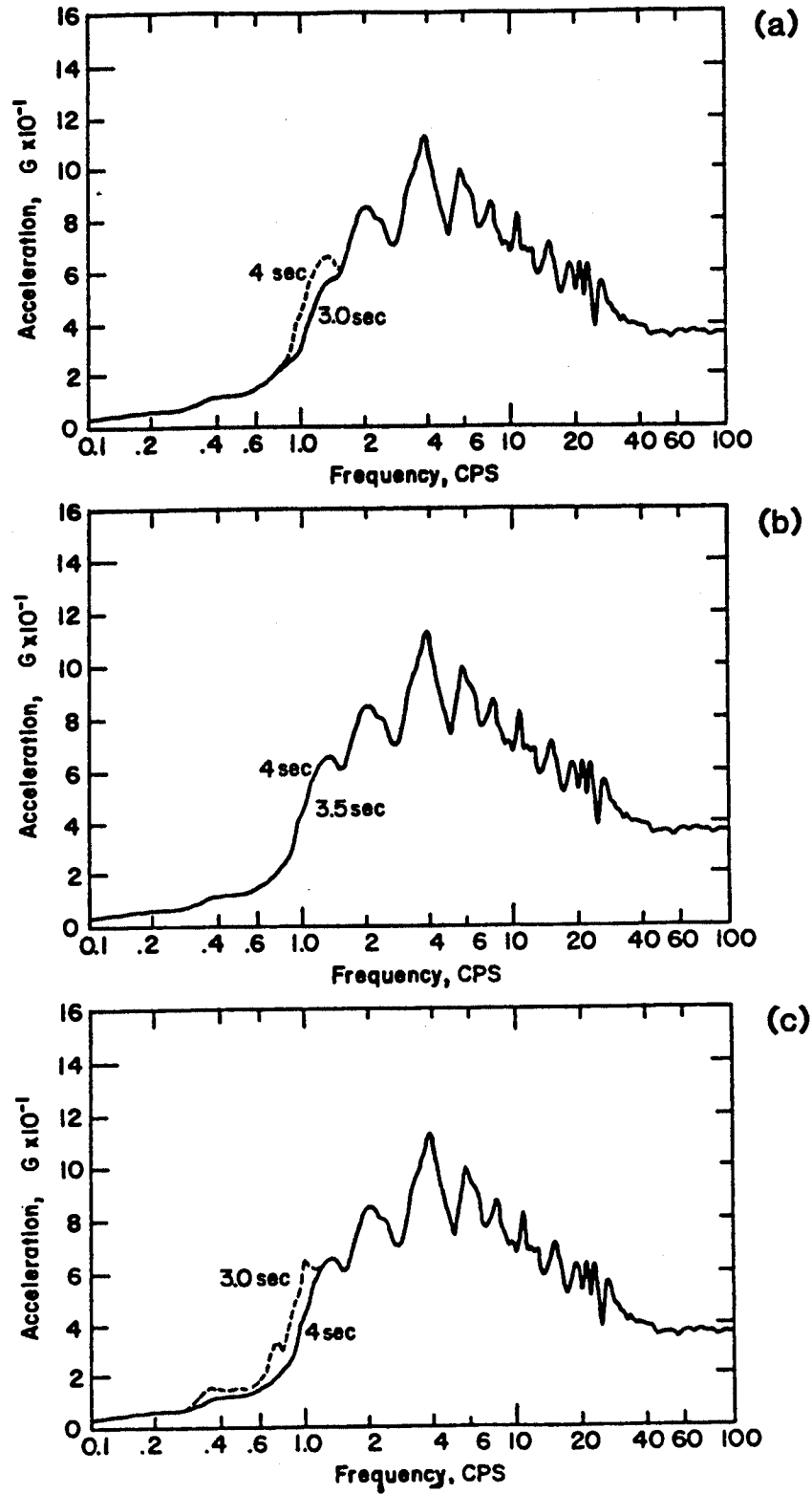
Figure 3.4   Development of Combined El Centro Response
Spectra with Increasing Time up to 4.0 Seconds
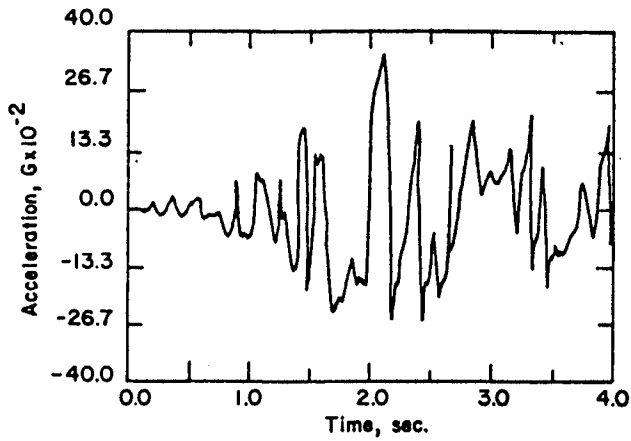
(1) Combined El Centro Time History
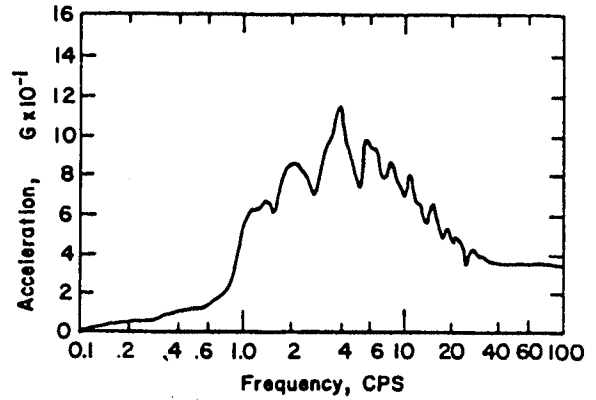
(2) Combined El Centro Response Spectrum
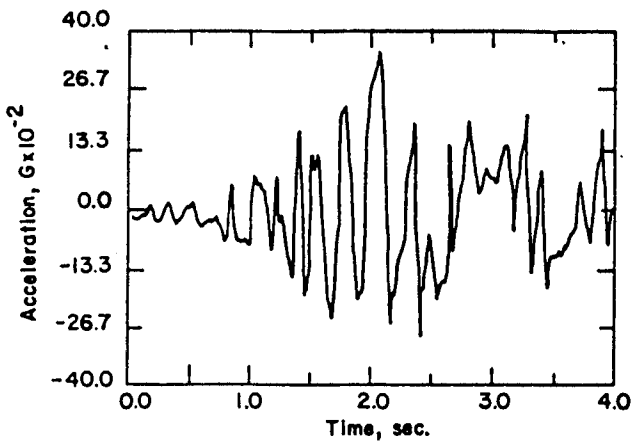
(3) Case II Time History
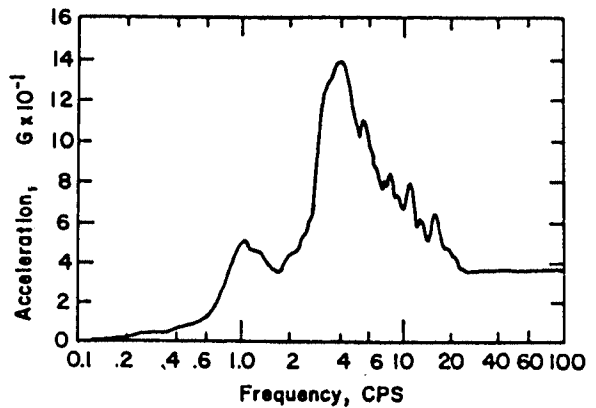
(4) Case II Response Spectrum

Figure 3.5   Effect of Modifying the Combined El Centro Time History Before the Occurrence of the Peak Acceleration
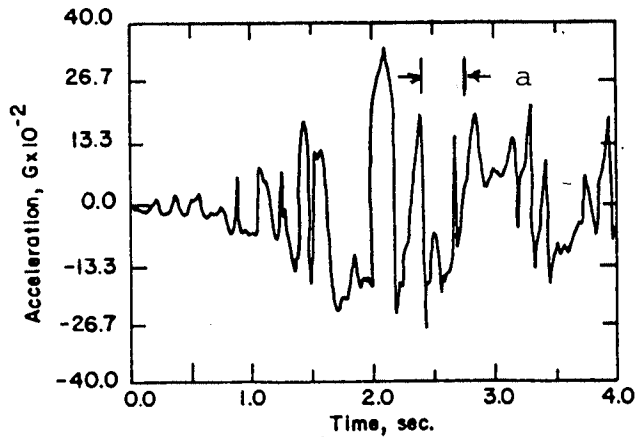
Figure 3.5 — Combined El Centro
(Repeated)   Time History
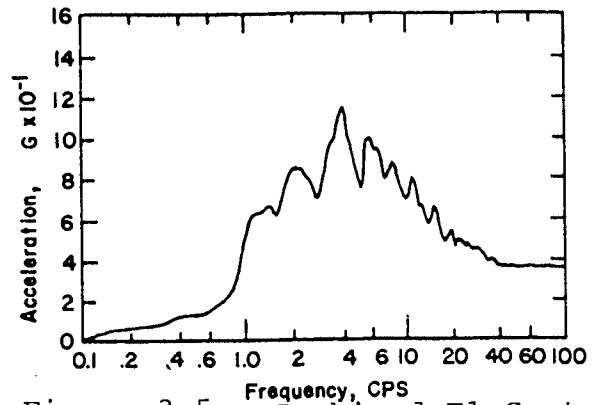
Figure 3.5 — Combined El Centro
(Repeated)   Response Spectrum
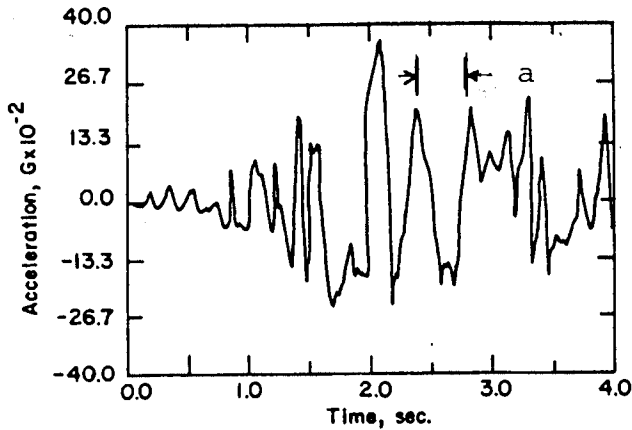
(1) Case III Time History
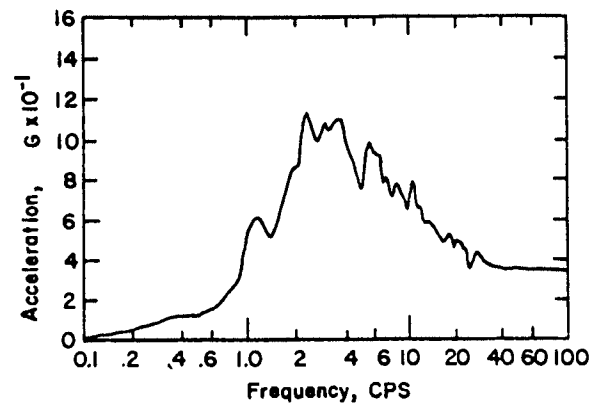
(2) Case III Response Spectrum
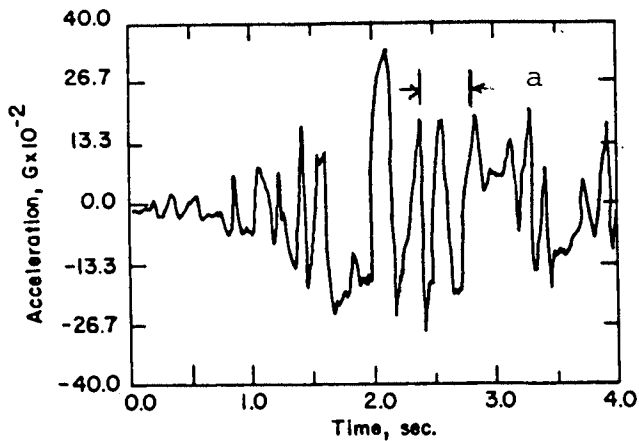
(3) Case IV Time History
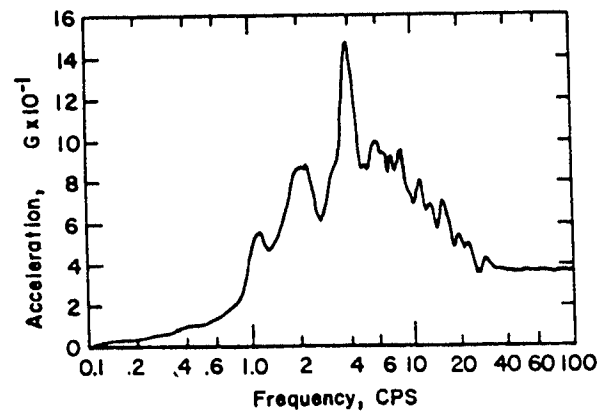
(4) Case IV Response Spectrum

Figure 3.6   Effect of Modifying the Combined El Centro Time History
After the Occurrence of the Peak Acceleration
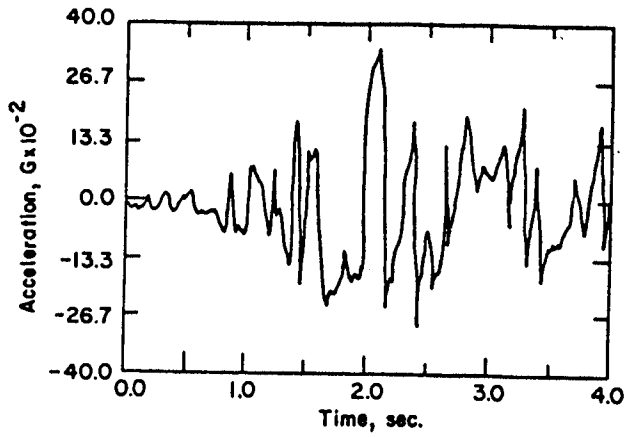
Figure 3.5 - Combined El Centro
(Repeated)   Time History
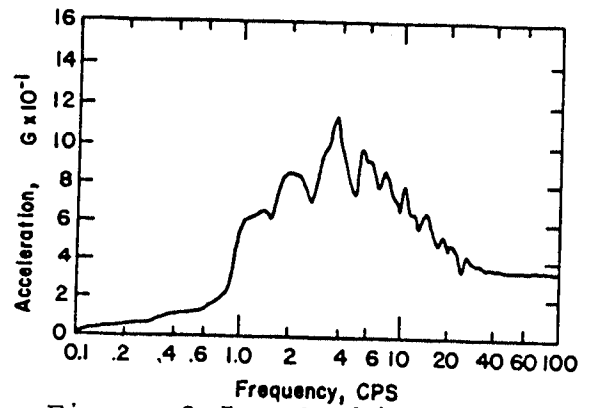
Figure 3.5 - Combined El Centro
(Repeated)   Response Spectrum
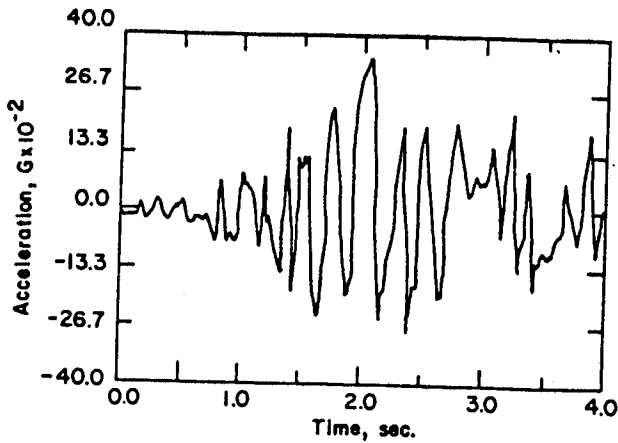
(1) Case **V** Time History

(Combination of Cases II and IV)
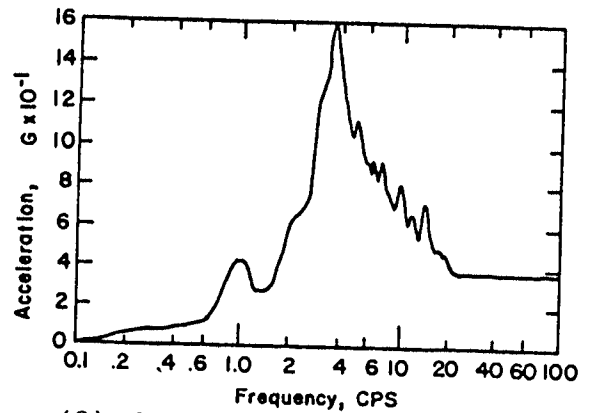
(2) Case **V** Response Spectrum
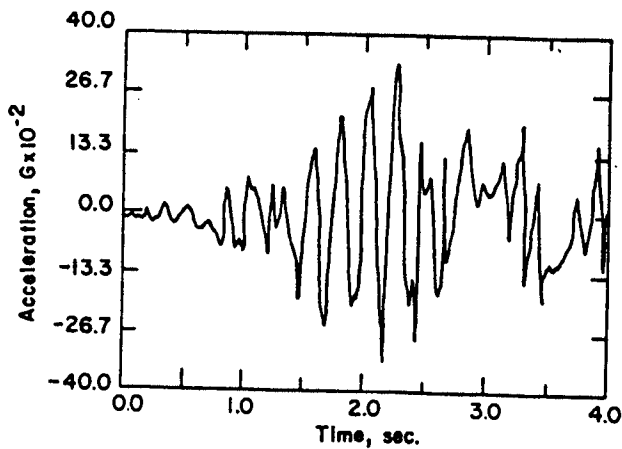
(3) Case VI Time History
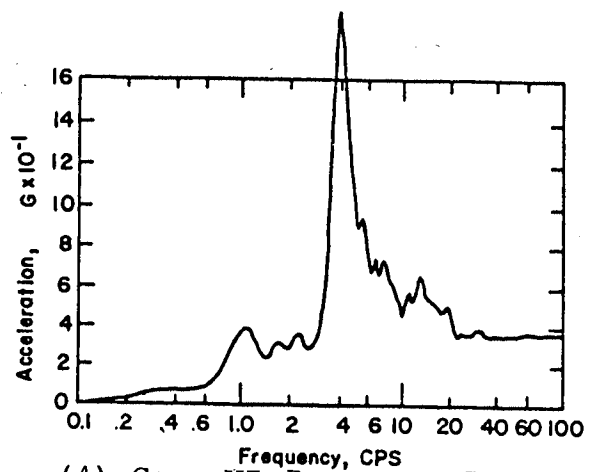
(4) Case VI Response Spectrum

Figure 3.7   Effect of Additional Modification to the Combined
El Centro Time History
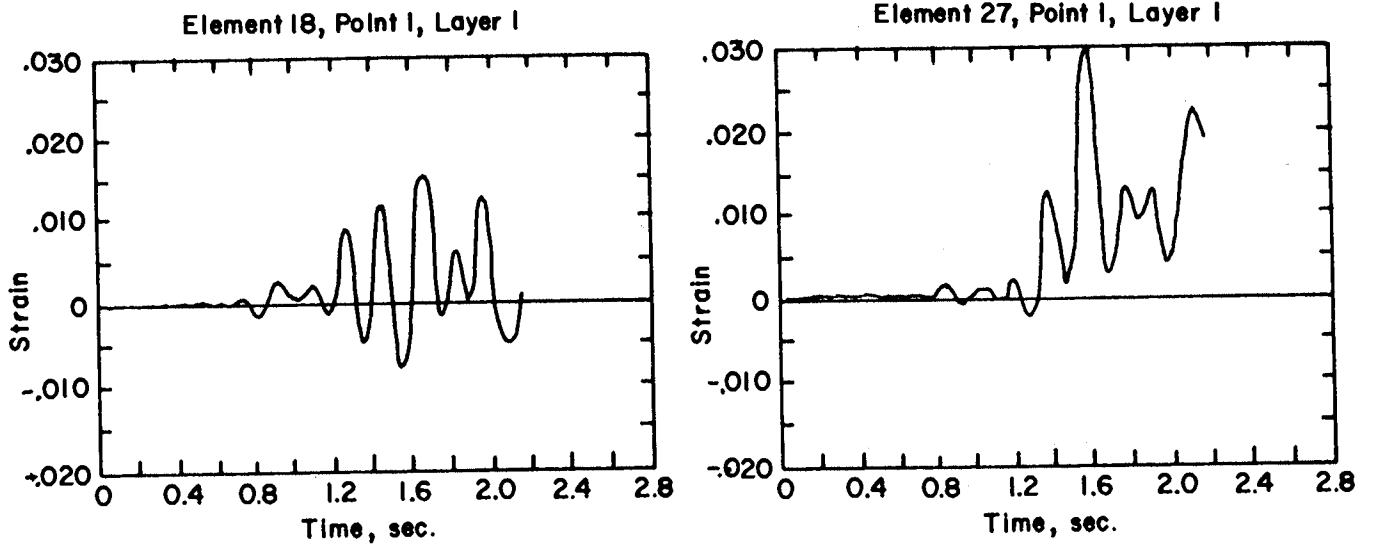
Figure 3.8   Time History of Hoop Strain in the Hot Leg
Elbow
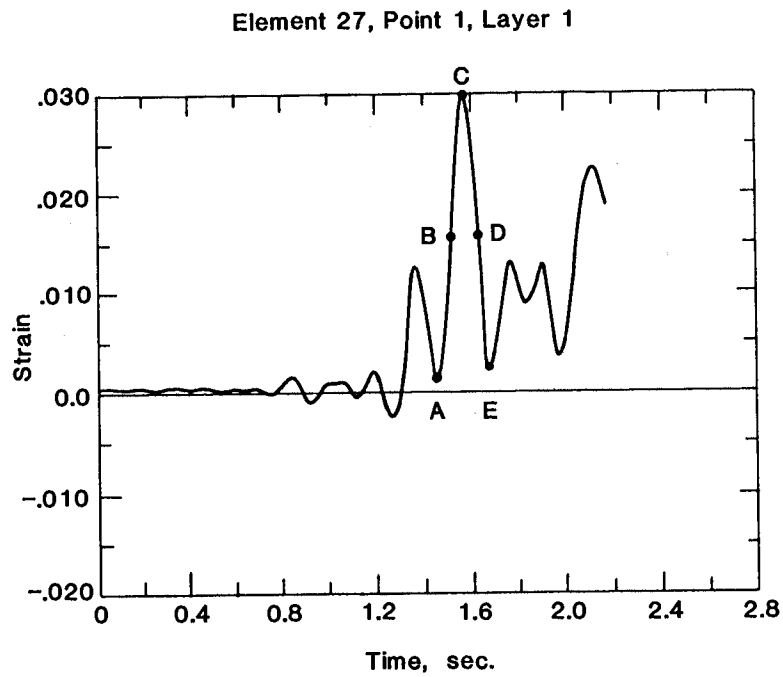
Figure 3.9   Selected Time Points for Evaluating Detuned
Natural Frequency
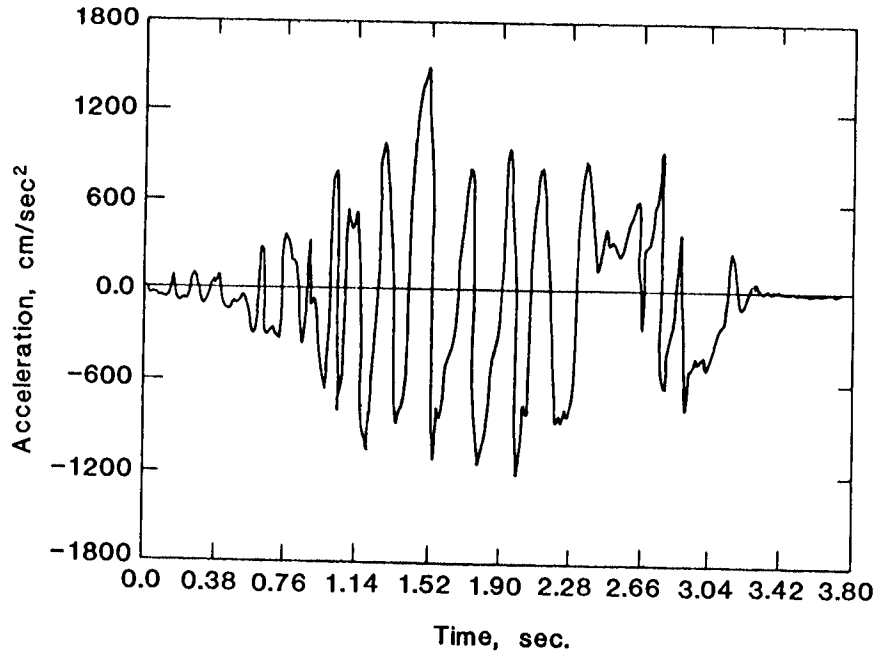
Figure 3.10   Excitation Time History for First Time
Segment of the Elastic-Plastic Analysis
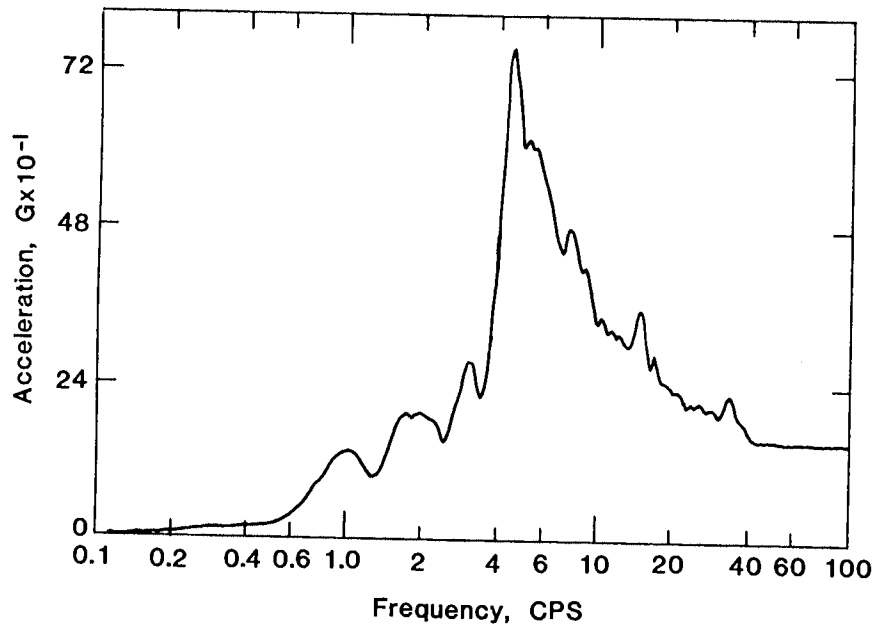
Figure 3.11   Response Spectrum for 5.0 Percent Damping
for Time History in Figure 3.10

3-18
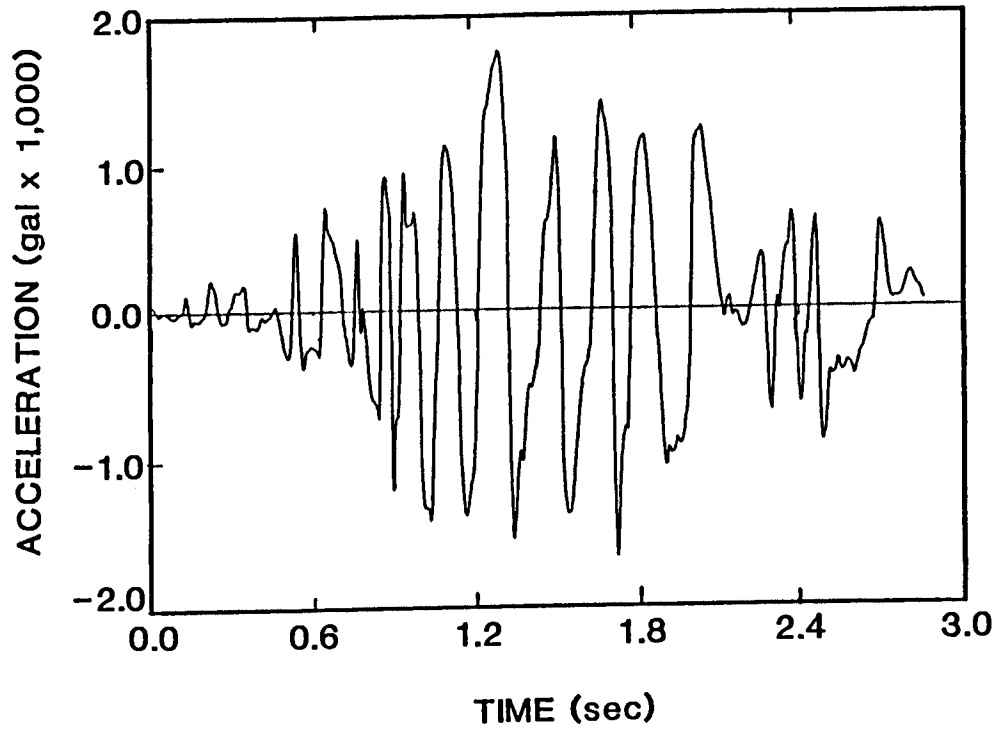
Figure 3.12 – Maximum Plastic Run (MPR) Time History –
Segment A
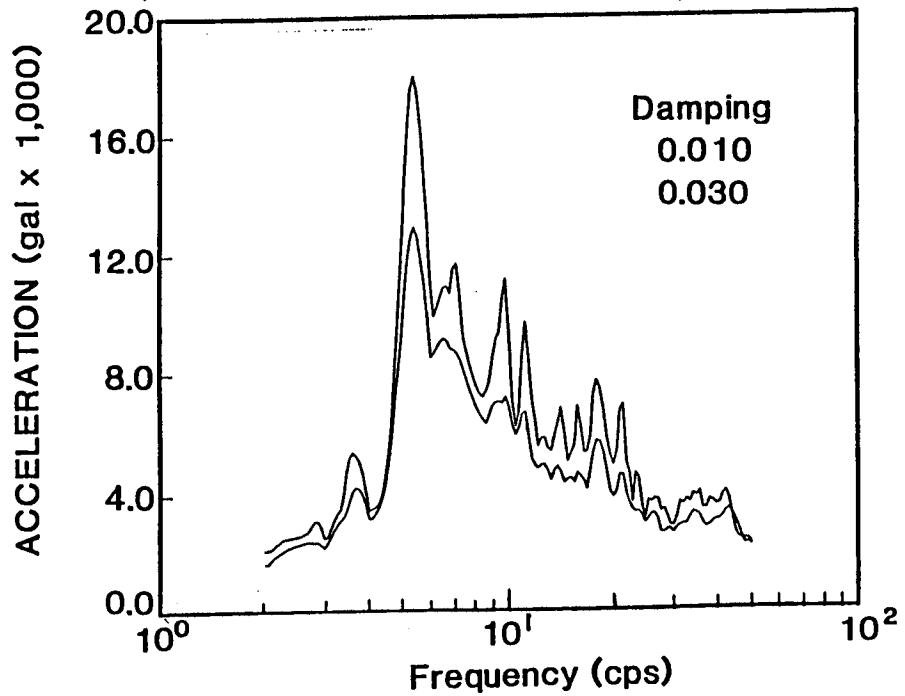
Figure 3.13   Response Spectra for MPR Time History –
Segment A
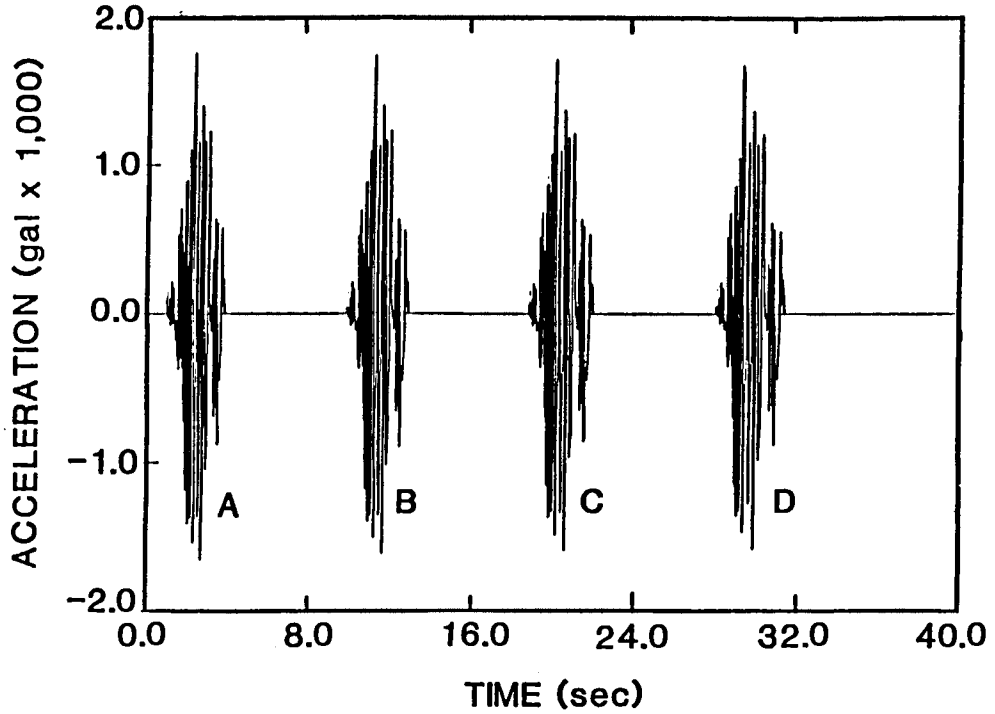
Figure 3.14 - Complete Maximum Plastic Run (MPR) Time History
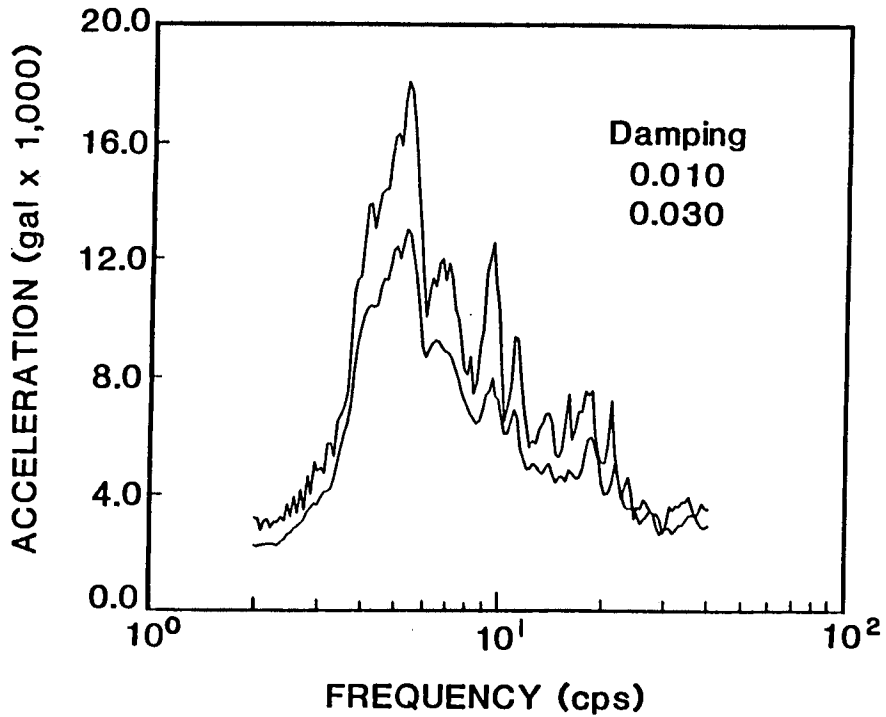
Figure 3.15   Response Spectra for Complete MPR Time History

4.0 PRE-TEST ANALYSIS

Selections had to be made regarding several aspects of the final pre-test analysis. A determination was made of the extent of the modeling detail that could be used to reflect a realistic but yet practical state-of-the-art analysis. At the same time, excitation conditions and dynamic parameters had to be chosen which anticipated some of the important operational characteristics that would affect the response when the test system was driven to failure at the maximum table capacity. Furthermore, maximizing the response required using the highest peak acceleration magnitude that the machine could produce. But the magnitude of the time history was dependent on where the frequency of the largest peak on the response spectra was located, and this could be determined only after the best estimate of the analytical natural frequency was computed.

This section discusses the details of the selections that were made, the final adjustments that were done to the excitation time history, the pre-test responses and failure predictions and comparisons of these predictions with some actual measurements obtained from the test results. The computer codes used in the analysis are the well-known codes such as MARC, ANSYS and ABAQUS.

4.1 Analysis Model Development

Various choices are available for finite element modeling and dynamic response analysis of complex systems. The libraries of different computer codes contain different elements which may be used to describe the HLVT test model. During the pre-test analysis some of these modeling choices were studied to examine the differences that would result in the computed elastic-plastic responses. Two different computer codes were used. These were MARC and a much simpler ANSYS model.

4.1.1 Description of Test Modeling

In Section 3, it was shown in a preliminary analysis that approximately 3% strain could be achieved with the selected time history applied at the maximum table capacity. For the final pre-test analysis, the finite element modeling was done in greater detail. The purpose was to generally improve the quality of the computations, to more accurately reflect the as-built character-istics of the system and to more closely identify the location of the maximum strain.

The modeling was refined at the hot leg elbow and at the support points of the steam generator and the reactor coolant pump. The number of elbow elements was increased by dividing it up into five axial sections, instead of the three that were previously used.

In addition, many more nodes and elements were used to describe the connection between the pin-type support and the lugs at the end of the structural support arms and the steam generator. Similarly, the connections between the reactor coolant pump and the three column support structure were modeled with more detail. The finite element description of the entire structural system designated as the MARC Elbow Model is shown in Figures 4.1(1) through 4.1(5).

The piping finite element modeling was also improved, as seen in Figure 4.1(3). Notice that an additional short element was placed at the location of the welded connection between the members. This was done to permit the identification of a junction where the material was different from the main body of the piping or elbow.

The element properties and corresponding material properties that were used with the MARC Elbow Model are listed in Table 4.1(1) and Table 4.1(2), respectively. The stress-strain relationships that were used in the elastic plastic analysis are shown in Figure 4.2.

4.1.2 ANSYS Model

The ANSYS Model uses simpler elements for both the elbow and the straight pipe parts. The pipe element approximately evaluates the average strain of the pipe cross section at eight points along the middle circle of the pipe shell thickness. The hoop strain is considered only as an equivalent static component (i.e. pressure is assumed as a constant load acting on the pipe without affecting its stiffness). Therefore, such effects as ovalization and strain distribution through the pipe thickness are not fully considered in the ANSYS analysis. But the non-linear analysis using ANSYS uses much less computer time than the same type of analysis using the highly detailed modeling with MARC. It was thought useful to compare the results with both computer codes.

4.1.3 Effect of Steam Generator Support Pad Modeling

The steam generator shell was supported on four support pads around its circumference. The structural connection at the support pad is neither fixed nor pinned. As the test progressed, the support in this region was drastically changed to a solid welded structure. A study was made of the effect of this stiffness change on the computed structural characteristics and on the responses. ANSYS was used in this analysis with the pads considered fixed (Run B) or with the pads free (Run B*).

The results of the computed natural frequencies for the first three modes are shown in Table 4.2. The response deflections and forces at the steam generator pads and the steam generator supporting pin are listed in Table 4.3. As is seen from the table, the differences in these responses are negligible.

4.1.4 Effect of Rolling Motion

An analysis was made of the effect of a small amount of rolling motion on the response of the system. This was designated as MARC run C*. The rolling motion was taken as a linear input of 4% of the X axis excitation. It was applied vertically at a distance along the Y axis of 630mm. This is shown in Figure 4.3.

The results were compared with the comparable MARC Run C which was done without the rolling motion. Table 4.4 gives a summary of the inelastic analysis results both with and without rolling motion. The effects of the rolling action is seen to be negligible and was therefore not further considered in either the pre-test or the post-test analyses.

4.1.5 Pre-Test Damping in Elastic Range

The preliminary pre-test analysis used a damping ratio of 3% for responses in the elastic range. The test measured the damping ratio as 0.86. Comparative computer runs were made with different damping values at an excitation level of 0.1 MPR. The results in Table 4.5 show an improved analytical prediction for run B where the damping ratio was closer to the measured value.

4.1.6 Selection of Time Scaling

The program was intended to maximize the response and to shorten the time to produce a failure. For a linear system, the maximum response is obtained when the response spectra peaks at the value of the natural frequency. But slightly different system characteristics are obtained from different analytical finite element solutions. Table 4.6 shows the first five natural frequencies as obtained by three different computer codes with the as-built finite element modeling. The maximum difference in the second mode is about 5%. This value exceeds the bandwidth ratio since the transfer function of the model with 0.8 percent damping is very narrow. Therefore, peak tuning could be done with only one model, the others would be somewhat detuned.

Because of the computational differences, and anticipating some detuning under the plastic response, it was decided to time shift the excitation so that the response spectra peak occurred at a frequency that was lower than the second mode natural frequency.

An analysis was made of the elastic-plastic responses that would result if three different ratios of RS peak frequency to second mode natural frequency were used. The ratios selected were 0.95, 0.90 and 0.80, on the basis of the SAP-5 calculation. Figure 4.4 shows the relative location of the three different runs, designated as A, B and C, with regard to the RS peak.

To take advantage of the vibration table capacity, the maximum value of the acceleration was changed, in accordance with the limiting displacement or velocity magnitude. Table 4.7(1) shows the input time history characteristics that were used for each of the three runs. Table 4.7(2) shows that the maximum displacement is attained in Run B when ANSYS was used and in Run C in the MARC analysis. However, the maximum axial strain response was obtained in Run A in MARC but in Run B in ANSYS. The hoop strain is also maximum in MARC. From these results, it was decided to use the tuning in Run B for all other studies and for the test time history.

4.1.7 Final Pre-Test Excitation Time History

The time history was further base-line adjusted to permit increasing the acceleration level without exceeding the limiting vibration table velocity or displacement characteristics. The final excitation time history that was used in the pre-test analysis (MARC Run D) is shown in Figure 4.5. The corresponding input velocity and displacement time histories are also shown in Figure 4.5. Figures 4.6(1) and 4.6(2) show the Response Spectrum and the Fourier Spectrum, respectively.

4.2 Pre-Test Responses

4.2.1 Pre-Test Response Predictions

The improved damping ratio and the selected time scaling were used in a series of computer runs carried out at excitation levels which produced piping strains in the plastic region. These were done at 0.4 MPR, 0.7 MPR, and 1.0 MPR. Table 4.8 shows a comparison of the pre-test predictions of the maximum strain with the corresponding test results.

Response time histories of some of the response motions and element strains for an excitation of 1.0 MPR (MARC Run D) are shown in Figures 4.7 through 4.13. The maximum responses are listed in Table 4.9. A maximum axial strain of 3.6 percent was predicted to occur at element 8 Point 3, ϵ_2 (see Figure 4.1(5)). This is the junction of the hot leg and the hot leg elbow. The location ϵ_2 signifies that the strain occurs at the top of the pipe.

4.2.2 Comparisons of Pre-Test Predictions with Test Measurements

The analytical predictions of the maximum displacement at the top of the steam generator for three different test run levels are shown in Figure 4.14. These results compare well with the test measurements which are also plotted in the same figure. Figure 4.14 compares the test and analysis results for the acceleration at the top of the steam generator. The analysis matches the test results for the test run prior to some modifications that were made to the steam generator support. After the modifications, the difference between the measured accelerations and the predicted accelerations increased.

A comparison of test and the pre-test MARC analysis results from Table 4.8 show that for all three run levels, the axial strains measured at the reactor vessel end were much higher than the analytical predictions. At the tapered transition joint the measured axial strains were also higher than the analysis results for the lower test level; however, the trend reversed for the higher test levels. For the hot leg elbow the axial strains measured during all test levels were much lower than analytical predictions. The differences were even greater for the hoop strains.

The maximum axial strain in these computer runs was 3.56% at strain gage 153X. This compares with the measured value of 2.28%. As noted in the table, this strain gage was damaged after the first portion of the excitation and so the value of 2.28% was deduced from the readings of other undamaged gages in this vicinity.

Based on the pre-test analysis results, the maximum axial strain (3.6%) was predicted to occur at the top of the hot leg pipe in the vicinity of the tapered transition joint with the hot leg elbow. In addition, a hoop strain of approximately 3% was predicted to occur at the top of the hot leg elbow on its inside surface near the middle of its arc. The analysis also indicated the possibility of significant hoop strain ratchetting in the hot leg elbow.

4.3 Pre-Test Fatigue Predictions

A ratchet-fatigue life analysis was performed prior to the test using the analysis results from Section 4.2.2 and the procedures outlined in NUREG/CR-5023 (Severud et al, 1988).

For this analysis, the increment of irrevocable yield per cycle is given by

$$\epsilon_R = \{3\sigma_y/(2\sigma_y - \sigma_H)\} \{\Delta\epsilon_t - (2\sigma_y - \sigma_H)/E\}$$

which becomes, for our case

$$\epsilon_R = 0.74 [\Delta\epsilon_t - 0.161] \qquad (1)$$

The ratchet-fatigue interaction effect is given by

$$N_{RF} = \left[\frac{(C - \epsilon_R N)}{\Delta\epsilon_p}\right]^2$$

where C is the effective fatigue ductility which is empirically derived, N is the number of cycles of effective strain range and $\Delta\epsilon_p$ is the plastic strain range which is the difference between the total strain range and the elastic range.

For our case, the ratchet-fatigue interaction equation becomes

$$N_{RF} = [(46 - \epsilon_R(\%)N)/(\Delta\epsilon_t(\%) - 0.1)]^2 \qquad (2)$$

Using equations (1) and (2), Table 4.10 shows the estimate of the ratchet-fatigue life. Ductility exhaustion occurs when $\sum N/N_{RF} = 1.0$.

The axial strain range in the hot leg pipe in the vicinity of the tapered transition joint was predicted to be between 5 to 7% with three cycles per segment when the excitation was at the 1.0 MPR level. This is shown by MARC Run D, in Figure 4.15(b). These strain ranges, coupled with estimates from earlier lower level runs, resulted in a prediction that a ratchet/fatigue failure could occur as early as the first run with the full four segment MPR time history. If ratchetting did not occur, but the same strain levels were achieved, it was predicted that a fatigue failure might occur after 5 to 6 MPR runs or longer. Recognizing the uncertainties in the above predictions, a ratchet/fatigue failure between the first and fifth MPR runs was considered to be within the realm of possibility if the predicted strains were achieved.

The above analytical predictions were made by BNL. Pre-test predictions were also performed by Westinghouse Hanford Company (Severud and Weiner, 1987) and Rockwell International (Jaquay and Larson, 1988) which are briefly summarized below.

Westinghouse Hanford utilized simplified elastic and inelastic analyses and concluded that the maximum axial strain range could be up to 4%. This estimate was based on an earlier version of the input wave which had a peak acceleration of 1.54g (1509 gal). Based on this work and updated pre-test analysis information

provided by BNL, they concluded that cracking and leaks in the piping were likely to occur during the first, second or third MPR run. Their best estimate was that cracking would occur during the second MPR run. These predictions were based on the assumption that the test would induce axial strain ranges in the 3 to 7% range.

Rockwell performed their pre-test predictions for EPRI based on analyses with the ABAQUS Code. They performed analyses up to the peak acceleration of the MPR time history. Based on these results, they estimated that each segment of loading at the MPR level would result in an accumulated hoop strain of 3 % with axial strain ranges from 2 to 7 %. Considering uncertainties of material properties, their time of failure prediction was between the fourth segment of the first MPR run to the second segment of the third MPR run. Their best estimate was that a ratchet/fatigue failure of the hot leg elbow would occur on the top side near its attachment weld to the hot leg straight pipe during the third segment of the second MPR run.

The actual test run sequence used during the test differed somewhat from the sequence used for the pre-test predictions. However, a crack did occur in the test model during the second full four segment run at the MPR level. Based on a review of the strain gage data in the region of the crack, it appears that the crack developed during the first segment of this run. Furthermore, the crack developed at the exact location as predicted in the above analyses. On the other hand, the axial strain ranges measured during the test were not as high as the pre-test analysis predictions. In addition, the large hoop strain ratchetting that was included in the calculations to predict the ratchet/fatigue life did not occur. Prior to the initiation of the crack, some bulging of the hot leg pipe at approximately one half to one diameter from the attachment weld to the hot leg elbow did occur. The possibility of such bulging was noted by P. Ibanez of ANCO Engineers, Incorporated who participated in a review of the final test plan.

Table 4.1 (1) MARC Elbow Model - Element Properties

ELEMENT No.	MATERIAL	EL. TYPE	P1*	P2*	P3*
1	E1	Pipe	10	20	
2	P1	Pipe	2.91	16.22	
3	P2	Pipe	2.91	16.22	
4-8	P3	Pipe	2.91	16.22	
9,20	P3	Shell	4.43		
10,19	P3	Shell	4.32		
11,18	P3	Shell	4.075		
12,17	P3	Shell	4.07		
13,16	P3	Shell	3.64		
14,15	P3	Shell	3.46		
21,32,33,44	P3	Shell	4.45		
22,31,34,43	P3	Shell	4.29		
23,30,35,42	P3	Shell	4.03		
24,29,36,41	P3	Shell	4.03		
25,28,37,40	P3	Shell	3.70		
26,27,38,39	P3	Shell	3.445		
45,56,57,68	P3	Shell	4.470		
46,55,58,67	P3	Shell	4.26		
47,54,59,66	P3	Shell	3.99		
48,53,60,65	P3	Shell	3.99		
49,52,61,64	P3	Shell	3.75		
50,51,62,63	P3	Shell	3.43		

*NOTE: Shell P1 = thickness (cm)
        Pipe   P1 = thickness (cm), P2 = middle radius (cm)
        Truss P1 = area, $A(cm^2)$
        Beam   P1 = $A(cm^2)$, P2 = $Ix(cm^4)$, P3 = $Iy(cm^4)$

Table 4.1 (1) MARC Elbow Model – Element Properties
(Continued)

ELEMENT No.	MATERIAL	EL. TYPE	P1*	P2*	P3*
69	P3	Pipe	3.98	17.32	
70	P4	Pipe	3.98	17.32	
71	P5	Pipe	4.02	17.79	
72,73,158	E1	Pipe	10.0	40.0	
185-200	E1	Pipe	10.0	40.0	
208-213	E1	Pipe	10.0	40.0	
75,86,87,98	P3	Shell	4.25		
76,85,88,97	P3	Shell	4.113		
77,84,89,96	P3	Shell	3.971		
78,83,90,95	P3	Shell	3.83		
79,82,91,94	P3	Shell	3.691		
80,81,92,93	P3	Shell	3.55		
103,114,115,126	P3	Shell	4.25		
131,142,143,154	P3	Shell	4.25		
104,113,116,125	P3	Shell	4.113		
132,141,144,153	P3	Shell	4.113		
105,112,117,124	P3	Shell	3.971		
133,140,145,152	P3	Shell	3.971		
106,111,118,123	P3	Shell	3.83		
134,139,146,151	P3	Shell	3.83		
107,110,119,122	P3	Shell	3.691		
135,138,147,150	P3	Shell	3.691		

*NOTE: Shell   P1 = thickness (cm)
        Pipe   P1 = thickness (cm), P2 = middle radius (cm)
        Truss   P1 = area, A(cm^2)
        Beam   P1 = A(cm^2), P2 = Ix(cm^4), P3 = Iy(cm^4)

Table 4.1 (1)   MARC Elbow Model — Element Properties
(Continued)

ELEMENT No.	MATERIAL	EL. TYPE	P1*	P2*	P3*
108,109,120,121	P3	Shell	3.55		
136,137,148,149	P3	Shell	3.55		
74,99-102	P3	Pipe	3.11	17.30	
127-130,155	P3	Pipe	3.11	17.30	
156	P5	Pipe	5.0	18.86	
159,160	P3	Pipe	2.75	15.345	
161,172,173,184	P3	Shell	3.895		
162,171,174,183	P3	Shell	3.768		
163,170,175,182	P3	Shell	3.642		
164,169,176,181	P3	Shell	3.515		
165,168,177,180	P3	Shell	3.388		
166,167,178,179	P3	Shell	3.26		
201-205	P5	Pipe	4.0	67.25	
157,206,207	P5	Pipe	6.86	32.01	
214-216	P5	Pipe	40.	43.6	
217-222	P5	Pipe	4.0	38.15	
223,226,229,232	E2	Beam	493.8	4.623 E+4	2.257 E+4
224,227,230,233	E2	Beam	413.0	4.488 E+4	4.553 E+4
225,228,231	E2	Beam	820.0	8.193 E+4	2.476 E+5
234-238	E2	Beam	820.0	8.193 E+4	2.476 E+5
239,242	E2	Beam	710.0	2.11 E+5	6.84 E+4
240,241	E2	Beam	720.0	4.755 E+5	9.6 E+4

*NOTE: Shell   P1 = thickness (cm)
         Pipe   P1 = thickness (cm), P2 = middle radius (cm)
         Truss   P1 = area, $A(cm^2)$
         Beam   P1 = $A(cm^2)$, P2 = $Ix(cm^4)$, P3 = $Iy(cm^4)$

Table 4.1 (1) MARC Elbow Model - Element Properties
(Continued)

ELEMENT No.	MATERIAL	EL. TYPE	P1*	P2*	P3*
243,245,246	P5	Beam	115.0	0.214 E+4	0.199 E+4
248,249,251	P5	Beam	115.0	0.214 E+4	0.199 E+4
244,247,250	P5	Beam	61.89	1.207 E+3	1.207 E+3
252	E3	Beam	38.4	205.0	73.7
253	E2	Beam	345.6	0.664 E+5	0.867 E+4
254-259	E2	Beam	300.0	1.0 E+4	0.01
260-261	E4	Truss	1.77 E+7		

*NOTE: Shell   P1 = thickness (cm)
         Pipe   P1 = thickness (cm), P2 = middle radius (cm)
         Truss   P1 = area, A(cm^2)
         Beam   P1 = A(cm^2), P2 = Ix(cm^4), P3 = Iy(cm^4)

Table 4.1 (2) MARC MODEL – Material Properties

MATERIAL NO.	TYPE	$E(kg/cm^2)$		$FY(kg/cm^2)$
E1	Elastic	1.0 E+7	-0.4	—
E2	Elastic	2.1 E+6	0.3	—
E3	Elastic	2.07 E+6	0.3	—
E4	Elastic	1.0	0.3	—
P1	Bilinear	1.96 E+6	0.3	4900
P2	Multilinear	1.99 E+6	0.3	(see Figure 4.2a)
P3	Multilinear	1.99 E+6	0.3	(see Figure 4.2b)
P4	Multilinear	1.99 E+6	0.3	(see Figure 4.2c)
P5	Bilinear	1.96 E+6	0.3	3620

Table 4.2   ANSYS Model Frequencies (HZ)

MODE	SG PAD FIXED	SG PAD PINNED
1	4.269	4.265
2	6.208	6.175
3	26.45	25.96

Table 4.3   Summary of Inelastic Analysis Results with SG Pad Supports Fixed and Pinned (Displacement-cm, Force-kg, Moment-kg-cm)

	ANSYS RUN B SG PAD SUPPORT FIXED	ANSYS RUN B* SG PAD SUPPORT PINNED
RELATIVE DISPLACEMENT TOP OF STEAM GENERATOR		
Ux	6.41	6.40
Uy	.45	.47
FORCE ON SG PIN SUPPORT		
Fx	187,900	182,700
Fy	6,644	6,800
Fz	70,840	71,000
Mx	1,218,000	1,266,000
My	0	0
Mz	1,570,000	1,520,000

Table 4.4 Summary of Inelastic Analysis Results
With and Without Rolling Motion
(Displacement-cm, Force-kg, Moment-kg-cm)

	MARC RUN C WITHOUT ROLLING MOTION	MARC RUN C* WITH ROLLING MOTION

RELATIVE DISPLACEMENT TOP OF STEAM GENERATOR

Ux	7.31	7.32
Uy	.57	(1.07) Absolute Value

FORCE ON SG PIN SUPPORT

Fx	210,000	210,000
Fy	8,620	10,200
Fz	72,300	76,900
Mx	1,480,000	2,140,000
My	0	0
Mz	1,260,000	1,360,000

Table 4.5   Comparison of Pre-Test MARC Analysis with Test

	TEST	RUN-A	RUN-B	RUN-C
SG				
Ux(cm)	0.95	0.73	0.81	0.81
Uy(cm)	0.14	0.08	0.06	0.10
Ax(gal)	1630	1130	1280	1280
Ay(gal)	212	71	55	55
PIN				
Fx(ton)	7.0	30	31.7	31.8
Mx(ton-m)	0.16	1.7	2.3	4.0
RCP				
Ux(cm)	0.021	0.017	0.021	0.02
Ax(gal)	395	220	195	195
SNUBBERS				
83x(ton)	2.66	1.9	2.0	1.9
84x(ton)	1.15	0.9	0.8	1.1
H.L.Strain(%)				
135x	0.08	0.053	0.06	0.06
153x	0.15	0.052	0.062	0.062
207x	0.10	0.033	0.042	0.042
207y	0.06	0.087	0.079	0.08

TEST: 0.1 MPR Test

A: Pre-Test Analysis (h = 3%)

B: h = 0.8%

C: h = 0.6%

Table 4.6 Natural Frequencies Obtained by Three Different Computer Codes

NATURAL FREQUENCIES (HZ)

MODE	SAP	MARC	ANSYS
1	4.2	4.63	4.27
2	6.09	6.44	6.21
3	23.24	28.45	26.45
4	29.86	31.17	29.91
5	31.49	35.00	31.49

Table 4.7 (1)   Summary of Input with Three Different Time Scalings

	INPUT TIME HISTORY				RESPONSE	
	MAX ACCEL cm/sec^2	MAX VEL cm/sec	MAX DISP cm	DURATION sec	MAX SPECTRAL ACCEL AT 1% DAMP cm/sec^2	FREQUENCY cps
MARC RUN A	1520.7	76.9	20.6	3.120	15700.	4.8
MARC RUN B	1707.8	70.1	7.45	2.770	17600.	5.5
MARC RUN C	1959.0	75.0	7.43	2.574	20066.	5.9
ANSYS RUN A	1463.4	75.0	18.9	3.24	14910.	4.8
ANSYS RUN B	1781.5	76.0	15.38	2.64	18151.	5.8
ANSYS RUN C	1908.8	76.0	15.86	2.5	19500.	6.2

NOTE: The time histories used for ANSYS RUN A, B and C are based
on the same time history used for MARC RUN A; however the
time step and magnification factor for each time history
were changed. For MARC RUN B, a different time history was
used which has a smaller displacement but an identical
response spectrum shape.   MARC RUN C used the same time
history as MARC RUN B but used a different time step and
magnification factor.

Table 4.7 (2) Summary of Inelastic Analysis Results
(Displacement-cm, Force-kg, Moment-kg-cm)

	MARC			ANSYS		
	RUN A	RUN B	RUN C	RUN A	RUN B	RUN C

RELATIVE DISPLACEMENT TOP OF STEAM GENERATOR

Ux	6.53	6.80	7.31	6.15	6.41	5.98
Uy	0.70	.53	.57	.745	.45	.54

SUMMARY OF INELASTIC ANALYSIS RESULTS

MAXIMUM AXIAL STRAIN (%)

MARC RUN A - Element 8, Point 3, ϵ_2 - 4.112
MARC RUN B - Element 8, Point 3, ϵ_2 - 3.441
MARC RUN C - Element 8, Point 3, ϵ_2 - 3.300
ANSYS RUN A - Element 7, Point 2* - 1.01
ANSYS RUN B - Element 7, Point 2* - 1.01
ANSYS RUN C - ELement 7, Point 2* - 0.94

MAXIMUM HOOP STRAIN (INSIDE) (%)

MARC RUN A - Element 32, Point 3 - 2.508
MARC RUN B - Element 32, Point 3 - 2.910
MARC RUN C - Element 32, Point 3 - 2.899
ANSYS RUN A - Element 8, Point 3* - 0.674
ANSYS RUN B - NOT CALCULATED

*ANSYS Element 7, Point 2 Close to MARC Element 8, Point 2, ϵ_3
 ANSYS Element 8, Point 3 Close to MARC Element 19, Point 2

NOTE: The difference in the maximum strain values between the MARC and ANSYS analyses may be attributed primarily to the difference in elements used in each analysis. In the MARC analysis, a general 3-D shell element is used for the elbow part, and a 3-D beam element for the straight part. In the ANSYS analysis, a much simpler element is used for both the elbow and straight parts. This element approximately evaluates the average strain of a pipe section at eight points along the middle circle of the pipe shell thickness, and the hoop strain is considered only as an equivalent static component (i.e., pressure is assumed as a constant load acting on the pipe without affecting its stiffness). Therefore, effects such as ovalization and strain distribution through the pipe thickness are not fully considered in the ANSYS analysis.

Table 4.8 Comparison of Strain (%) Along Hot Leg Pipe for Three Test Levels
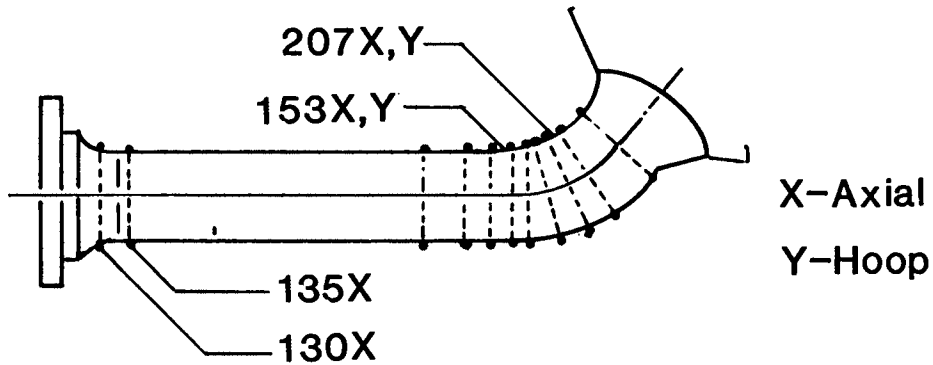
GENERAL LOCATION	STRAIN GAGE NO.	.4MPR(4/19/88)		.7MPR(4/20/88)		1.0MPR(4/22/88)	
		TEST	MARC	TEST	MARC	TEST	MARC
RV Nozzle	130X	0.34	0.18	0.45	0.20	0.55	0.21
Hot-Leg Near RV Nozzle	135X	0.34	0.23	0.79	0.47	1.18	0.73
Tapered Trans-istion Joint	153X	0.83	0.52	1.35$^{(2)}$	2.31	2.28$^{(1)}$	3.56
	153Y	0.16	–	0.19$^{(2)}$	–	0.34	–
Hot-Leg Elbow	207X	0.39	0.46	0.57	1.12	0.83	1.54
	207Y	0.24	0.86	0.32	1.80	0.41	2.32

Notes: 1. Strain Gages 153X and 153Y were damaged after recording Segment A of 1.0MPR Test of 4/22/88.

2. Gages 153X and 153Y were damaged. Previous run at this level prior to modification recorded the following strains 135X – 0.49%, 153X – 1.19%, 153Y – 0.25%. For this test clip gage readings are tabulated (46X for 153X and 47Y or 153Y).

Table 4.9   Summary of Results for MARC Run D
(3% Damping)

<u>TOP OF STEAM GENERATOR</u>

Relative Displacement -   Ux   -   7.15
(cm)   Uy   -   0.56

Acceleration   -   Ax   -   6356
(gal)   Ay   -   476

<u>MAXIMUM AXIAL STRAIN (%) IN HOT-LEG PIPE</u>

Element 8, Point 3, ϵ_2 -   3.557
Element 8, Point 1, ϵ_2 -   3.370

<u>MAXIMUM STRAINS (%) IN HOT-LEG ELBOW</u>

Hoop (Inside)   - Element 32, Point 3   -   3.000
                   Element 20, Point 3   -   2.911

Hoop (Outside)   - Element 32, Point 1   -   2.319
                   Element 21, Point 3   -   2.288

Axial (Inside)   - Element 21, Point 2   -   1.310

Axial (Outside) - Element 31, Point 2   -   1.538
                   Element 19, Point 3   -   1.375

Table 4.10 Ratchet/Fatigue Life of Hot Leg Pipe –
Accounting for Ductility Exhaustion

RUN	$\Delta\epsilon_t\%$	N	$\epsilon_R\%$	$N\epsilon_R$	$\Sigma N\epsilon_R$	N_{RF}	N/N_{RF}	$\Sigma N/N_{RF}$
8+8′	.8	5	.47	2.35	2.35	3888	0	
	.6	5	.32	1.60	3.45	7073	0	
	.7	5	.40	2.00	5.45	4456	0	
9′	3.9	1	2.77	2.77	8.72	96	.01	.01
	2.7	1	1.88	1.88	10.60	185	.005	.015
	3.2	1	2.25	2.25	12.85	114	.009	.024
10′	6.9	1	4.99	4.99	17.84	17	.06	.084
	4.9	1	3.51	3.51	21.35	26	.04	.124
	5.6	1	4.02	4.02	25.37	14	.07	.194
10A	6.9	1	4.99	4.99	30.36	5.3	.19	.384
	4.9	1	3.51	3.51	33.87	6.2	.16	.544
	5.6	1	4.02	4.02	37.89	2.2	.45	.994

NOTES: 1. $\epsilon_R\%$ based on Eq(1) in Section 4.3
2. N_{RF} based on Eq(2) in Section 4.3
3. Strain Ranges ($\Delta\epsilon_t$) for Runs 8+8′ – see Figure 4.15(a)
4. Strain Ranges ($\Delta\epsilon_t$) for Runs 10+10′ – see Figure 4.15(b)
5. Strain Ranges ($\Delta\epsilon_t$) for Runs 9′ based on average of Figures 4.15(a) and 4.15(b)

If strains are achieved and pressure is maintained near 157 kg/cm^2 a ratchet/fatigue could occur during Run 10.
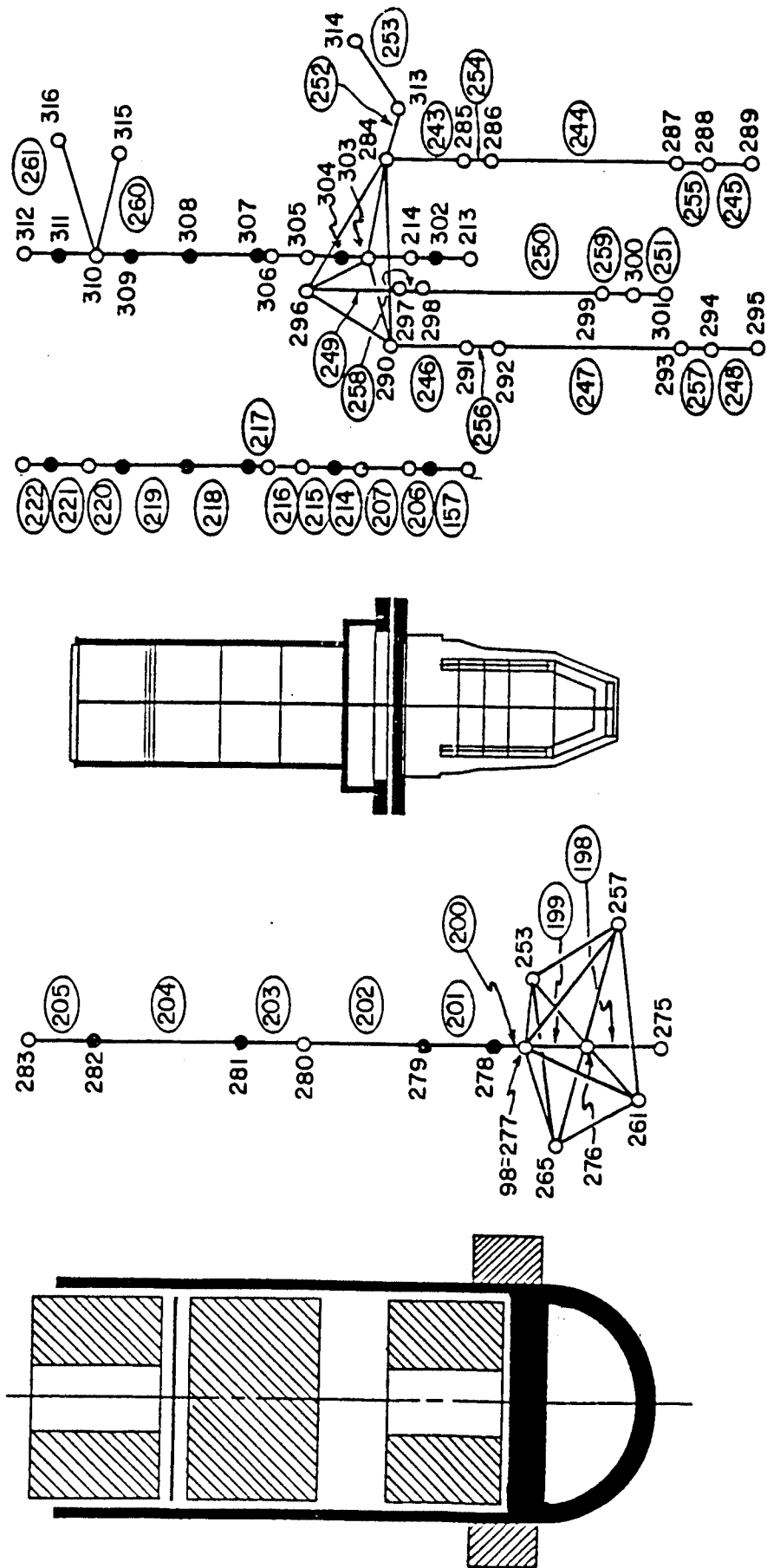
Figure 4.1 (1)   MARC Elbow Model - (Steam Generator and Reactor Coolant Pump)
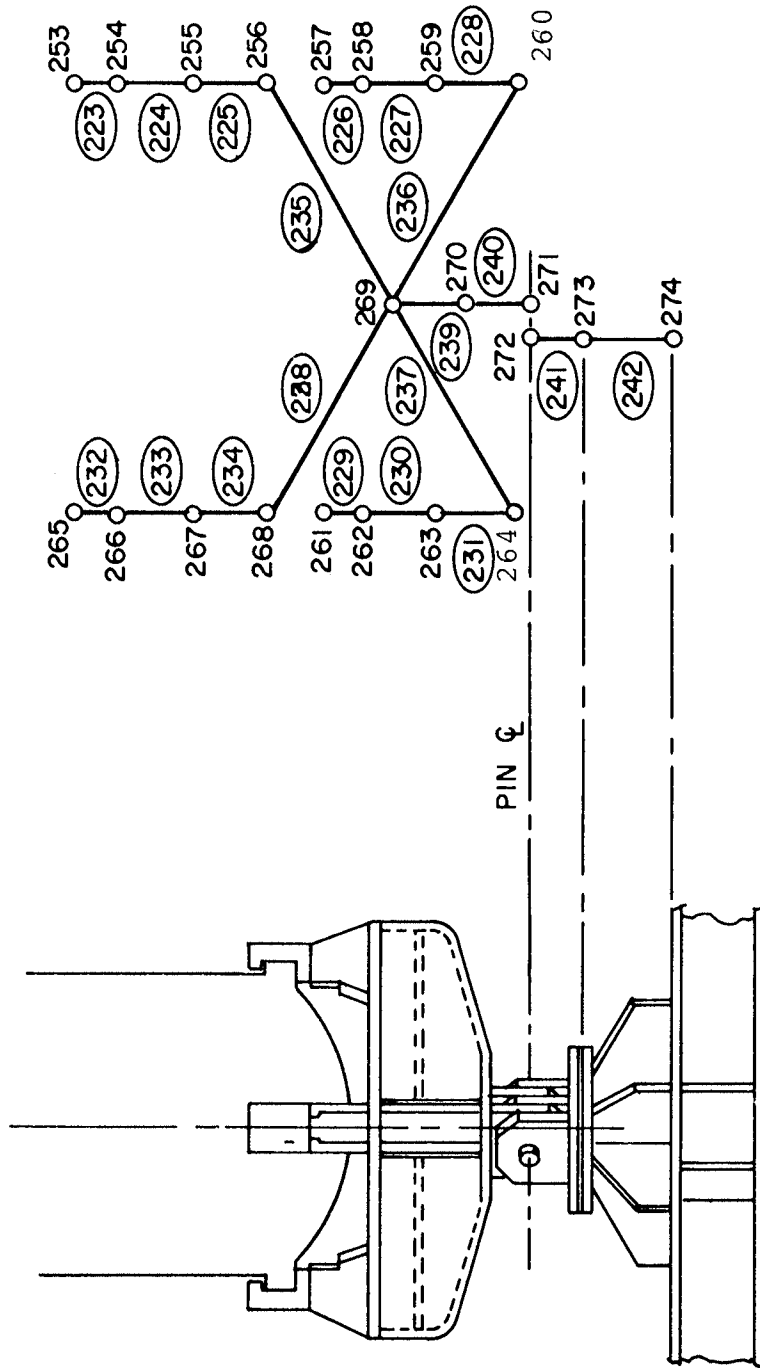
Figure 4.1 (2) MARC Elbow Model — (Steam Generator Support)
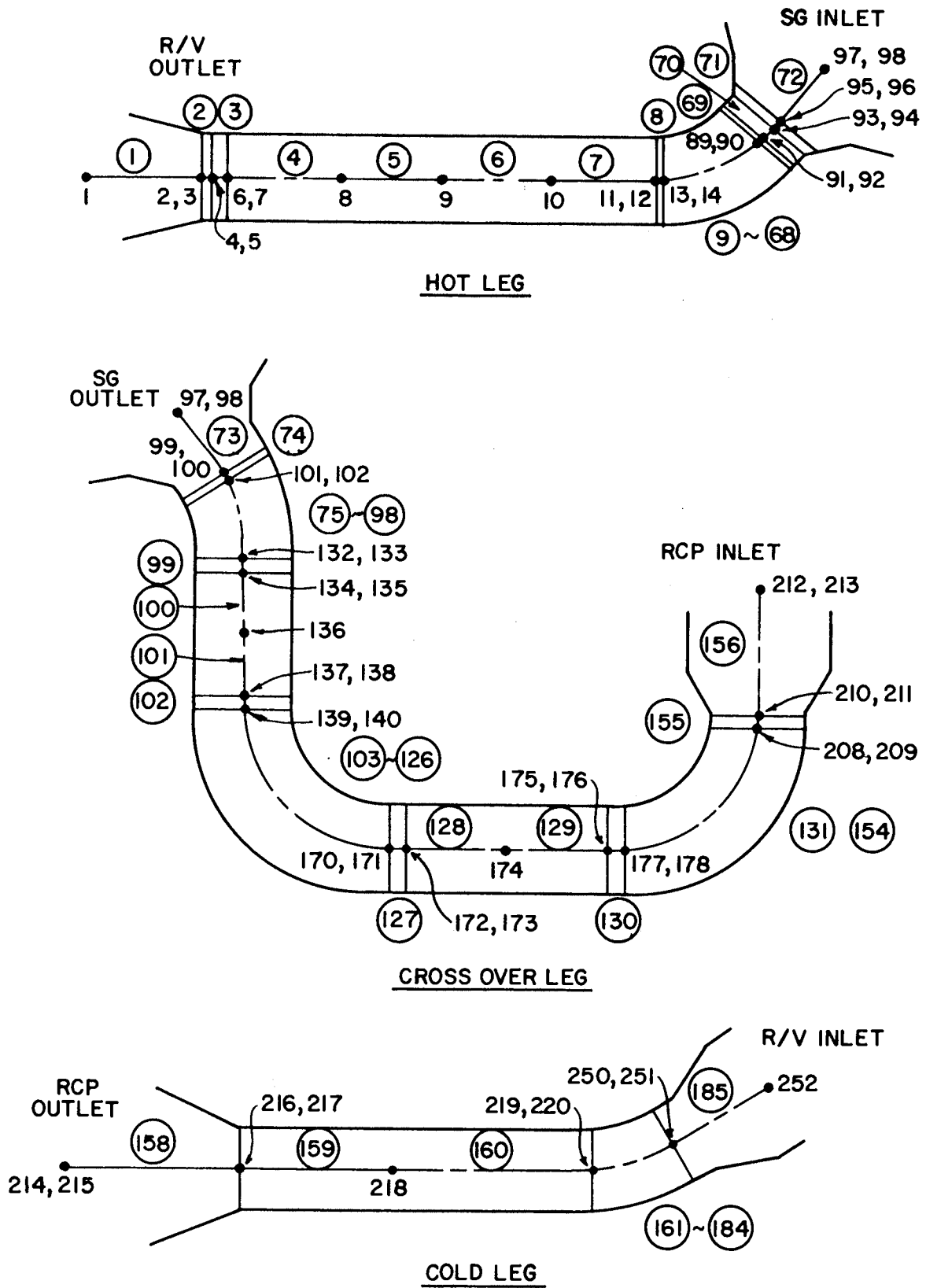
Figure 4.1 (3)   MARC Elbow Model - (Piping)

(Hot-Leg Elbow)
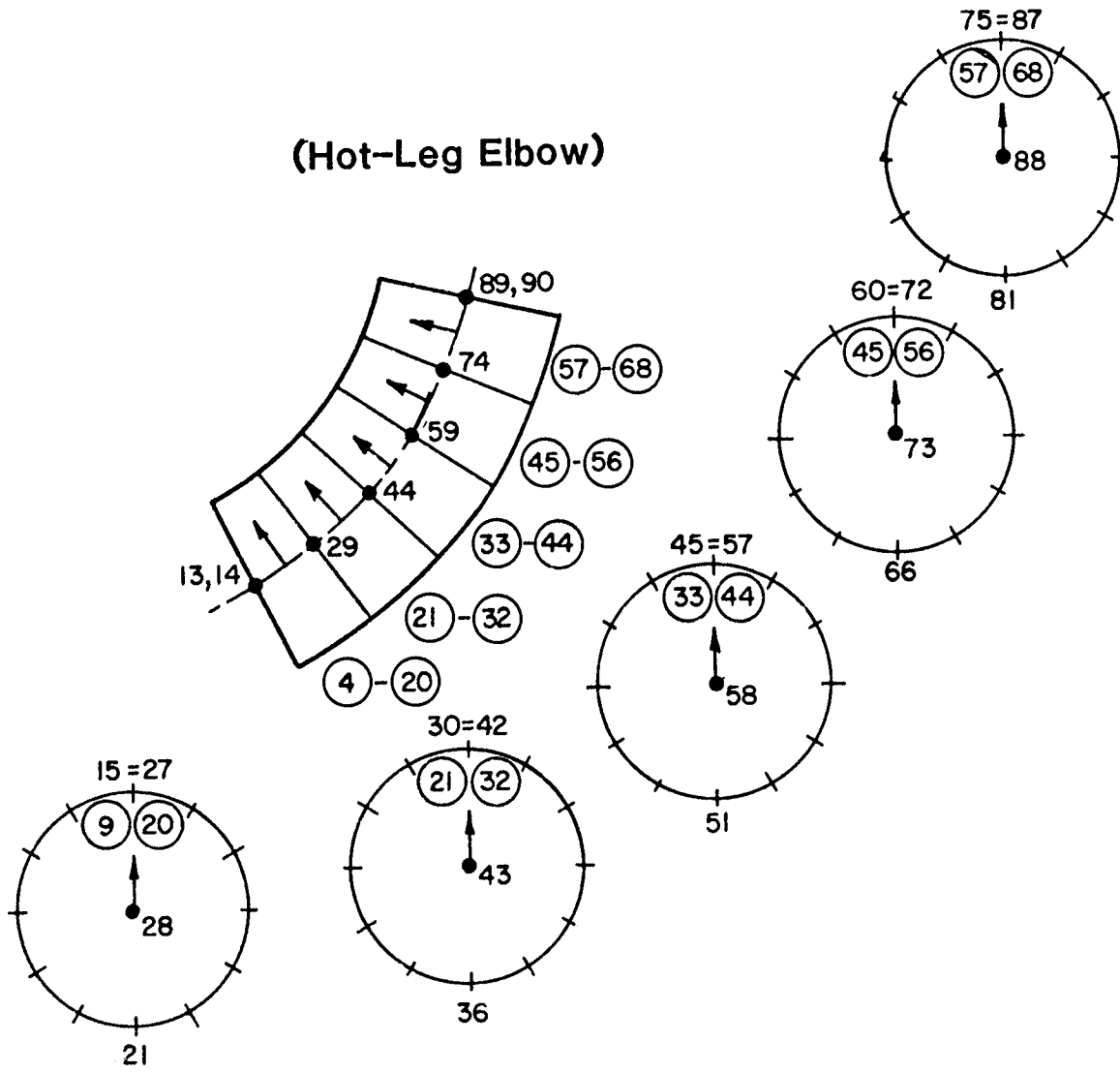
(Cold-Leg Elbow)
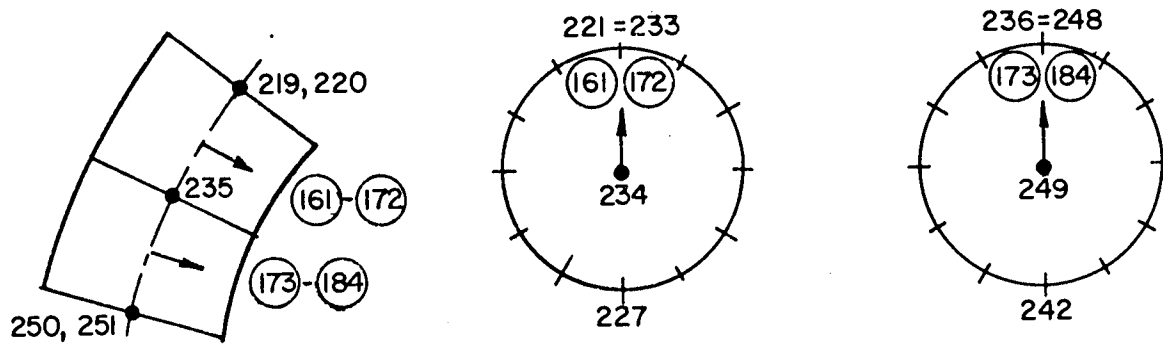
Figure 4.1 (4) MARC Elbow Model – (Node and Element Numbers for Hot Leg and Cold Leg Elbows)
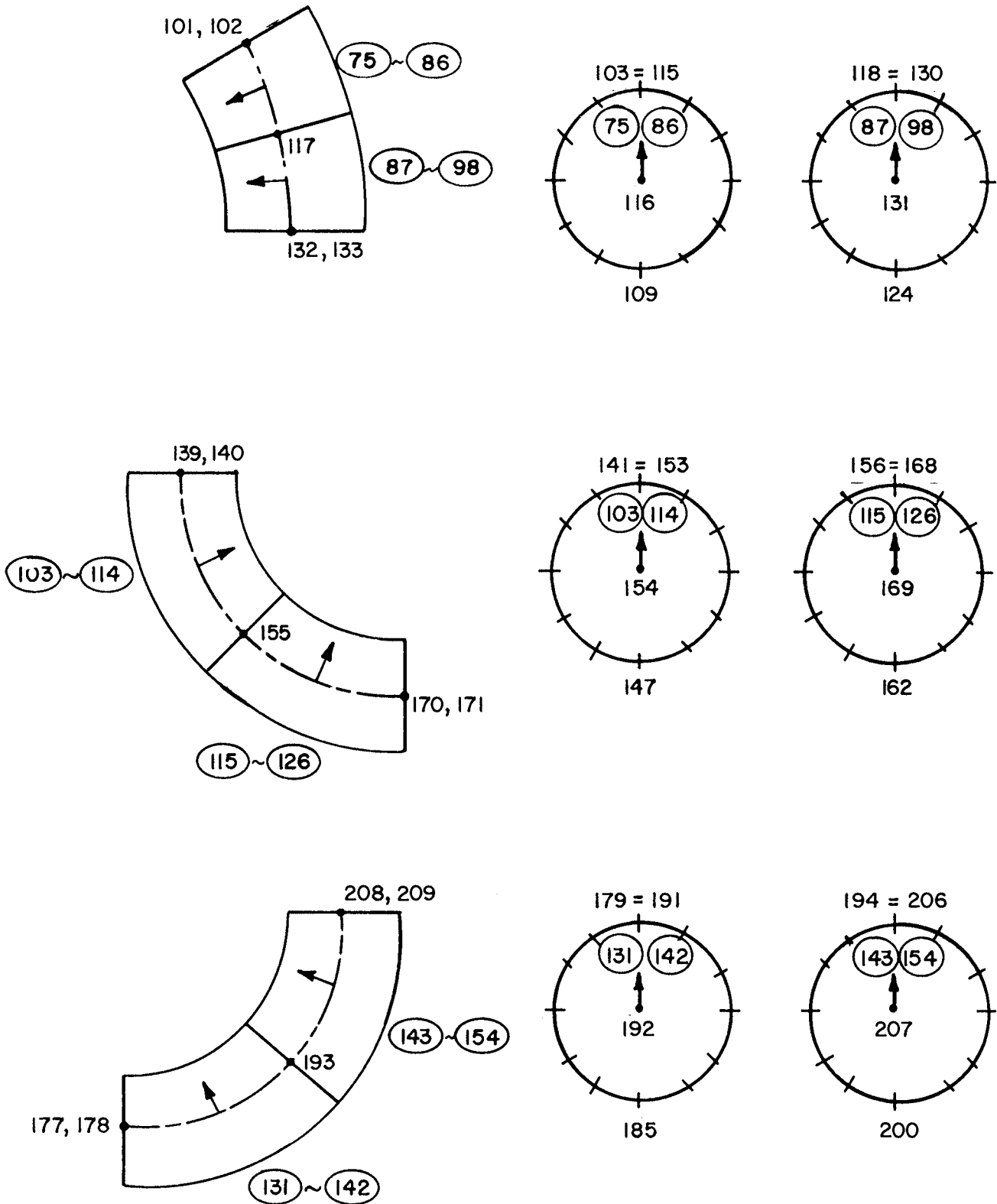
Figure 4.1 (5)   MARC Elbow Model – (Node and Element Numbers for Crossover-Leg Elbows)
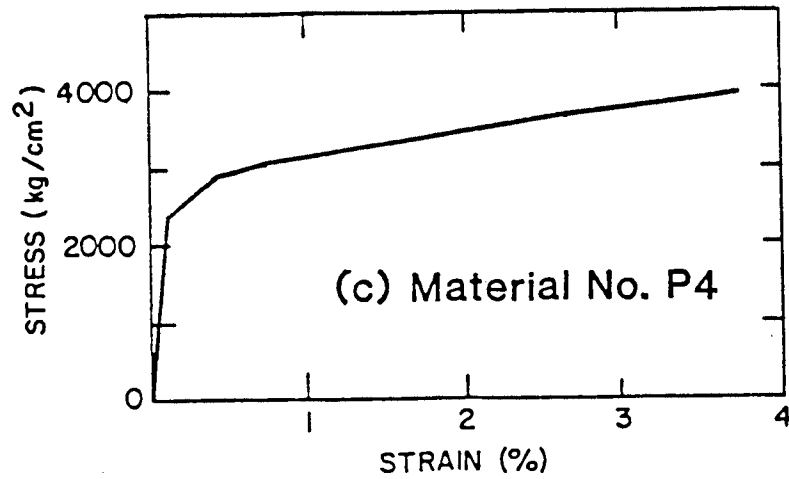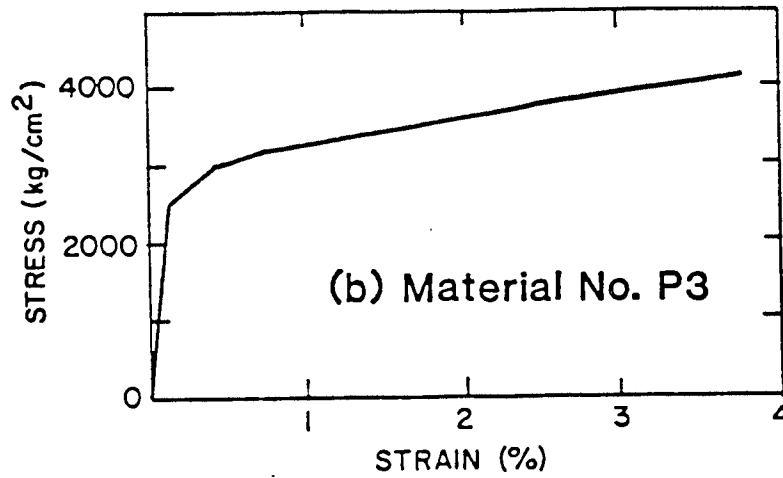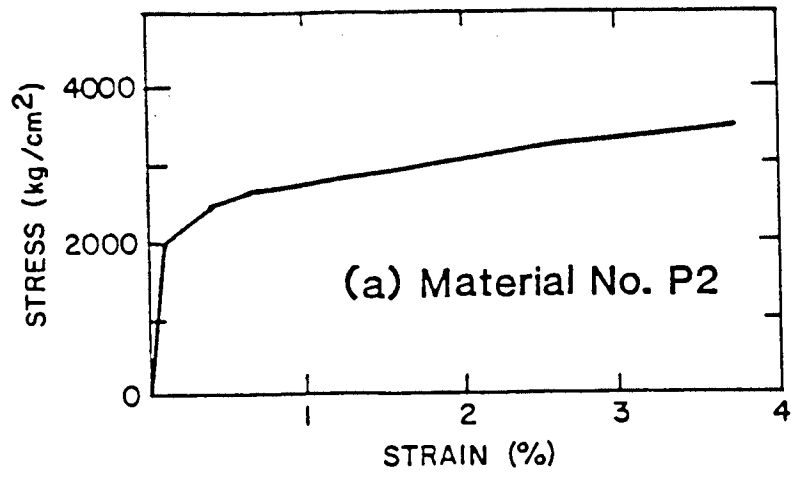
Figure 4.2   Stress-Strain Relationship Used for Material
Nos. P2, P3, and P4 in MARC Analysis

$$\ddot{\theta} = 0.04 \times \left(\frac{\ddot{X_o}}{630} \right)$$

$$\ddot{Y} = -(Z+133) \cdot \ddot{\theta}$$

$$\ddot{Z} = Y \cdot \ddot{\theta}$$

$$\ddot{X} = \ddot{X_o}$$
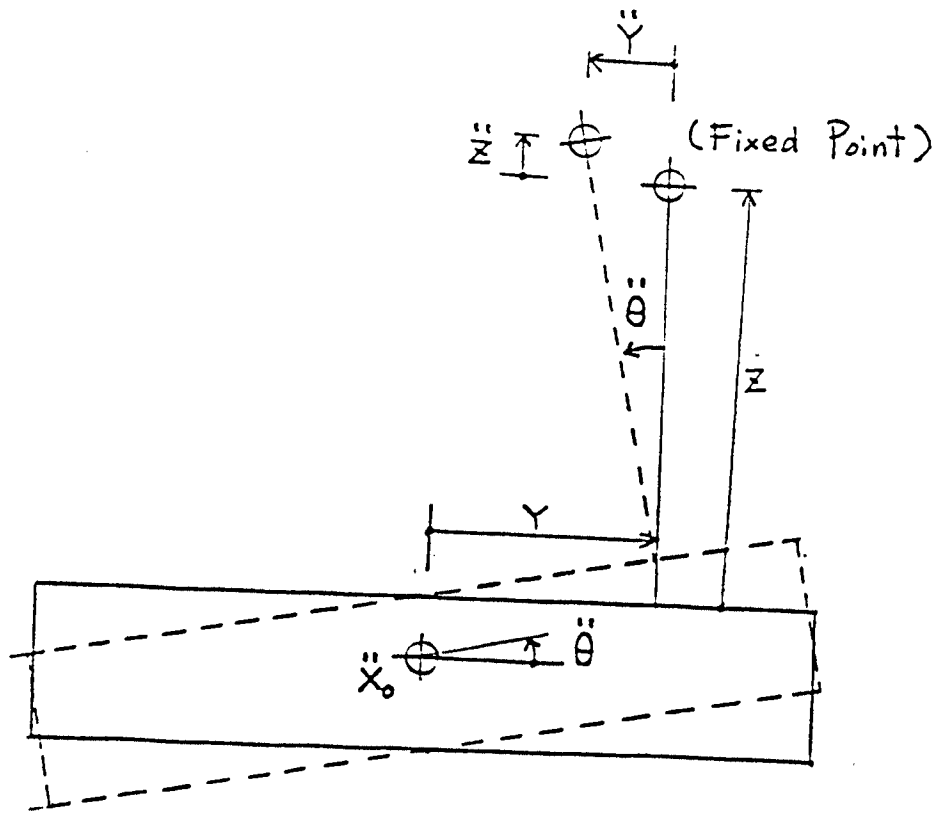
$\left. \phantom{\begin{array}{c} a \\ a \\ a \\ a \end{array}} \right\}$ input for fixed points.

Figure 4.3   Determination of Effect of Rolling Motion
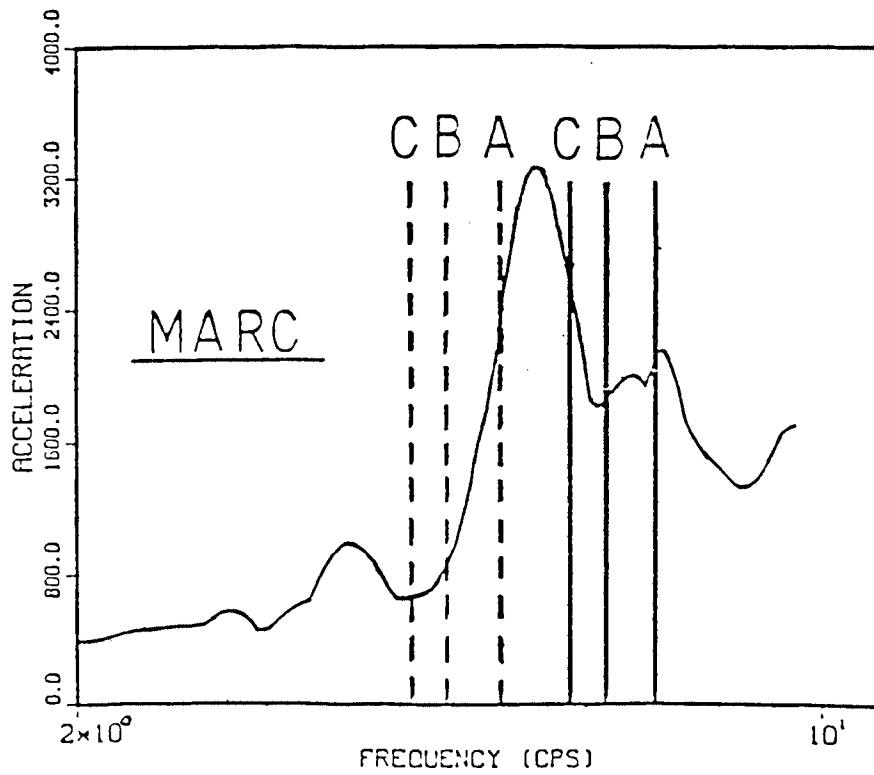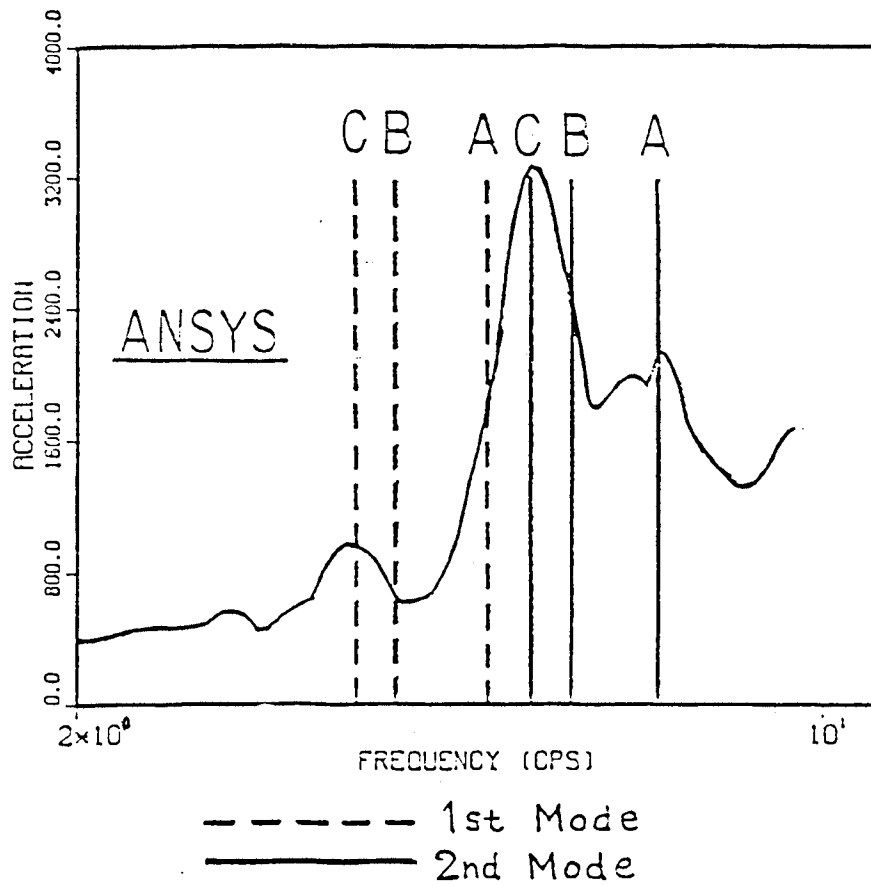
Figure 4.4   Comparison of Time Scaling Choices in
            ANSYS and MARC
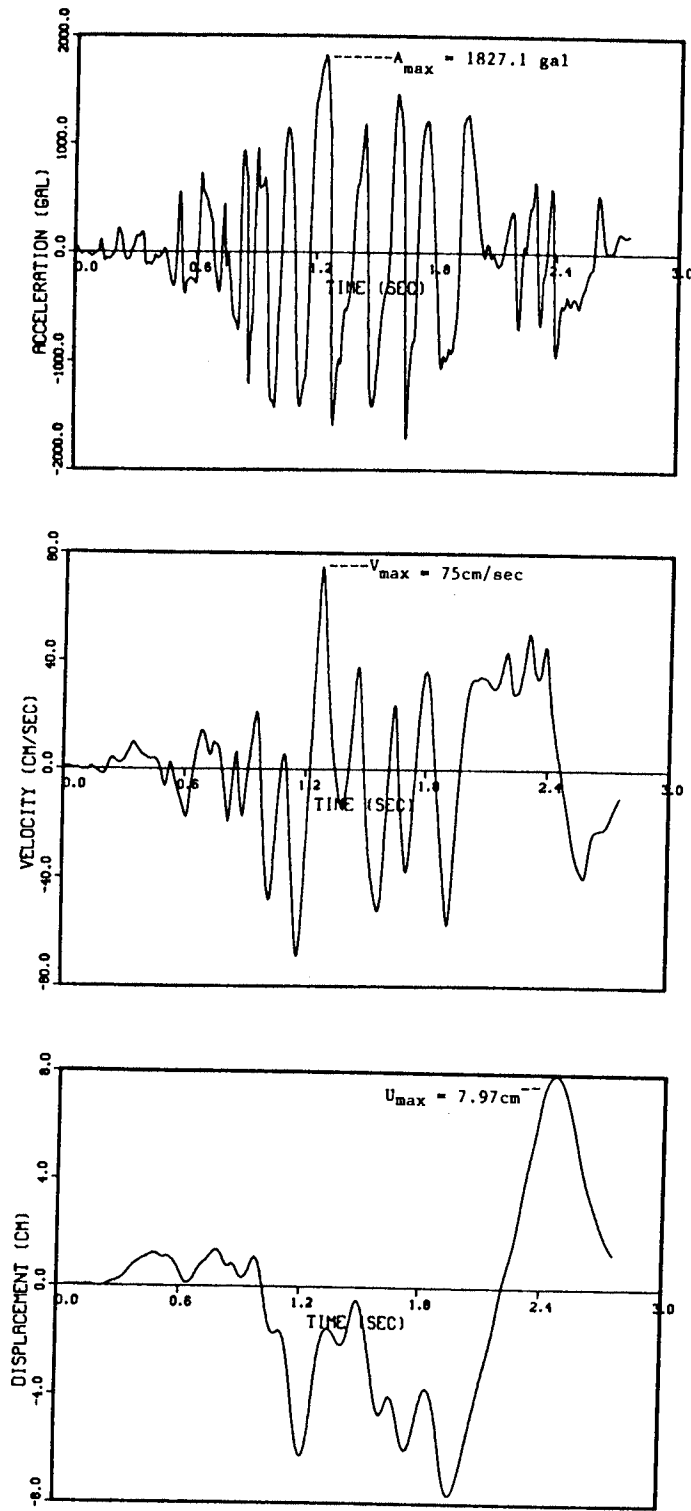
Figure 4.5   MARC Run D - Input Motion Time
History

ACCELERATION
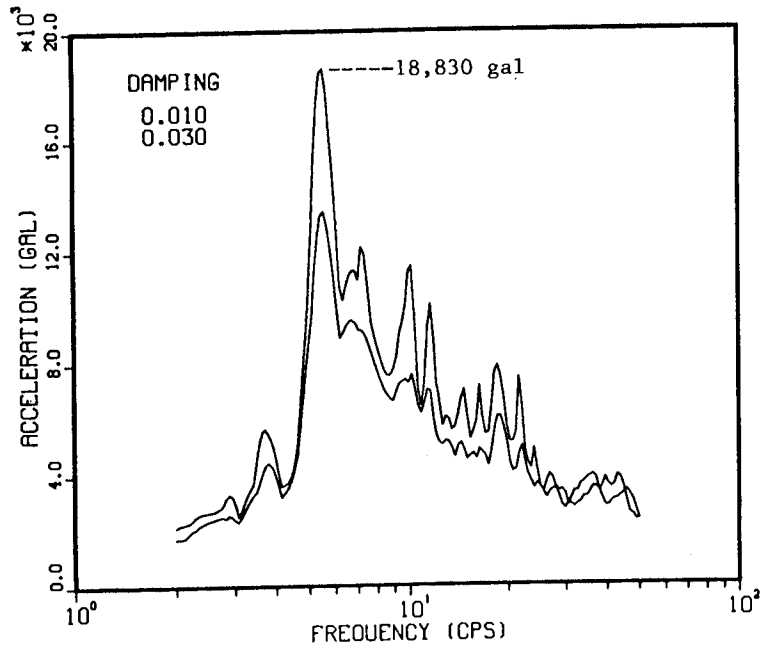
Figure 4.6 (1)   MARC RUN D - Response Spectrum
                  of Input Time History

FOURIER
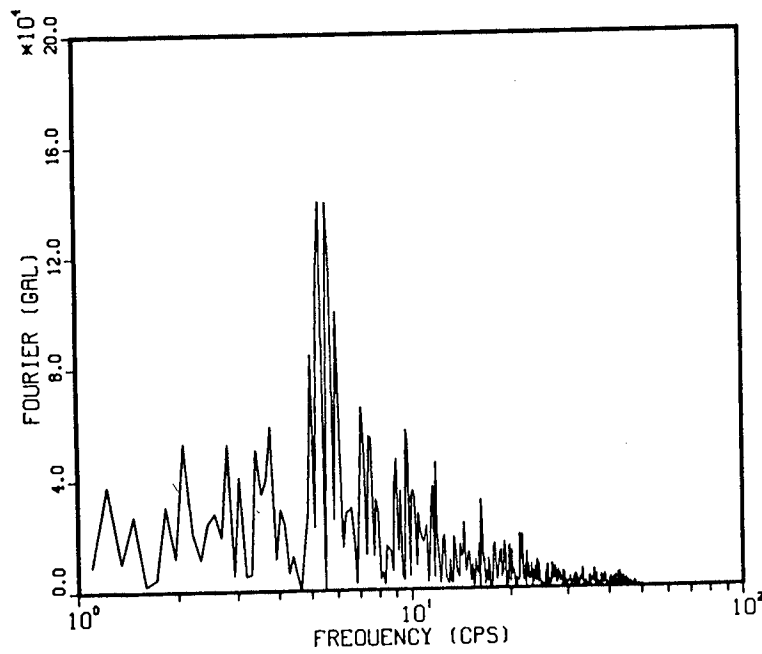
Figure 4.6 (2)   MARC Run D - Fourier Spectrum
                  of Input Time History
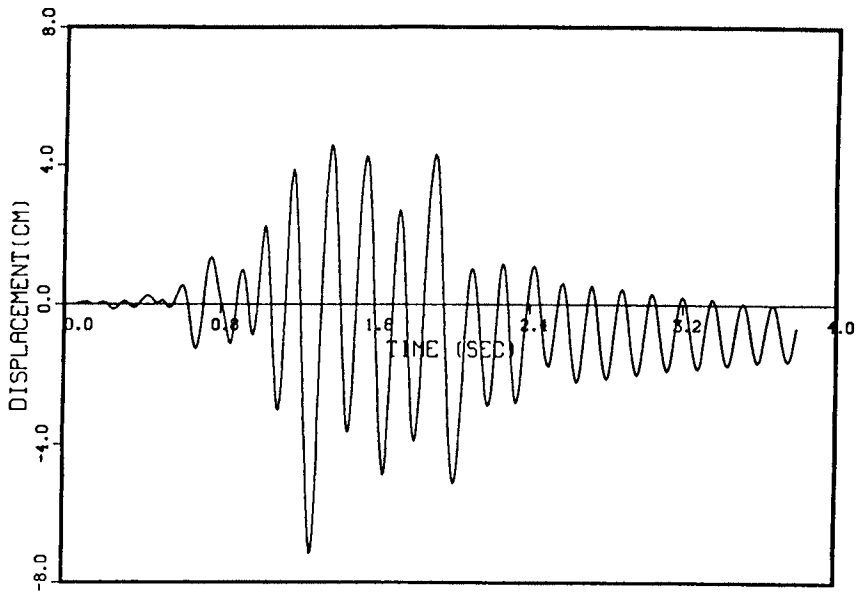
Figure 4.7 (1)   Relative Displacement in X-Direction,
Node 283
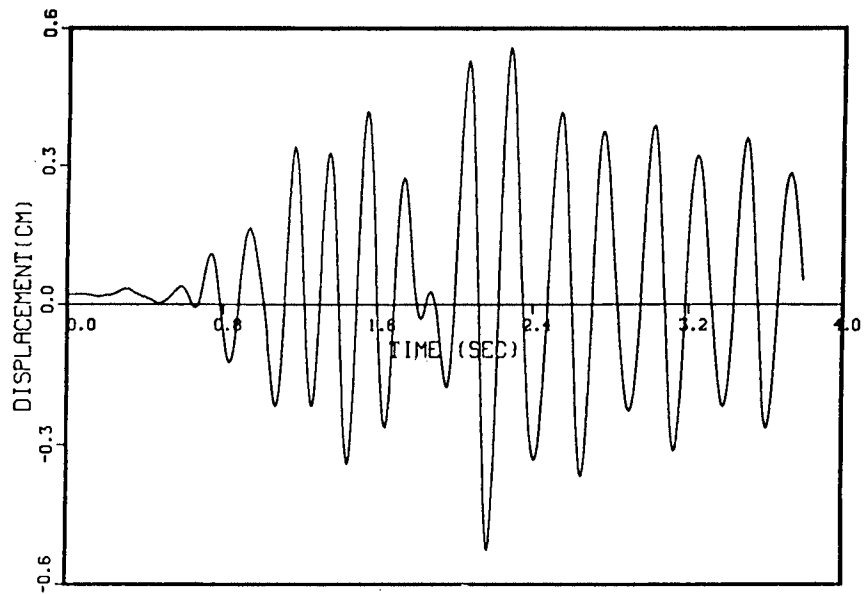
Figure 4.7 (2)   Relative Displacement in Y-Direction,
Node 283
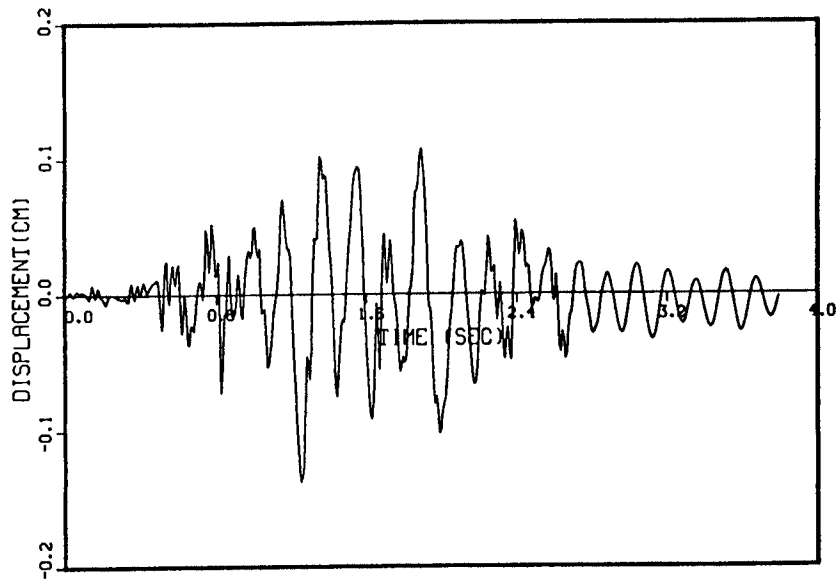
Figure 4.7 (3) MARC Run D - Relative Displacement
in X-Direction, Node 312
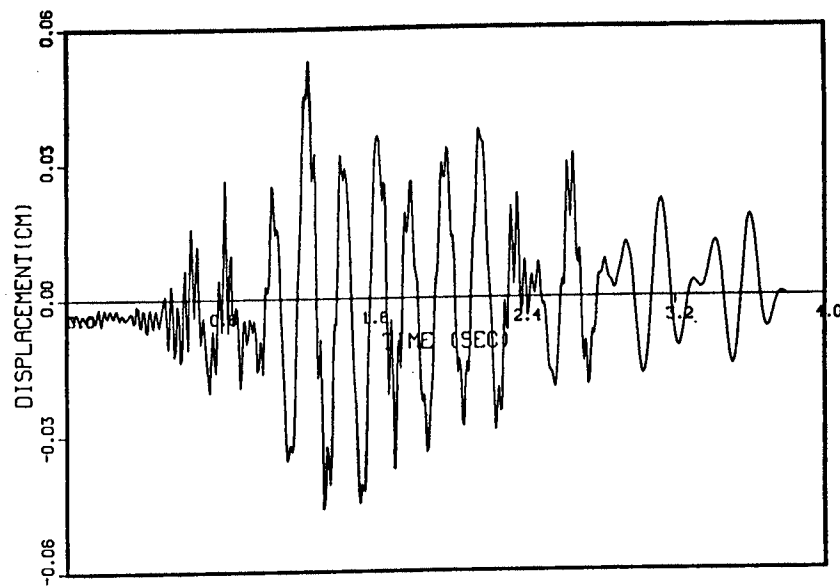
Figure 4.7 (4) MARC Run D - Relative Displacement
in Y-Direction, Node 312

4-33
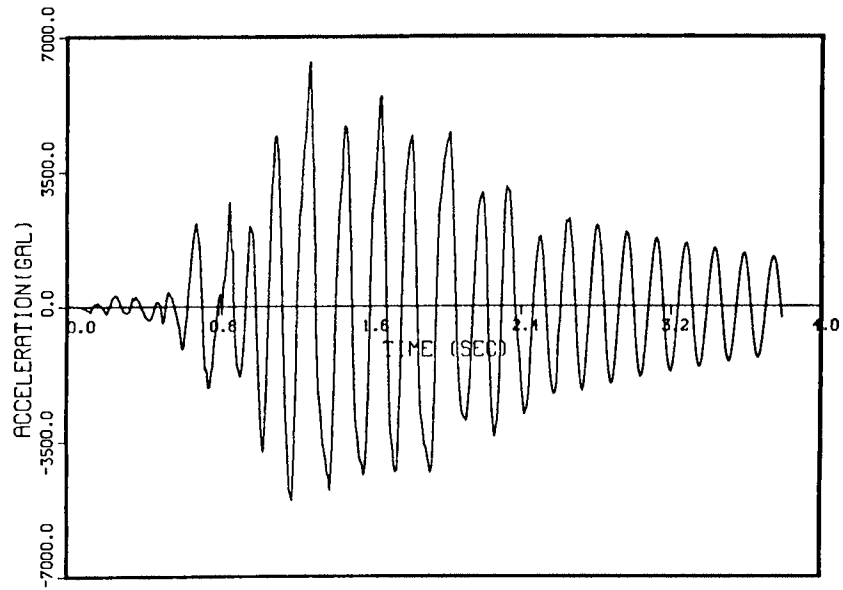
Figure 4.8 (1)   MARC Run D - Acceleration in
                  X-Direction, Node 283
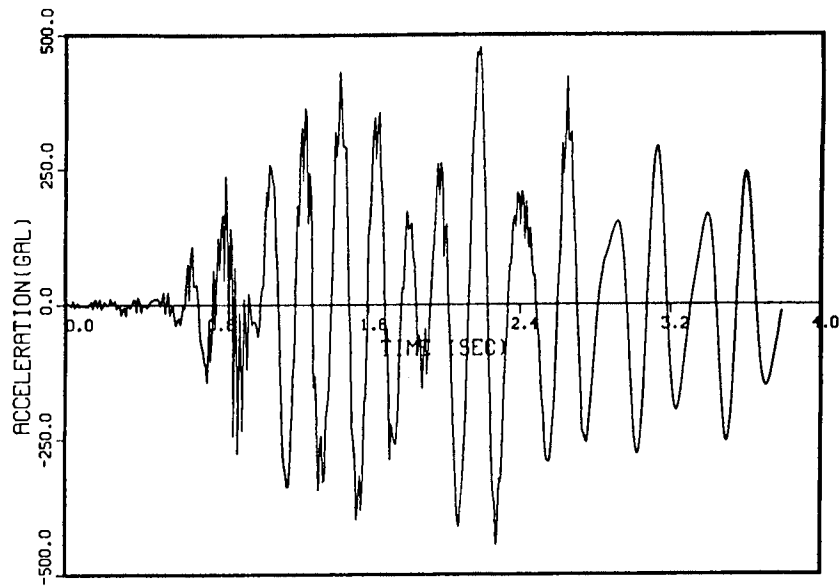
Figure 4.8 (2)   MARC Run D - Acceleration in
                  Y-Direction, Node 283
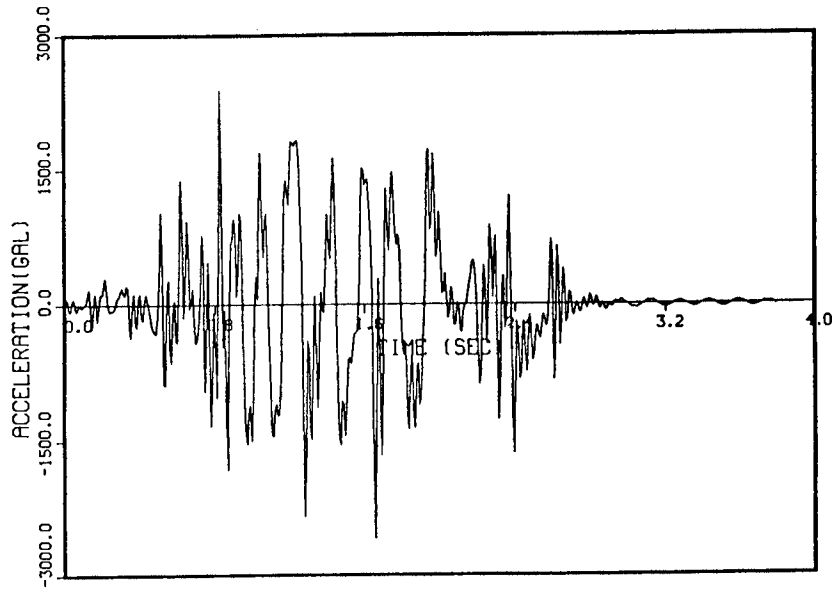
Figure 4.9 (1)   MARC Run D - Acceleration in
X-Direction, Node 312
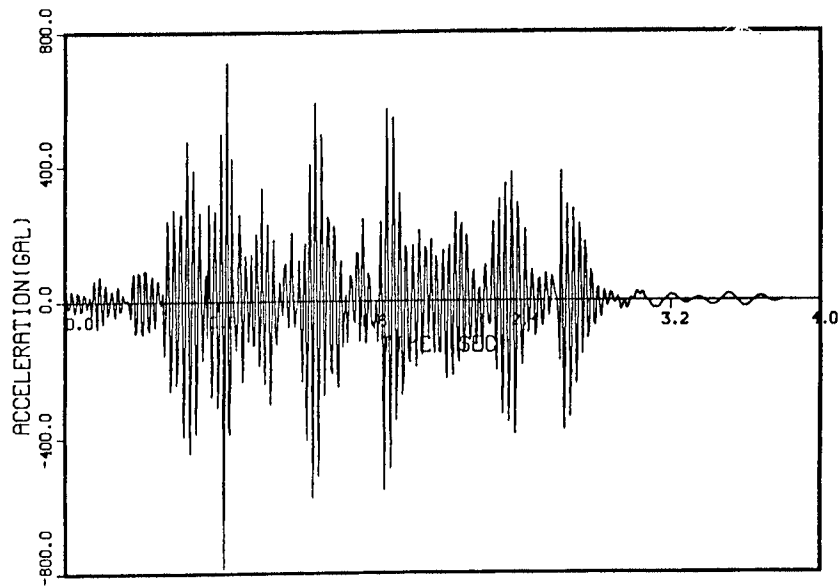
Figure 4.9 (2)   MARC Run D - Acceleration in
Y-Direction, Node 312

4-35
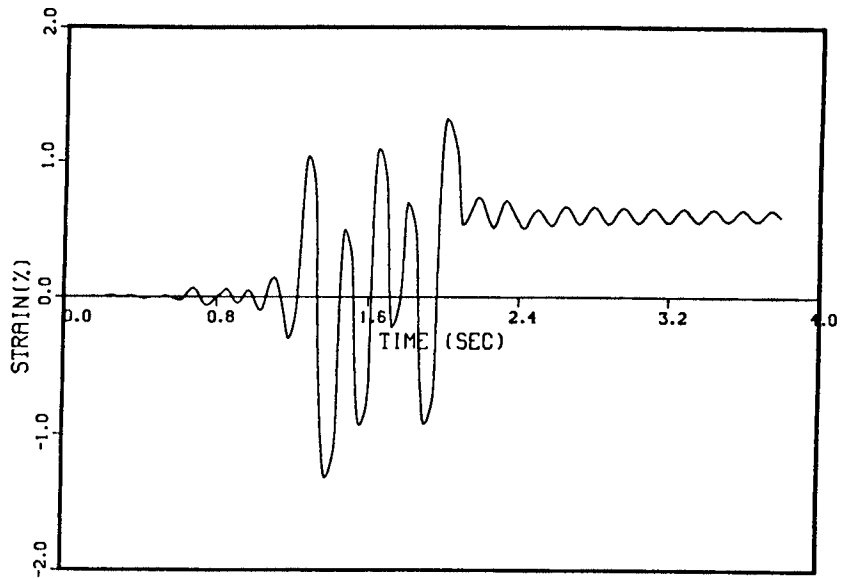
Figure 4.10 (1) MARC Run D - Axial Strain (ε_1) at Element 8, Point 3
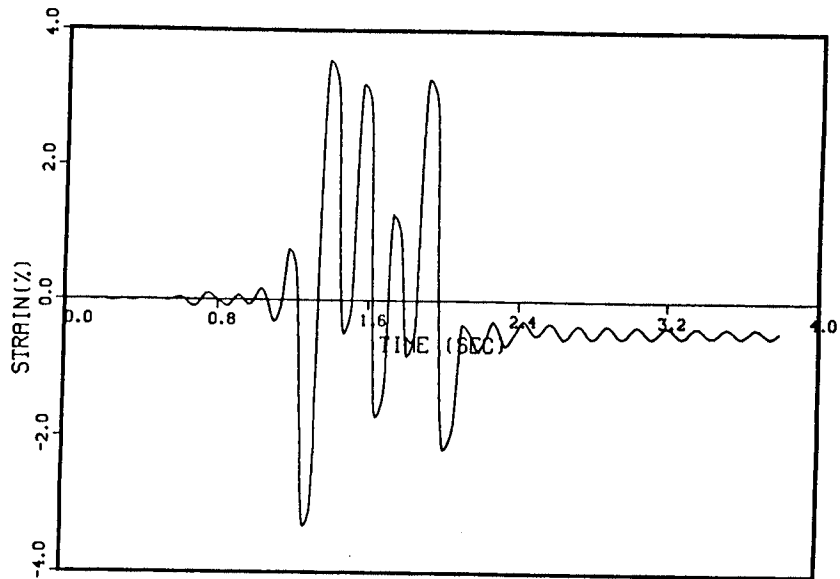
Figure 4.10 (2) MARC Run D - Axial Strain (ε_2) at Element 8, Point 3
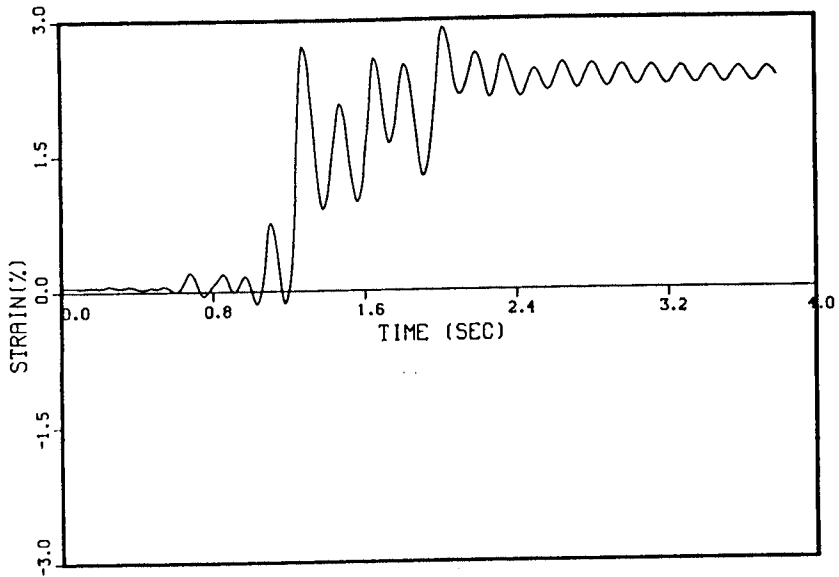
Figure 4.11 (1) MARC Run D - Hoop Strain (Inside)
at Element 20, Point 3
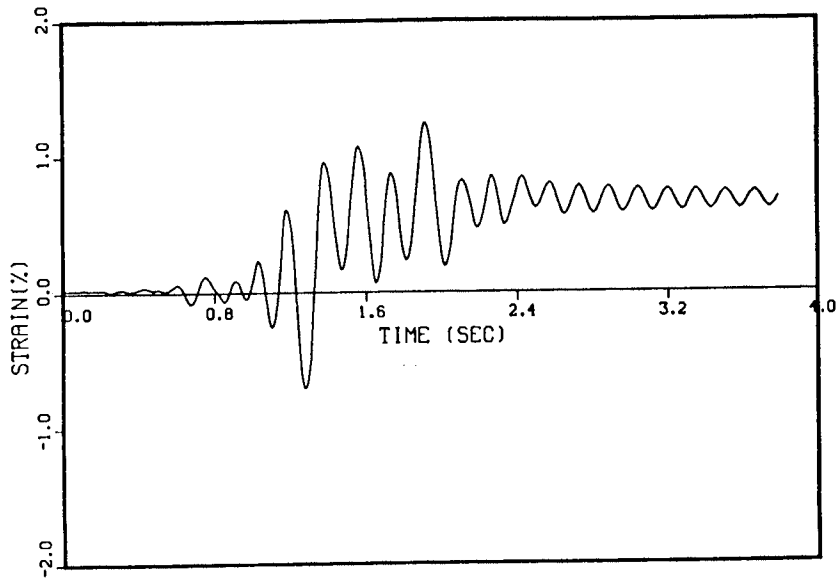
Figure 4.11 (2) MARC Run D - Hoop Strain (Outside)
at Element 20, Point 3
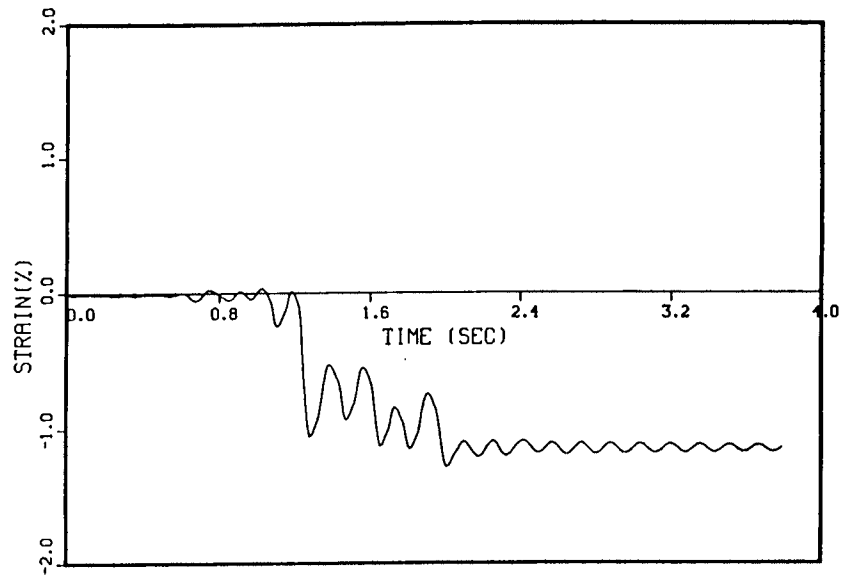
Figure 4.12 (1)   MARC Run D – Axial Strain (Inside)
                   at Element 21, Point 1
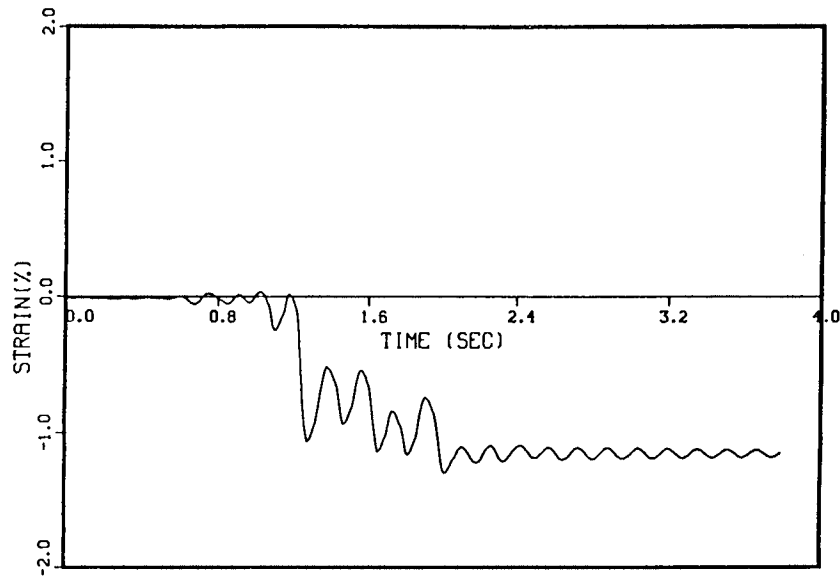
Figure 4.12 (2)   MARC Run D – Axial Strain (Outside)
                   at Element 21, Point 1
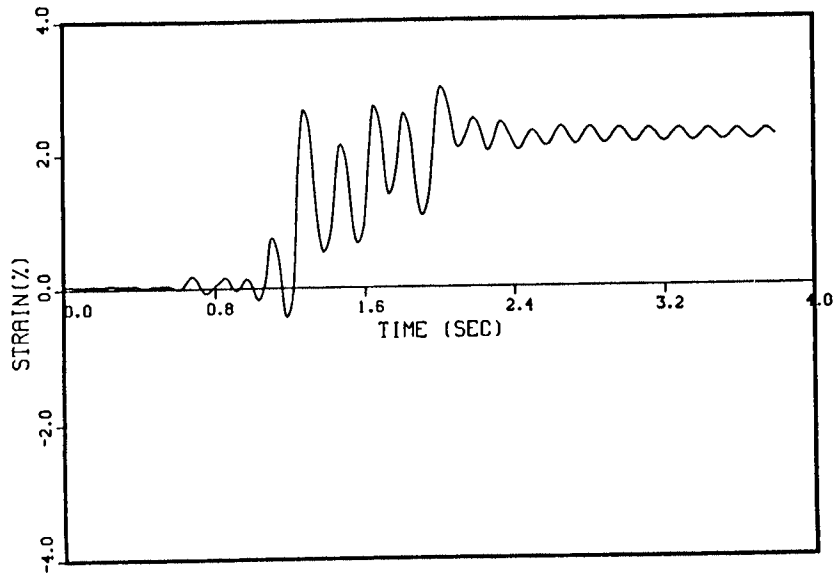
Figure 4.13 (1)   MARC Run D - Hoop Strain (Inside)
                   at Element 32, Point 3
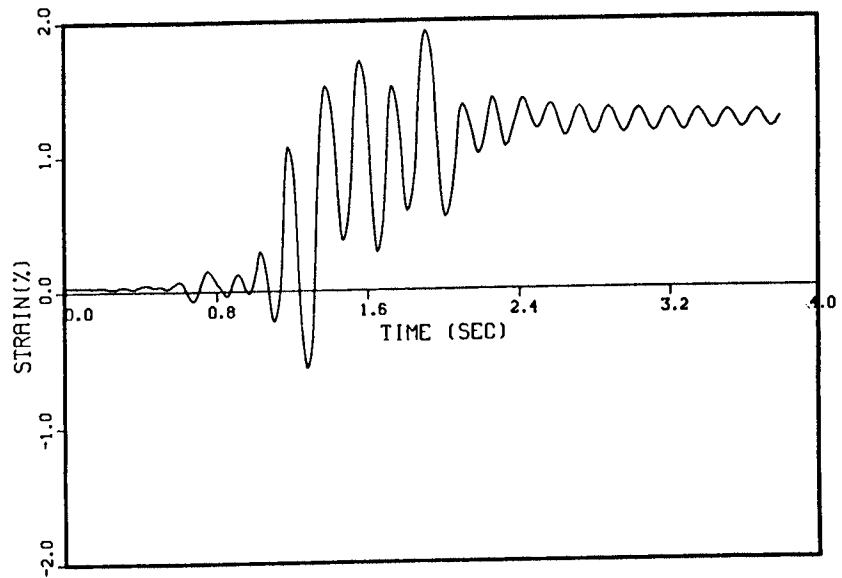
Figure 4.13 (2)   MARC Run D - Hoop Strain (Outside)
                   at Element 32, Point 3
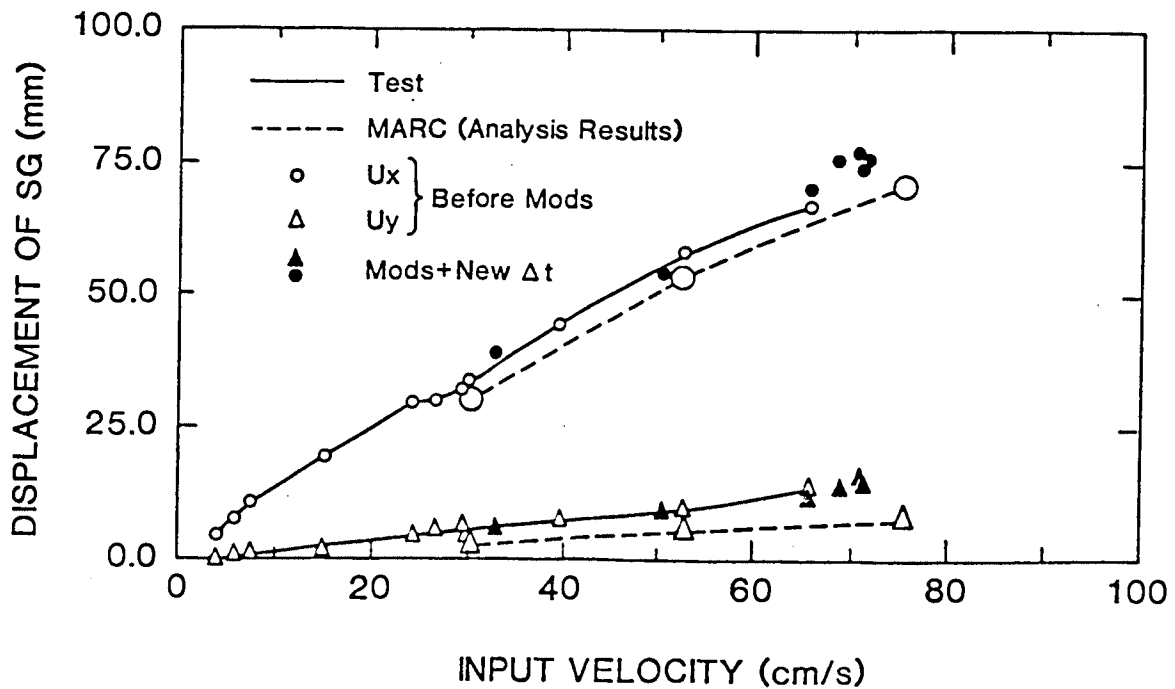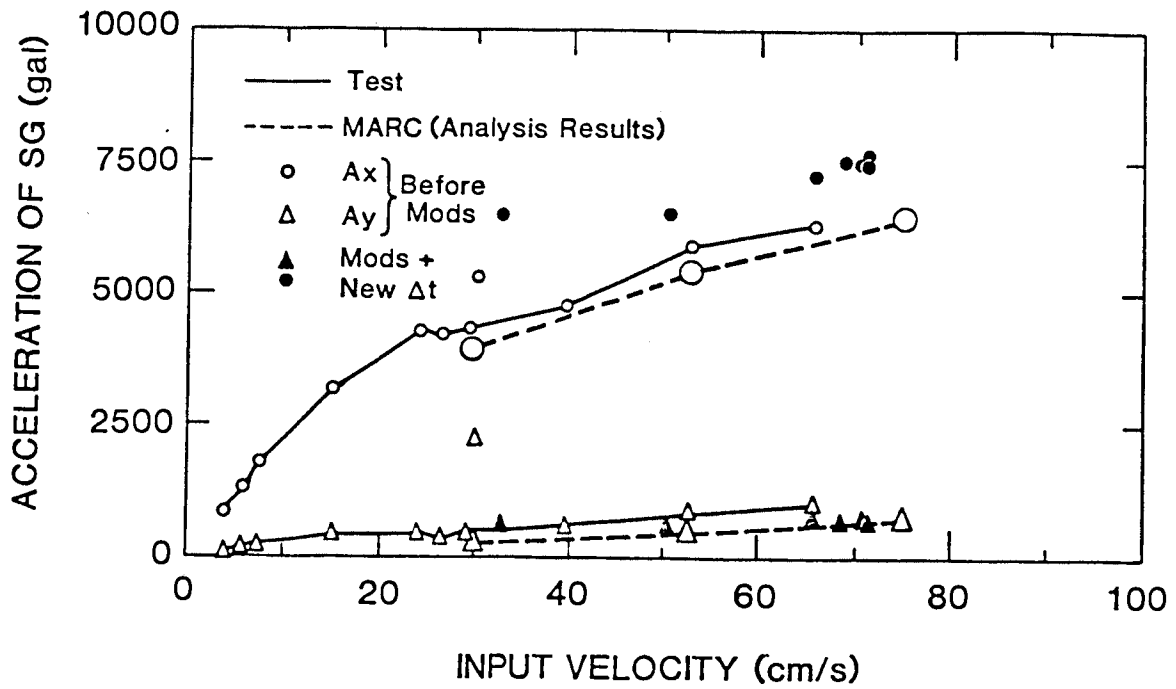
Figure 4.14   Comparison of Analysis and Test Response at
the Top of the Steam Generator
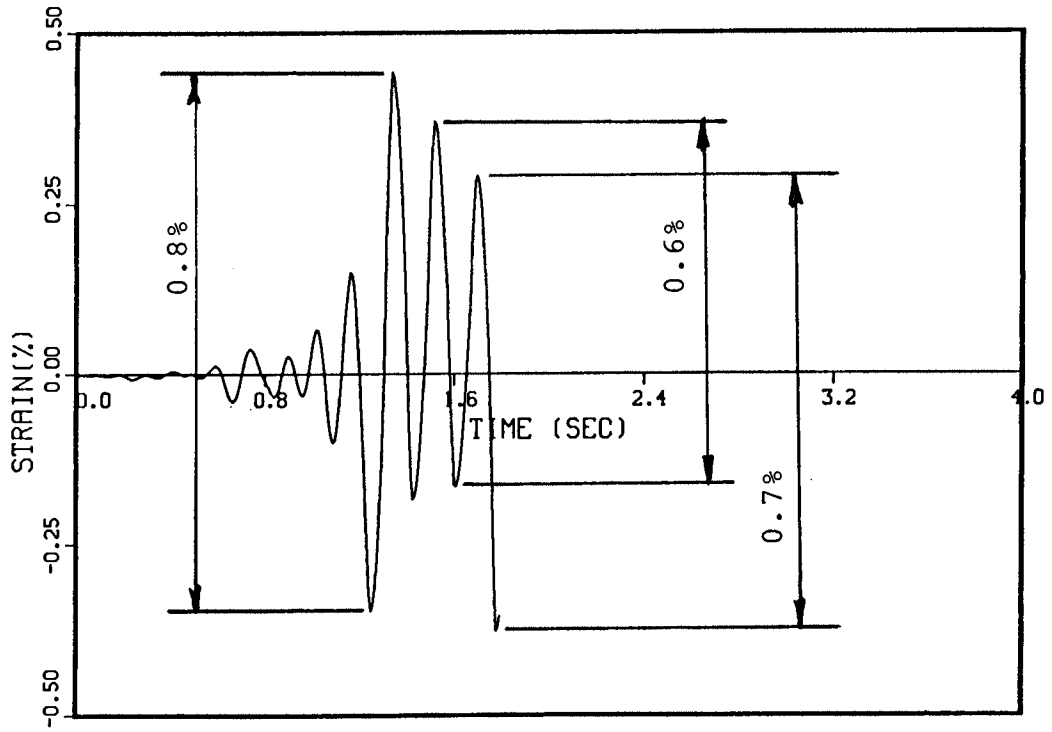
(a) MARC Run D* (0.4 MPR) - Axial Strain (ε_2) at
Element 8, Point 3
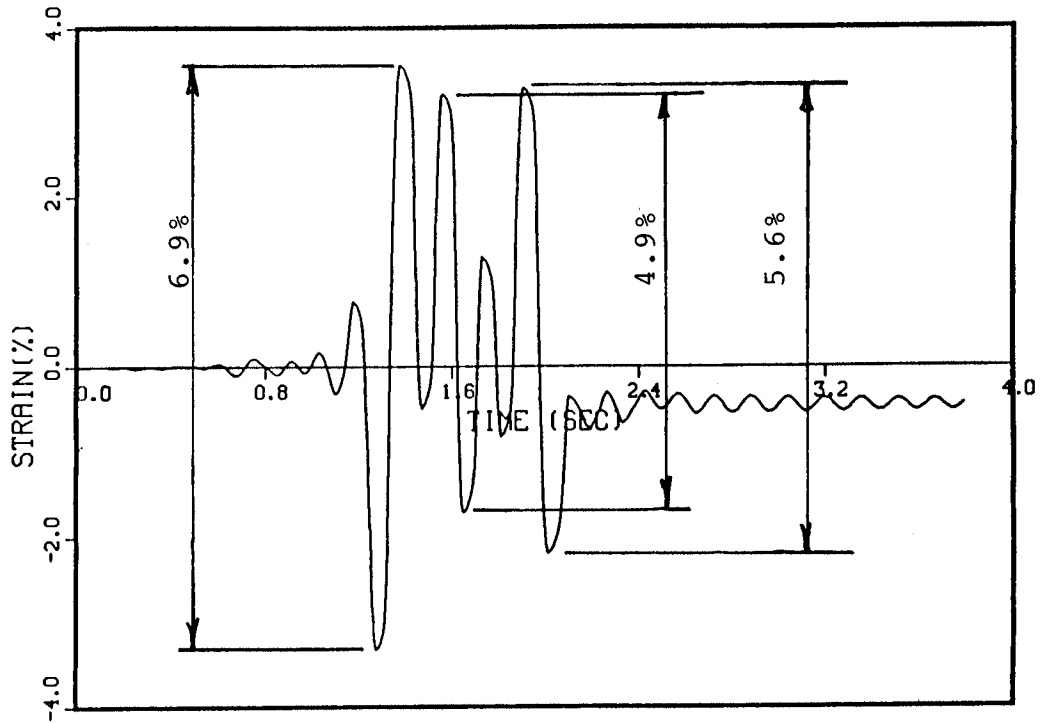
(b) MARC Run D (1.0 MPR) - Axial Strain (ε_2) at
Element 8, Point 3

Figure 4.15   Strain Range Evaluation for Fatigue Failure
Prediction at Element 8

5. TEST RESULTS

5.1 Test Procedure

A total of 45 tests were carried out with the test model including sinusoidal and random vibration tests to obtain the characteristics of the test model. Table 5-1 lists the HLVT runs and gives an outline of the test procedures. Figure 5-1 illustrates the test procedure and identifies the nomenclature assigned to the various test stages. Also, Table 5-2 lists the details of all the tests performed and shows the entire test history of the test model. The excitation level of the vibration table is denoted by the ratio to the maximum excitation run (MPR). The test was divided into three stages, i.e., preliminary test, high level vibration test part 1, and high level vibration test part 2. With the exception of some early preliminary tests, all tests were conducted with the piping at a constant pressure of 157 kg/cm^2. Photographs of the test model are included in Appendix A. Details of the transducers and measuring points are provided in Appendices B and C, respectively.

Appendix D provides a summary of some of the data that was recorded during the test program. It contains table operating data as well as response information. Representative data is presented for each of the three test stages, that is, from the preliminary tests (up to 0.1 MPR), the high level vibration test, Part 1 (0.2 and 0.4 MPR), and the high level vibration test, Part 2 (0.4 and 1.0 MPR). The 0.4 MPR test was repeated because of structural modifications that were done at that time. At each test stage, information is plotted to show:

- Response spectra (table excitation)
- Maximum response distributions
- Instantaneous response distributions
- Transfer function (SG response to table input)
- Hysteresis loops
- Time history response

The major test runs are described in the following subsections.

5.1.1 Preliminary Test

Low-level excitation tests up to run 4 are included in this stage. The main objective of this stage is to determine the dynamic characteristics of the test model-vibration table system in the elastic range. Therefore, the maximum strain response of the test model was kept to a micro-strain below 2000 (0.2% strain). The test procedure and objective of each run are described below.

Tapping test - The natural frequencies in the X and Y-direction were measured by tapping the top of the steam generator (SG). The free vibration responses were recorded by accelerometers mounted on the top of the SG.

Warm-up tests - A warm-up test was performed using a low-amplitude sinusoidal motion. The polarity of all sensors was determined during this test.

Random tests - Random motions were used to determine the transfer function of the combined system of the model and the shaking table. Applied excitations were uncompensated pink-noise with a duration of 10 seconds and the peak acceleration described in Table 5-2 in terms of 3σ.

Sinusoidal tests - Sine-sweep tests were performed to identify the vibration frequencies and damping values.

Run 1 - Two input motions, i.e., A-A-A-A and A-B-C-D were scaled to 5% of full-scale.

Runs 2, 3 and 4 - Low level excitation runs at 0.075 MPR and 0.1 MPR were performed to refine the transfer function and establish the linear responses. The 0.1 MPR test was repeated twice since the trip was triggered after segment-C by the strain reading of 153X.

5.1.2 High Level Vibration Test Part 1

Runs 5 through 10 are included in this stage, and the excitation level is increased from 0.2 MPR to 1.0 MPR. In order to minimize the fatigue damage due to intermediate level excitations, only the first segment was excited in runs 9 (0.6 MPR), 9* (0.8 MPR) and 10 (1.0 MPR).

A banging sound occurred inside the test frame during runs 7 and 8. After run 9* the cause of the sound was found to be due to the slippage of the baseplate at the SG pin-support. The pretension in the bolts of the baseplate was increased up to the limit for run 10, but it was not sufficient to prevent the slippage. Therefore, attention should be paid to unexpected non-linearities in the data evaluation of these runs (runs 9, 9*, and 10').

5.1.3 High Level Vibration Test Part 2

After run 10' the model was reinforced. Excitations after the reinforcement, i.e. runs 8* through 14' are included in this stage. Inelastic fatigue cracks initiated during run 11, and continued to grow at each input at the 1.0 MPR level. Inspection of the cracks was conducted after each subsequent run. The testing was completed after run 14'.

5-2

5.1.4 Inspection Method

The as-built dimensions of the test model were established on the basis of design dimensions, shop dimensional records and measurements at Tadotsu during the overall check of the test model. Reference points were marked on the test model and on the support frame structure. The distance between two reference points was measured before the test (after modification of test model) and after completion of the last HLVT run for comparison. Ten (10) sets of scratch marks were indicated on the SG inlet elbow around selected strain gages to measure the permanent strain induced by the HLVT runs. Diameters in two directions and circumferences of the pipe and the elbows were measured after modification of the test model (for establishment of the initial condition) and after each test run if the test run induced large strains above yield. These measurements were made at the hot leg elbow, both ends of the straight portion of the hot leg pipe and the crossover leg elbow closest to the SG. Reference points were marked for diameter measurements before the initial measurement. Visual inspection (TV) was performed after each test run to check the integrity of the test model. Liquid penetrant examination (PT) was performed on the applicable portions after test runs which induced large strains. A metallurgical investigation of the highly strained portion of the pipe was also conducted and is fully discussed in Section 6.0.

5.2 Results of Preliminary Test

5.2.1 Sine-Sweep Excitation

Test conditions of the sine-sweep excitation are listed below.

(Excitation Level)	(Frequency Range)	(Frequency Increment)
10 gal	2 ~ 30Hz	0.2Hz
10 gal	2 ~ 7.8Hz	0.05Hz

The frequency responses of the horizontal and pitching components of the table acceleration are shown in Figure 5-2. Although the excitation level is very small, the vibration table is well controlled and the fluctuation of the excitation level in the frequency range up to 30Hz is within 20% of the target level.

The response of typical measuring points on the SG are shown in Figure 5-3 in the form of a transfer function. Figure 5-3 illustrates the transfer function measurement of natural frequencies. Based on these results, the vibration frequencies were determined as:

5-3

Y-direction: f = 3.2Hz
X-direction: f = 6.4Hz

The damping for the X-direction vibration mode was found to be 0.86% as shown in Figure 5.4. At the higher frequency region, the following two peaks were recognized:

f = 20.2Hz (SG torsion)
f = 28.0Hz (RCP vibration)

Figure 5-5 shows the vibration mode shape of the predominant mode at 6.4Hz.

5.2.2 Low-Level Earthquake Excitation

Test conditions of the earthquake wave excitation are shown in Table 5-3, where runs 2 though 4 are defined as the preliminary test. As a typical case of the preliminary test, the results of run 4 (0.1 MPR) are discussed below.

Response spectrum: The response spectrum of the table acceleration is a measure of the controllability of the vibration table. As shown in Figure D.1, the response spectrum of the horizontal table acceleration was within about 10% of the target spectrum, and the pitching, rolling and yawing components were also well suppressed to less than about 10% of the horizontal acceleration.

Maximum response distribution: Figure D.2 shows the maximum response distribution at run 4 (0.1 MPR). The maximum value is defined as the largest absolute response value that occurred during the full four segment excitation. The maximum strain of the piping was observed at the cross section HR3A, which is the interface of the straight pipe and the elbow of the hot leg. A discontinuity of the pipe wall thickness exists there. Relatively large strain was distributed over the upper part of the piping in the vicinity of this portion. The axial strain was the largest component at most measuring points.

Instantaneous response distribution: Figure D.3 shows the instantaneous response distribution at the time when the maximum strain was recorded. The tensile strain at the upper part of cross section HR3A and the lower part of the reactor vessel (RV) nozzle (cross section HR1A) was produced when the SG is at the furthest distance from the RV.

Transfer function: Figure D.4 shows the transfer function of the SG top acceleration to table acceleration as calculated by the FFT method. The peak frequency of the earthquake wave response obtained from the transfer function is about the same as the natural frequency measured by the sine-sweep excitation.

5-4

<u>Hysteresis loop</u>: The inertia force acting on the SG estimated from the acceleration records at the SG top and bottom is plotted against the displacement of the SG top as shown in Figure D.5. Since the area enclosed by this loop corresponds for the most part to the dissipated energy of the test model, the equivalent damping ratio is approximately calculated as follows;

$$\varsigma = \frac{1}{4\pi} \cdot \frac{E_D}{E_P} \tag{5.1}$$

where,

ς : equivalent damping ratio
E_D: dissipated energy
E_P: potential energy

<u>Time history of response</u>: Figure D.6 shows the response time history of typical measuring points.

5.3   High Level Vibration Test Part 1

Runs 5 through 10 are included in this stage, during which the excitation level was increased from 0.2 MPR to 1.0 MPR. Runs 5 (0.2 MPR) through 8 (0.4 MPR) were four-segment excitations (A-B-C-D) and runs 9 (0.6 MPR) through 10 (1.0 MPR) were one-segment excitations using only the first A-segment.

During run 5 (0.2 MPR), a high pitching ratio of 20% was obtained in the table motion. The next excitation, run 6 (0.3 MPR), was used as the first input to restart the compensation for the subsequent compensation process. Since the 0.3 MPR test was not compensated, a relatively large difference was observed between the target and actual table motions. In subsequent runs 7 and 8, the table control was acceptable. It was found later that the slippage of the baseplate at the SG pin-support started during these tests.

During run 9 (0.6 MPR) and 9* (0.8 MPR), a rattling sound was created by the slippage of the baseplate. The pretension of the bolts of the baseplate was increased to eliminate the slippage. At the 0.8 MPR test, the achieved peak velocity was only 53cm/sec, making the intended 0.8 MPR test equivalent to 0.7 MPR. This reduction of the table motion was caused by the vibration of the test model.

During run 10 (1.0 MPR), a loud banging noise was heard again. A newly installed transducer recorded a maximum slippage of the baseplate of 5mm. Based on the response spectrum ratio of the table acceleration, the actual excitation level was calculated to be about 0.85 MPR. After this test, it was decided to reinforce both the baseplate and the SG pad support joints.

The results of run 5 (0.2 MPR) and 8 (0.4 MPR) are discussed below as the typical cases of this stage.

Table motion: Due to repeated compensation runs, good table control accuracy was achieved in a period range of less than 0.1 second, as shown in Figure D.7.

Maximum response distribution: The maximum strain distribution of the hot leg pipe during runs 5 and 8 are illustrated in Figure D.8. A high plastic strain is observed in the axial strain at the upper half of the pipe in the vicinity of the cross-section HR3A.

Instantaneous response distribution: The instantaneous response distributions of the strain in the hot leg pipe and the SG displacement during runs 5 and 8 are shown in Figure D.9. The ratio of the strain values and the displacement values is the same as those of the preliminary test.

Transfer function: It is observed in run 8 (Figure D.10) that the predominant frequency is reduced and the peak is broadened compared with those of run 5 due to the increased plastic action.

Hysteresis loops: Figure D.11 shows the hysteresis loops of the shear force and the top relative displacement of the SG. The area of the hysteresis loops seems to be increased with the excitation level. Some additional damping due to the slippage of the baseplate may be included in these loops.

Time history response: Typical measuring points for runs 5 and 8 are shown in the time history plots (Figure D.12). It can be observed that all four segments of the input motion produced a similar peak response. Also, a drift is observed in some of the strain readings, particularly for the hoop strain at HR3B-BY.

Excitation level and maximum responses: The relationship of the maximum response values of selected measuring points are plotted against the peak velocity of the table motion in Figure 5.6. The same plots are shown for the predominant frequency and the equivalent damping ratio in Figures 5.7 and 5.8. Since the measured responses at higher excitation levels may contain the unexpected nonlinear effects due to the slippage of the baseplate, the results obtained in Part 2 should be used for comparing the analysis and test results. In Figure 5.6 (3), the maximum value of the shear force at the SG pin-support has a tendency to level off at higher excitation levels. It may be further evidence of the occurrence of slippage.

5.4 High Level Vibration Test Part 2

The high level excitation tests after the reinforcement of the SG support, i.e., runs 8** through 14' are included in this stage. The details of the reinforcement of the pad-support and baseplates are shown in Appendix E.

After the reinforcement of the test model, the time scale of the input motion was changed because the elastic frequency of the test model increased from 6.38Hz to 6.64Hz. The corresponding plastic frequency was estimated to be 5.8Hz compared with 5.35Hz which had been used before the reinforcement. Therefore, the new time interval, Δt, was calculated as,

$$\Delta t = 0.005 \text{ sec. x } 5.35\text{Hz}/5.8\text{Hz} = 0.004612 \text{ sec.}$$

The peak values of the input motion were changed as follows:

Acceleration: 1908.8 gal
Velocity: 75 cm/sec.
Displacement: 16.74 cm

After run 9 (0.75 MPR), slight bulging was observed on the top of the straight part of the hot leg pipe about a distance of one pipe diameter away from the elbow. After run 10 (1.0 MPR), the bulging was clearly recognized. However, no significant pressure drop was observed during the test. After run 11 (1.0 MPR), surface cracks were found at the upper part of the hot leg pipe, near the transition point of the straight and elbow parts. The maximum crack depth was 2.5mm and the maximum length was 15mm. These cracks were separated from each other, and some of them were too small to clearly recognize.

During the subsequent 1.0 MPR runs, the cracks grew and merged together to form a large crack. At the same time, the bulging seemed to stop growing as the crack growth continued. Only the first segment (A-segment) was used for the final run (No. 14') to avoid the possibility of any table damage due to pipe leakage or a catastrophic failure.

As the typical cases of this stage, the results of run 8** (0.4 MPR), run 11 (1.0 MPR) and run 14' (1.0 MPR; one-segment excitation) are discussed below.

Table motion: As described above, the time scale of the input motion was changed for run 8**. This run was used as the initial input for the following compensation process. Therefore, the motion of this run had a relatively large deviation from the target spectrum (Figure D.13). The iterative compensation was conducted in the following runs 9, 10 and 11, and good control accuracy was achieved in run 11. The input motion of run 11 was used for the subsequent runs 12, 13 and 14' without compensation.

<u>Maximum response distribution</u>: The maximum strain distributions of the hot leg pipe are illustrated in Figure D.14 for runs 8**, 11 and 14'. There is no significant difference in the strain distribution between these three runs. The highest measured strain of 2.28% occurred during the run 11 at the top of the cross section HR3A.

<u>Instantaneous response distribution</u>: The instantaneous response distribution of the strain in the hot leg pipe and the SG relative displacement are shown in Figure D.15 for runs 8** and 11. It can be observed that there is no significant change in the ratio from the previous runs.

<u>Transfer function</u>: The transfer functions of the SG top acceleration to the table acceleration are shown in Figure D.16. The peak of run 8** (0.4 MPR) shows that the natural frequency of the test model slightly increased due to the reinforcement. Also, the peaks of runs 11 and 14' are broadened considerably due to the plastic action.

<u>Hysteresis loops</u>: A comparison of Figures D.11 (2) and D.17 (1) for the 0.4 MPR runs indicates that the shape of the hysteresis loops of the shear force and the top relative displacement of the SG are quite similar, but the peak shear force increased after the reinforcement.

<u>Time history response</u>: Figure D.18 shows time history responses of typical measuring points for runs 8**, 11 and 14'. The time history of the strain in the hot leg pipe at HR3A-BX in run 11 produced the highest strain of 2.28% in compression, and the strain response reduced suddenly after recording this peak. The inspection after this run showed that one of the cracks was located 3.5mm from the strain gage HR3A-BX and it might have caused de-bonding of the gage. Also, a significant drift or ratchetting is observed in the responses of HR3B-BY (hoop strain). This gage is the closest to the peak of the bulge near the hot leg elbow.

<u>Excitation level and maximum responses</u>: The maximum response values of the SG responses and the strains in the hot leg pipe are plotted against the peak velocity of the vibration table in Figure 5.9. It can be seen from Figure 5.9 (3) that the measured value of the shear force at the SG pin-connection is considerably higher than those from the Part 1 tests and analytical values. Figures 5.10 and 5.11 show some plots for the predominant frequency and the equivalent damping ratio calculated from the hysteresis loops.

The maximum test responses that were recorded after run 4, run 8** and run 11 are listed in Table 5.4.

5.5 Inspection results

5.5.1 Dimension of the Test Model

In order to evaluate the amount of permanent deformation of the test model during the HLVT runs, some dimensions of the test model were measured. The procedure and results are shown below. The figures and tables pertaining to this discussion are included in Appendix F.

As-built test model location: Figure F.1 shows the as-built test model location (plane location). Dimensional measurements were conducted 3 times (just after the modification, just after the SG support reinforcement and after completion of the HLVT runs). The results of these measurements were essentially the same.

Relative Movement of the Test Model: Reference points were marked on the test model and the support frame structure to measure the relative movement due to dynamic testing. The distance between two points was measured 3 times (just after the modification, just after the SG support reinforcement and after completion of the HLVT runs) by using a measuring tape. Figures F.2 through F.5 show the measured points and Tables F.1 through F.11 show the results of the measurements.

From the results of the measurements as shown in Figures F.6 and F.7 the following conclusions were drawn: 1) the top of the SG moved toward the opposite side of RV nozzle in the X-direction and toward the opposite side of the RCP in the Y-direction, 2) there was no other remarkable change other than the aforesaid.

5.5.2 Piping Diameter and Circumference

In order to evaluate the amount of plastic deformation in the piping, the diameter and the circumference of the piping were measured. The procedure and results are shown below.

Method of measurement: The outside diameter was measured by using a micrometer. Circumferential length was measured by using a wire.

Time and item measurement: The time and item of measurement are shown in Table F.12 and the measurement locations are shown in Figures F.8 through F.10. Additional measurements were made on the swelling location of the hot leg pipe after completion of the HLVT as shown in Figure F.11.

Results of measurements: Results of the measurements are shown in Tables F.13 and F.14. A visible change in the pipe diameter was observed on the hot leg straight pipe. The maximum increase in the circumferential length of that portion was measured to be about 1%. The dimensional changes in the swelling portion of the pipe are shown in Figures F.12 and F.13.

The records show that the diameter and circumferential length of H' became unexpectedly larger after Run 9. Judging from the data of adjacent locations of H' such as G' and F', whose records did not show such a change, the diameter and circumferential length of H' probably did not become larger, but may have been measured at the incorrect point and circumference. The strain and circumferential length of H' are shown in Figure F.14. There were no large strains such as to produce the plastic deformation.

Accuracy of measurement: The document "The Accuracy of Measurement of Component Location" (ZKS-A036 Rev. 0) refers to the accuracy of the measurements. The resultant accuracy is summarized as follows;

	Accuracy referred in the document (ZKS - A036)	Resultant accuracy assumed	Reason
1	The diameter of the pipe measurement; within 0.06mm	within 0.5mm	(i) The top of anvil and spindle of outside micrometer used at HLVT was not pin-shaped but thick and flat. (ii) The surface of the pipe was not ideal plane. These made it difficult to set the anvil and spindle of the outside micrometer on 2 reference points on the pipe in the complete same manner, and caused the error.
2	The circumferential length of the pipe measurement; within 1mm	within 2mm	(i) The length of wire varied with the tension force. (ii) On measuring the circumferential length the wire was wound around the circumference of the pipe and the wire was set on 4 reference points marked on the pipe. When the wire was set on 4 reference points again, it could not be set precisely on the same circumference of the pipe as before.

5.5.3 Crack Propagation

Figure 5.12 illustrates the observed size of the crack after each excitation run. The crack depth measured by the Electro-Resistance Method is shown in Figure 5.13. The crack depth was also measured by directly installing a thin piano wire into the crack. It showed the crack depth was more than about 24mm.

Note that the results of the crack depth measurements were obtained as the ratio of the crack depth to the thickness of the pipe wall, and the measured results in Figure 5.12 and 5.13 are shown as the percentage of the crack depth to the wall thickness. The crack growth process and the final crack profile are illustrated in Figure 5.14.

5.5.4 Cumulative Strain and Displacement

The cumulative strain distribution of the hot leg pipe is shown in Figure D.19. Relatively large cumulative strains were observed at both the top of the elbow side and the bottom of the RV side of the hot leg straight piping.

The cumulative displacement of the SG top is shown in Figure D-20. After the reinforcement, the SG moved gradually toward the opposite side of the RV.

5.6 Evaluation of Test Results

5.6.1 Behavior of Test Model Under Earthquake Response

1) Dynamic Characteristics

The predominant vibration mode of the test model, as illustrated in Figure 5.5, represents a rigid body-like rotation of the SG around the pin-support. The damping ratio and vibration frequency regarding this particular mode are studied below.

Figure 5.15 illustrates the estimation of the transfer function (SG top displacement/table acceleration) natural frequency and the damping ratio using the AR method during runs 4, 8** and 11. In this calculation, the entire four-segment records are used for the numerical processing.

Figure 5.16 compares the damping ratios obtained by the AR method and those calculated from the hysteresis loops. These results indicate that the damping values calculated from the hysteresis loops are much higher than those obtained by the AR methods using the entire time history data. The above difference is clearly illustrated by the time history of plastic strain energy in Figure 5.17. The plastic energy increases at the predominant part of the response, and the equivalent damping was calculated using the hysteresis loops at this portion of the response.

Therefore, the damping ratio of 0.86% measured in the elastic region (sinusoidal excitation) should be compared with those estimated by the AR transfer function, and the equivalent damping ratio calculated from hysteresis loops may be regarded as a measure of the energy consumption due to plastic deformation.

Figure 5.18 shows comparisons of natural frequencies evaluated by the transfer functions using the FFT method and the AR method. The natural frequencies evaluated by both the methods agree well.

In order to investigate the frequency content of the response, the vibration period of the displacement time history at top of the SG was measured, as shown in Figure 5.19. The results show that the frequency at the predominant part of the response decreased when the excitation level increased. On the other hand, the frequency at the free vibration part of the response seems to be constant. Generally, the transient response of the structure consists of the natural frequency component excited by the shock input and the forced vibration component which has the same frequency as the input motion. In the case of the HLVT, it is found that the predominant component of the response changes from the free vibration component to the forced vibration component when the excitation level increased.

2) Relationship between input level and peak responses

The peak SG top displacement and acceleration are plotted against the input peak velocity for all runs in Figures 5.20 and 5.21. The acceleration responses tend to level off at higher excitations, and the corresponding response magnification factor reduces as the equivalent damping ratio increases.

Figure 5.22 shows the same plots for the peak strain values of the hot leg pipe. At locations where higher strain values are recorded, a significant plastic strain increase is observed at the higher excitation level, indicating the development of a localized concentration of plasticity.

5.6.2 Estimation of Member Force

Force and moment acting on the piping were estimated from measured strains as described in Appendix G. The strain distribution was assumed to be that of an elastic uniform beam, and Young's modulus normally used for design (E=1.99 x 10^4kg/mm^2) was assumed. The estimated member forces for typical test cases are shown in Table 5.5. The instantaneous strain distribution when the SG top achieved its maximum displacement was used for the estimation.

The results show that the estimated member forces in different cross sections of the hot leg in the elastic run (run 4:0.1MPR) agree well with each other and these values seem to be reliable. On the other hand, the estimated values become very large in the plastic runs (Runs 8** and 11) due to the local plastic strain at cross sections HR1 and HR3C. Because of the assumption of an elastic strain distribution, it is difficult to estimate the member forces in the plastic runs quantitatively. More refined analysis is required to better estimate the member forces in the plastic runs.

5.6.3 Fatigue Damage

The fatigue usage factor was evaluated using the strain measurements and the following procedure. The axial stress was estimated by

$$\sigma_x = \frac{E}{1-\nu^2} K \cdot (\varepsilon_x + \nu \varepsilon_y) \tag{5.2}$$

where

σ_x: Axial Stress
ε_x: Axial Strain (measured strain at HR3A - BX)
ε_y: Hoop Strain (measured strain at HR3A - BY)
ν: Poisson Ratio (=0.5)
E: Young's modulus ratio (=1.99 x 10^4 kg/mm^2)

The K-value in the above equation represents the ratio of the actual strain at the crack location to the measured strain. This value was assumed to be K = 1.35 as described in Appendix H.

The stress amplitude and number of stress cycles were determined using the rain flow method. The fatigue damage factor was evaluated as

$$D_j = \sum_{i=1}^{k} \frac{n_i}{N_i}$$

where,

D_j: Fatigue damage factor at run j
N_i: Fatigue life at stress level i
n_i: Equivalent number of stress cycles at level i
k : Number of divisions of stress level (=64)

As illustrated in Figure 5.23, three fatigue strength curves were used.

The calculated fatigue damage factors are given in Table 5.6. Using the fatigue curve obtained from the post-test examination data, the fatigue usage factor exceeds 1.0 during run 14'. During that test the crack almost penetrated the pipe wall. Using the design fatigue curve, the final damage value was calculated to be 3.8, indicating the conservative estimate of fatigue life in the design formulation.

It is known that ratchet strain is one of the major factors affecting the failure mechanism of pressurized piping. In the HLVT test, the total accumulated ratchet strain was 2 to 3% (after run 11) compared to the ultimate elongation of the material of about 40%. Therefore, ratchetting does not appear to be a major factor for the HLVT. Based on the above evaluation, it can be judged that the failure of the test model was mainly due to low-cycle fatigue damage under high-amplitude loading reversals.

5.6.4 Evaluation of the Safety Margin

The safety margin for the HLVT model can be expressed in the following form:

Safety Margin = A/B

where,

A = The maximum base input acceleration level which was withstood during the test without collapse.

B = The allowable base input acceleration level using Class 1 piping stress limits.

The criteria for piping systems is based on ASME Section III. The evaluation of the primary stress is as follows:

$$S = \frac{B_1 P D_\theta}{2t} + \frac{B_2 D_\theta M_1}{2I} \leq 3Sm$$

where

B_1, B_2 = Stress Indices
P = Pressure
D_θ = Outside pipe diameter
t = Wall thickness
I = Moment of inertia
M_1 = Resultant moment due to dead weight and seismic loading
$3Sm$ = Allowable stress for SSE earthquake loading

The allowable stress limit for primary stress is 3Sm. The primary stress consists of dead weight, pressure and seismic stresses. For the piping of the HLVT model, $3Sm = 42kg/mm^2$, the pressure stress = 4.8 kg/mm^2 and the dead weight stress = 0.1 kg/mm^2. Therefore, the maximum allowable seismic stress is found to be 37.1kg/mm^2.

Linear elastic time history analysis was performed on the HLVT model using the same input wave as the test. The allowable base input loading for the seismic stress (37.1kg/mm^2) was obtained by scaling the input wave for the HLVT. The fatigue usage for the allowable base input was also estimated.

The calculated results are summarized below:

1) The maximum base input loading confirmed during the test
   (A)........ 1895 gal

2) The maximum allowable base input loading (B)........ 240 gal

3) The fatigue usage factor for the allowable base input motion was found to be 0.2; therefore, it was confirmed that at this level the primary stress limits of the code would control rather than fatigue.

4) Based on (1) and (2), it is estimated that the safety margin is (A)/(B) = 7.9.

In summary, it was found that the current code allowable level based upon linear elastic analysis is approximately 8 times less than the maximum test level.

Table 5.1
Test Procedures

Run No.	Contents	Notes
Run 2	0.075 MPR	Runs 2 through 4 were performed as a series of interactive compensation excitations. Target level was set as 0.10 MPR and excitation gain was adjusted properly to increase table acceleration gradually. The transfer function of the vibration table measured during the proving test phase 2 was employed for table control.
Run 3	0.10 MPR	
Run 4	0.10 MPR	
-	Measurement of the transfer function of the vibration table.	Excitation level was set as large as possible keeping the response of the test model within the elastic region.
-	Discussion of data	Review data of Runs 2 through 4 and determine excitation wave for elastic-plastic excitation (after run 5).
Run 5	0.20 MPR	Runs 5 through 8 were performed following the same procedure as those of Runs 1 through 4 (i.e., interactive compensation with target level 0.40 MPR and increase excitation level gradually).
Run 6	0.30 MPR	
Run 7	0.35 MPR	
Run 8	0.40 MPR	
-	Discussion of data	Review data of Runs 5 through 8 and determine excitation level of Runs 9' and 9*'.
Run 9'	0.60 MPR	Compensated input wave run achieved in Run 8 was scaled-up and only first one segment was applied.
9*'	0.80 MPR	
-	Discussion of data	Review data of Runs 9'and 9*' and determine excitation level of Run 10'.
-	0.05 MPR	Compensated input wave achieved in Run 8 was scaled-down and only first one segment was applied at 0.05 MPR.
Run 10'	1.0 MPR	Compensated input wave achieved in Run 8 was scaled-up and excited at 1.0 MPR. Only first one segment was applied.

Table 5.1 - Continued
Test Procedures

Run No.	Contents	Notes
—		Reinforcement of the model and restoration of the instruments.
Run 8*	0.4 MPR	The same input wave of Run 8 was employed and excited at 0.4 MPR.
Run 8**	0.4 MPR (revised time scale)	The time scale of input wave was changed and excited at 0.4 MPR
—	0.05 MPR	Compensated input wave achieved in Run 8 was scaled-down and only first one segment was excited at 0.05 MPR.
Run 9 Run 10	0.75 MPR 1.0 MPR	Input wave of Run 8** was scaled-up and excited at 0.75 and 1.0 MPR.
—	Discussion of data	Review data of Runs 9 and 10.
Run 11	1.0 MPR (2nd run)	Same as Run 10.
—	Inspection of the crack	
Run 12	1.0 MPR (3rd run)	Same as Run 10.
Run 13	1.0 MPR (4th run)	Same as Run 10.
Run 14'	1.0 MPR (5th run)	Same as Run 10, but only first one segment was applied.
—	Discussion of data	Review all data and decide to finish the test.
—	Inspection of the test model	

Table 5.2 Detail of Each Run

Run No.	Input Wave	Direction	Peak Acceleration (gal)	Note
	Tapping Test	X		f = 6.84Hz, h = 0.5-0.9% (X-direction)
	Tapping Test	Y		f = 3.13Hz, h = 0.7-1.0% (Y-direction)
	Sine Wave	X	50	Warming-up test to check polarity of censors
	Sine Wave	V	50	"
	Pink Noise	X	50	Trial Random Test to determine excitation level
	"	V	25	"
	"	P	40	"("P" represents pitching motion)
	"	X	250	Random tests to obtain transfer functions (repeated 8 times)
	"	V	100	"
	"	P	150	"
	Sine Wave	X	10	Preliminary Sinusoidal Test, f = 2-7.8Hz, Δf = 0.05
	"	V	20	"
	"	P	10	"
	Sine Wave	X	10	Sine Sweep Test, f = 2-7.8Hz, Δf = 0.2Hz
	Sine Wave	X	10	Sine Sweep Test, f = 7.8-15.6Hz, Δf = 0.2Hz
	"	X	10	Sine Sweep Test, f = 15.6-30Hz, Δf = 0.2Hz
	"	X	10	Sine Sweep Test, f = 2-7.8Hz, Δf = 0.05Hz
1	AAAA, 0.05MPR	X	99	f = 6.38Hz, h = 0.86% (X-direction)
	"	X	97	f = 3.15Hz, (Y-direction) U_x = 4.9mm, U_y = 0.5mm (S/G), ε_{max} = 0.076% Input signal was compensated to improvie table motion
1*	ABCD, 0.05MPR	X	103	"
	"	X	-97	U_x = 5.3mm, U_y = 0.6mm (S/G), ε_{max} = 0.083%
	"	X	93	Input signal was compensated to improve table motion
2	ABCD, 0.075MPR	X	97	"
3	ABC, 0.1MPR	X	150	U_x = 7.6mm, U_y = 0.9mm, ε_{max} = 0.12%
		X	185	U_x = 10.1mm, U_y = 1.0mm, ε_{max} = 0.3% Trip triggered after Segement C by strain at 153X (0.2%)

Table 5.2 Detail of Each Run

Run No.	Input Wave	Direction	Peak Acceleration (gal)	Note
4	ABCD, 0.1MPR	X	185	High Strains at pads
	Pink Noise	V	200	Random test to obtain transfer function of table (8 times)
5	ABCD, 0.2MPR	X	390	$Ux = 19.9mm$, $Uy = 2.5mm$, $\varepsilon_{max} = 0.58\%$ Negative strain drift of 0.25% at 153X
6	ABCD, 0.3MPR (0.4MPR)	X	705	$Ux = 30.0mm$, $Uy = 5.0mm$, $\varepsilon_{max} = 0.73\%$ Table motion was not compensated. Actual MPR-0.4
7	ABCD, 0.35MPR	X	741	$Ux = 30.0mm$, $Uy = 5.5mm$, $\varepsilon_{max} = 0.55\%$
8	ABCD, 0.4MPR	X	816	$Ux = 31.9mm$, $Uy = 6.1mm$, $\varepsilon_{max} = 0.59\%$
	A, 0.05MPR	X	89	Low-level excitation to obtain elastic frequency (6.38Hz)
9	A, 0.6MPR	X	1250	$Ux = 45.2mm$, $Uy = 7.6mm$, ε_{max} 0.83% Banging noise occurred inside frame. Source unknown
9*	A, 0.8MPR (0.71 MPR)	X	1850	$Ux = 59.5mm$, Uy 9.6mm, $\varepsilon_{max} = 1.2\%$ Banging noise attributed to slippage of base plate supporting SG/pin. Pre-tension was increased
	A, 0.05MPR	X	89	Low-level excitation to obtain elastic frequency (6.38Hz)
10'	A, 1.0MPR (0.87 MPR)	X	2350	$Ux = 68.2mm$, $Uy = 13.6mm$, $\varepsilon_{max} = 1.48\%$ Big banging noise due to slippage of base-plate of 5mm. Strain at pads increased significantly. Ratcheting hoop strain observed at 143Y.
	AFTER RUN-10' BOTH BASEPLATE AND PADS WERE REINFORCED			
8*	ABCD, 0.4MPR	X	829	Repeat Run 8 Frequency of model changed to 6.54Hz
8**	ABCD, 0.4MPR (0.43MPR)	X	1099	using new $\Delta t = 0.004612sec$ (will use this afterwards) $Ux = 38.7mm$, $Uy = 3.9mm$, $\varepsilon_{max} = 0.78\%$

Table 5.2   Detail of Each Run

Run No.	Input Wave	Direction	Peak Acceleration (gal)	Note
	A, 0.05MPR	X	89	Low-level excitation to obtain elastic frequency (6.64Hz)
9	ABCD, 0.75MPR (0.67MPR)	X	1786	Ux = 55mm, Uy = 9.5mm. Gages at 153X, Y were damaged due to temperature increase
10	ABCD, 1.0 MPR (0.87MPR)	X	2420	Ux = 70.9mm, Uy = 12.3mm. Bulging observed at top of hot-leg pipe about 0.5D from elbow
11	ABCD, 1.0MPR (0.95MPR)	X	2431	Ux = 75.7mm, Uy = 14.4mm, ϵ_{max} = 2.28% (153X) Gages 153, 144, 148 were damaged after recording Segment-A. Bulging at 143Y more clear (0.6%). Cracks found at transition of straight and elbow parts of hot let. (maximum depth 2.5mm)
12	ABCD, 1.0MPR (0.95MPR)	X	2431	Repeat Run 11 Cracks grow (depth 5mm)
13	ABCD, 1.0MPR	X	2431	Repeat Run 11 Three major cracks form (depth 15mm)
14'	A, 1.0MPR	X	2431	Final test. Crack depth reached 27-30mm (wall thickness is about 32mm)

Table 5.3　Test Condition of Earthquake Wave Excitation

Run No.	Target excitation level		Excitation wave		Note
	MPR	Acceleration (gal)	Four segment (A+B+ C+D)	One segment (A)	
Run 2	0.075	133	◯		
Run 4	0.1	177	◯		
Run 5	0.2	354	◯		
Run 6	0.3	532	◯		
Run 7	0.35	620	◯		
Run 8	0.4	709	◯		
Run 9'	0.6	1063		◯	
Run 9'*	0.8	1489		◯	
Run 10'	1.0	1772		◯	
Run 8*	0.4	709	◯		
Run 8**	0.4	758	◯		Time scale was shifted
Run 9	0.75	1421	◯		↑
Run 10	1.0	1895	◯		↑
Run 11	1.0	1895	◯		↑
Run 12	1.0	1895	◯		↑
Run 13	1.0	1895	◯		↑
Run 14'	1.0	1895		◯	↑

Table 5.4 Maximum Test Response (A-Segment)

	RUN 4 (0.1 MPR)	RUN 8** (0.4 MPR)	RUN 11 (1.0 MPR)
Top of SG			
Ux (cm)	0.95	3.88	7.64
Uy (cm)	0.14	0.92	3.04
Ax (cm)	1630	5470	7280
Ay (cm)	212	510	600
Top of RCP			
Ux (cm)	0.021	0.076	0.104
Uy (cm)	0.011	0.04	0.05
Ax (gal)	395	1610	3800
Ay (gal)	175	825	1230
SG Pin Support			
Fx (ton)	7.0	254	402
Fz (ton)	9.0	90	152
Mx (ton-m)	0.16	3.68	6.14
RCP Snubbers			
83x (ton)	2.66	13.5	23.7
84x (ton)	1.15	6.6	11.6

Strain in Piping (%)*

		RUN 4 (0.1 MPR)	RUN 8** (0.4 MPR)	RUN 11 (1.0 MPR)
Hot Leg at RV-end	(135X)	0.078	0.39	1.18
	(135Y)	0.006	0.026	0.08
Hot Leg at Tapered Joint	(153X)	0.153	0.78	2.28
	(153Y)	0.038	0.19	0.34
Hot leg at Elbow	(207X)	0.10	0.39	0.78
	(207Y)	0.059	0.22	0.37
Crossover Leg at SG-end	(Axial)	0.02	0.08	0.14
	(Hoop)	0.01	0.035	0.06

*X-axial strain, Y-hoop strain

Table 5.5   Estimated Member Force

Location	Cross Section		RUN 4 (0.1 MPR)	RUN 8** (0.4 MPR)	RUN 11 (1.0 MPR)
Hot Leg	HR1	Fx	- 154.642	818.907	- 2280.910
		My	23.086	- 116.020	307.069
		Mz	- 1.778	1.494	5.383
	HR3C	Fx	- 141.906	880.179	- 2011.125
		My	-20.483	100.278	- 214.869
		Mz	2.718	- 9.778	- 17.482
	HR5	Fx	-150.679	566.325	- 637.928
		My	- 18.047	33.655	14.703
		Mz	4.809	- 6.820	- 5.317
Cross Over Leg	XR3	Fx	14.197	- 52.118.	92.910
		Fy	21.376	- 61.734	82.153
		Fz	8.455	- 35.653	- 67.239
		Mx	1.355	-2.453	1.650
		My	4.178	- 15.349	22.875
		Mz	- 11.599	39.761	- 74.047
	XR9	Fx	- 5.241	- 20.282	36.234
		My	- 1.578	- 5.561	- 10.483
		Mz	6.049	22.394	43.210
Cold Leg	CR1	Fx	4.886	- 14.809	35.955
		My	- 1.324	3.365	- 4.842
		Mz	3.756	- 9.966	13.255
	CR3	Fx	4.351	- 17.817	41.603
		My	0.619	- 1.720	2.065
		Mz	- 1.622	3.763	- 4.421
S/G Inartial Force		Fx	47.1	-156.8	171.4
Support Leg		Fx	12.0	249.6	- 404.4
		Fz	9.9	87.3	139.0
		Mx	0.2	3.9	6.0

UNIT :   Force   : Ton

Moment : Ton·m

Table 5.6   Fatigue Damage Calculation

Fatigue Curve / Run	Design		ASME best-fit		Post-test Exam	
	U.F.	Total	U.F.	Total	U.F.	Total
2	0.015	0.015	0.000	0.000	0.000	0.000
3	0.013	0.028	0.000	0.000	0.000	0.000
4	0.025	0.053	0.000	0.000	0.000	0.000
5	0.077	0.130	0.003	0.003	0.001	0.001
6	0.032	0.162	0.001	0.004	0.001	0.002
7	0.088	0.250	0.004	0.008	0.003	0.005
8	0.096	0.346	0.005	0.013	0.005	0.010
9'	0.007	0.353	0.000	0.013	0.000	0.010
9''	0.066	0.419	0.006	0.019	0.008	0.018
10'	0.115	0.534	0.013	0.032	0.042	0.060
8 *	0.187	0.721	0.012	0.044	0.014	0.074
8 **	0.101	0.822	0.006	0.050	0.005	0.079
9	0.471	1.293	0.040	0.090	0.074	0.153
10	0.467	1.760	0.042	0.132	0.094	0.247
11	0.629	2.389	0.099	0.231	0.244	0.491
12	0.629	3.018	0.099	0.330	0.244	0.735
13	0.629	3.647	0.099	0.429	0.244	0.979
14'	0.157	3.804	0.025	0.454	0.061	1.040

excitation level

1.0MPR

Note : Prime (')denotes
one segment
wave excitation

run	level	
run 2	(0.075MPR)	
run 3	(0.10MPR)	
run 4	(0.10MPR)	
run 5	(0.20MPR)	
run 6	(0.30MPR)	
run 7	(0.35MPR)	
run 8	(0.40MPR)	
run 9'	(0.60MPR)	
run 9*'	(0.80MPR)	
	(0.05MPR)	
run 10'	(1.0MPR)	

preliminary
test

high level
vibration
test part 1

◁ Reinforcement

run	level
run 8*	(0.4MPR)
run 8**	$\left(\begin{array}{c}\text{frequency}\\\text{shifted}\\\text{0.4MPR}\end{array}\right)$
	(0.05MPR)
run 9	(0.75MPR)
run 10	$\left(\begin{array}{c}\text{1.0MPR}\\\text{1st run}\end{array}\right)$
run 11	$\left(\begin{array}{c}\text{1.0MPR}\\\text{2nd run}\end{array}\right)$
run 12	$\left(\begin{array}{c}\text{1.0MPR}\\\text{3nd run}\end{array}\right)$
run 13	$\left(\begin{array}{c}\text{1.0MPR}\\\text{4th run}\end{array}\right)$
run 14'	$\left(\begin{array}{c}\text{1.0MPR}\\\text{5th run}\end{array}\right)$

high level
vibration
test part 2

Figure 5.1 Test Procedure

5-25

Figure 5.2 Frequency Response of Table Acceleration

Displacement of S/G top X-direction

Displacement of S/G top Y-direction
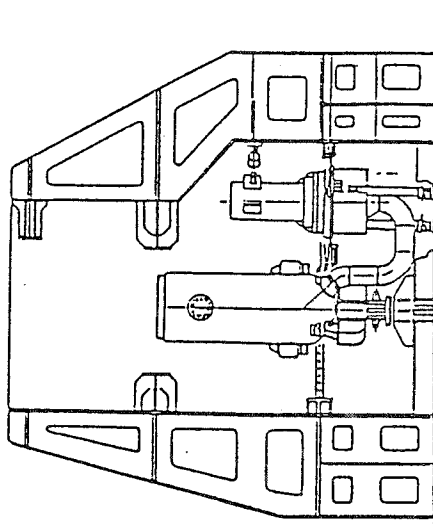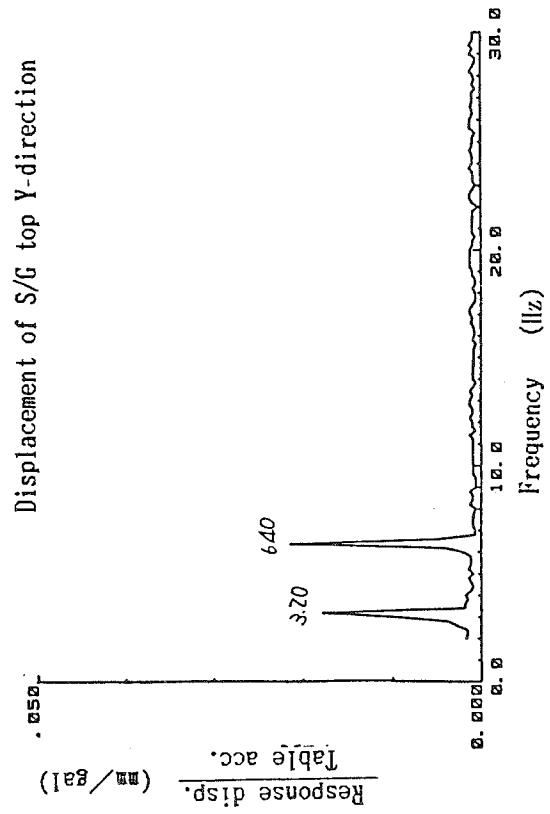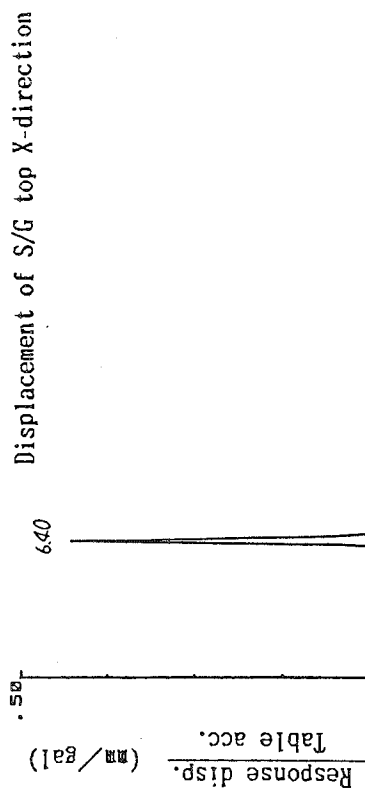
Figure 5.3 (1) Transfer Function (Displacement)
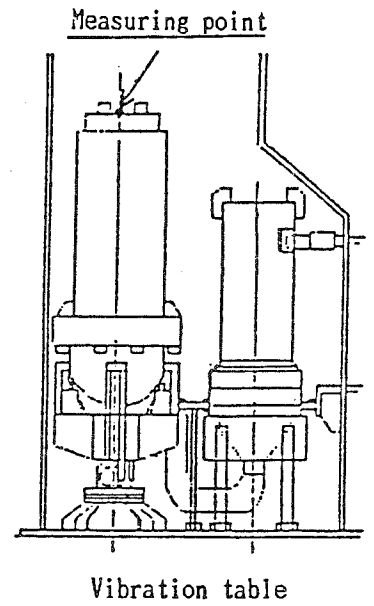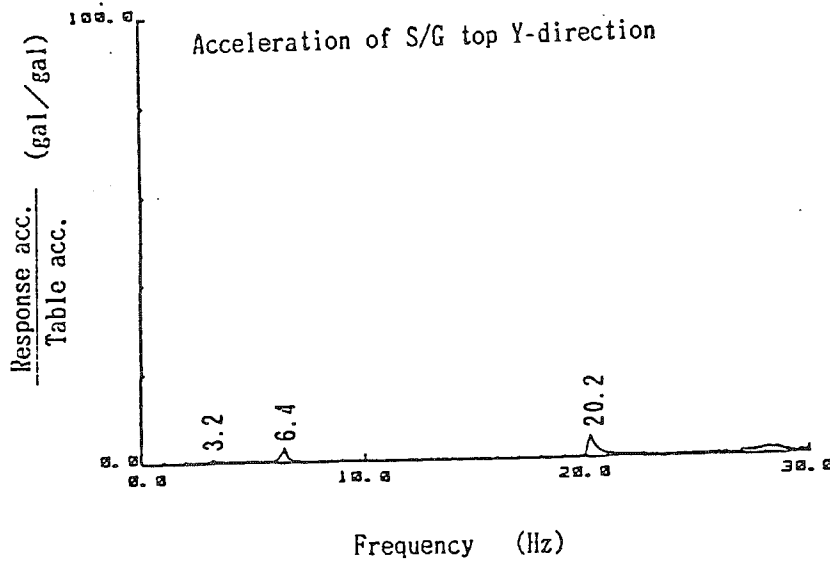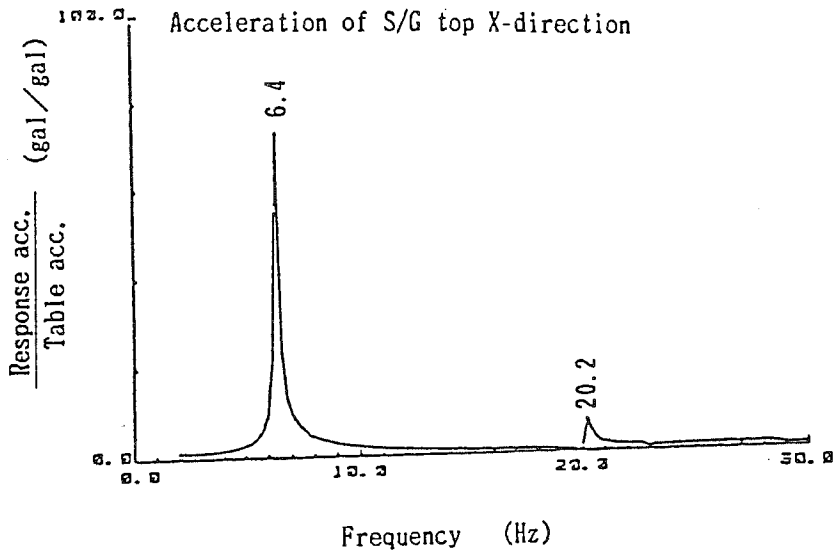
Figure 5.3 (2) Transfer Function (Acceleration)
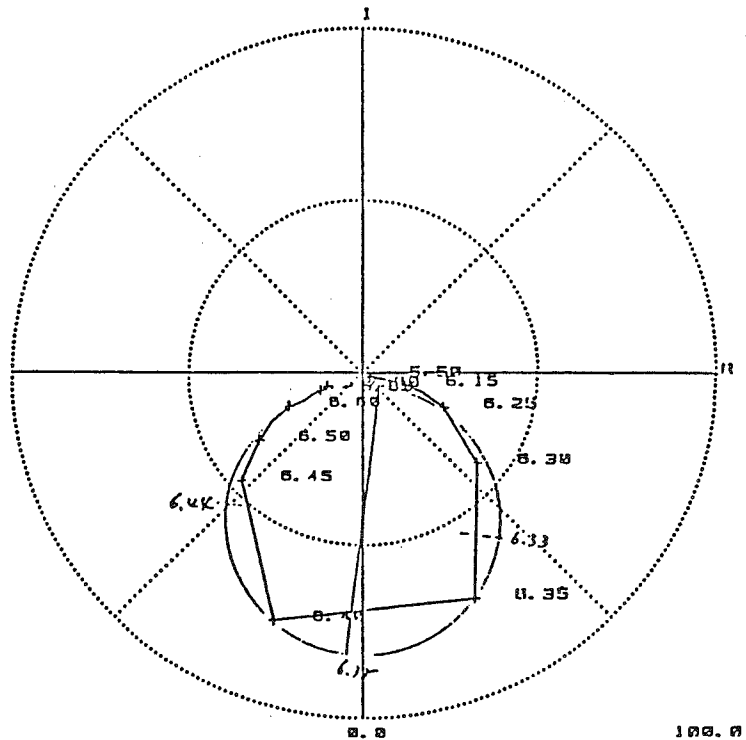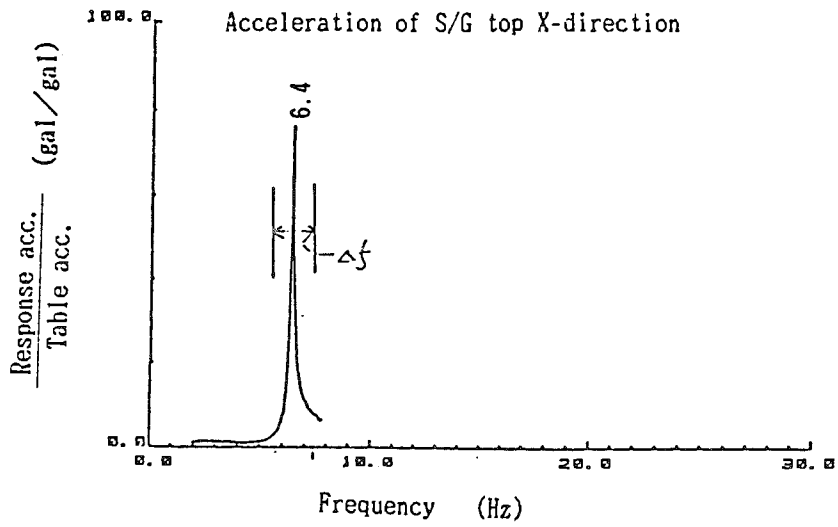
$$\text{Modal damping ratio} ; h = \frac{6.44 - 6.33}{2 \times 6.38} \times 100 = 0.86\%$$

Figure 5.4 Transfer Function (Nyquist Diagram)
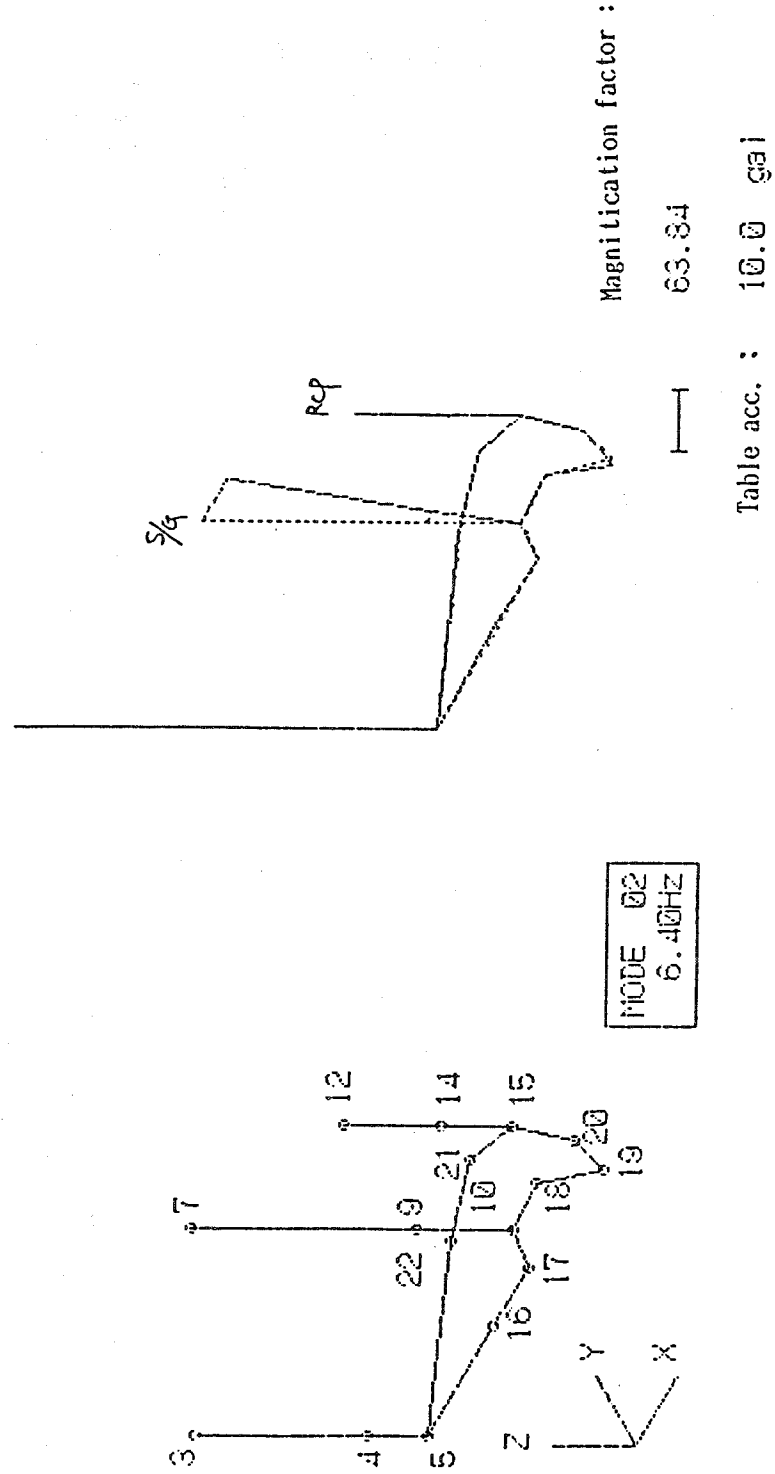
Figure 5.5 Vibration Mode Shape

○: X-direction
△: Y-diruction
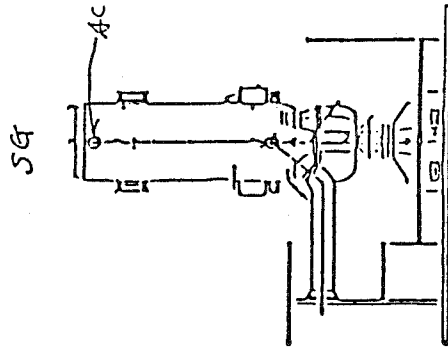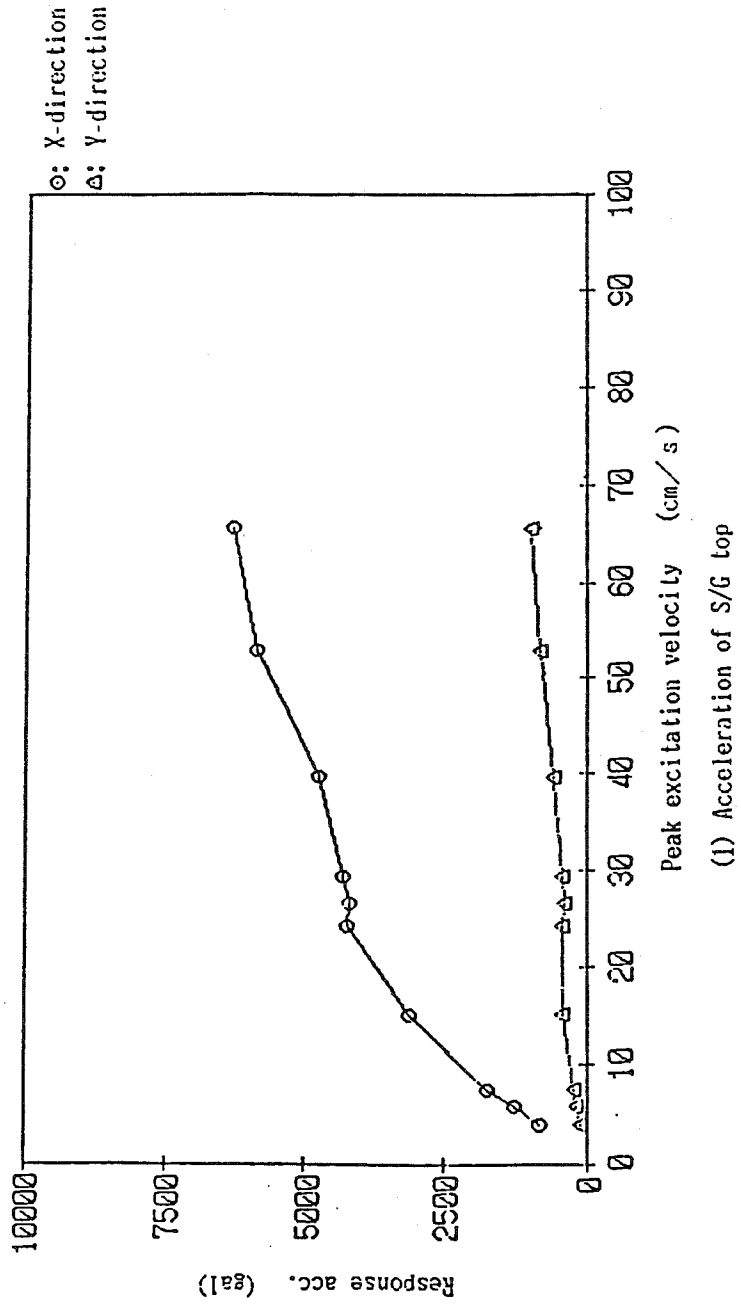
Figure 5.6 (1) Maximum Response Versus Excitation Level
(Acceleration)

(1) Acceleration of S/G top

Peak excitation velocity (cm/s)

Response acc. (gal)
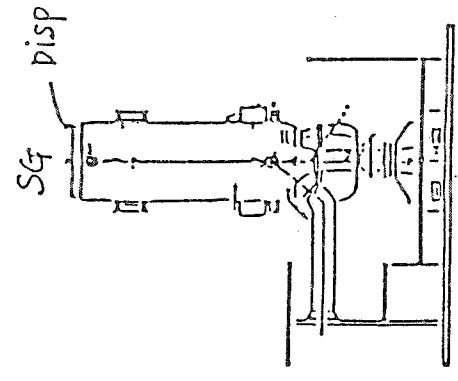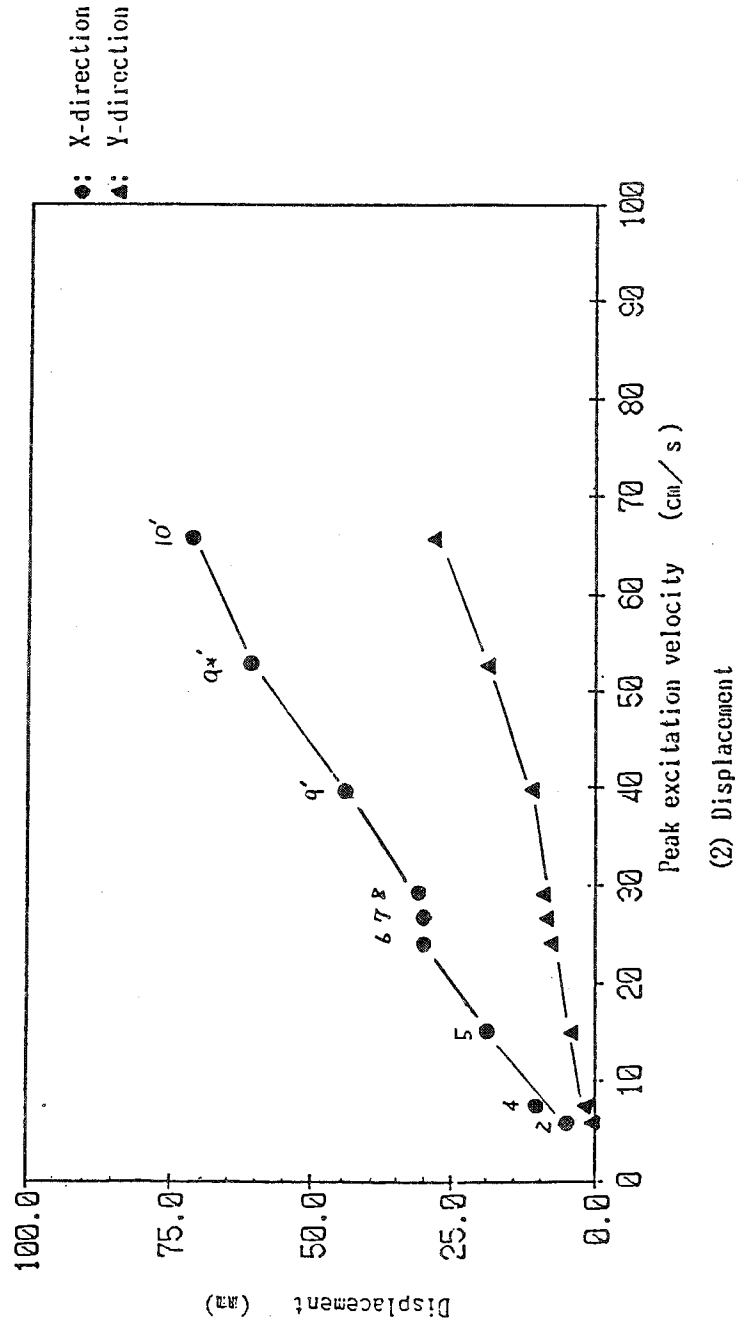
(2) Displacement

Figure 5.6 (2)   Maximum Response Versus Excitation Level
(Displacement)

O : Shear force
△ : Vertical force

Force (ton)

Peak excitation velocity (cm/s)

(3) Reaction force of S/G support
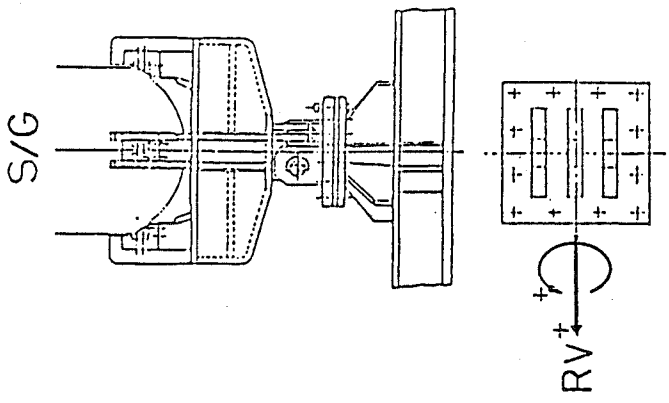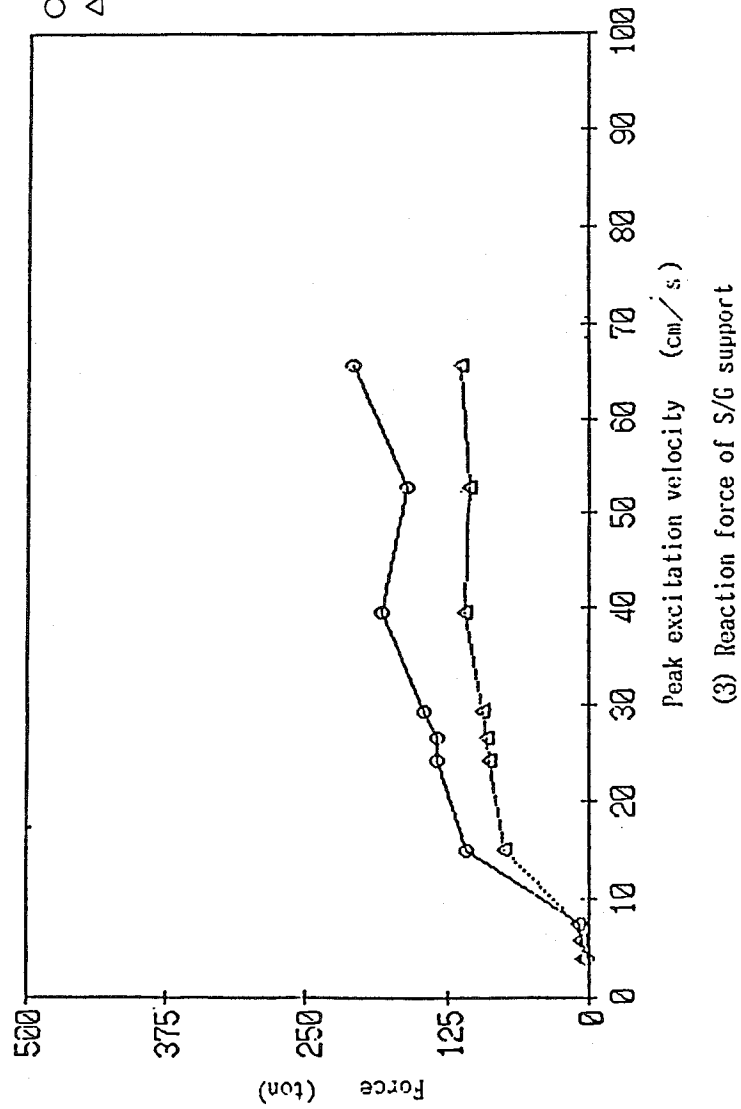
Figure 5.6 (3) Maximum Response Versus Excitation Level
(Force at SG Pin)

5-33
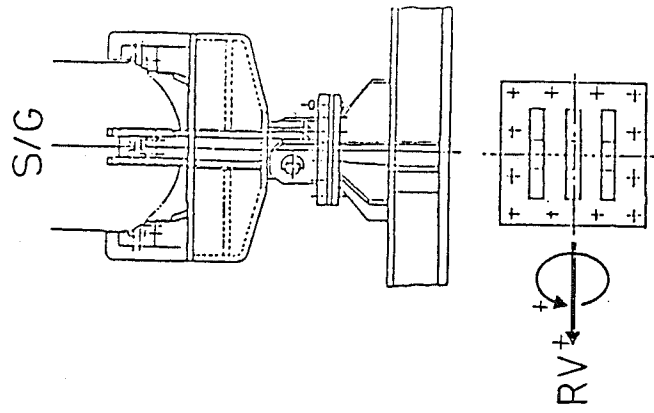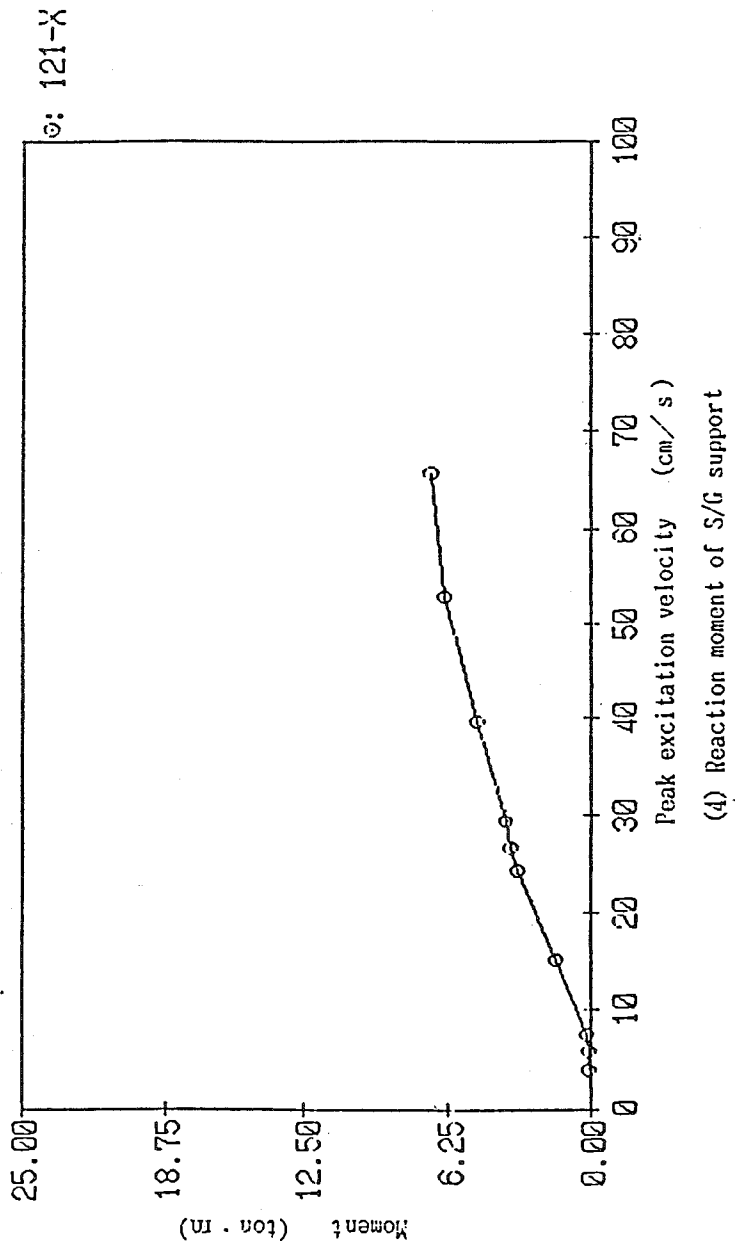
Figure 5.6 (4)   Maximum Response Versus Excitation Level
(Moment at SG Pin)
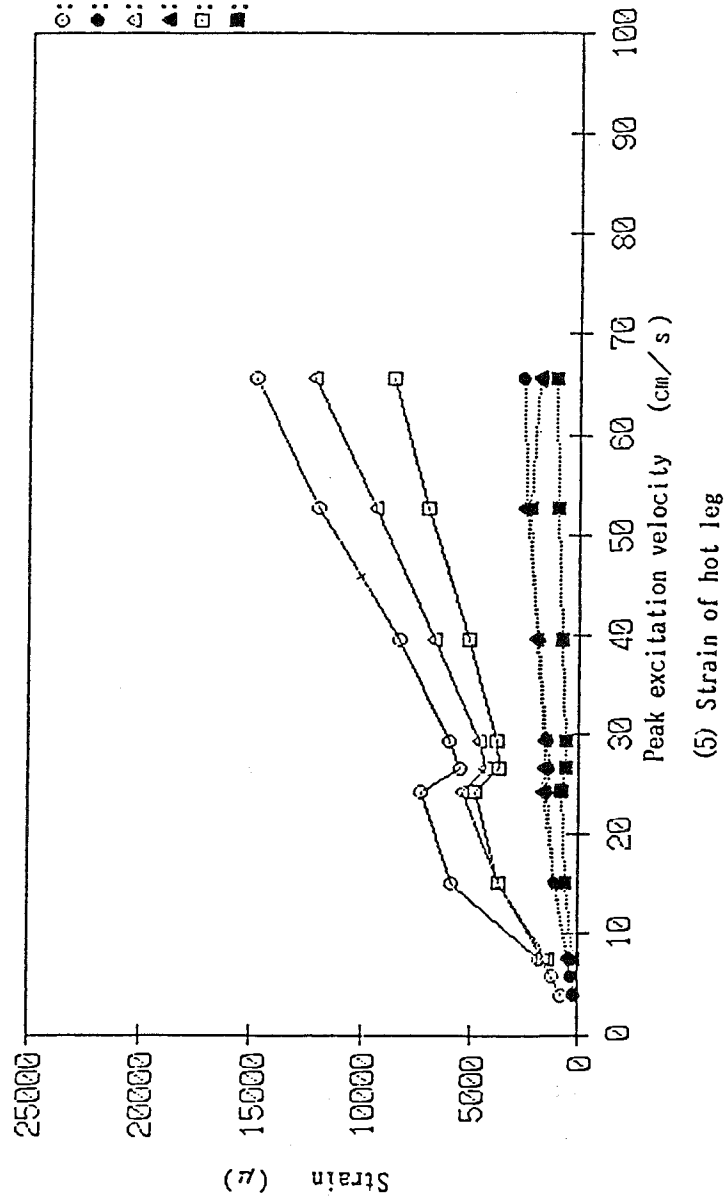
Figure 5.6 (5)   Maximum Response Versus Excitation Level
(Strain)
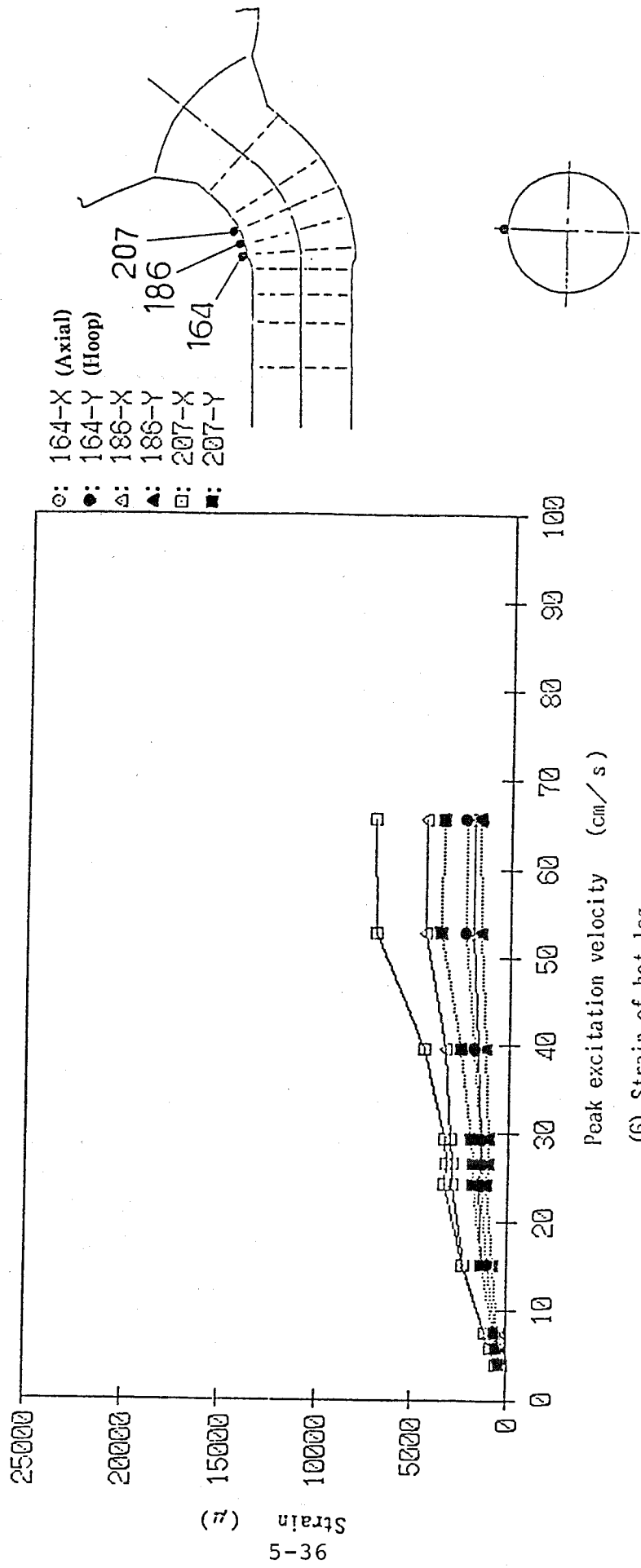
Figure 5.6 (6) Maximum Response Versus Excitation Level (Strain)
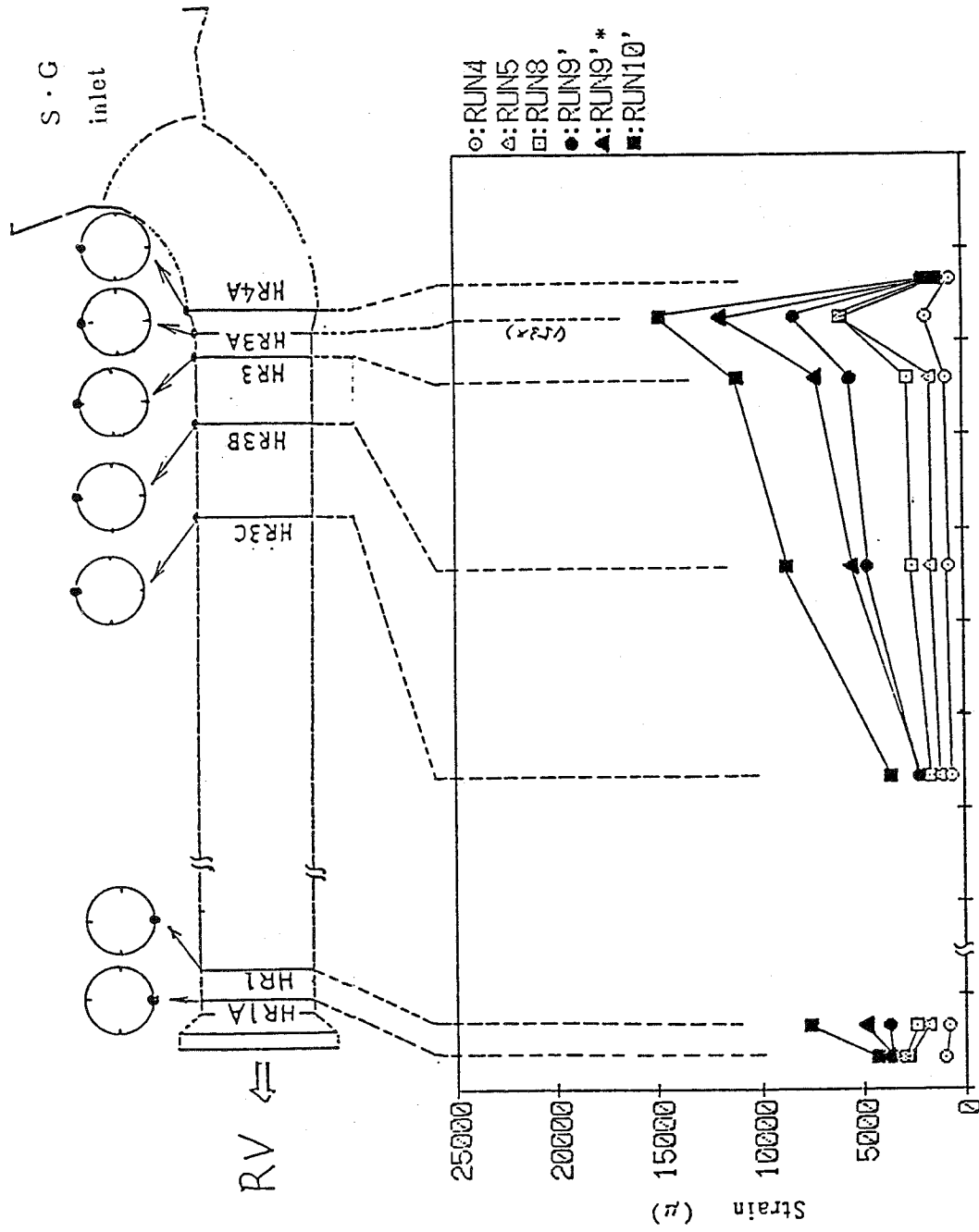
(6) Strain of hot leg

(7) Strain distribution of hot leg (Axial strain)

Figure 5.6 (7) Maximum Response Versus Excitation Level (Strain)
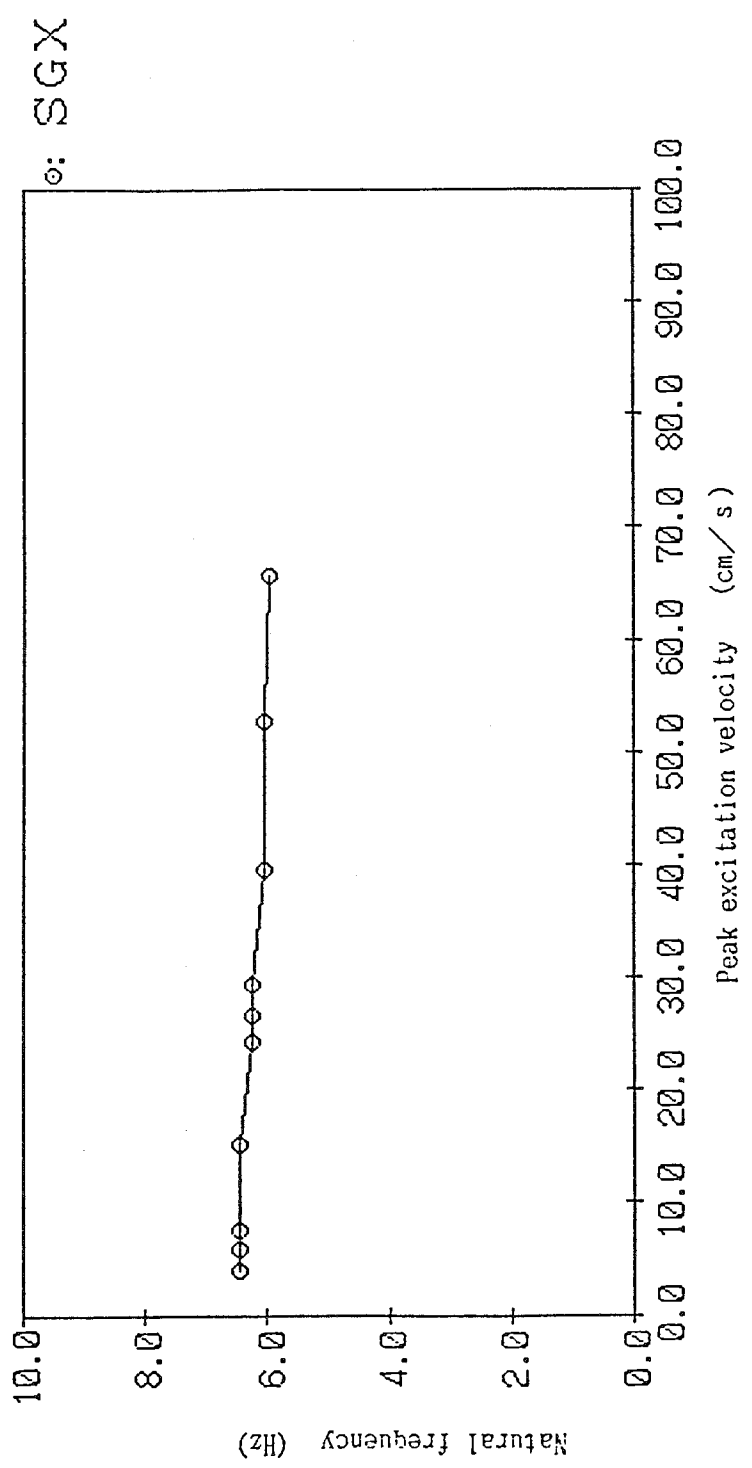
Figure 5.7 Natural Frequency Versus Excitation Level
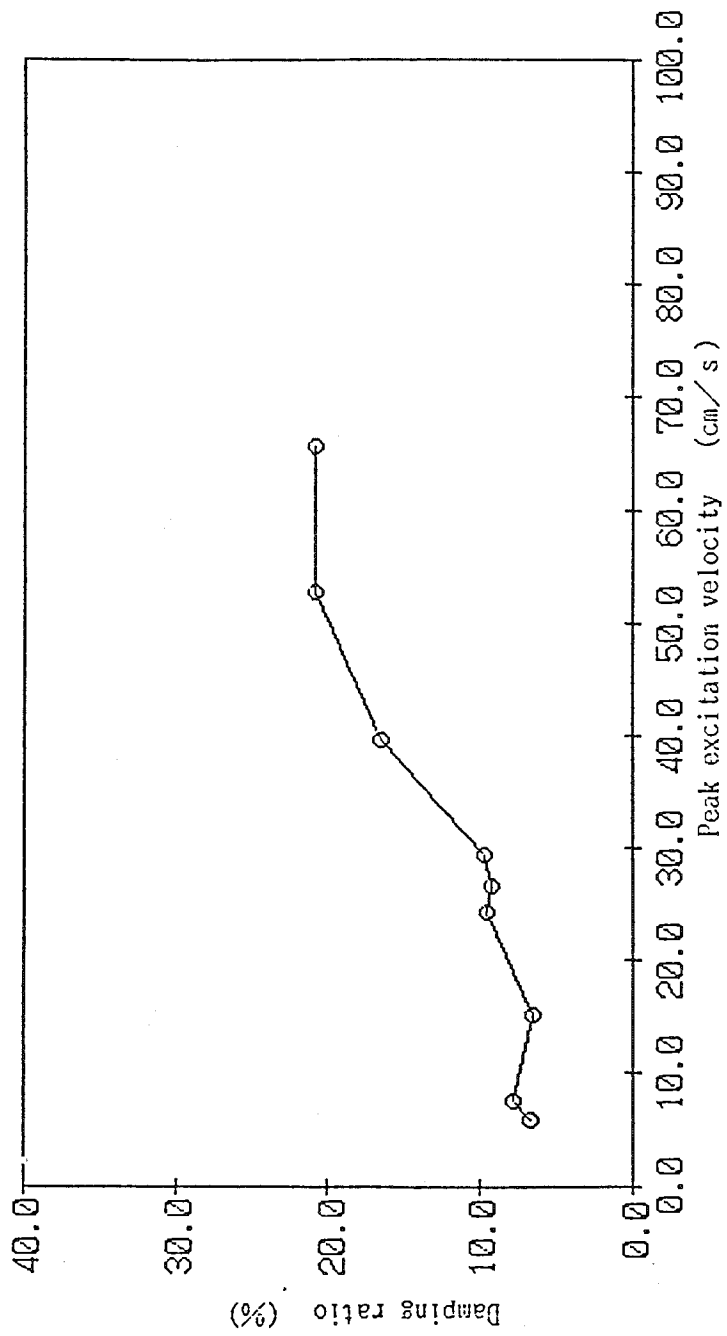
Figure 5.8 Damping Ratio Versus Excitation Level

(1) Acceleration of S/G top
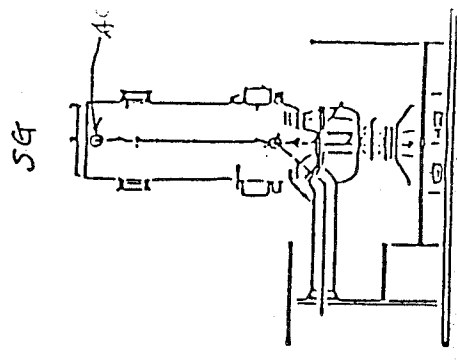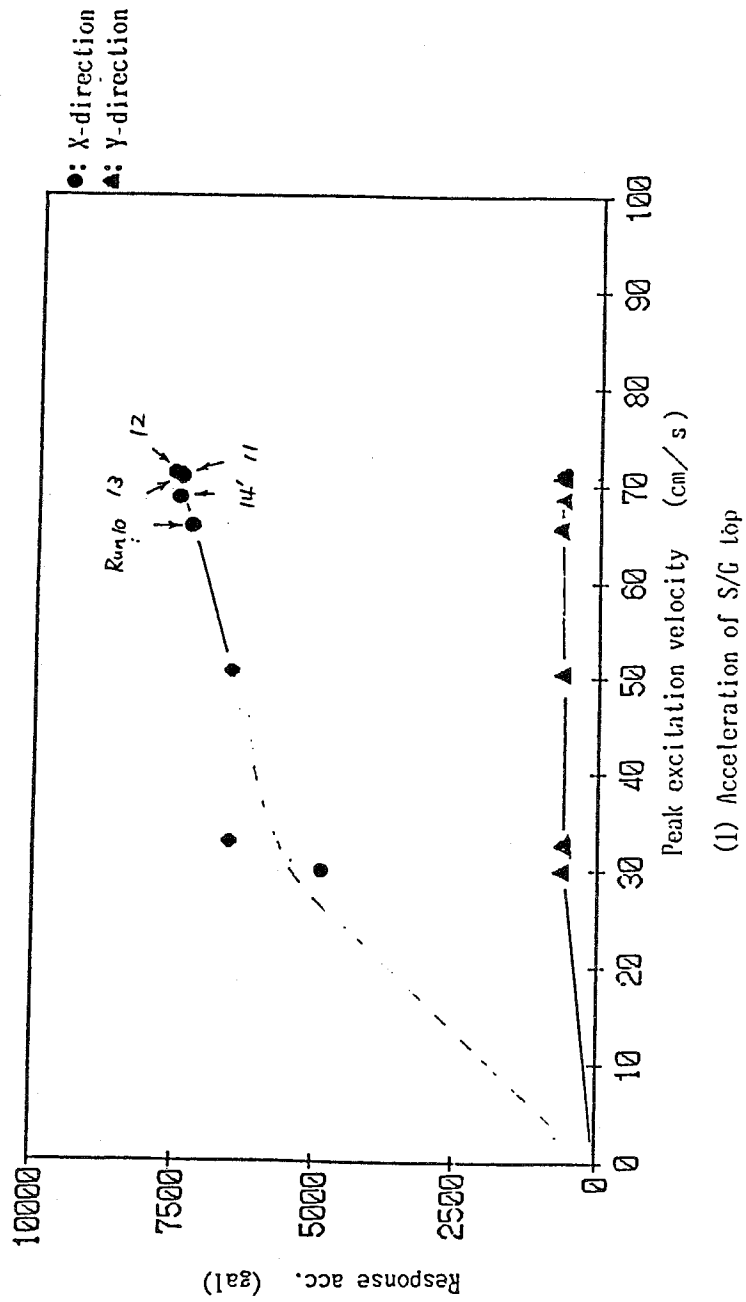
Figure 5.9 (1)   Maximum Response Versus Excitation Level
(Acceleration)

(2) Displacement of S/G top
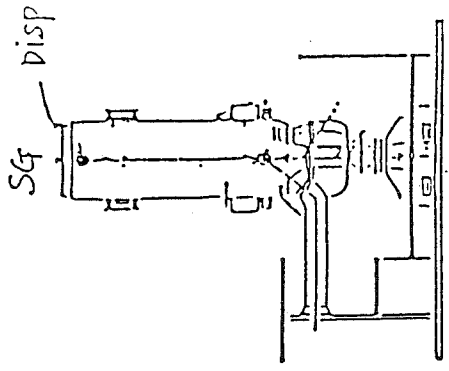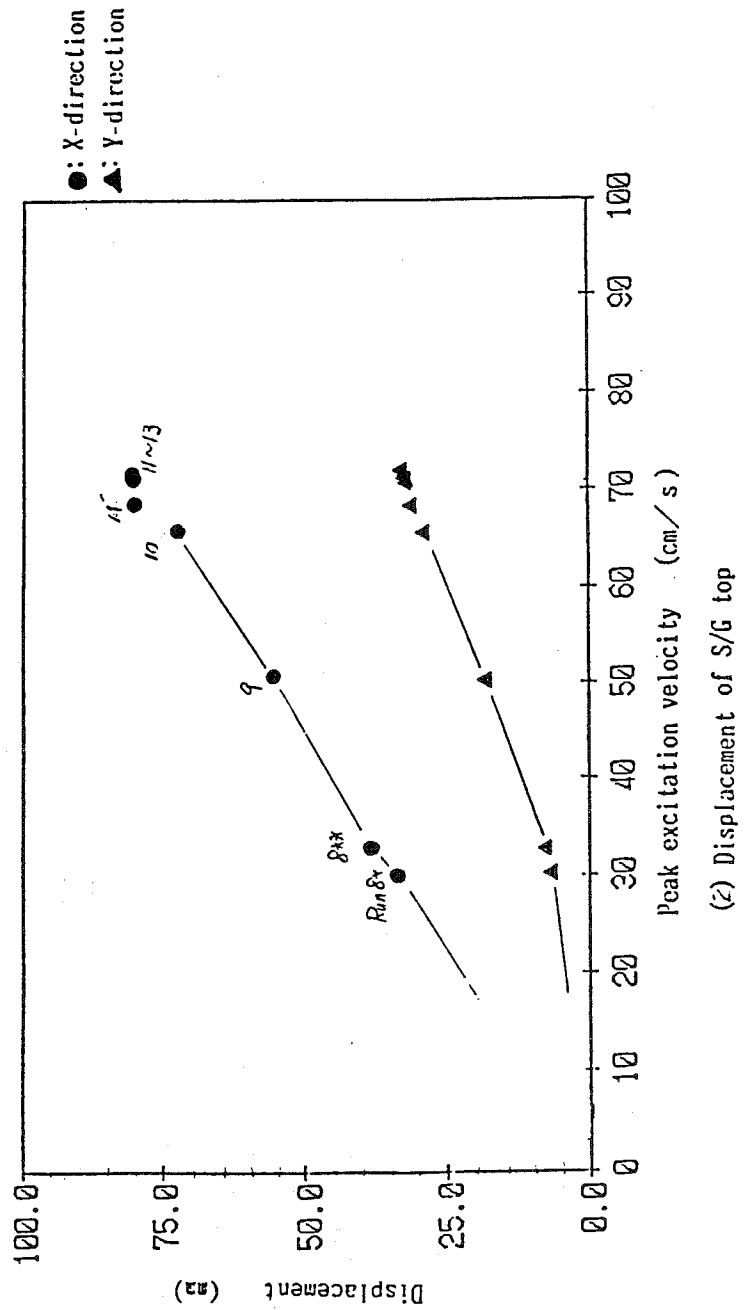
Figure 5.9 (2)   Maximum Response Versus Excitation Level
(Displacement)
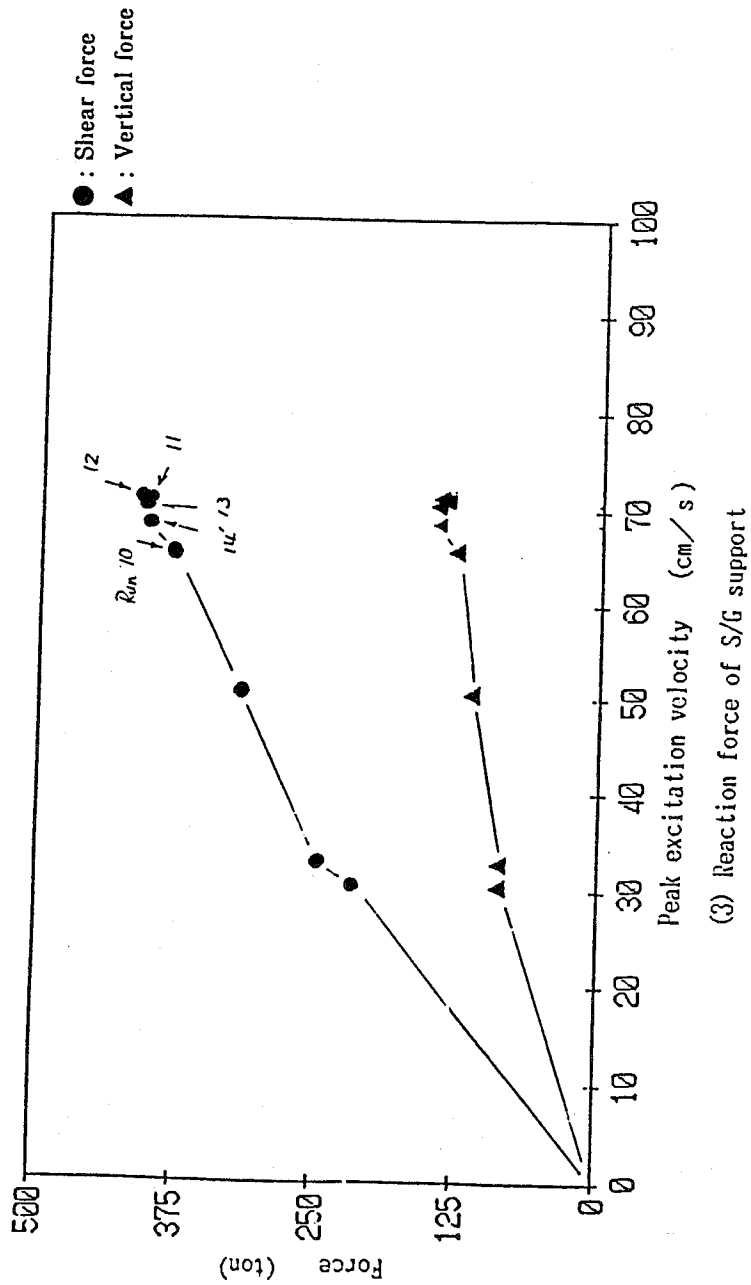
Figure 5.9.(3) Maximum Response Versus Excitation Level
(Force at SG Pin)
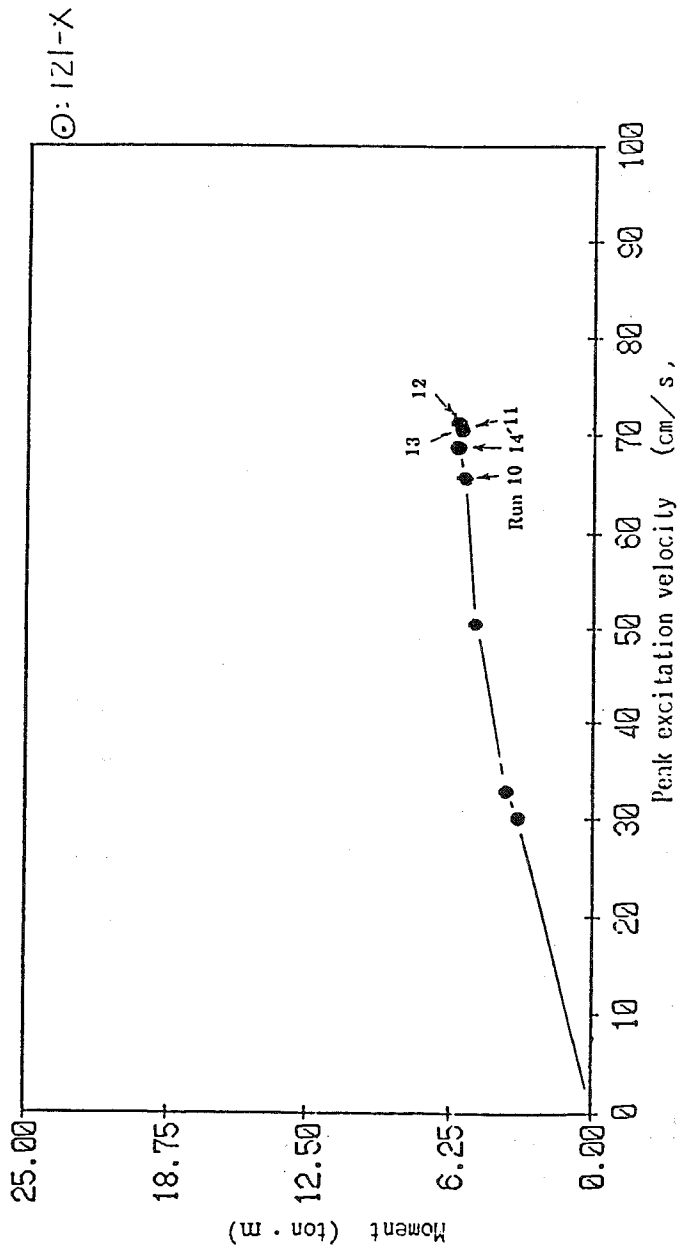
Figure 5.9 (4)   Maximum Response Versus Excitation Level
(Moment at SG Pin)
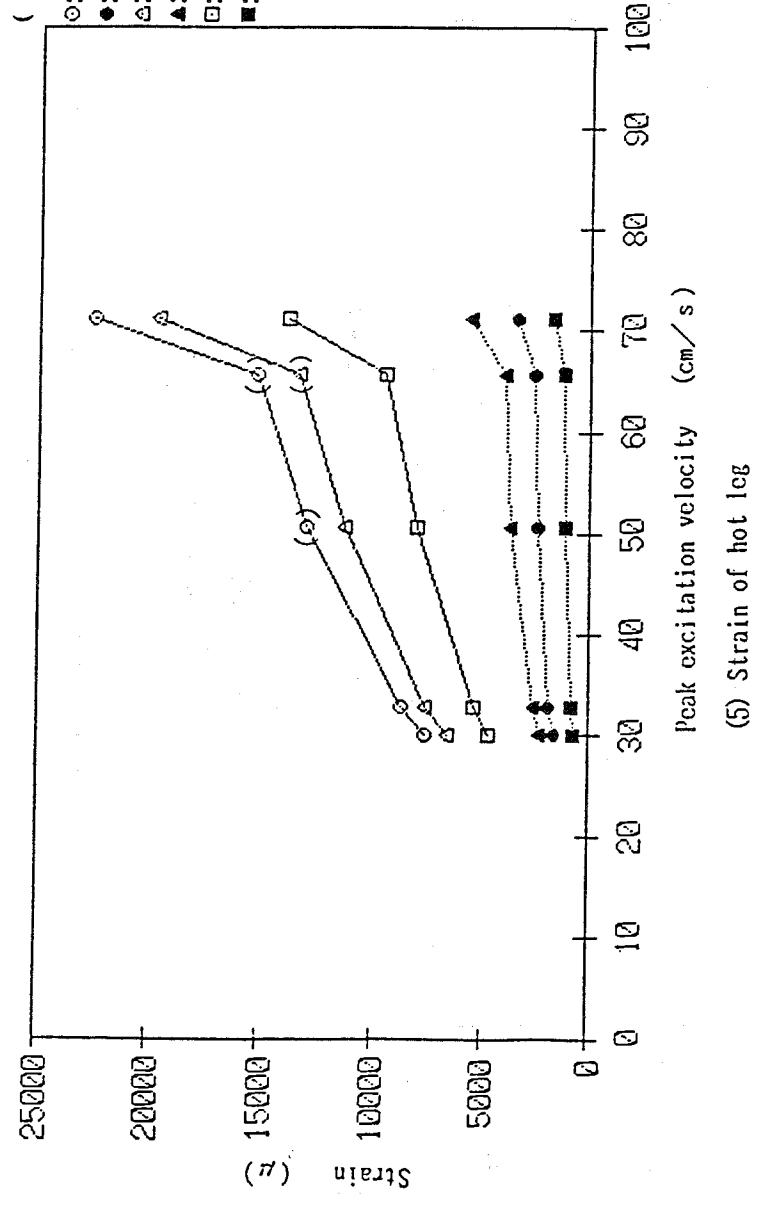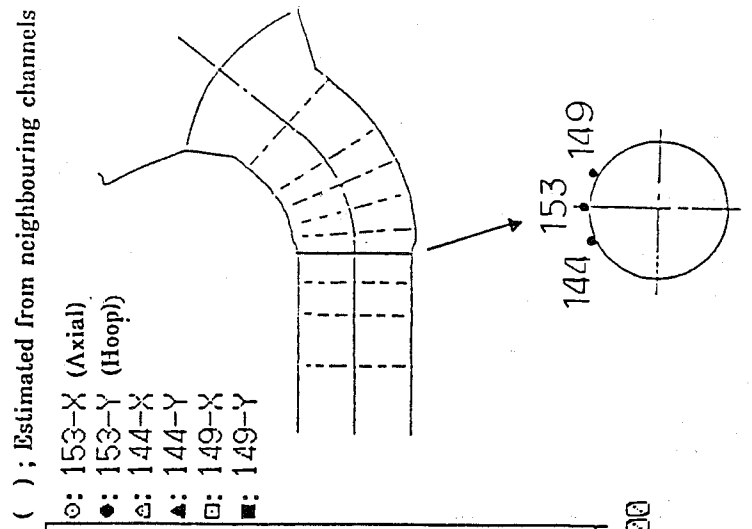
Figure 5.9 (5) Maximum Response Versus Excitation Level
(Strain)

164-X (Axial),
164-Y (Iloop)
186-X
186-Y
207-X
207-Y

⊙: 164-X (Axial),
●: 164-Y (Iloop)
△: 186-X
▲: 186-Y
□: 207-X
■: 207-Y

Strain (μ)

25000
20000
15000
10000
5000
0

0 10 20 30 40 50 60 70 80 90 100

Peak excitation velocity (cm/s)

(6) Strain of hot leg
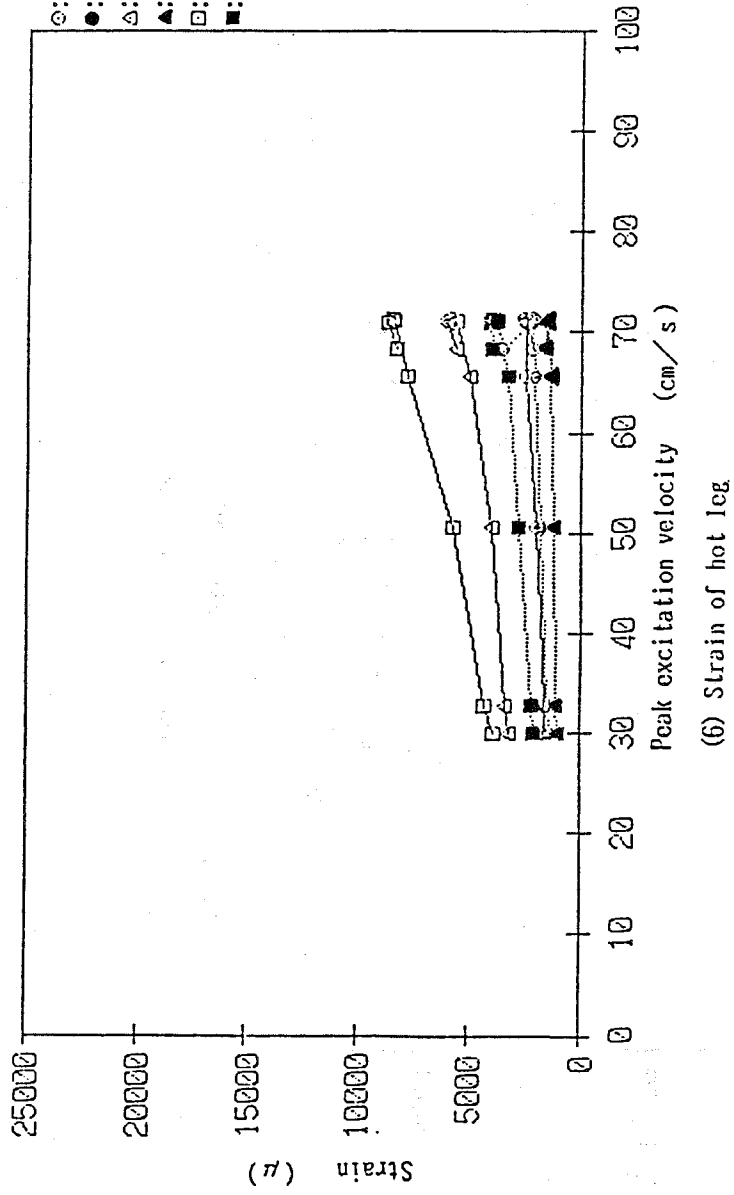
Figure 5.9 (6)   Maximum Response Versus Excitation Level
(Strain)

5-45

(7) Strain distribution of hot leg (Axial strain)
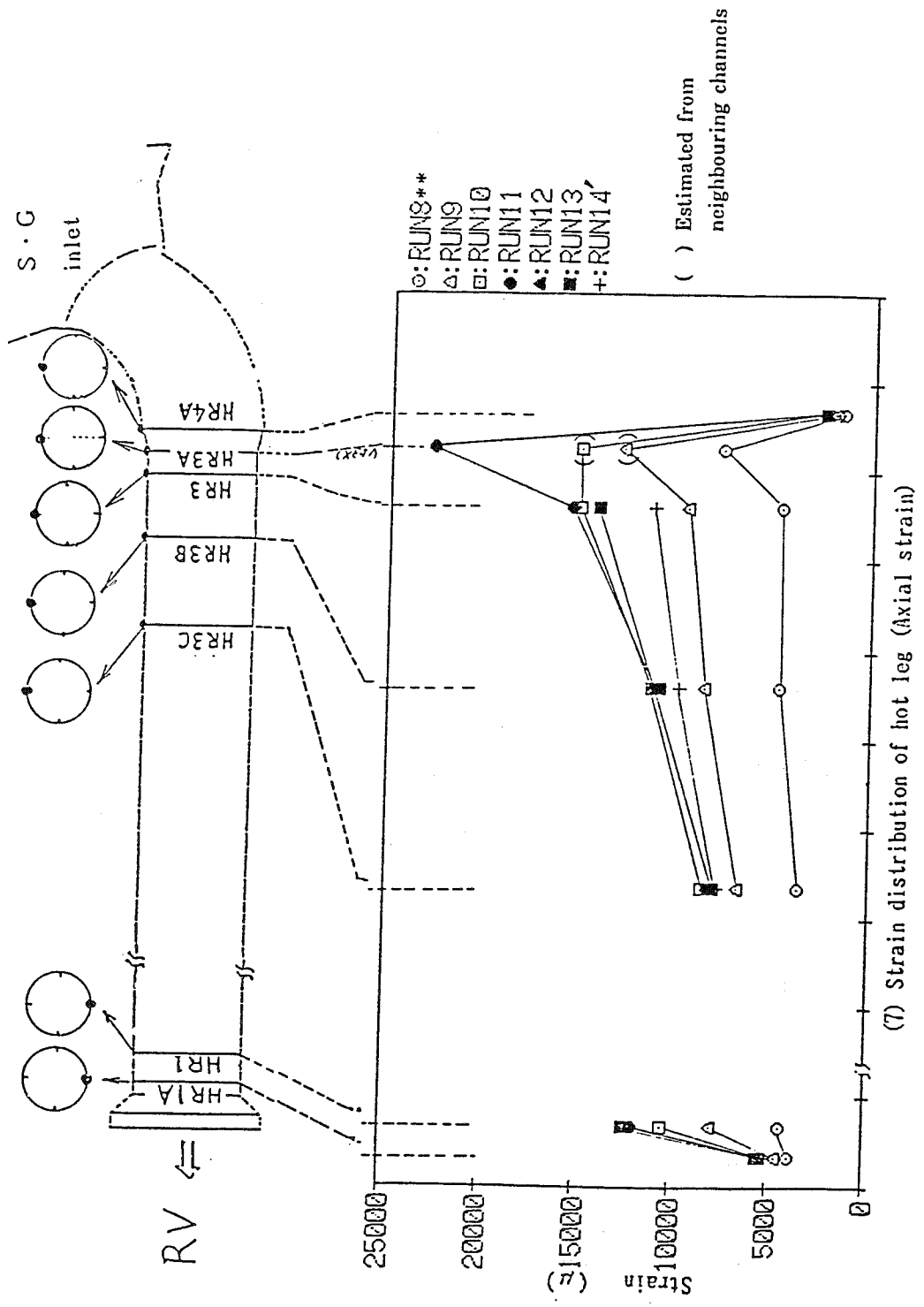
Figure 5.9 (7)　Maximum Response Versus Excitation Level
(Strain)
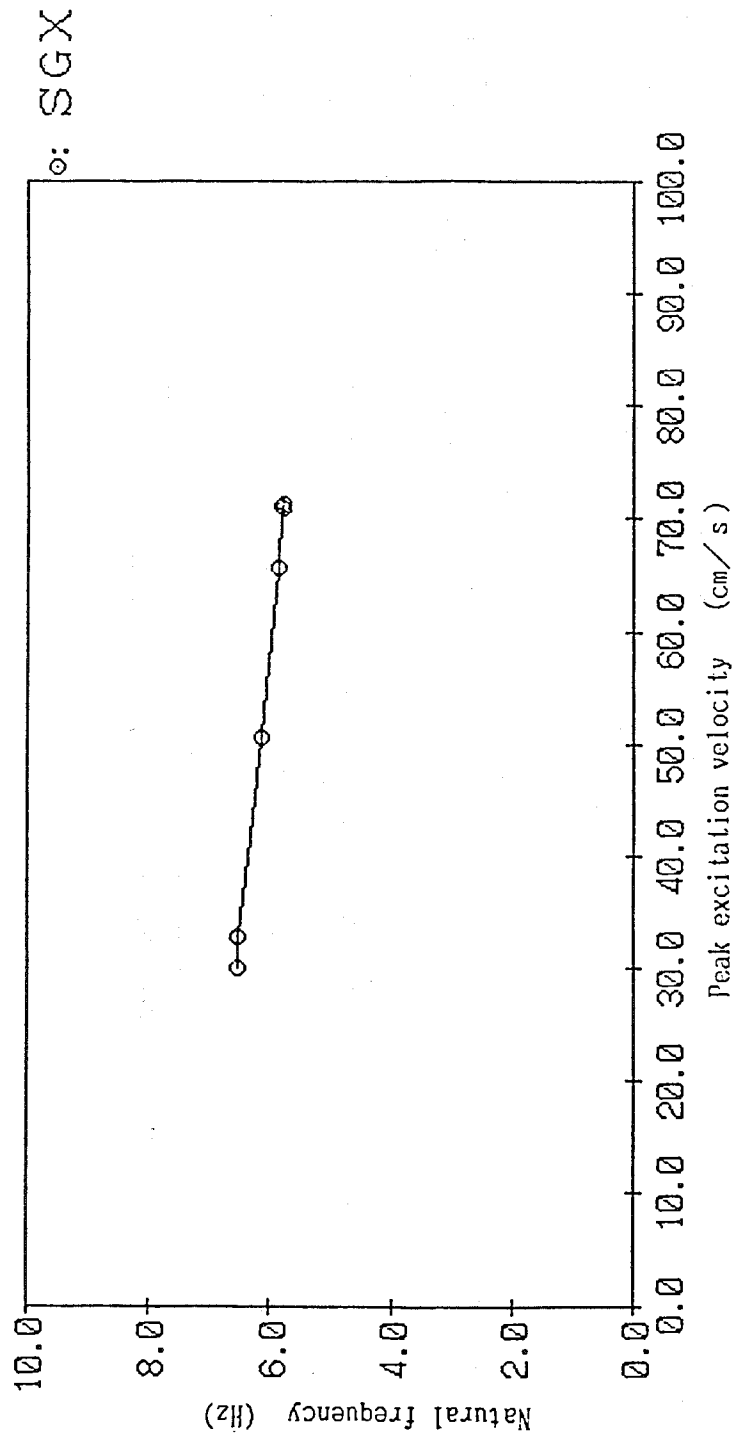
Figure 5.10 Natural Frequency Versus Excitation Level
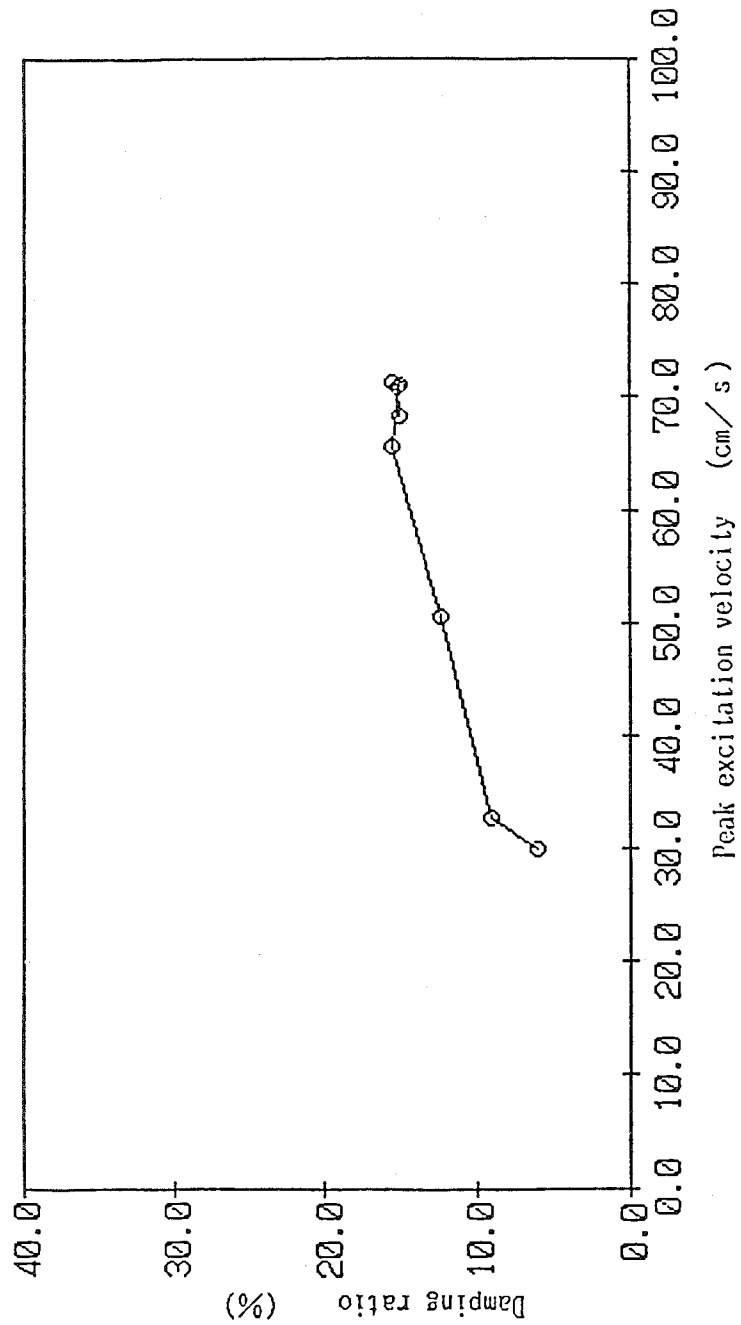
Figure 5.11 Damping Ratio Versus Excitation Level
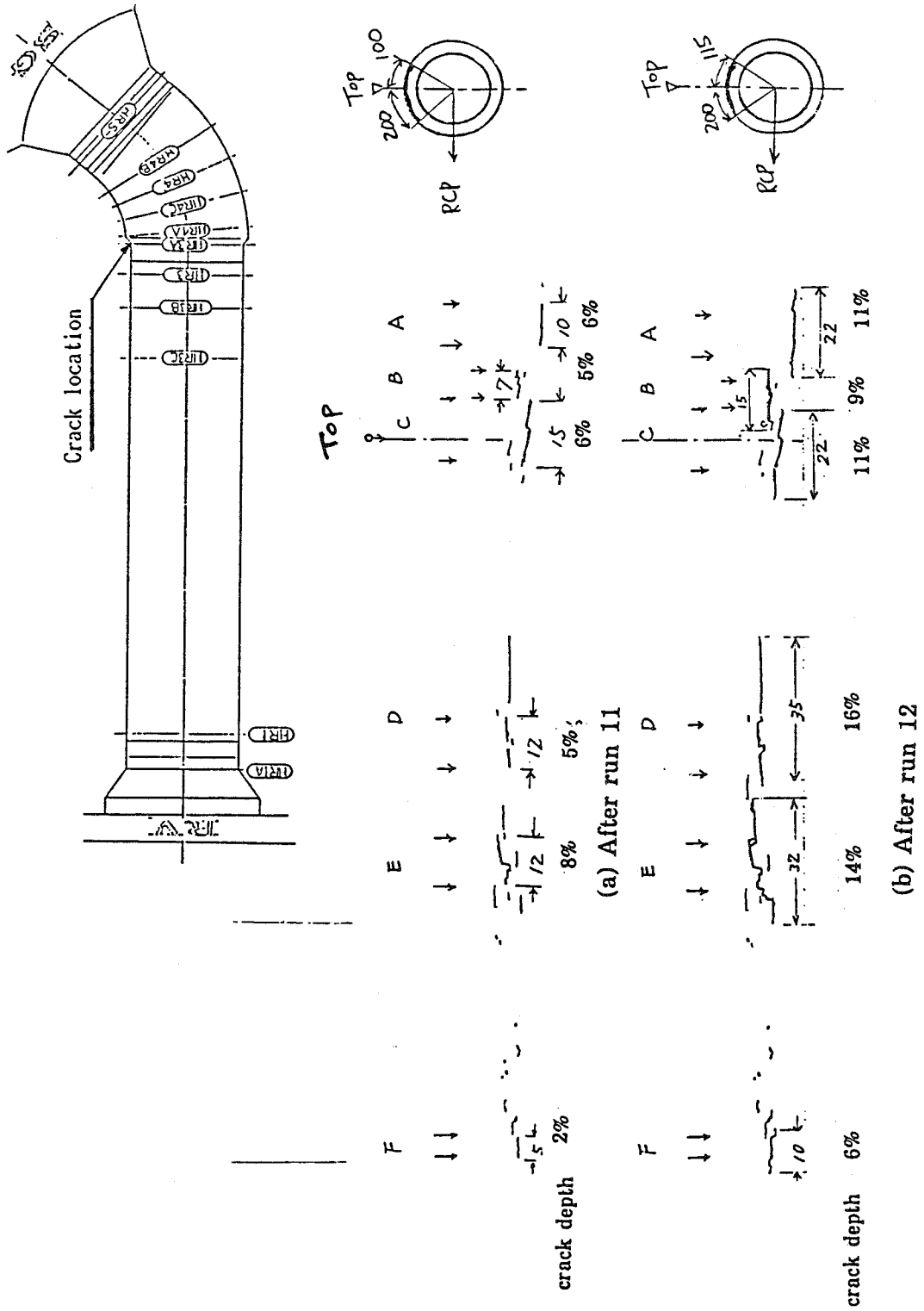
Figure 5-12 (1) Observed Crack Dimension

(c) After run 13

Opening 0.6mm
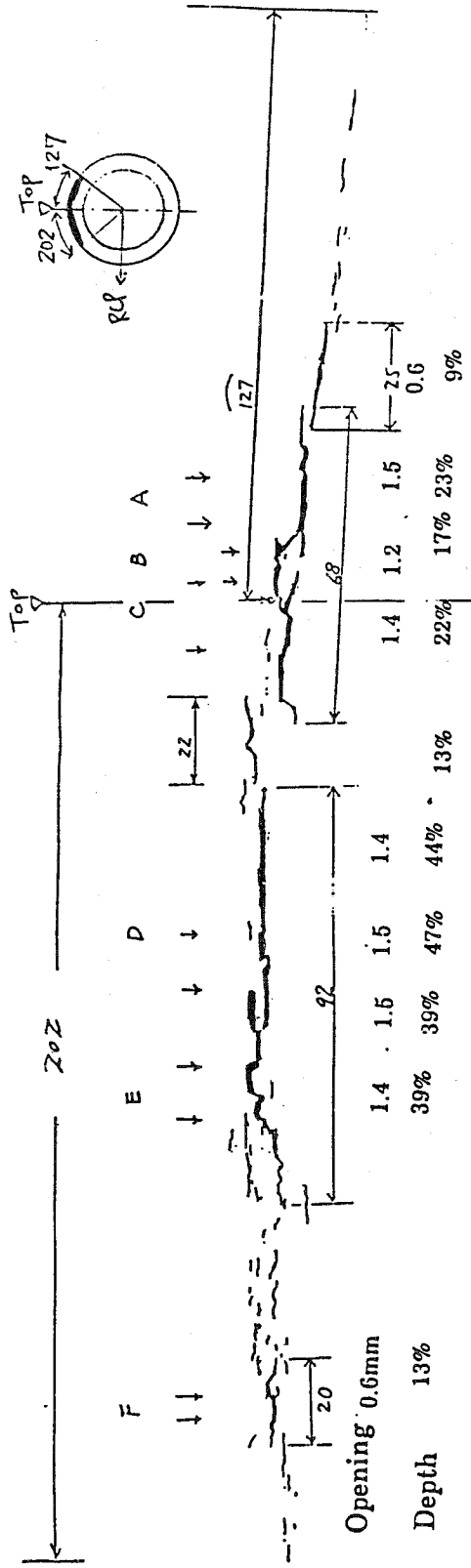
Depth 13%
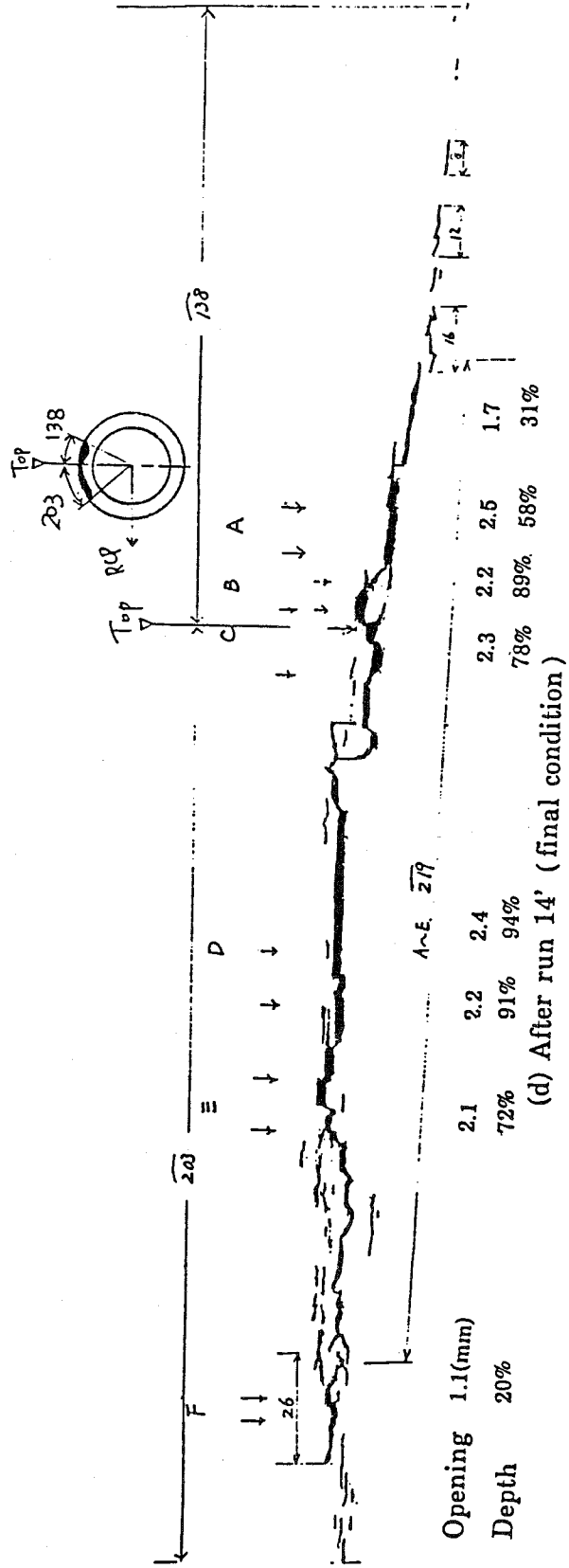
(d) After run 14' (final condition)

Opening 1.1(mm)

Depth 20%

Figure 5.12 (2) Observed Crack Dimension (Continued)
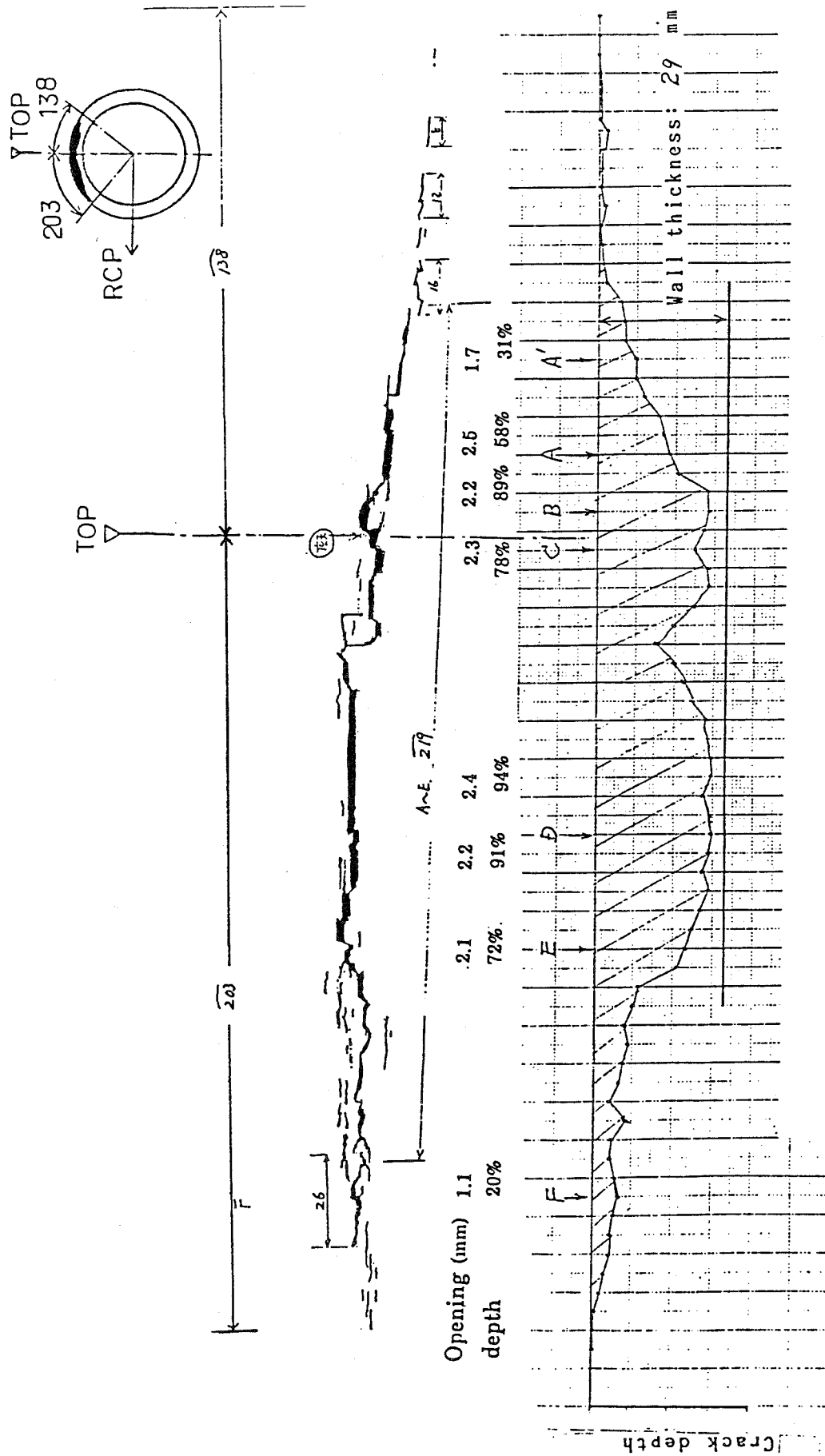
Figure 5.13   Measured Crack Depth (After run 14'; Final Condition)

5-51

| Opening(mm) | 1.1 | | 2.1 | 2.2 | 2.4 | | 2.3 | 2.2 | 2.5 | 1.7 |
| Depth | 20% | | 72% | 91% | 94% | | 78% | 89% | 55% | 31% |

Figure 5.14   Crack Growth

SG Top Disp./Table Acceleration

(1) R U N   4

MAX=.500000

88940801 (58X+69X)/2 / X^9
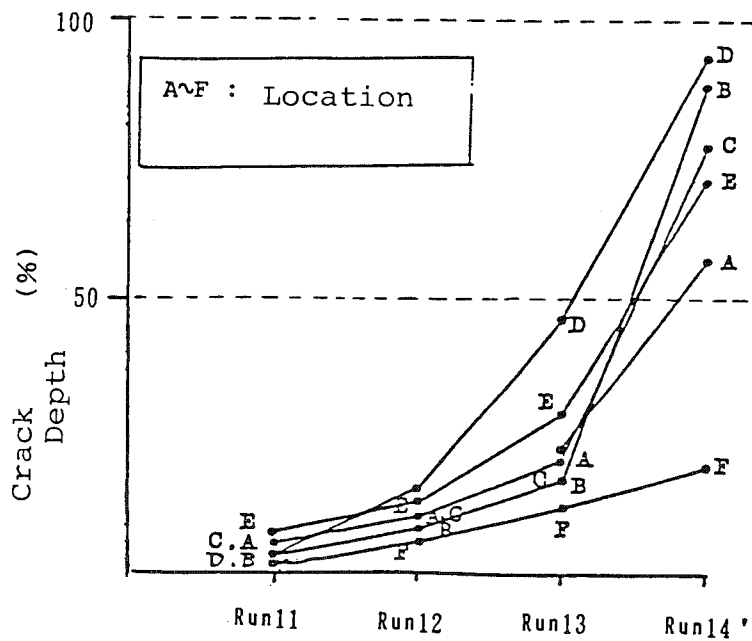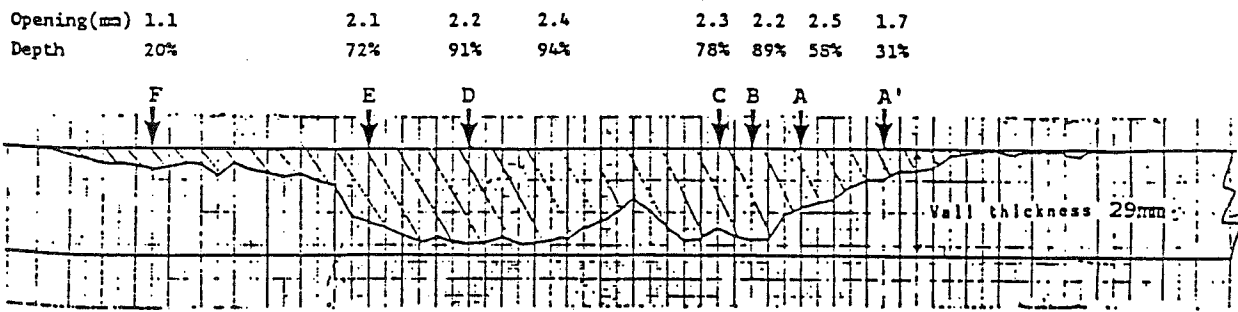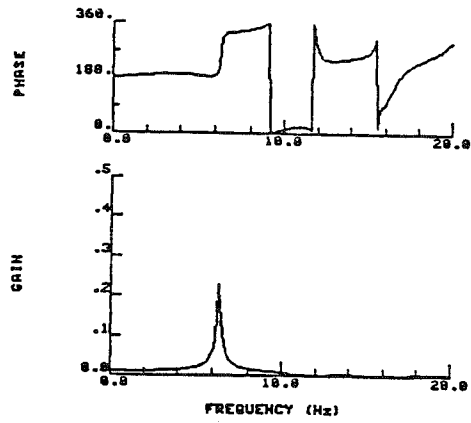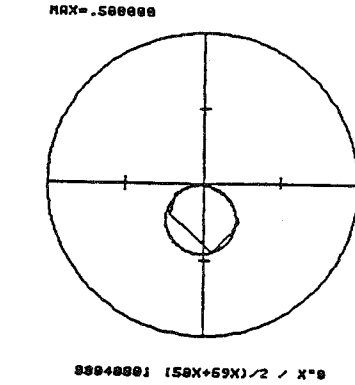
MODE	FREQ (Hz)	DAMPING
1	6.328E+00	2.315E-02

(2) R U N   8 ✳✳

MAX=.100000

88041782 (58X+59X)/2 / X^9
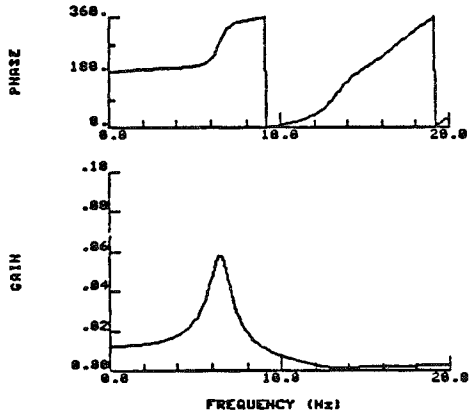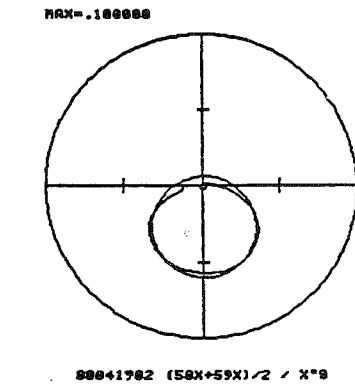
MODE	FREQ (Hz)	DAMPING
1	6.491E+00	8.274E-02

(3) R U N   1 1

MAX=.100000

88042201 (58X+59X)/2 / X^9
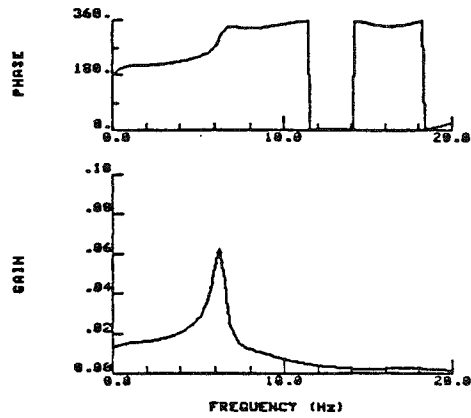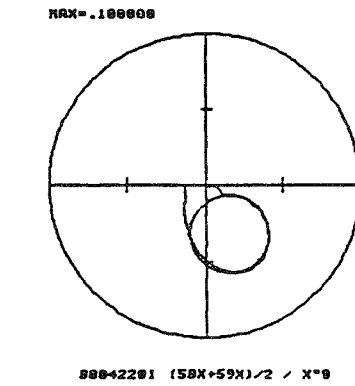
MODE	FREQ (Hz)	DAMPING
1	6.247E+00	7.035E-02

Figure 5.15   Transfer Function by AR-Method

○ : Equivalent Damping (at Maximum Response)

● : Transfer Function (from whole wave)
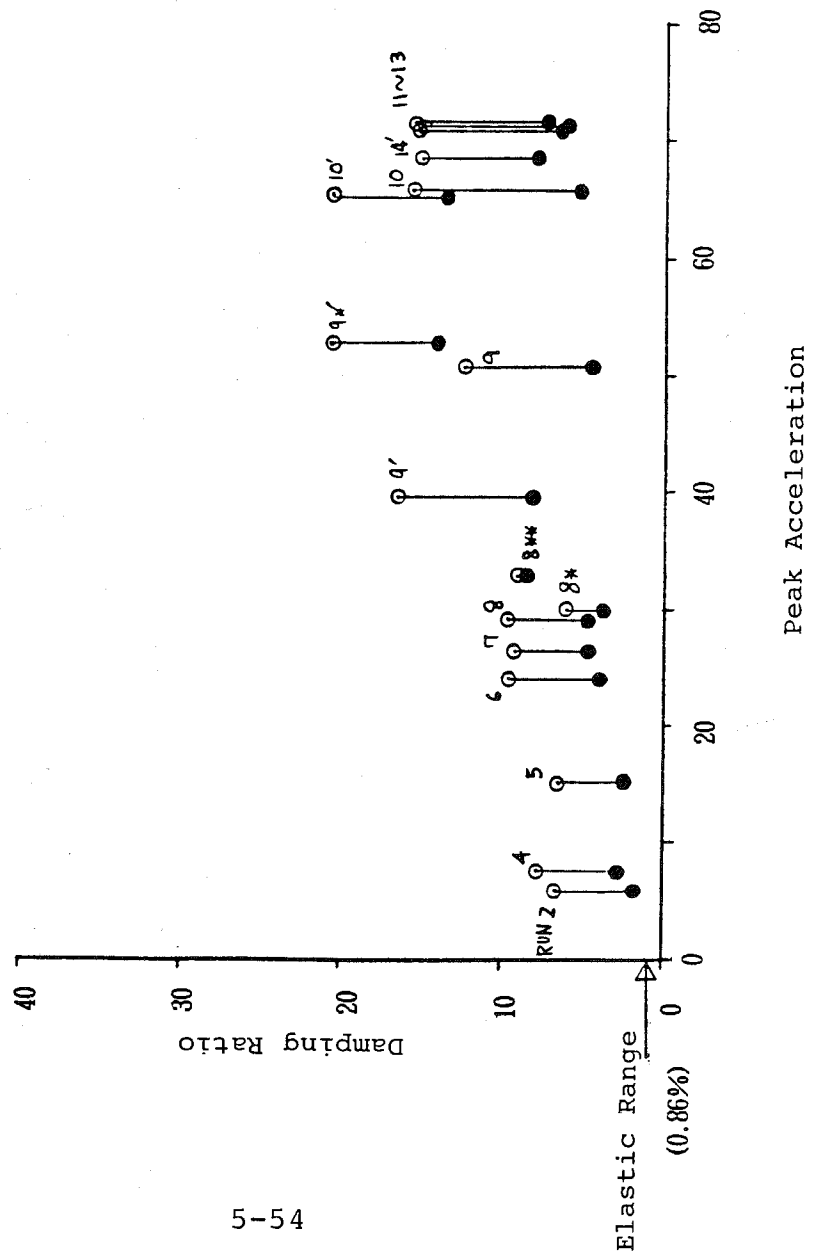
Figure 5.16 Comparison of Damping Ratio

5-54
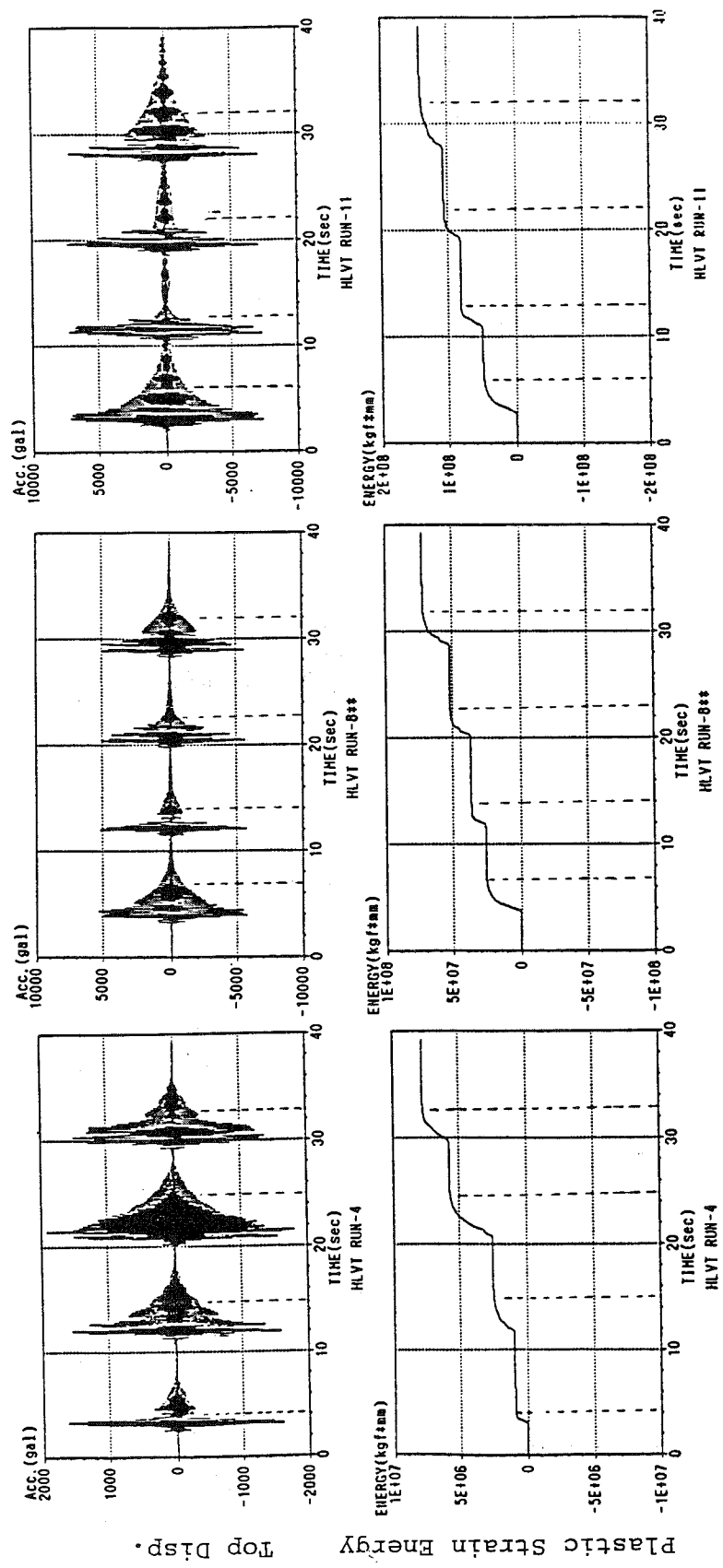
Figure 5.17 Time History of Plastic Strain Energy

Peak Accleration   Comparison of Natural Frequency
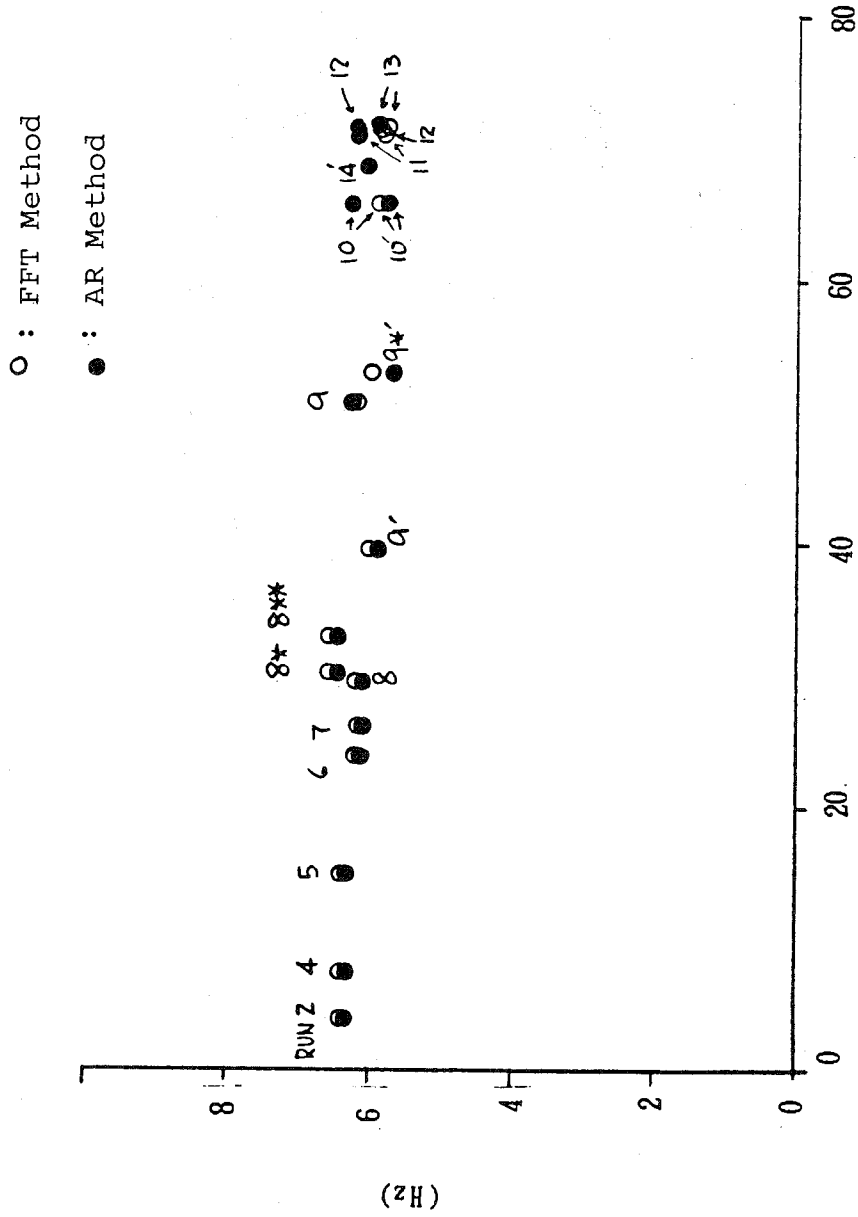
Figure 5.18   Comparison of Natural Frequency
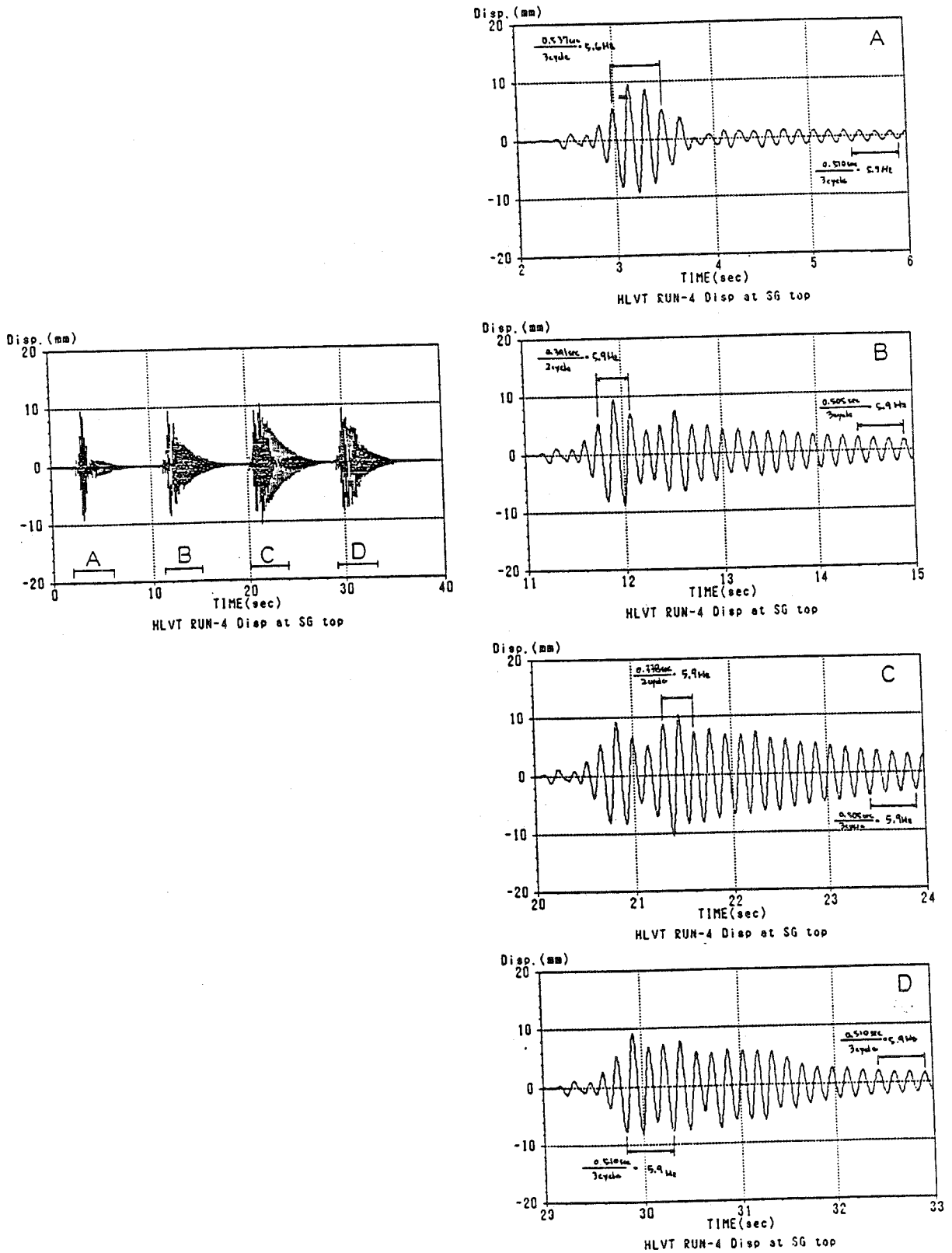
Figure 5.19 (1) Predominant Frequency (run 4)

5-57
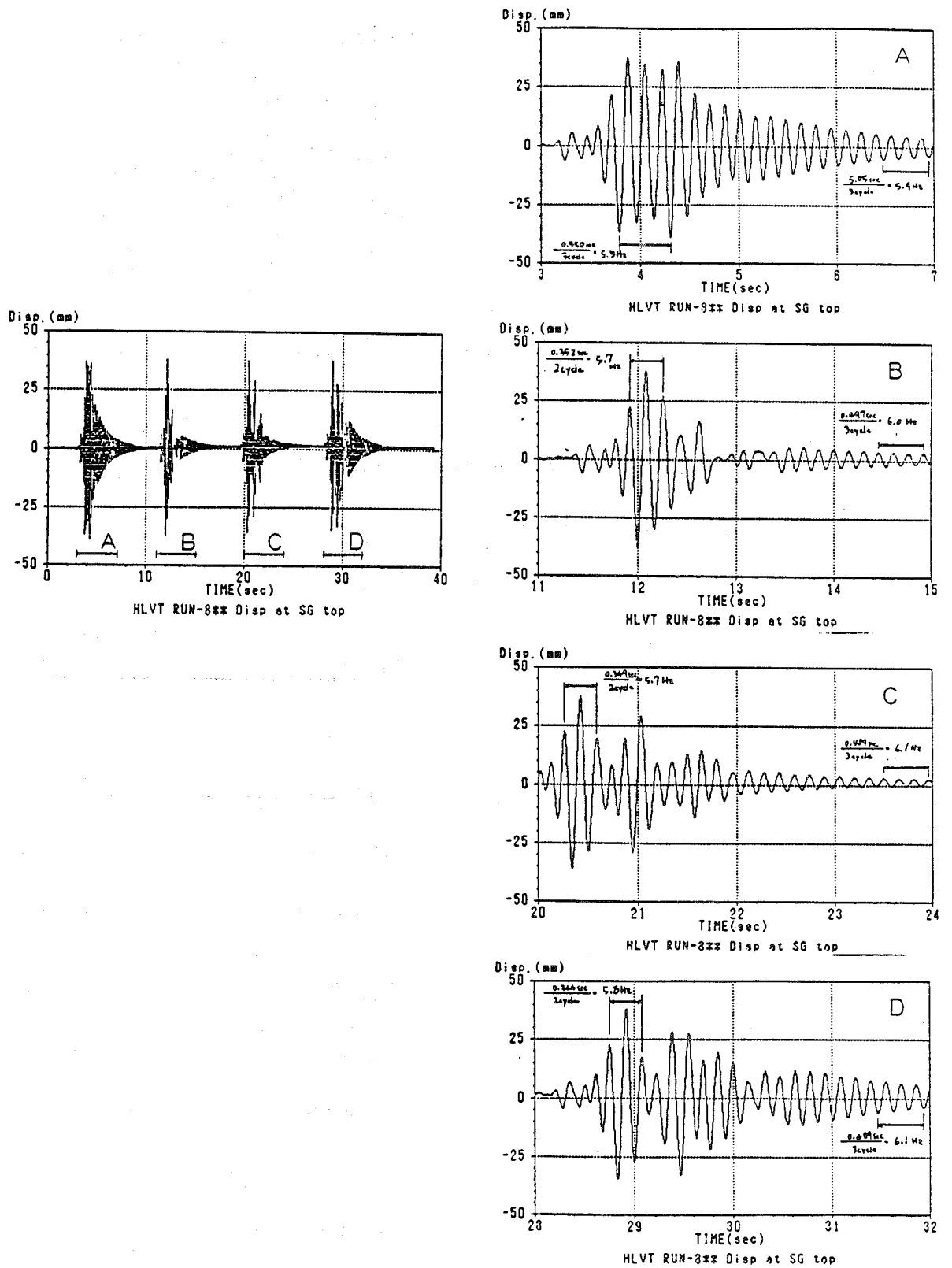
Figure 5.19 (2) Predominant Frequency (run 8**)
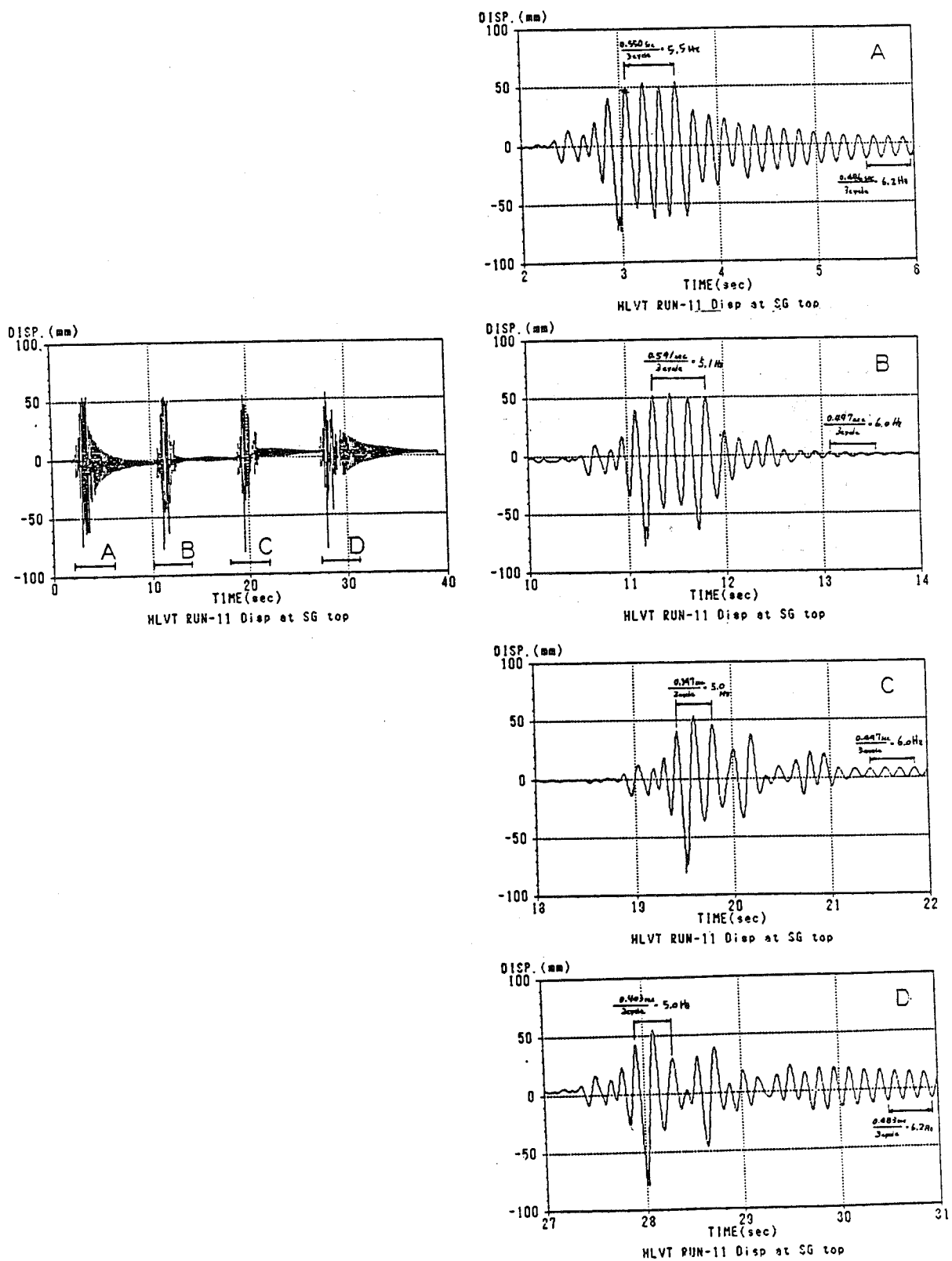
Figure 5.19 (3) Predominant Frequency (run 11)

5-59
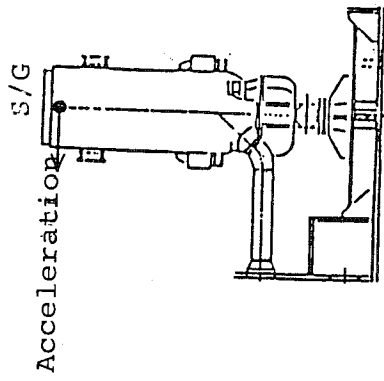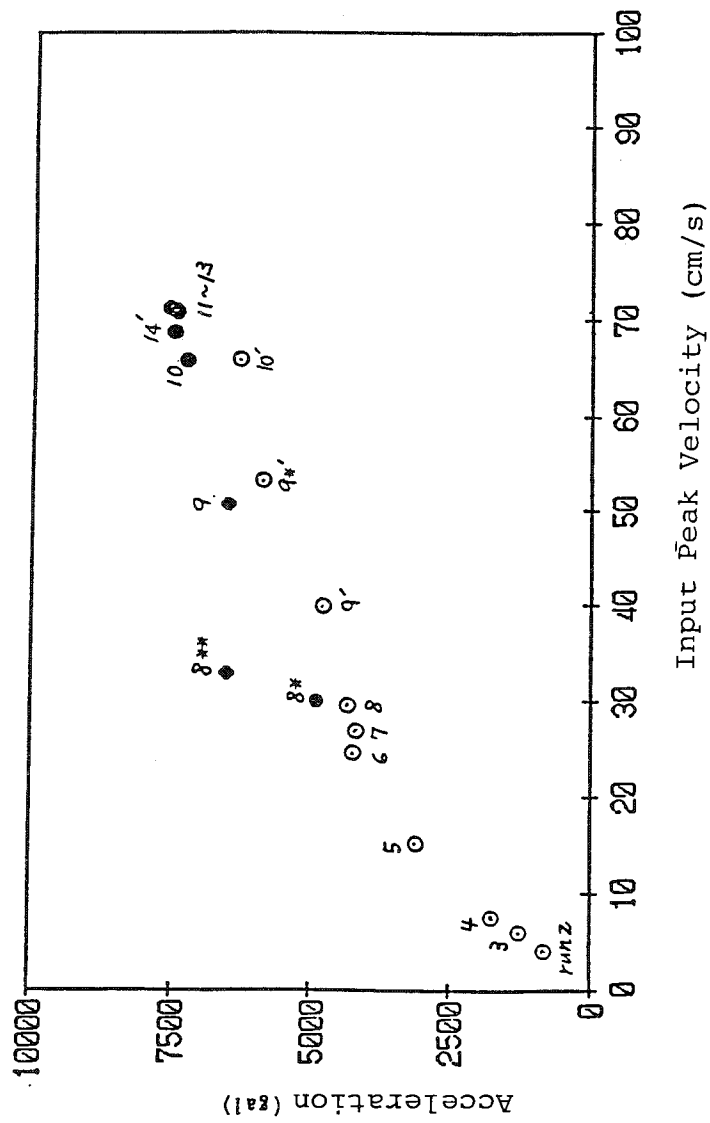
Figure 5.20   Input Level and SG Acceleration
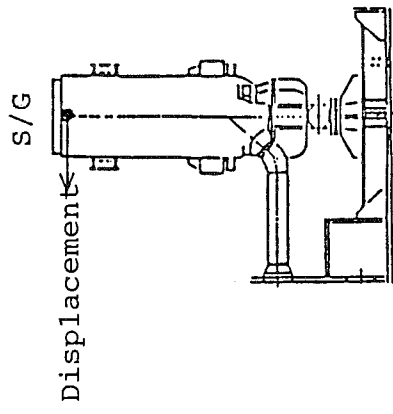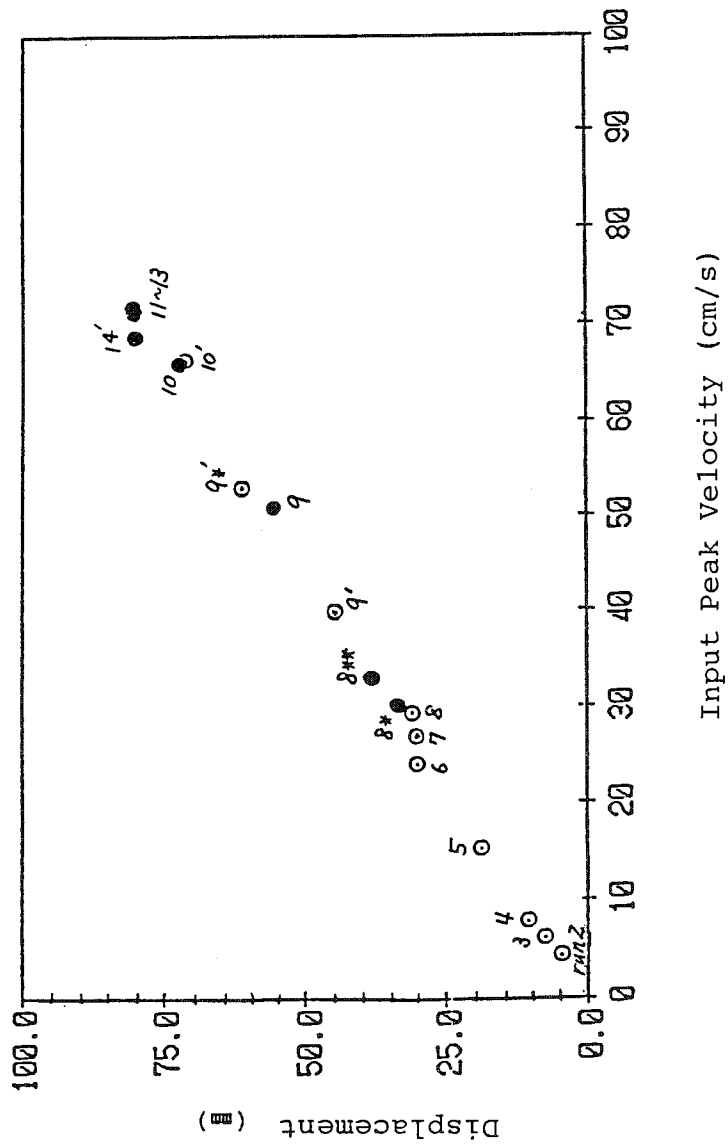
Figure 5.21   Input Level and SG Displacement
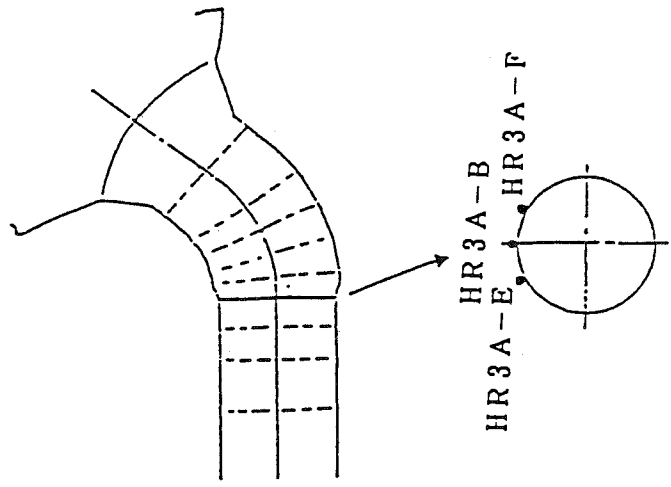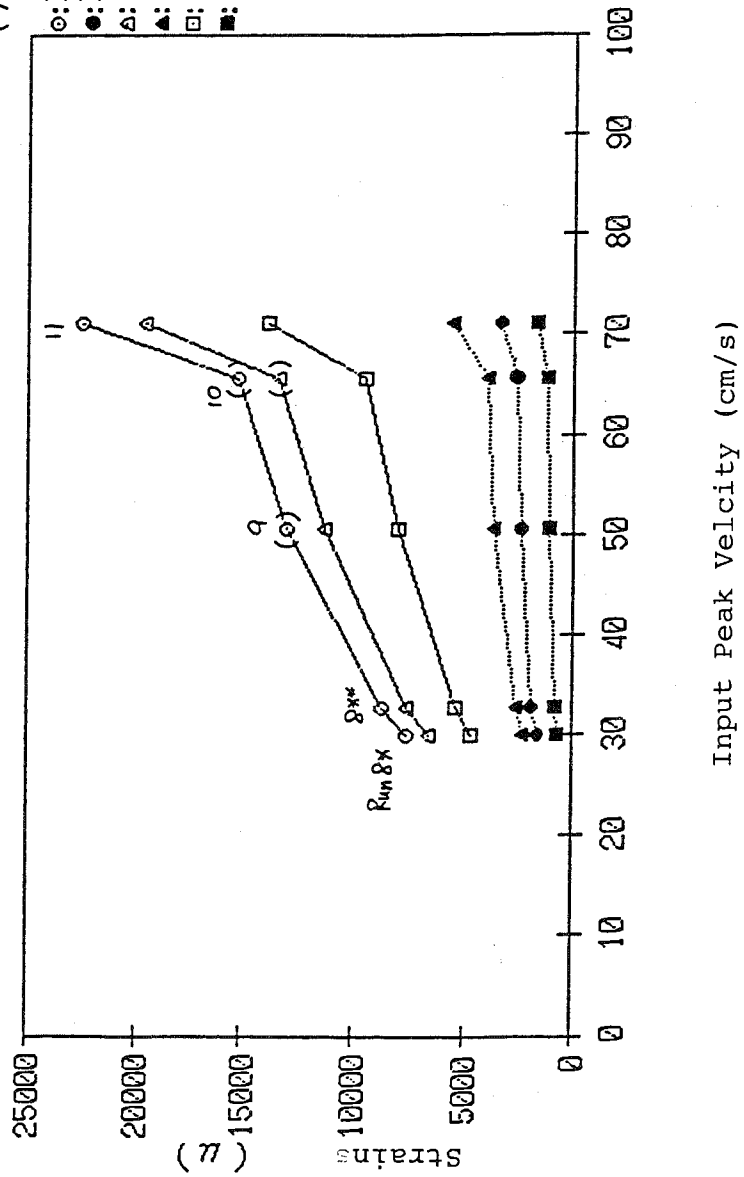
Figure 5.22 Input Level and Strains
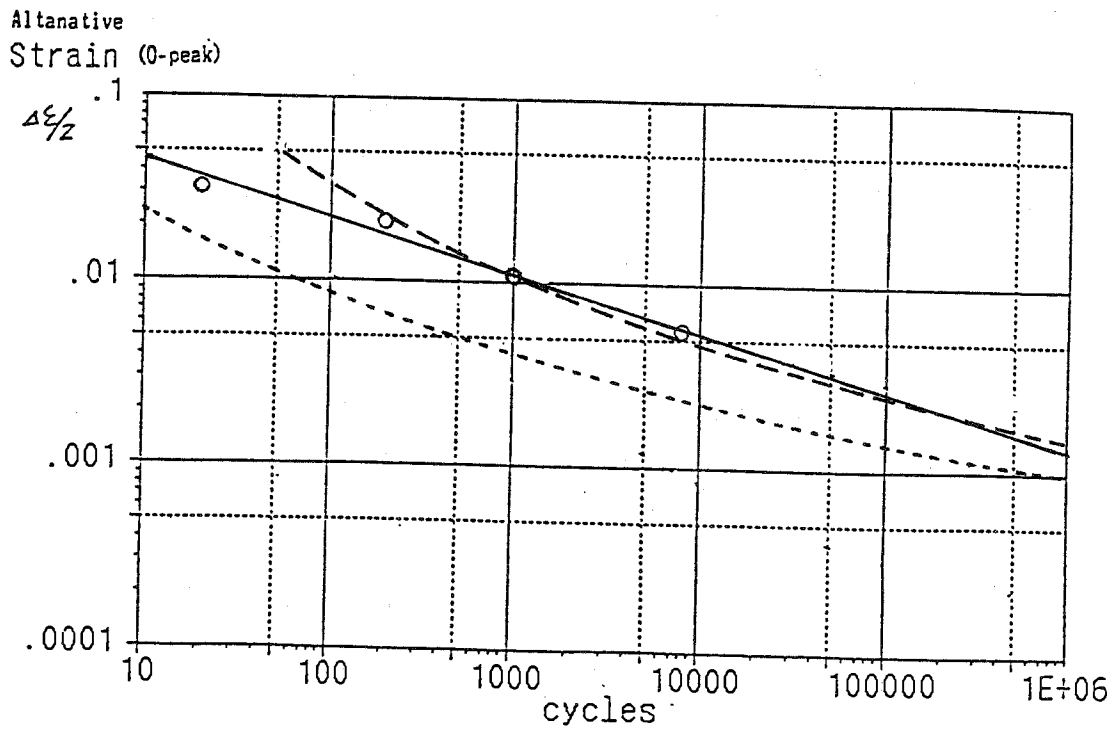
Altanative
Strain (0-peak)

Figure 5.23 Comparison of Fatigue Strength Curves

6.0 POST-TEST EXAMINATION OF HOT LEG

6.1 Objective

The cracks and bulging in the hot leg pipe that were observed after the HLVT are illustrated in Figure 6.1. The details of the crack growth process are shown in Figures 5.12 to 5.14. To support the evaluation of the HLVT results, detailed measurements were made of the bulging and cracks, and material properties were investigated. Included in this chapter are discussions of the following items:

(1) Investigation of cracks which were not identified during the vibration tests.

(2) Measurements of dimensions of the hot leg pipe

(3) Crack behavior

(4) Measurements of tensile strength and low cycle fatigue strength

(5) Others

6.2 Post-Test Examination Plan

6.2.1 Test Items

The test items included in the post-test examination program are shown in Table 6.1. Selected items are further discussed below.

The existance of any cracks other than the dominant crack as shown in Figure 5-12 was determined by visual inspections and dye penetrant tests on the inner surface of the piping. The dimensions and locations of any additional cracks were measured.

For the bulged regions, the extension of bulging and change of wall thickness were measured. The actual size of the dominant crack was also measured after the crack surface was exposed. Crack growth behavior was investigated by fractography.

As for the piping material properties, metallurgical tests and mechanical tests were performed. Tensile tests of the bulged pipe material were conducted to obtain data concerning the effect of bulging on the tensile properties of the straight pipe. Fatigue initiation and crack growth tests of the elbow material were carried out to obtain data necessary to analyze the initiation and propagation of the dominant crack.

6.2.2 Cutting Plan

To conduct the post-test examination program described above, it was necessary to cut the test pipe properly and obtain sufficient test specimens. The cutting process is shown in Figure K.1 of Appendix K. First, the test pipe was cut circumferentially into four blocks. Block #1 for the elbow, Block #2 for the cracked area, Block #3 for the non- damaged straight pipe and Block #4 for the end segment to the pressure vessel.

Then, blocks #1, 2 and 4 were cut longitudinally for the inspection of their inner surface. Specimens for macro and micro structures were cut from blocks #2A, and 4A. Macro and micro specimens for cross sections were also cut from blocks #2A, 2B, 4A and 4B.

Tensile specimens were cut from the straight pipe at the bulged region. Specimens for fatigue crack initiation and propagation were cut from the elbow. Dimensions of these specimens are shown in Figure K.2. Details of all the examined locations are shown in Figure 6.2.

6.2.3 Test Procedures

The test procedures are summarized in Figure 6.3 and discussed below. All tests were done at room temperature.

(1) Tensile Tests

Specimens with fillets were used to perform the tensile tests. During the loading, the displacement between the fillets was recorded. Stresses and strains were calculated as follows:

$$
\begin{array}{ll}
\text{nominal stress} & \sigma_N = P/A \\
\text{nominal strain} & \epsilon = \Delta d/d \\
\text{true stress} & \sigma_A = (1+\epsilon)\sigma_N \\
\text{true strain} & e = \ln(1+\epsilon)
\end{array}
$$

where, P was the load, A was the cross sectional area, and d was distance between the fillets.

(2) Low Cycle Fatigue Tests

As the cracked region had been subjected to high strain cycling during the HLVT, low cycle fatigue tests were done at very high strain levels. Hourglass type specimens were used and their diametral displacement was controlled at four levels. During the test, hysteresis loops were recorded. The number of cycles to crack initiation and failure were measured. Crack initiation was

defined as the number of cycles at which the applied load decreased. Diametral strain was converted to longitudinal strain by the following equation:

$$\triangle \varepsilon_t = 2 \ln \frac{Dc}{Dt} + \frac{1 - 2v}{E} \triangle \sigma_N$$

where, Dc is the diametral strain in compression, Dt is the diametral strain in tension, v is Poisson's ratio, and E is Young's modulus.

(3) Fatigue Crack Growth Rate Tests

Low cycle fatigue crack growth rates were measured by compact specimens. Since the HLVT showed a high rate of crack growth, tests were conducted in the plastic deformation region where the J-integral is used as a parameter. During the test, the load-displacement was recorded. The crack length was calculated from the load to load-displacement relationship of the unloading process by the unloading compliance method. The crack length was approximated to polynomials of the applied cycles and the crack growth rate was calculated from the derivatives of the polynomials. The J-integral value was calculated from the load displacement curve as follows:

$$\triangle J = \frac{2A}{Bb} \cdot \frac{1 + \eta}{1 + \eta^2} \qquad \triangle K = \sqrt{\frac{E \triangle J}{1 - V^2}}$$

where, A is the applied energy, B is the thickness, b is the ligament length, and η is the shape factor.

6.3 Test Results

6.3.1 Appearance

(1) Visual Inspection and Dye Penetrant Test

The overall view of the hot leg pipe when it arrived at the Takasago R&D Center is shown in Figure 6.4. A close up view of the dominant crack is shown in Figure 6.5.

This pipe was cut into several blocks and inspected. Four small circumferential cracks, about 3 to 5 mm long, were identified on the inner surface of block #2A. No cracks were found on the inner surfaces of any other blocks. Luder's band marks were identified on the inner surfaces around the weld joints and in the bulged regions. Details of the inner surface examinations are shown in Figures K.3 to K.6 of Appendix K.

(2) Small Cracks on the Inner Surface

The depth of the small cracks which were found by dye penetrant testing was measured by a Crack Depth Meter based on the electric resistance method developed by Mitsubishi Heavy Industries. As shown in Figure K.7, the depth of these cracks ranged from 1 to 3 mm.

(3) Dimensions

The thickness of the pipe was measured by a Sonick detector and by a Mitsutoyo micrometer. As shown in Figure K.8, there was no remarkable change of thickness found at the bulging region compared with the undamaged part.

The diameter and circumferential length of the pipe were measured by a Mitsutoyo large micrometer and an ordinary scale. The results are shown in Table 6-2 and Figure K.9. There was about a 3 mm increase in the diameter and about a 10 mm increase in the circumferential length at the cross section of the bulged region on the top side of the pipe. There was also about a 1.5 mm increase in the diameter and about a 3 mm increase in the circumferential length at the cross section of the bulged region.

6.3.2 Metallugical Test

(1) Macro- and Microstructures

Macrostructures of the longitudinal cross section of the pipe at the crack location are shown in Figure 6.6. Additional macrostructures of the longitudinal and circumferential cross sections are shown in Figures K.10 to K.12 of Appendix K. Reasonable structures common to dual phase stainless steels are recognized at the regions of crack initiation and bulging. Crack origins were located at the outer surface of the elbow and were about 45 mm from the center of the pipe-to-elbow weld joint.

Microstructures of the cross sections at the crack initiation, bulged and undamaged regions are shown in Figures K.13 to K.16. As in the case of the macrostructures, only reasonable structures were observed.

2. Fractography

The fracture surface of the dominant crack was broken open at low temperature and is shown in Figures 6.7 and 6.8. On the fracture surface, several beach marks were identified and the crack was observed to have grown almost to the inner surface. The remaining ligament was only about 1.5 mm in thickness.

Typical crack origins are shown in Figure 6.9. It is obvious that the crack initiations were caused by fatigue. Near the origin, striations were observed by Scanning Electron Microscope (SEM) examinations. Apart from the origin, deformation slips and dimples dominated the fracture surface. In this area, periodic characteristics related to high amplitude cyclic load were recognized. The SEM observations are shown in Figures K.17 and K.18 of Appendix K.

In summary, the cracks were initiated by cyclic load and propagated slowly at first. Then, as the crack grew, the growth rate increased.

6.3.3 Mechanical Property Tests

(1) Hardness

Hardness in the region of crack initiation and bulging, which was subjected to high strain during the HLVT, was higher than in others areas. The distribution of the diamond pyramid hardness measured on the macro specimens is shown in Figure K.19.

(2) Tensile Strength

Tensile test results are shown in Table 6-3. Tensile properties for the virgin condition are also shown in the same table. The 0.2% proof stress and tensile strength after the HLVT were higher than those for the virgin condition. The tensile strength was not increased much by the HLVT; however, the 0.2% proof stress was increased by about 43%. The stress-strain relationships are shown in Figure 6.10. The specimens after the test are shown in Figure K.20. The surface became rugged because of the large grain and inhomogeniety of the test material. The tensile test results for the weld metal are also shown in Figure 6.10. The 0.2% proof stress is higher than the base metal and the tensile strength is also slightly higher.

(3) Low Cycle Fatigue Strength

Low cycle fatigue tests were conducted on the MTS servo-hydraulic testing machine as shown in Figure K.21. The test was strain controlled. Loads (stresses) during the test are shown in Figure K.22 and hysteresis loops are shown in Figure K.23.

The test results are shown in Table 6-4 and Figure K.24. The data are compared with the low cycle fatigue strength of Japanese austenitic stainless steels as shown in Figure K.25. The current data are in good agreement with these data. In Figure K.25, the results of the low-cycle fatigue tests of weld metals are also shown. These results indicate there is no significant difference in fatigue strength between the weld metal and the base metal.

The appearance of the specimens after the tests is shown in Figure K.26. Their surfaces are rugged and the irregularity increased for the specimens with higher applied strain.

(4) Fatigue Crack Growth Rate

Fatigue crack growth rate tests were done on another MTS testing machine as shown in Figure K.27. In order to obtain the same order of crack growth rate as experienced during the HLVT, a high-amplitude load was applied. During the test, the maximum load was kept constant. As shown in Figure K.28, as load was cycled more, the plastic deformation of the specimen increased. The crack length and J-integral are shown in Figures K.29 and K.30 as a function of the applied number of load cylces.

The test results are shown in Figure K.31. The crack growth rate is:

$$da/dN = 5.67 \ X \ 10^{-13} \Delta K^{3.84}$$

Test results are compared with low cylce fatigue crack growth rates of Japanese austenitic stainless steels in Figure K.32. Current data are in good agreement with these data. The appearance of the specimens after the tests is shown in Figure K.33.

6.4 Summary of Post-Test Examination

The hot leg pipe of the HLVT model was investigated at the Takasago R&D Center of MHI. Conclusions are as follows:

(1) No large cracks, other than the dominant crack on the outer surface, were found. The dominant crack initiated and propagated by cyclic forces.

(2) Several small cracks on the inner surface were found opposite the outer crack portion.

(3) The outer surface of the dominant crack portion had been repaired by shielded metal arc welding, prior to the HLVT by the material manufacturer.

(4) At the top bulged portion, the diameter and circumferential length increased slightly ($\approx$ 0.8% and $\approx$ 0.9%, respectively). A thickness change was not clearly identified.

(5) Metallurgical examination of the fracture surface of the dominant crack revealed a series of beach marks. Based on Scanning Electron Mircroscope (SEM) examinations, it appears that locations where striations clearly dominated were limited to Runs 11 and 12 and the beginning of Run 13. The crack propagated by fatigue during these runs. The fracture surface also shows increasing amounts of dimple rupture starting in

Run 11 and increasing to the point that the evidence of striations has disappeared by the end of Run 13. The crack propagation in most of Run 13 and all of Run 14 was due to dimple rupture. During these last two runs, rapid crack propagation is observed due to the ductile tearing on each of the load cycles.

(6)   Test specimens taken from the top bulged portion showed strain hardening, i.e. the 0.2% proof stress increased compared with that of the virgin material.

(7)   Low cycle fatigue tests were conducted with $\Delta\epsilon_t$ from $\approx$ 1% to $\approx$ 6%. The low cycle fatigue strength of the base metal and the weld metal were in good agreement with that of Japanese austenitic stainless steels. Also, the low cycle fatigue strength of the weld metal was found to be the same as that of the base metal.

(8)   Based on the macrostructure examinations, the bulged portions had the same metallurgical structure as the non-bulged portion.

(9)   Crack Propagation Mechanism

- Cracks were caused and propagated by fatigue.

- When the crack was small, it propagated slowly and left striations.

- As the crack grew, it propagated fast and left deformation slips and dimples.

- For the region where striations were observed, the applied load cycles were roughly calculated from the striation spacings. In addition, the applied load cycles were roughly estimated from the intervals of the fracture surface characteristics.

- Cracks were subjected to very high, plastic range, stresses. Furthermore, the loading amplitudes were varied. These conditions made it difficult to estimate the number of applied load cycles from the fracture surface examination. With this limit in mind, the total number of applied cycles was roughly estimated to be about 500-700 cycles.

- The actual applied load cycles were about 800, based on the time history responses, and it was concluded that the above estimated value fell within a reasonable range.

Table 6.1 Items Examined and Conditions

	Items Examined	Notes	Stage Examined or Coupon Taken			Location Investigated	
			Before HLVT	During HLVT	After HLVT	Straight Pipe	Elbow
1	Visual appearance	VI and PT	X	X[2]	X	X (Entire surface)	X (Entire surface)
2	Crack depth	(1) ERT and, visual measurement		X[4]	X		X (Crack portion)
3	Thickness	micrometer	X[3]		X	X (Bulging and non-bulging portion)	X (Near crack portion)
4	Dimension	Tape measure for circumference, micrometer for diameter	X	X	X	X (Full length)	X (Near crack portion)
5	Macro-structure	—			X	X (Bulging and non-bulging portion)	X
6	Micro-structure	Optical microscope			X	X (Bulging portion)	X (Crack portion)
7	Fracto-graphy	Visual and SEM			X	X (Bulging portion)	X (Crack surface)
8	Hardness	Vickers			X	X (Bulging portion)	X (Crack portion)
9	Tensile	At ambient temp. (5D, G.L. = 50 mm for specimen)	X		X	X (Bulging portion)	
10	Low cycle fatigue	Strain controlled (R = −1, Hour-glass type specimen)			X		X (Low stress portion)
11	Crack growth rate	$\Delta J \rightarrow \Delta K$			X		X (Low stress portion)

(1) ERT : Electric Resistance Test   (2) VI only for outer surface   (3) Typical portion   (4) ERT only

6-8

Table 6.2 Diameter and Circumferential Length

(View from P/V to S/G)

O'clock

Direction

S/G

R/V

Top side Bulging
Cracked location
Bottom side bulging

(50) Measuring interval

(Unit : mm)

X

Loca-tion / Direction	0	1	2	3	4	5	6	7	8	9	10	11	12
1~7	352.80	352.63	355.94	356.87	356.26	355.07	354.17	353.09	353.57	353.65	353.63	353.60	353.49
2~8	353.44	353.26	356.00	356.68	356.26	355.19	354.31	353.77	353.50	353.43	353.25	353.22	353.21
3~9	353.56	352.66	355.75	356.58	355.89	354.86	354.15	353.67	353.32	353.15	353.05	353.06	353.01
4~10	353.50	352.55	355.74	356.92	356.10	354.96	354.06	353.65	353.35	353.19	353.10	353.15	353.10
5~11	353.43	351.63	354.53	356.39	355.78	354.61	353.97	353.58	353.48	353.48	353.51	353.48	353.39
6~12	352.36	351.50	353.90	356.17	355.56	354.40	353.88	353.81	353.72	353.75	353.80	353.60	353.55
Circumferential length	1109.00	1107.30	1117.30	1120.50	1118.50	1119.70	1112.50	1111.30	1110.70	1110.70	1110.50	1110.30	1110.00

K

Loca-tion / Direction	K
1~7	353.16
2~8	353.21
3~9	353.22
4~10	353.20
5~11	353.16
6~12	353.15
Circumferential length	1110.00

Y

Loca-tion / Direction	1	2	3	4	5	6	7
1~7	350.84	353.27	354.44	354.46	354.09	353.76	353.41
2~8	350.94	353.25	353.92	354.12	353.85	353.70	353.48
3~9	350.98	353.13	353.80	353.90	353.77	353.68	353.44
4~10	351.22	353.28	354.14	354.04	353.79	353.74	353.46
5~11	351.98	353.38	354.32	354.44	354.05	353.76	353.42
6~12	350.50	353.48	354.55	354.48	354.10	353.82	353.32
Circumferential length	1102.50	1109.00	1113.00	1113.00	1112.00	1111.30	1110.70

Table 6.3   Tensile Test Results

Tensile Properties / Base Metal		0.2 % proof stress σ 0.2 (kgf / mm^2)	Tensile Strength (%)	Elongation (%)	Reduction of Area (%)	Remarks
Specification SCS 14 A - CF		> 21.0	≧ 49.0	≧ 33.0	—	d = ø 14 GL = 70
Specification SA - 351 CF8M		> 21.1	≧ 49.2	≧ 30.0	—	d = ø 12.7 GL = 50.8
Before HLVT (Straight pipe)	MCP1*	22.7	51.3	47.6	63.9	d = ø 10 GL = 50
	MCP2*	23.0	51.5	47.0	66.3	d = ø 10 GL = 50
	MCP3*	23.4	51.9	44.4	67.8	d = ø 10 GL = 50
After HLVT (Bulged pipe)	2A1	32.1	53.8	46.0	79.8	d = ø 10 GL = 50
	2A1	33.7	55.0	39.0	77.5	d = ø 10 GL = 50

*   Internal test data of virgin material MHI

Table 6.4 Low Cycle Fatigue Test Results

Material Temperature	Strain Rate $\dot{\varepsilon}$ (%/SEC)	T.P.	Toral Strain Range $\triangle \varepsilon$ t (%)	Range at Nf/2 cycle (%, kgf/mm²)			Nc (cycles)	Nf (cycles)
				Plastic strain $\triangle \varepsilon$ p	elastic strain $\triangle \varepsilon$ e	stress $\triangle \sigma$		
SCS 14A R.T.	0.4	4	6.28	5.50	0.78	163.0	20	25
		3	4.20	3.46	0.74	93.9	200	220
		2	2.16	1.53	0.63	76.3	1000	1270
		1	1.12	0.72	0.40	56.7	8000	8642
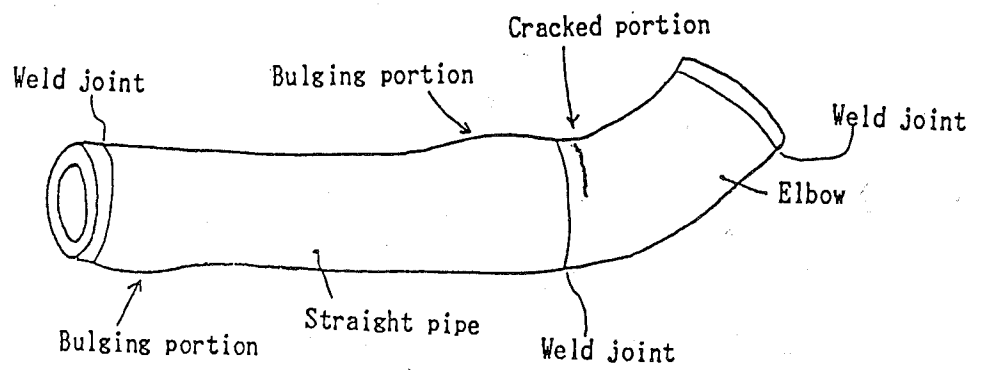
Figure 6.1   Bulging of the Test Pipe
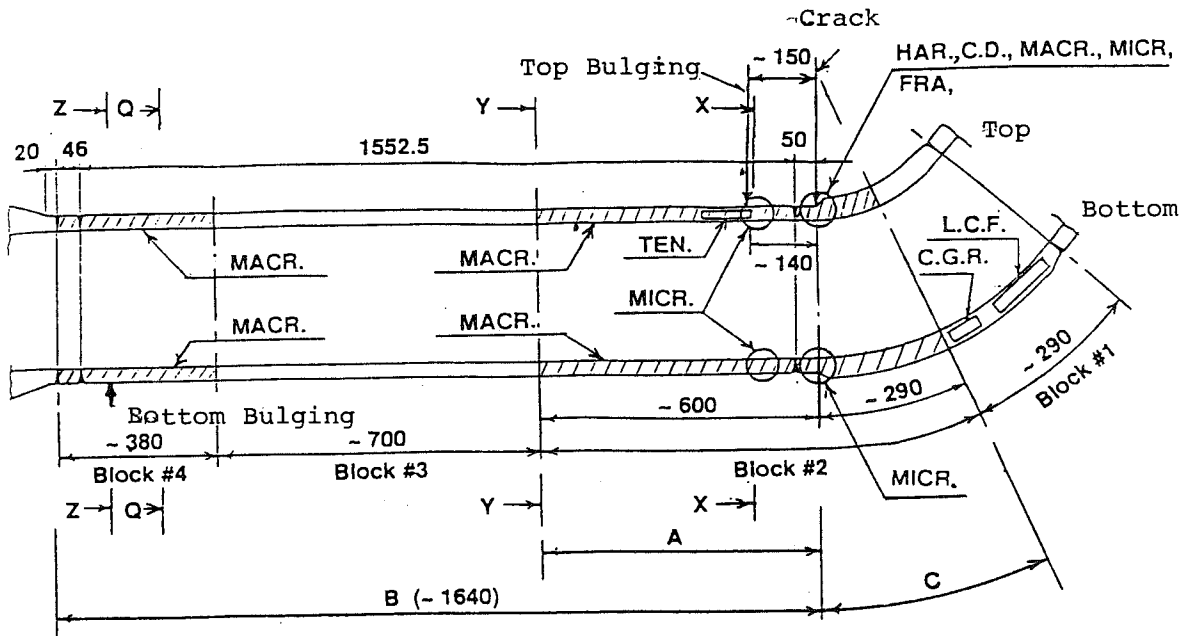
(Longitudinal Section - Top and Bottom)

Range   A : THK., HAR.

B : DIM. (Dia, Circum. length)

C : THK., HAR.

(Transverse Section)

X-X : THK., MACR.

Y-Y : THK.,

Z-Z : THK., MACR.

Q-Q : MACR.

C.D. :	Crack Depth
THk. :	Thickness
DIM. :	Dimension
MACR.:	Macrostructure
MICR.:	Microstructure
FRA :	Fractrography
HAR. :	Hardness
TEN. :	Tensile
L.C.F:	Low Cycle Fatigue
C.G.R:	Crack Growth Rate
(FCR :	Fatigue Crack Propagation

Figure 6.2   Details of Examined Location
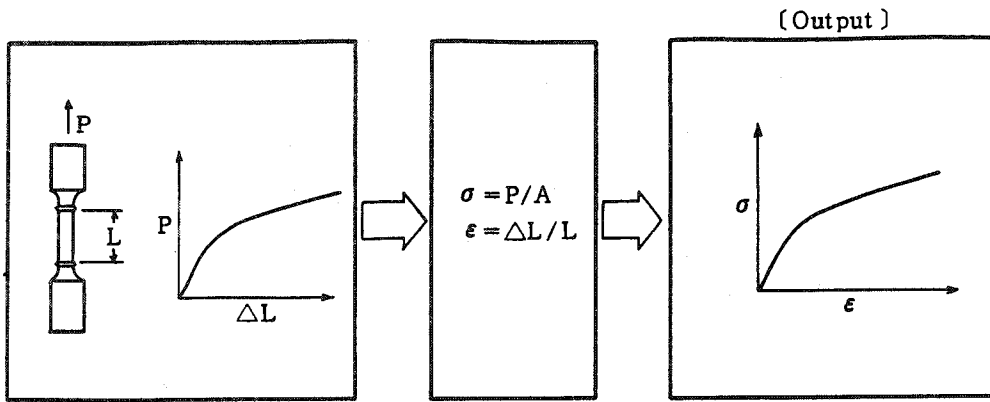
Tensile Test
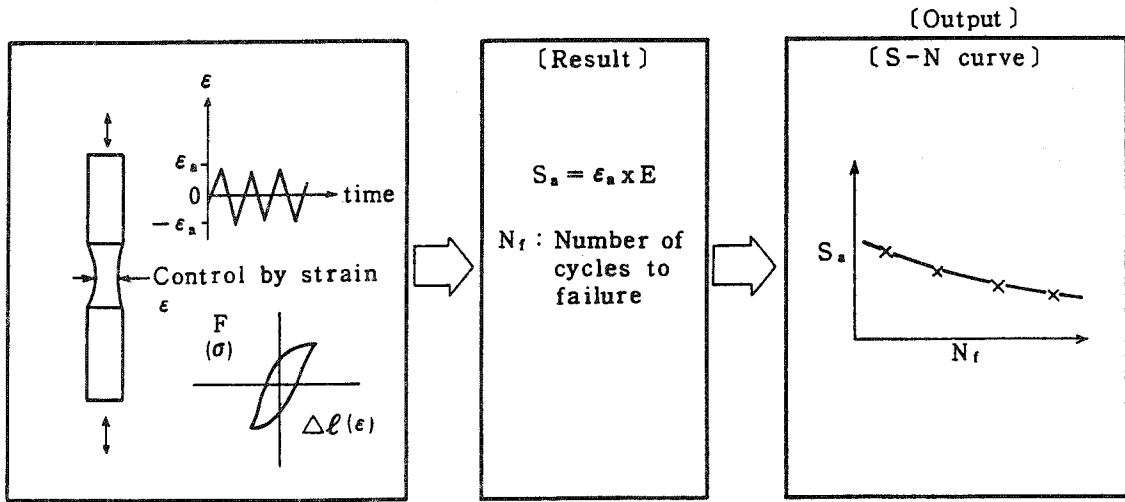
(2) Low Cycle Fatigue Test

S_a ; Stress amplitude
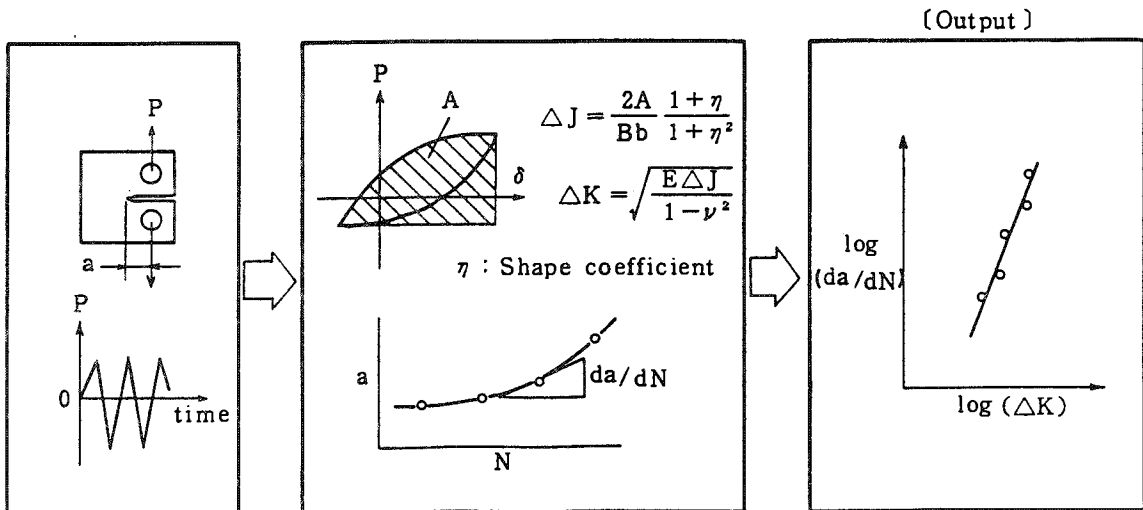
(3) Fatigue Crack Growth Rate

Figure 6.3   Test Procedures

S/G

↑

Cracked location →

Bulged area →

←— Bulged area

↓

R/V
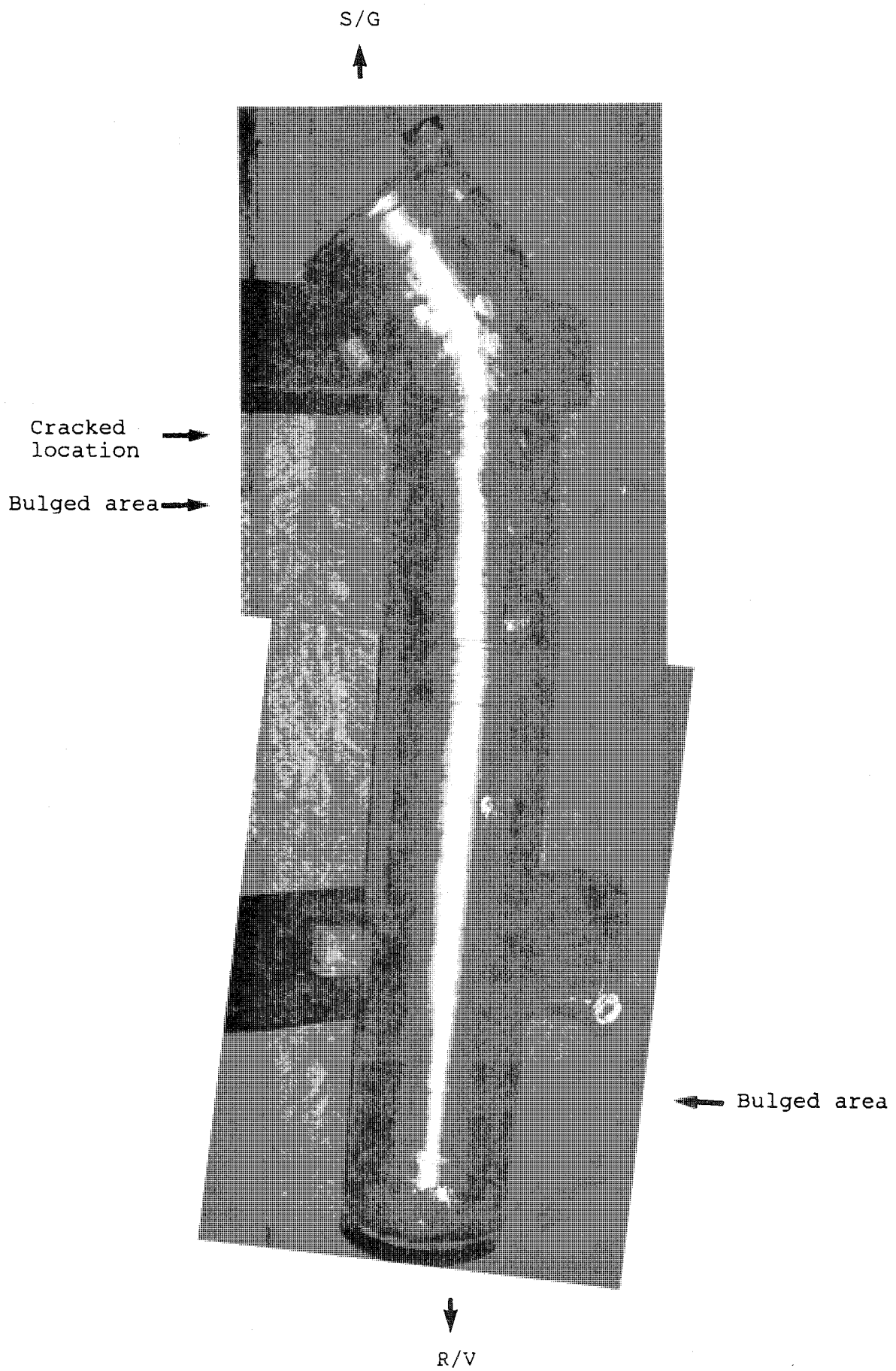
Figure 6-4   Overall View of the Hot Leg Pipe
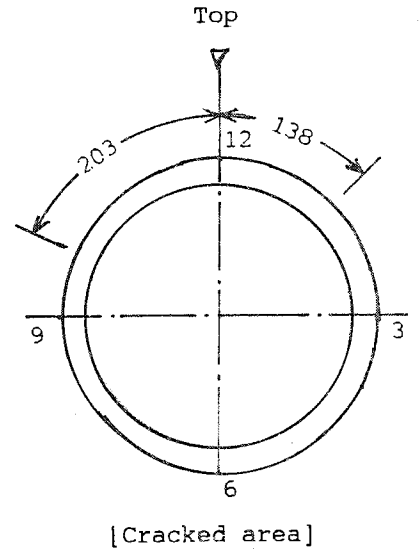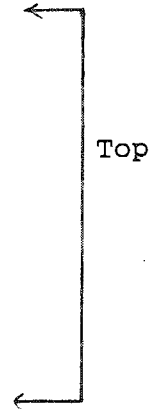
Figure 6.5 Outer Surface of Cracked Area
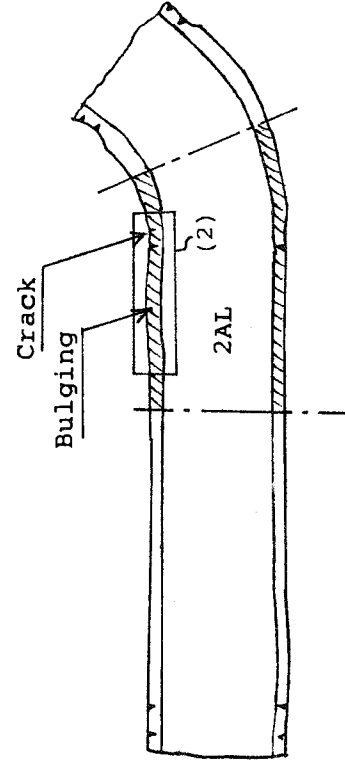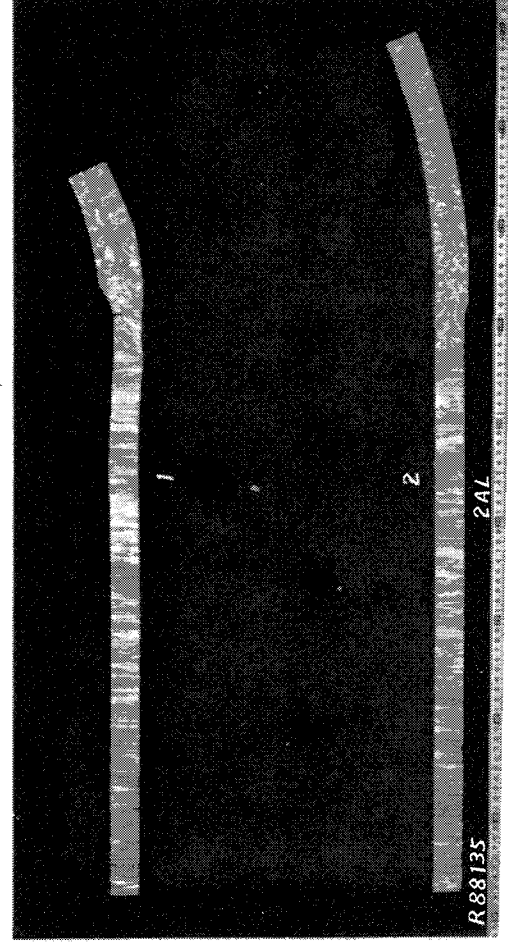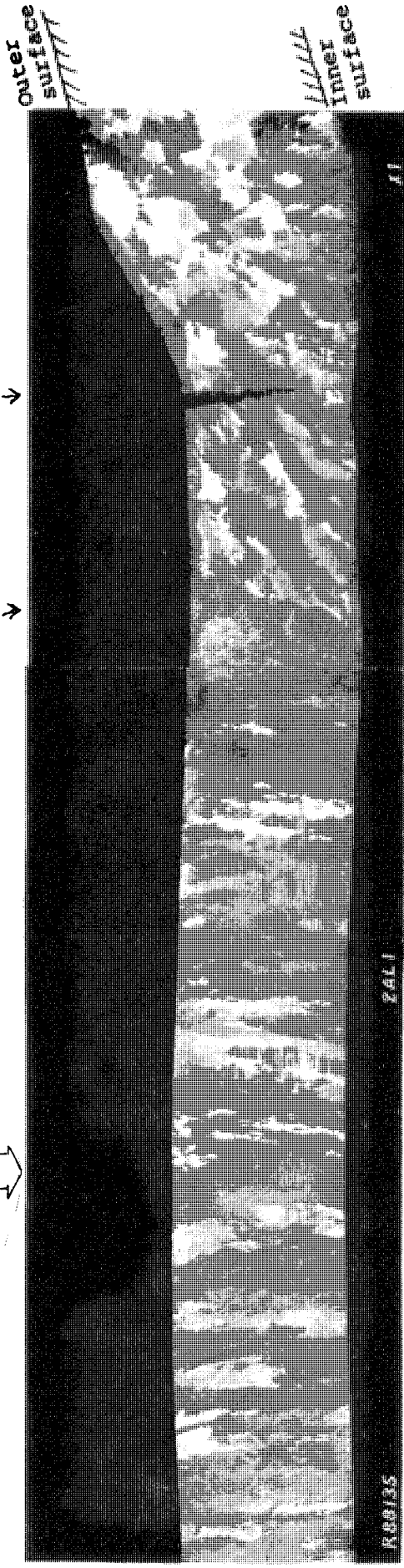
Figure 6.6 Macrostructure of Block #2A Longitudinal Cross Section

6-17

Top (12 O'clock)

C B A

A ∿ F designate crack-origins.

D

E

F

outer surface

D
25
20.
12.0
15.0
21.0
26.0
28.0
4.5mm

E

Fatigue

C B A

Forced Opened Surface

‡ × 1

inner surface

F

Saw Cut
(to reduce
Uncracked Ligament)

· Values on beach marks show
  distance from D.
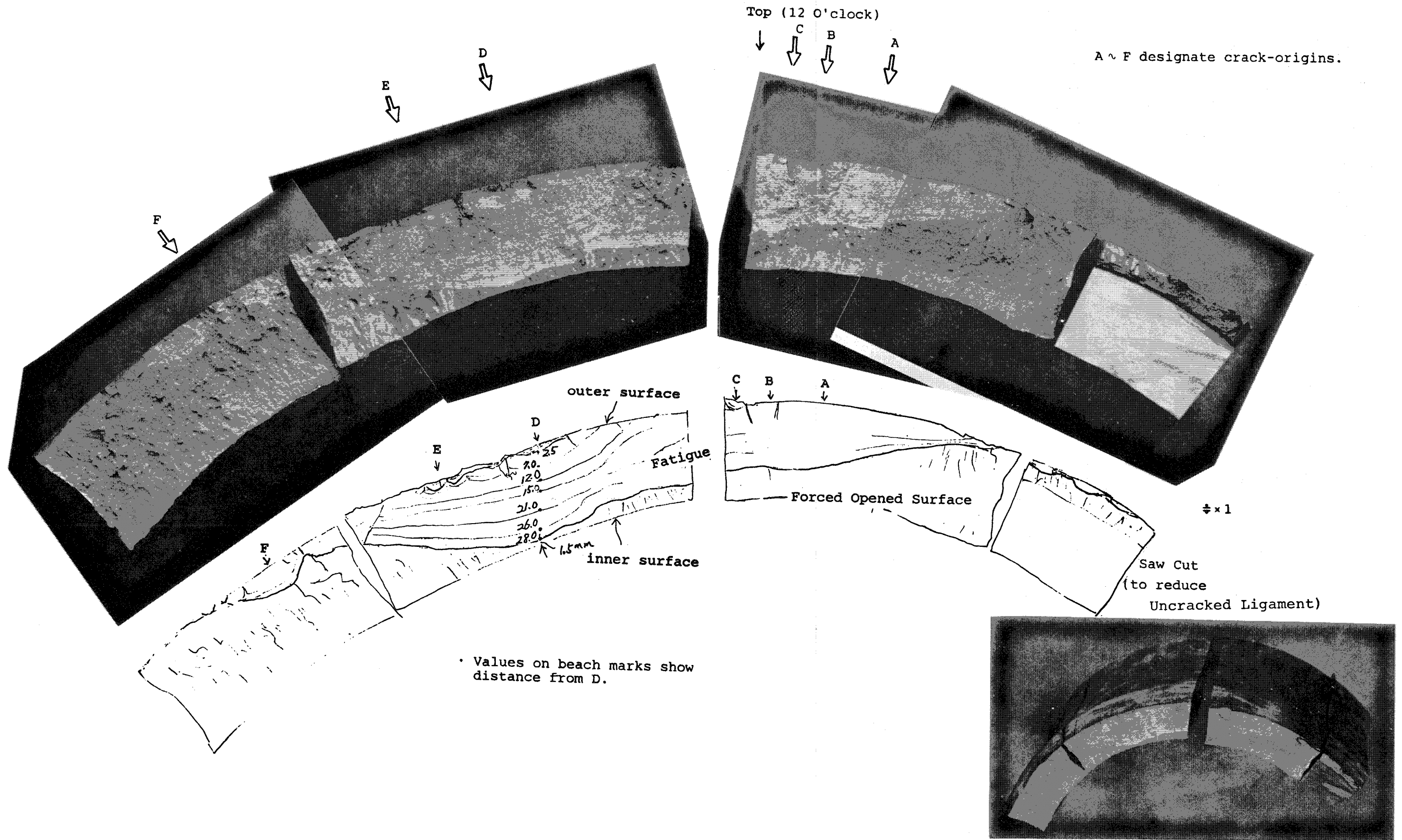
Figure 6.7   Crack Propagation Behavior

×0.33
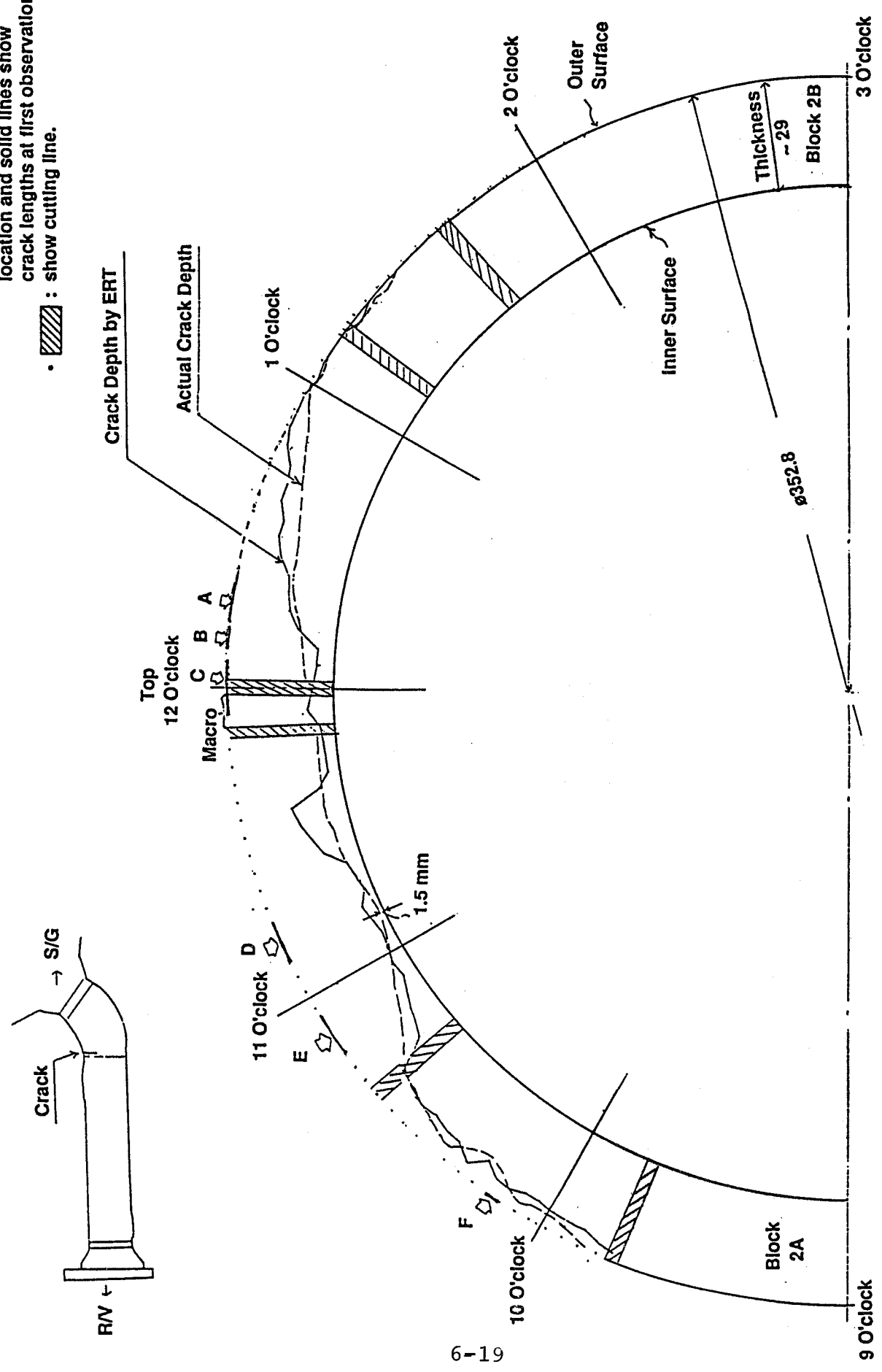
Figure 6.8 Comparison of Crack Depth Measured by ERT with Actual Depth

6-19
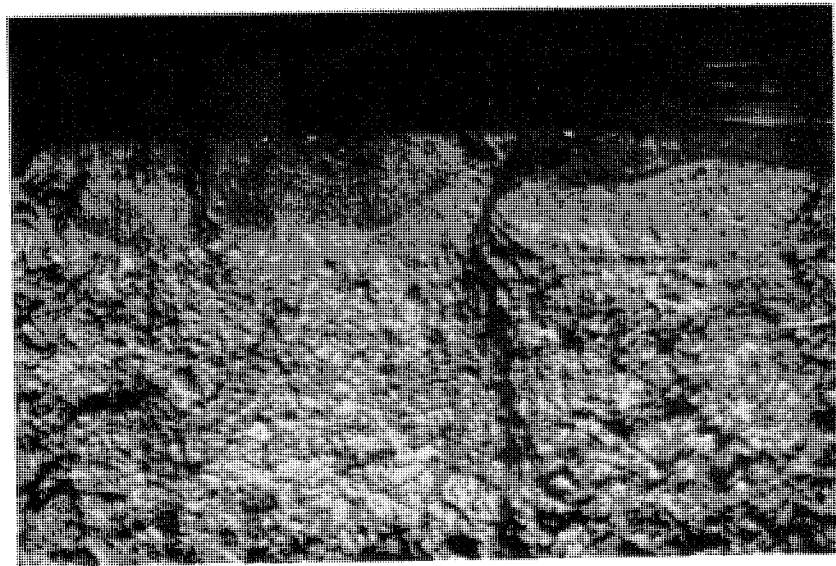
Location E

× 5.5

Location D

Location F

× 5.5

Location B

× 5.5
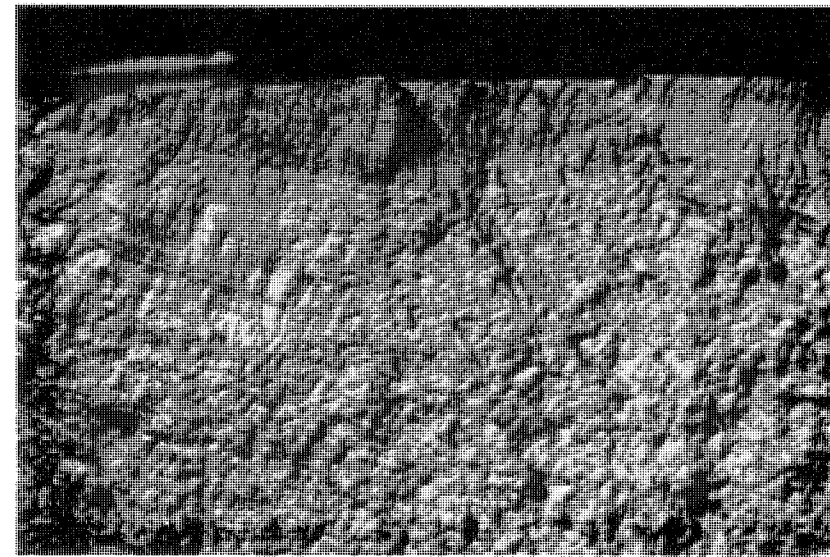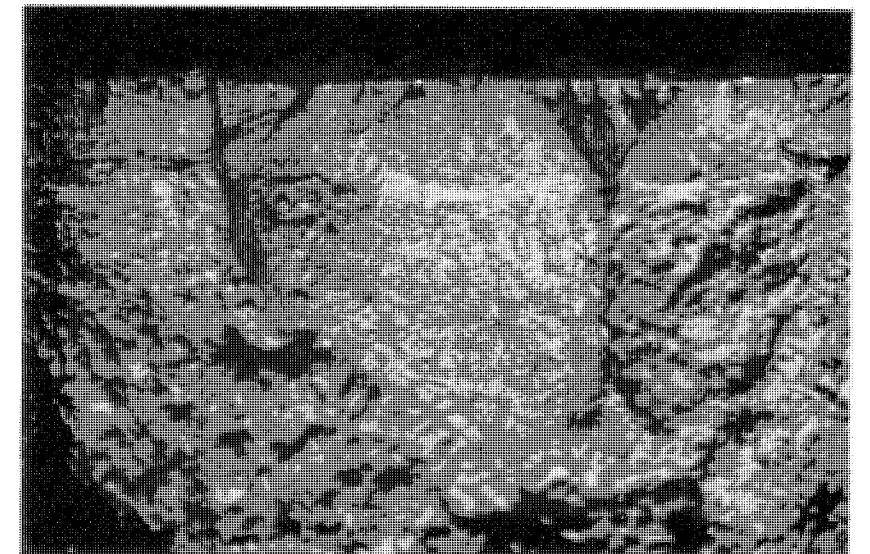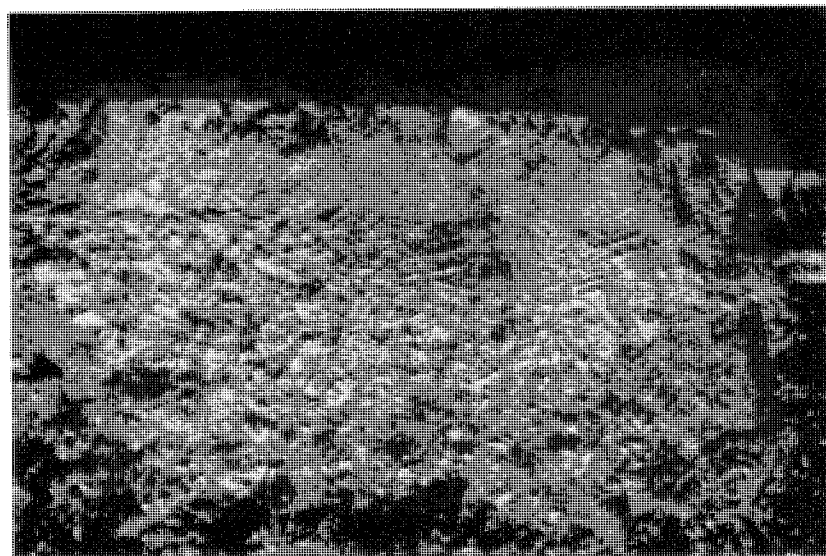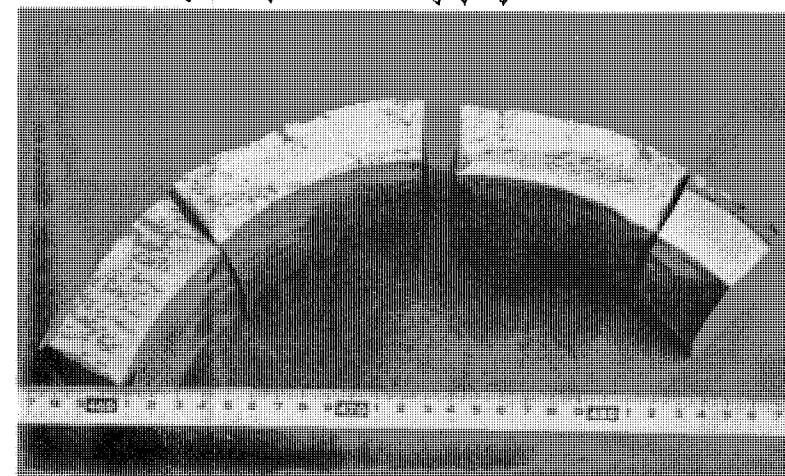
Overall view

Figure 6.9   Details of Crack Origins

Test Temp. = 23 (°C)

Top graph (Nominal Stress vs Nominal Strain):
- Y-axis: Nominal Stress (kgf/mm²), 0 to 100
- X-axis: Nominal Strain (%), 0 to 20

TP No.
◇ : 2A · 1
○ : 2A · 2

Labels: Weld Joint, Bulging Portion, Cracked Portion, Weld Joint, Elbow, Bulging Portion, Straight Pipe, Weld Joint

Current Data (After HLVT) : Base Metal

2A-2
2A-1 } Current Data (Base Metal)

Virgin (Straight Pipe)

Weld Metal

ø10   H18

Weld Metal :
Represent
repair weld

25 — 50 — 25
120

Test Temp. = 23 (°C)

Bottom graph (True Stress vs True Strain):
- Y-axis: True Stress (kgf/mm²), 0 to 100
- X-axis: True Starin (%), 0 to 20

Weld Metal

2A-2
2A-1 } Current Data (Base Metal)

Virgin (Straight Pipe)

Nominal stress $\sigma_N = P / A$
Nominal strain $\varepsilon = \Delta d / d$
True stress $\sigma_A = (1 + \varepsilon) \sigma_N$
True strain $e = \ln (1 + \varepsilon)$

Where, P was load, A was cross section, d was distance between fillets.

Figure 6-10   Stress-Strain Curves

6-21

7.0 POST-TEST ANALYSIS

7.1 Input Motion

The accelerogram input to the seismic simulator is shown in Figure 7.1. The recorded table motion during Run 11 on April 22, 1988 is also shown in Figure 7.2 for comparison. Although the peak acceleration is increased by 27% from the original input signal (1909 gal to 2431 gal), the response spectrum and peak velocity value, which may be more representative of the actual response potential, are closely reproduced. The three recorded table motions during Run 4 (0.1 MPR), Run 8** (0.4 MPR) and Run 11 (1.0 MPR) were selected in the post-test analysis to represent a mostly elastic, a moderately plastic and a fully plastic response, respectively. Moreover, only the first segment (A-segment) was used in the analysis as shown in Figures 7.3 to 7.5. An analysis has indicated that the table motion components other than the excited motion, e.g., pitching and rolling motions, have negligible effects on the responses of the test model. Therefore, only the excited motion, i.e., A_x, was used in the subsequent analysis.

7.2 Analysis Model Description

7.2.1 General

In addition to the MARC elbow model used in the pre-test prediction analysis, four other models were developed using the MARC and ABAQUS Codes for the post-test analysis. These are designated as the MARC plate model, the ABAQUS elbow model, the ABAQUS beam model and the ABAQUS shell model. Among these models, the ABAQUS shell model was used only for a static analysis to study the strain concentration near the crack location in the hot leg pipe. The other four models were used to study the differences in calculated responses due to different codes and different modeling at three excitation levels. The details of each analysis model are described below.

7.2.2 MARC Elbow Model

The same model as shown in Figure 4.1 was used with a few minor changes. For the SG pin-connection, all the rotational components are assumed free while all the translational components are restricted, making the connection an ideal pin in all three directions. This is to reflect the existence of a gap at the pin connection. The same assumption is applied to all the following analysis models. Moreover, to simulate the reinforcement at the pad-support performed between Run 10' and Run 8*, the elements directly connected to the SG channel head, i.e. elements 223, 226, 229, and 232 in Figure 4.1, are assumed to be rigid for the analysis of Run 8** and 11. The rest of the model is identical to the one used in the pre-test analysis.

7.2.3 MARC Plate Model

The foregoing MARC elbow model simplifies piping modeling by using 3-D beam elements for a straight segment and axisymmetric shell elements with a uniform strain along the pipe axis for a pipebend segment. The MARC plate model was developed to investigate possible differences in strain responses around the hot leg elbow when the above simplifications in modeling are eliminated. The four-node flat-plate element (element 75) was used to model the critical portion of the hot leg pipe as shown in Figure 7-6. Twenty four elements are used around the circumference; therefore, a cross-section has forty eight integration points.

A significant simplification was made to save memory space for the parts of the model which are expected to stay in the elastic range. The truss elements to model the SG channel head as well as the SG support beams were replaced by the equivalent rotational springs, K_x and K_y. The rotational spring constant was determined based on a linear static analysis using the foregoing MARC elbow model as,

$$K_x = K_y = 1.2 \text{ E} + 9 \text{ (kg·cm/rad)} \ldots \text{before reinforcement}$$
$$1.6 \text{ E} + 9 \text{ (kg·cm/rad)} \ldots \text{after reinforcement}$$

Moreover, the RCP, crossover leg and the cold leg pipes were replaced by a "super element," which is connected to the SG at Node 331 (see Figure 7-6). The ANSYS Code was used to obtain the properties of the "super element" as follows:

- Translational springs (kg/cm)
  $K_x = 3.47 \text{ E}+4$, $K_y = 6.65 \text{ E}+4$, $K_z = 5.21 \text{ E}+4$
- Rotational springs (kg·cm/rad)
  $K_x = 2.27 \text{ E}+9$, $K_y = 1.09 \text{ E}+9$, $K_z = 8.0 \text{ E}+8$
- Translational masses (kg·sec^2/cm)
  $M_x = 0.62$, $M_y = 0.89$, $M_z = 0.96$
- Rotational masses (kg·cm·sec^2)
  $I_x = 1.16 \text{ E}+4$, $I_y = 2.72 \text{ E}+3$, $I_z = 5.94 \text{ E}+3$

In developing the above model, the use of curved shell elements, which seemed to be a logical choice, was attempted. This was not successful due to a serious numerical instability problem even during the 0.1 MPR level analysis. The same numerical problem, although to a smaller degree, was experienced during a full-plastic analysis using the flat-plate element. Because of this, only the peak portion of the input motion (from 1.0 sec to 1.6 sec) was analyzed for the 1.0 MPR excitation.

7.2.4 ABAQUS Elbow Model

In addition to the two MARC models, the ABAQUS Code was used to compare time history responses using different computer codes. The elbow elements in the MARC Code are formulated based on Fourier interpolation around the circumference and linear or quadratic interpolation along the pipe axis. In this formulation, the ovalization of a cross-section is approximated by Fourier series, called the "ovalization modes" in the documentation of the ABAQUS Code, which are truncated after M terms.

To model the piping of the test model, the two-node elbow element, "ELBOW 31," was used for straight pipes, and the three-node elbow element, "ELBOW 32," was used for pipebends. Linear polynomials are used for "ELBOW 31," and quadratic polynomials are used for "ELBOW 32," to interpolate strains along the pipe axis. Twelve integration points and three ovalization nodes were used for both of the elbow elements. A comparison with a more detailed model using eighteen integration points and six ovalization nodes showed no noticeable improvement, both in the overall responses of the SG and the strain responses of the piping. Therefore, the above piping modeling was used throughout the analyses discussed below. Figures 7.7 to 7.11 show the analysis model and Table 7.1 lists the element properties. The model is identical with the MARC elbow model except for the piping modeling and a few details, reflecting differences in codes. The non-uniform pipe thickness around the circumference is not considered in modeling elbows since the ABAQUS elbow element assumes uniform thickness. The hinge connections at the leg-supports of the RCP (nodes 301 and 302, etc. in Figure 7.9) are modeled by constraint equations without using additional beam elements (i.e., elements 254 and 255 in Figure 4.1). Moreover, the snubbers are modeled as a parallel combination of a spring and a dashpot (see Table 7.1).

7.2.5 ABAQUS Beam Model

The piping of the test model, especially the elbows, is a relatively thick-wall design. The piping modeling of the foregoing analysis models, however, are based on thin-wall shell assumptions. An additional analysis model was developed to obtain responses without the shell-type deformation of piping in order to compare with the foregoing models. The above ABAQUS elbow model was modified for this purpose by replacing the elbow elements, "ELBOW 31" and "ELBOW 32," by nonlinear beam elements, "B31" and "B32," respectively. Therefore, in this modeling, the effect of the internal pressure is not included.

7.2.6 ABAQUS Shell Model

The ABAQUS shell model was developed to examine the detailed strain distribution at the critical section of the hot leg pipe where cracks occurred. Only static analysis was performed using this model. As illustrated in Figure 7.12, the model is very similar to the foregoing MARC plate model. In this model, eight-node doubly curved thick-shell elements, "S8R," are used to model the critical part of the hot leg pipe. Twelve shell elements are used around the circumference. Nonlinear beam elements are used for the remaining part of the hot leg pipe.

7.2.7 Material Properties

No changes were made regarding the material properties for the MARC Models as shown in Figure 4.2 and Table 4.1. A multi-linear curve was used to model the stress-strain relationship of the stainless steel virgin material used for the piping. In using the ABAQUS Code, however, a bilinear curve as listed in Table 7.2 is used for the same material, since it is the only available option. In using both the MARC and ABAQUS Codes, the kinematic hardening rule was used to prescribe the hysteretic behavior of the material. More advanced plastic material modeling, such as the Oak Ridge Model, is not available in current commercial codes in such a way that the complex hardening behavior, resulting from random cyclic strain reversal, can be reproduced to fit the stress-strain curves obtained from laboratory tests. Since the kinematic hardening rule is "history-independent," the effect of previous loadings could not be incorporated in the analyses. Therefore, each analysis was performed as an isolated run.

Viscous damping was assumed to be 0.8% at the vibration frequency in the excited direction. The damping matrix was assumed proportional to the mass matrix.

7.3 Analysis Results

7.3.1 Vibration Frequencies

The measured and calculated vibration frequencies are listed in Table 7.3. The mode shapes of the first three modes of the ABAQUS elbow model are also shown in Figures 7.13 to 7.15. The calculated frequency in the excitation direction ranges from 6.46Hz to 6.81Hz compared with the measured value of 6.64Hz. For the vibration frequency in the direction orthogonal to the table motion, however, the range is much higher, i.e., from 2.23Hz to 3.81Hz compared with the measured value of 3.15Hz. In both the MARC and ABAQUS elbow models, the analysis overestimated the frequency in the Y-direction by about 20%. This difference may be

largely attributed to the additional flexibility caused by the gap at the SG pin-connection. The effect of the flexibility of the supporting frame at the RV-end of the hot leg pipe seems negligible. By including additional springs at the connection, the vibration frequency in the X-direction decreased by only 0.6%.

7.3.2 Response of Steam Generator

The maximum responses during the first segment of the selected three runs are listed in Tables 7.4 to 7.6, including displacement and acceleration at the top of the SG and the RCP, forces at the SG pin-connection and snubbers, and selected strain values. In the MARC analysis, the plate model was used only for the 0.1 MPR and the 1.0 MPR tests. Moreover, time history responses for the 1.0 MPR test were not obtained since only the peak part of the base motion was analyzed due to numerical instability problems. In the ABAQUS analysis, two sets of material properties were used as listed in Table 7.2 for the 0.4 MPR and 1.0 MPR tests. Thus, there was a total of four analyses for each run, except for the 0.1 MPR test in which only the original yield stress values were used.

In Figures 7.16 to 7.18, the relationship of the peak input velocity versus the peak responses of the SG, (i.e., the top relative displacement, the top absolute acceleration and the shear force at the pin-connection) are shown in which the analysis values from Table 7.4 to 7.6 are indicated by a range. From these comparisons, it can be said that the acceleration and displacement responses of the SG in the X-direction agree fairly well, especially at lower excitation levels. The ABAQUS elbow model gives the best prediction at the 0.1 MPR level. However, at the 1.0 MPR level, the MARC analyses have slightly better results than the ABAQUS analyses.

In spite of the above agreement in the responses in the X-direction, all the analyses underestimate the responses of the SG in the Y-direction, as well as the shear force at the pin-connection in both directions. After the reinforcement of the SG support, the shear force at the pin-connection increased considerably. However, the analyses, which are more representative of the test specimen conditions after the reinforcement, follow the lower shear force values obtained before the reinforcement.

The hysteretic behavior of the SG hot leg pipe system is illustrated in Figures 7.19 to 7.21 in terms of the top SG relative displacement and the shear force at a cross-section of the SG right above the hot leg connection nozzle. The reversed S-shape type nonlinearity observed in the hysteresis loops at the 0.1 MPR test, which may be attributed to the gap at the SG pin-connection, is not present in the analysis results as shown in Figure 7.19. Other than this difference, the ABAQUS analysis results agree fairly well

with the observed hysteretic behavior at the 0.1 MPR and 0.4 MPR tests. However, at the 1.0 MPR test, the calculated hysteretic loops show a slightly lower yield strength and higher hysteretic damping compared to the test results (see Figure 7.21).

The comparison of time histories are shown in Figures 7.22 to 7.51 for selected channels. The time histories relevant to the responses of the SG are Figures 7.22, 7.32 and 7.42 for the relative displacement in the X-direction, Figures 7.23, 7.33 and 7.43 for the relative displacement in the Y-direction, Figures 7.25, 7.35 and 7.45 for the absolute acceleration in the X-direction, and Figures 7.26, 7.36 and 7.46 for the shear force at the pin-connection. A clear similarity can be observed between test and analyses for the SG responses in the X-direction and the shear force. However, all the analyses underestimate the responses in the Y-direction. Moreover, the observed one-sided biased response in U_y was not reproduced in the analysis. The biased response may be caused by the nonlinear behavior at the SG pin-connection due to the gap which is not reflected in the analysis models.

7.3.3 Response of Reactor Coolant Pump

The response of the steam generator is dominated by the inertia force of the large mass of the SG itself and the inelastic resistance of the hot leg pipe. The contribution by the crossover leg pipe is very minor based on the calculated forces in the pipes. For the response of the RCP, the effect of the transmitted force through the crossover leg pipe is not negligible, considering the relatively small mass of the RCP. The time histories of the RCP given in Figures 7.24, 7.34, 7.44 show a little more complex nature of the RCP responses due to the contributions by the inertia force of the RCP, the transmitted forces by the crossover leg pipe and the resistance by the hot leg pipe.

The comparison of the peak responses in Table 7.4 to 7.6 shows that the analyses agree fairly well at the 0.1 MPR level, especially the ABAQUS models. However, at higher excitation levels, the analyses overestimate the displacement response and under-estimate the acceleration response in the X-direction. The peak snubber forces are relatively well predicted especially in the ABAQUS analyses.

7.3.4 Strain in Hot Leg Pipe

The hot leg pipe was the most heavily instrumented part of the test model since major plastic action, as well as crack initiation, was expected. About 140 strain gages were used to monitor the elastic-plastic deformation behavior of the pipe. The corresponding analysis results are described in detail in this report. In Tables 7.4 to 7.6, comparisons of the peak strain values at nine key locations are listed. The location 135 is at

7-6

the bottom of the RV end; the locations 143, 148 and 153 are at the top of the straight portion near the elbow; and the locations 164 and 207 are at the top of the elbow near the SG end. Similar comparisons in the strain time histories are also shown in Figures 7.27 to 7.31 for the 0.1 MPR test, Figures 7.37 to 7.41 for the 0.4 MPR test, and Figures 7.47 to 7.51 for the 1.0 MPR test. Figures 7.52 to 7.54 illustrate the axial strain distribution of the test and analyses for each of three runs. The comparisons of the circumferential strain distribution are also given for both axial and hoop strains in Figures 7.55 to 7.66. In addition, strain time histories at eight locations are shown for each analysis run in Figures 7.67 to 7.82.

At the 0.1 MPR level, the peak responses in Table 7.4 indicate that all the analyses underestimate the axial strain at 153X. Comparisons in Table 7.4 and Figure 7.52 show that the ABAQUS elbow model gives the best prediction and the MARC plate model also provides a fairly good prediction. The MARC elbow model consistently underestimates the axial strain and overestimates the hoop strain compared to test results and other analysis results. It should be noted that the initial yield strain of the stainless steel used for the hot leg pipe is about 0.1%. Since the strains calculated using the MARC elbow model and the ABAQUS beam model are within this yield limit, these two analysis results are purely elastic solutions. For the ABAQUS elbow model, a purely elastic analysis gives a lower strain value for 153X (e.g., by assuming the linear property in the ABAQUS elbow model, the peak strain value at 153X is reduced from 0.124% to 0.11%). The circumferential strain distributions, particularly by the ABAQUS elbow model, agree well with the measured ones (see Figures 7.58 and 7.59) except the axial strain distribution obtained by the MARC elbow model (see Figure 7.55).

At the 0.4 MPR and 1.0 MPR levels, discrepancies between analysis and test results become clearer. The comparisons of strain time histories in Figures 7.37 to 7.41 and Figures 7.47 to 7.51 show a "ratchetting phenomenon" in the analysis results using elbow models which is not present in the test results. These time histories indicate a significant bulge in the hot leg pipe and the axial strains drift to either the tension or the compression side. These trends are more prominent in the ABAQUS analyses than in the MARC analyses. During the tests, bulging was observed in the hot leg pipe about one pipe diameter from the transition point. However, the observed bulging is much smaller than the elbow model analyses indicate. Moreover, virtually no drifts are observed in the measured time histories of axial strain. The comparisons of the peak strains at the 1.0 MPR level in Table 7.6 and Figure 7.54 indicate that the ABAQUS beam model gives a much better prediction of axial strain than the MARC and ABAQUS elbow models. Since the beam model yields no shell-type deformations, these comparisons

indicate that the elbow models overestimate the ovalization of the HLVT hot leg pipe which may be classified as a thick-walled pipe (thickness ratio is 0.09 for straight part and 0.11 for elbow part).

The ovalization behavior can be more clearly compared in the form of circumferential strain distributions. Figures 7.62 and 7.63 show the comparison of the circumferential strain distribution by the MARC elbow model at the time the analysis predicted the peak axial strain at 153X location. Clearly, the analysis considerably overestimates the ovalization deformation in the plastic region. Figures 7.64 to 7.66 show the comparisons using the MARC plate model and the ABAQUS elbow model at the time the analysis predicted the peak displacement of the steam generator. Fairly good agreement can be seen in these comparisons. However, the "ratchetting" starts right after this peak in these analyses.

In the ABAQUS elbow model, it was found that the assumed yield stress values have a significant impact on the calculated strain values. Comparisons of peak and time history responses indicate that the use of higher yield stress values significantly reduces the "ratchetting phenomenon" and, thus, leads to a better prediction. In order to determine the material properties correctly for each run, the stress increase due to prior loading reversals should be evaluated. This is not possible in the foregoing analyses since the currently available commercial codes are not capable of reproducing the complex hardening behavior under cyclic loadings. As mentioned before, the kinematic hardening rule is used in both the MARC and ABAQUS analyses since it is the best available option for nonlinear dynamic analyses of piping. A more sophisticated material modeling should be developed to improve the capability of shell-type analysis under nonlinear loading reversals.

As an overall comparison regarding the prediction of strains in the hot leg pipe, the ABAQUS elbow model and MARC plate model produce fairly good results at the 0.1 MPR level. However, at higher excitation levels, both the MARC and ABAQUS elbow models overestimate the ovalization effect and a "ratchet-like" effect appeared in the analyses. At the highly plastic region, a simpler modeling using beam elements seems to produce better results for the thick-walled HLVT piping. Although both the MARC and ABAQUS elbow models produced similar "ratchet-like" effects at higher excitation levels, one remarkable difference was noticed between the two analyses at all the excitation levels. In the MARC elbow model, the largest strain in the hot leg elbow occurs at the inside hoop strain, whereas in the ABAQUS elbow model it is at the outside axial strain.

7.4 Additional Static Analysis

To supplement the above dynamic analyses in which the shell-type deformations were approximated by use of beam, elbow and plate elements, an additional static analysis was performed using eight-node doubly curved thick shell elements as shown in Figure 7.12. The specific objective of this analysis was to obtain the detailed strain distribution around the critical part of the hot leg pipe. A lateral displacement was applied at the top and bottom of the SG in the X-direction and monotonically increased up to the recorded peak values at the 1.0 MPR test (U_x = 7.64 cm). The original stress-strain relationship was used in the analysis.

Figure 7.83 shows the calculated relationship between the applied SG top displacement and strain values at several locations. Within the element nearest to gage 153X, the axial strain varies from 2% to 4% along the pipe axis. Also, the ratio of the average strain over the gage length of 153X to the strain value at the crack location was calculated to be about 1.3 based on the shape function of the shell element. From the same figure, it can be observed that plastic strains around 153X develop rapidly after reaching the yield value. Figures 7.84 and 7.85 show the strain contours at 20% and 100% of the SG displacement, respectively. A clear formation of a plastic hinge is observed at the transition point from the straight and elbow parts of the hot leg pipe. The strain concentration around gage 153X increases at larger displacement levels. However, the hoop strain is much less concentrated. At the maximum displacement level, the calculated shear force at the SG pin-connection is 218.0 tons; which is closer to the value of the ABAQUS elbow model than the recorded value.

7.5 Conclusions from Post-Test Analysis

Based on the comparisons of analyses and test results, the following conclusions can be drawn:

- The input base motion was very accurately reproduced in terms of response spectrum and peak velocity.

- For the SG and RCP responses, i.e., relative displacement and absolute acceleration, all the analyses agree reasonably well with recorded values at all the excitation levels.

- The snubber forces were well predicted. However, the shear force at the SG pin-connection was underestimated by as much as 50%.

- At load levels corresponding to the onset of plasticity, e.g., at the 0.1 MPR level, the ABAQUS elbow model reproduced the recorded responses very well, including the ovalization effect at and near the hot leg pipe elbow.

- At the higher plastic ranges, e.g., at the 0.4 MPR and 1.0 MPR levels, both the MARC and ABAQUS elbow models exhibit a "ratchet-like phenomenon" in the strain responses of the hot leg elbow which was not present in the test results. The simpler model using beam elements produced a better result than the elbow models for the plastic deformation for the thick-walled HLVT piping.

- Material properties, especially the hardening due to previous cyclic loadings, have a significant impact on the calculated strain responses using shell-type elements.

- Currently available commercial computer codes are not capable of reproducing the complex strain hardening behavior of steel under earthquake-like cyclic loads.

- According to a detailed static analysis, the maximum strain near the cracks may have been higher than the recorded value of 2.3% at gage 153X.

Table 7.1 ABAQUS Elbow Model-Element Properties

Element No.	Material	Element Type	D1*	D2*	D3*
(HOT LEG PIPE)					
1,20	E1	Pipe	10	50	
2	P1	Straight Elbow	2.91	17.67	
3	P2	Straight Elbow	2.91	17.67	
4-11	P3	Straight Elbow	2.91	17.67	
12,13	P3	Straight Elbow	2.8	17.67	
14	P3	Elbow	3.71	18.43	
15	P3	Elbow	3.76	18.74	
16	P3	Elbow	3.81	19.05	
17	P3	Elbow	3.86	19.36	
18	P3	Elbow	3.91	19.66	
19	P4	Straight Elbow	3.11	18.86	
(CROSSOVER LEG PIPE)					
41	E1	Pipe	10	50	
42,44,46	P3	Elbow	3.91	19.66	
43,45	P3	Straight Elbow	3.11	18.86	
(COLD LEG PIPE)					
66,70	E1	Pipe	10	50	
67,68	P3	Straight Elbow	2.75	17.72	
69	P3	Elbow	3.515	17.485	
(S/G)					
33,34,35	E2	Pipe	10	50	
36-40	E2	Pipe	4	69.25	
(S/G SUPPORT)					
71,72,73,74	E3	Rigid Beam			
75,76,77,78	E3	Beam	413	4.488E+4	4.553E+4

Table 7.1 (Cont'd)

Element No.	Material	Element Type	D1*	D2*	D3*
79-86	E3	Beam	820	1.76E+5	2.47E+5
87,90	E3	Rigid Beam			
88,89	E3	Beam	720	1.16E+5	9.6E+4
		(RCP)			
47-50	E2	Pipe	6.86	35.435	
57-58	E2	Pipe	40	43.5	
59	E2	Pipe	4	51.5	
60-65	E2	Pipe	4	38.16	
102,103		Snubbers	1.5E+5	0.15	
		(RCP-SUPPORT)			
91-96	E2	Beam	115.2	2.14E+3	1.99E+4
97,98,99	E2	Pipe	1.59	7.0	
100	E2	Beam	38.4	205	73.7
101	E2	Beam	345.6	6.64E+4	8.67E+3

*NOTE:

Pipe	D1 = thickness (cm), D2 = Outsite radius (cm)
Elbow	D1 = thickness (cm), D2 = Outside radius (cm)
Beam	D1 = A (cm^2), D2 = Ix (cm^4), D3 = Iy (cm^4)
Snubbers	D1 = Axial Stiffness (kg/cm), D2 = Damping ratio

Table 7.2 ABAQUS MODEL-MATERIAL PROPERTIES

No. Material	Type	$E(kg/cm^2)$	$fy(kg/cm^2)$	$Ep(kg/cm^2)$
E1	Elastic	4.0E+6		
E2	Elastic	1.96E+6		
E2	Elastic	2.10E+6		
P1	Bilinear	1.99E+6	4900	1.0E+3
P2	Bilinear	1.99E+6	3086(4051)	4.94E+4
P3	Bilinear	1.99E+6	2430(3190)	3.89E+4
P4	Bilinear	1.99E+6	2928(3844)	4.68E+4

NOTE:

(1) Ep is the post-yield modulus.

(2) Yield stress within parenthesis is used for additional analyses to account for the yield stress increase due to prior runs.

TABLE 7.3 COMPARISON OF VIBRATION FREQUENCIES

	SG-X	SG-Y
Test		
(Before Reinforcement)	6.38 Hz	3.15 Hz
(After Reinforcement)	6.64 Hz	3.15 Hz
MARC Elbow Model (B.R.)	6.35 Hz	3.81 Hz
MARC Elbow Model (A.R.)	6.46 Hz	3.61 Hz
MARC Flat-Plate Model	6.81 Hz	2.23 Hz
ABAQUS Elbow Model	6.59 Hz	3.76 Hz
ABAQUS Beam Model	6.68 Hz	3.80 Hz
ABAQUS Shell Model*	6.55 Hz	2.71 Hz

* Model used for static analysis

TABLE 7.4 COMPARISON OF PEAK RESPONSES AT 0.1 MPR (A-Segment)

| | Test | MARC ANALYSIS | | ABAQUS ANALYSIS | |
		Elbow Model	Plate Model	Elbow Model	Beam Model
SG					
Ux(cm)	0.95	0.808	1.04	0.95	0.945
Uy(cm)	0.14	0.062	0.070	0.093	0.074
Ax(gal)	1630	1276	1606	1580	1610
Ay(gal)	212	55	25	102	80
RCP					
Ux(cm)	0.021	0.016	–	0.021	0.020
Uy(cm)	0.011	0.0035	–	0.003	0.003
Ax(gal)	395	188	–	220	221
Ay(gal)	175	13	–	29	39
PIN					
Fx(ton)	7.0	31.6	34.1	33.9	32.2
Mx(ton-m)	0.16	0.32	0.58	0.51	0.29
SNUBBERS					
83x(ton)	2.66	1.9	–	2.85	2.66
84x(ton)	1.15	0.9	–	1.48	1.5
H.L.Strain(%)					
135x	0.078	0.053	0.086	0.058	0.058
143x	0.068	0.048	0.067	0.058	0.063
148x	0.073	0.057	0.083	0.086	0.080
153x	0.153	0.062	0.114	0.124	0.083
153y	0.038	–	0.019	0.030	–
164x	0.054	0.030	0.067	0.078	0.062
164y	0.045	0.070	0.022	0.036	–
207x	0.10	0.028	0.051	0.081	0.061
207y	0.059	0.080	0.003	0.033	–

TABLE 7.5   COMPARISON OF PEAK RESPONSES AT 0.4 MPR (A-Segment)

	Test	MARC ANALYSIS Elbow Model	Elbow Model	ABAQUS ANALYSIS Elbow* Model	Beam Model	Beam* Model
SG						
Ux(cm)	3.88	3.32	3.38	3.75	3.55	3.68
Uy(cm)	0.92	0.31	0.41	0.44	0.31	0.33
Ax(gal)	5470	3928	4400	5180	4450	5240
Ay(gal)	510	309	371	402	284	327
RCP						
Ux(cm)	0.076	0.067	0.079	0.084	0.081	0.085
Uy(cm)	0.04	0.02	0.015	0.019	0.016	0.017
Ax(gal)	1610	1196	1210	1210	1210	1270
Ay(gal)	825	186	292	254	408	447
PIN						
Fx(ton)	254	119	110	124	105	116
Mx(ton-m)	3.68	0.8	0.9	1.17	0.93	1.05
SNUBBERS						
83x(ton)	13.5	8.2	10.5	11.1	10.9	11.3
84x(ton)	6.6	3.0	5.8	6.3	5.9	6.4
H.L.Strain(%)						
135x	0.39	0.25	0.80	0.48	0.36	0.29
143x	0.43	0.16	0.83	0.36	0.25	0.23
148x	0.46	0.21	2.05	1.38	1.15	0.88
153x	0.78	0.73	4.04	2.28	1.42	1.17
153y	0.19	-	1.90	0.90	-	-
164x	0.16	0.42	1.92	0.79	0.24	0.22
164y	0.15	0.54	1.63	0.64	-	-
207x	0.39	0.49	0.49	0.28	0.21	0.22
207y	0.22	0.70	0.22	0.10	-	-

* Analysis using the increased yield stress

TABLE 7.6 COMPARISON OF PEAK RESPONSES AT 1.0 MPR (A-Segment)

	Test	MARC ANALYSIS			ABAQUS ANALYSIS		
		Elbow Model	Plate Model	Elbow Model	Elbow* Model	Beam Model	Beam* Model
SG							
Ux(cm)	7.64	7.10	7.43	6.41	6.84	6.38	6.79
Uy(cm)	3.04	0.56	–	0.69	0.75	0.47	0.55
Ax(gal)	7280	5853	6669	6400	7460	6330	7250
Ay(gal)	600	495	–	566	622	516	611
RCP							
Ux(cm)	0.104	0.11	–	0.127	0.142	0.137	0.149
Uy(cm)	0.05	0.036	–	0.03	0.03	0.03	0.03
Ax(gal)	3800	3049	–	2970	2950	3470	3480
Ay(gal)	1230	776	–	720	694	1060	949
PIN							
Fx(ton)	402	203	272	178	200	161	182
Mx (ton-m)	6.14	1.45	1.22	1.40	1.40	1.38	1.56
SNUBBERS							
83x(ton)	23.7	14.6	–	17.1	19.2	18.5	20.0
84x(ton)	11.6	4.9	–	9.4	10.6	9.3	10.1
H.L.Strain(%)							
135x	1.18	0.72	0.88	1.85	1.08	1.20	1.06
143x	1.10	0.36	0.55	1.77	0.87	0.59	0.49
148x	1.38	0.42	0.93	2.08	1.67	2.42	2.51
153x	2.28	3.59	2.03	4.94	3.32	2.73	2.90
153y	0.34	–	0.30	4.26	1.81	–	–
164x	0.24	1.14	0.52	3.34	1.37	0.46	0.46
164y	0.21	1.23	0.35	3.76	1.06	–	–
207x	0.78	0.94	0.47	0.69	0.57	0.34	0.39
207y	0.37	0.83	0.27	0.79	0.38	–	–

*Analysis using the increased yield stress
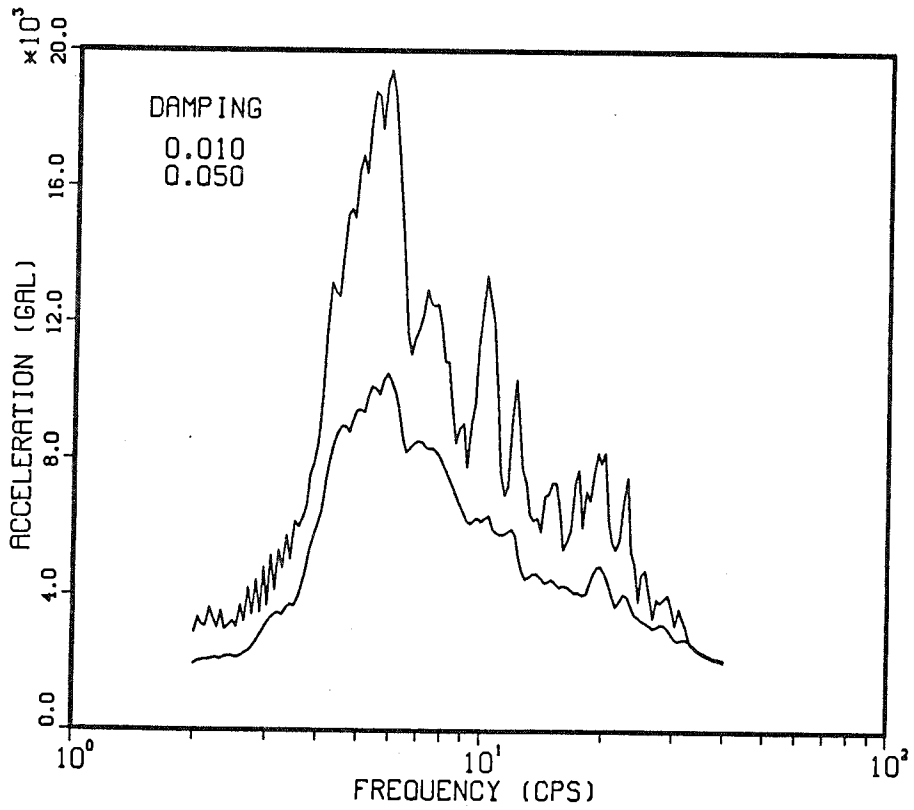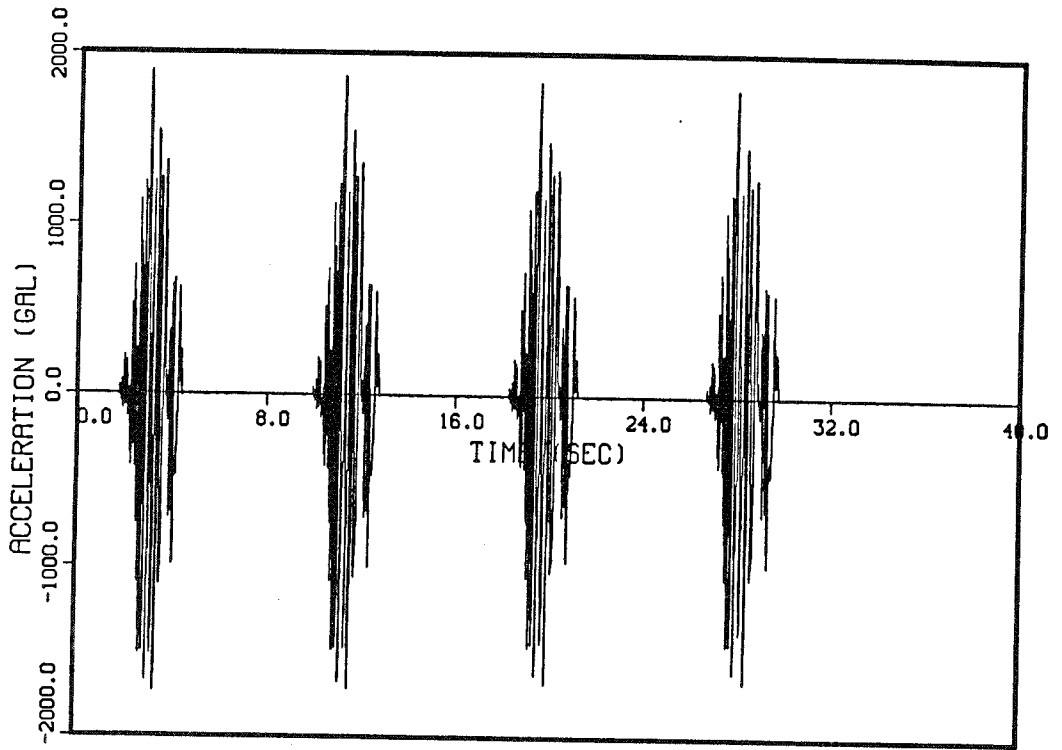
Figure 7.1 Original Accelerogram Input for Shaking Table (1.0 MPR)
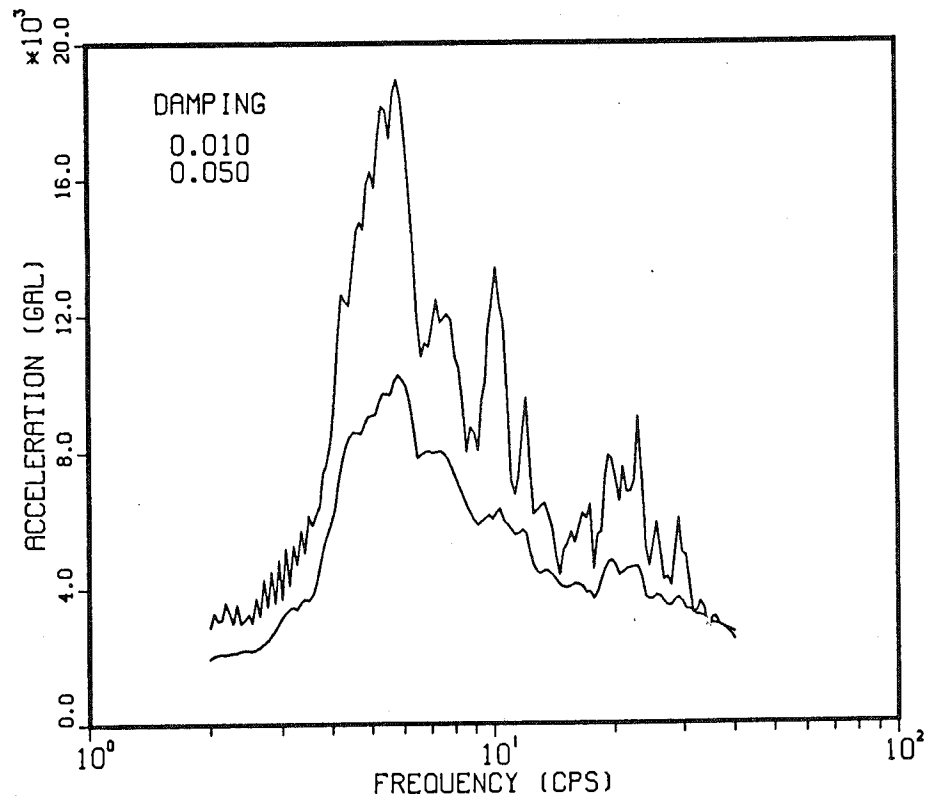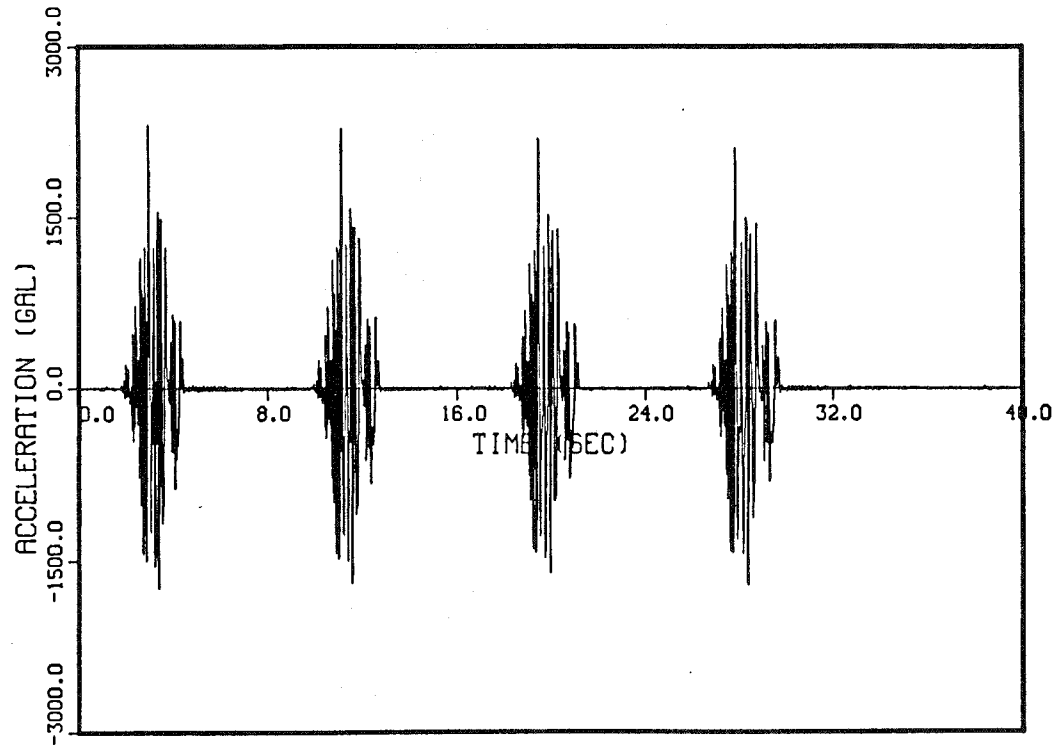
Figure 7.2   Recorded Horizontal Table Motion at 1.0 MPR Test on 4/22
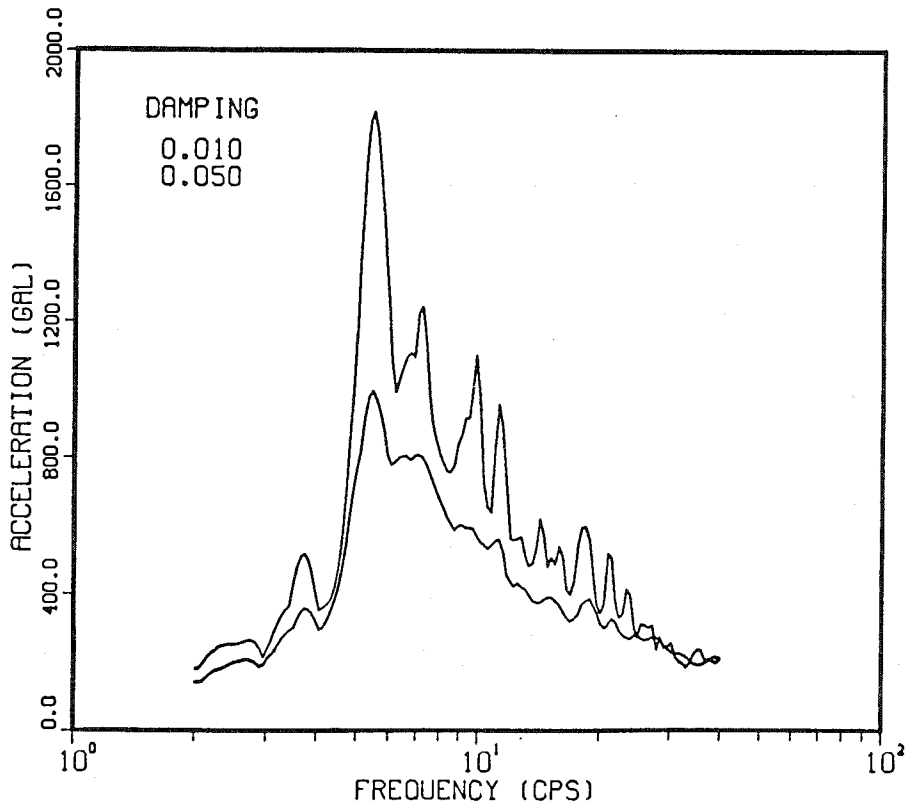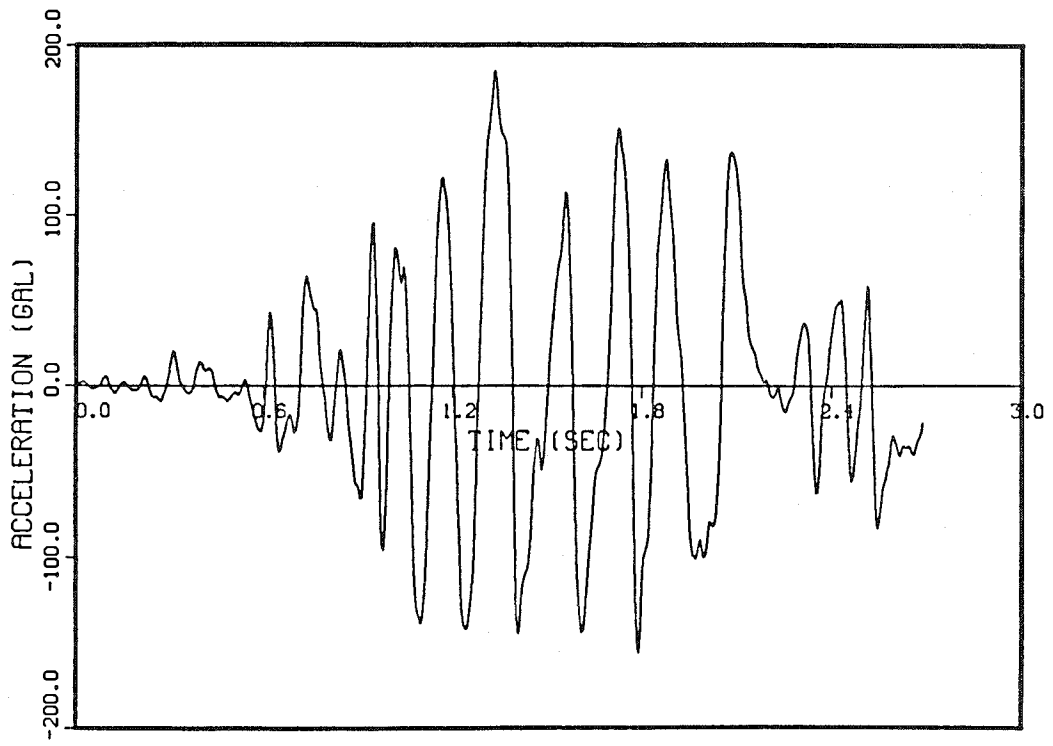
Figure 7.3   Recorded Horizontal Table Motion at 0.1 MPR Test on 4/4
             (A-Segment)
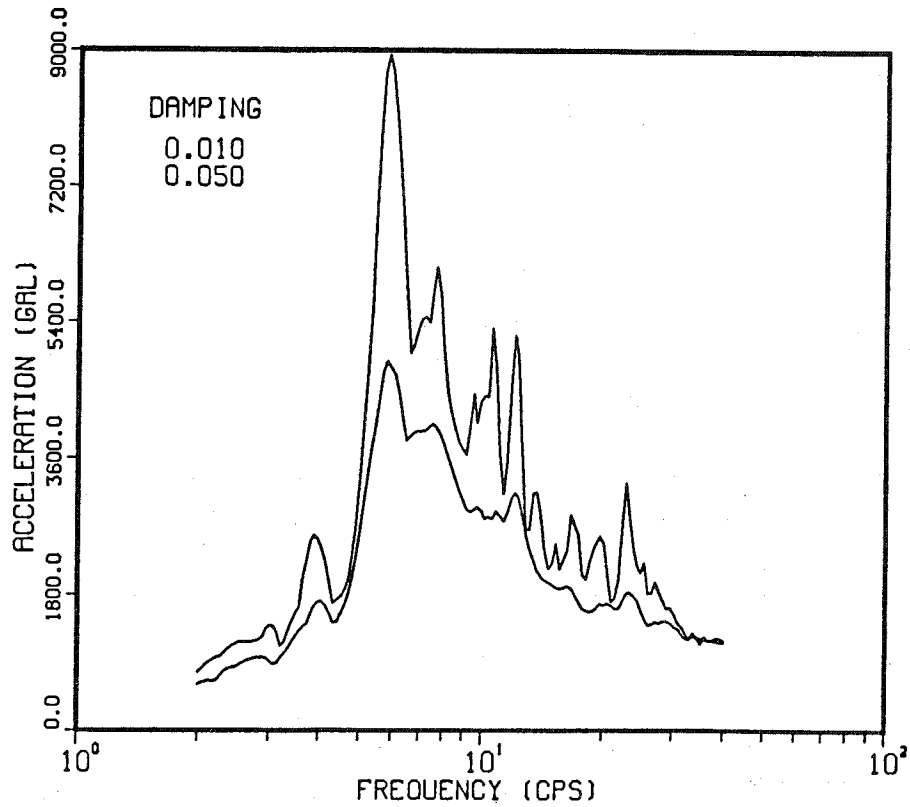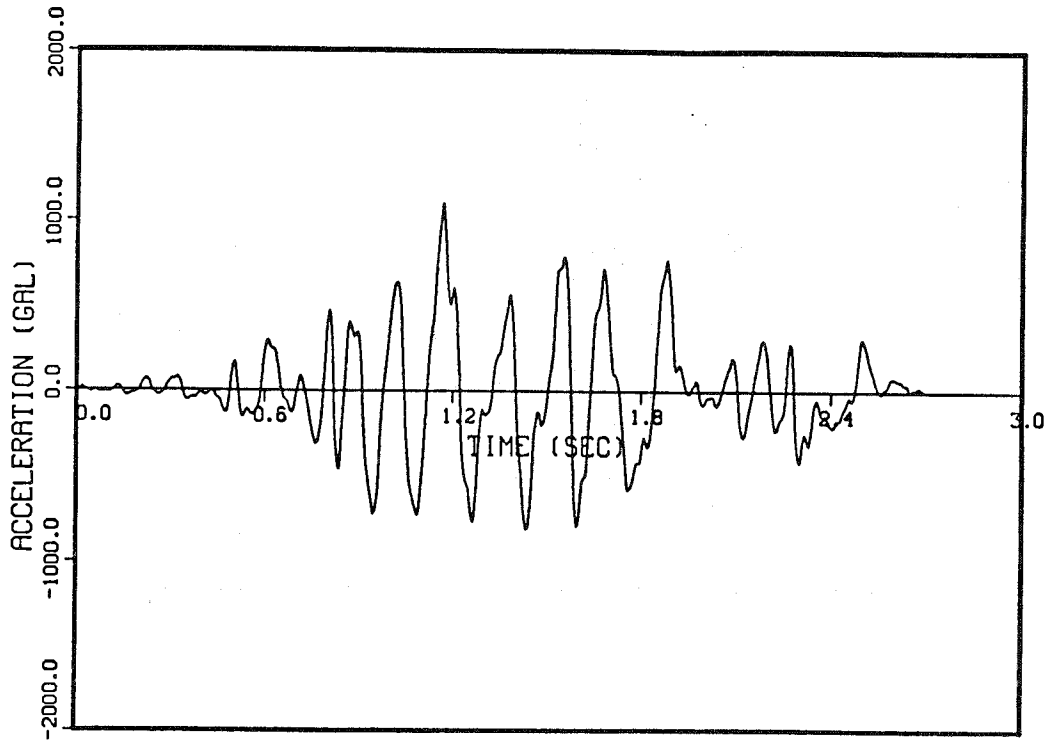
Figure 7·4   Recorded Horizontal Table Motion at 0.4 MPR Test on 4/19
(A-Segment)
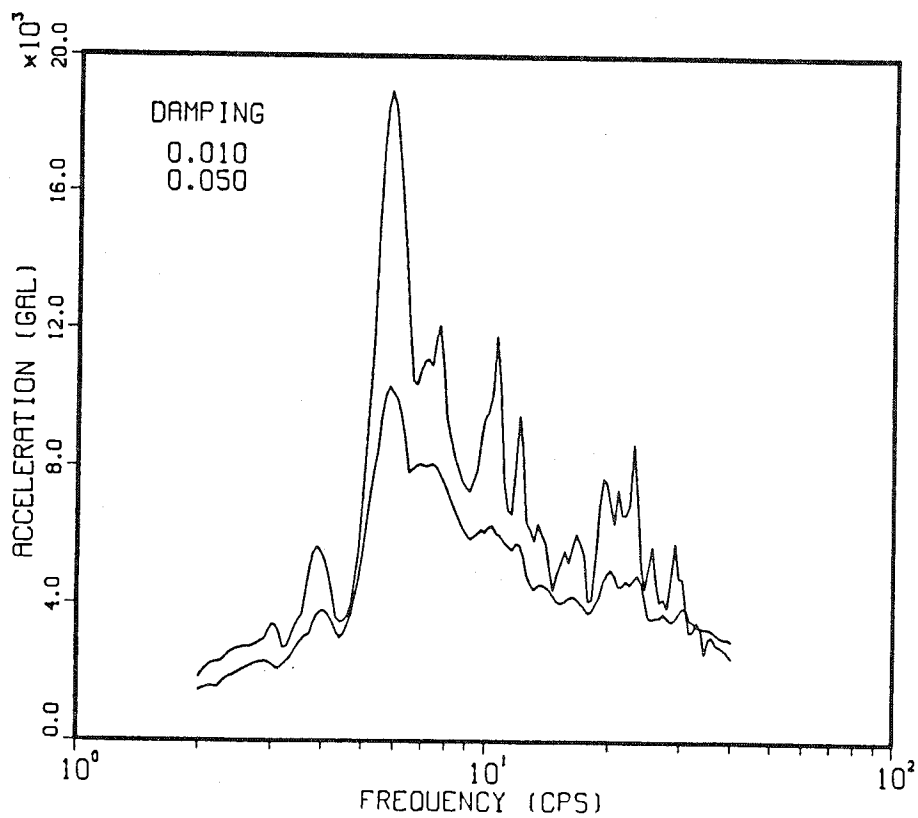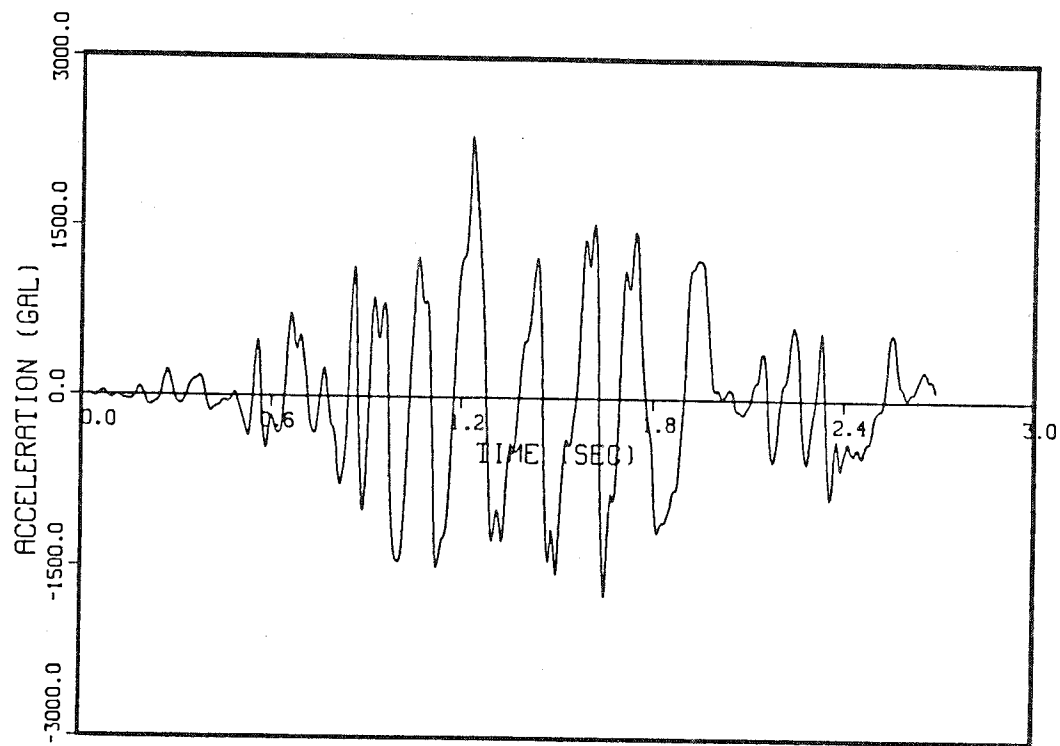
Figure 7.5   Recorded Horizontal Table Motion
at 1.0 MPR Test on 4/19 (A-Segment)
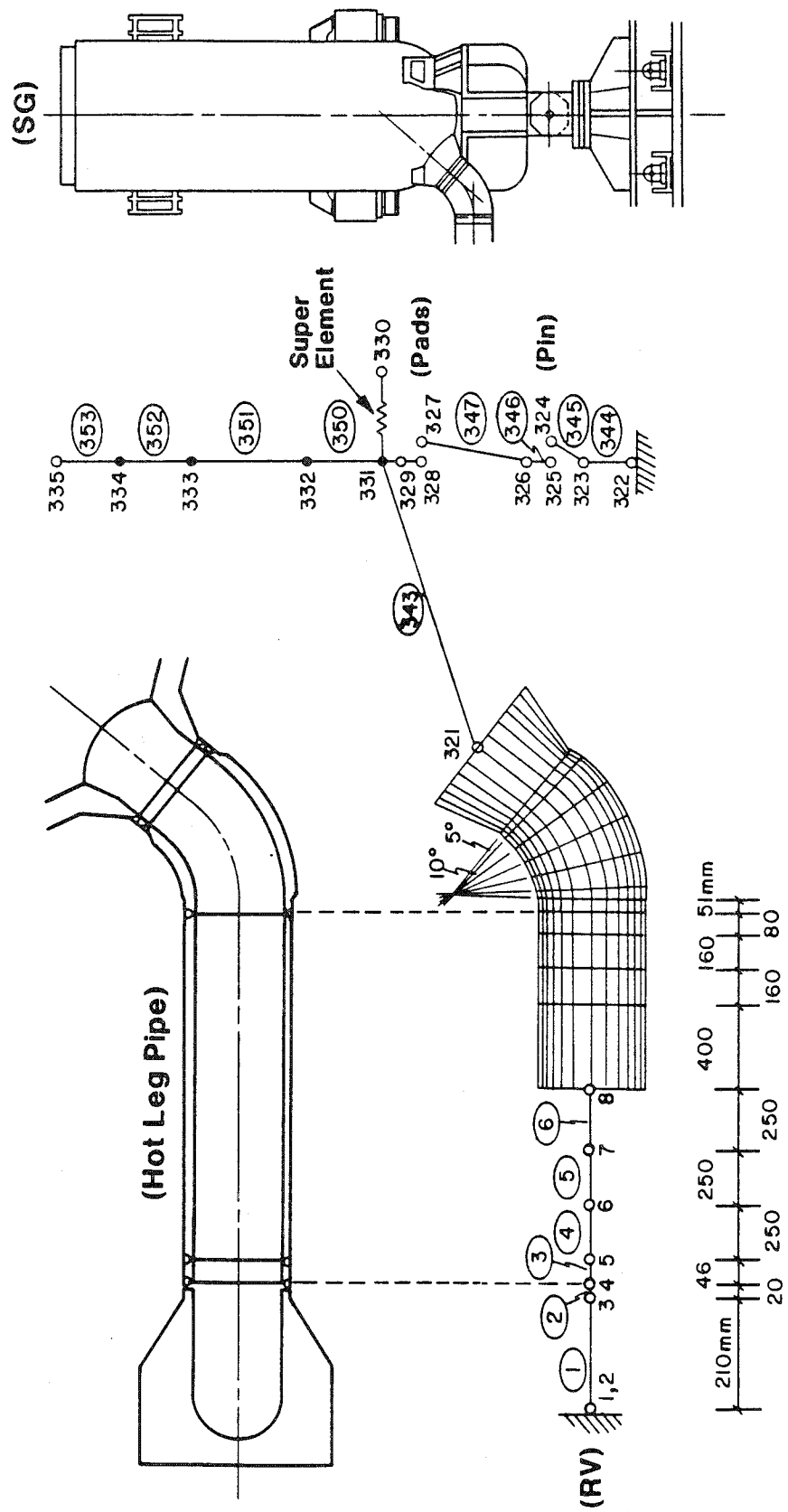
Figure 7.6 MARC Flat-Plate Model

Figure 7.7 Node Numbers of ABAQUS Elbow (& Beam) Model

Figure 7.8 Element Numbers of ABAQUS Elbow (& Beam) Model
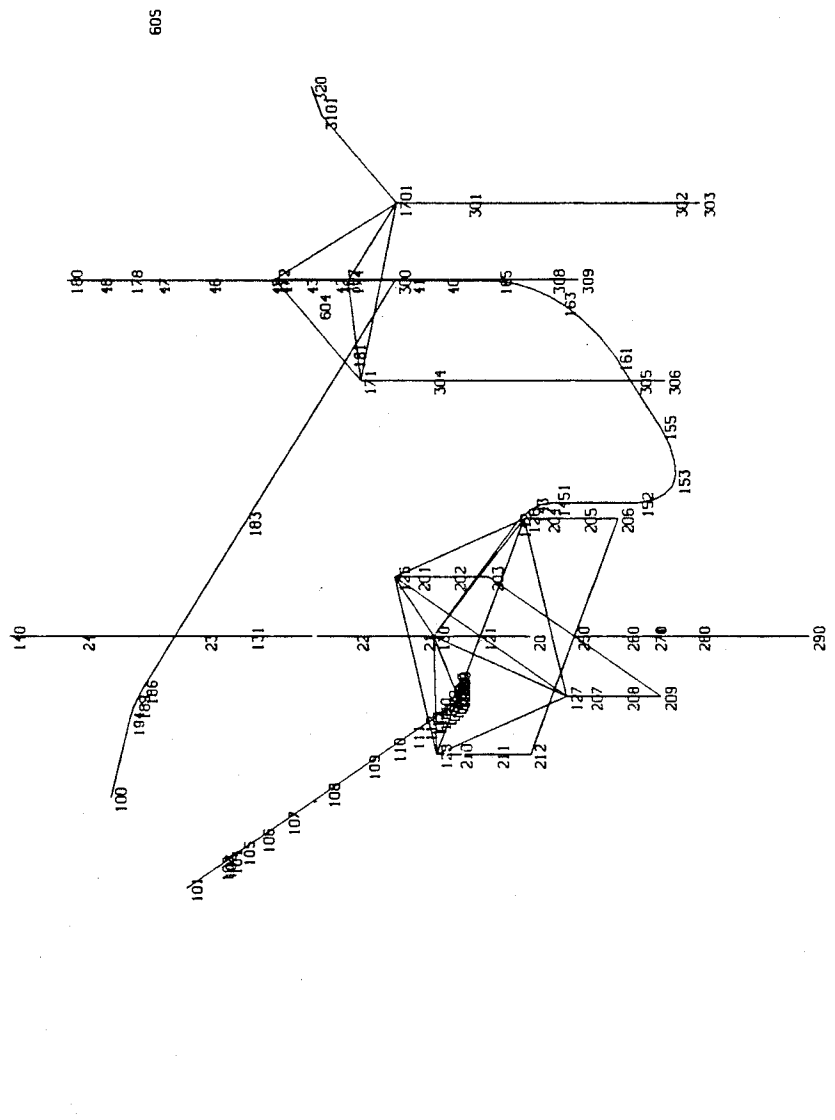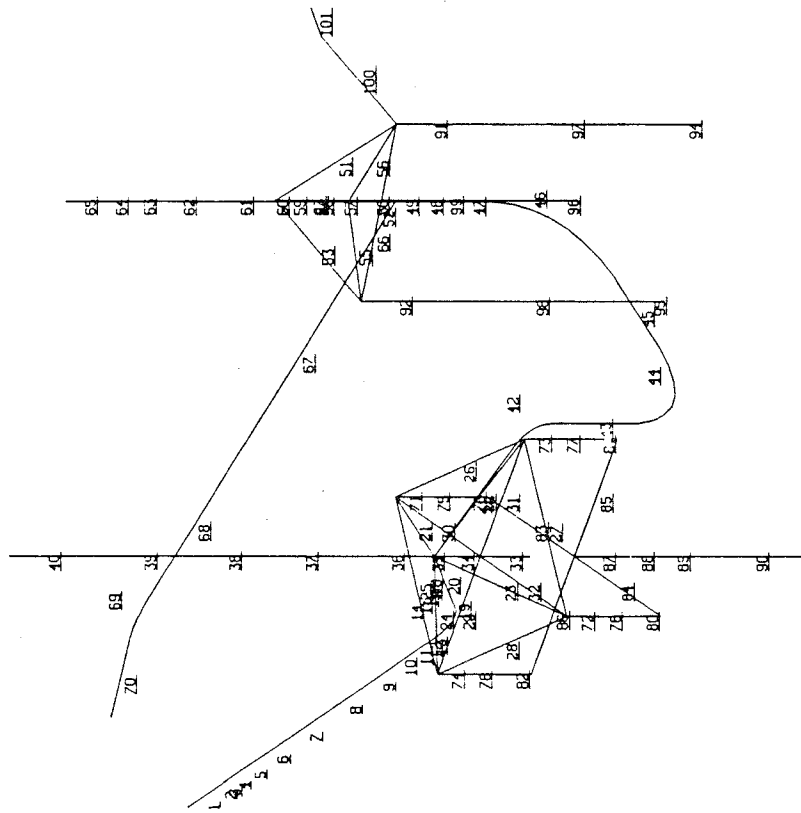
HLVT ABAQUS MODEL
ABAQUS VERSION 4-7-1   DATE: 3/27/89   TIME: 16:25: 3
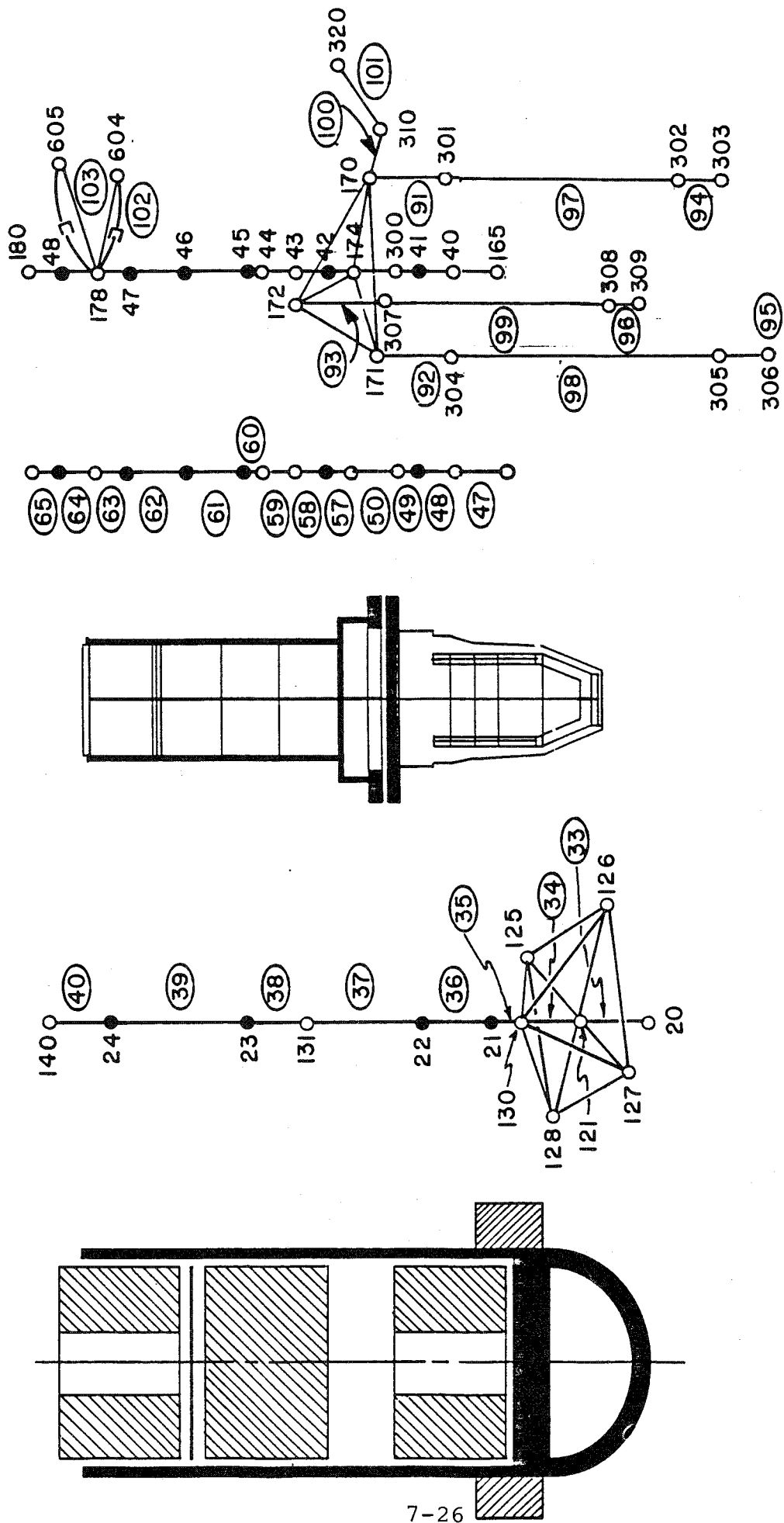
Figure 7.9   ABAQUS Elbow Model (Steam Generator and
Reactor Coolant Pump)
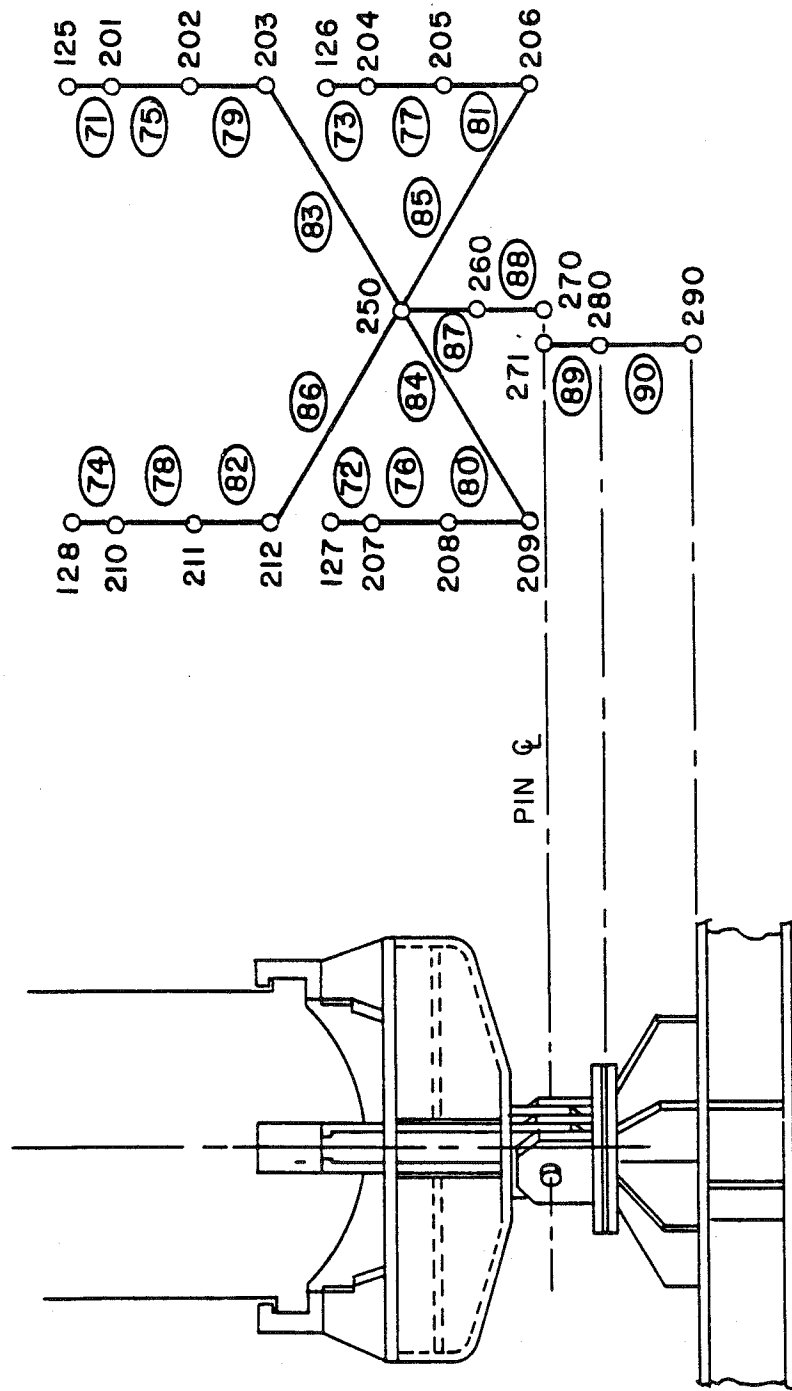
Figure 7.10 ABAQUS Elbow Model (Steam Generator Support)
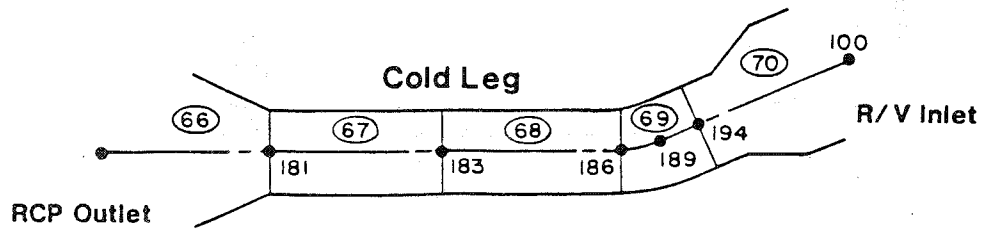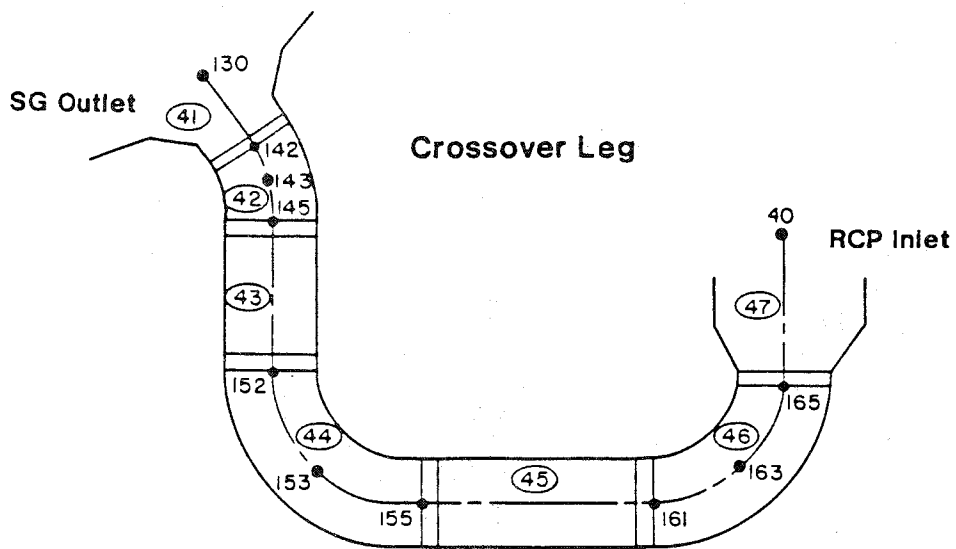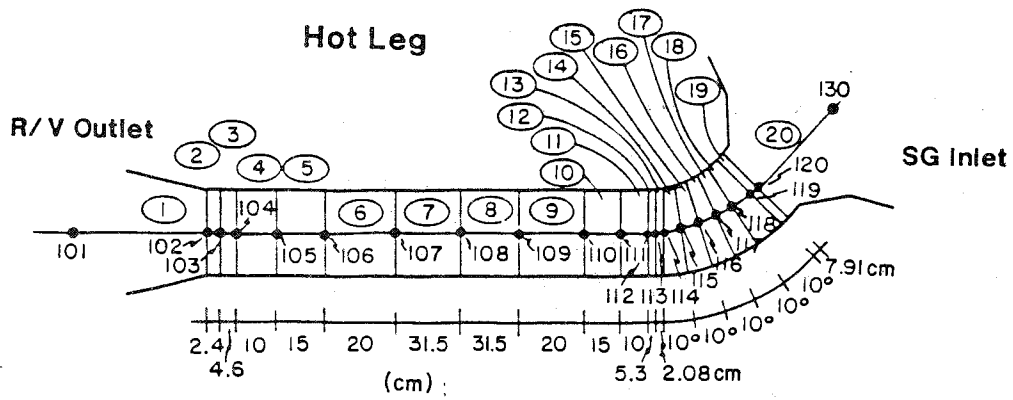
Figure 7.11 ABAQUS Elbow Model (Piping)
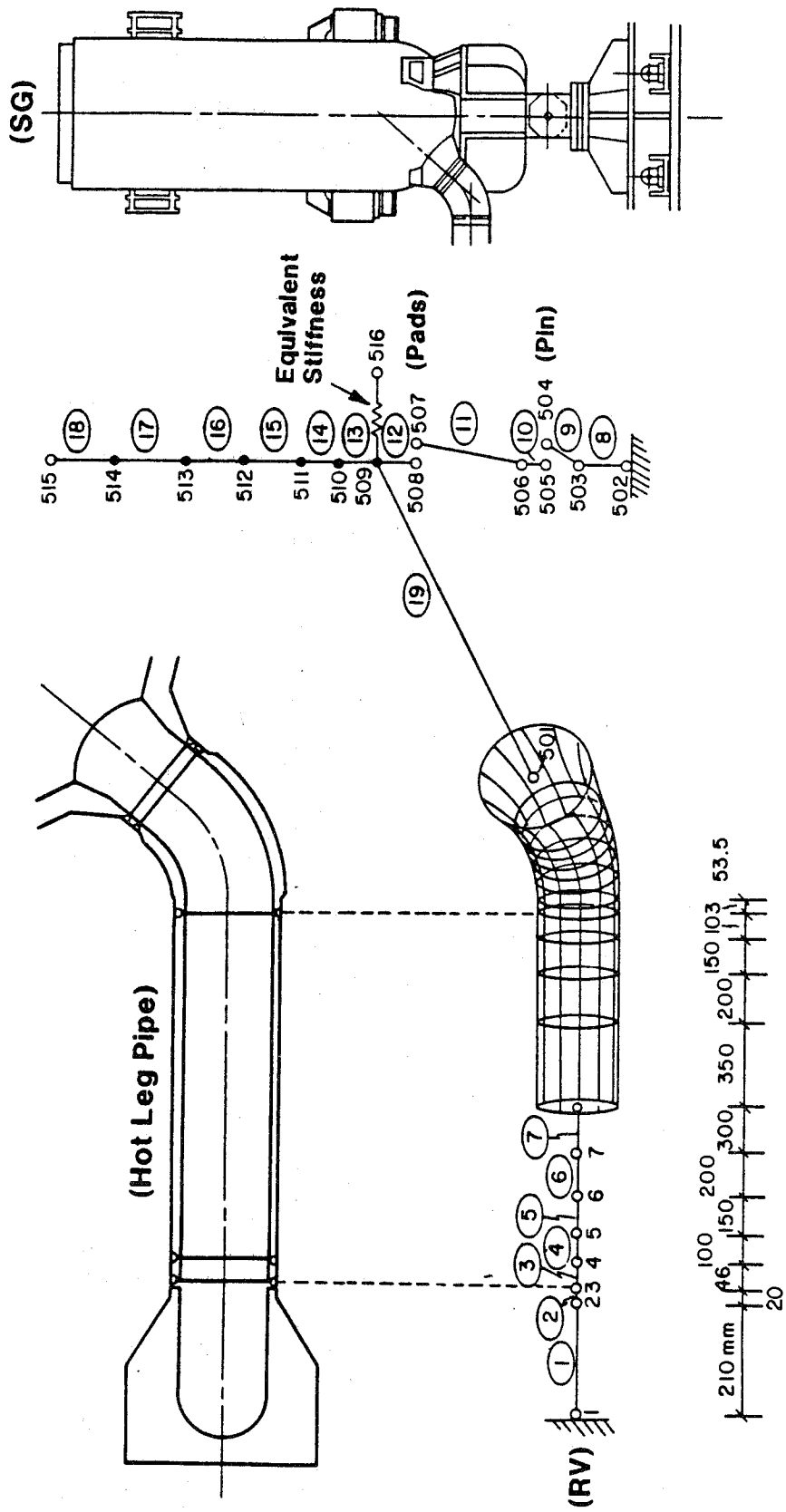
Figure 7.12 ABAQUS Shell Model

7-29

U
MAG. FACTOR = +2.4E+01
SOLID LINES - DISPLACED MESH
DASHED LINES - ORIGINAL MESH
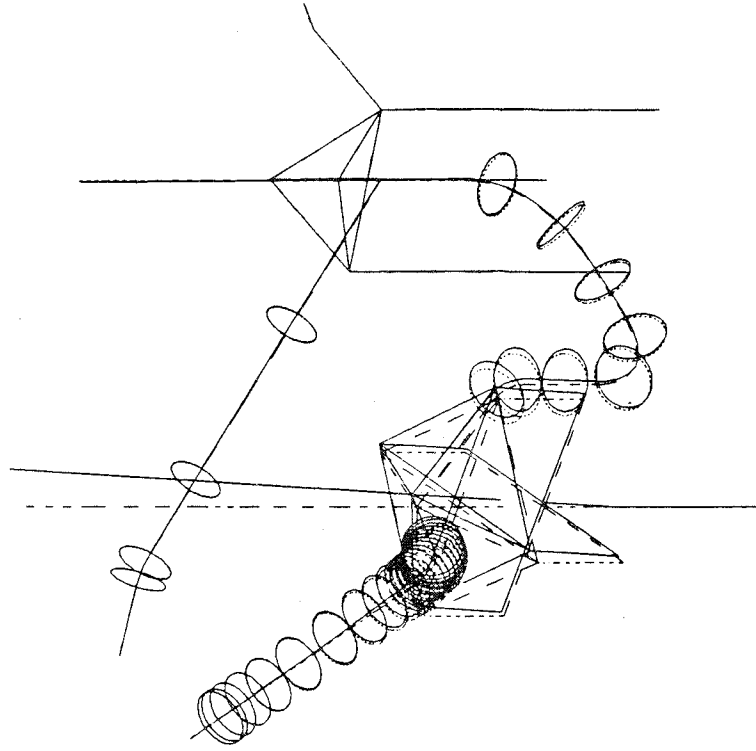
HLVTOE---EIGENVALUE ANALYSIS

EIGENVALUE = +5.566E+02

ABAQUS VERSION 4-7-1   DATE: 3/27/89   TIME: 16:25:54

Figure 7.13 First Mode of ABAQUS Elbow Model (3.76Hz)
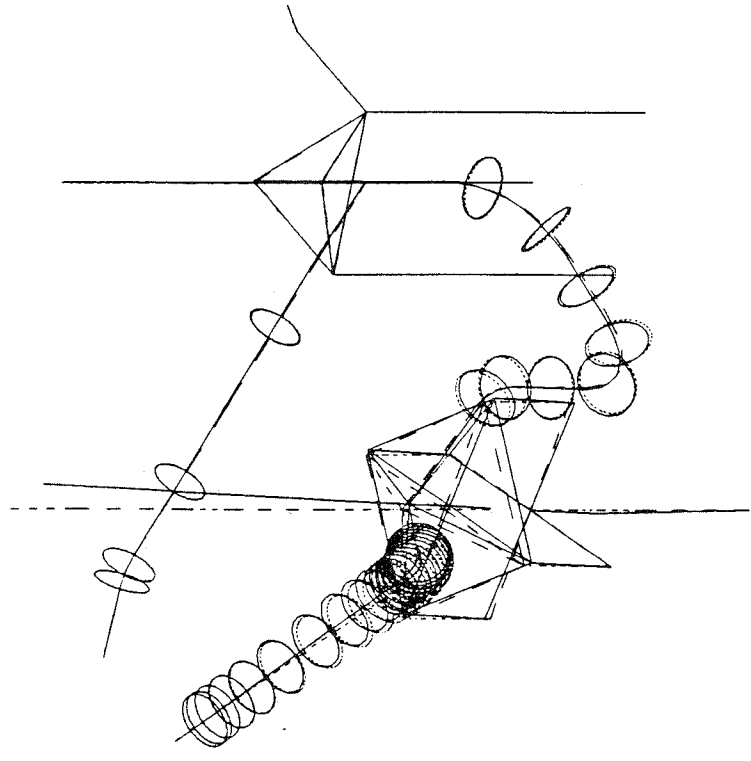
U
MAG. FACTOR = +2.8E+01
SOLID LINES - DISPLACED MESH
DASHED LINES - ORIGINAL MESH
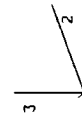
HLVTOE---EIGENVALUE ANALYSIS

EIGENVALUE = +0.000E+00

ABAQUS VERSION 4-7-1   DATE: 3/27/89   TIME: 16:25:54

Figure 7.14 Second Mode of ABAQUS Elbow Model (6.59Hz)

U
MAG. FACTOR = +2.3E+01
SOLID LINES - DISPLACED MESH
DASHED LINES - ORIGINAL MESH
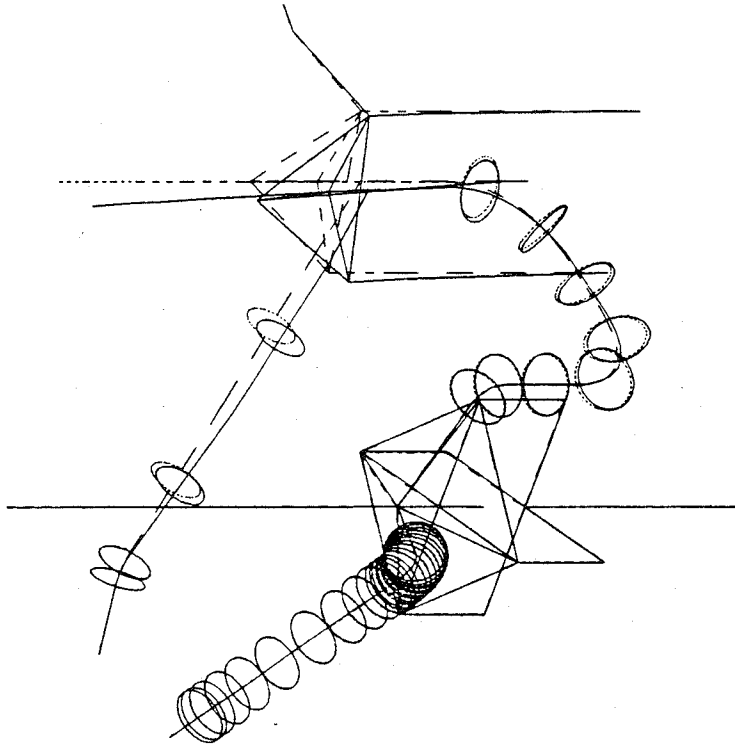
HLVTOE---EIGENVALUE ANALYSIS

EIGENVALUE = +0.000E-00

ABAQUS VERSION 4-7-1   DATE: 3/27/89   TIME: 16:25:54

Figure 7.15 Third Mode of ABAQUS Elbow Model (32.09Hz)
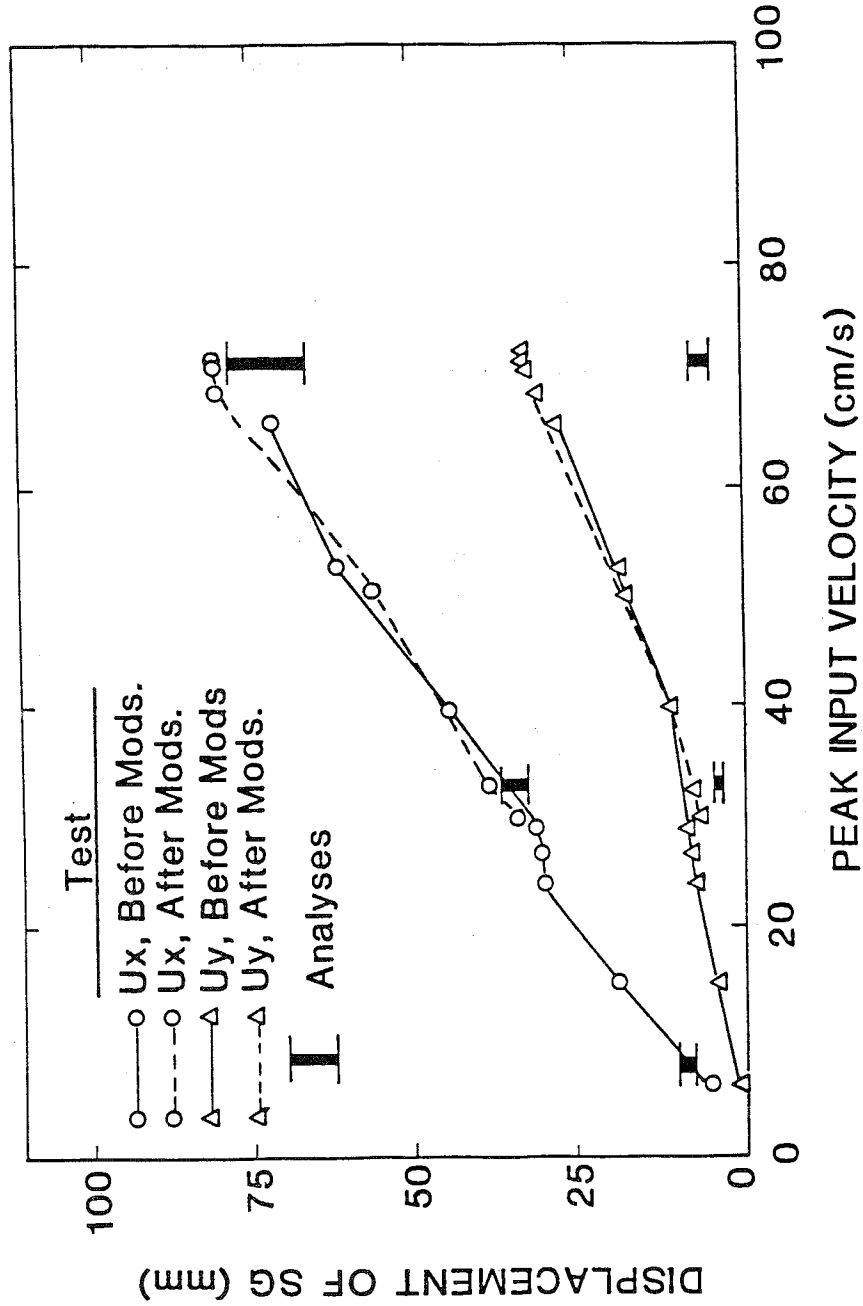
Figure 7.16 Peak Displacement Response of Steam Generator
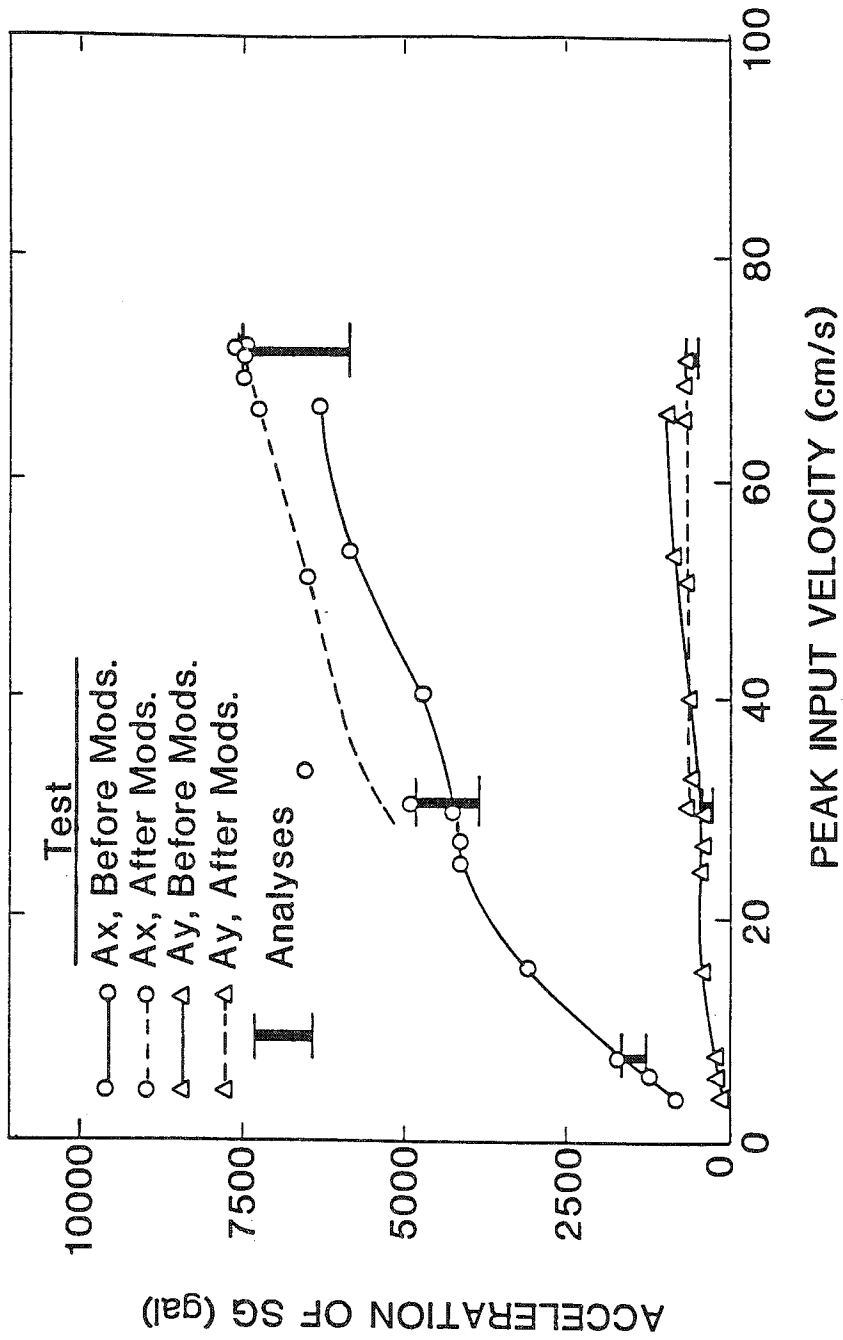
Figure 7.17 Peak Acceleration Response of Steam Generator
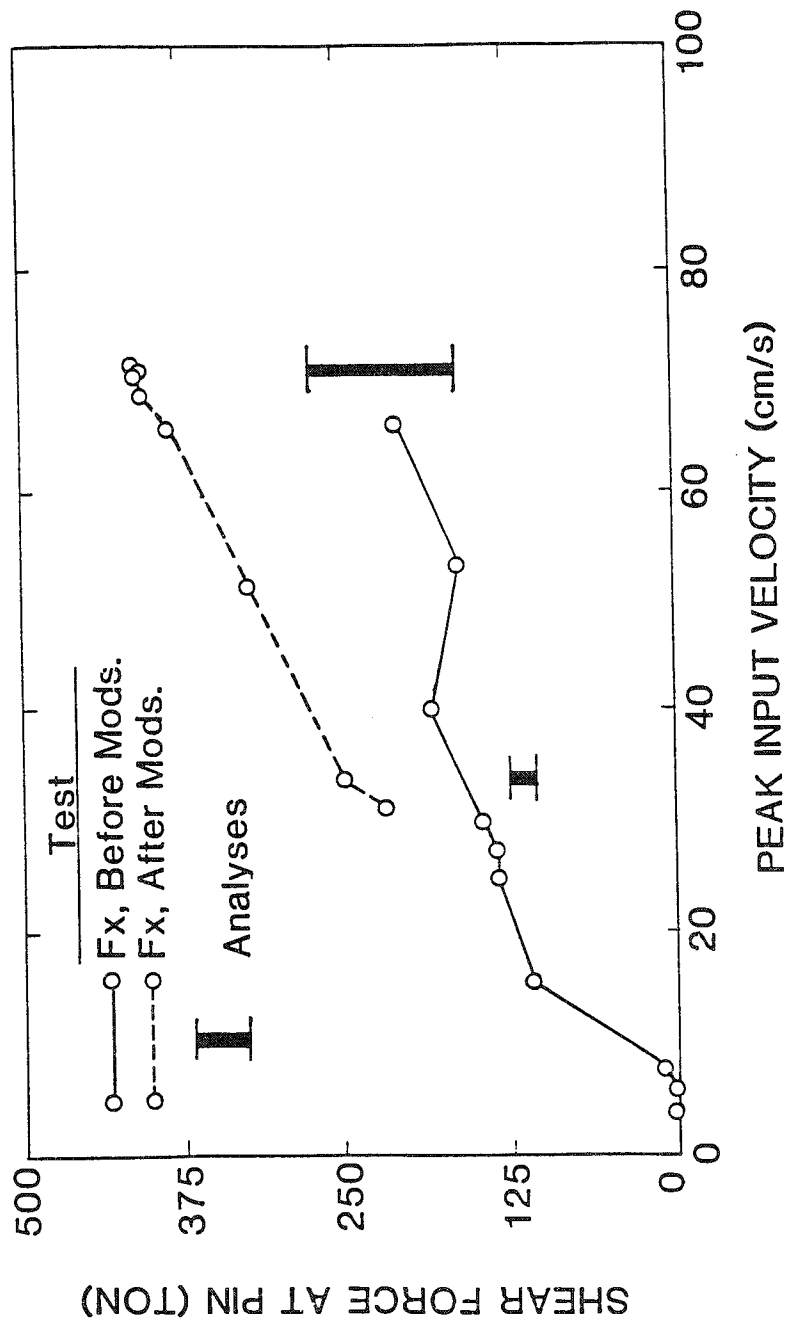
Figure 7.18 Peak Shear Force at Steam Generator Support
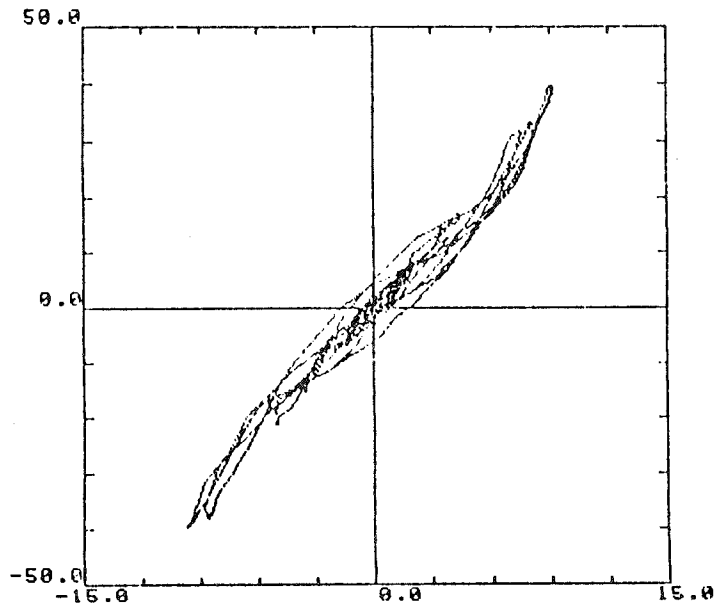
(a) Test Results
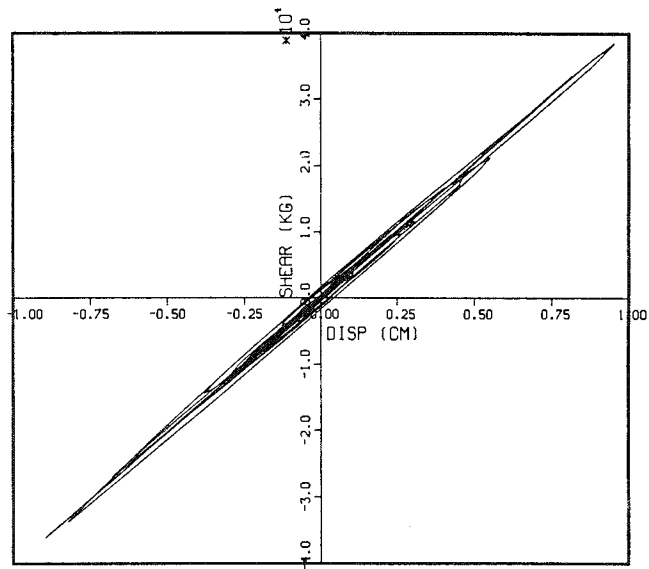
(b) ABAQUS Elbow Model Analysis

Figure 7.19 Shear Force-Top Displacement Relationship of SG
at 0.1 MPR
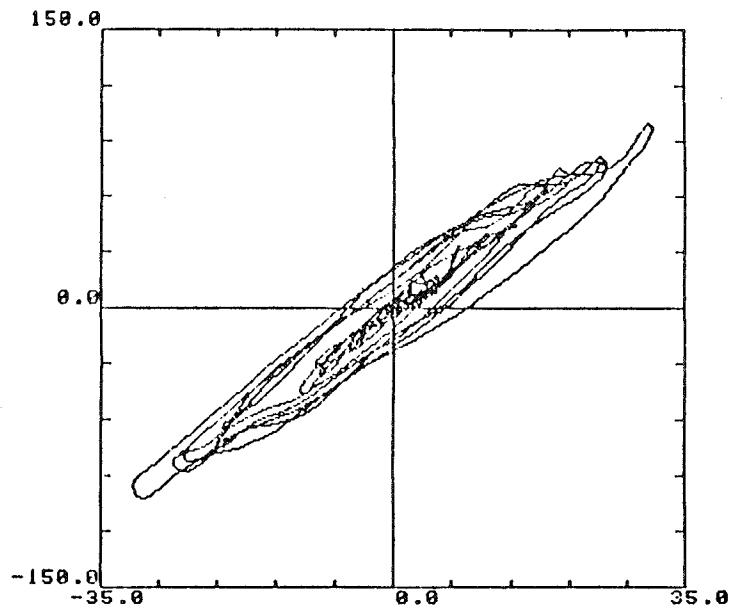
(a) Test Results
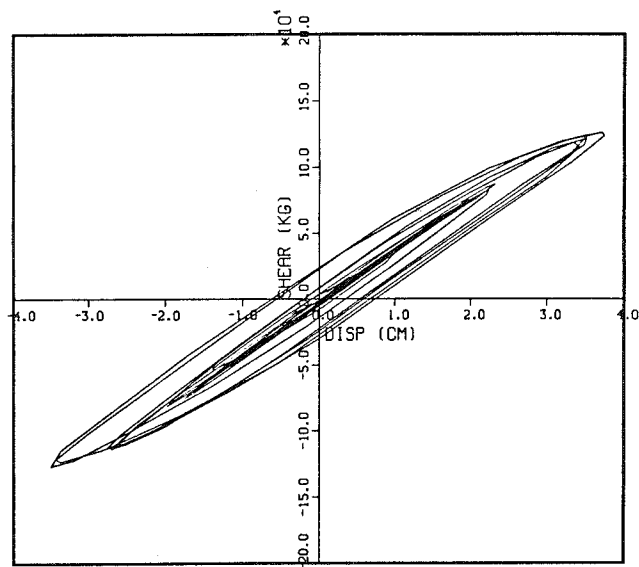
(b) ABAQUS Elbow Model Analysis

Figure 7.20 Shear Force-Top Displacement Relationship of SG
at 0.4 MPR
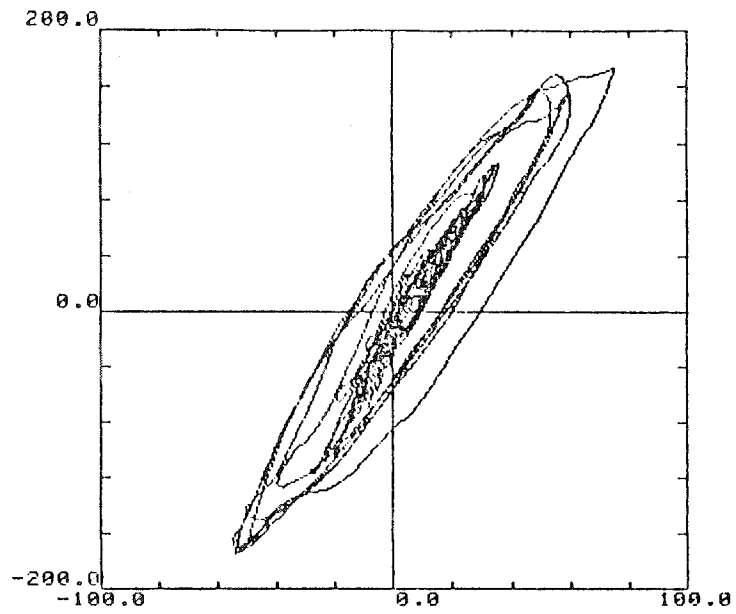
(a) Test Results
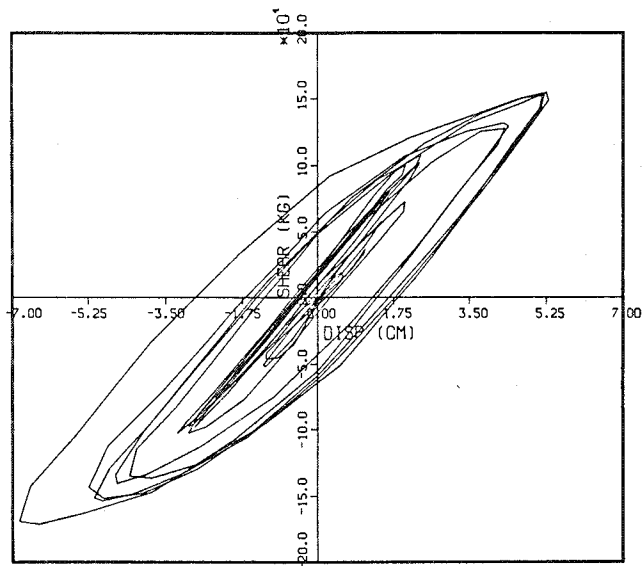
(b) ABAQUS Elbow Model Analysis

Figure 7.21 Shear Force-Top Displacement Relationship of SG
at 1.0 MPR
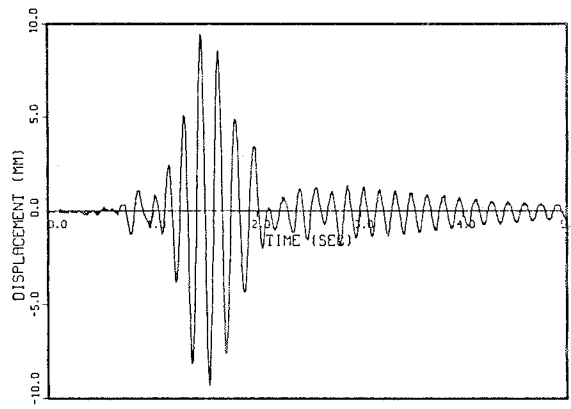
(a) Test Result
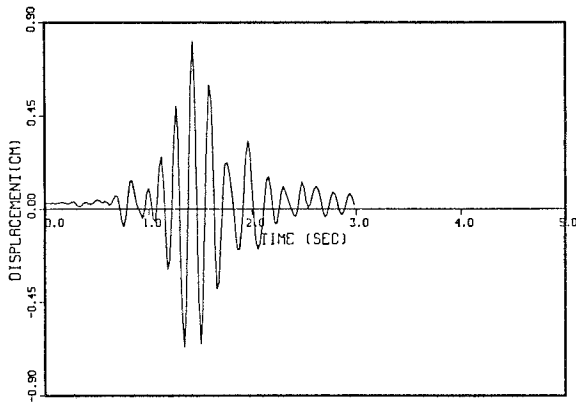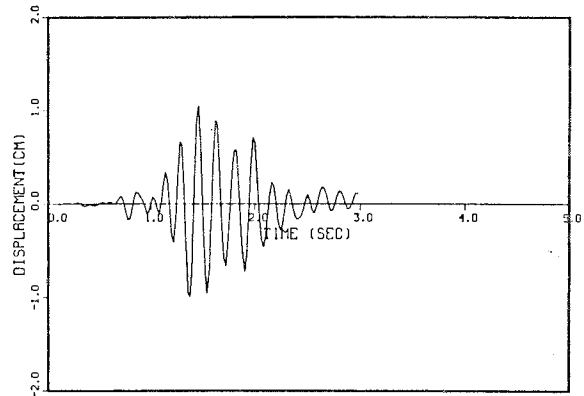
(b) MARC Elbow
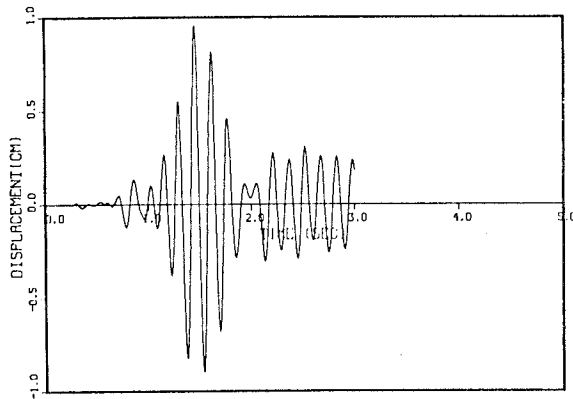
(c) MARC Plate
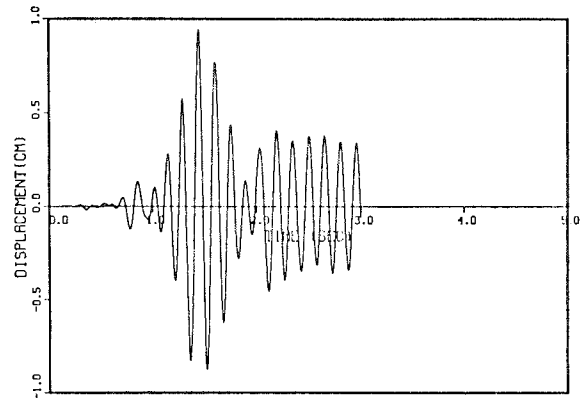
(d) ABAQUS Elbow

(e) ABAQUS Beam

Figure 7.22 Displacement at Top of S/G, Ux (0.1 MPR)
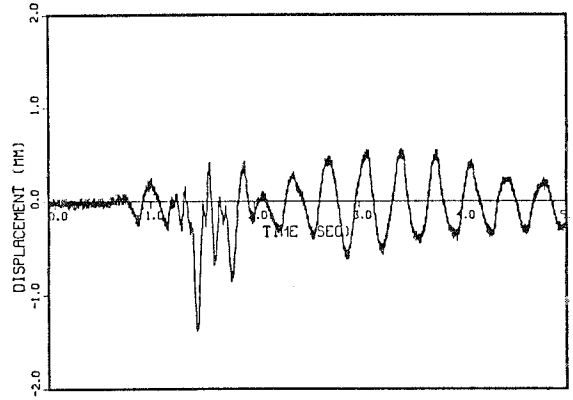
(a) Test Result
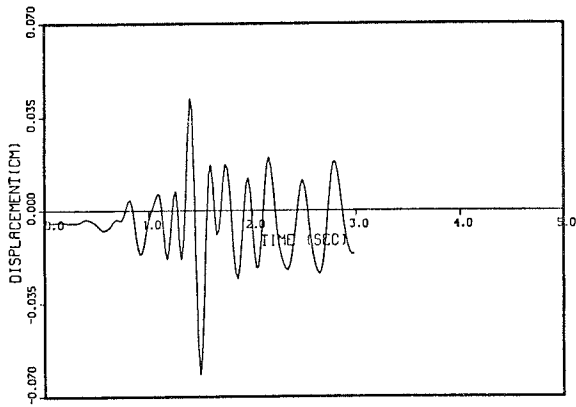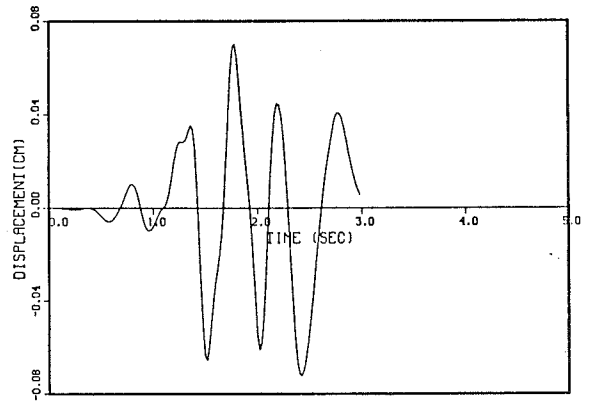
(b) MARC Elbow
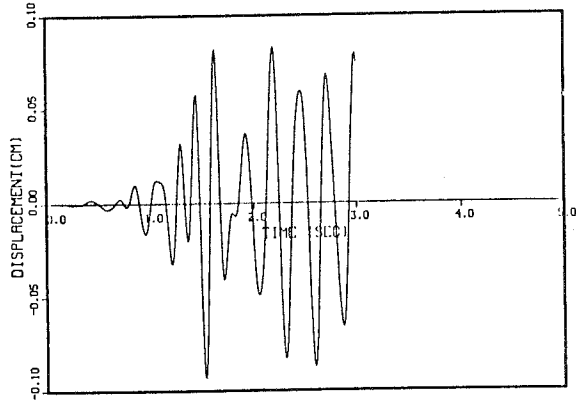
(c) MARC Plate
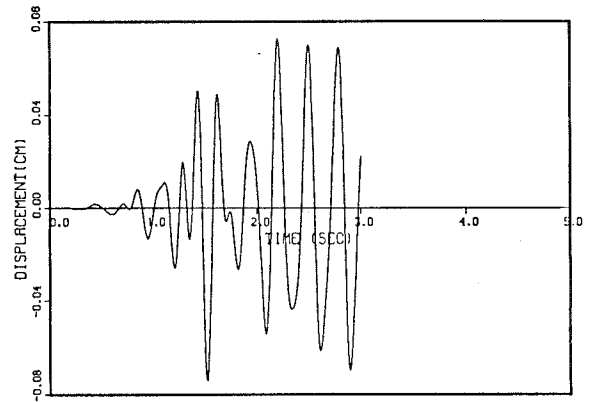
(d) ABAQUS Elbow

(e) ABAQUS Beam

Figure 7.23 Displacement at Top of S/G, Uy (0.1 MPR)
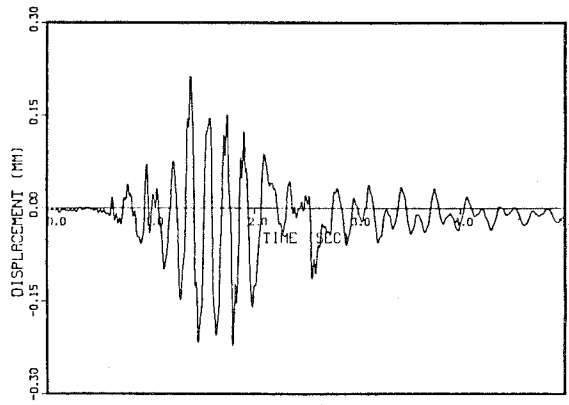
(a) Test Result
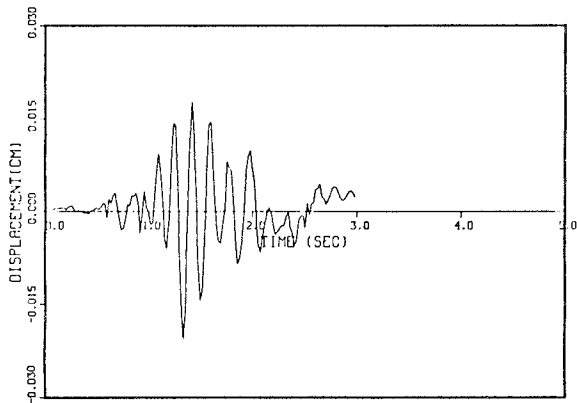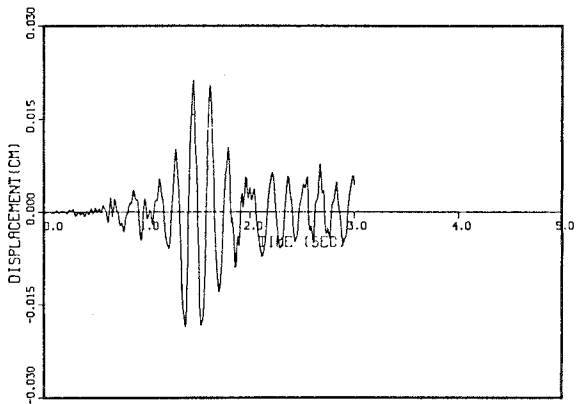
(b) MARC Elbow
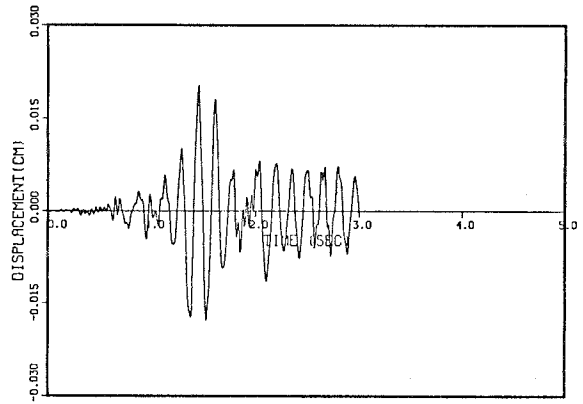
(c) ABAQUS Elbow

(d) ABAQUS Beam

Figure 7.24 Displacement at Top of RCP, U_x (0.1 MPR)
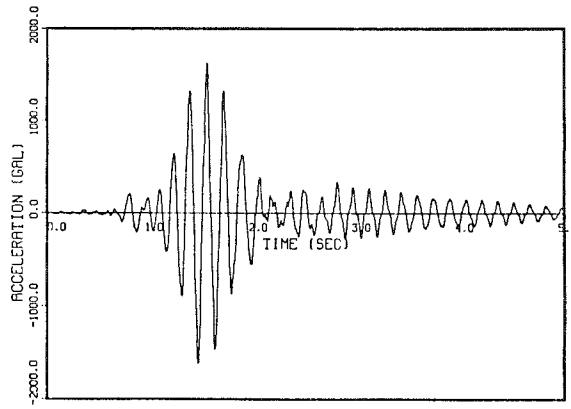
(a) Test Result
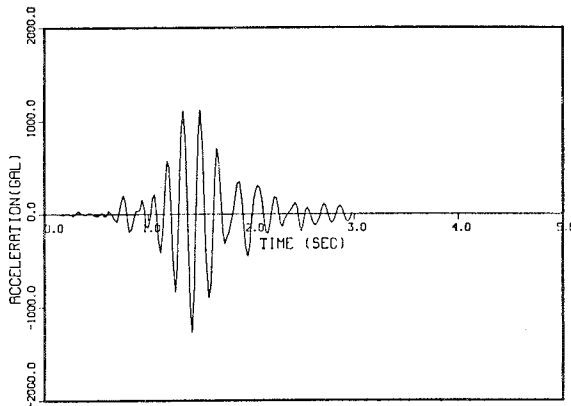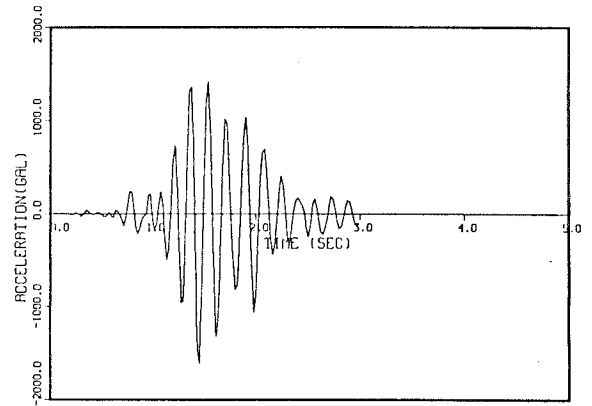
(b) MARC Elbow
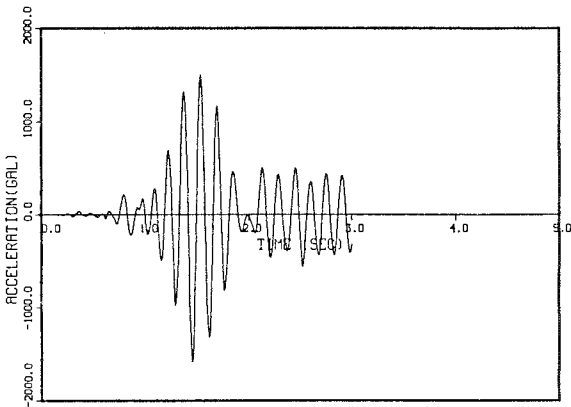
(c) MARC Plate
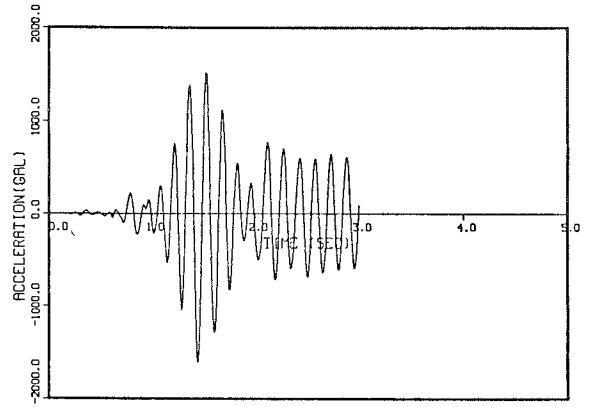
(d) ABAQUS Elbow

(e) ABAQUS Beam

Figure 7.25 Acceleration at Top of S/G, Ax (0.1 MPR)

7-42
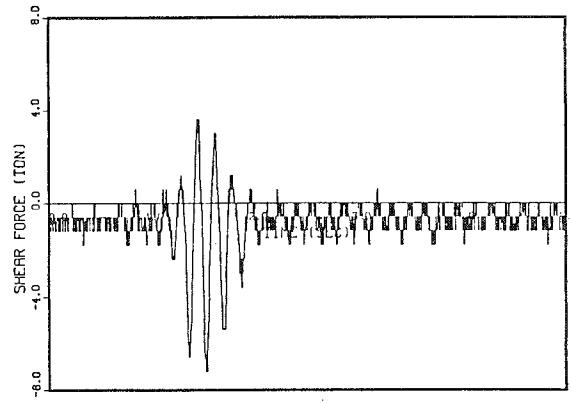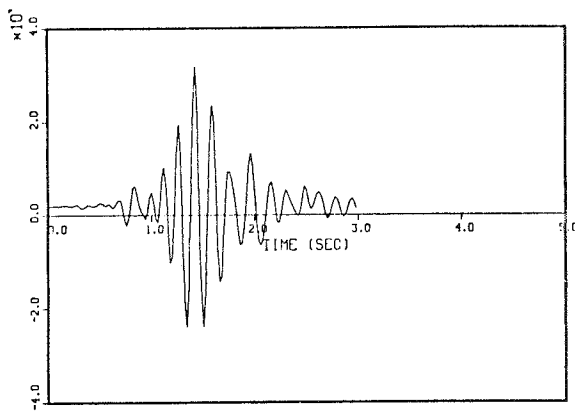
(a) Test Result
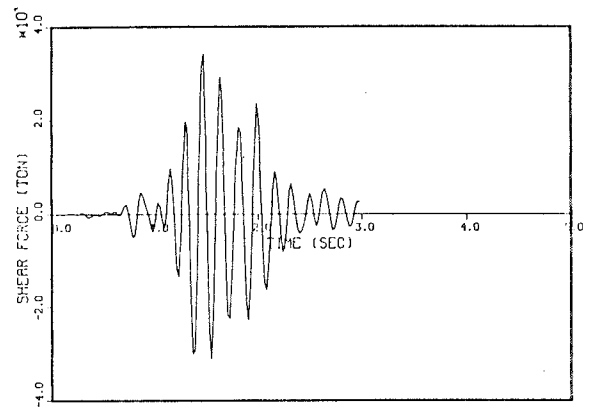
(b) MARC Elbow
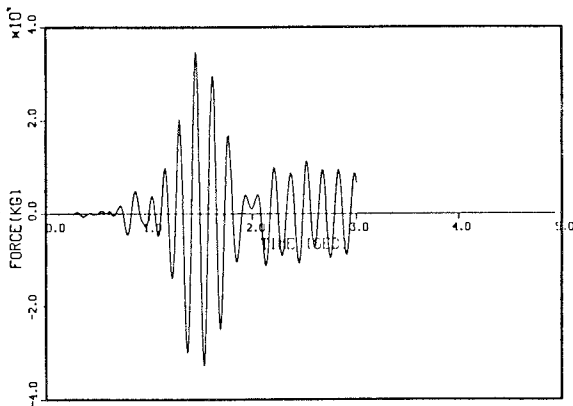
(c) MARC Plate
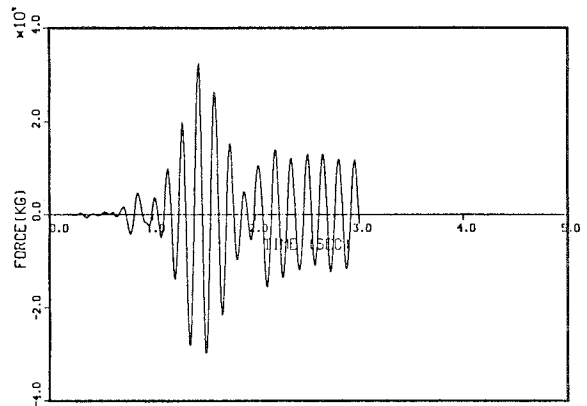
(d) ABAQUS Elbow

(e) ABAQUS Beam

Figure 7.26 Shear Force at Pin-Support, Qx (0.1 MPR)
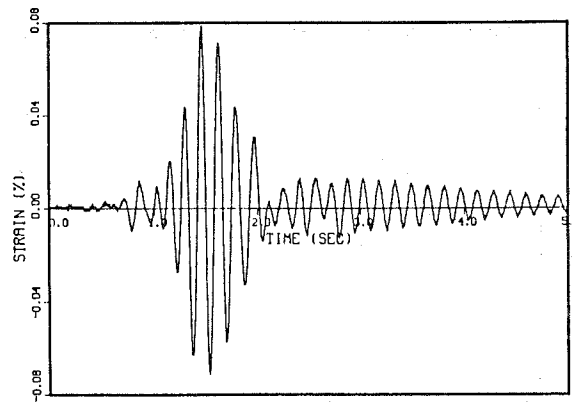
(a) Test Result
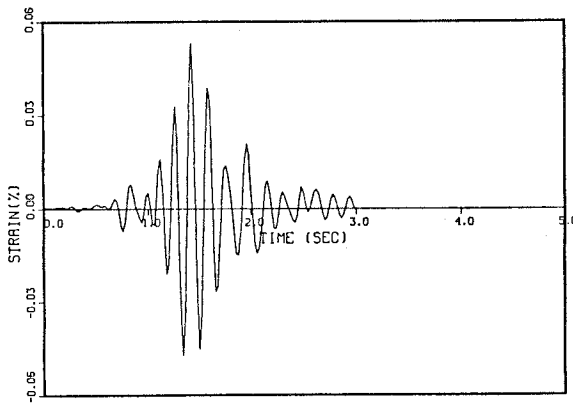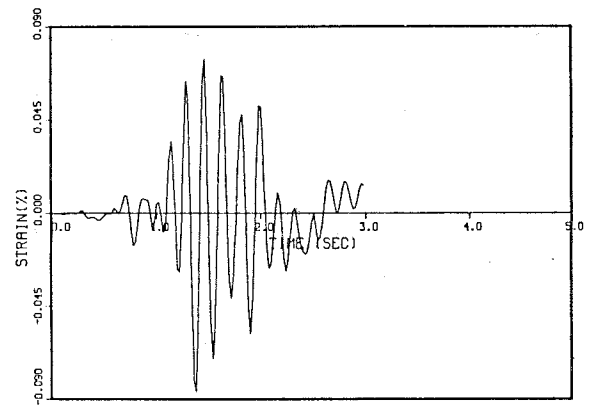
(b) MARC Elbow
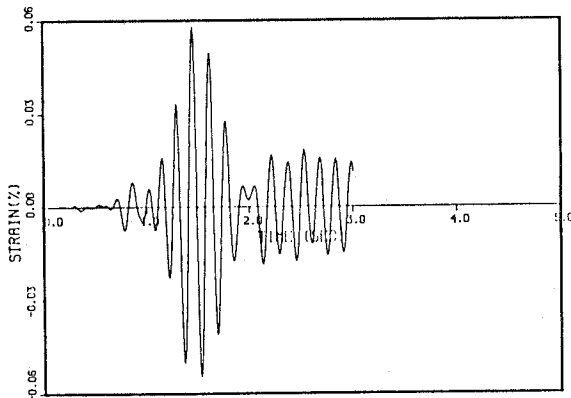
(c) MARC Plate
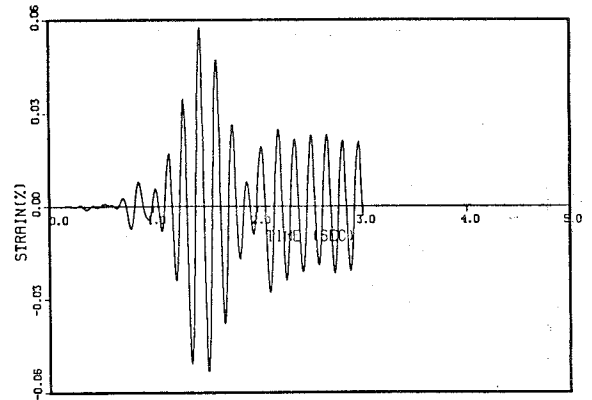
(d) ABAQUS Elbow

(e) ABAQUS Beam

Figure 7.27 Axial Strain at 135X (0.1 MPR)
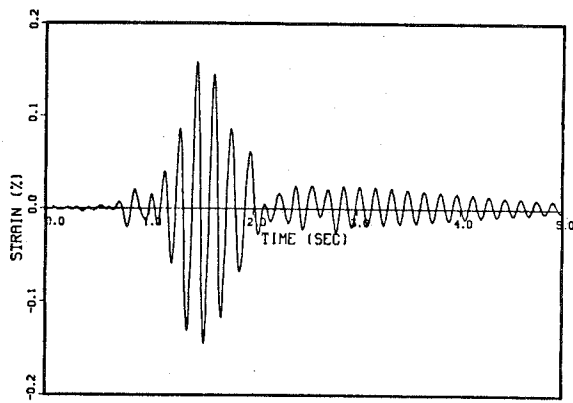
(a) Test Result
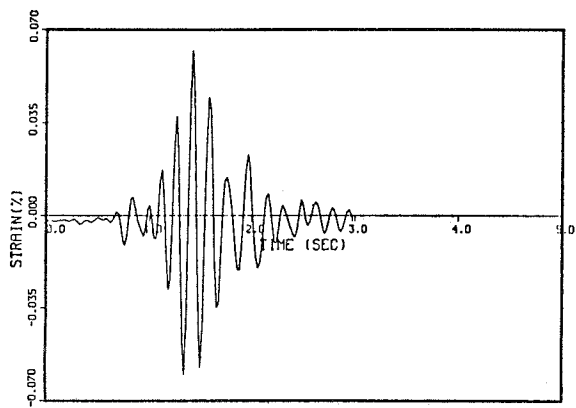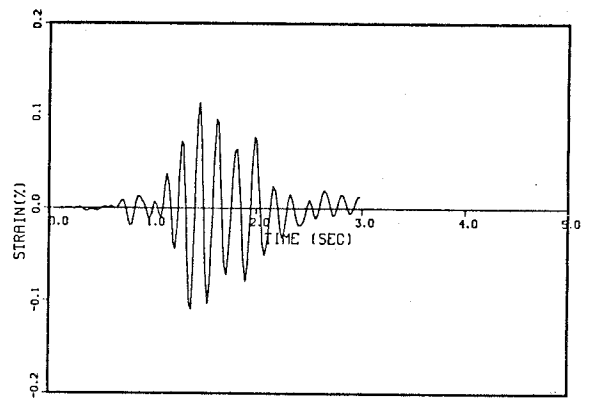
(b) MARC Elbow
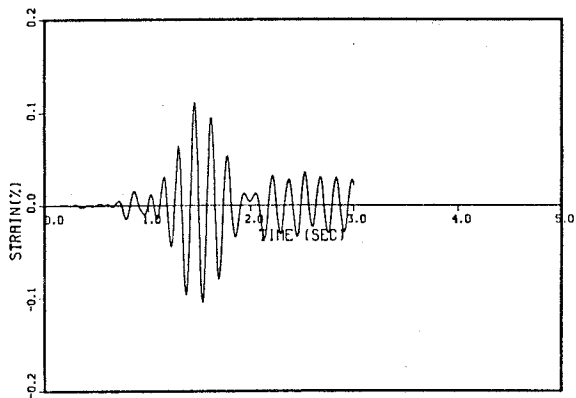
(c) MARC Plate
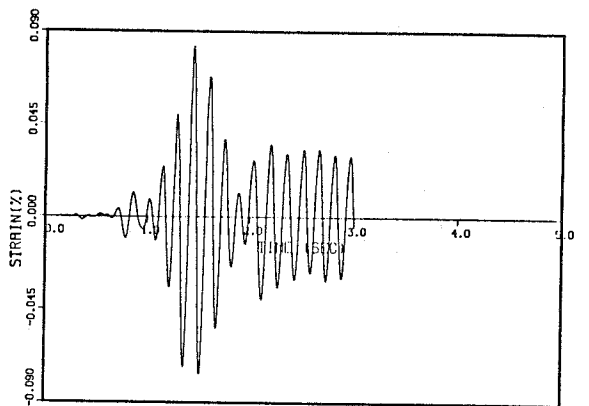
(d) ABAQUS Elbow

(e) ABAQUS Beam

Figure 7.28 Axial Strain at 153X (0.1 MPR)
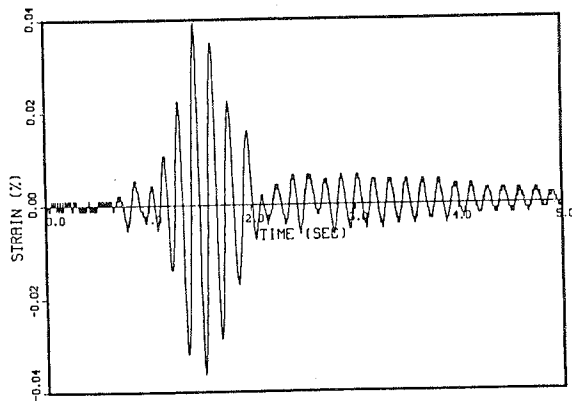
(a) Test Result
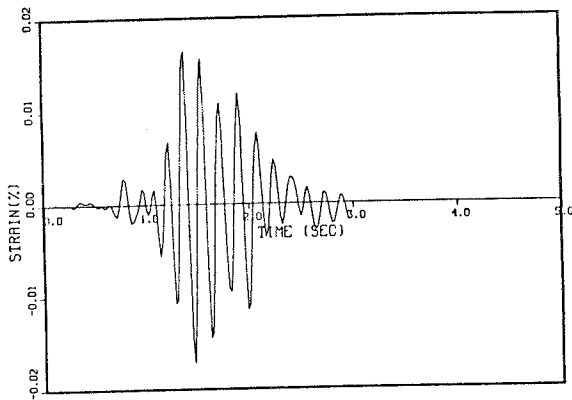
(b) MARC Plate
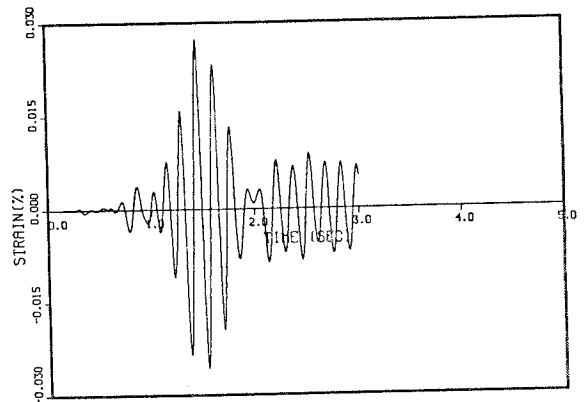
(c) ABAQUS Elbow

Figure 7.29 Hoop Strain at 153Y (0.1 MPR)
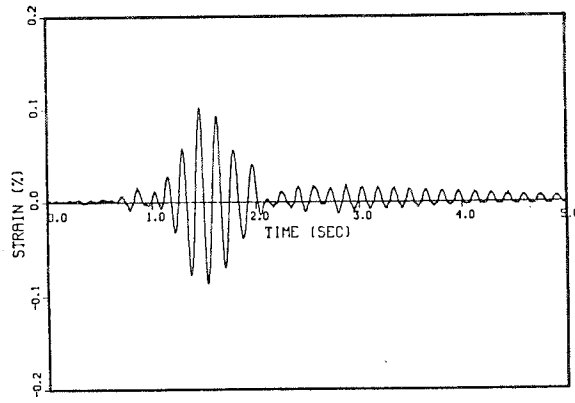
(a) Test Result
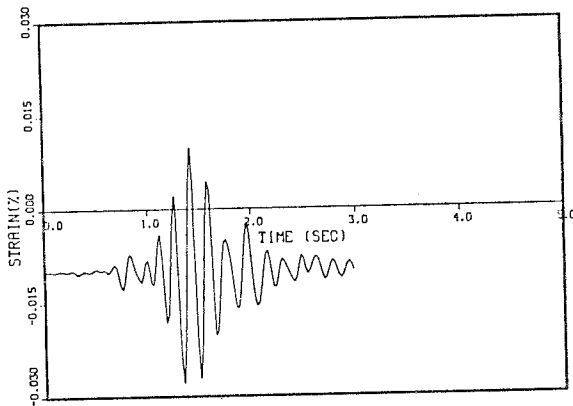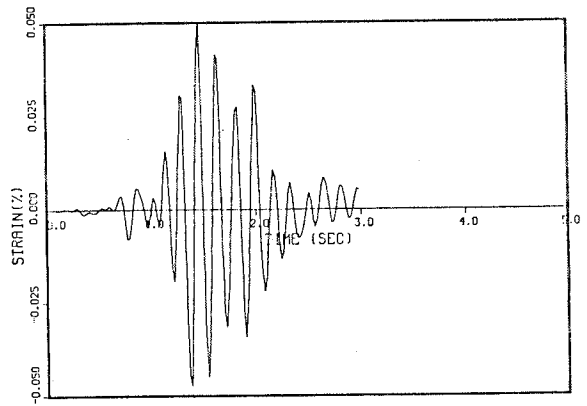
(b) MARC Elbow
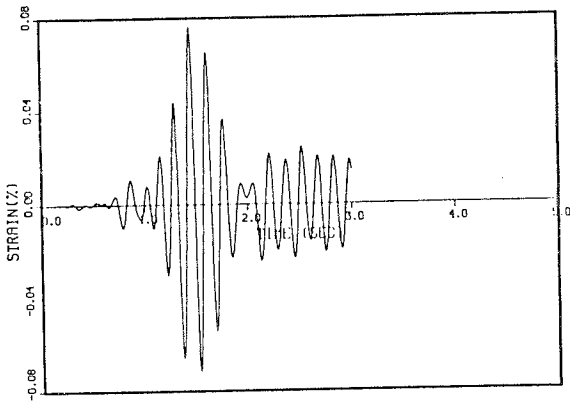
(c) MARC Plate
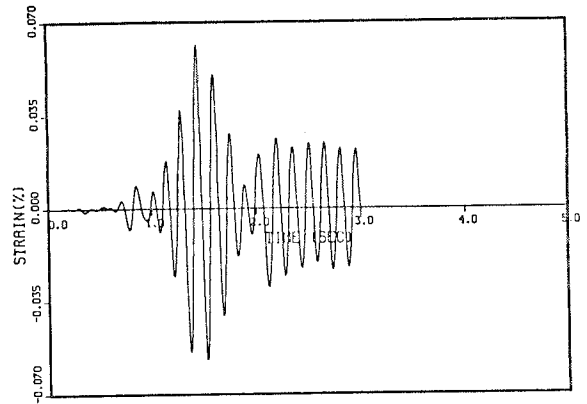
(d) ABAQUS Elbow

(e) ABAQUS Beam

Figure 7.30 Axial Strain at 207X (0.1 MPR)

7-47
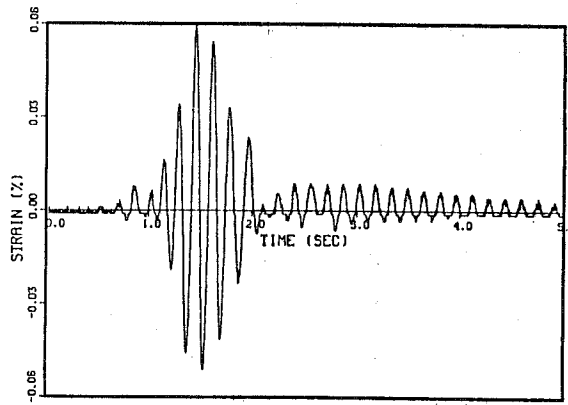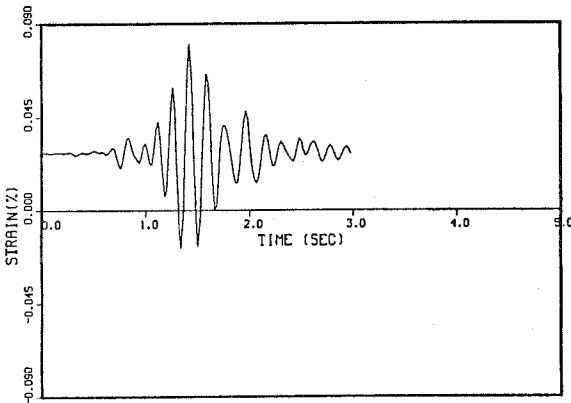
(a) Test Result
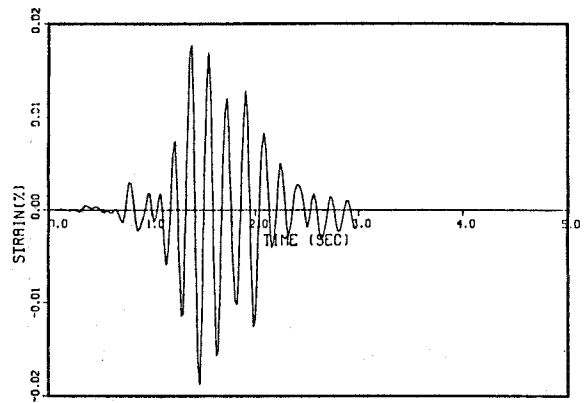
(b) MARC Elbow

(c) MARC Plate
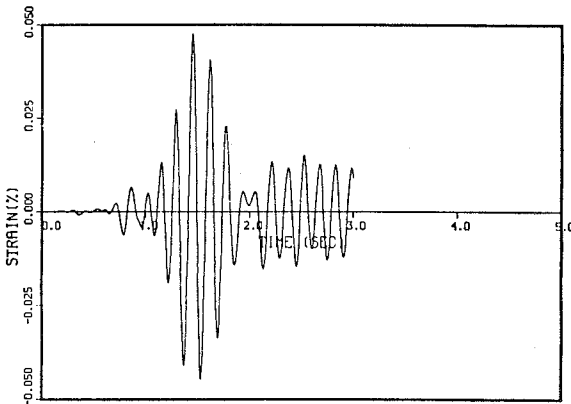
(d) ABAQUS Elbow

Figure 7.31 Hoop Strain at 207Y (0.1 MPR)
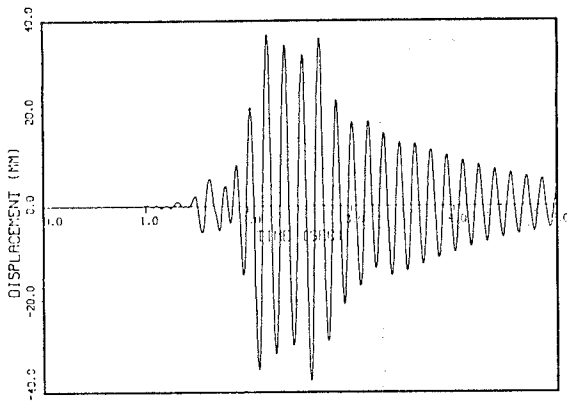
(a) Test Result
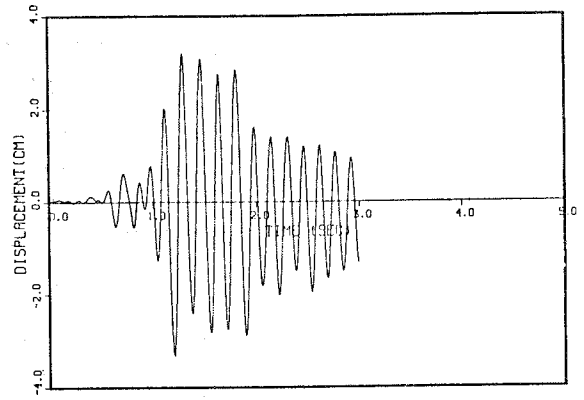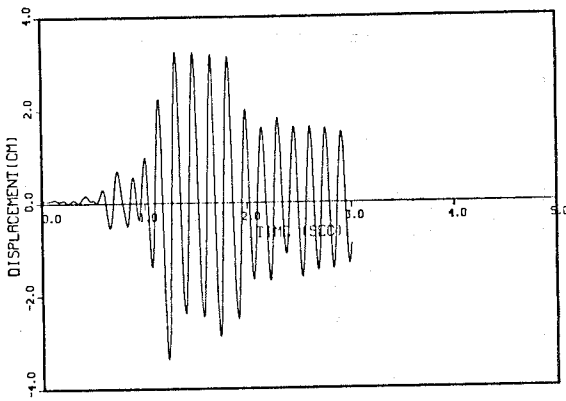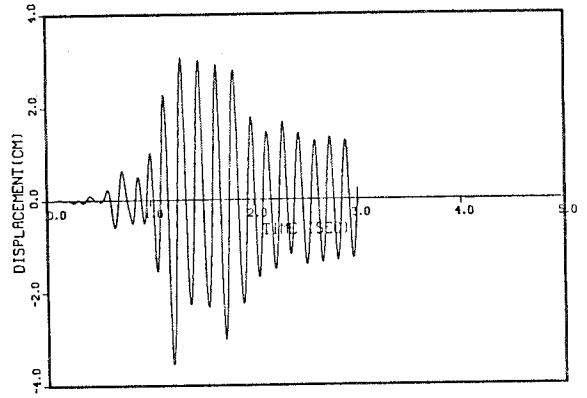
(b) MARC Elbow

(c) ABAQUS Elbow
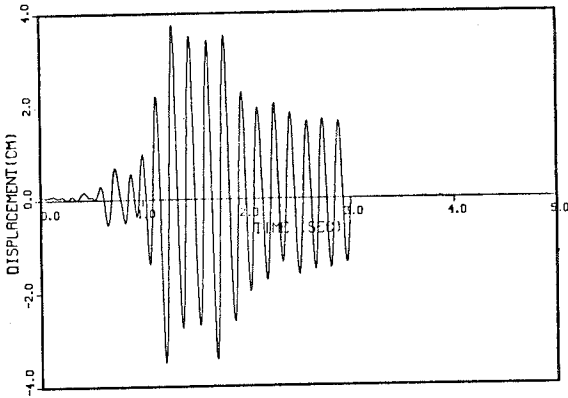
(d) ABAQUS Beam

(e) ABAQUS Elbow
     (Higher Yield Stress)
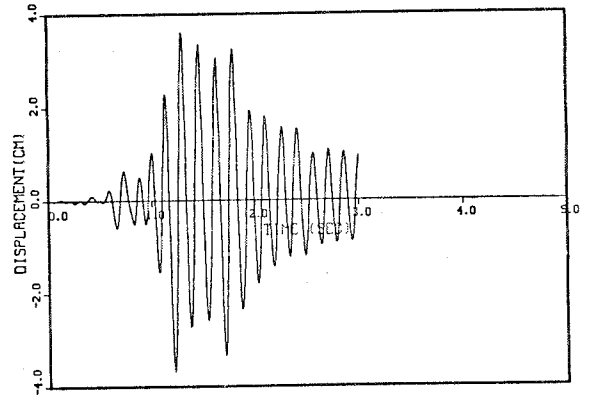
(f) ABAQUS Beam
     (Higher Yield Stress)

Figure 7.32 Displacement at Top of S/G, Ux (0.4 MPR)
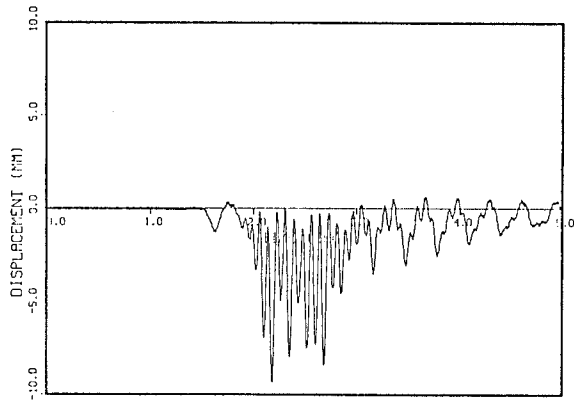
(a) Test Result
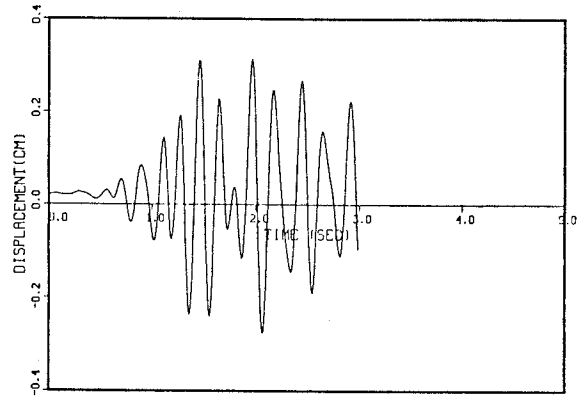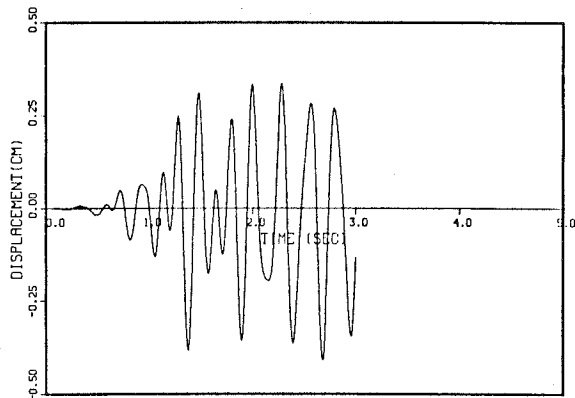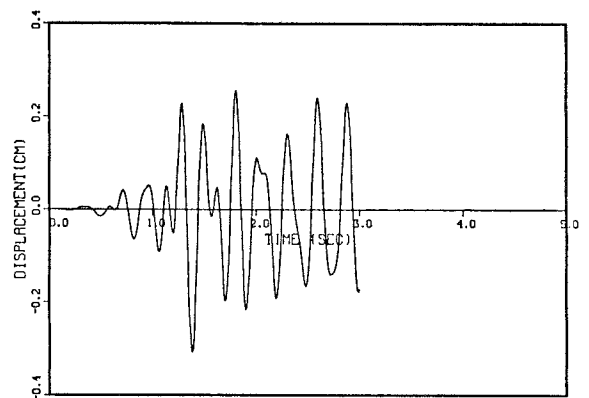
(b) MARC Elbow

(c) ABAQUS Elbow
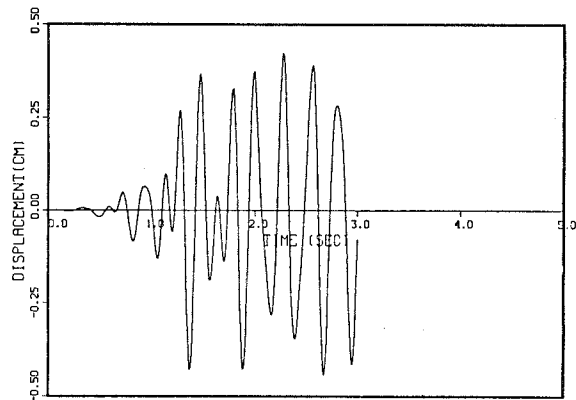
(d) ABAQUS Beam

(e) ABAQUS Elbow
    (Higher Yield Stress)
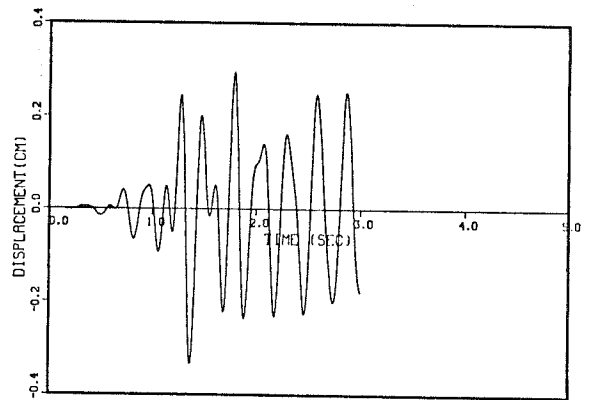
(f) ABAQUS Beam
    (Higher Yield Stress)

Figure 7.33 Displacement at Top of S/G, Uy (0.4 MPR)
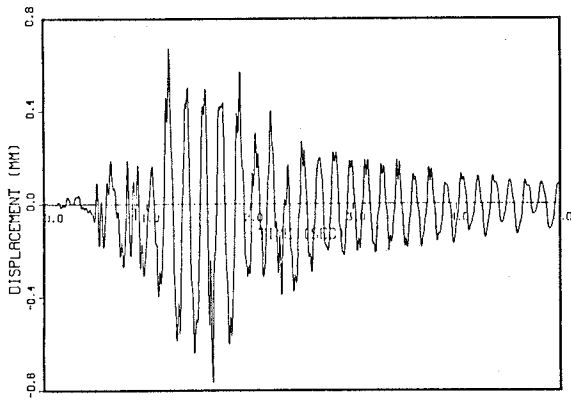
(a) Test Result   (b) MARC Elbow
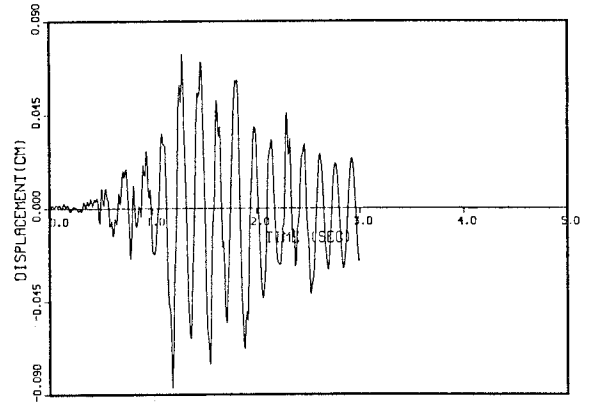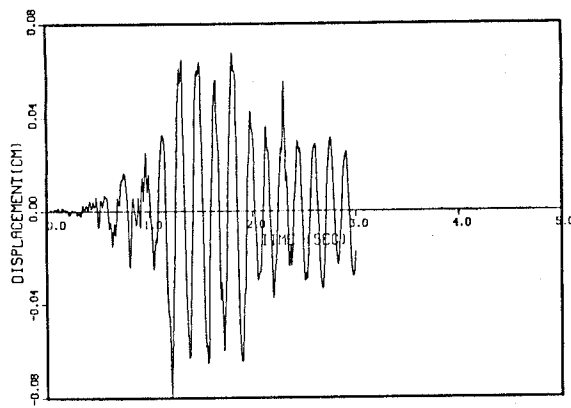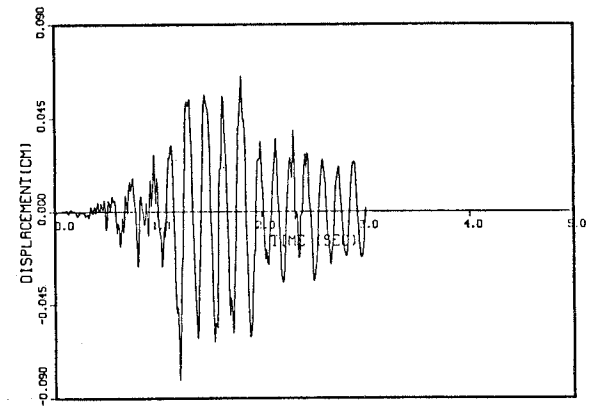
(c) ABAQUS Elbow   (d) ABAQUS Beam
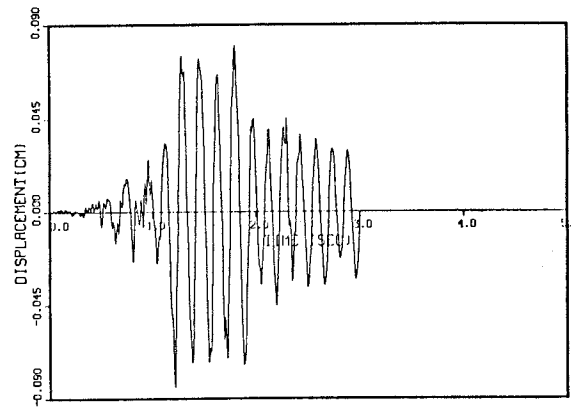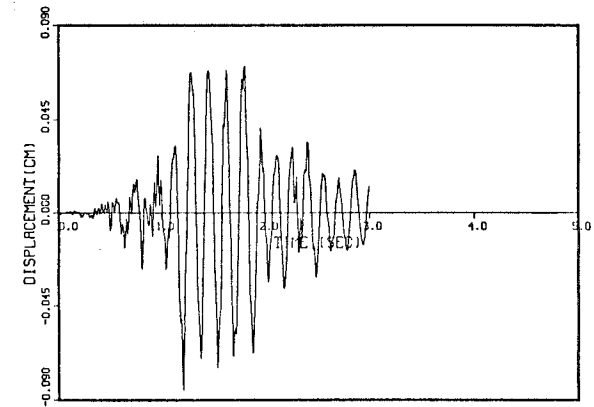
(e) ABAQUS Elbow   (f) ABAQUS Beam
     (Higher Yield Stress)   (Higher Yield Stress)

Figure 7.34 Displacement at Top of RCP, Ux (0.4 MPR)
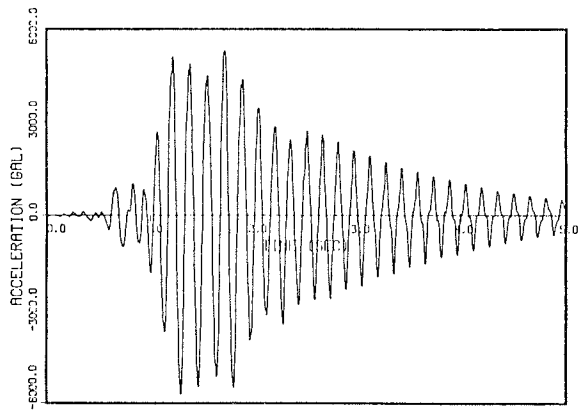
(a) Test Result
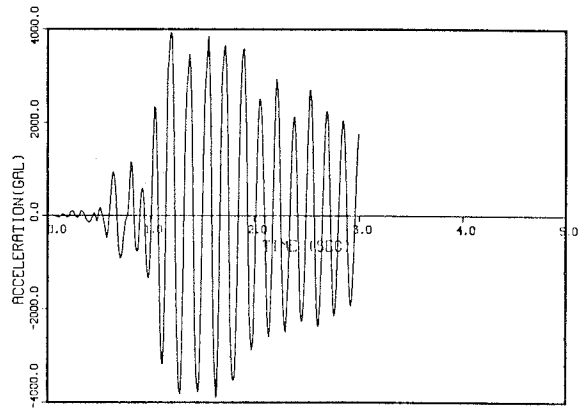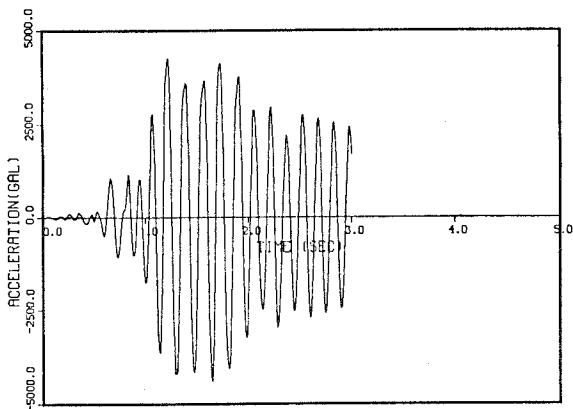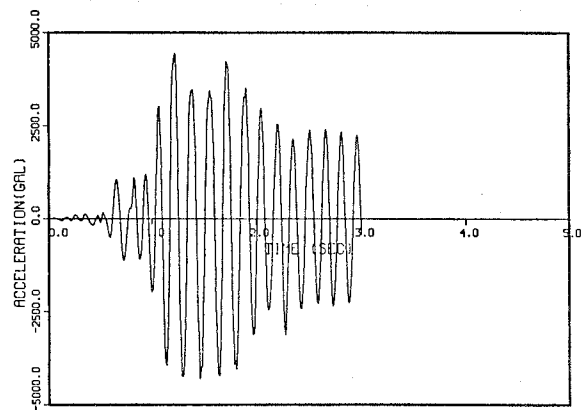
(b) MARC Elbow

(c) ABAQUS Elbow
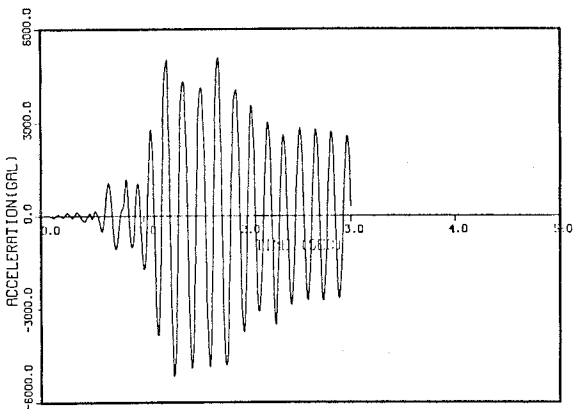
(d) ABAQUS Beam

(e) ABAQUS Elbow
    (Higher Yield Stress)
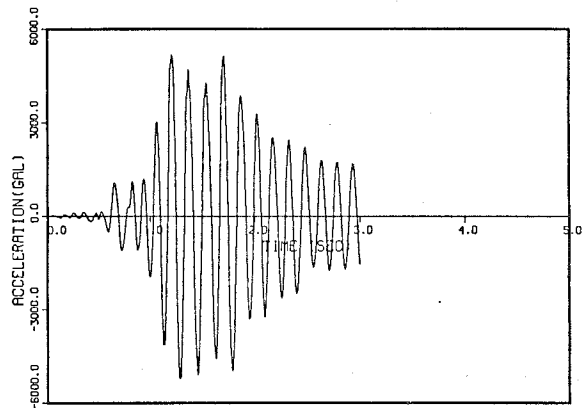
(f) ABAQUS Beam
    (Higher Yield Stress)

Figure 7.35 Acceleration at Top of S/G, Ax (0.4 MPR)
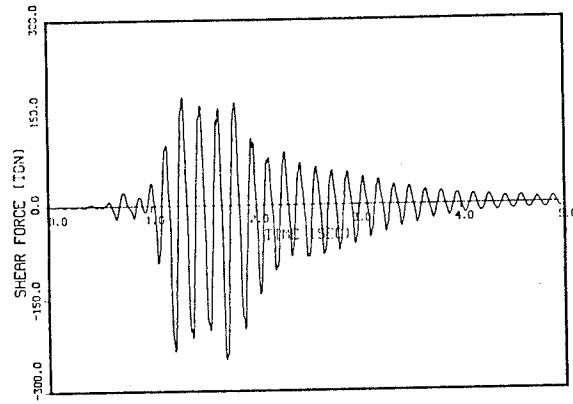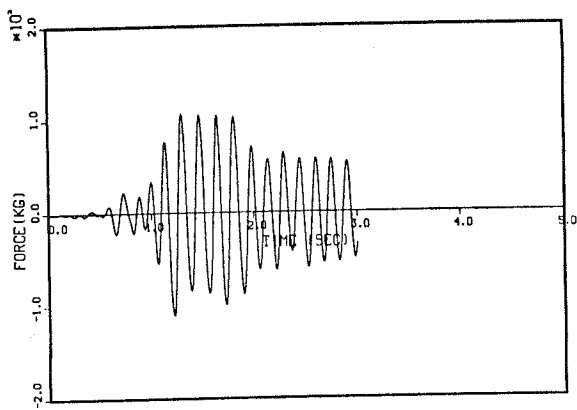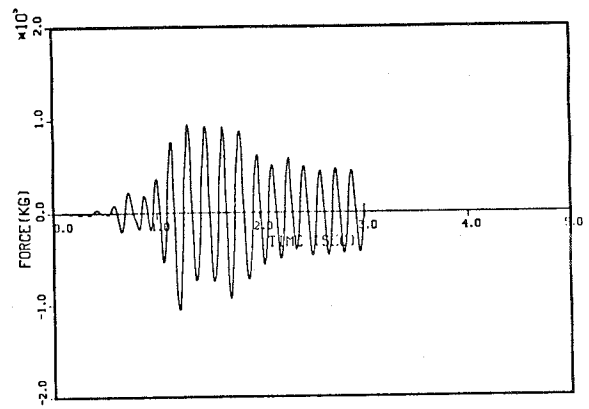
7-52

(a) Test Result

(b) ABAQUS Elbow
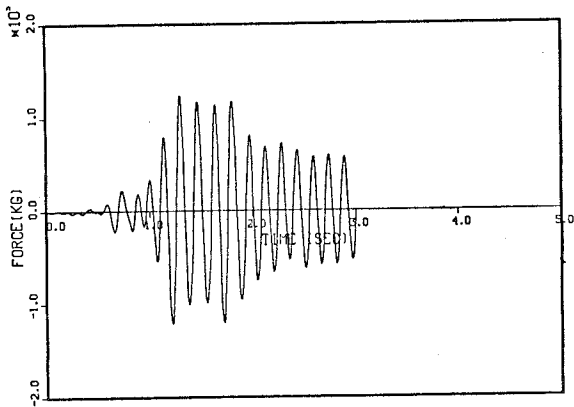
(c) ABAQUS Beam

(d) ABAQUS Elbow
    (Higher Yield Stress)
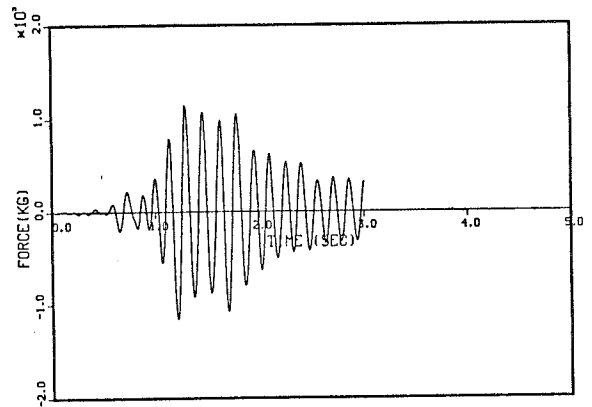
(e) ABAQUS Beam
    (Higher Yield Stress)

Figure 7.36 Shear Force at Pin-Support, Qx (0.4 MPR)
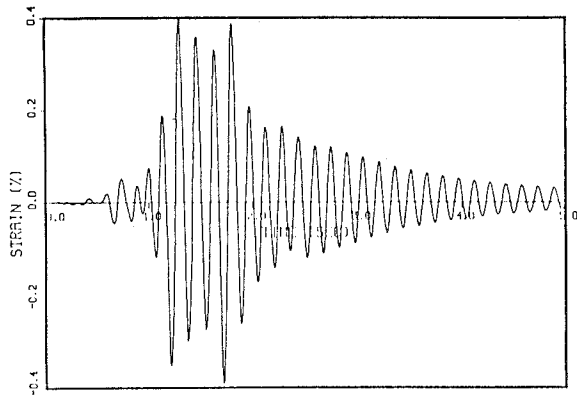
(a) Test Result
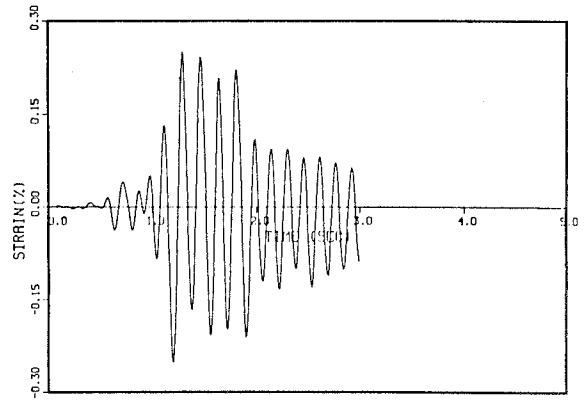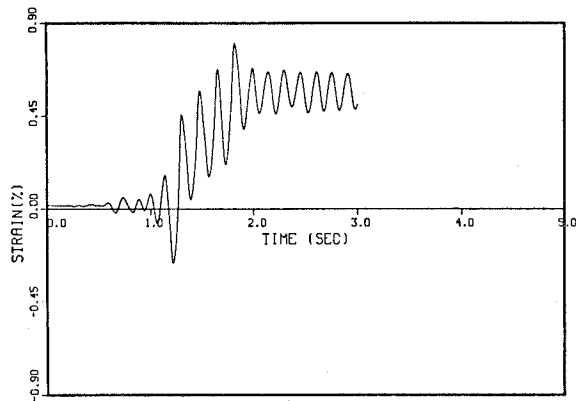
(b) MARC Elbow
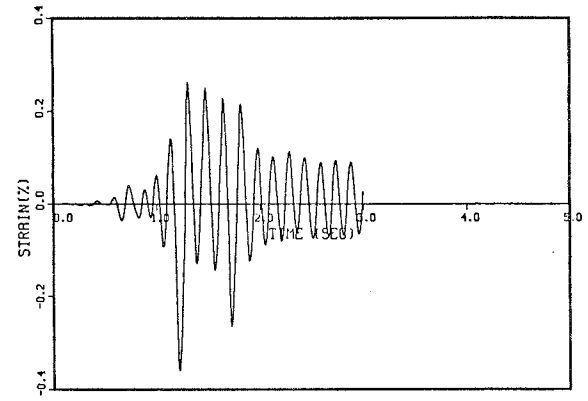
(c) ABAQUS Elbow
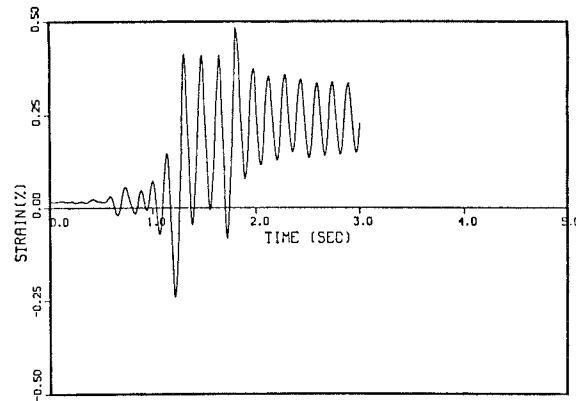
(d) ABAQUS Beam

(e) ABAQUS Elbow
    (Higher Yield Stress)
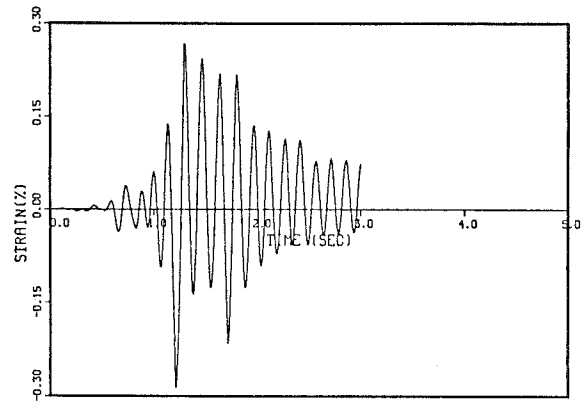
(f) ABAQUS Elbow
    (Higher Yield Stress)

Figure 7.37 Axial Strain at 135X (0.4 MPR)
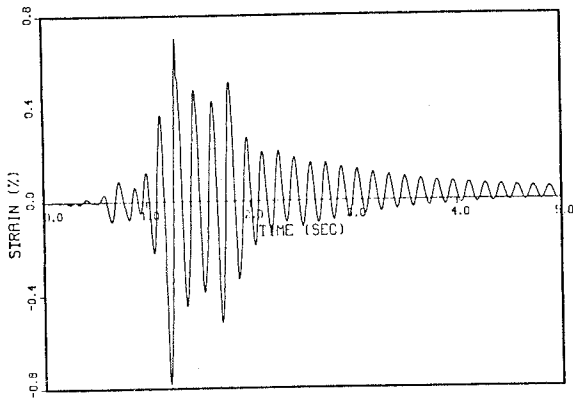
(a) Test Result
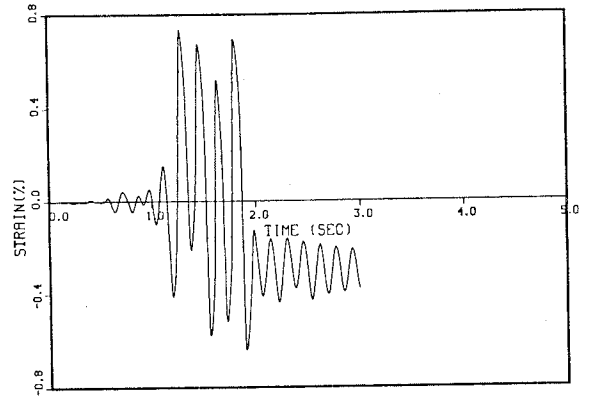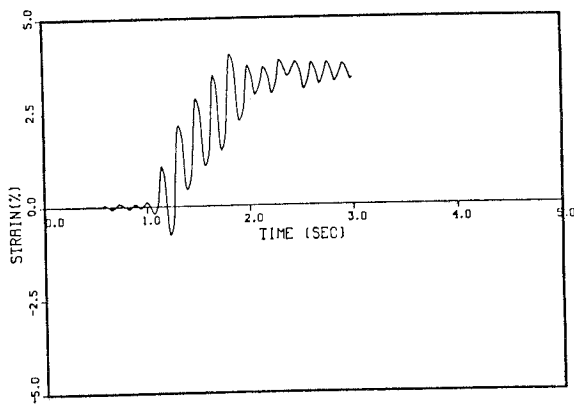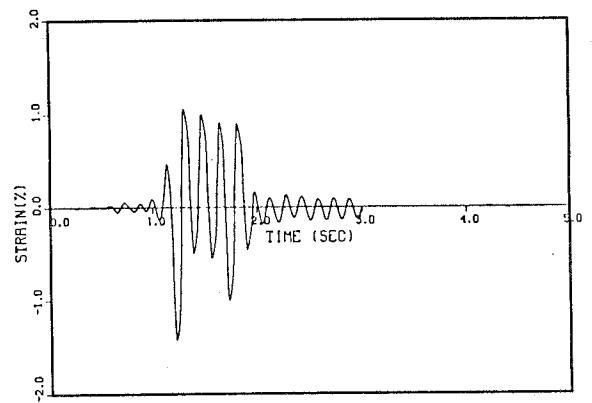
(b) MARC Elbow

(c) ABAQUS Elbow
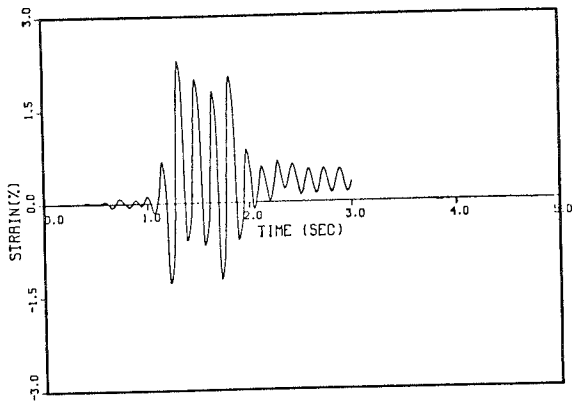
(d) ABAQUS Beam

(e) ABAQUS Elbow
     (Higher Yield Stress)
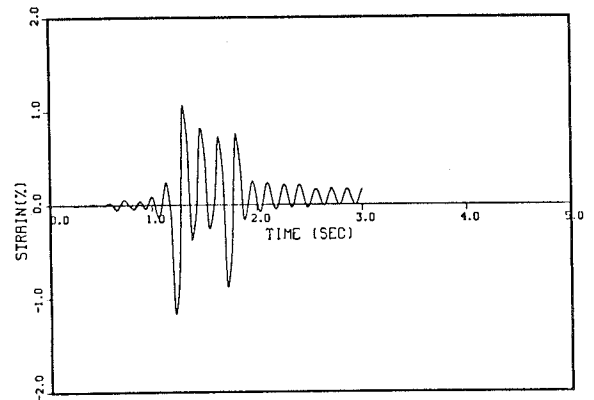
(f) ABAQUS Beam
     (Higher Yield Stress)

Figure 7.38 Axial Strain at 153X (0.4 MPR)

7-55
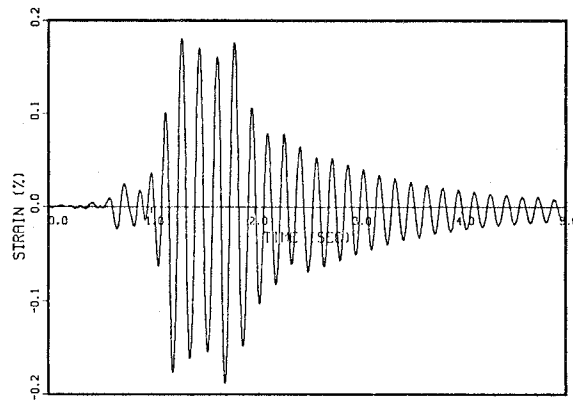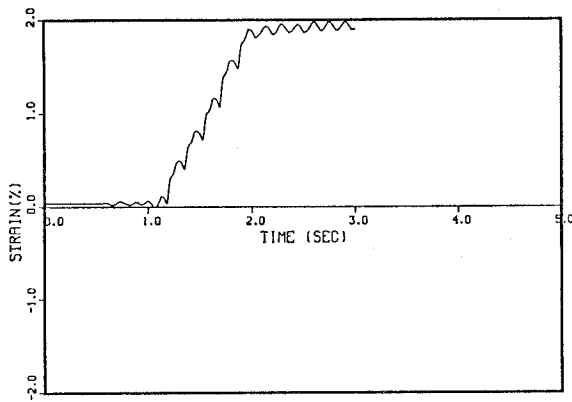
(a) Test Result
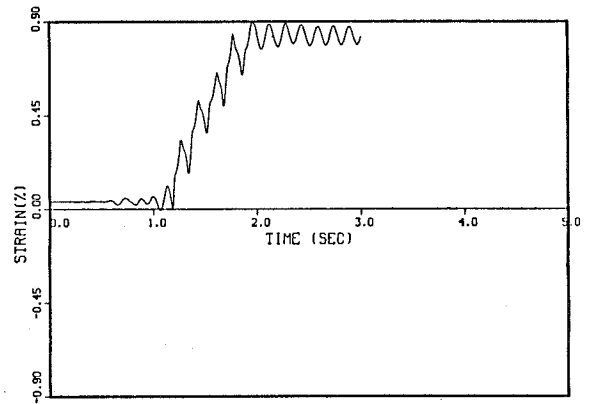
(b) ABAQUS Elbow

(c) ABAQUS Elbow
(Higher Yield Stress)

Figure 7.39 Hoop Strain at 153Y (0.4 MPR)
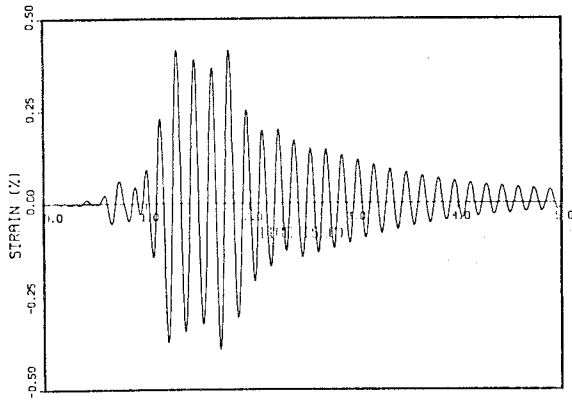
(a) Test Result
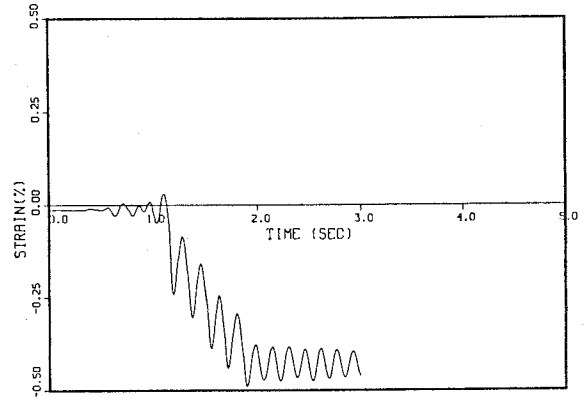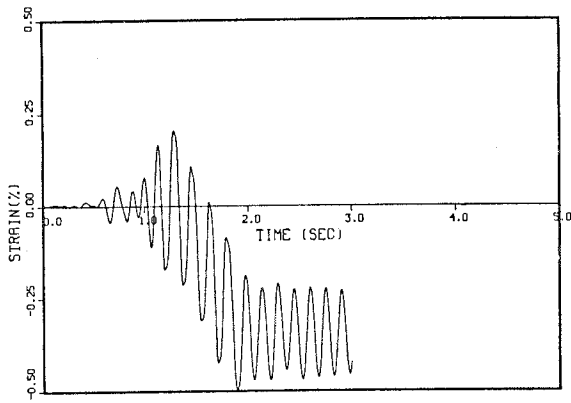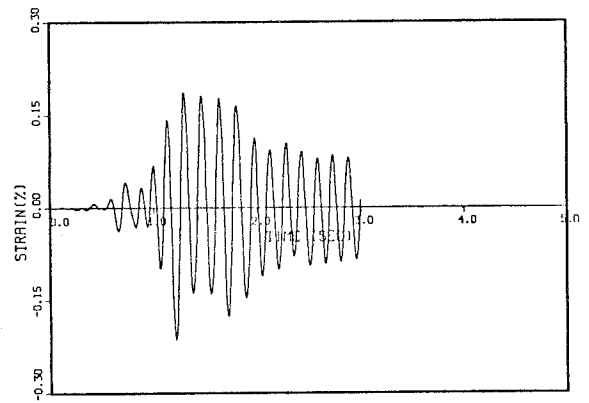
(b) MARC Elbow

(c) ABAQUS Elbow
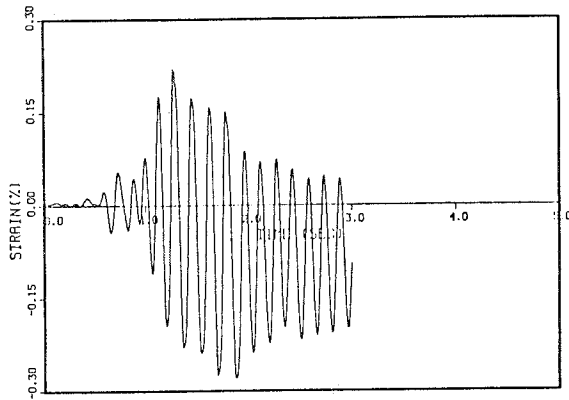
(d) ABAQUS Beam

(e) ABAQUS Elbow
(Higher Yield Stress)
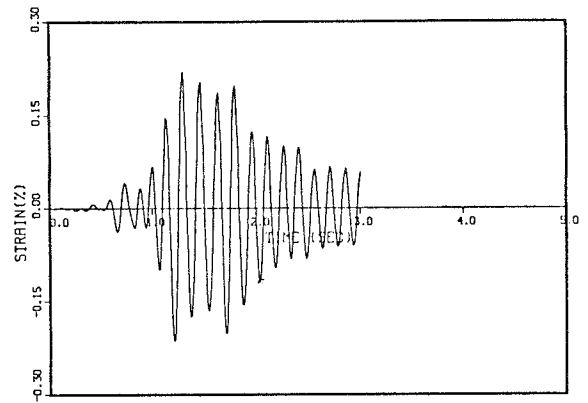
(f) ABAQUS Beam
(Higher Yield Stress)

Figure 7.40 Axial Strain at 207X (0.4 MPR)
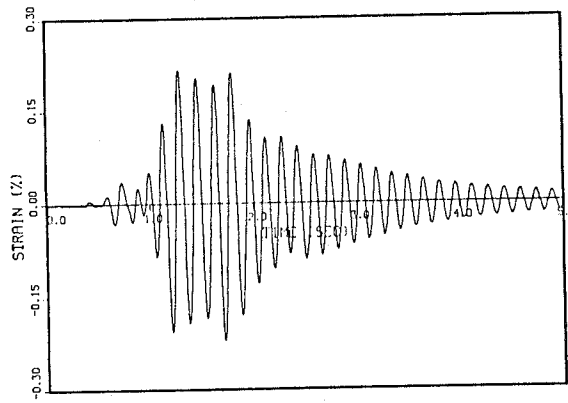
(a) Test Result
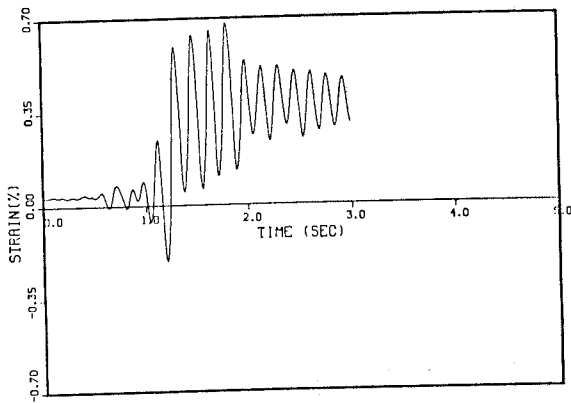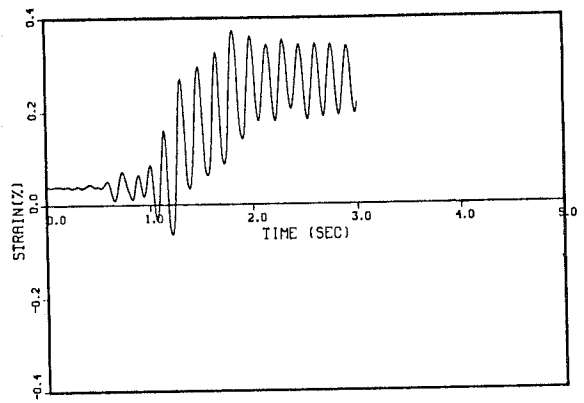
(b) MARC Elbow
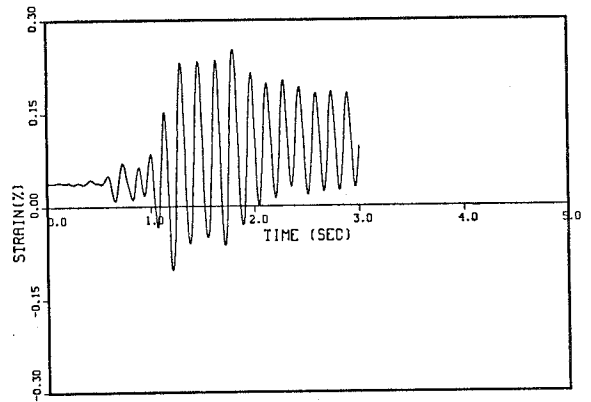
(c) ABAQUS Elbow

(d) ABAQUS Elbow
(Higher Yield Stress)

Figure 7.41 Hoop Strain at 207Y (0.4 MPR)
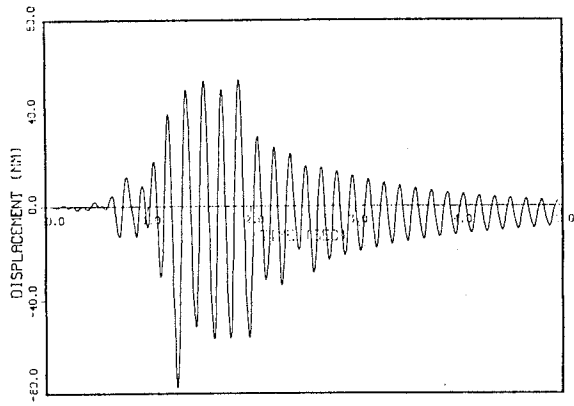
(a) Test Result
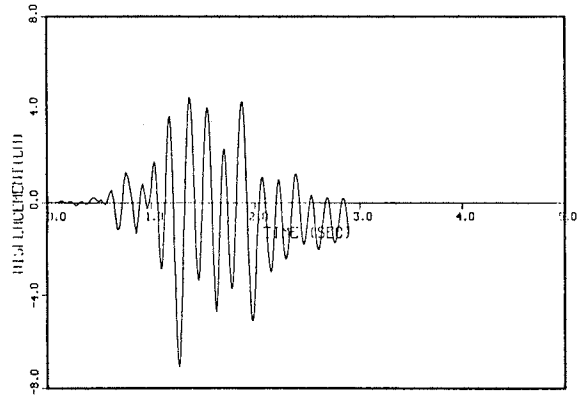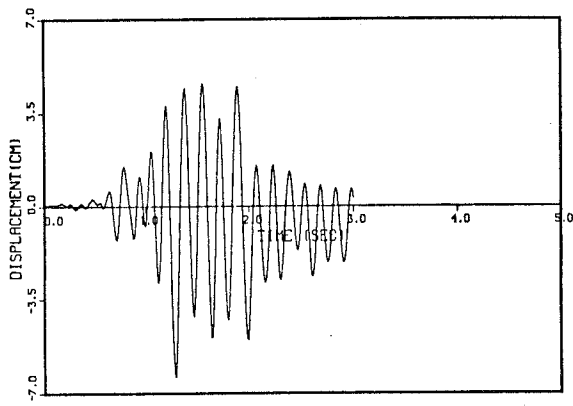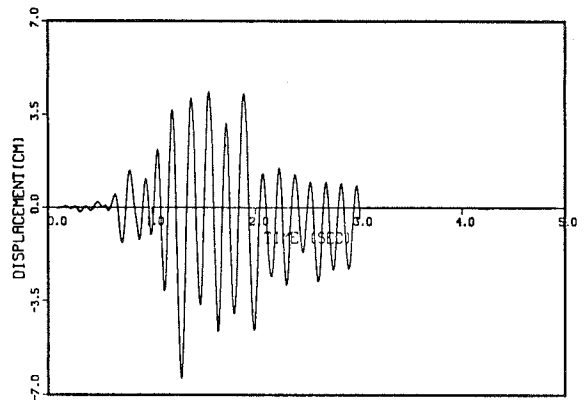
(b) MARC Elbow

(c) ABAQUS Elbow
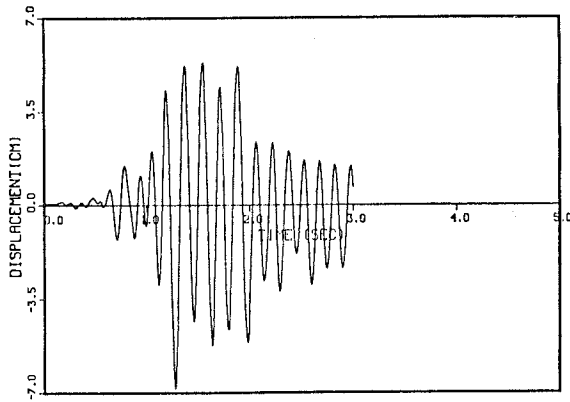
(d) ABAQUS Beam

(e) ABAQUS Elbow
(Higher Yield Stress)
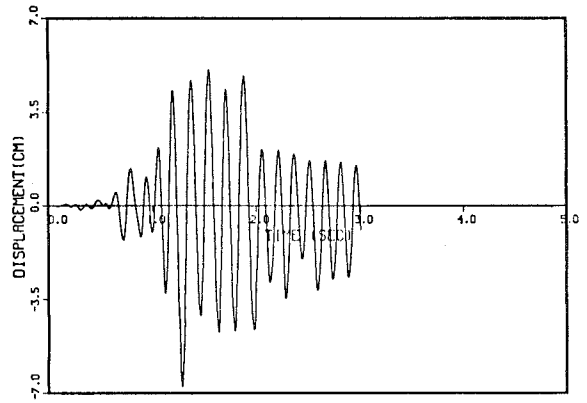
(f) ABAQUS Beam
(Higher Yield Stress)

Figure 7.42 Displacement at Top of S/G, Ux (1.0 MPR)
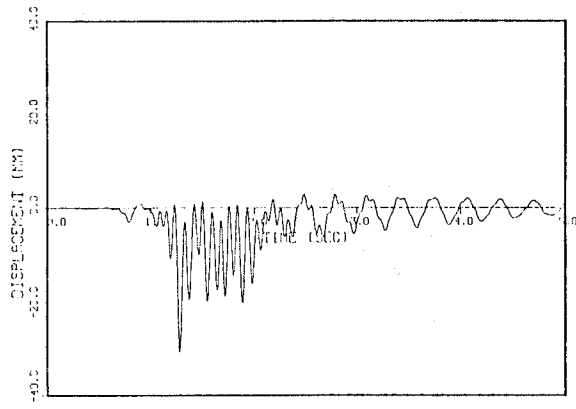
(a) Test Result
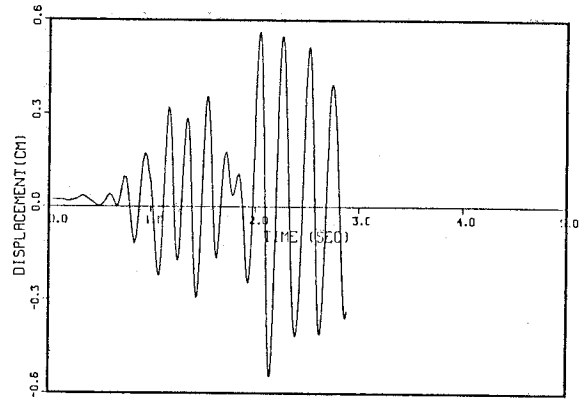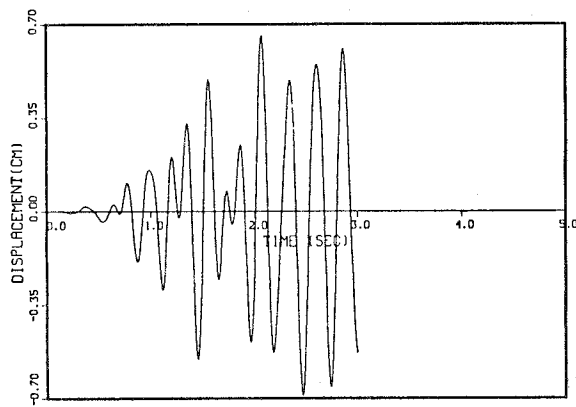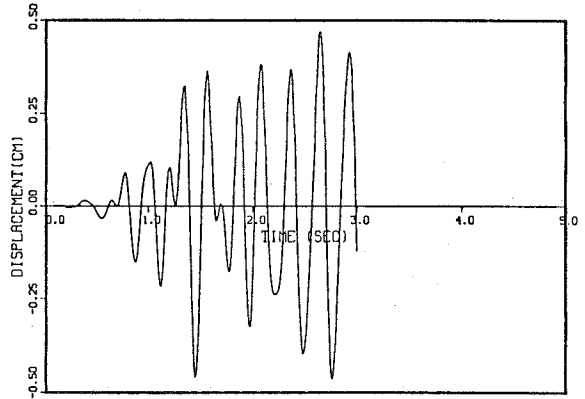
(b) MARC Elbow

(c) ABAQUS Elbow
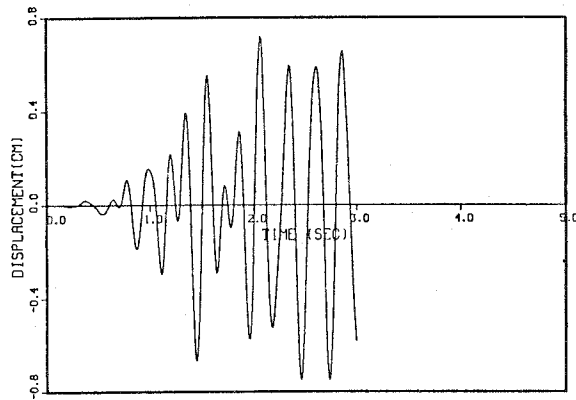
(d) ABAQUS Beam

(e) ABAQUS Elbow
    (Higher Yield Stress)
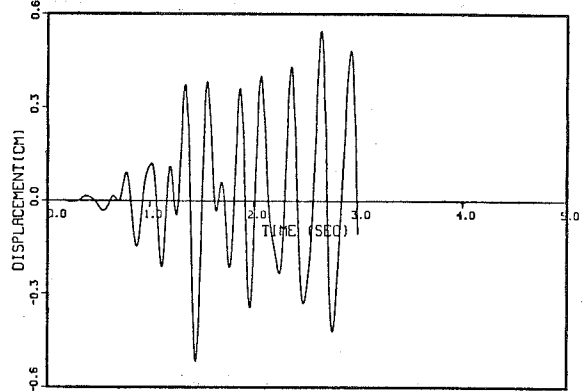
(f) ABAQUS Beam
    (Higher Yield Stress)

Figure 7.43 Displacement at Top of S/G, Uy (1.0 MPR)
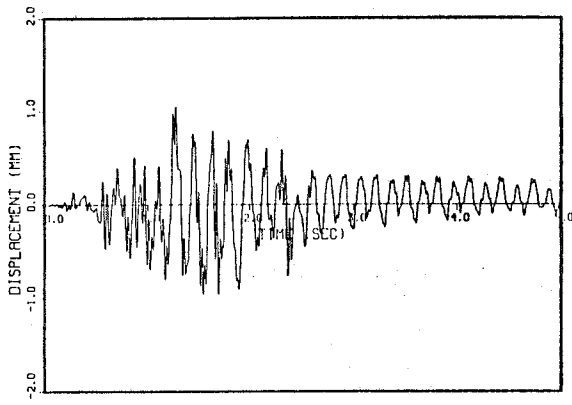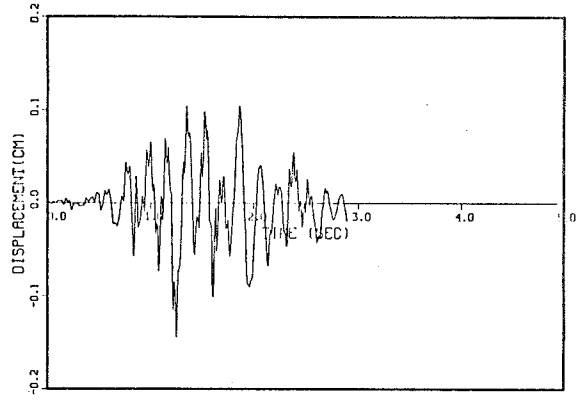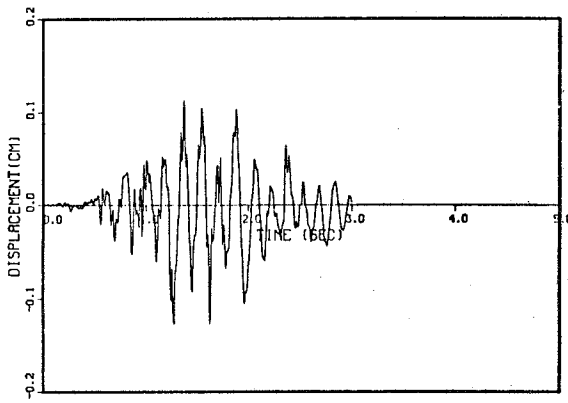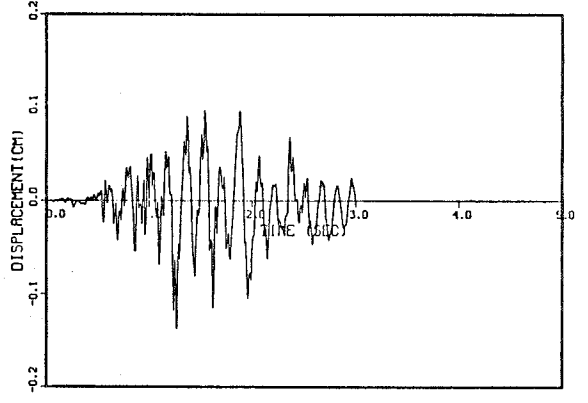
7-60

(a) Test Result

(b) MARC Elbow

(c) ABAQUS Elbow
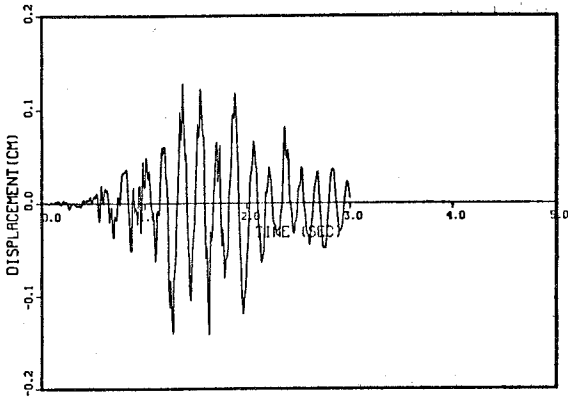
(d) ABAQUS Beam

(e) ABAQUS Elbow
(Higher Yield Stress)
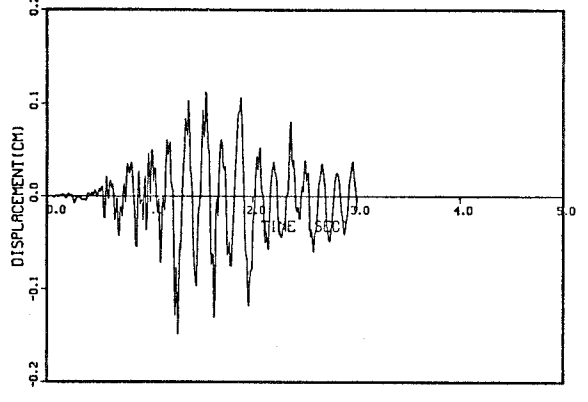
(f) ABAQUS Beam
(Higher Yield Stress)

Figure 7.44 Displacement at Top of RCP, Ux (1.0 MPR)
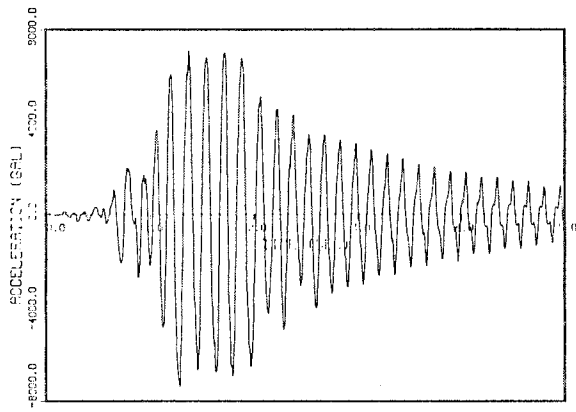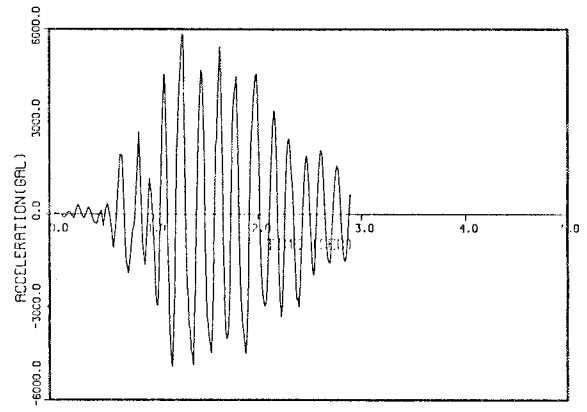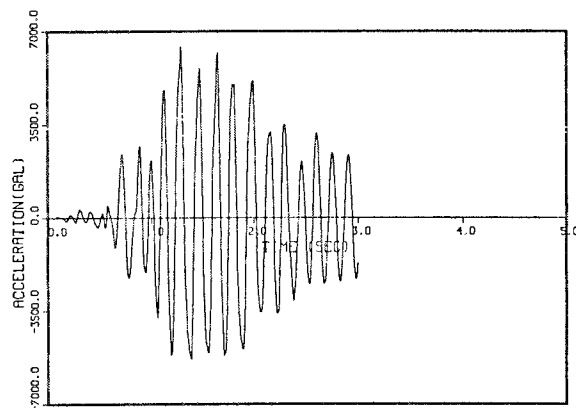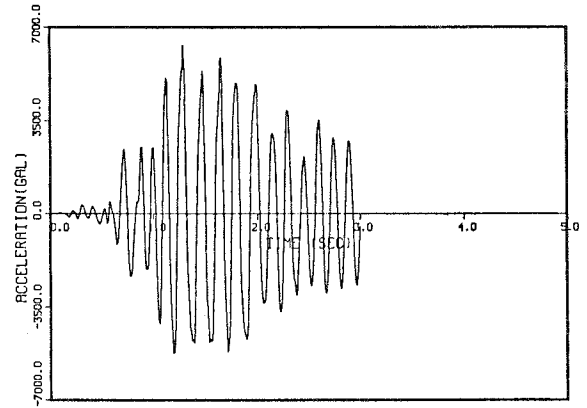
7-61

(a) Test Result

(b) MARC Elbow

(c) ABAQUS Elbow
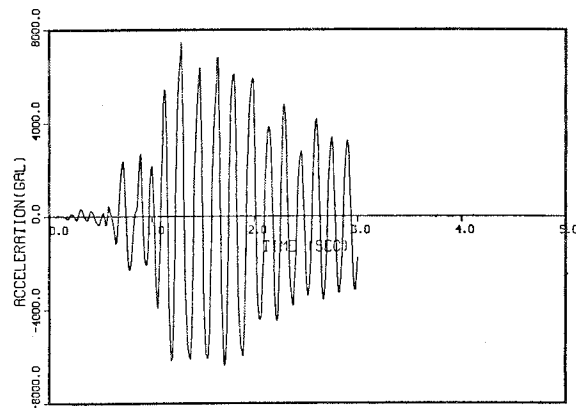
(d) ABAQUS Beam

(e) ABAQUS Elbow
    (Higher Yield Stress)
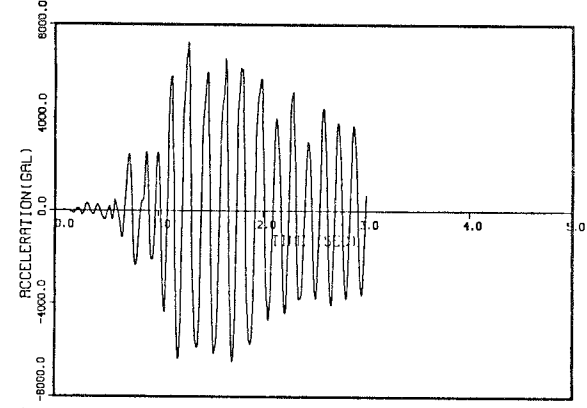
(f) ABAQUS Beam
    (Higher Yield Stress)

Figure 7.45 Acceleration at Top of S/G, Ax (1.0 MPR)
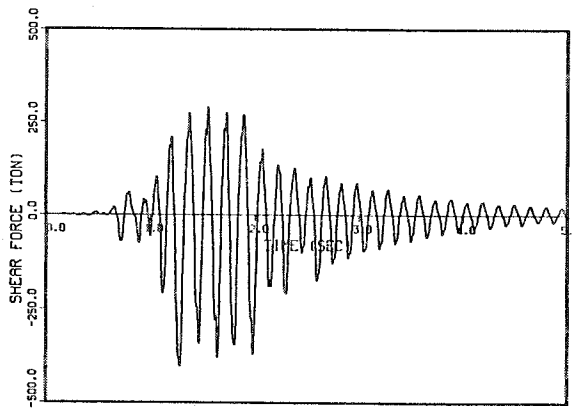
(a) Test Result
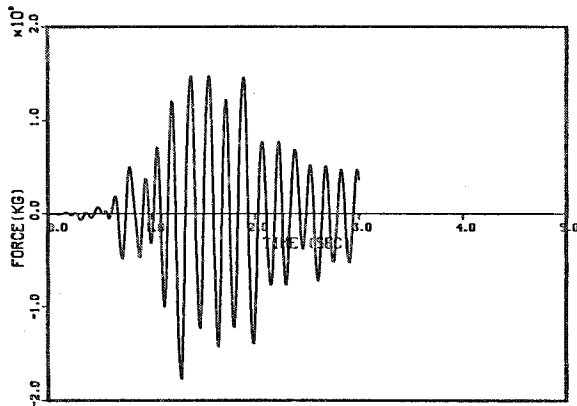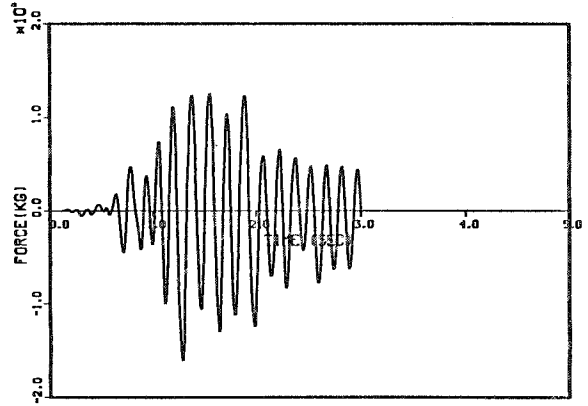
(b) ABAQUS Elbow
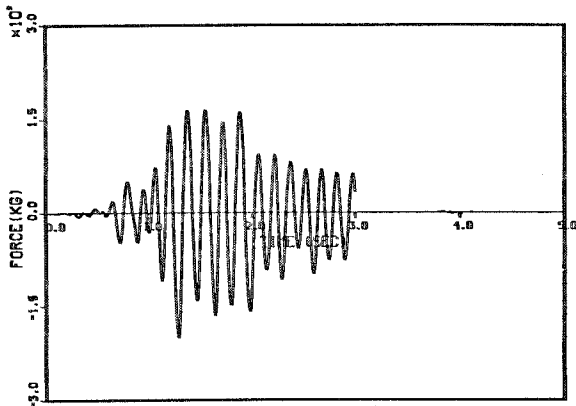
(c) ABAQUS Beam

(d) ABAQUS Elbow
(Higher Yield Stress)
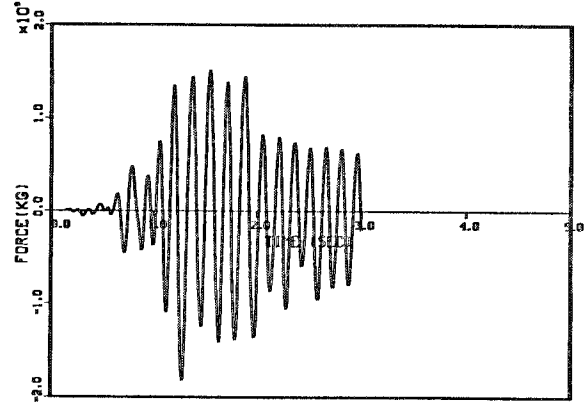
(e) ABAQUS Beam
(Higher Yield Stress)

Figure 7.46 Shear Force at Pin-Support, Qx (1.0 MPR)
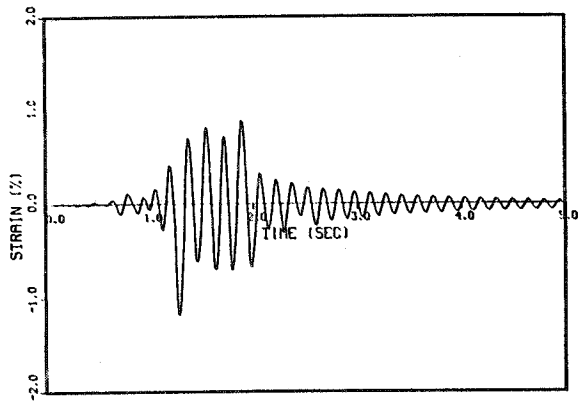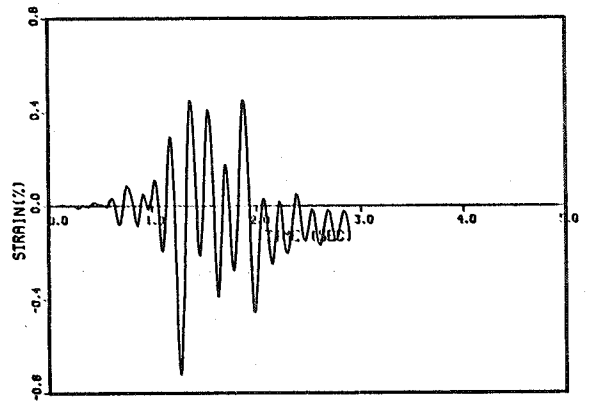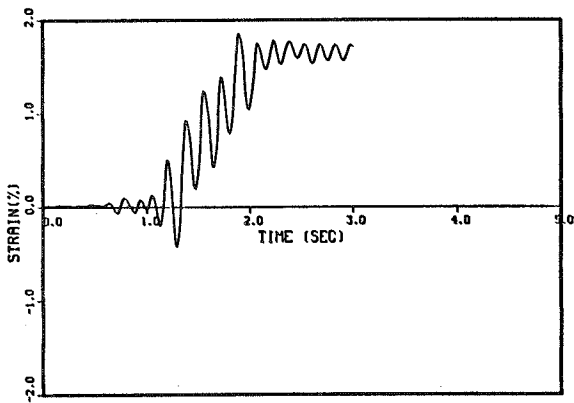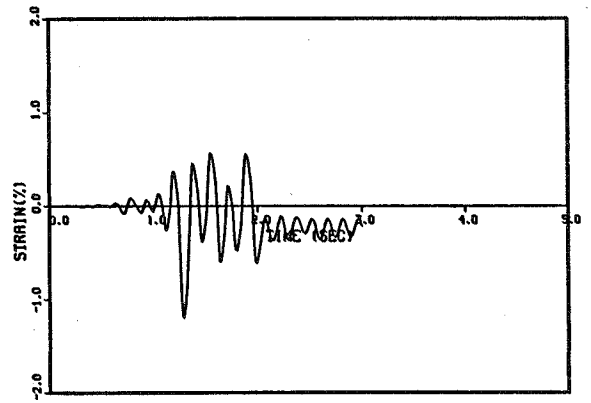
7-63

(a) Test Result

(b) MARC Elbow

(c) ABAQUS Elbow
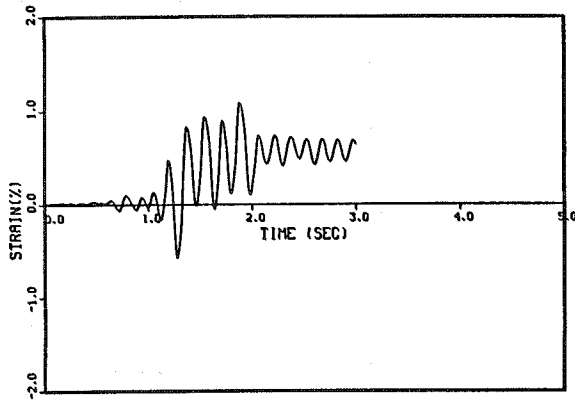
(d) ABAQUS Beam

(e) ABAQUS Elbow
(Higher Yield Stress)
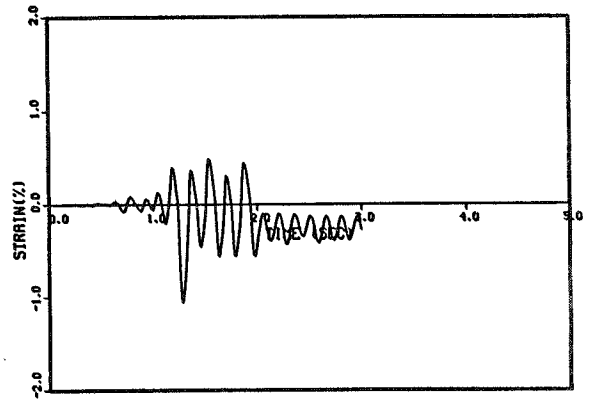
(f) ABAQUS Beam
(Higher Yield Stress)

Figure 7.47 Axial Strain at 135X (1.0 MPR)
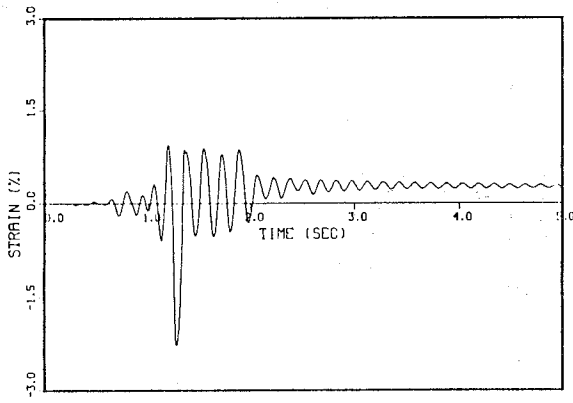
(a) Test Result
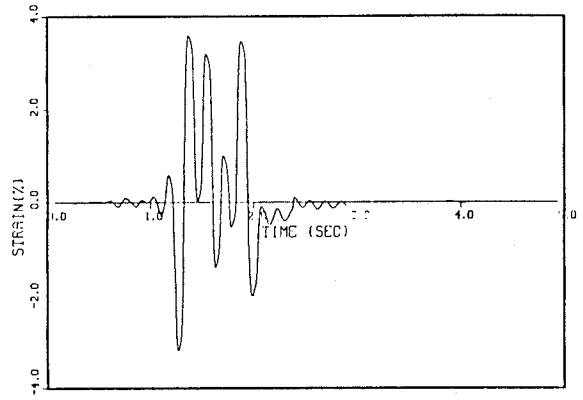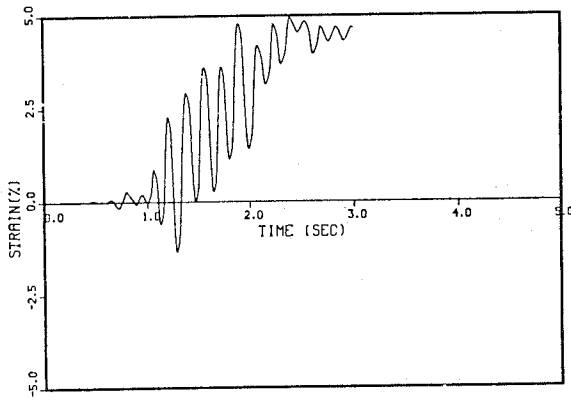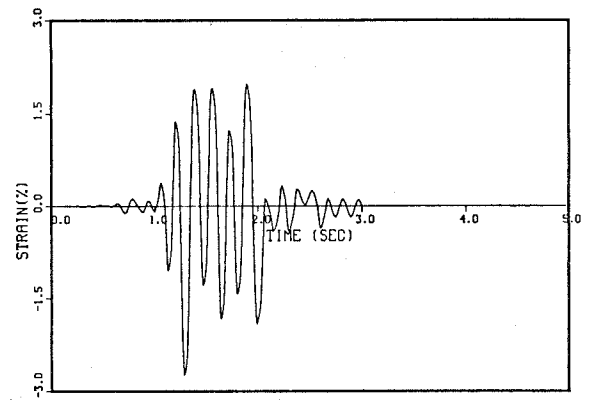
(b) MARC Elbow

(c) ABAQUS Elbow
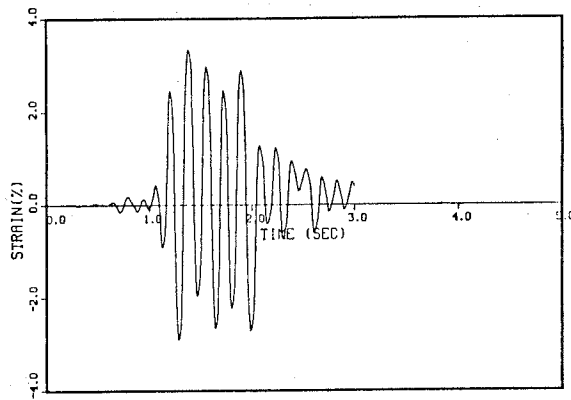
(d) ABAQUS Beam

(e) ABAQUS Elbow
(Higher Yield Stress)
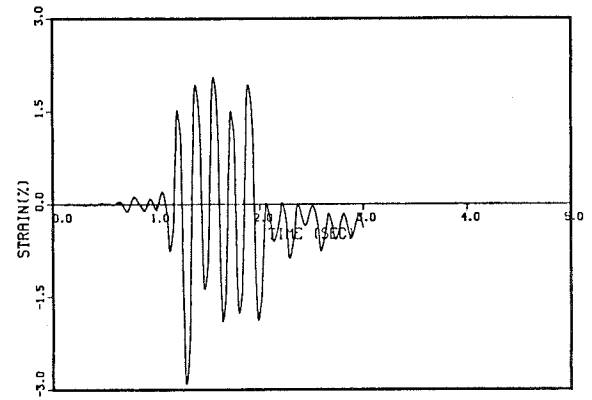
(f) ABAQUS Beam
(Higher Yield Stress)

Figure 7.48 Axial Strain at 153X (1.0 MPR)
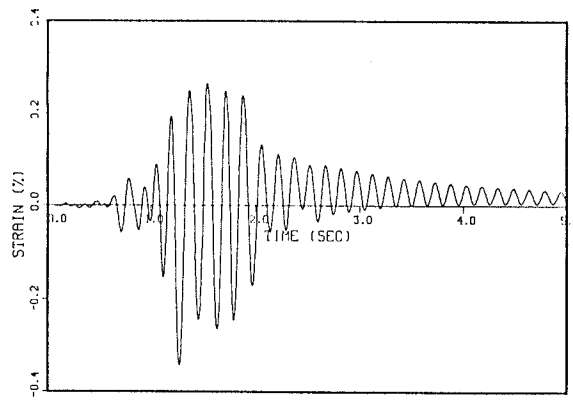
(a) Test Result
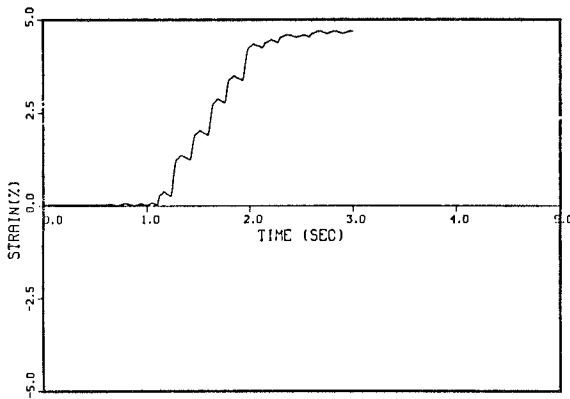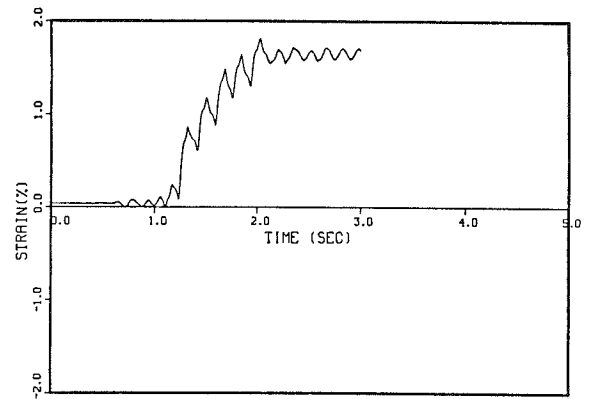
(b) ABAQUS Elbow

(c) ABAQUS Elbow
(Higher Yield Stress)

Figure 7.49 Hoop Strain at 153Y (1.0 MPR)
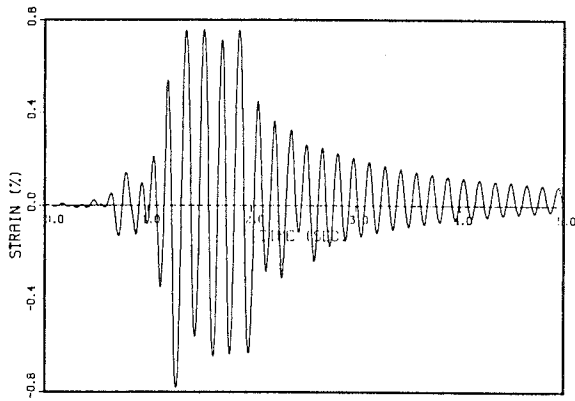
(a) Test Result
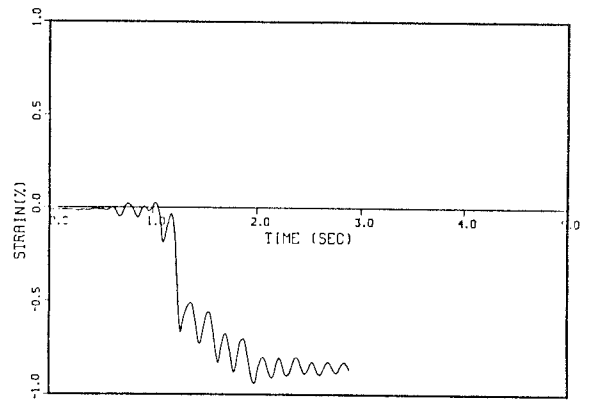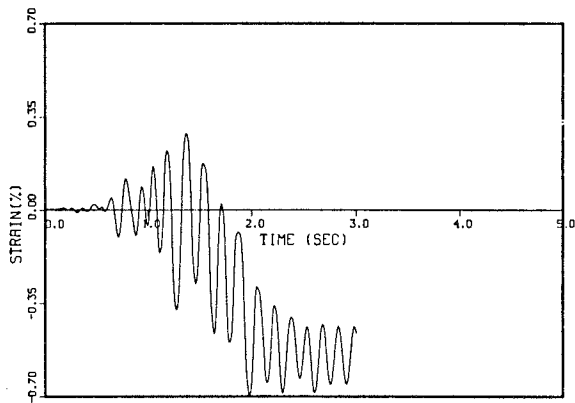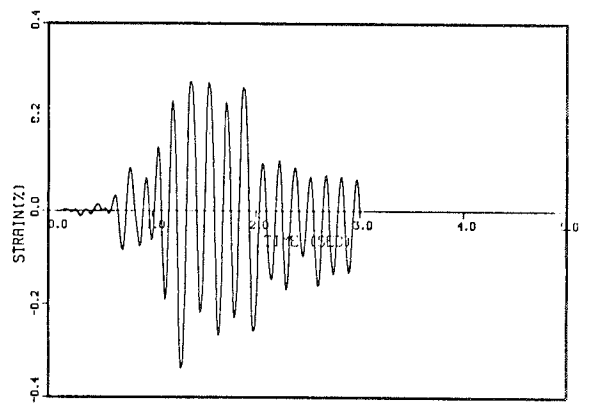
(b) MARC Elbow

(c) ABAQUS Elbow
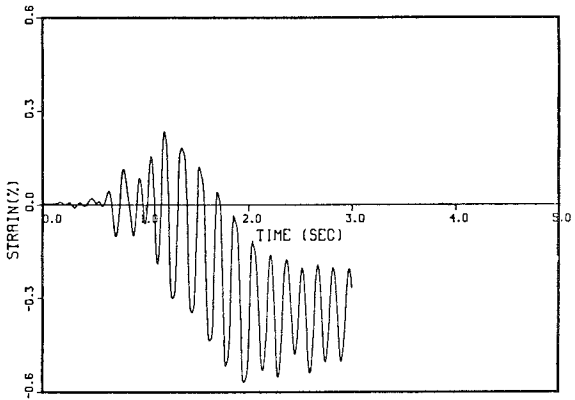
(d) ABAQUS Beam

(e) ABAQUS Elbow
     (Higher Yield Stress)
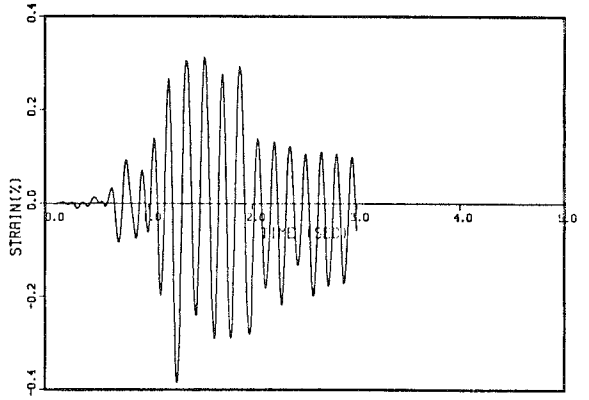
(f) ABAQUS Beam
     (Higher Yield Stress)

Figure 7.50 Axial Strain at 207X (1.0 MPR)
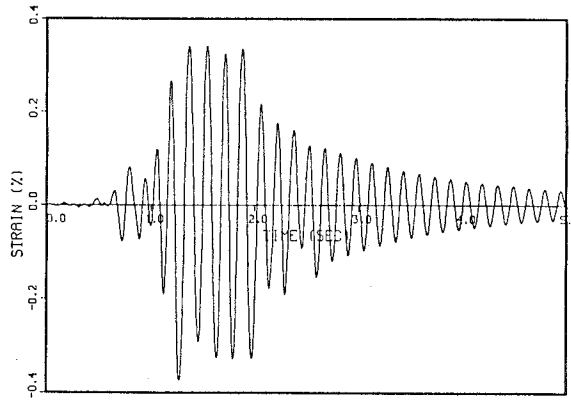
(a) Test Result
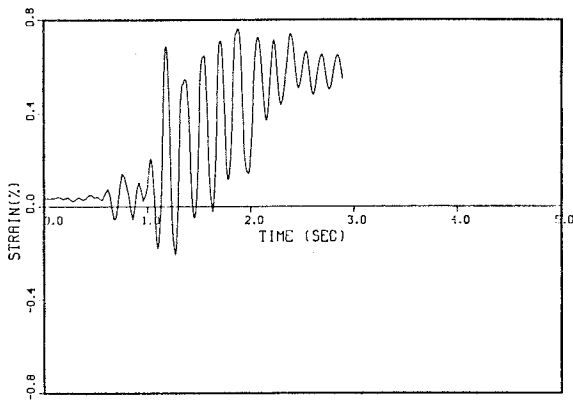
(b) MARC Elbow
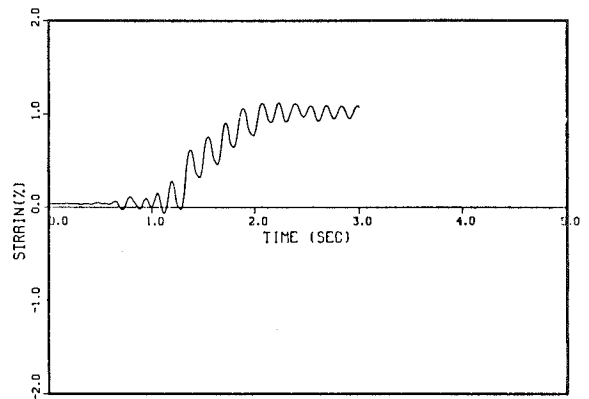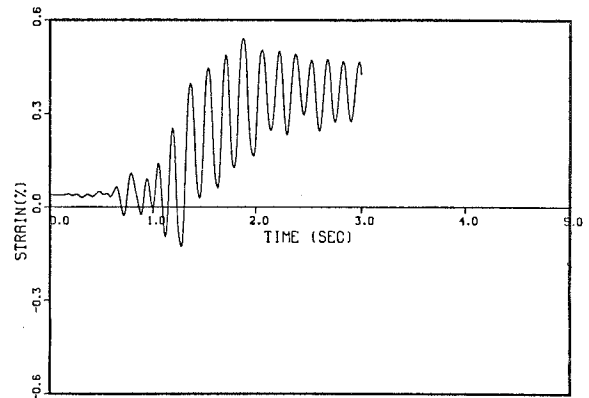
(c) ABAQUS Elbow

(d) ABAQUS Elbow
    (Higher Yield Stress)

Figure 7.51 Hoop Strain at 207Y (1.0 MPR)
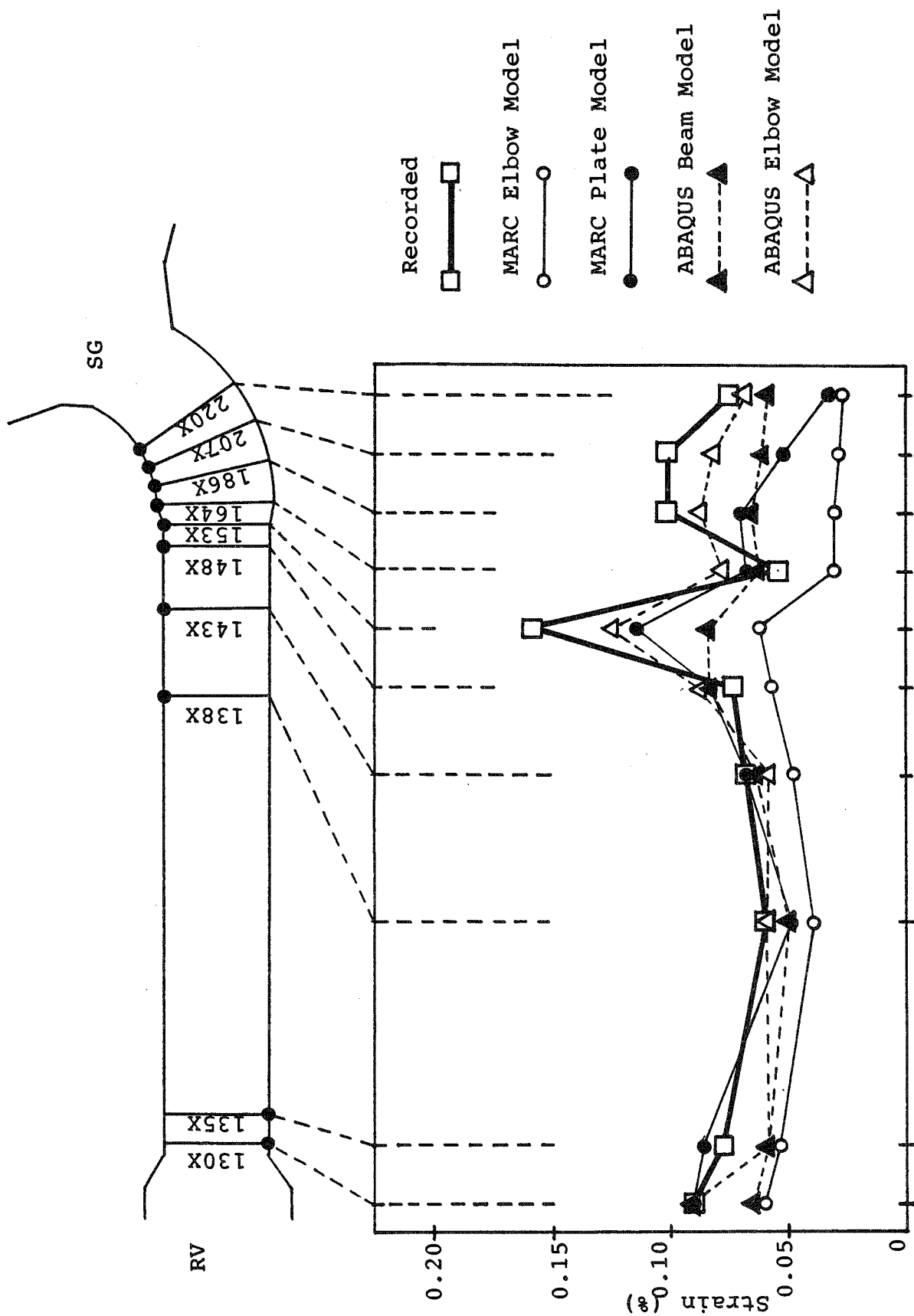
Figure 7.52 Axial Strain Distribution at 0.1 MPR (A-Segment)
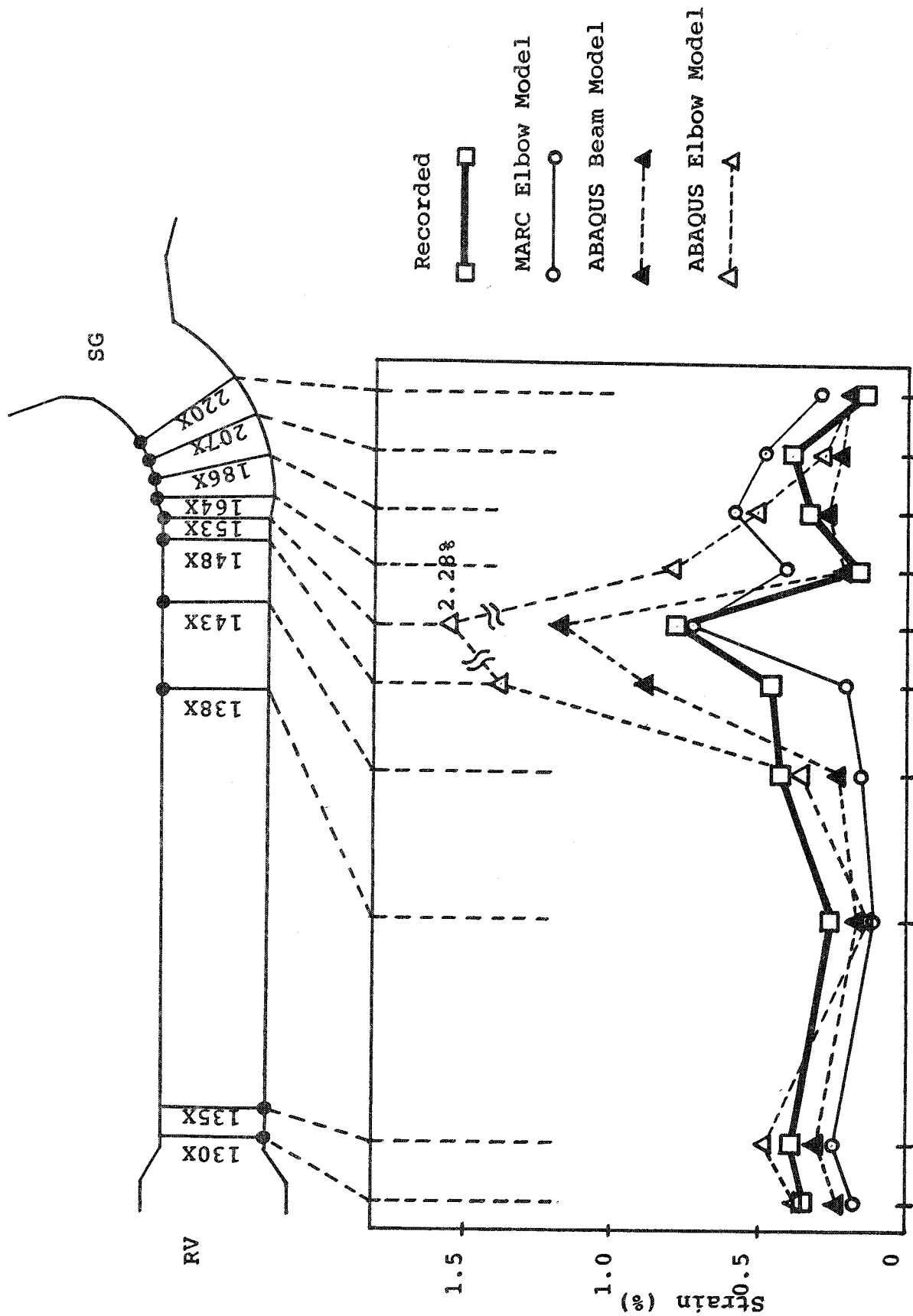
Figure 7.53 Axial Strain Distribution at 0.4 MPR (A-Segment)
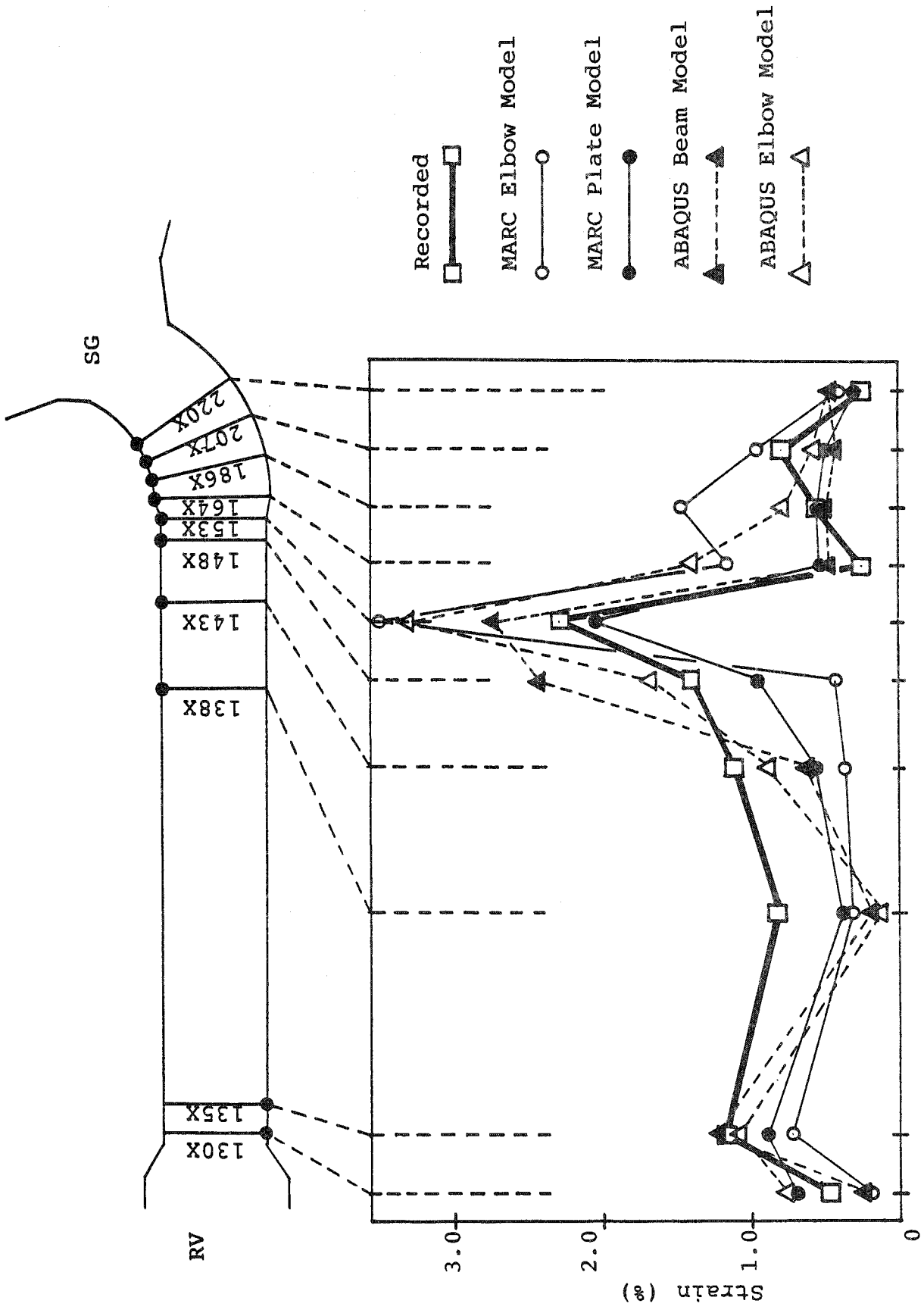
Figure 7.54 Axial Strain Distribution at 1.0 MPR (A-Segment)

7-71

KEY FOR FIGURES 7.55 - 7.66

● TEST DATA

——— ANALYSIS (OUTSIDE SURFACE)

- - - ANALYSIS (INSIDE SURFACE)

(HR4A)

(HR4)
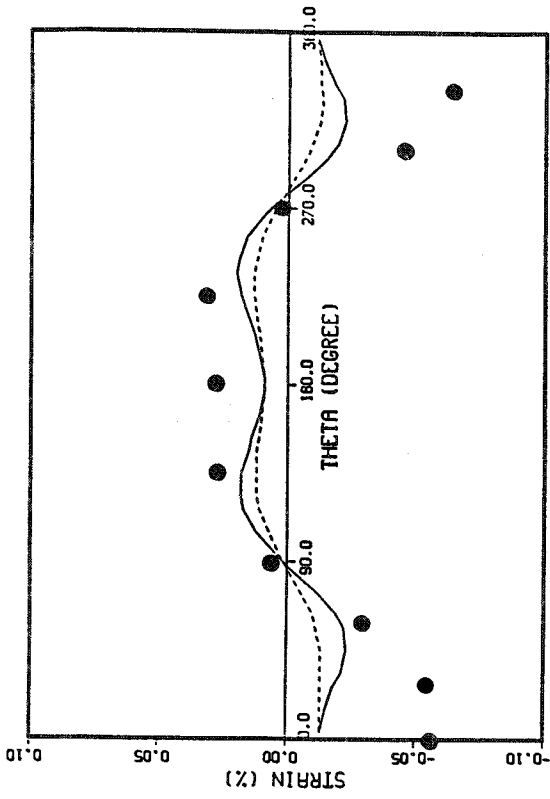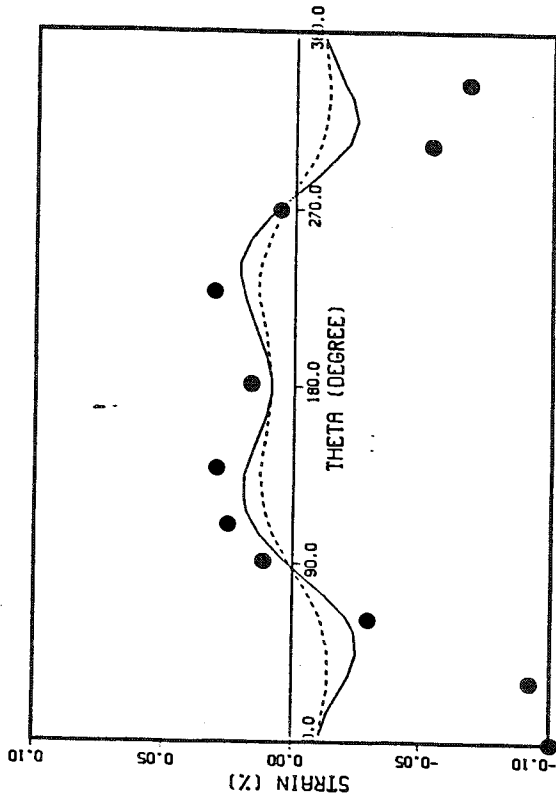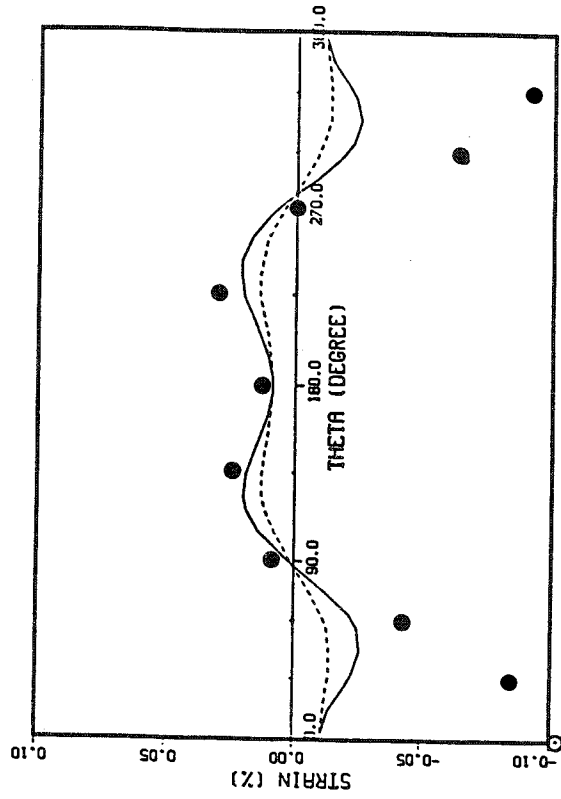
(HR4C)

Figure 7.55 Axial Strain Distribution at Maximum Peak Response of 0.1 MPR by MARC Elbow Model
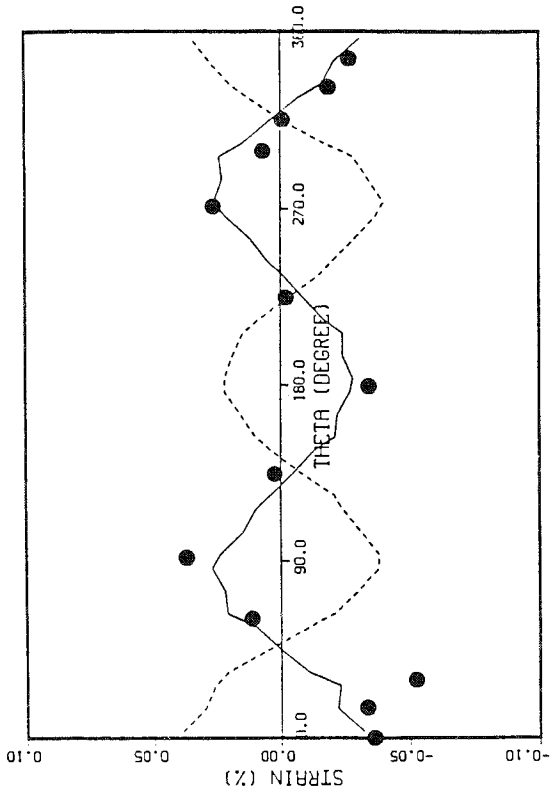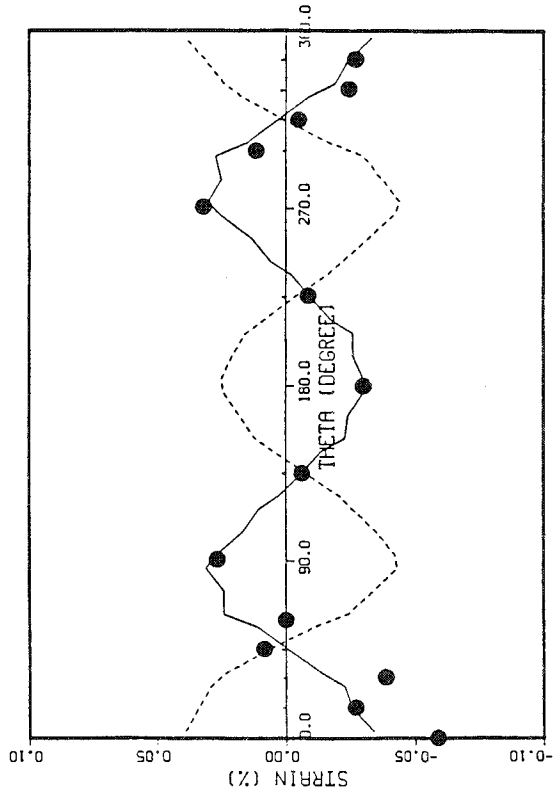
(HR4A)

(HR4)
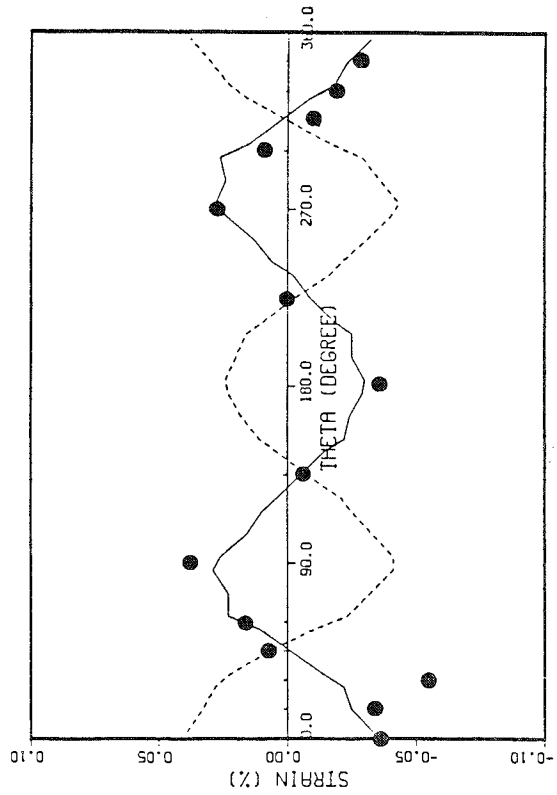
(HR4C)

Figure 7.56 Hoop Strain Distribution at Maximum Peak Response
of 0.1 MPR by MARC Elbow Model
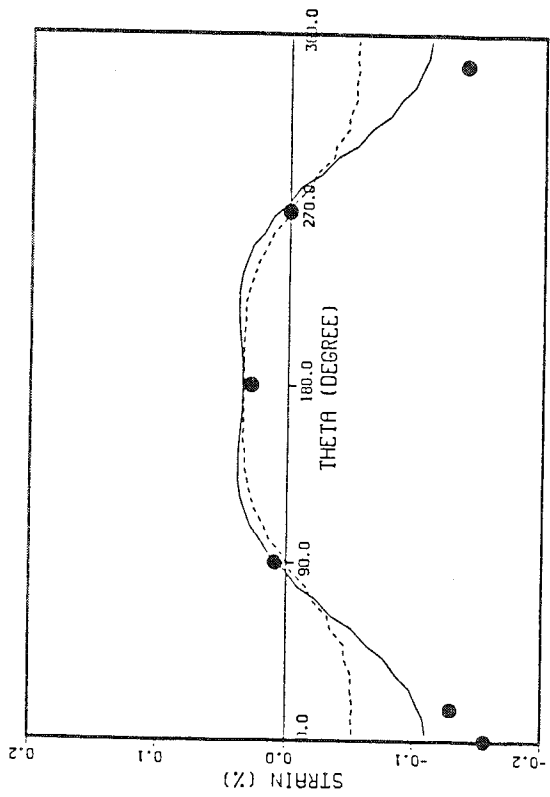
(Axial Strain at HR4A)
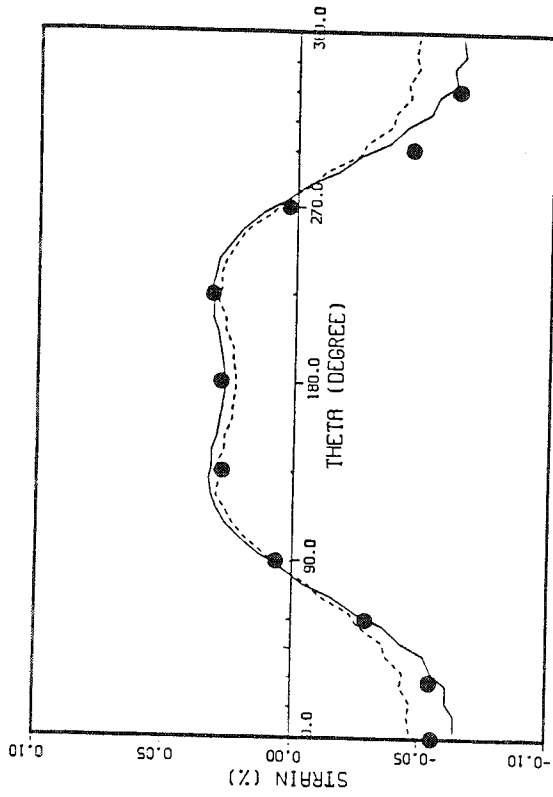
(Hoop Strain at HR4A)
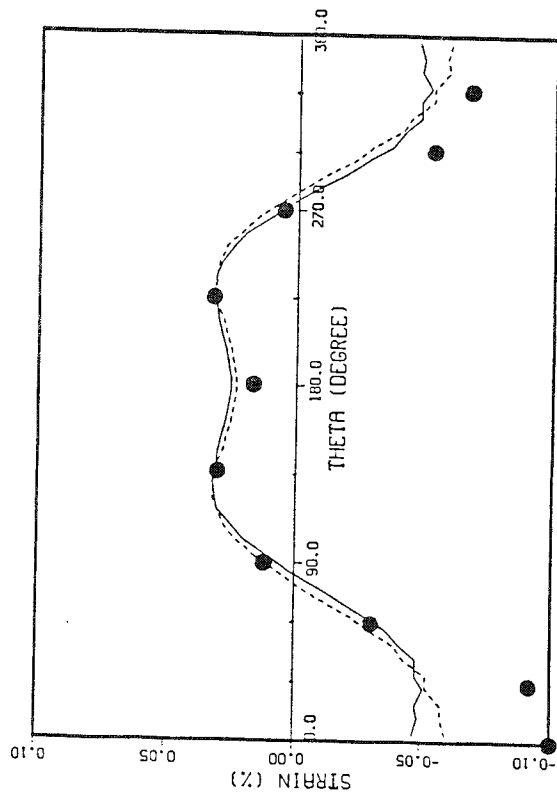
(Axial Strain at HR3A)
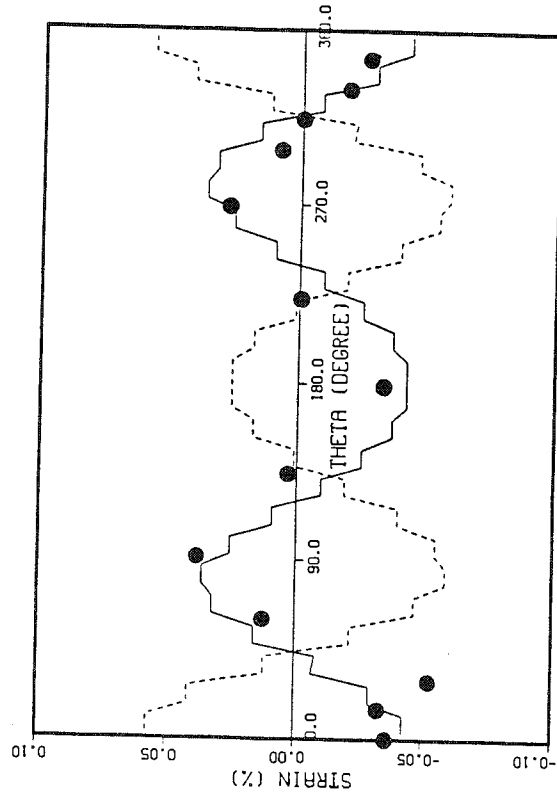
(Axial Strain at HR4C)

Figure 7.57 Strain Distribution at Maximum Peak Response
of 0.1 MPR by MARC Flat-Plate Model

7-74
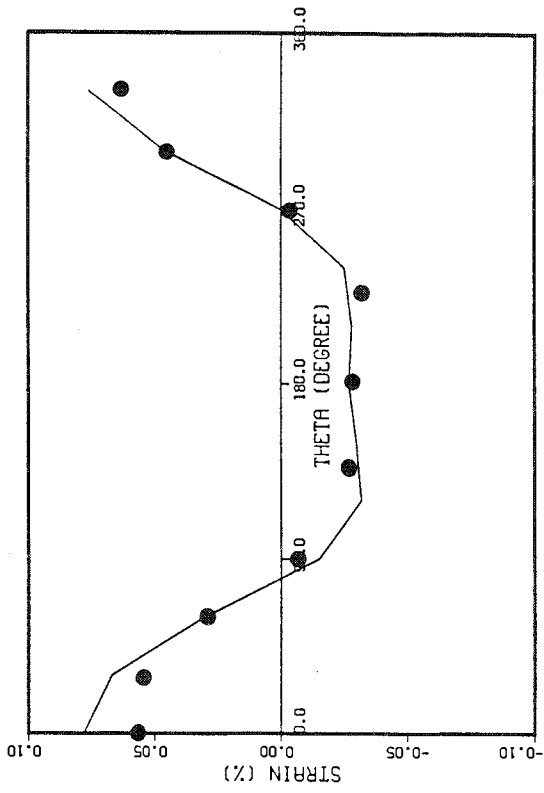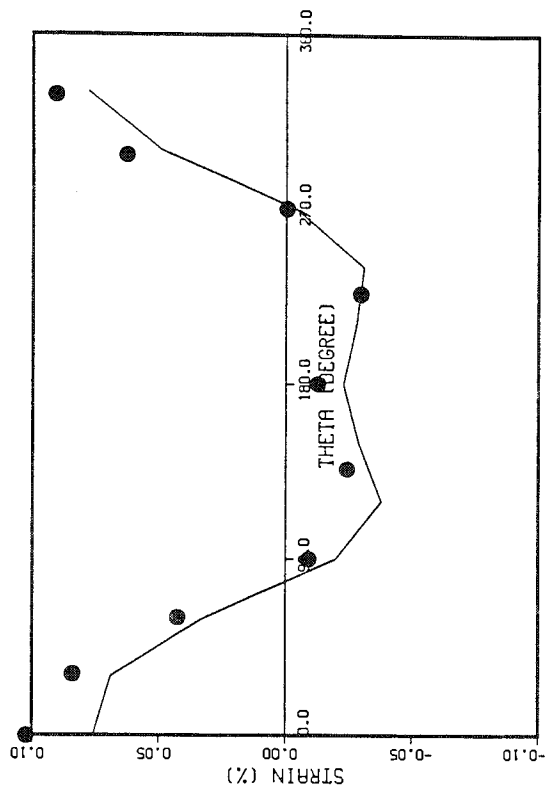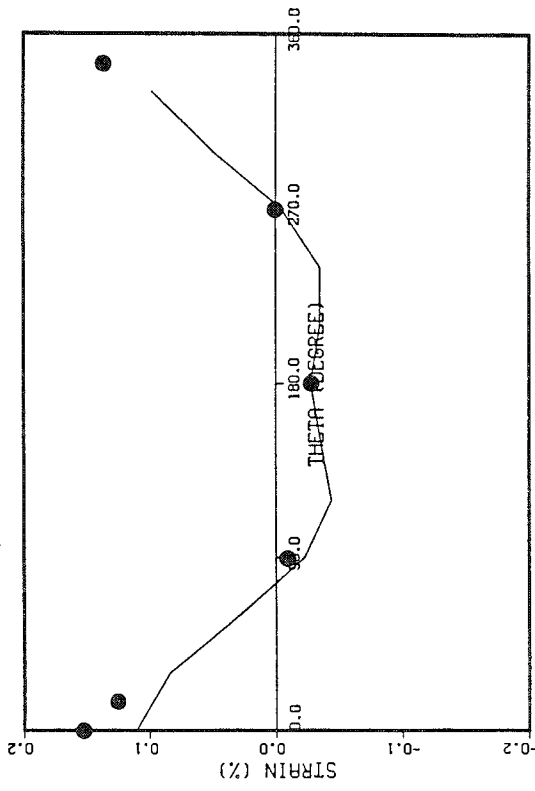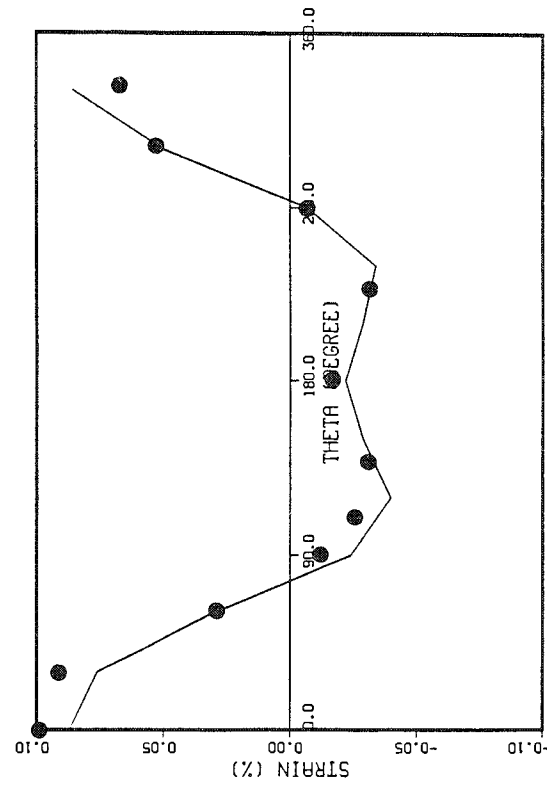
Figure 7.58   Axial Strain Distribution at Maximum Peak Response
of 0.1 MPR by ABAQUS Elbow Model
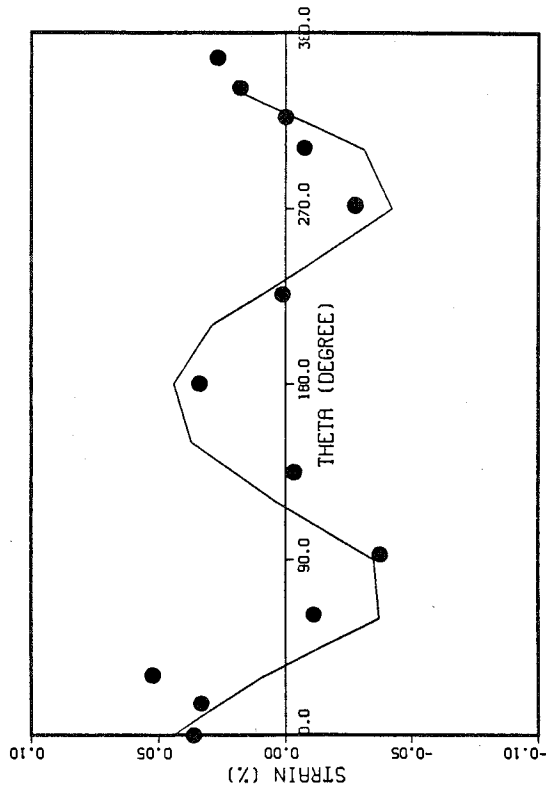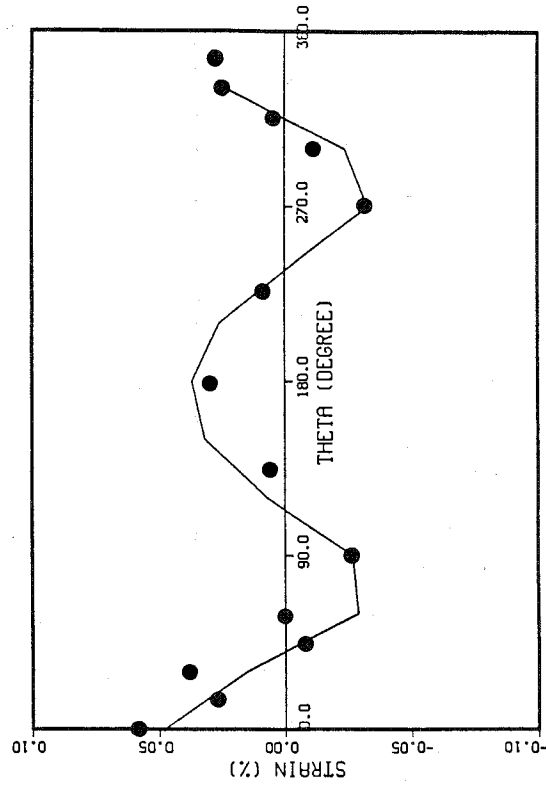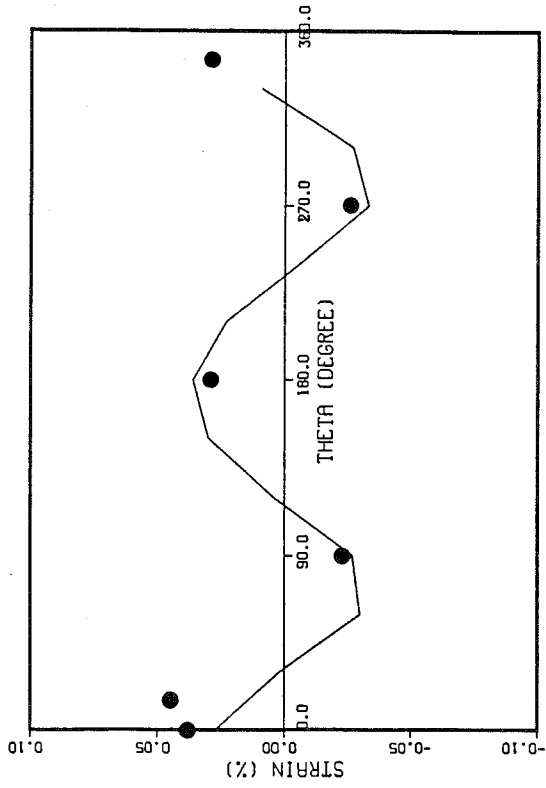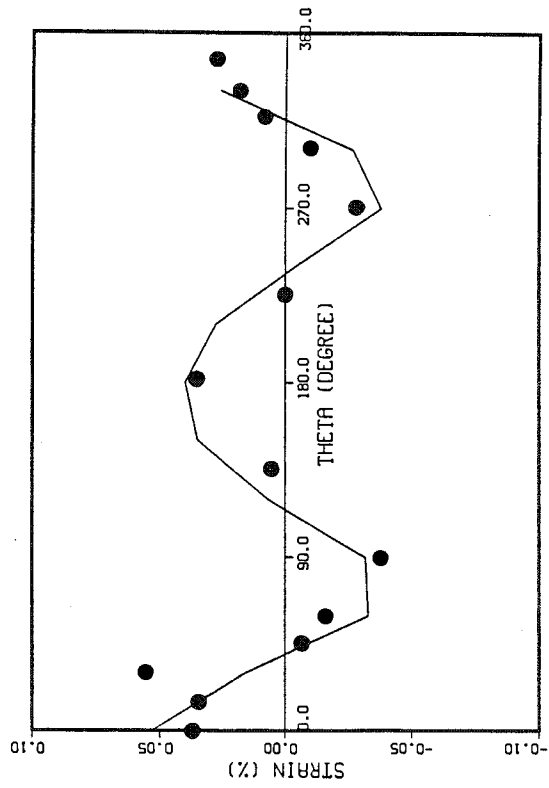
Figure 7.59 Hoop Strain Distribution at Maximum Peak Response
of 0.1 MPR by ABAQUS Elbow Model
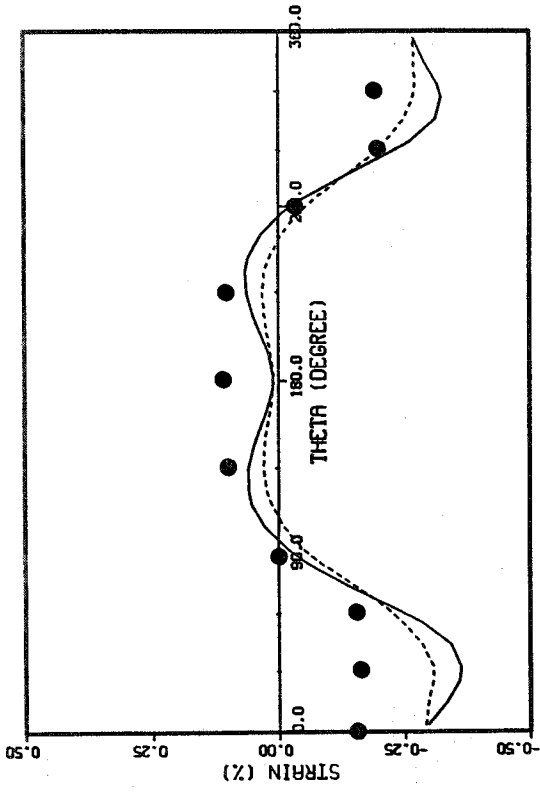
(HR4A)
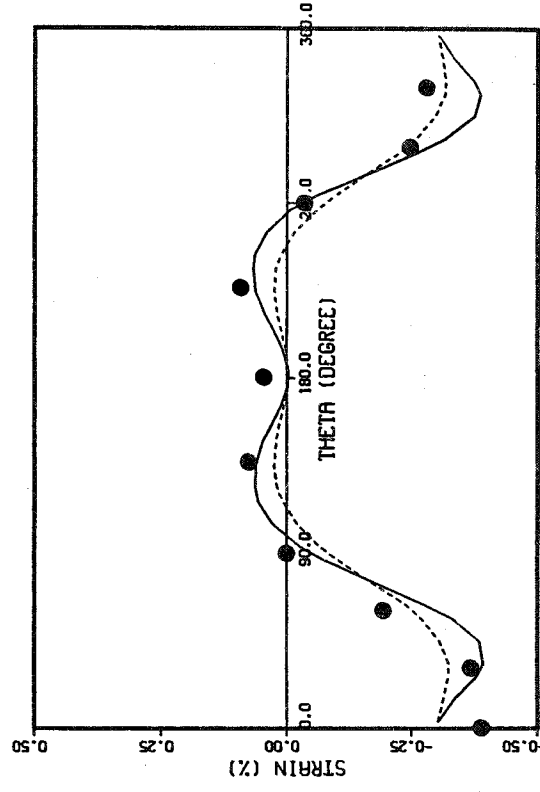
(HR4)
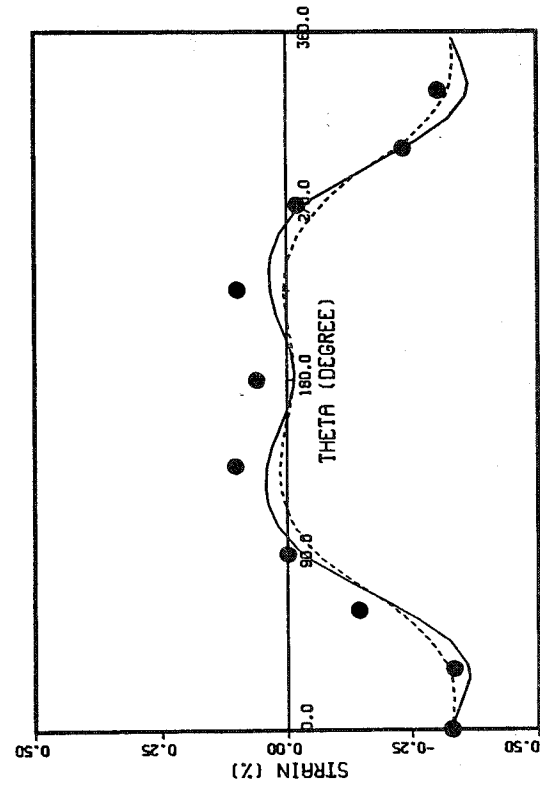
(HR4C)

Figure 7.60 Axial Strain Distribution at Maximum Peak Response
of 0.4 MPR by MARC Elbow Model

(HR4A)

(HR4)
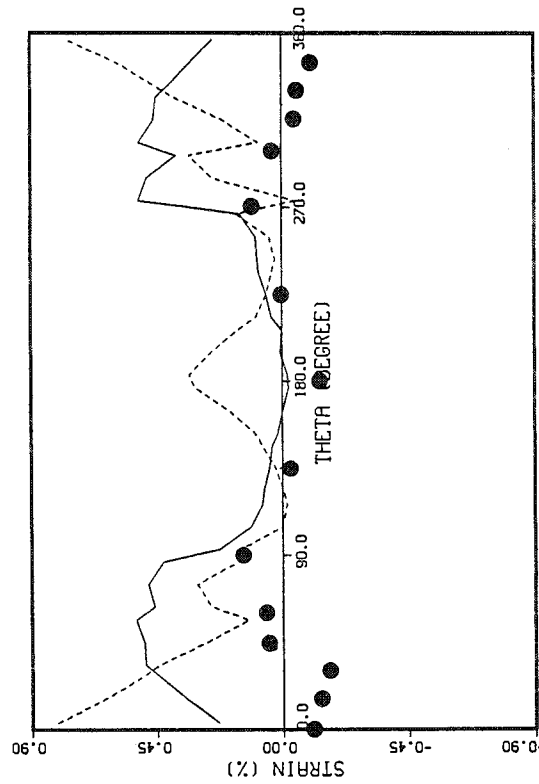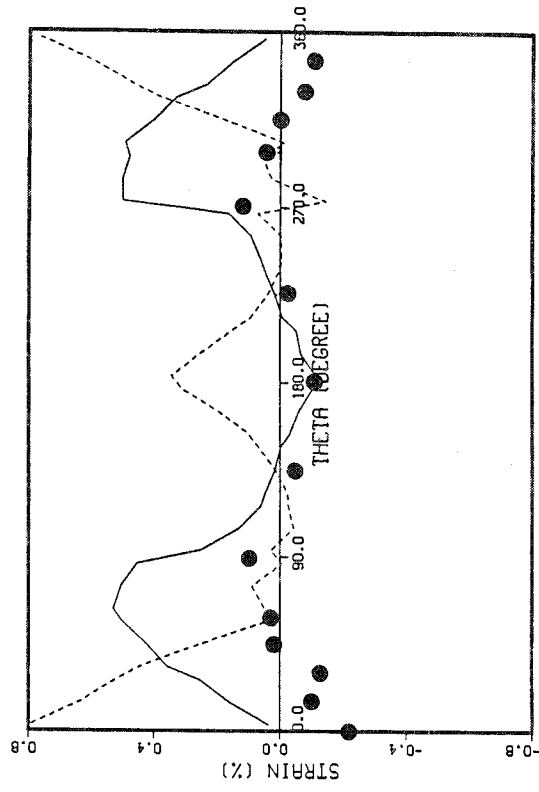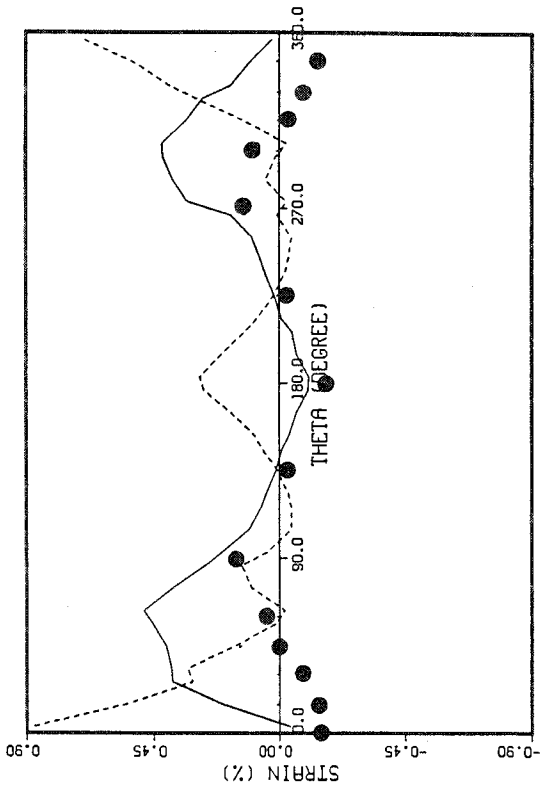
(HR4C)

Figure 7.61 Hoop Strain Distribution at Maximum Peak Response of 0.4 MPR by MARC Elbow Model
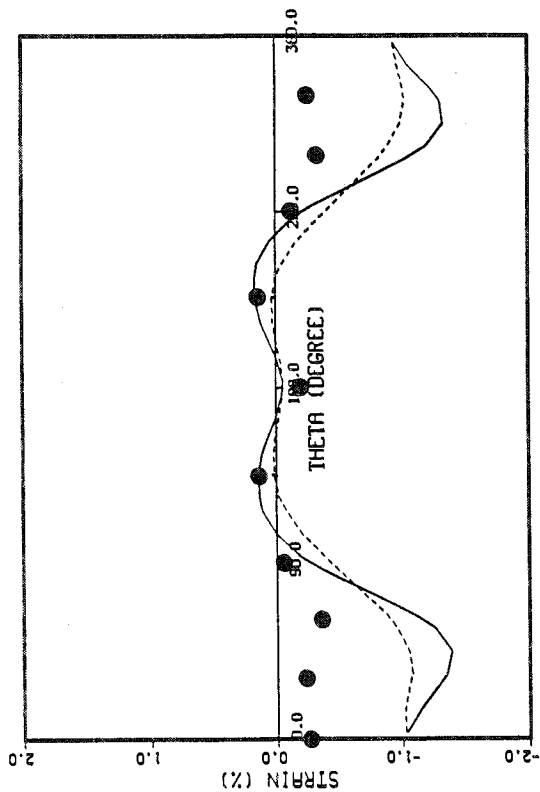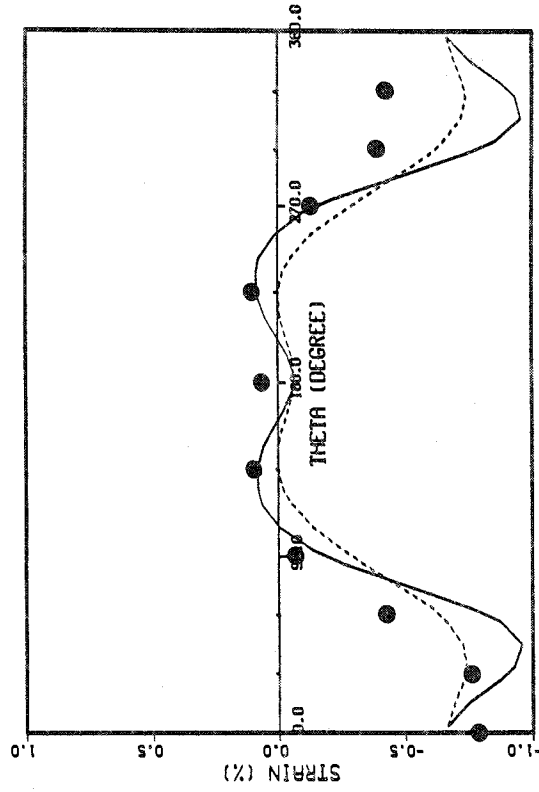
(HR4A)

(HR4)
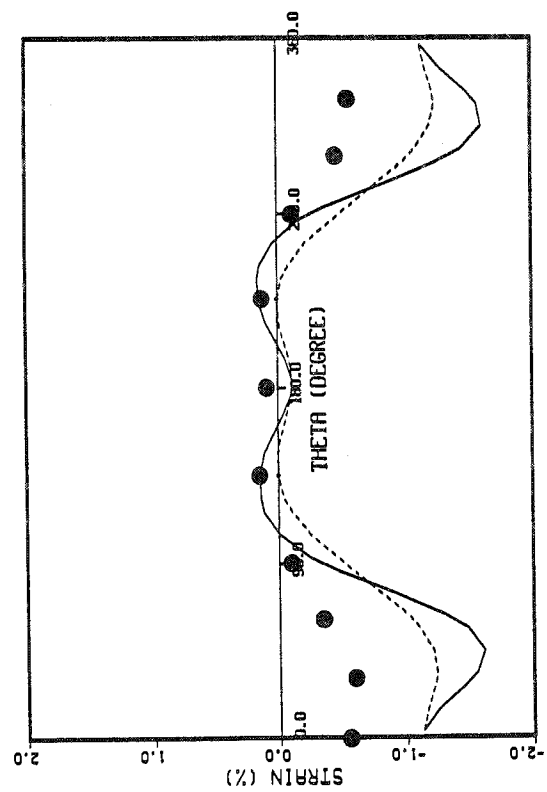
(HR4C)

Figure 7.62 Axial Strain Distribution at Maximum Peak Response
of 1.0 MPR by MARC Elbow Model
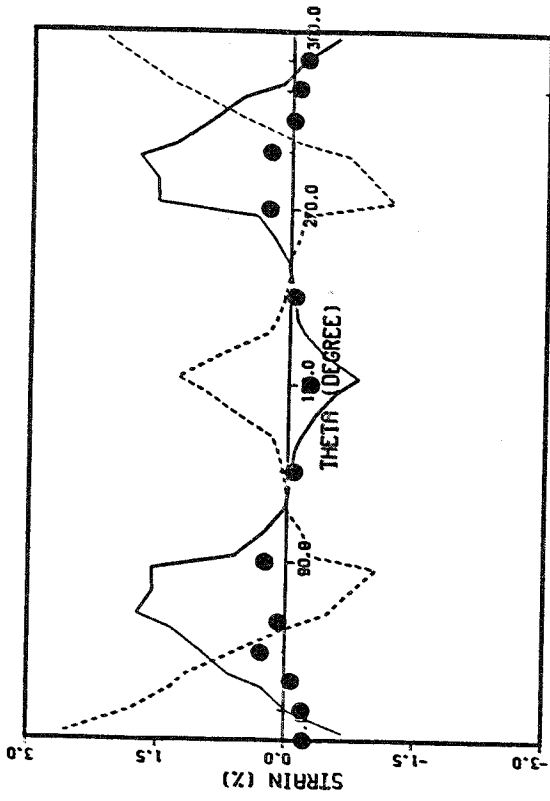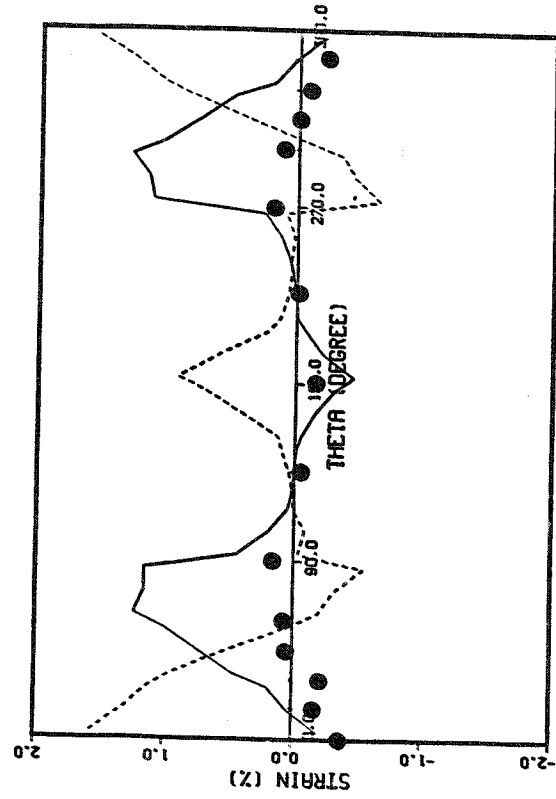
(HR4A)

(HR4)
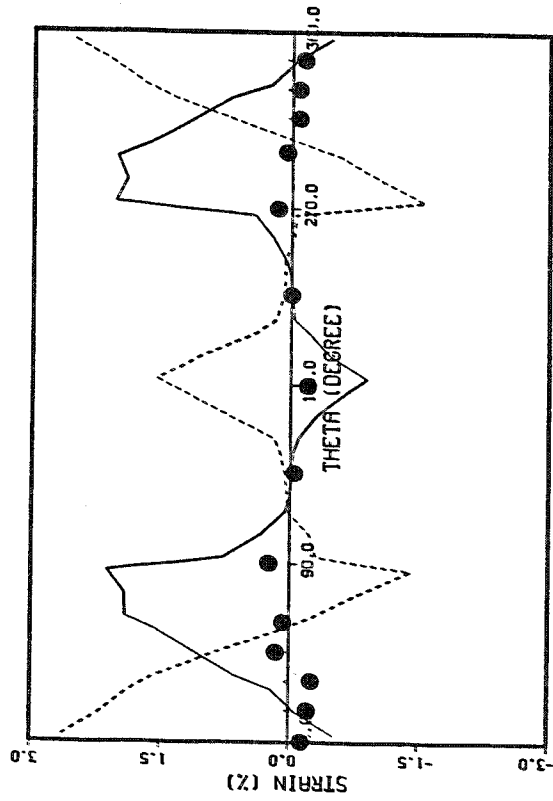
(HR4C)

Figure 7.63 Hoop Strain Distribution at Maximum Peak Response
of 1.0 MPR by MARC Elbow Model

7-80
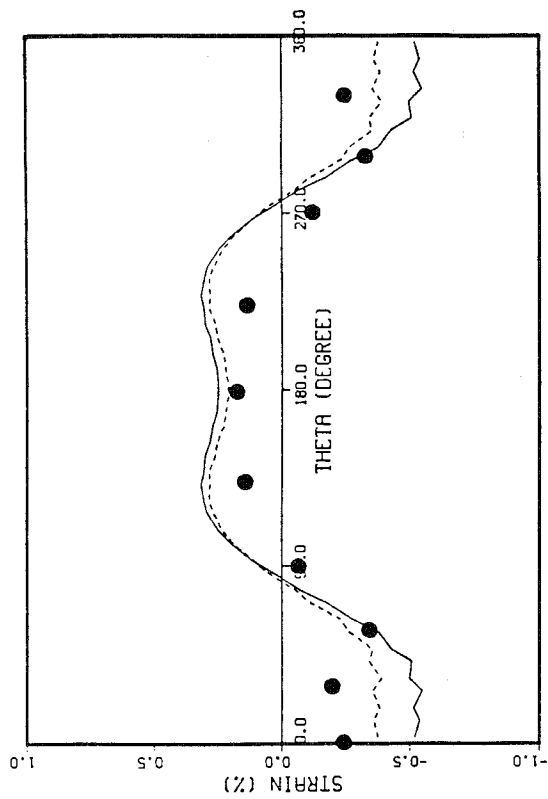
(Axial Strain at HR4A)

(Hoop Strain at HR4A)

(Axial Strain at HR3A)

(Axial Strain at HR4C)

Figure 7.64 Strain Distribution at Maximum Peak Response
of 1.0 MPR by MARC Flat-Plate Model
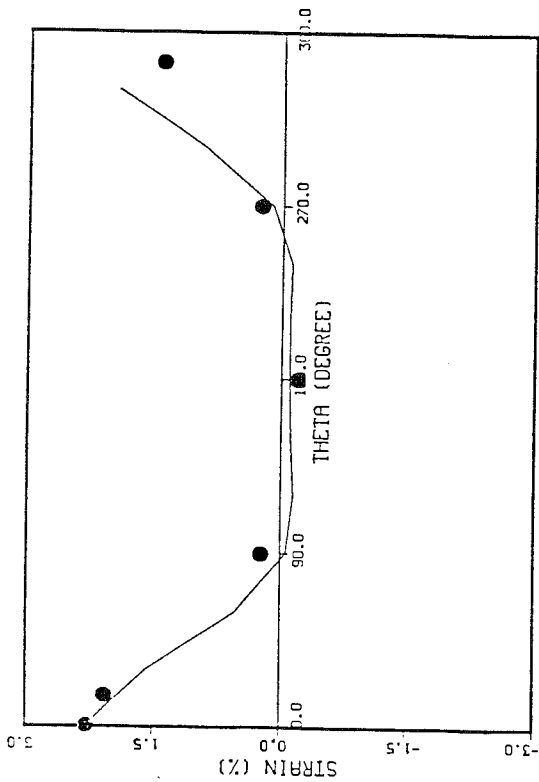
(HR3A)
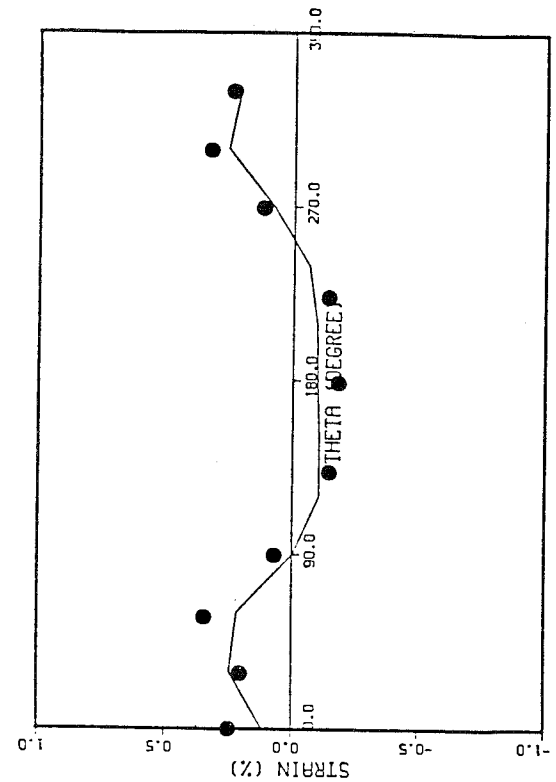
(HR4C)

(HR4A)
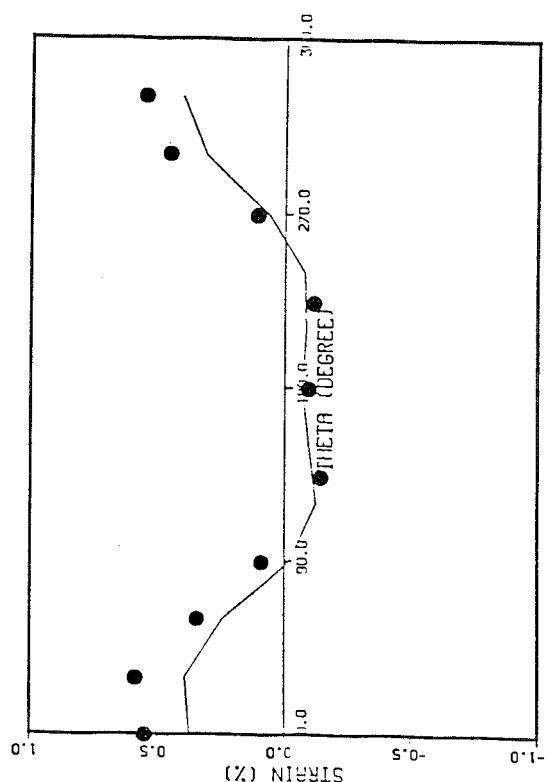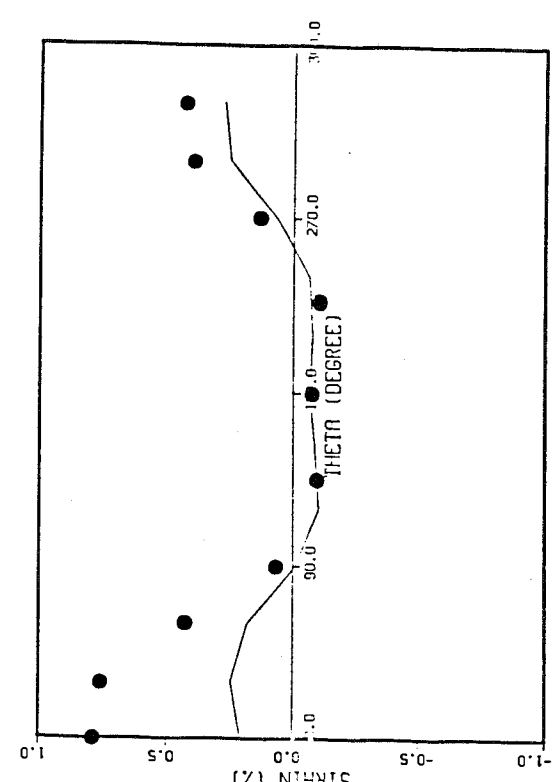
(HR4)

Figure 7. 65 Axial Strain Distribution at t = 1.2 sec. of 1.0
MPR by ABAQUS Elbow Model

7-82

(HR4A)

(HR3A)

(HR4)

(HR4C)
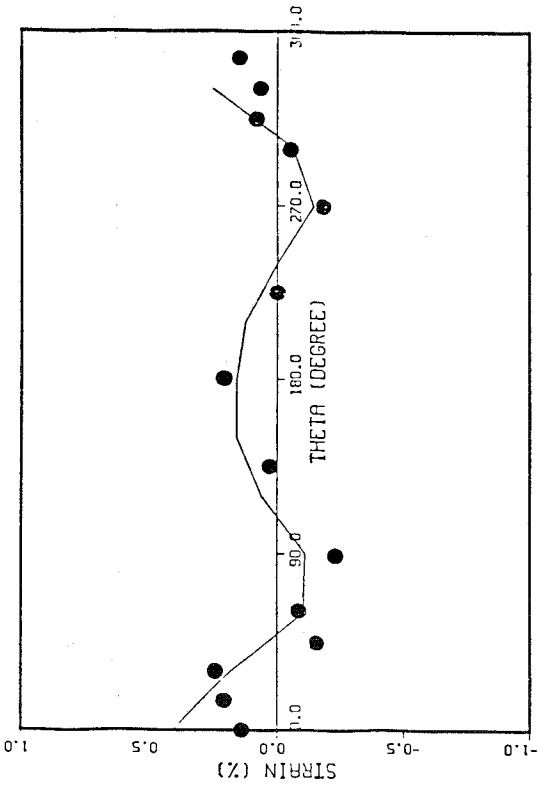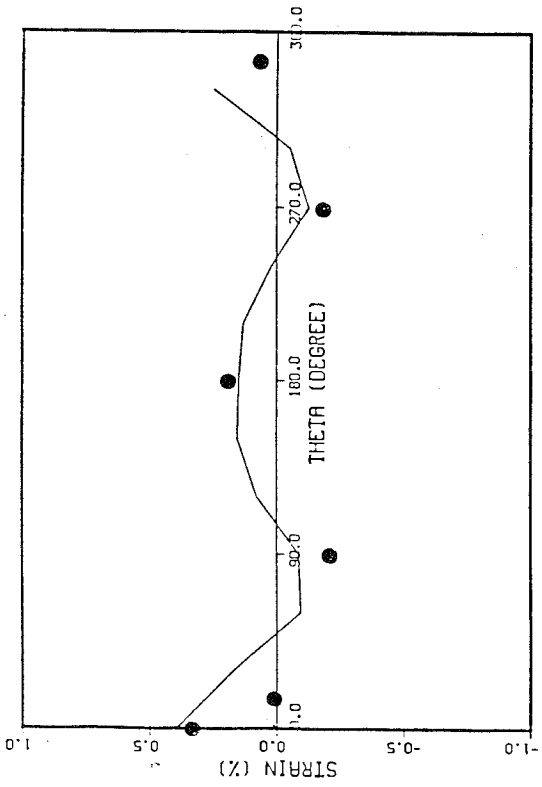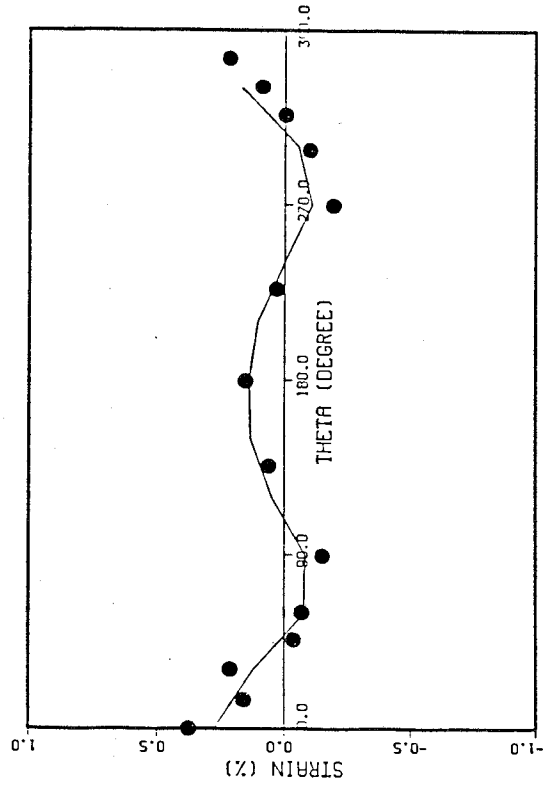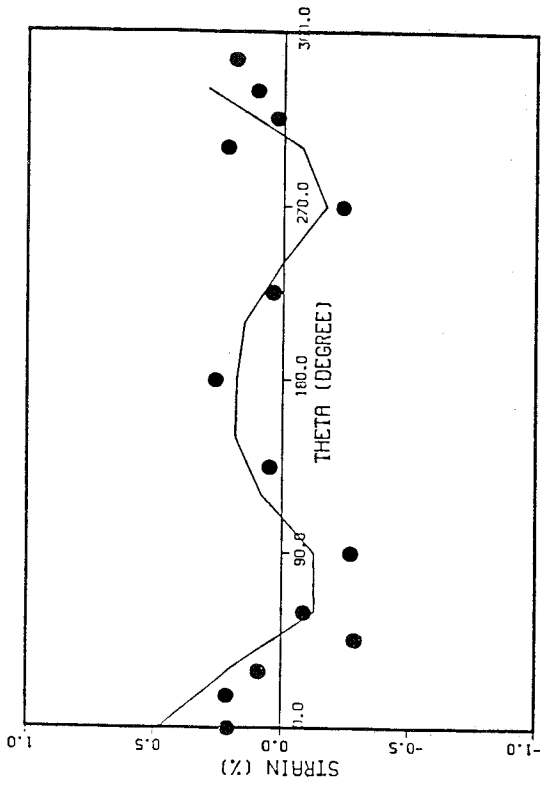
Figure 7.66 Hoop Strain Distribution at t = 1.2 sec. of 1.0
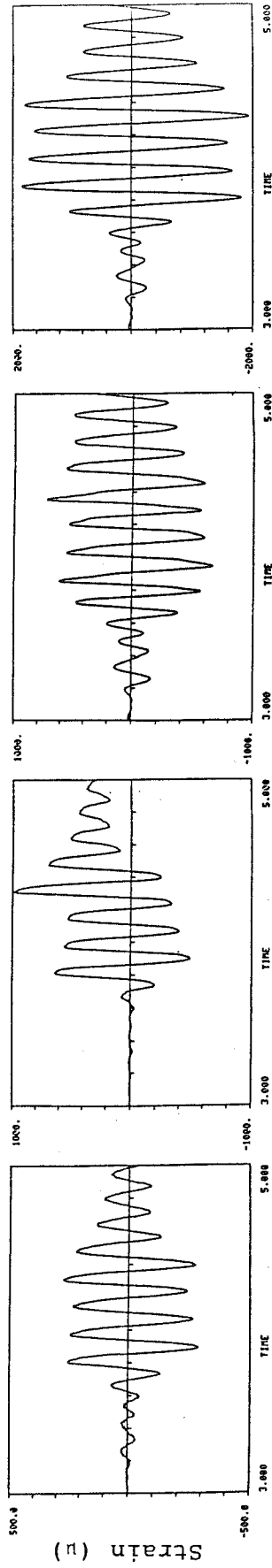MPR by ABAQUS Elbow Model
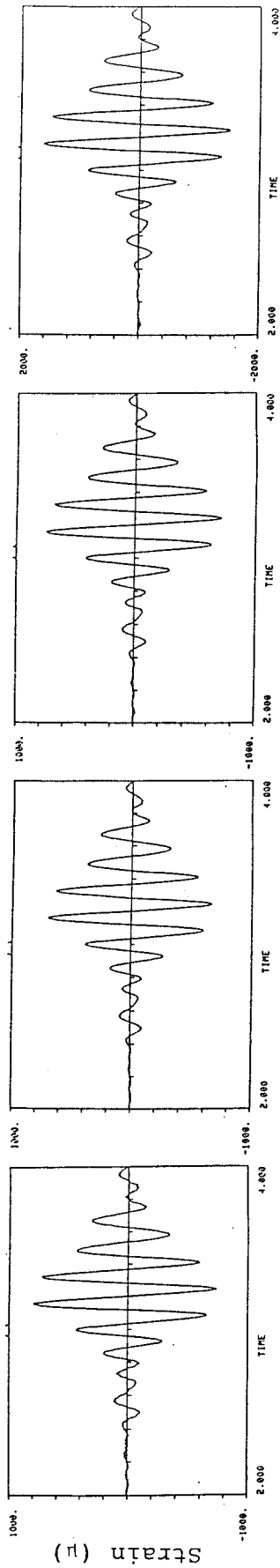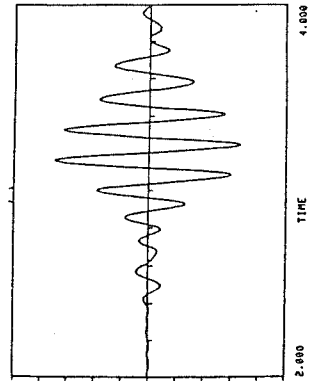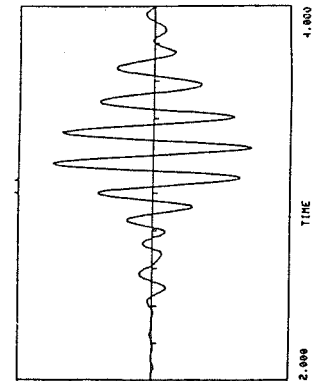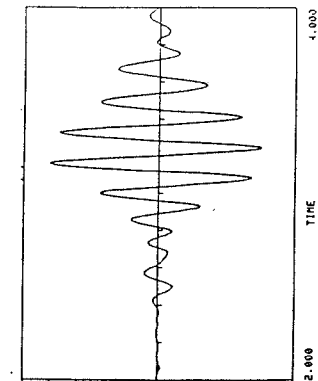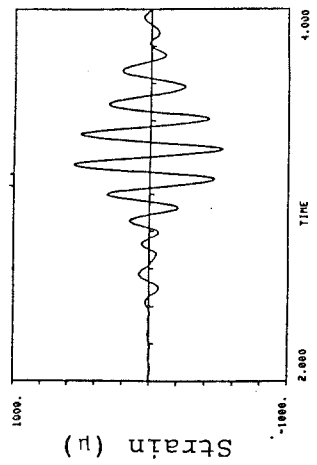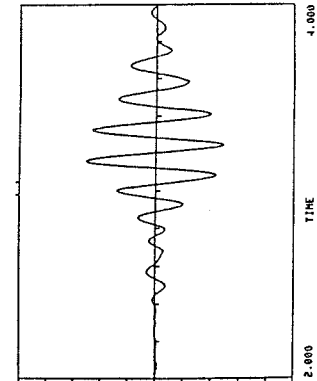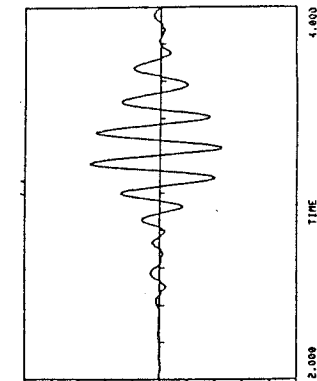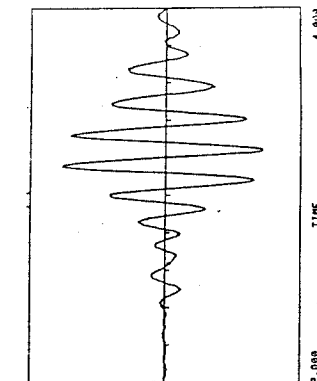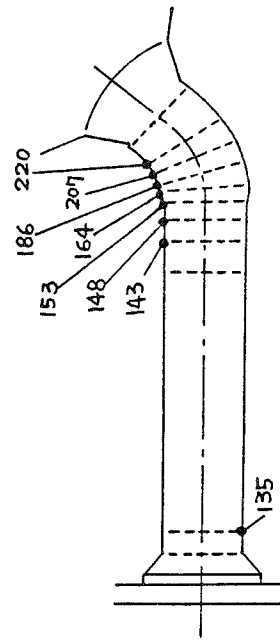
Figure 7.67   Test Results for Axial Strain at 0.1 MPR
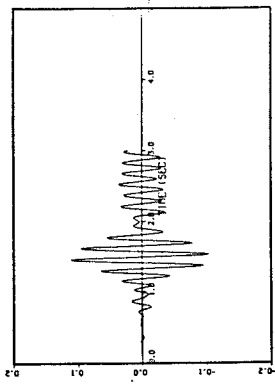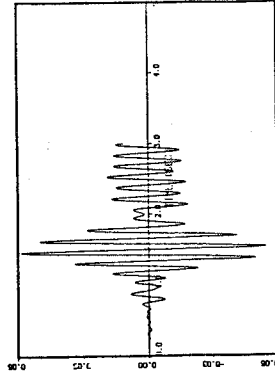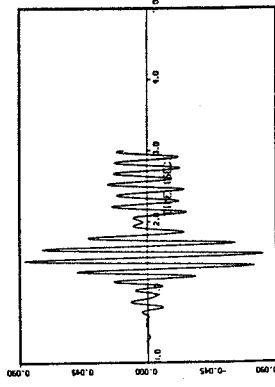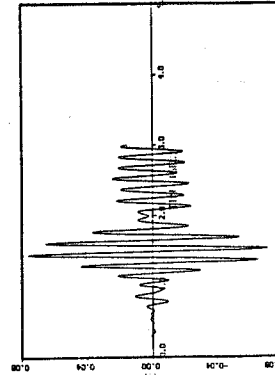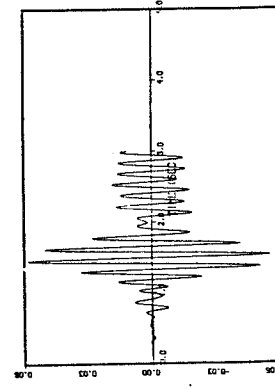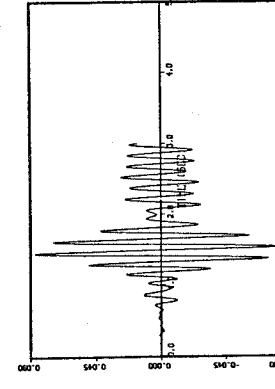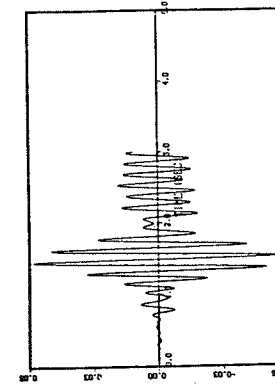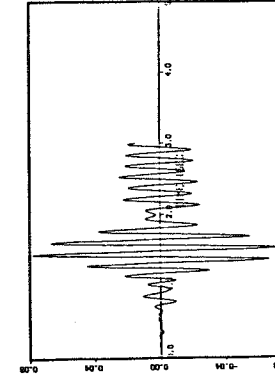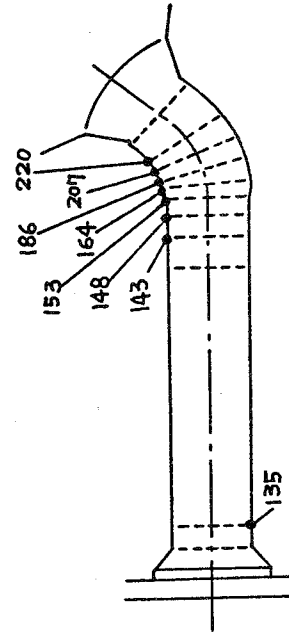
Figure 7.68 Axial Strain at 0.1 MPR by ABAQUS Elbow Model
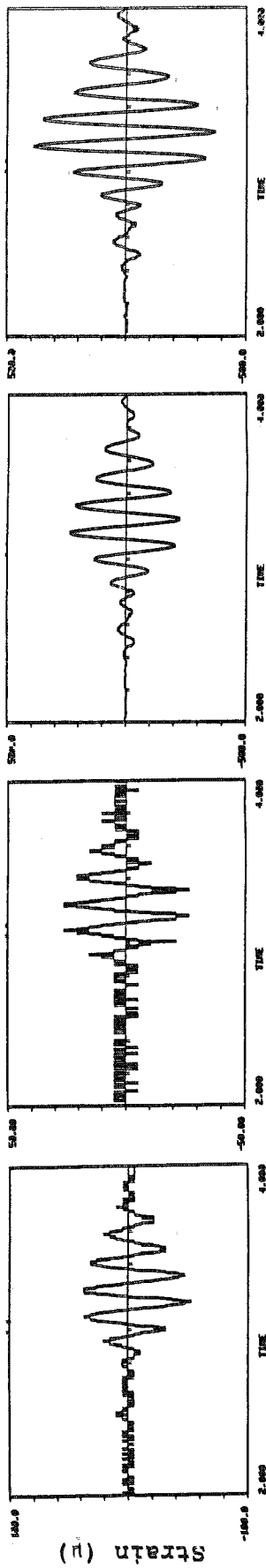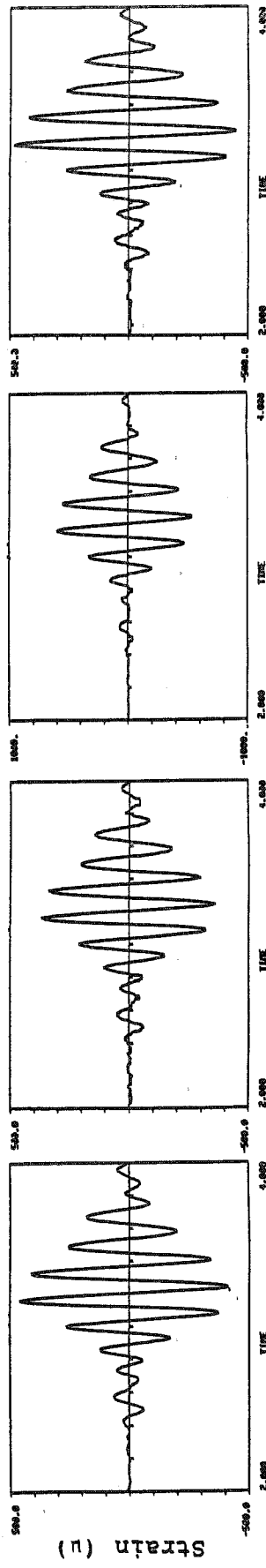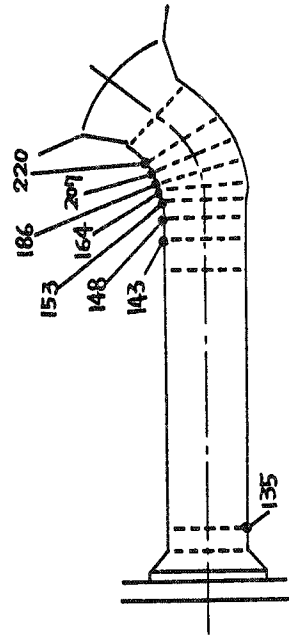
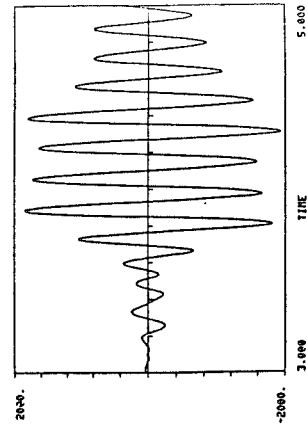Figure 7.69   Test Results for Hoop Strain at 0.1 MPR

7-86
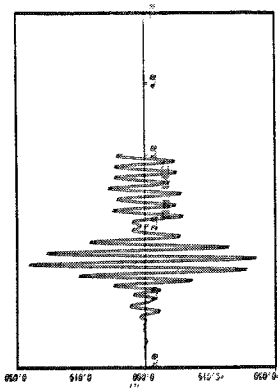
(153Y)
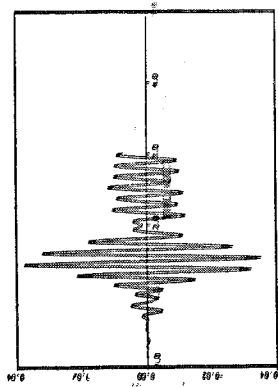
(148Y)

(143Y)

Strain %

(220Y)
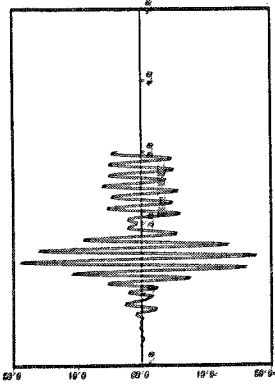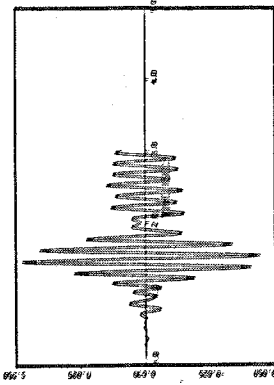
(207Y)
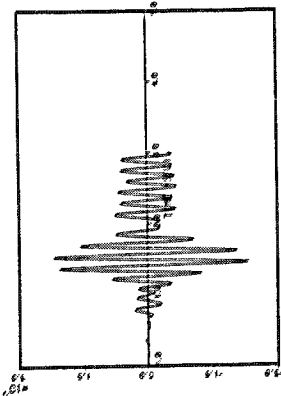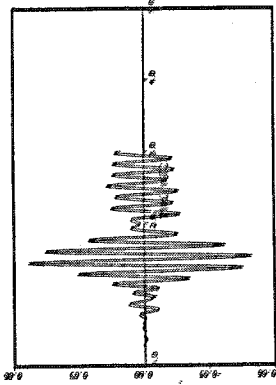
(186Y)
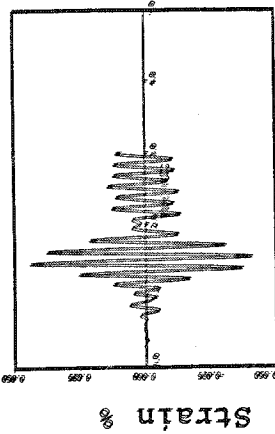
(164Y)
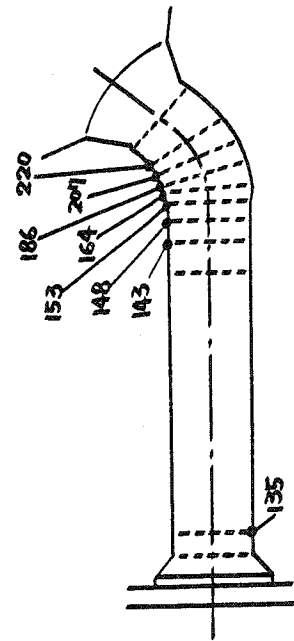
Strain %

Figure 7.70 Hoop Strain at 0.1 MPR by ABAQUS Elbow Model
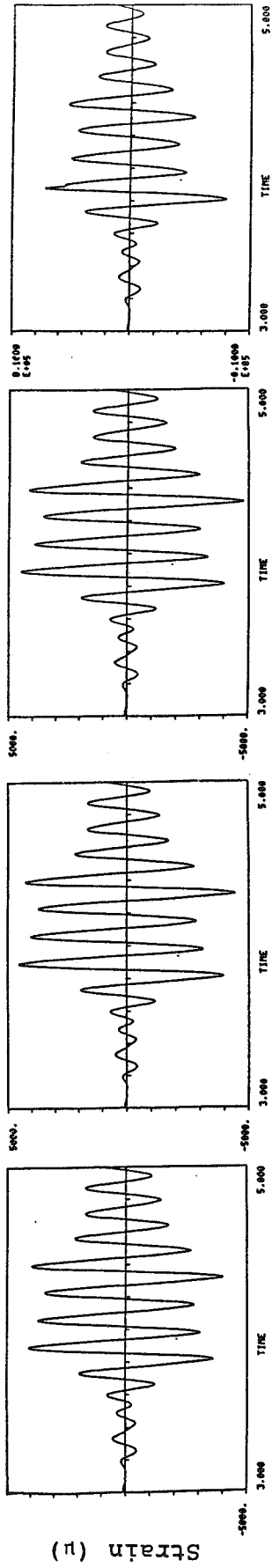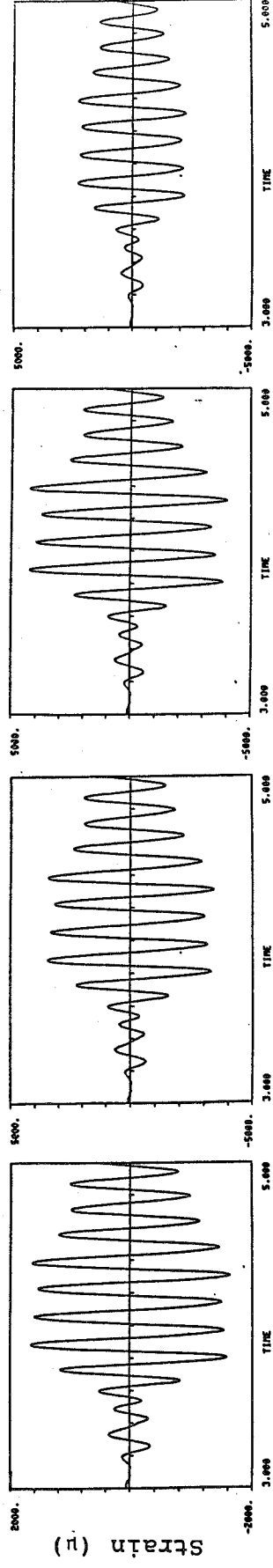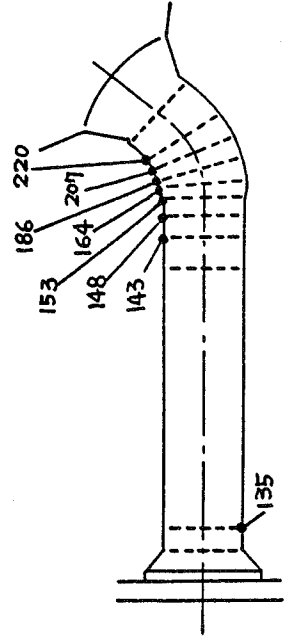
Figure 7.71 Test Results for Axial Strain at 0.4 MPR
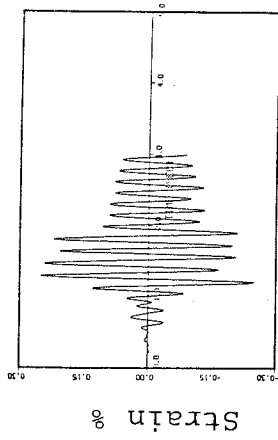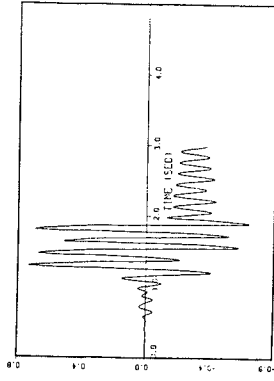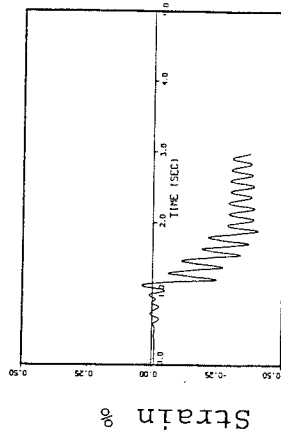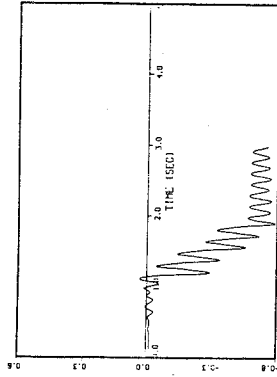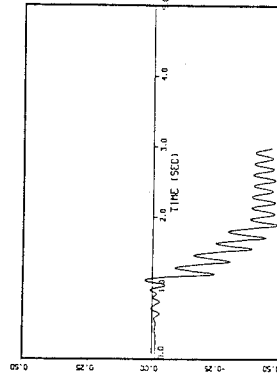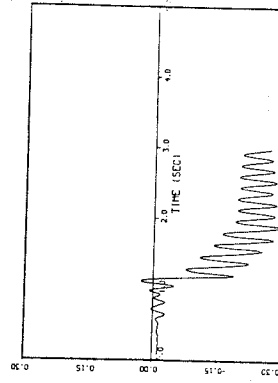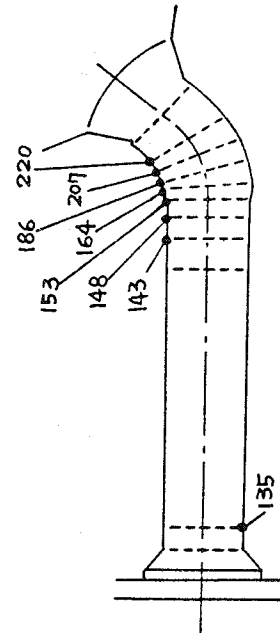
Figure 7.72 Axial Strain at 0.4 MPR by MARC Elbow Model
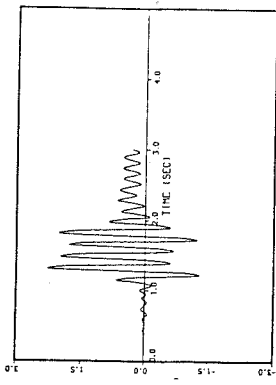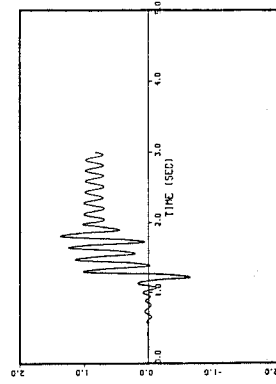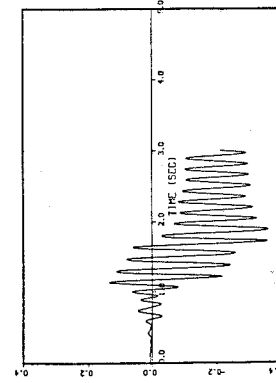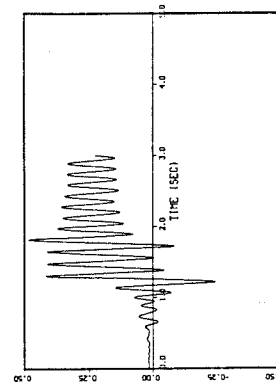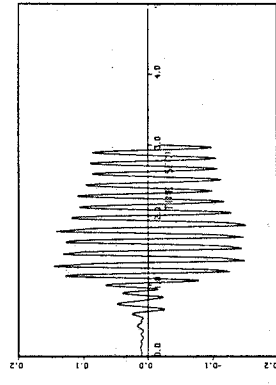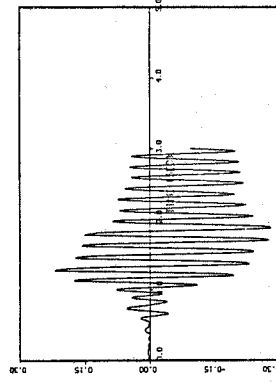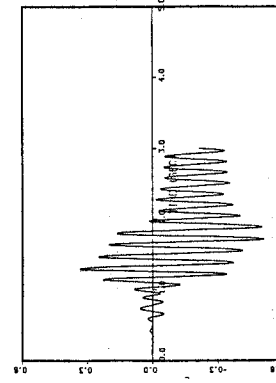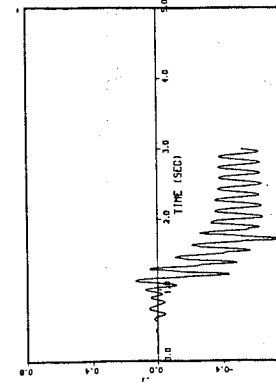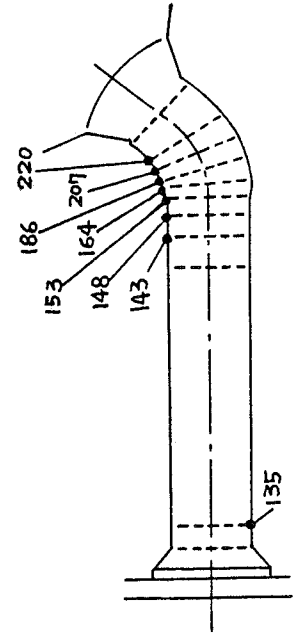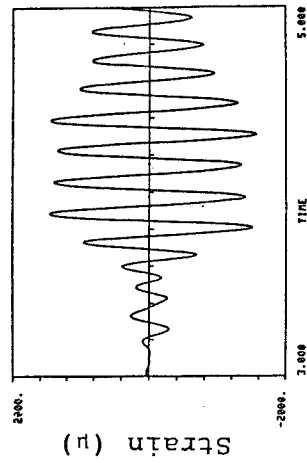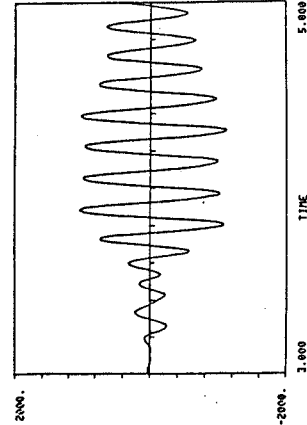
Figure 7.73 Axial Strain at 0.4 MPR by ABAQUS Elbow Model
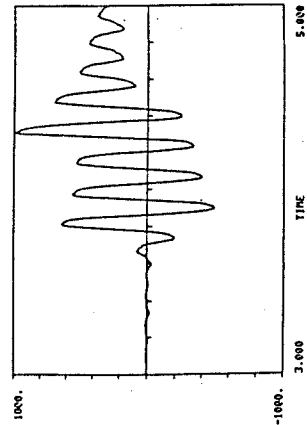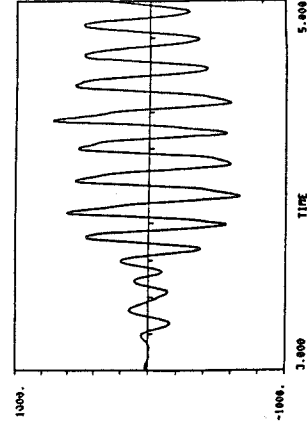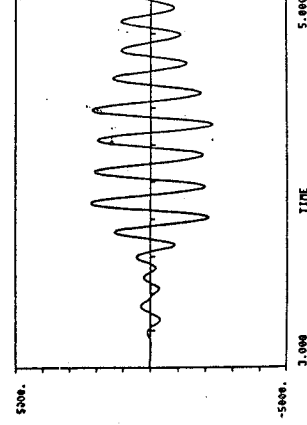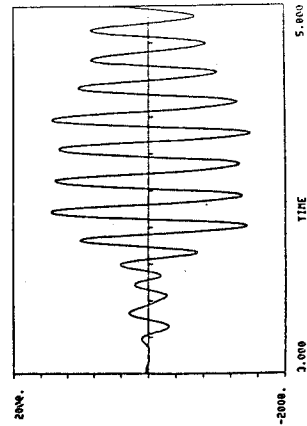
Figure 7.74   Test Results for Hoop Strain at 0.4 MPR
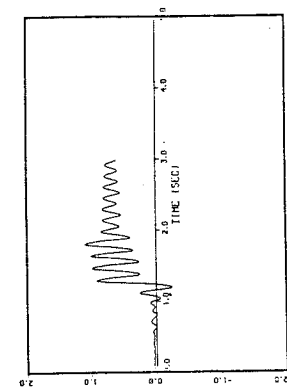
(220Y)

(207Y)
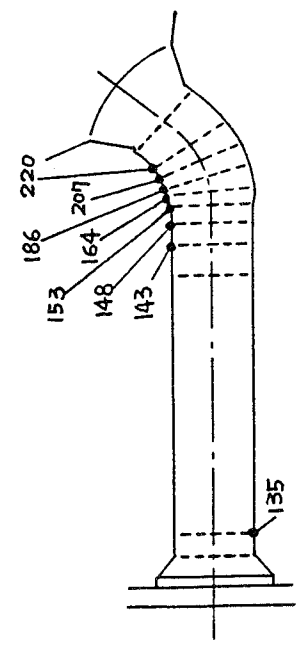
(186Y)

(164Y)

Strain %

Figure 7.75 Hoop Strain at 0.4 MPR by MARC Elbow Model

Figure 7.76 Hoop Strain at 0.4 MPR by ABAQUS Elbow Model

Strain %
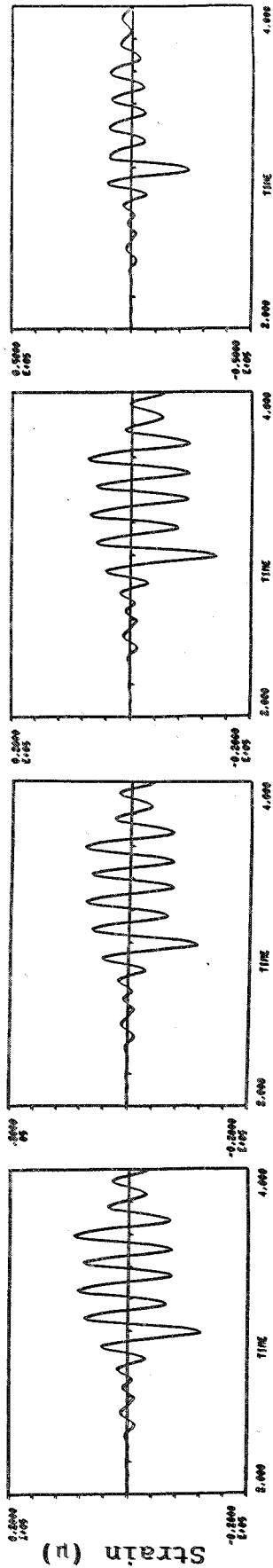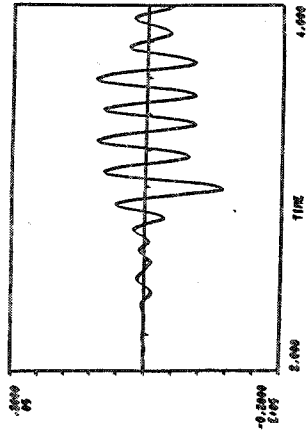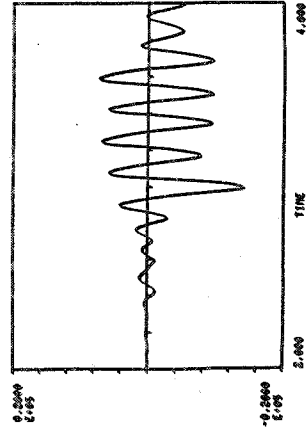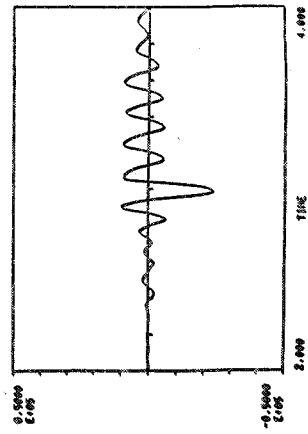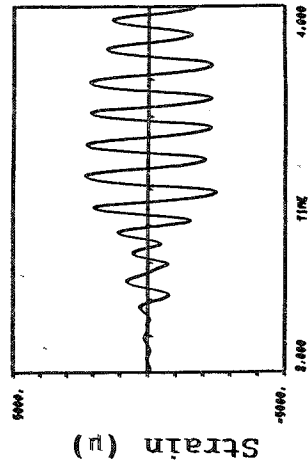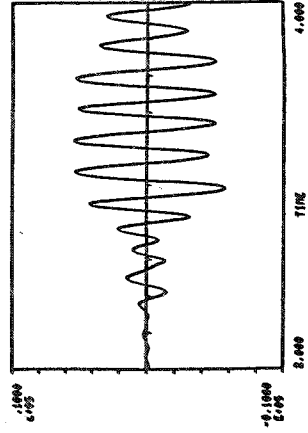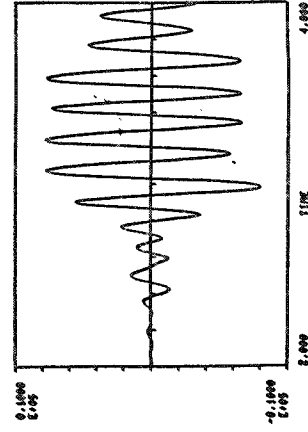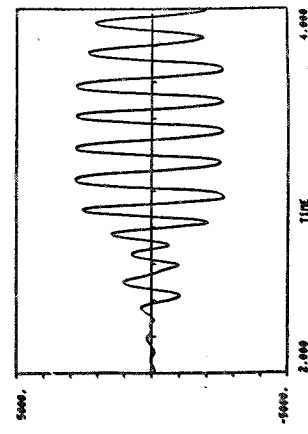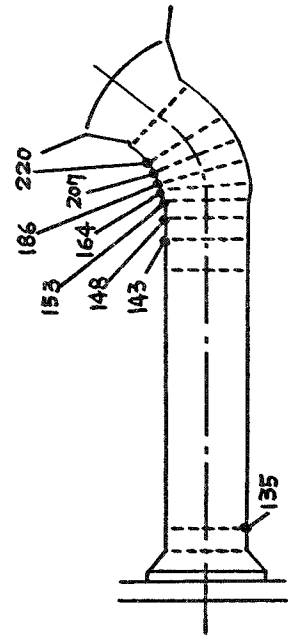
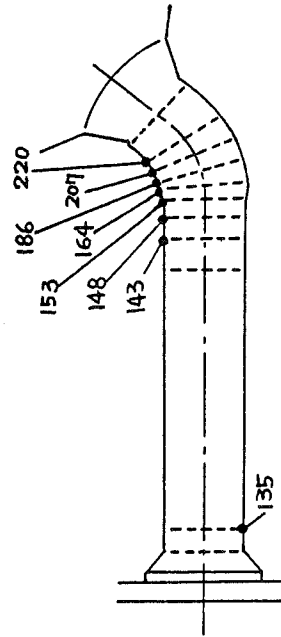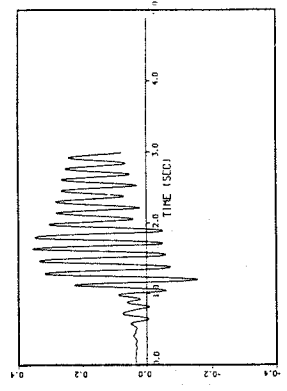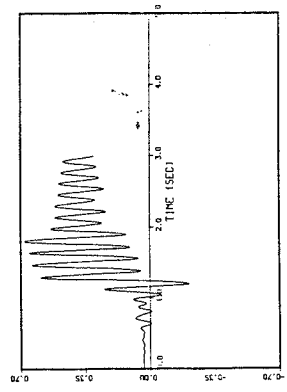Figure 7.77 Test Results for Axial Strain at 1.0 MPR
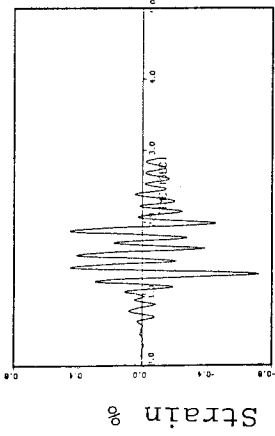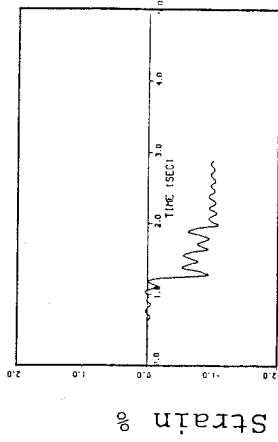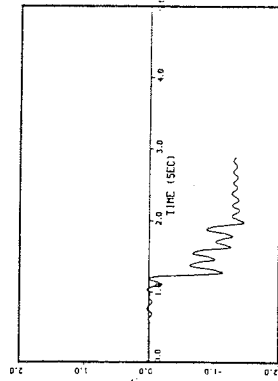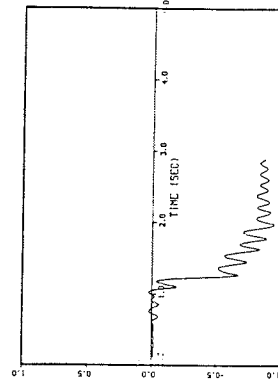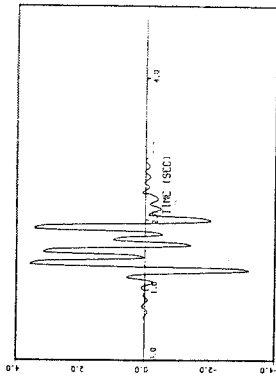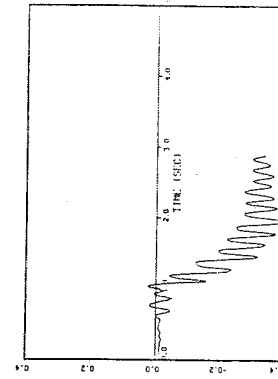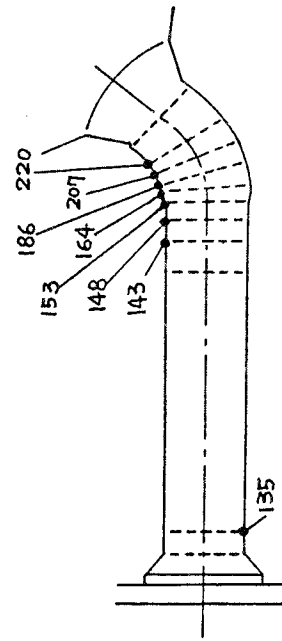
Figure 7.78 Axial Strain at 1.0 MPR by MARC Elbow Model
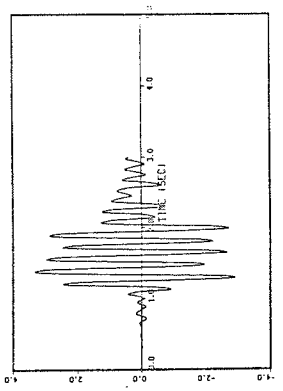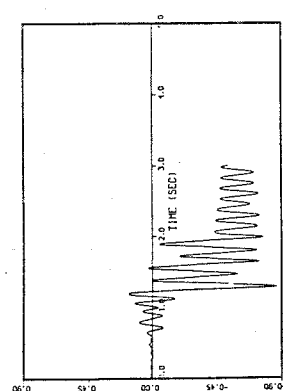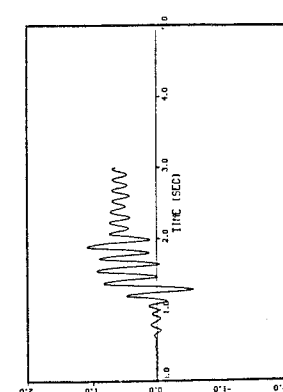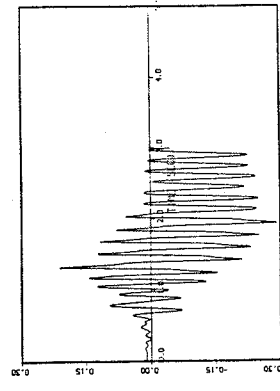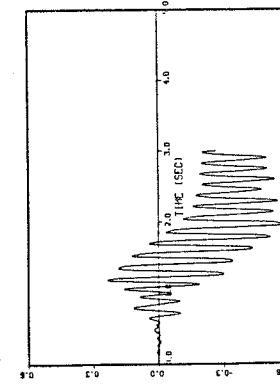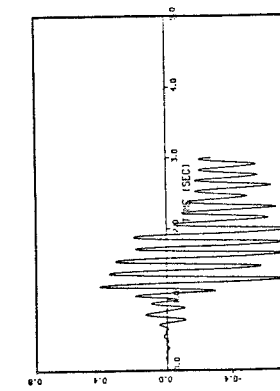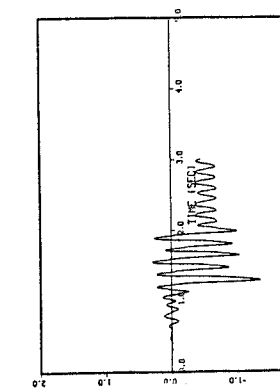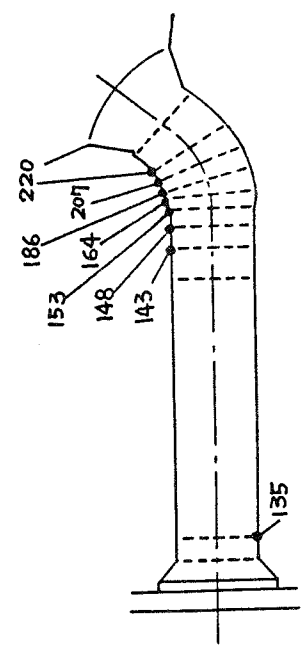
Figure 7.79 Axial Strain at 1.0 MPR by ABAQUS Elbow Model
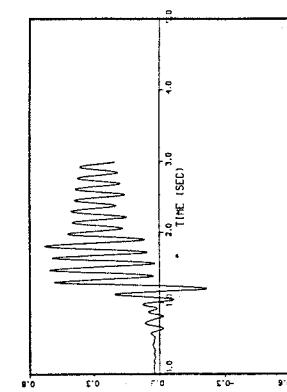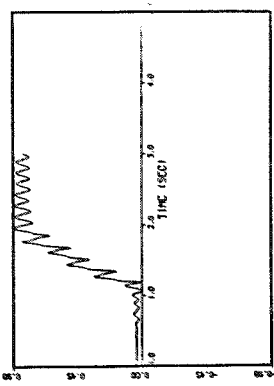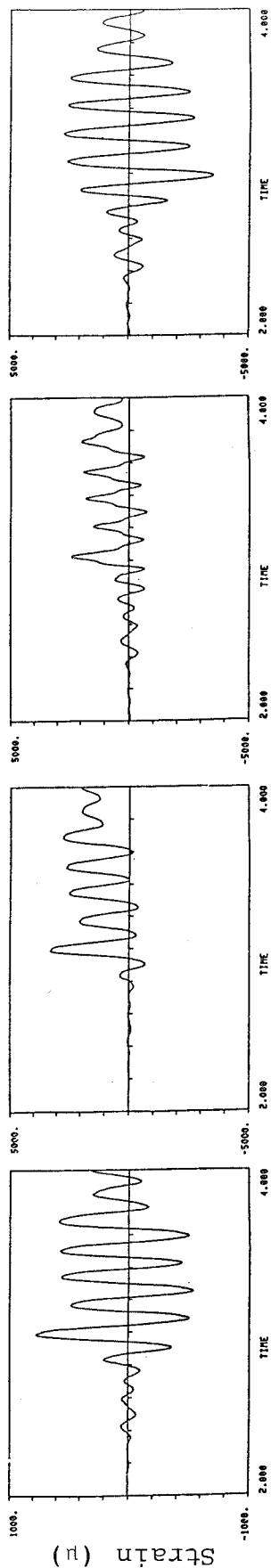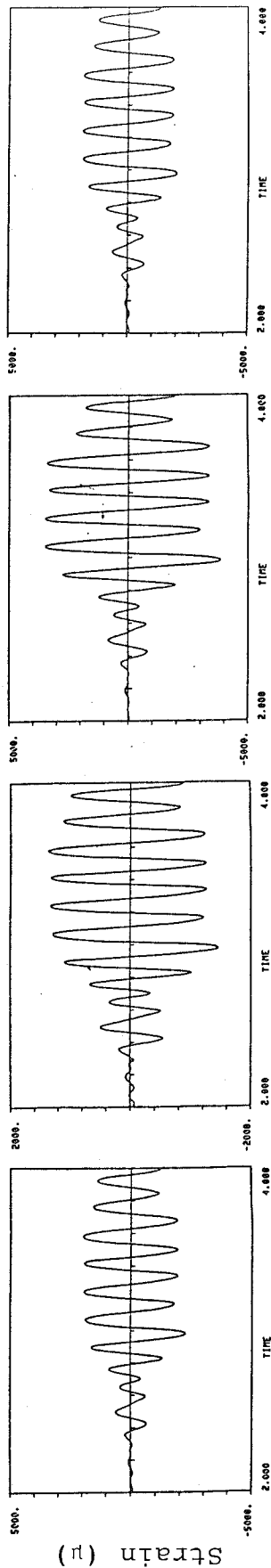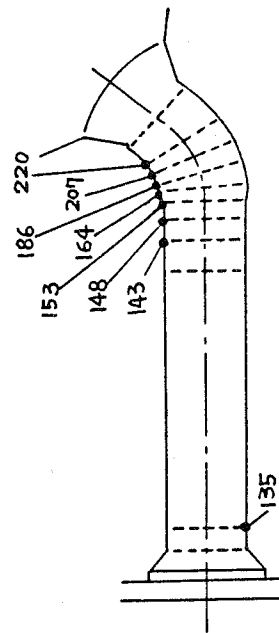
Figure 7.80 Test Results for Hoop Strain at 1.0 MPR
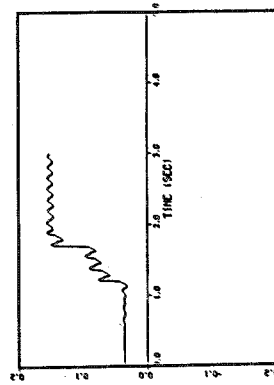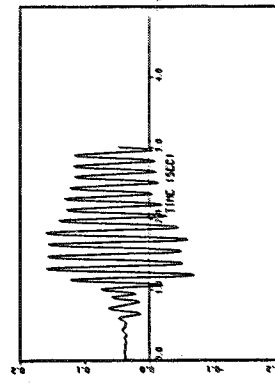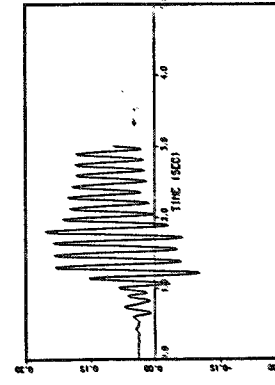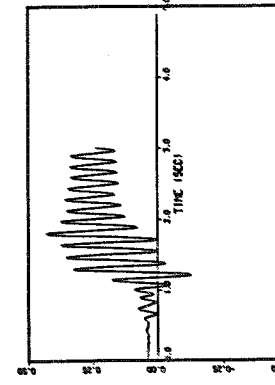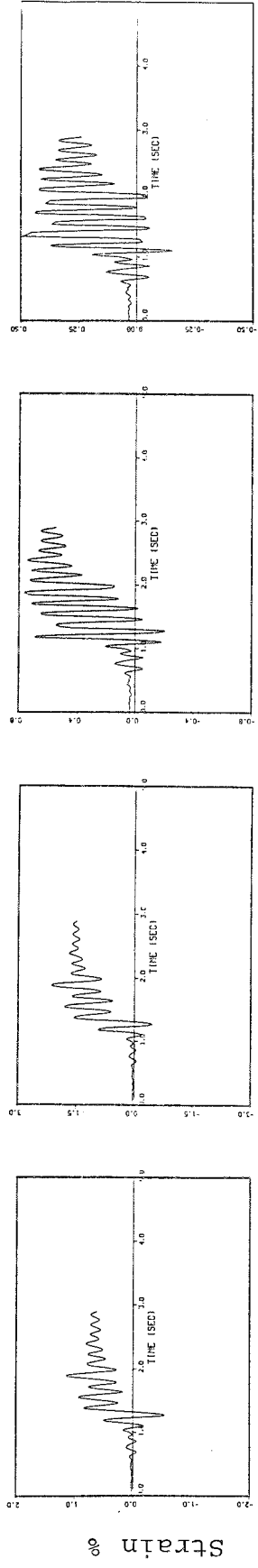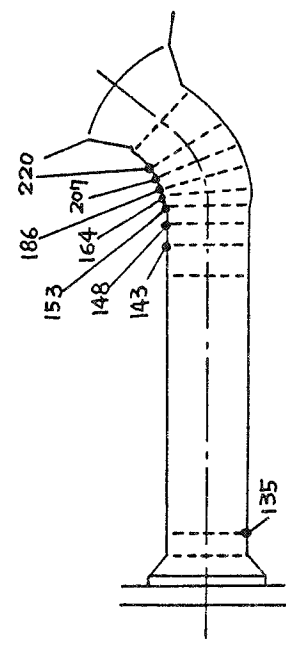
Figure 7.81   Hoop Strain at 1.0 MPR by MARC Elbow Model
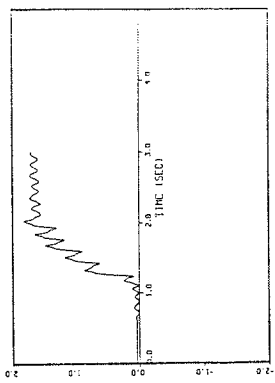
(153Y0)
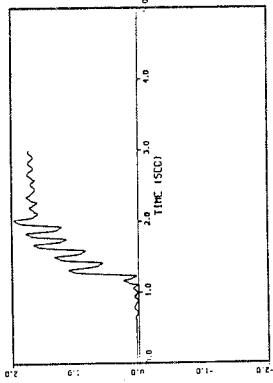
(148Y)
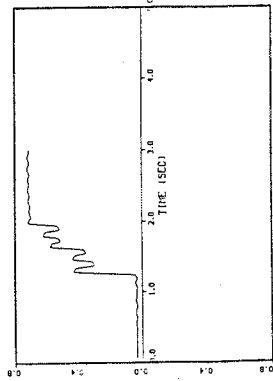
(143Y)
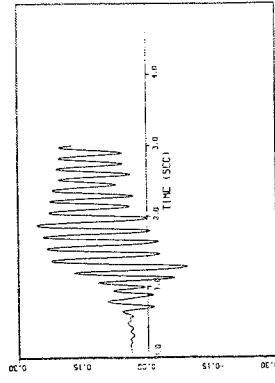
(220Y)
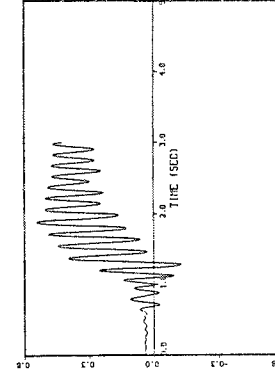
(207Y)
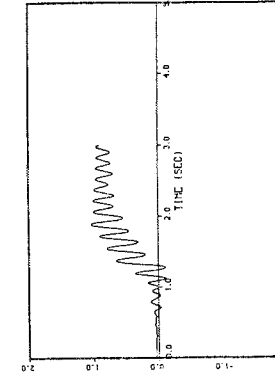
(186Y)
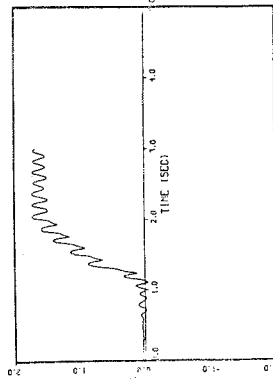
(164Y)

Strain %

Strain %
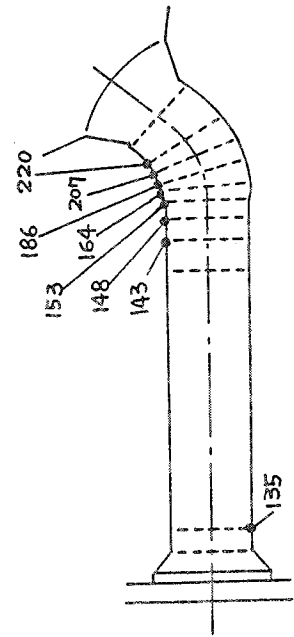
Figure 7.82   Hoop Strain at 1.0 MPR by ABAQUS Elbow Model
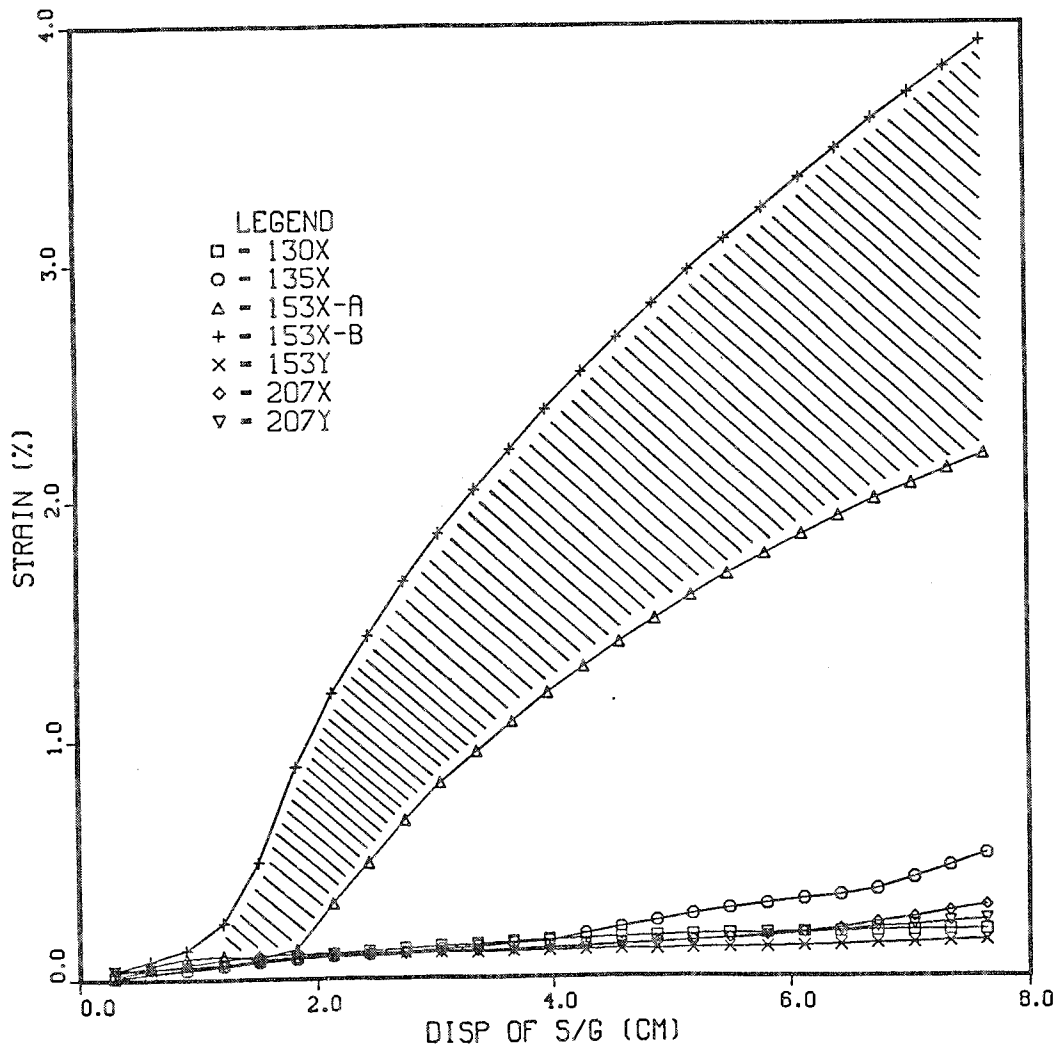
Figure 7.83 Results of Static Analysis (Displacement at Top of S/G vs. Strain in Hot Leg Pipe)

(Top View)

	VALUE
1	-9.99E-04
2	-4.99E-04
3	+4.99E-10
4	+5.00E-04
5	+1.00E-03
6	+1.49E-03
7	+1.99E-03
8	+2.49E-03
9	+2.99E-03
10	+3.49E-03
11	+3.99E-03
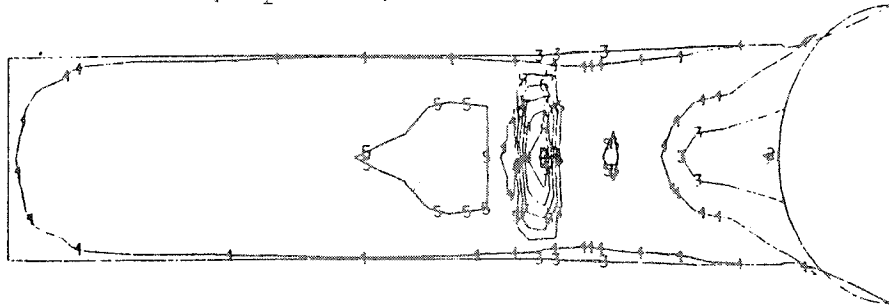
(Bottom View)

	VALUE
1	-9.99E-04
2	-7.99E-04
3	-5.99E-04
4	-3.99E-04
5	-1.99E-04
6	+1.99E-10
7	+2.00E-04
8	+4.00E-04
9	+5.99E-04
10	+7.99E-04
11	+9.99E-04
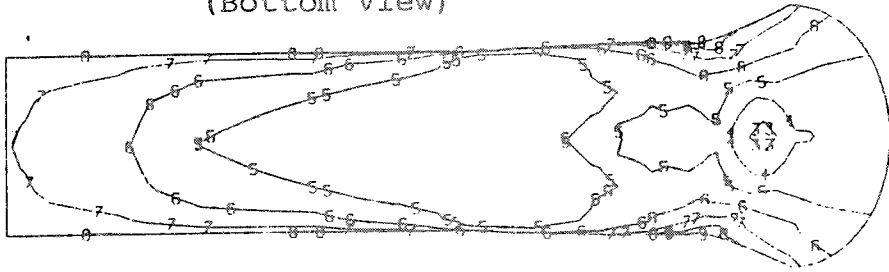
(a) Axial Strain

(Top View)

	VALUE
1	-9.99E-04
2	-7.99E-04
3	-5.99E-04
4	-3.99E-04
5	-1.99E-04
6	+1.99E-10
7	+2.00E-04
8	+4.00E-04
9	+5.99E-04
10	+7.99E-04
11	+9.99E-04
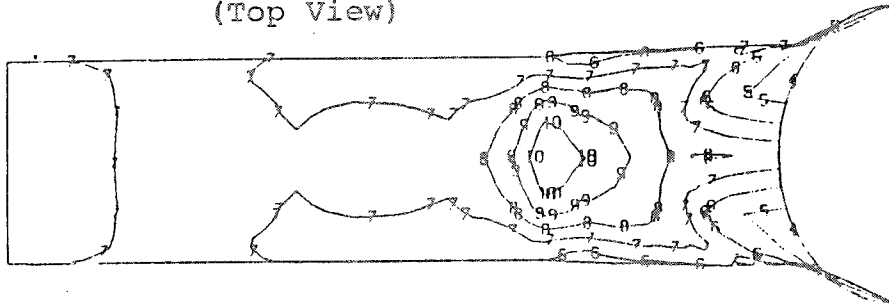
(Bottom View)

	VALUE
1	-9.99E-05
2	-9.99E-06
3	+8.00E-05
4	+1.69E-04
5	+2.59E-04
6	+3.49E-04
7	+4.39E-04
8	+5.29E-04
9	+6.19E-04
10	+7.09E-04
11	+7.99E-04
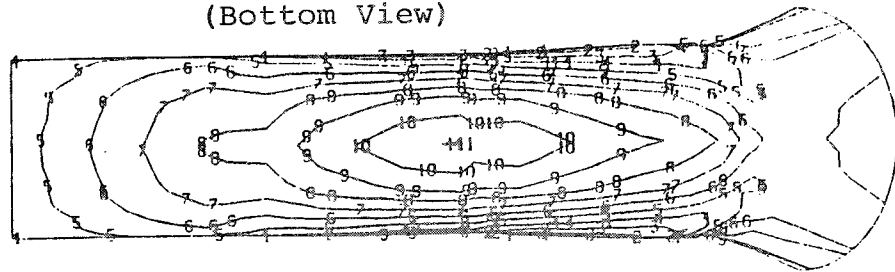
(b) Hoop Strain

Figure 7.84   Contour Plots for Strain of Hot Leg Pipe
from Static Analysis (at Ux = 1.53 cm)

7-101

(Top View)

VALUE	
1	-9.99E-03
2	-5.99E-03
3	-1.99E-03
4	+2.00E-03
5	+6.00E-03
6	+1.00E-02
7	+1.40E-02
8	+1.80E-02
9	+2.20E-02
10	+2.60E-02
11	+3.00E-02

(Bottom View)

VALUE	
1	-4.99E-03
2	-3.99E-03
3	-2.99E-03
4	-1.99E-03
5	-9.99E-04
6	+9.99E-10
7	+1.00E-03
8	+2.00E-03
9	+2.99E-03
10	+3.99E-03
11	+4.99E-03

(a) Axial Strain

(Top View)

VALUE	
1	-3.99E-03
2	-3.19E-03
3	-2.39E-03
4	-1.59E-03
5	-7.99E-04
6	+7.99E-10
7	+8.00E-04
8	+1.60E-03
9	+2.39E-03
10	+3.19E-03
11	+3.99E-03

(Bottom View)

VALUE	
1	-1.99E-03
2	-1.39E-03
3	-7.99E-04
4	-1.99E-04
5	+4.00E-04
6	+1.00E-03
7	+1.59E-03
8	+2.19E-03
9	+2.79E-03
10	+3.39E-03
11	+3.99E-03

(b) Hoop Strain

Figure 7.85   Contour Plots for Strain of Hot Leg Pipe
from Static Analysis (at Ux = 7.64 cm)

8.0 CONCLUSIONS

The previous sections have discussed the details of the high level vibration test and analysis program which was carried out jointly between the United States and Japan. Conclusions have already been stated as the material has been reviewed in the individual sections. This section provides a summary of the more important conclusions, together with a general overview of the accomplishments of the entire program.

8.1 TEST RESULTS

8.1.1 Characterization of Dynamic Response

Forty five tests were performed during the test program, including low-level random and sinusoidal tests to identify the dynamic characteristics of the test model. The natural frequency of the test model was 6.4 Hz in the elastic range and decreased by approximately 10% at the maximum excitation level. Based on the test results, the equivalent viscous damping ratio was measured to be 0.9% in the elastic range. The damping increased at high excitation levels and was estimated to be between 6 and 10% in the intermediate plastic strain range and 10 to 15% at the high level strain. A maximum axial strain of 2.3% was measured on the outer surface at the top of the hot leg pipe in the vicinity of the tapered transition joint with the hot leg elbow.

From the test results, it was confirmed that the development of the input wave, the table control techniques and the test procedure were adequate to achieve the goals of the HLVT. After Run 10, bulging was observed in the hot leg pipe approximately one pipe diameter from the transition joint. Crack initiation was detected after Run 11 in the vicinity of the strain gage where the maximum strain was measured. Crack growth was monitored in subsequent excitation runs. The final maximum crack depth was estimated to be 94% of the wall thickness and the crack extended approximately 110 degrees around the outside of the pipe.

8.1.2 Post-Test Examinations

Post-test examinations were conducted to provide data for post-test analyses and evaluation of failure modes. Measurements of bulging and crack growth were made and material properties were investigated. Dimensional measurements showed that the diameter and circumference increased by about 3 mm and 10 mm, respectively, at the cross section of the bulged region closest to the hot leg elbow. Slight bulging in the hot leg pipe near the reactor vessel end was also detected.

In addition to the cracks on the outer surface, visual examinations of the hot leg pipe showed that four small circumferential cracks had also occurred on the inner surface. They were approximately 3 to 6 mm long and 1 to 3 mm in depth.

The mechanical property tests showed that the hardness of the material in the region of the crack initiation and bulging was higher than the hardness of the material in the virgin condition. This region was subjected to many cycles of high strain during the HLVT. The low cycle fatigue test results and the fatigue crack growth behavior were in agreement with available data for Japanese austenitic stainless steels.

Metallurgical examination of the fracture surface revealed a series of beach marks. Based on Scanning Electron Microscope (SEM) examinations, it appears that locations where striations clearly dominated were limited to Run 11 and 12 and the beginning of Run 13. The crack propagated by fatigue during these runs. The fracture surface also shows increasing amounts of dimple rupture starting in Run 11 and increasing to the point that evidence of striations has disappeared by the end of Run 13. The crack propagation in most of Run 13 and all of Run 14' was due to dimple rupture. During these last two runs the rapid crack propagation appears to be due to ductile tearing on each of the load cycles.

8.2 ANALYSIS RESULTS

8.2.1 Pre-Test Dynamic Analysis

Prior to the testing, prediction analyses were performed to ensure the success of the test and optimize the input table motion. Linear and elastic-plastic responses were analyzed by using various finite element analysis programs and simplified analysis techniques. Good agreement was obtained regarding the vibration frequency in the excitation direction. However, the frequency in the direction orthogonal to table motion was overestimated by 20 to 30%.

The overall displacement and acceleration responses of the steam generator in the direction of excitation are in good agreement with the test results at all levels of excitation. The analytical results for axial strain were higher at some points and lower at others when compared with the test measurements. The only qualitative comparisons that appeared to be generally true are that the analytically determined axial strains at low excitation levels underestimated the actual response. In addition, the calculated hoop strains were much higher than the measured values. However, at the maximum excitation level, the maximum axial strain was computed to be between 3 and 4 percent, depending on the relationship between the natural frequency and the frequency of the peak of the response spectra. This compares with the test measurement of 2.3%. The analysis showed that the location of the maximum

strain was at the junction between the elbow and the hot leg pipe and this is where the actual crack was observed to start. Although the actual test run sequence used during the test differed somewhat from the original plan, cracking did occur in the test model at approximately the same time as predicted by the pre-test analysis. On the other hand, the large hoop strain ratchetting that was included in the calculations to predict the ratchet/fatigue life did not occur.

8.2.2 Post-Test Dynamic Analysis

In addition to the pre-test analysis models, post-test analysis finite element models of the problem were developed. The results were compared with the test measurements.

It is noted that the post-test analytical results were closer to the test results than the pre-test analysis, but the pre-test general conclusions are still valid. The computed natural frequency range for all methods and all models is less than 7% for the predominant mode. The analytically determined displacement and acceleration at the top of the steam generator compare very well with the measured values. This holds at all levels of excitation and for all methods and all models. The time histories of these dynamic responses from test measurements and from the analytical results are strikingly similar.

The snubber forces were well predicted by analyses at all excitation levels, however, the shear force at the steam generator pin-connection was underestimated by as much as 50%.

The analytical results of the axial and hoop strains were generally underestimated at 10% of the maximum excitation level. However, for some models there was a good comparison between the test and analysis results. At higher excitations, the hoop strains determined analytically were very much higher than the test measurements. "Ratchet-like" effects appear extensively in the analytical results but did not show up to any great extent in the tests. These analysis results indicate that the material properties, especially the hardening due to previous cyclic loadings, have a significant impact on the calculated strain responses in shell-type elements. Improvements are clearly necessary in nonlinear computer codes since the currently available commercial codes are not capable of reproducing the complex strain hardening behavior under strong seismic motions.

In general, the pin forces and the strain magnitudes that were calculated were significantly different from the measured values at the higher levels of excitation. At some points, they were higher and at others they were lower. No one method or model was consistently better for all measured items and at all excitation levels.

In summary, it appears that finite element codes, as is, cannot predict well inelastic strains at or near failure locations. However, further blind post-test predictions utilizing various simplified and detailed analysis techniques are being performed to study this matter further. Based on the analysis results to date, the HLVT program has identified some areas where further studies and development are needed to improve nonlinear computer codes. These include the use of strain hardening models that can follow the cycle to cycle characteristics of a particular material. Furthermore, numerical instability problems are easily encountered in these lengthy calculations and ways to eliminate or reduce this effect should also be explored. With such improvements, nonlinear computer codes could be better utilized to assess the margin of safety in structures and components.

8.3 FAILURE MODE ASSESSMENT

8.3.1 Fatigue Damage

The fatigue damage factor after Run 14' exceeds 1.0 when the fatigue strength data obtained from the post-test examinations are employed. This factor agrees fairly well with the actual condition of failure of the test model. Although it is well known that the permanent strain due to ratchetting affects the failure mechanism, the measured permanent strain at the cracked portion (2-3%, after Run 11) is significantly smaller than the elongation of the material (39-47.6%). Therefore, it is considered that the dominant cause of the failure is not ratchetting but low cycle fatigue. However, since some ratchetting did occur during the test it would be useful to perform further studies to understand the occurrence of mixed failure modes involving ratchetting and fatigue. Such studies could assist in possible future design code revisions concerning this subject.

8.3.2 Crack Propagation Mechanism

The cracks were initiated and propagated by fatigue. When the crack was small, it propagated slowly and striations were observed. As the crack grew, it propagated faster and deformation slips and dimples developed. For the region where striations appeared, the applied load cycles were roughly calculated from the striation spacings. In the region where striations were not observed, applied load cycles were roughly estimated from the intervals of the fracture surface characteristics. The cracks were subjected to a very high, plastic range cyclic stress. Furthermore, amplitudes were varied. These conditions made it difficult to estimate the number of applied load cycles from the fracture surface examination. Under these limited conditions, a total number of applied cycles was roughly estimated as 500-700 cycles. Since the number of actual applied load cycles was about 800, the estimated value fell within a reasonable range.

8-4

8.4 EVALUATION OF SAFETY MARGIN

The safety margin of the HLVT model piping was evaluated by comparing the maximum base input loading for the HLVT test with the allowable base input loading for Class I piping based on the current standard design analysis practice.

The maximum base input loading, related to the allowable stress limit for the design basis earthquake, was found to be 240 gals, while the maximum base input acceleration for the HLVT test was 1895 gals.

Comparing these base input levels, it is estimated that the maximum test loading level is approximately eight times greater than the current code allowable design loading. Therefore, the tests demonstrated that there is a safety margin of at least a factor of eight for the HLVT model piping.

8.5 GENERAL SUMMARY

The objective of the HLVT was to use the NUPEC vibration table to drive a large diameter nuclear piping structure to a condition of substantial strain with an earthquake-like excitation. The test results were to be compared with state-of-the-art analyses. These program objectives were attained. The specified high level vibration table motion was satisfactorily reproduced and large plastic strains and cracks were developed in the piping up to the point of imminent failure.

The program has enhanced the understanding of the behavior of large-size piping systems under severe dynamic loading. It provided extensive test data to evaluate elastic and inelastic dynamic analysis techniques, as well as data to assess the conservatisms in current criteria and to investigate improved criteria which could be used in the future for seismic design. In addition, unique test data were obtained to understand fatigue crack initiation and crack growth under seismic loading conditions. The program showed that there is a significant seismic margin in nuclear power plant piping.

Finally, the HLVT program demonstrated the ability to successfully plan and execute a major cooperative seismic testing program between the United States and Japan.

9.0 REFERENCES

1. Jaquay, K. and Larson, J. (1988). Best Bet Pre-Test Failure Prediction for HLVT Tests. Letter Report to H.T. Tang of EPRI dated April 5, 1988.

2. Severud, L. and Weiner, E. (1987). Pre-Test Analysis of HLVT Pipe System for High Level Vibration Response and Failure. HEDL Report EA/BNL-1.

3. Severud, L. et al (1988). High Level Seismic Response and Failure Prediction Methods for Piping. NUREG/CR-5023, pp. 56-57.

Appendix A

Photographs of Test Model
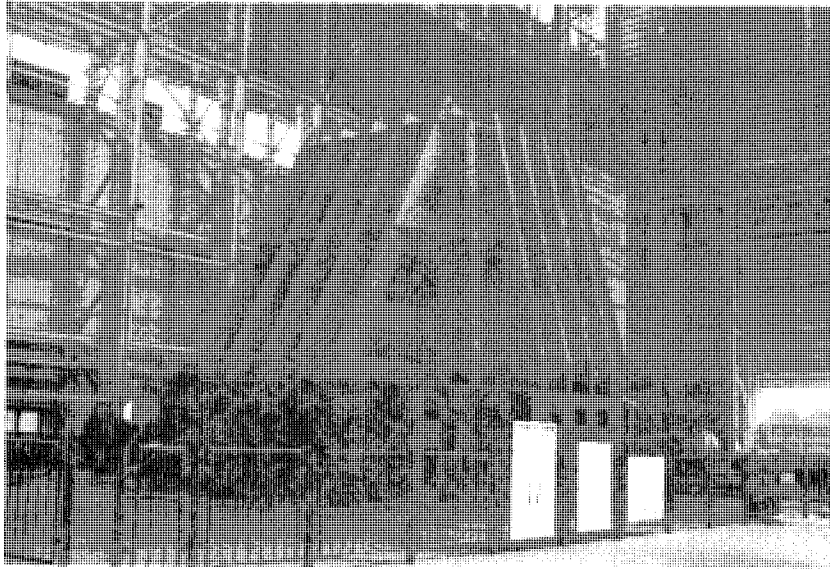
Figure A.1   Test Model on Shaking Table
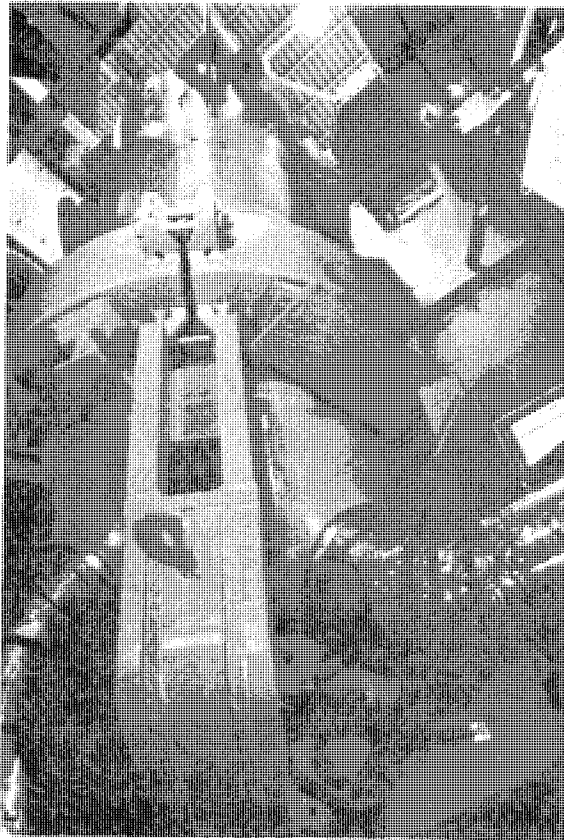
Figure A.2   Steam Generator

A-2
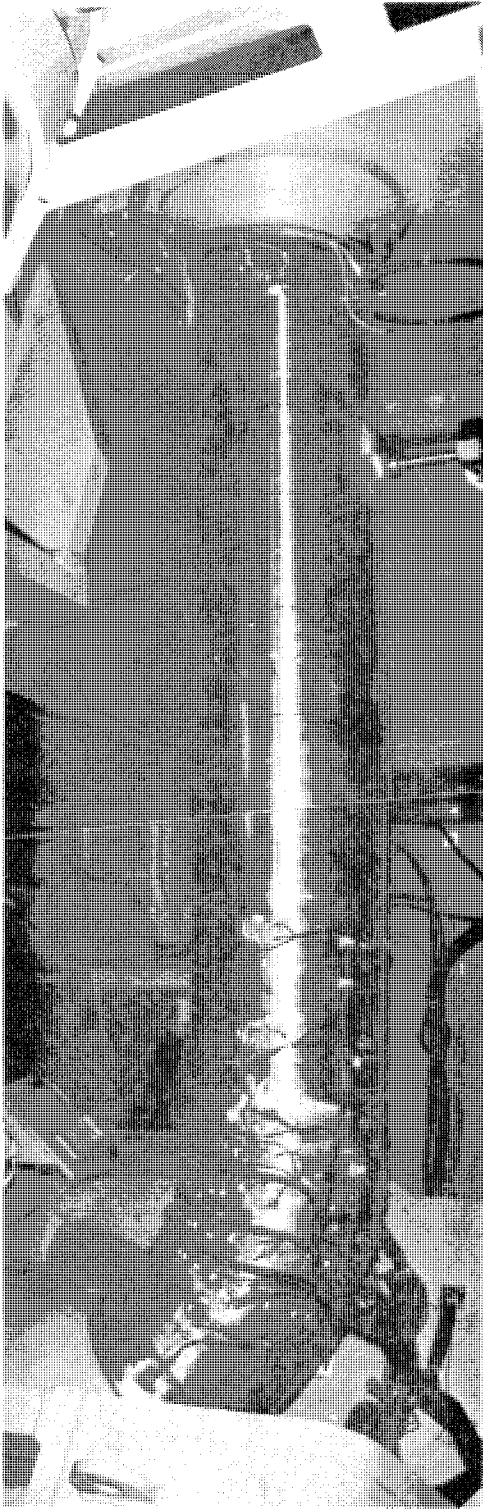
Figure A.3 Hot Leg Piping
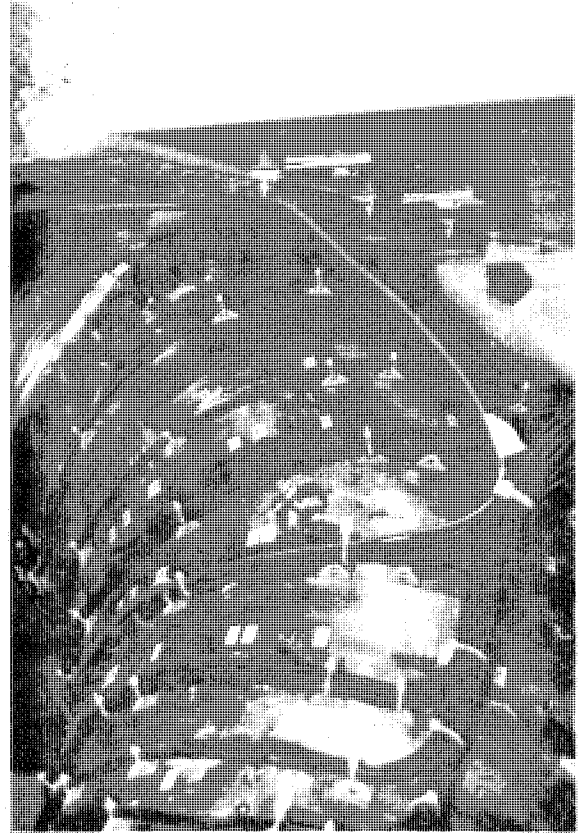
Figure A.4 Hot Leg Elbow
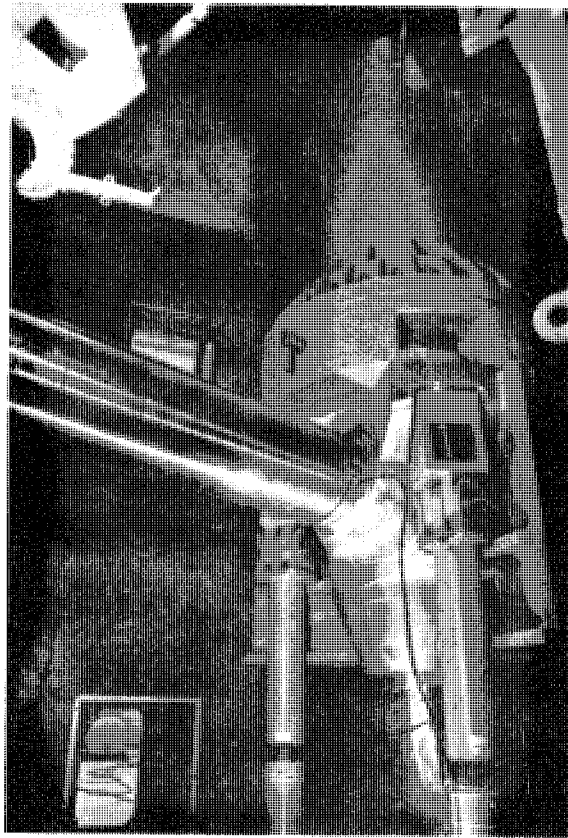
Figure A.5 Reactor Coolant Pump
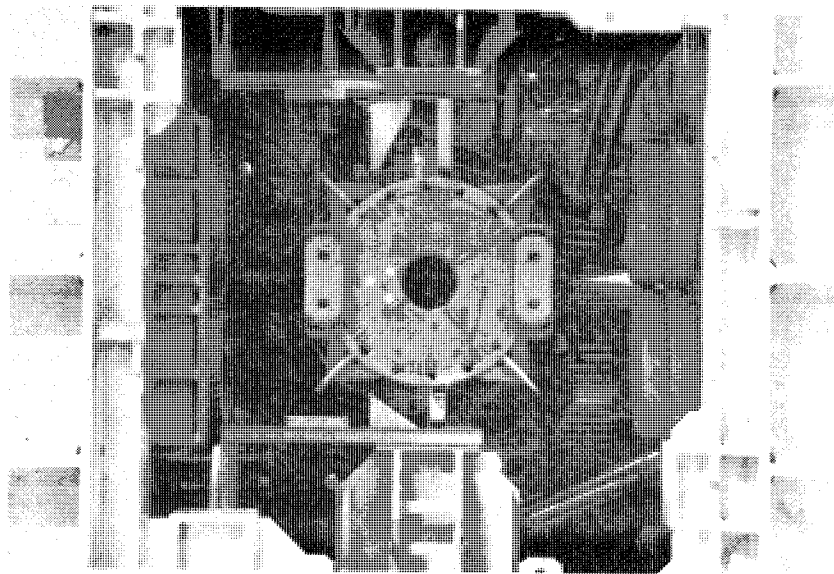
Figure A.6 Top View of Steam Generator
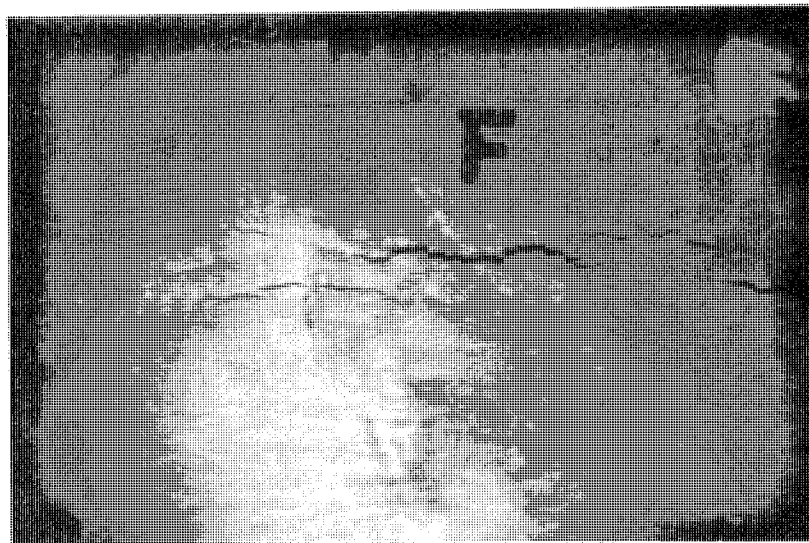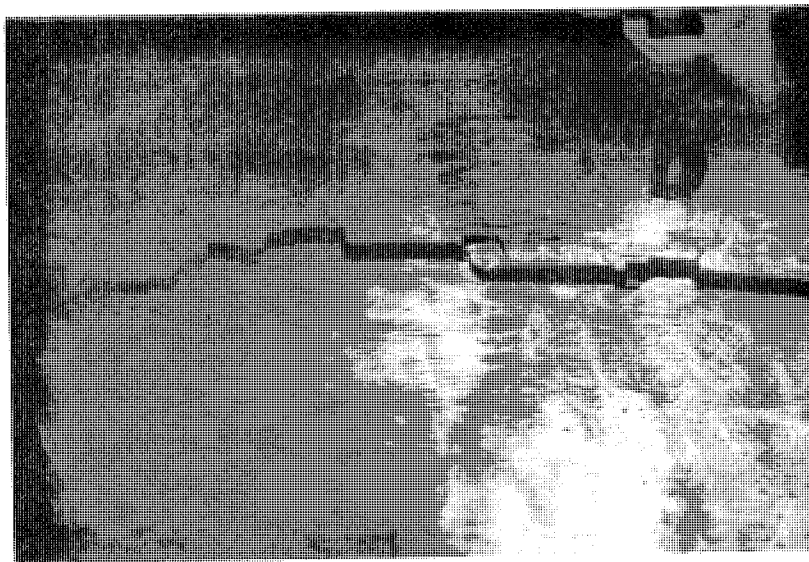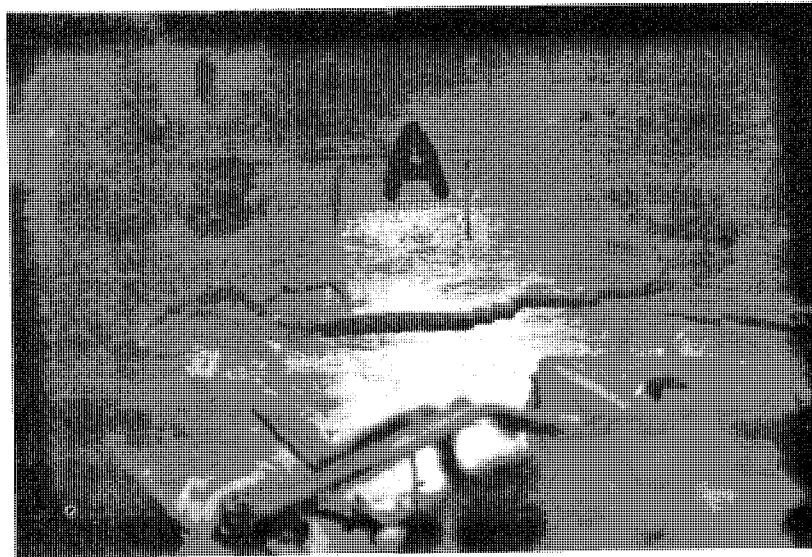
Figure A.7   Crack Opening (After Run 14':   Final Stage)

A-5

Appendix B

Specification of Transducers

Table B.1 Specification of Transducers

item	manufuctrure/type	specifications	note
Accelerometer	ENDEVCO /7751-500	type : piezoelectric with integrated amprifier range : MAX. 10g freq. renge : 0.2~500Hz	° prepared in proving test
Strain gage	KYOWA /KFC-5-C1 -16L500-3	type : foil type range : (for elastic strain) gage length : 5mm	° for estimated max. strain <0.2%
	KYOWA /KLM-6-A9	type : foil type range : max. 20% strain gage length : 6mm	° for estimated max. strain >0.2%
$\left(\begin{array}{c}\text{Back-up for}\\\text{strain gage}\end{array}\right)$	Displacement transducer ("clip gage")	type :strain type measuring range : ±10% material : stainless steel mounting : spot welding	
displacement sensor	AEC DPU-50	type : eddy current range : max. 25mm$_{p-p}$ freq. range: DC~5KHz	° prepared in proving test
	GENISCO PT-10 PT-15	type : wire type renge : max. 254mm(10")$_{p-p}$ or 381mm (15") $_{p-p}$ freq. range : DC~more than 30Hz	
Pressure transducer	KYOWA PAV-200KES	type : strain type runge: max. 200kgf/cm^2	° prepared in proving test

Appendix C

Details of Measuring Points

Table C.1 (1) (1/2) Measuring Point

component	Measuring item	Measurig point	Notation	Number of points	Directions	Measuring channels
Main coolant piping	Accele-ration	Hot leg	H 1	1	3	3
		Cross over leg	X 2	1	3	3
		Cold leg	C 2	1	3	3
	Strain	R/V nozzle	HRIA	2	2	4
		Hot leg	HR1	4	2	8
		↑	HR3C	4	2,3	9
		↑	HR3B	4	2,3	9
		↑	HR3	4	2,3	9
		↑	HR3A	4	2,3	13
		SG inlet elbow	HR4A	14	1,2,3	25(4)
		↑	HR4C	14	1,2,3	25(4)
		↑	HR4	14	1,2,3	25(4)
		↑	HT4B	4	2	8
		SG inlet nozzle	HR5	4	2	8
		SG outlet nozzle	XR2A	8	1,2	12
		SG outlet elbow	XR2B	8	2	16
		Cross over leg	XR3	4	3	12
		RCP inlet elbow	XR9	4	1	4
		Cold leg	CR1	4	1	4
		↑	CR3	4	2	8
	Dis-placement	Cross over leg	XD1	1	2	2
		Hot-leg and SG	HD1A	1	1	1
Steam Generator	Accele-ration	Top	S1X1	1	1	3
			S1X2	1	1	
			S1Y	1	1	
		Channel head	S5X	1	1	3
			S5Y	1	1	
			S1Y	1	1	
	Dis-placement	Top	SD9A,9B	2	1	3
			SD10	1	1 .	
		Channel head	SD11-13	3	1	3
	Strain	Inlet nozzle	SR1A	1	2	2
		Pad	SR2A-5A	4	2	8
		Pin bracket	SR6A-8A	1	3	3
		Frange	SR9A	1	2	2
Coolant pump	Accele-ration		R2X1	1	1	2
			R2Y	1	1	
		Bottom	R4X	1	1	3
			R4Y	1	1	
			R4Z	1	1	
	Dis-placement	Top	RD1	1	1	2
			RD2	1	1	
		Bottom	RD3	1	1	3
			RD4	1	1	
			RD5	1	1	

( ) : back - up

Table C.1 (2) (2/2) Measuring Point

Component	Measuring item	Measurig point	Notation	Number of points	Directions	Measuring channels
RCP	Load	Sunabber	RR1, RR2	2	1	2
		Tie rod	RR3	1	1	1
		Support column	RR4-6	3	1	3
Support frame	Acceleration	RCP upper support	F3X1, Y1	1	2	4
			F3X2, Y2	1	2	
		Control point	F4X1-X4	4	1	9
			F4Z1-Z4	4	1	
			F4YA	1	1	
		R/V wall	F5X-Z	1	3	3
		Bottom	F6XA	1	1	3
			F6ZA, ZB	2	1	
	Load	Bolt	BR1, BR2	2	1	2
Piping	Pressure	Internal press.	EP	1	1	1
	Temperature	SG inlet elbow	ET	1	1	1
Table controll parameter	Acceleration	Target (H)	XT	—	—	1
		Average (H)	X0	—	—	3
		Average (Pitch)	Zθ			
		Average (Roll)	Zφ			
		Controll (H)	X0	—	—	3
		Point (Pitch)	Zθ			
		(Roll)	Zφ			
	Hydraulic pressure	Horizontal	PLH0	—	—	5
		Vertical	PLV0			
		Pitching	PLθ			
		Rolling	PLφ			
		Yawing	PLΨ			

Summary of measuring channel

		Number of measuring channels
· Main coolant piping	Acceleration	9 ·
	Strain	199 (back-up:12)
	Relative displacement	3
	Pressure and Temperature	2
· Steam generator	Acceleration	6
	Relative displacement	6
	Strain	12
	Support load	3
· Reactor coolant pump	Acceleration	6
	Relative displacement	5
	Support load	6
· Support frame	Acceleration	19
	Load of bolt	2
· Vibration table	Control parameter	12

Total   290 (+back-up:12)

Figure C.1 Strain Gauge Installation Location of Hot Leg

Symbol	HR1A	HR1	HR1C	HR3B	HR3	HR3A	HR4A	HR4C	HR4	HR4B	HR5
Type of gauge installation	D	C	A	A	A	A	B	B	B	B	C
Number of channel	4	8	6	6	6	6	25	25	25	25	8
Location	R/V outlet nozzle	Vicinity of R/V outlet nozzle safe-end	Horizen straight run close to S/G Inlet	Horizen straight run close to S/G Inlet	Horizen straight run close to S/G Inlet	Location of thickness change at the beginning of elbow bend	50° Elbow near horizontal straight run	50° Elbow near horizontal straight run	Middle point of 50° Elbow	50° Elbow near S/G Inlet nozzle	S/G Inlet nozzle (safe end)

Weld

Beginning point of elbow bend   Installed on S/G side from beginning point of elbow bend

Weld |Weld

Installed on R/V side from beginning point of radius work

Beginning point of radius work

※ ◯内数値は B/VL推奨値
  Value enclosed with ◯ are recommended by BHL.

Refer to Appendix 1
※添付 1 参照

Total of channels number
(excluding the channel number)

C-4

ゲージ取付記号 Symbol	XR2A	XR2B	XR3	XR9
取付位置 Type of gauge installation	40°エルボ	40°エルボ	40°エルボ (と直管の 溶接部)	90°エルボ (とRCP・A入口 管との溶接部)
ゲージ取付タイプ	E	F	G_T	H
チャンネル数 Number of channel	12	16	12	4
Location	40° Elbow near S/G outlet nozzle	40° Elbow near vertical straight run	Vertical straight run near 40° Elbow	RCP side 90° Elbow near RCP inlet nozzle

Total of channels number

チャンネル数小計 44

XR9

XR2A

XR2B

XR3

20°

10°

10°

Weld
溶接線

Weld
溶接線
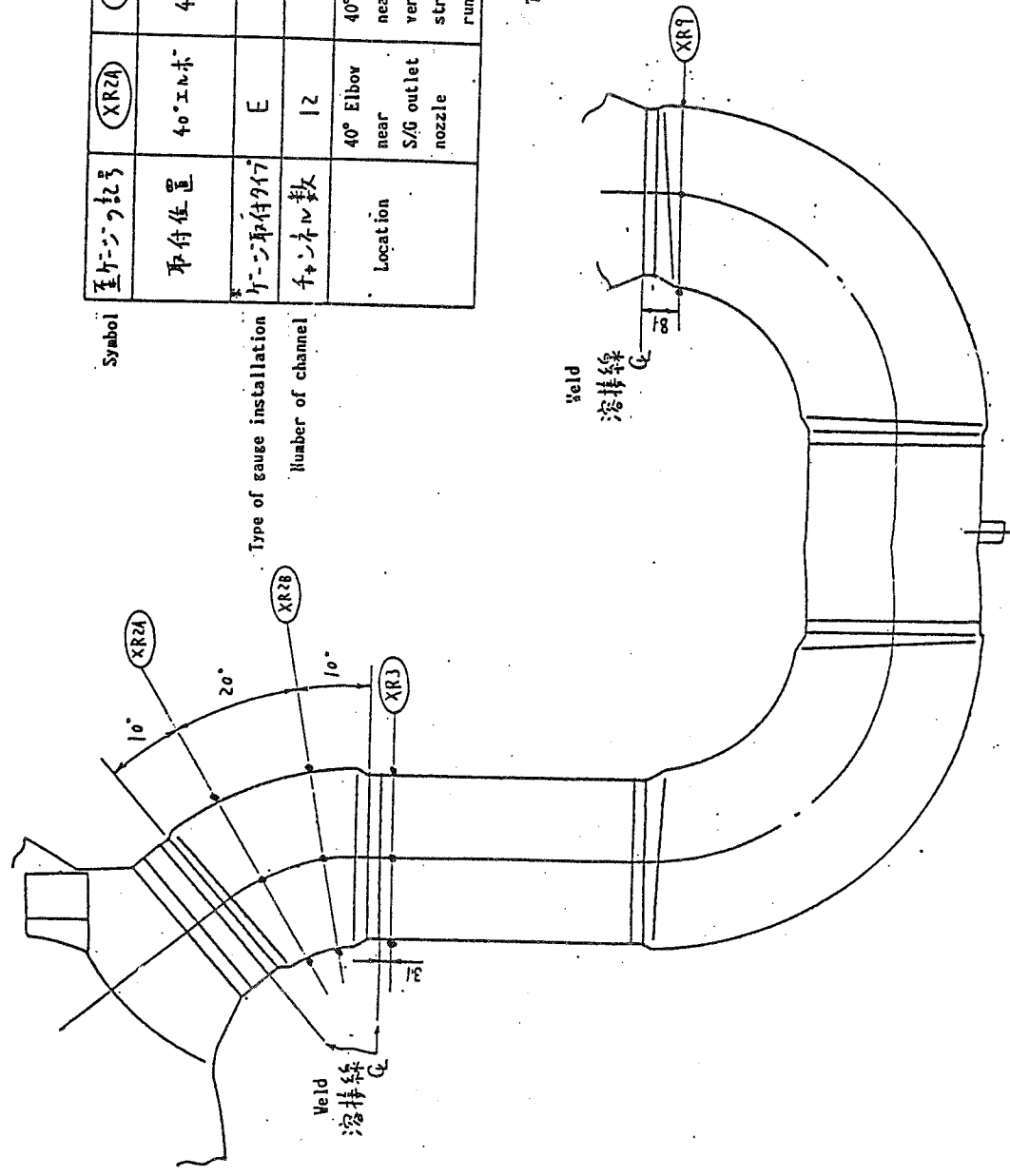
Figure C.2　Strain Gauge　Installation Location of Cross-Over Leg

※ Refer to Fig.A3-4

Symbol モトゲージの記ちう	CR1	CR3
取付位置 Type of gauge installation	RCPpa出妾管る (と継合う溶部分)(と継合う溶部)	22°Iルホ゛ (と継合う溶接部)
ゲーンに取付9イプ	H	C
チャンネル数 Number of channel	4	8
Location	Vicinity of RCP outlet nozzle	Horizontal straight run close to 22° Elbow

Total of channels number
チャンネル数小計 12

Weld
溶接線
ℂ

30

CR1

Weld
溶接線
ℂ

30

CR3
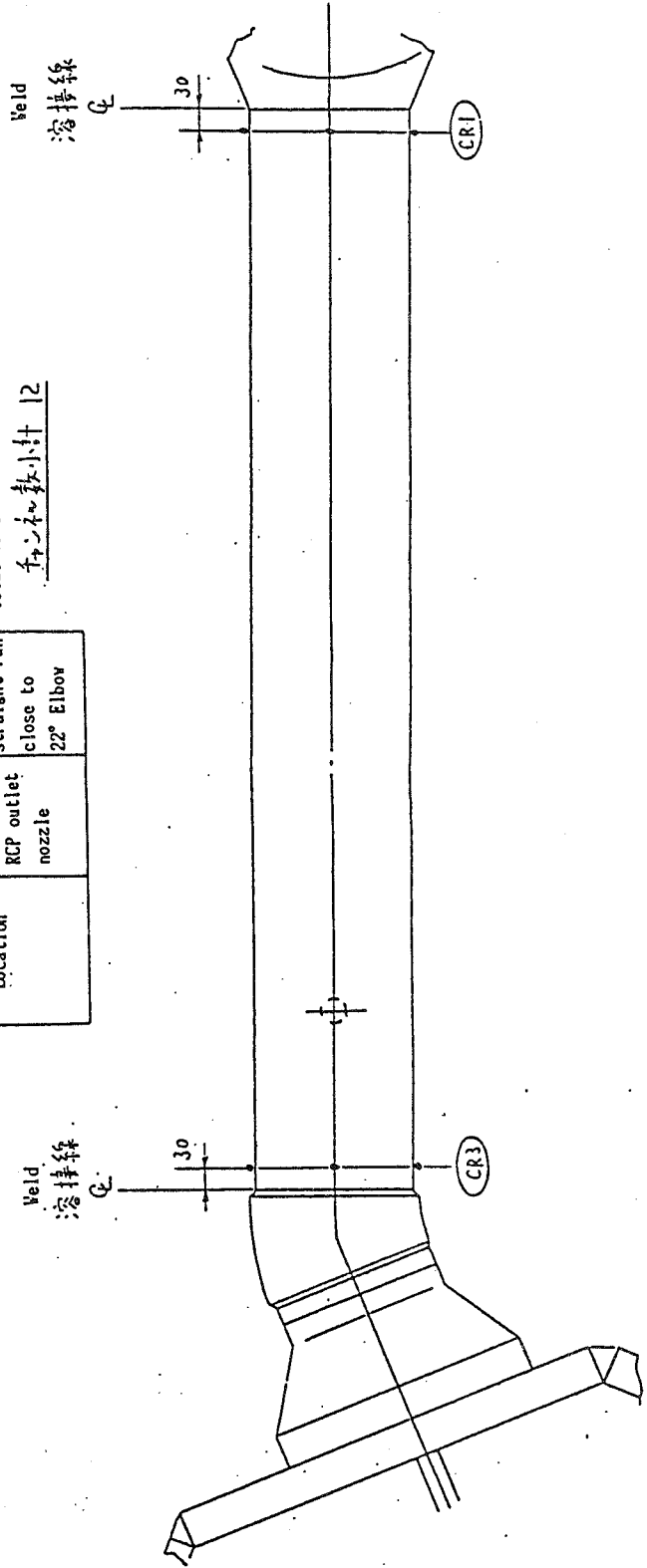
Figure C.3 Strain Gauge Installation Location of Cold Leg

Type A

Type B

Type C

Type D

Type E

Type F

Type G

Type H

Type A'

◫: 1軸ゲージ (円周方向) 1 direction gauge (circumferential)
●: 2軸ゲージ 2 direction gauge
▲: 3軸ゲージ 3 direction gauge
□: 1軸 バックアップ ゲージ (円周方向) 1 direction back-up gauge
✕: 1軸ゲージ (軸方向)   (circumferential)
  1 direction gauge (axial)
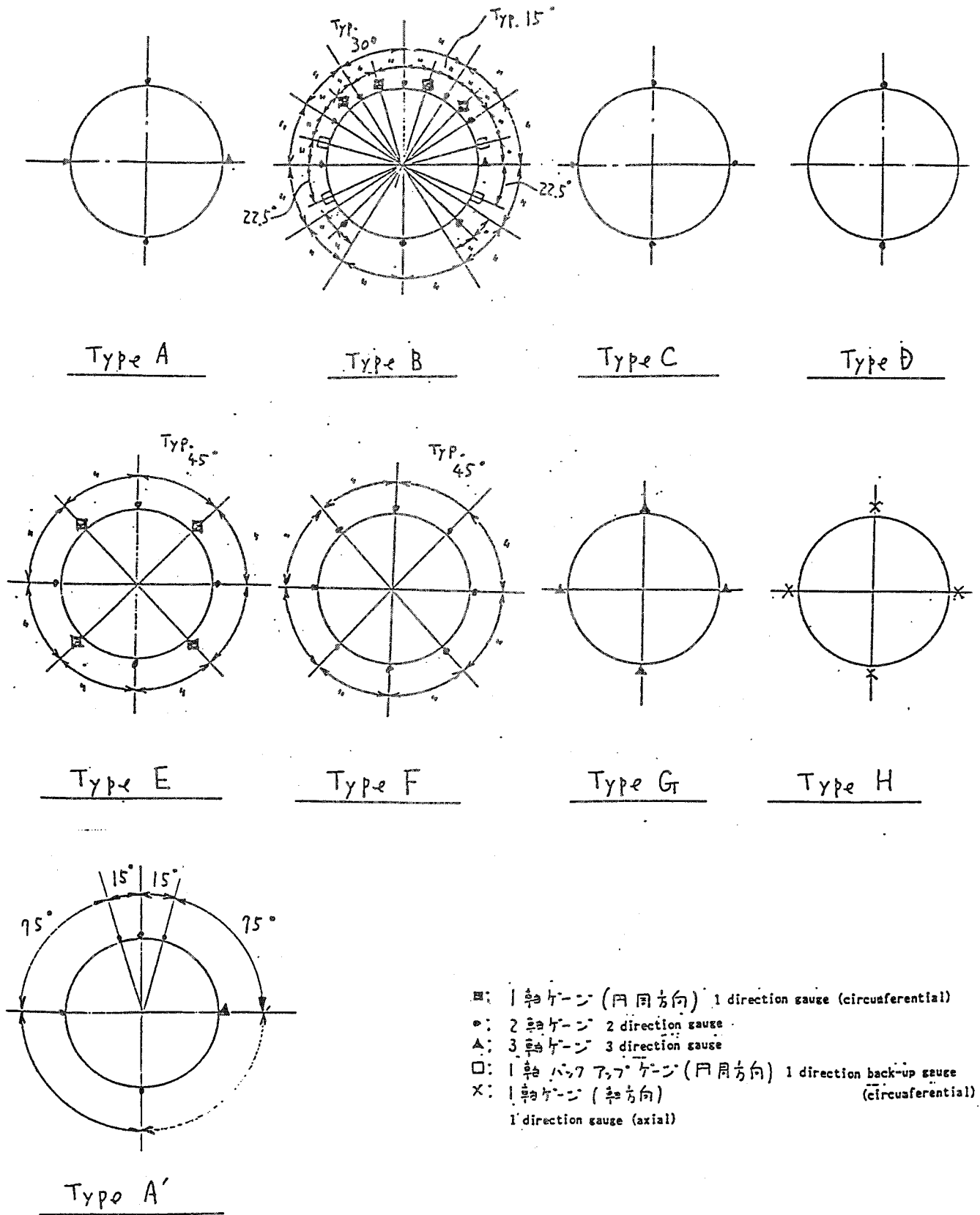
Figure C.4   Type of Gage Installation
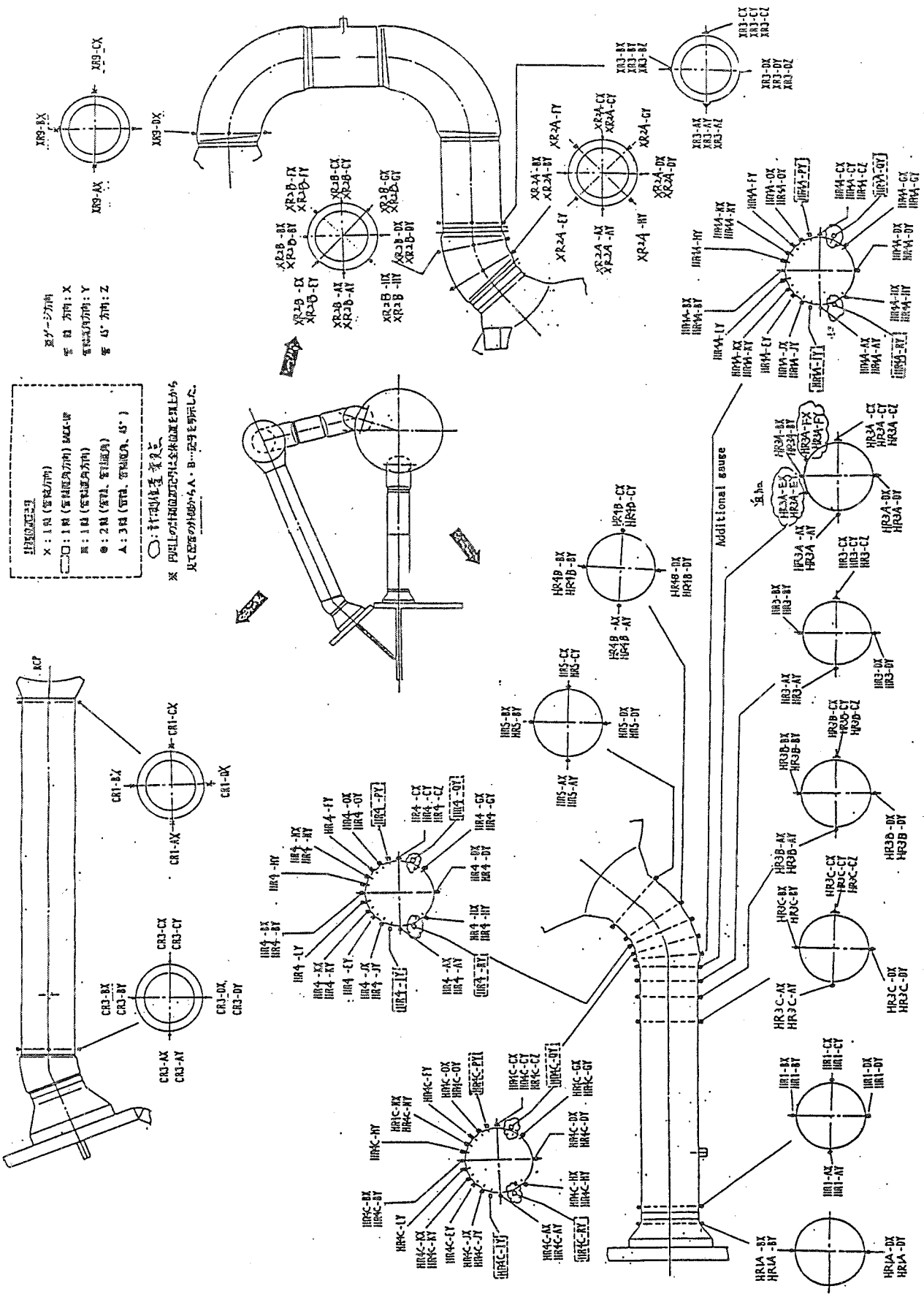
Figure C.5 Location of Measuring Points (Strain)

C-8

Figure C.6　Location of Measuring Points
(Acceleration Displacement and Force)

C-9

Appendix D

Summary of Test Results

Horizontal acceleration

Target acceleration

Pitching acceleration

Pitching acceleration
─────────────────────
Horizontal acceleration

Rolling acceleration

Yawing acceleration
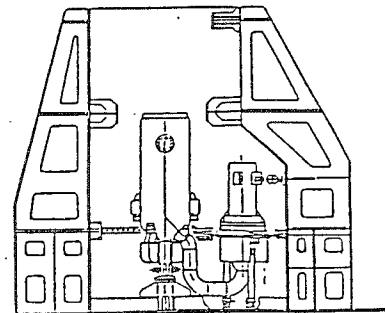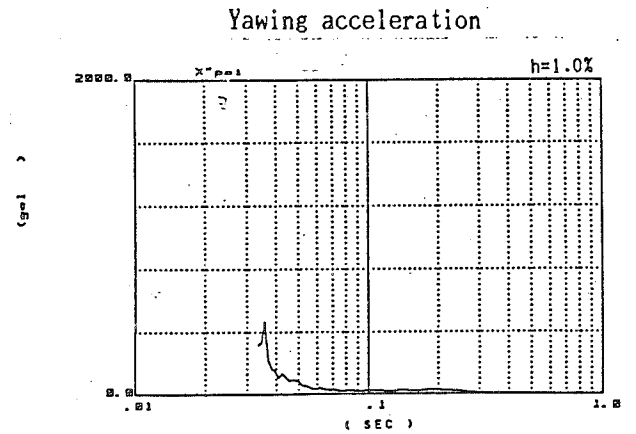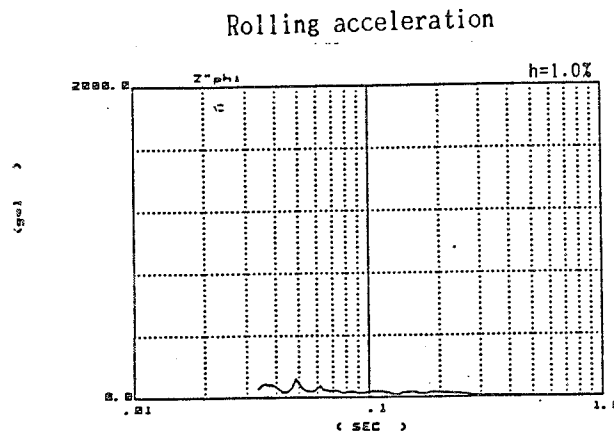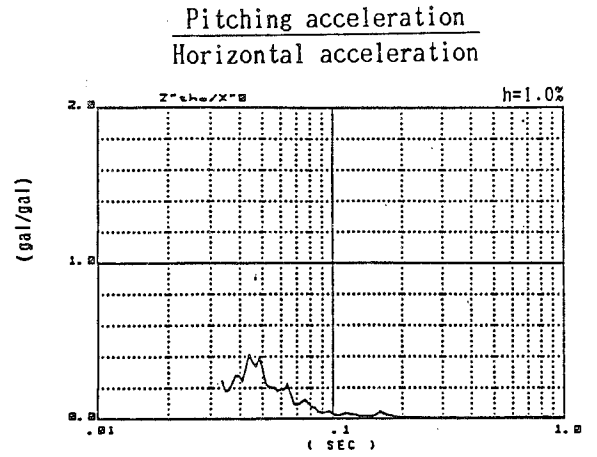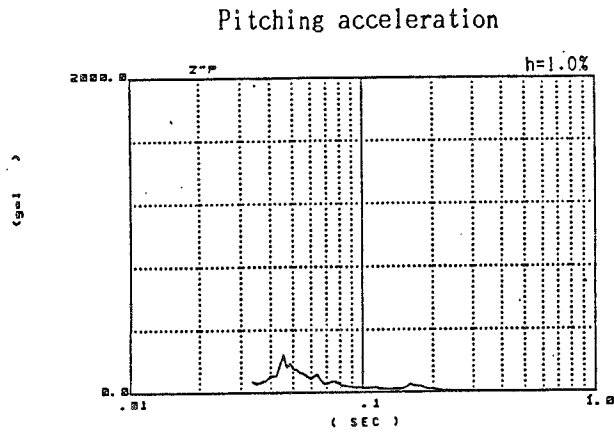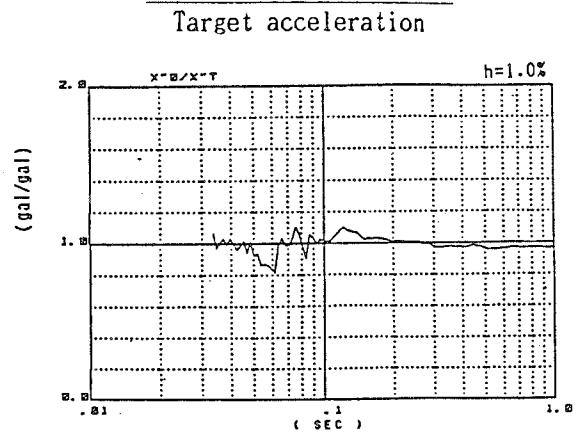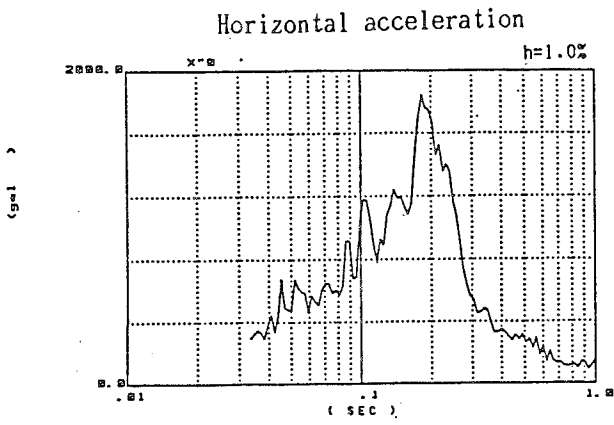
Figure D.1 Response Spectrum (Run 4 ; 0.1 MPR)
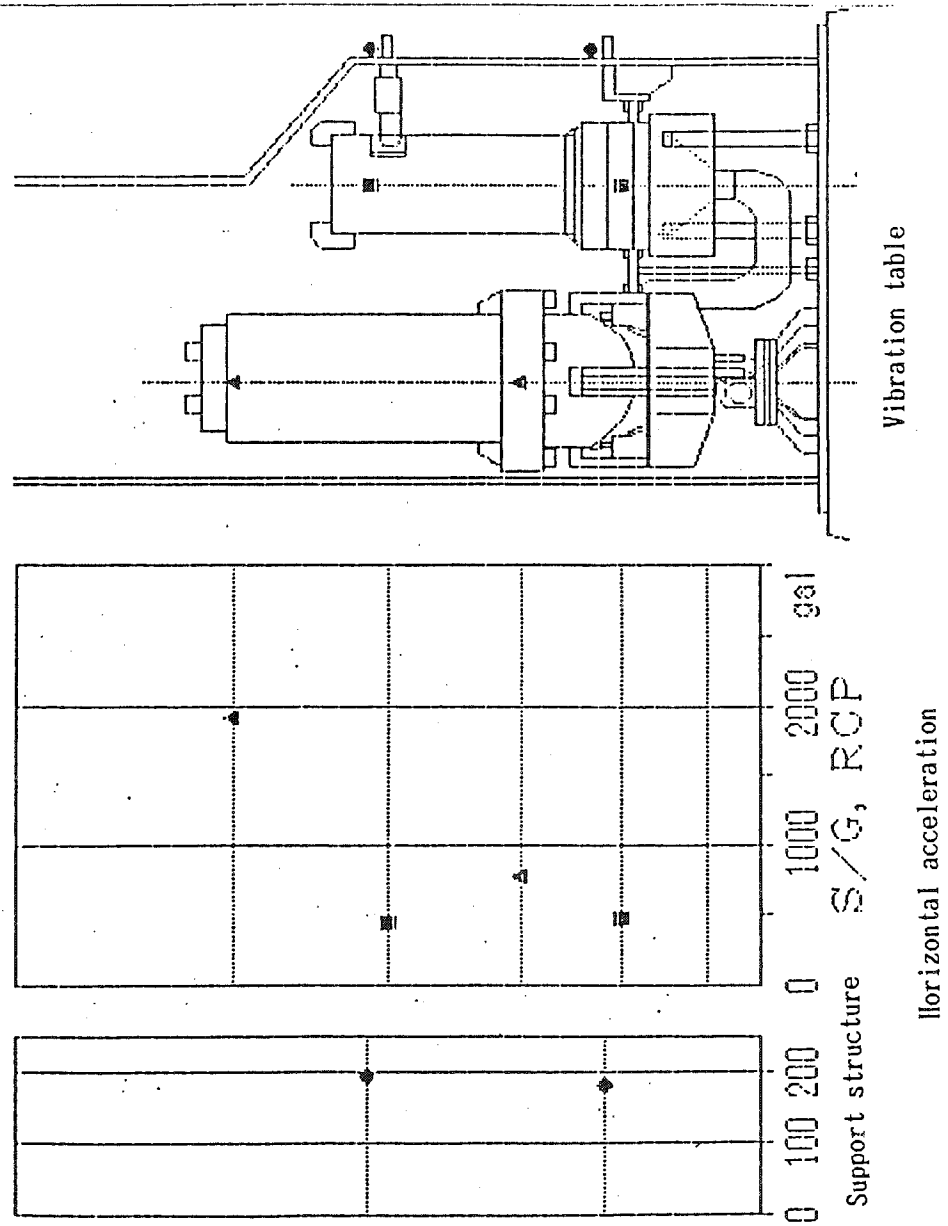
Figure D.2 (1)   Maximum Response Distribution
(Acceleration of S/G and RCP, Run 4 ; 0.1 MPR)

10 mm
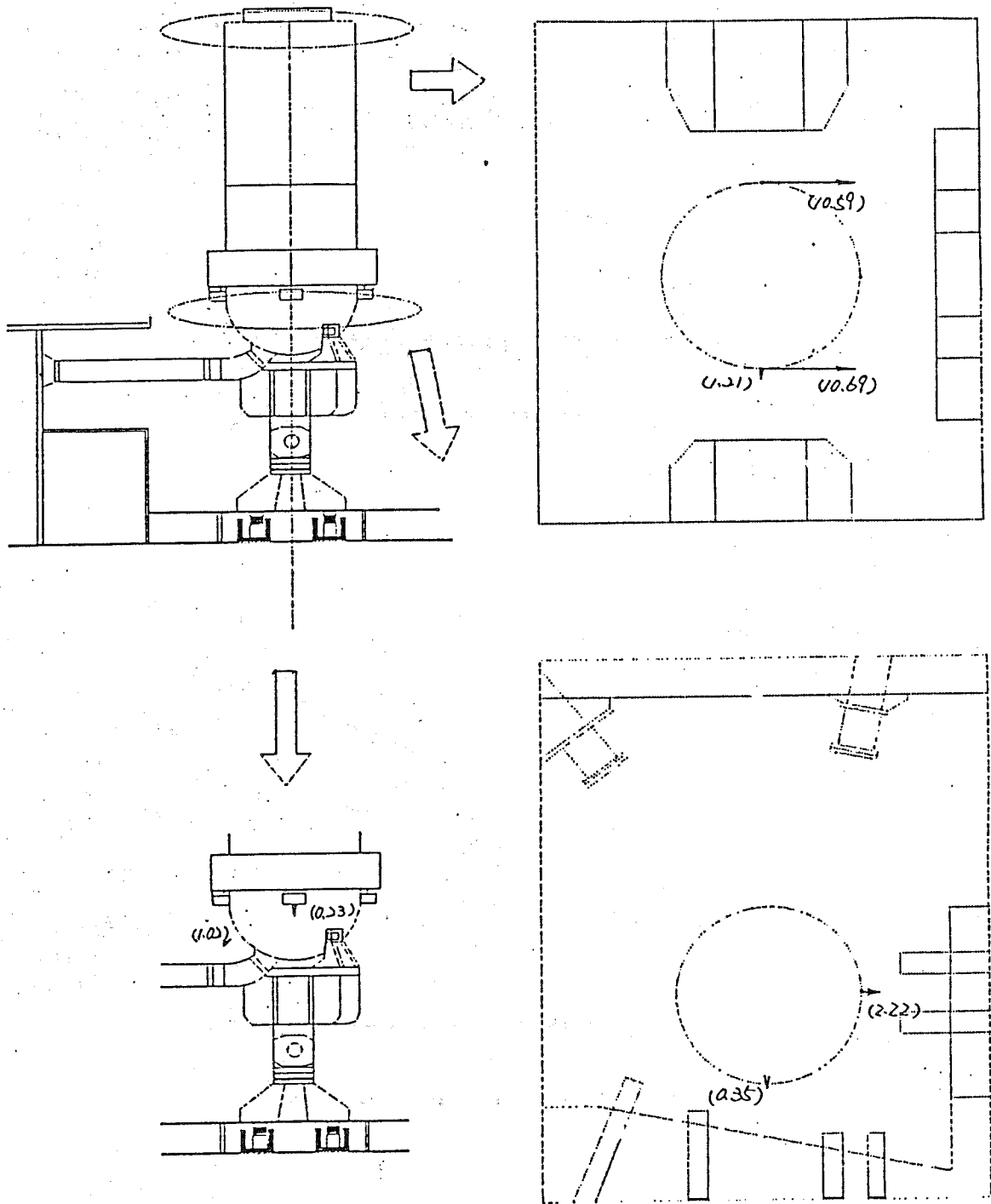
Figure D.2 (2)   Maximum Response Distribution
(Displacement of S/G, Run 4 ; 0.1 MPR)

Acceleration $\underset{\longrightarrow}{500\,gal}$

Dislacement $\underset{\longmapsto}{10\,mm}$
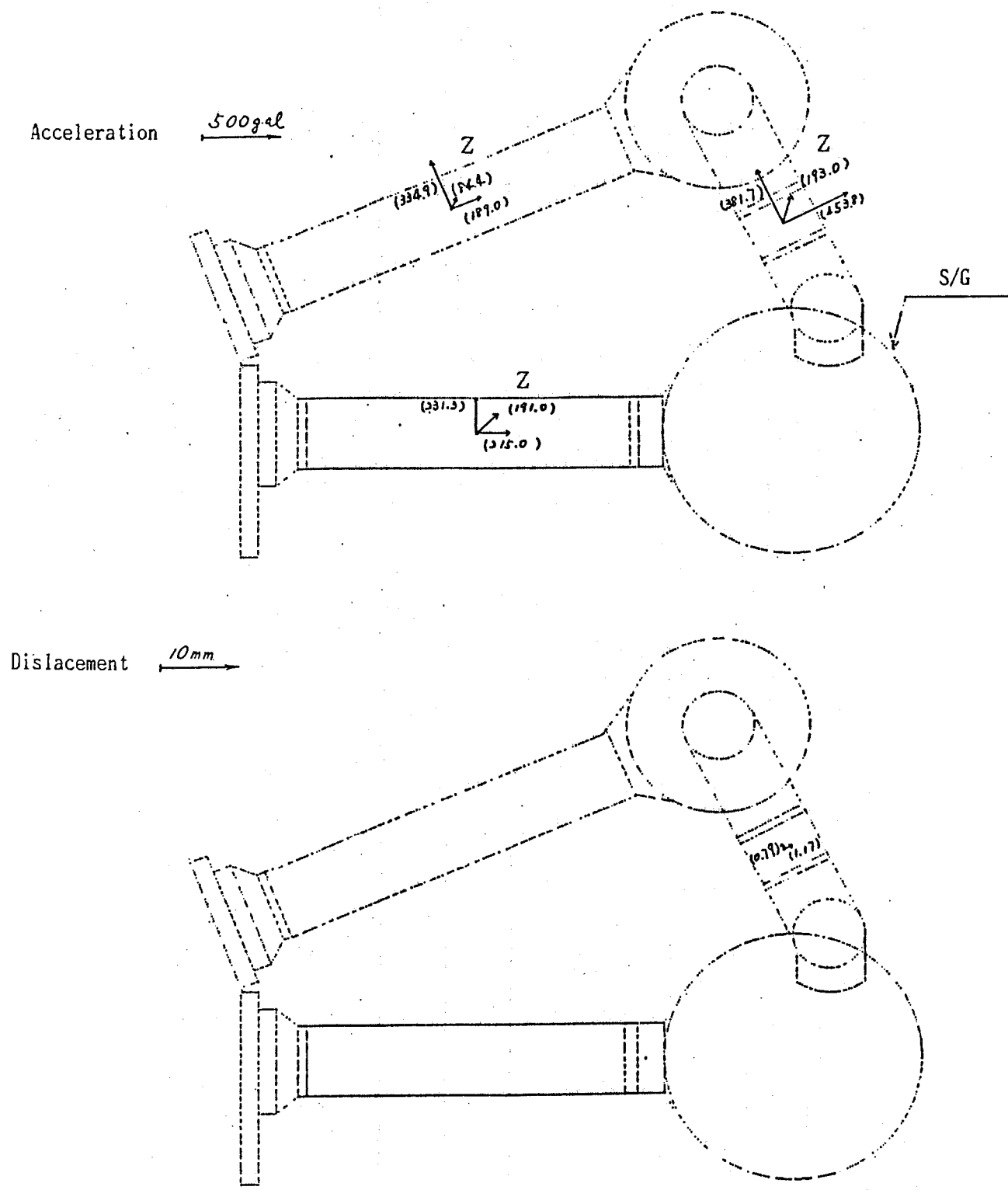
Figure D.2 (3)   Maximum Response Distribution
                 (Acceleration and Displacement
                 of Piping, Run 4 ; 0.1 MPR)
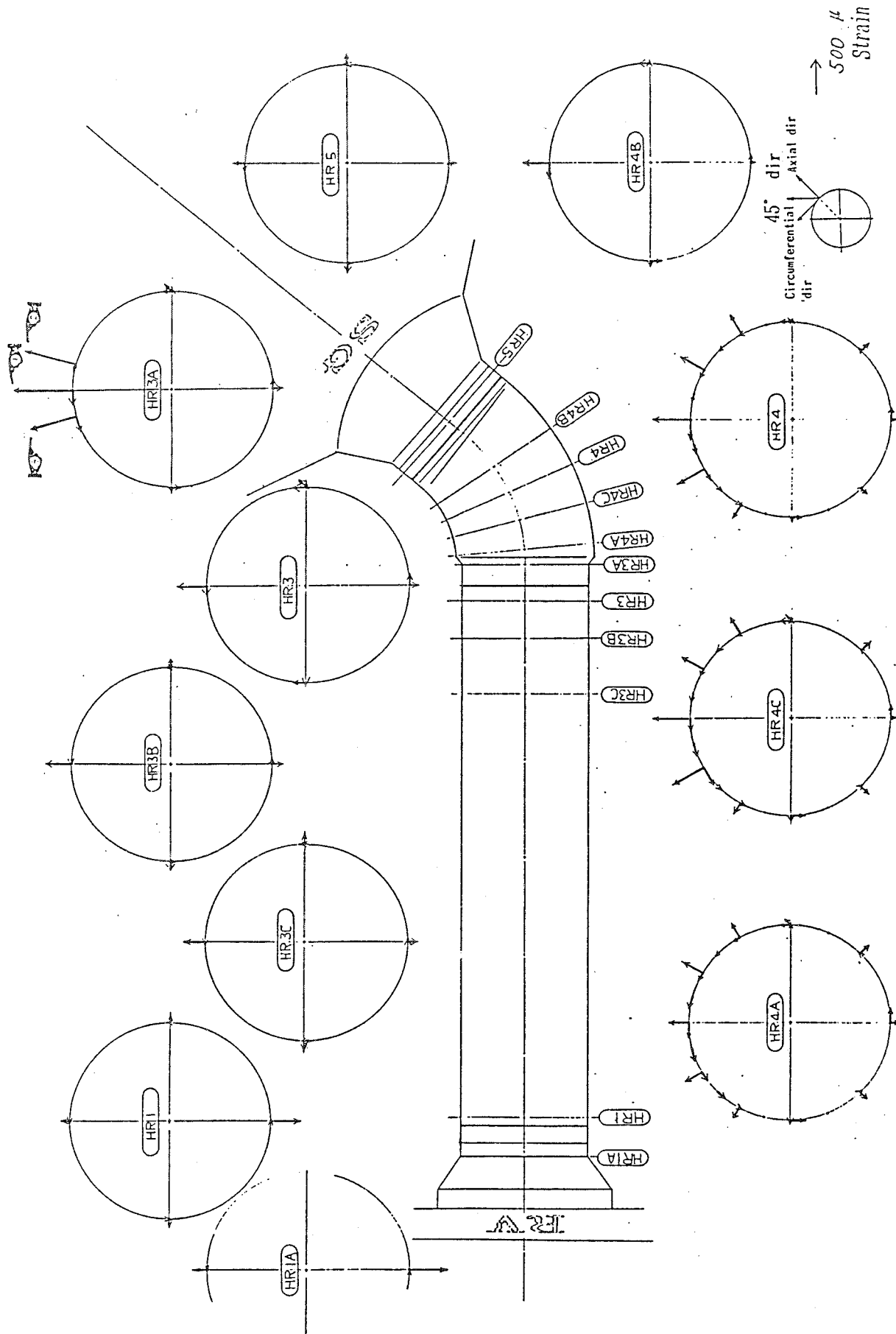
Figure D.2 (4) Maximum Response Distribution
(Strain of Hot Leg, Run 4 ; 0.1 MPR)

D-6
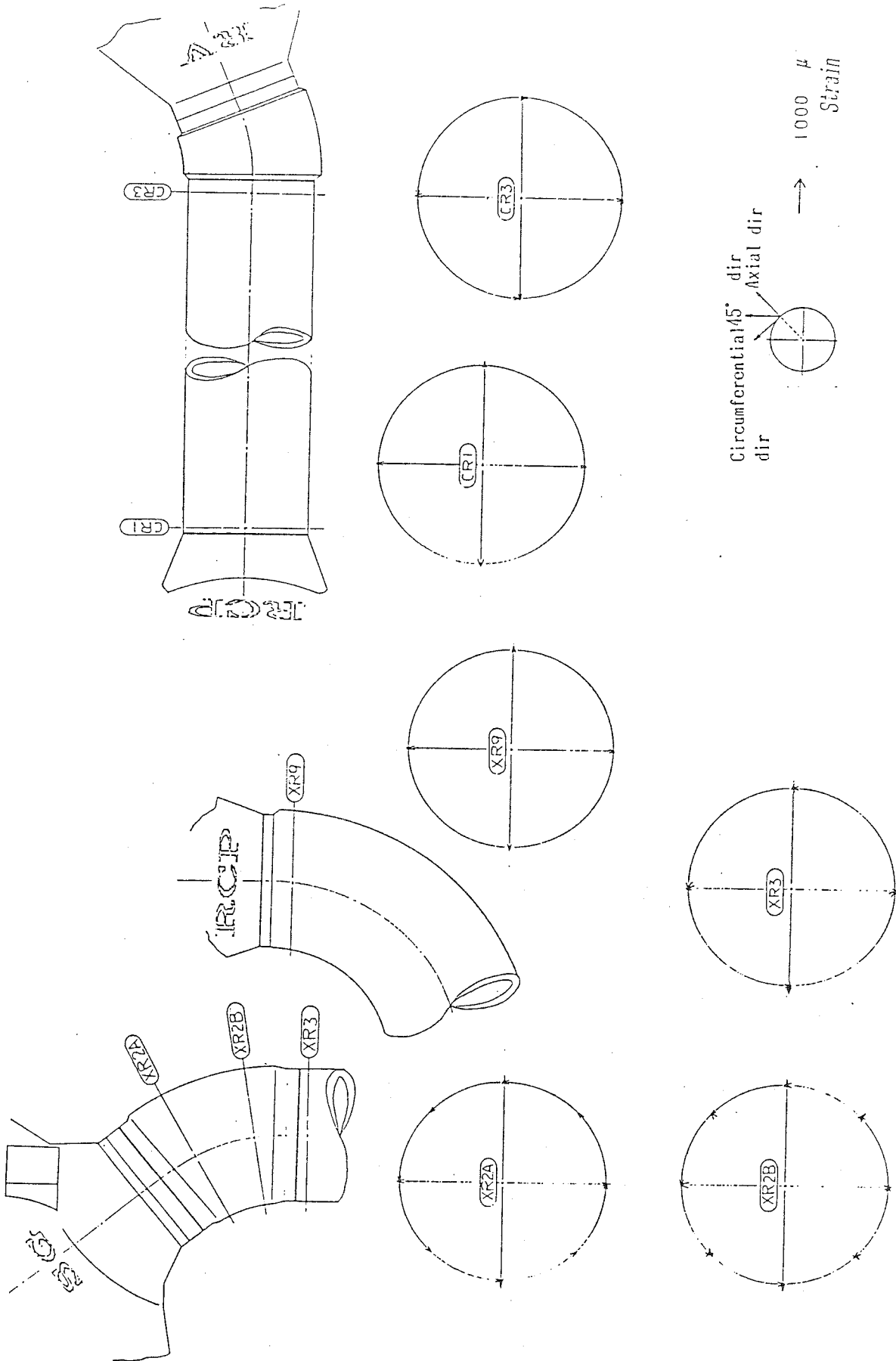
Figure D.2 (5)　Maximum Response Distribution
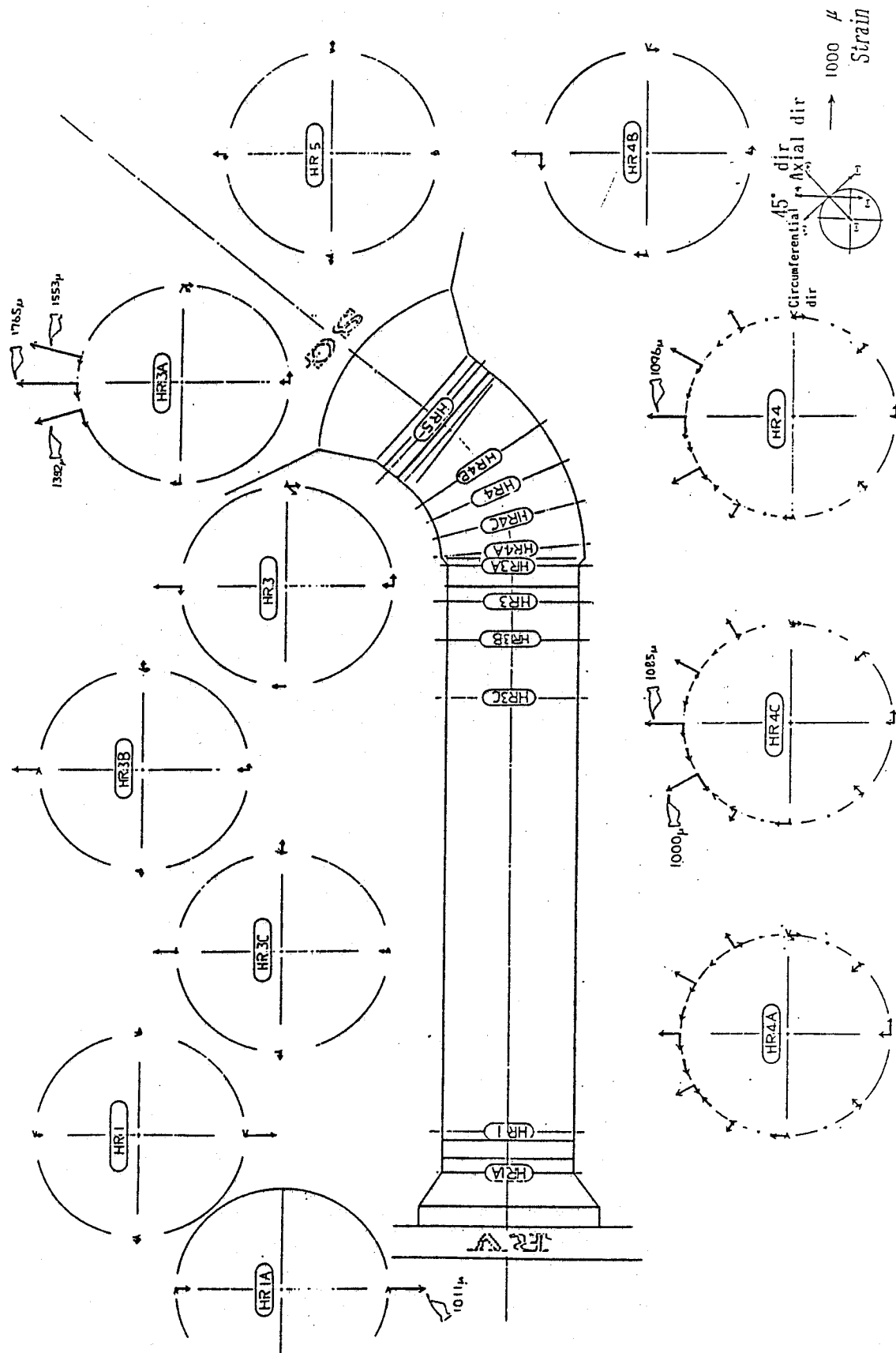(Strain of Cross-over Leg and Cold Leg, Run 4 ; 0.1 MPR)

D-7

Figure D.3 (1)   Instantaneous Response Distribution
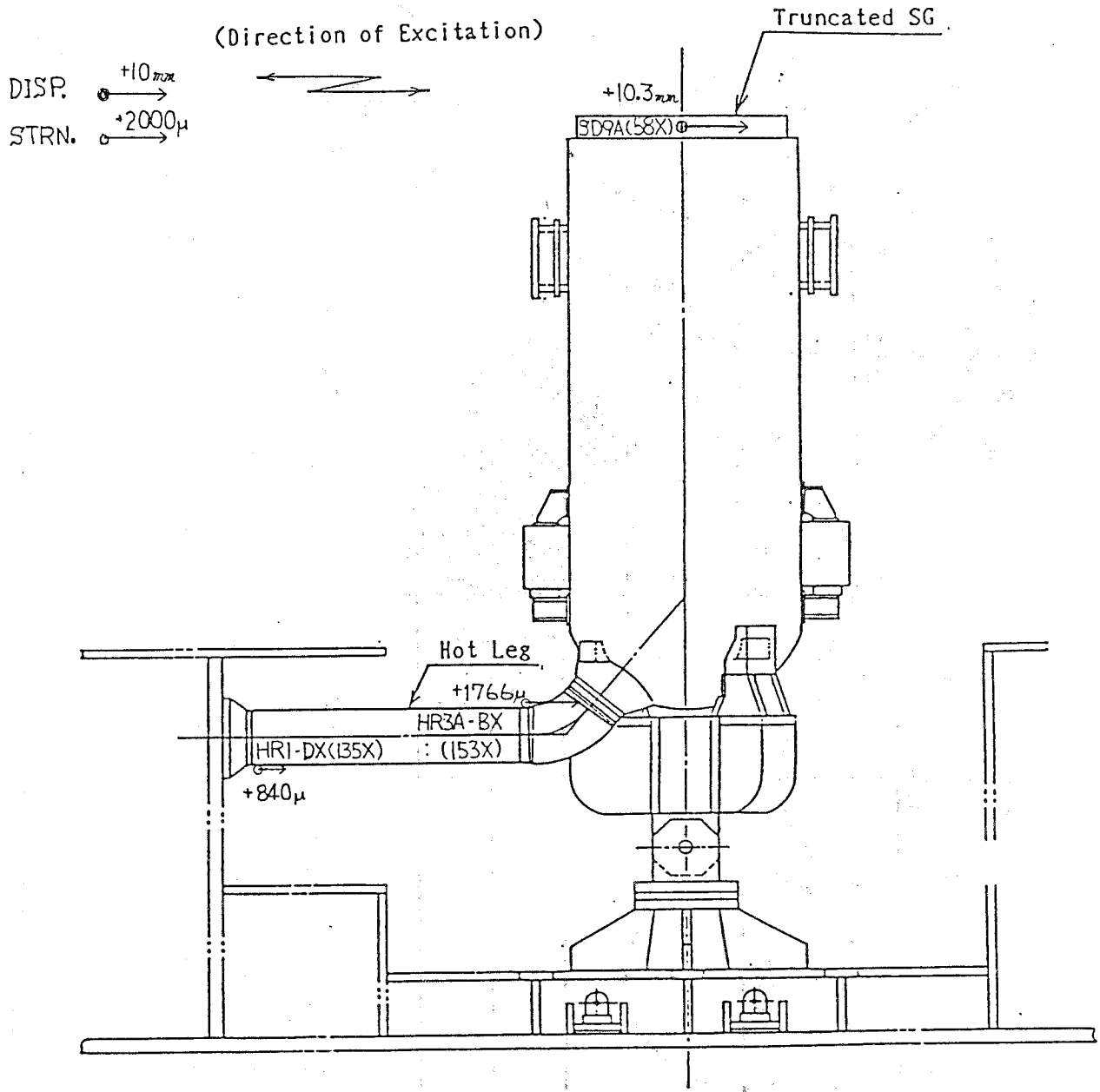(Strain of Hot Leg, Run 4 ; 0.1 MPR)

D-8

(Direction of Excitation)

DISP. $\circ \xrightarrow{+10_{mm}}$

STRN. $\circ \xrightarrow{+2000\mu}$

Truncated SG

$+10.3_{mm}$

3D9A(58X)$\circ \longrightarrow$

Hot Leg

$+1766\mu$

HR3A-BX

HR1-DX(135X) : (153X)

$+840\mu$

Figure D.3 (2)   Instantaneous Response Distribution
(Displacement of S/G and Strain of Hot
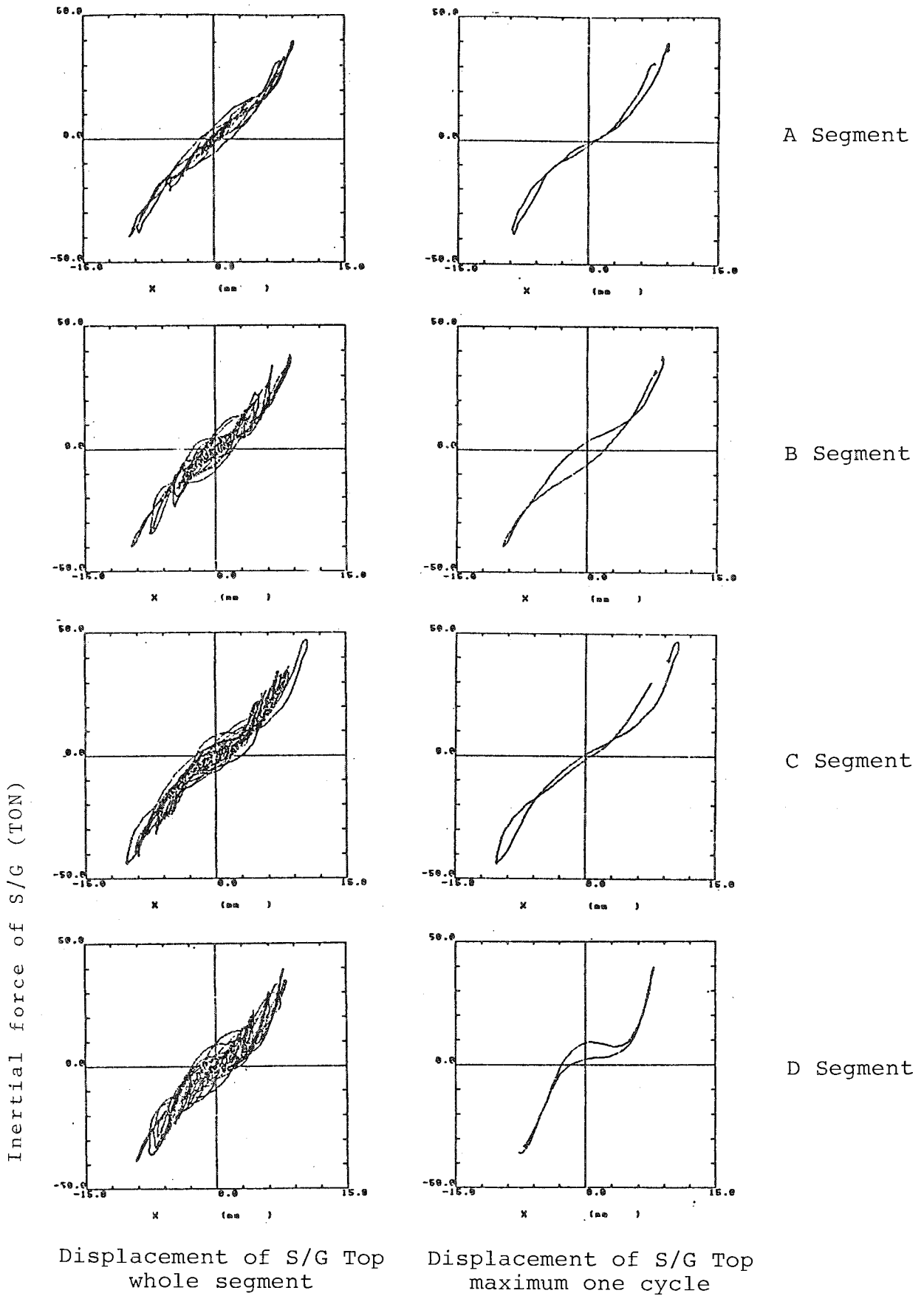Leg Run 4; 0.10 MPR
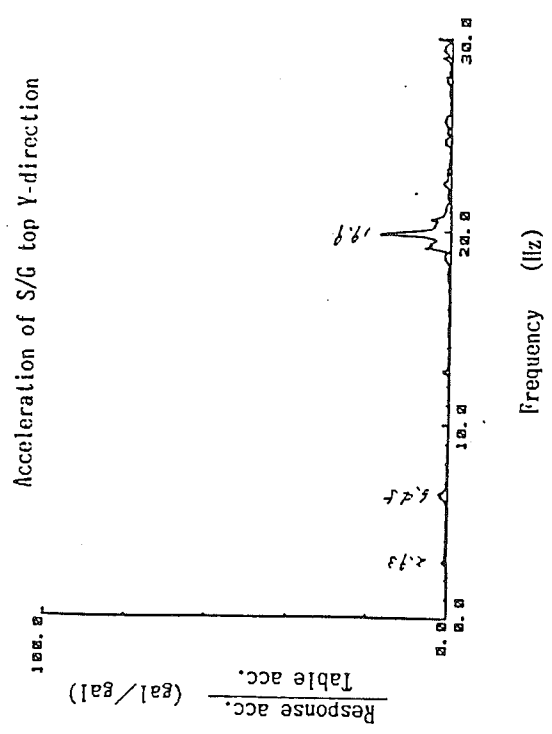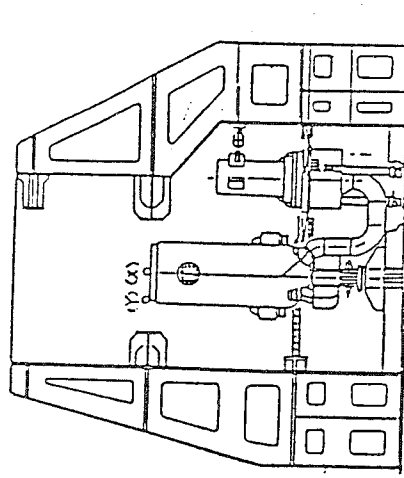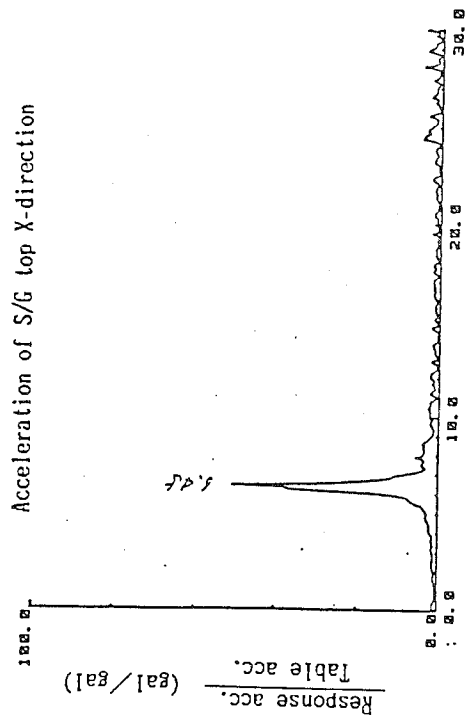
Figure D.4 Transfer Function (Run 4 ; 0.1 MPR)

A Segment

B Segment

C Segment

D Segment

Inertial force of S/G (TON)

Displacement of S/G Top
whole segment

Displacement of S/G Top
maximum one cycle

Figure D.5   Hysteresis Loop of Force and Displacement of
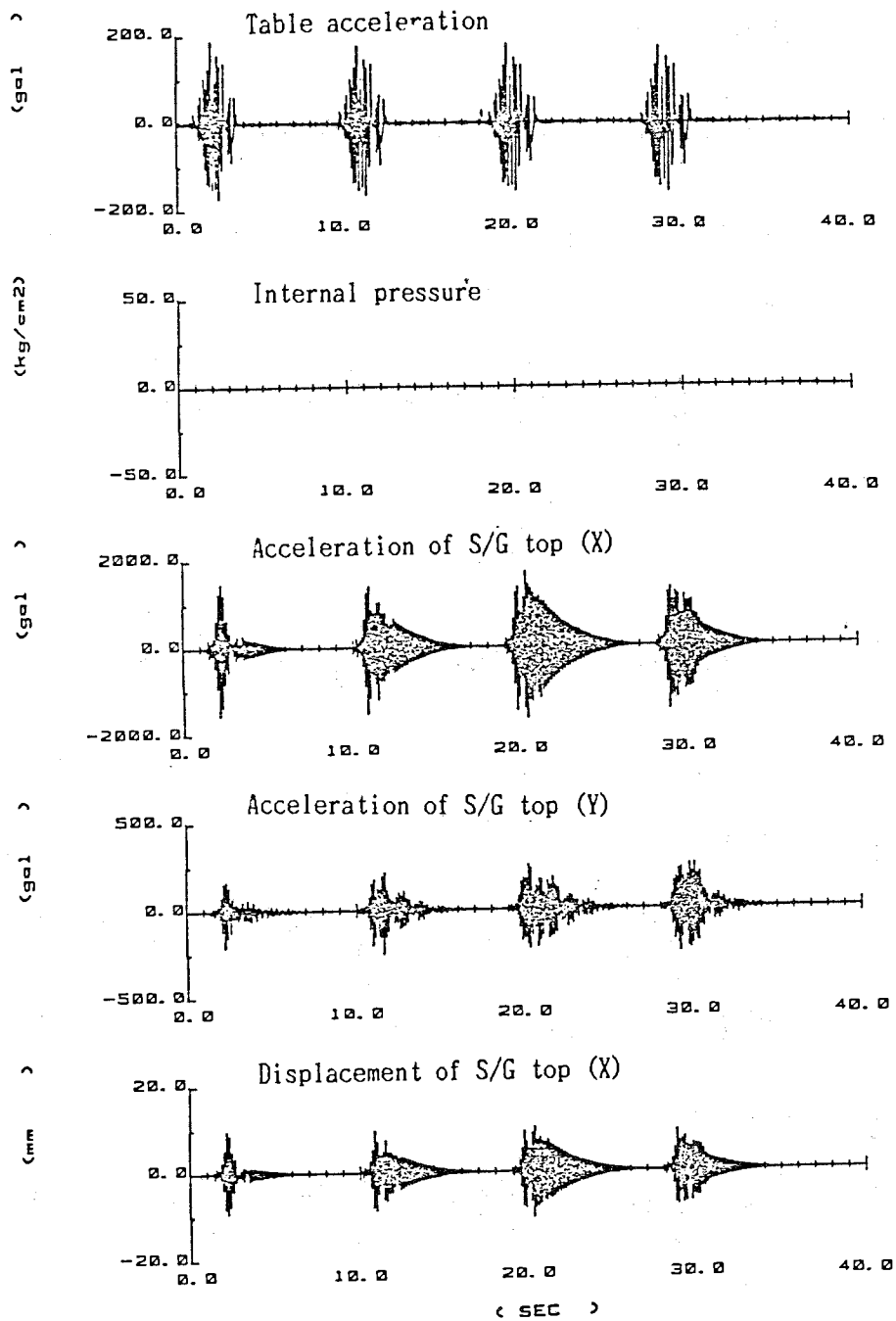S/G (Run 4; 0.1 MPR)

D-11

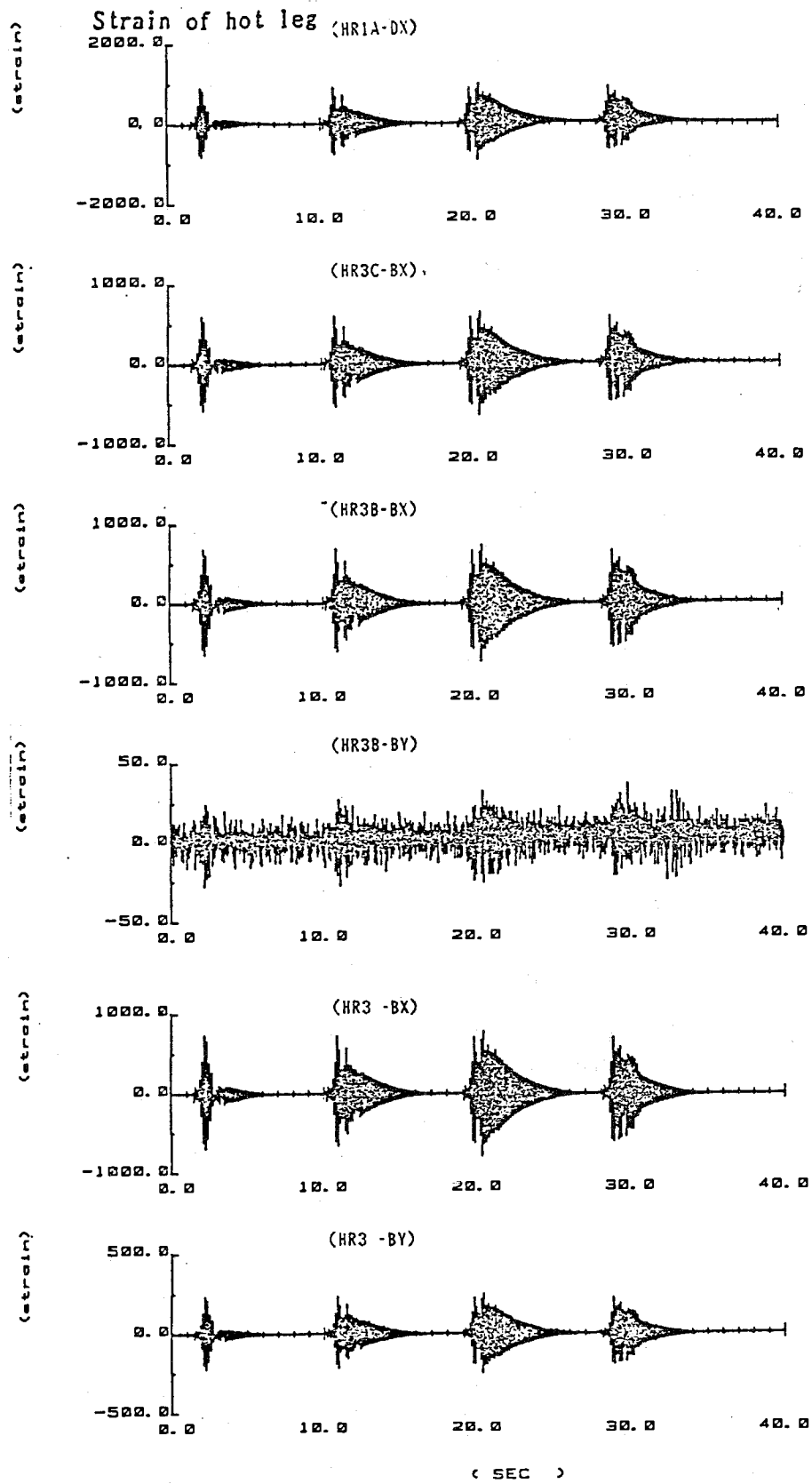Figure D.6 (1)   Time History of Response (Run 4 ; 0.1 MPR)

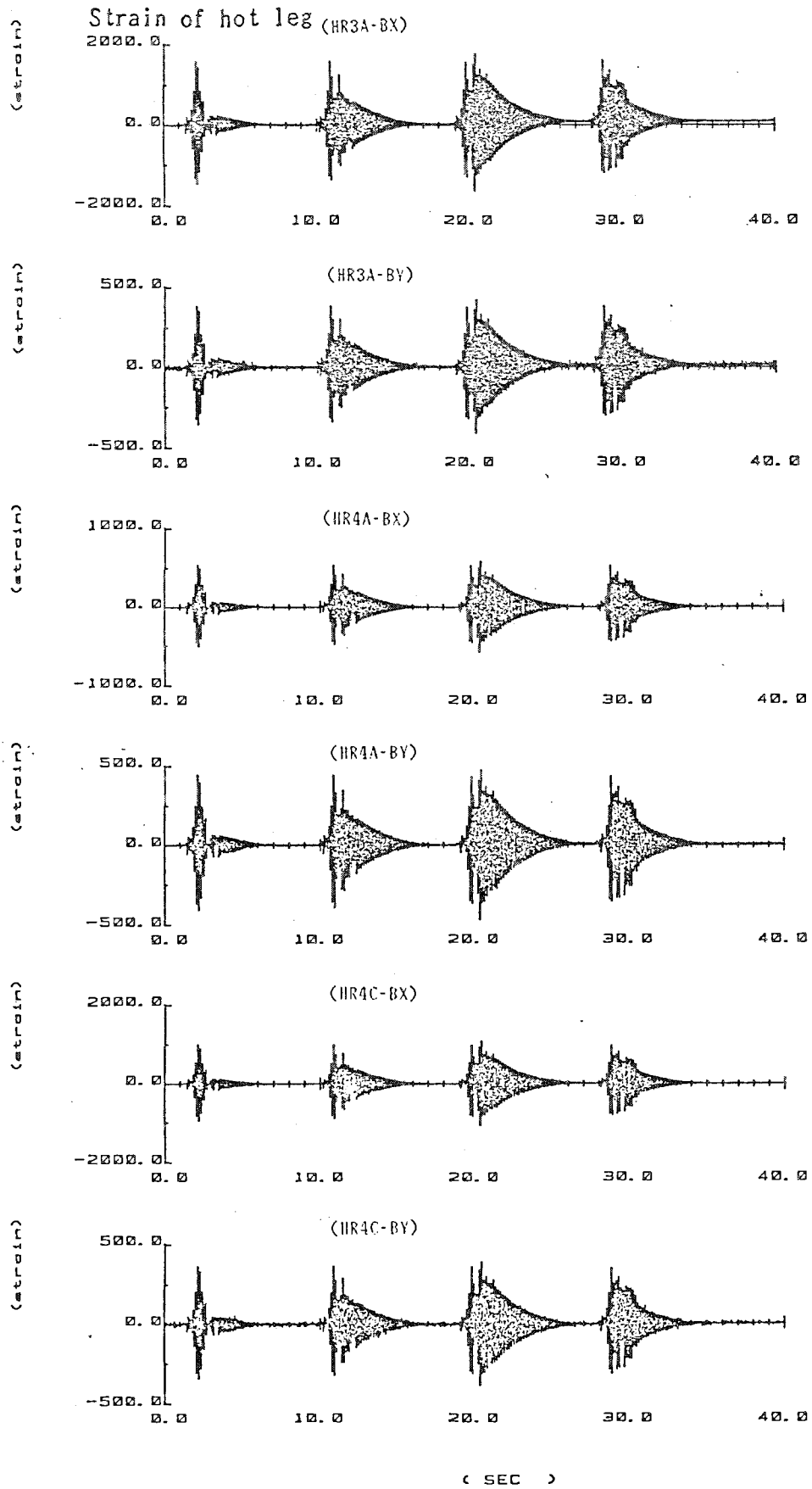Figure D.6 (2) Time History of Response (Run 4 ; 0.1 MPR)

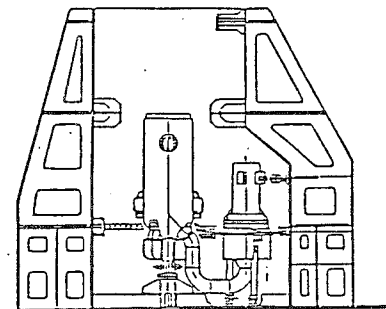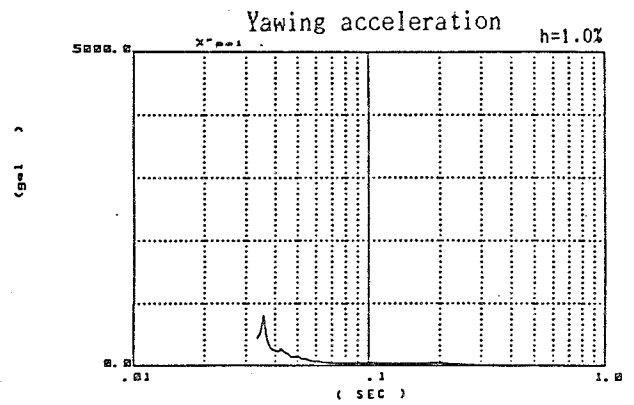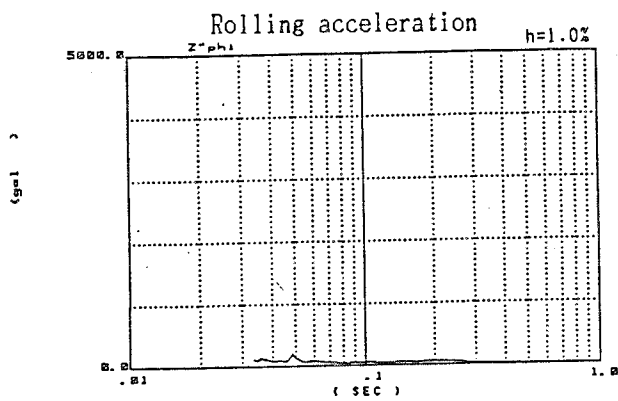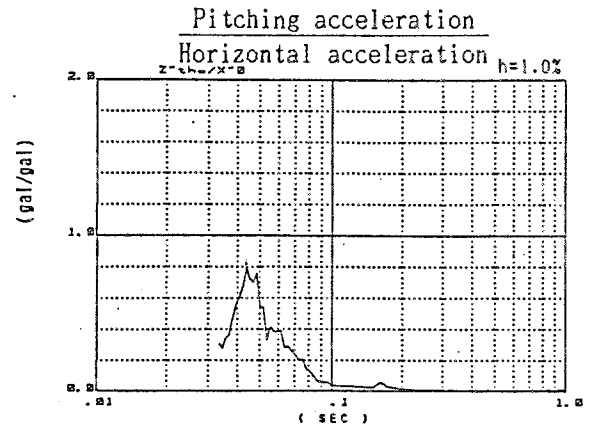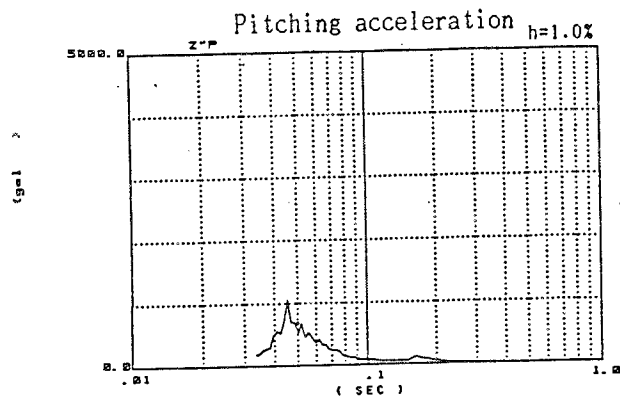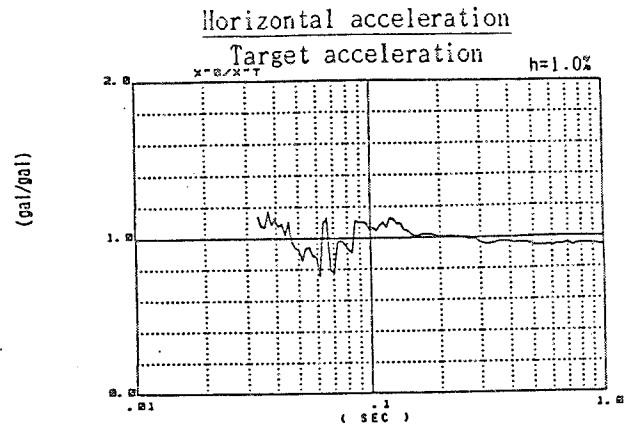Figure D.6 (3)   Time History of Response (Run 4 ; 0.1 MPR)
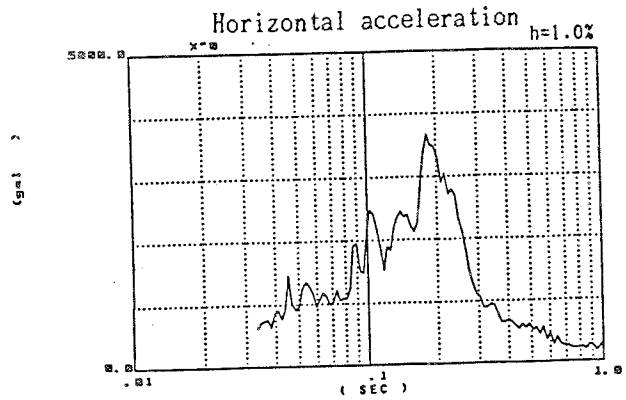
Figure D.7 (1)   Response Spectrum (Run 5 ; 0.2 MPR)
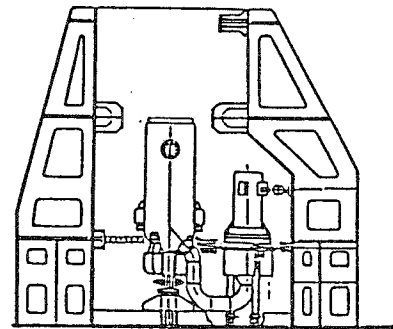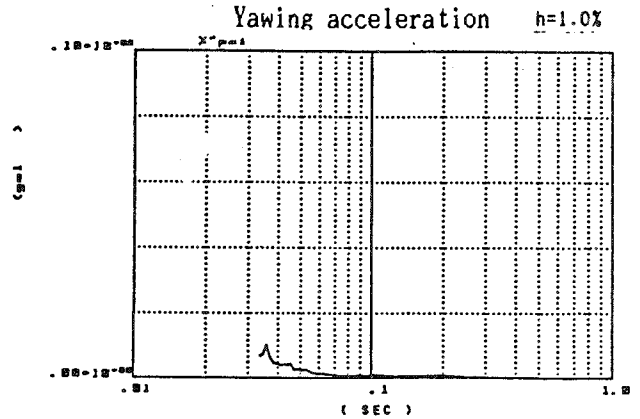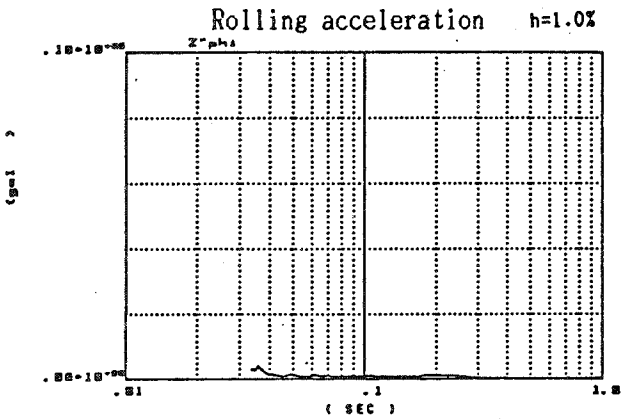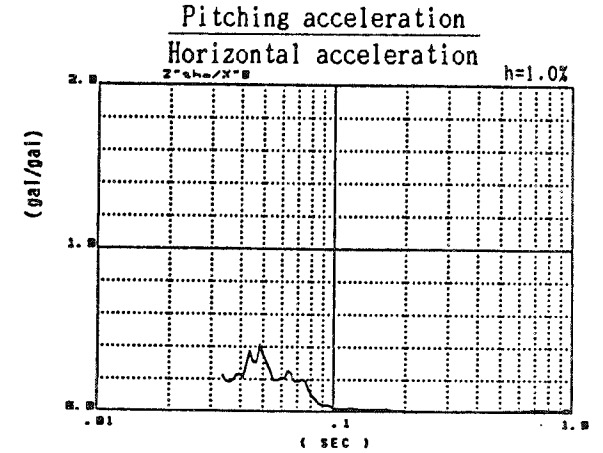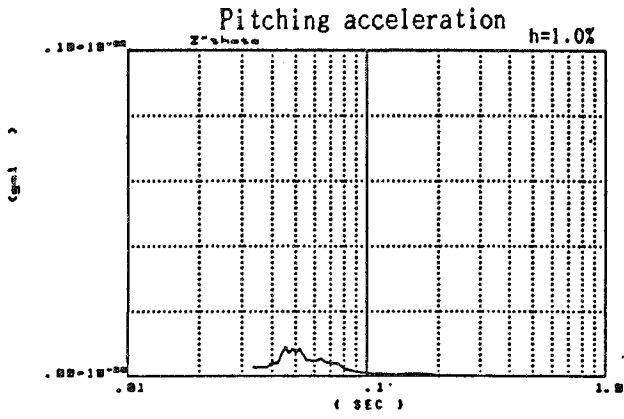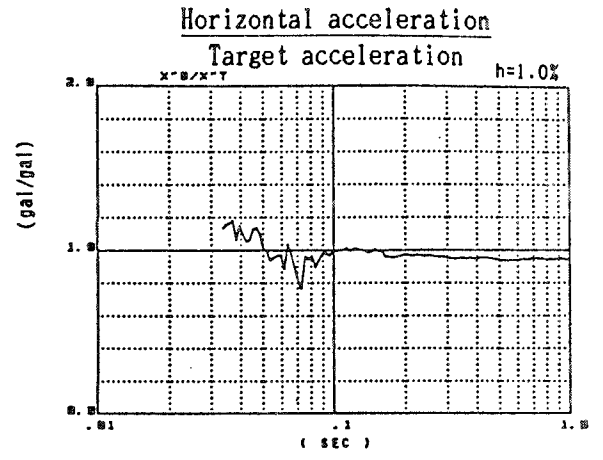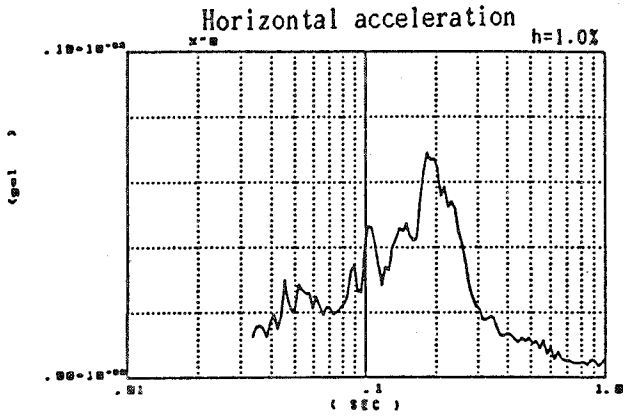
Figure D.7 (2)   Response Spectrum (Run 8; 0.4 MPR)
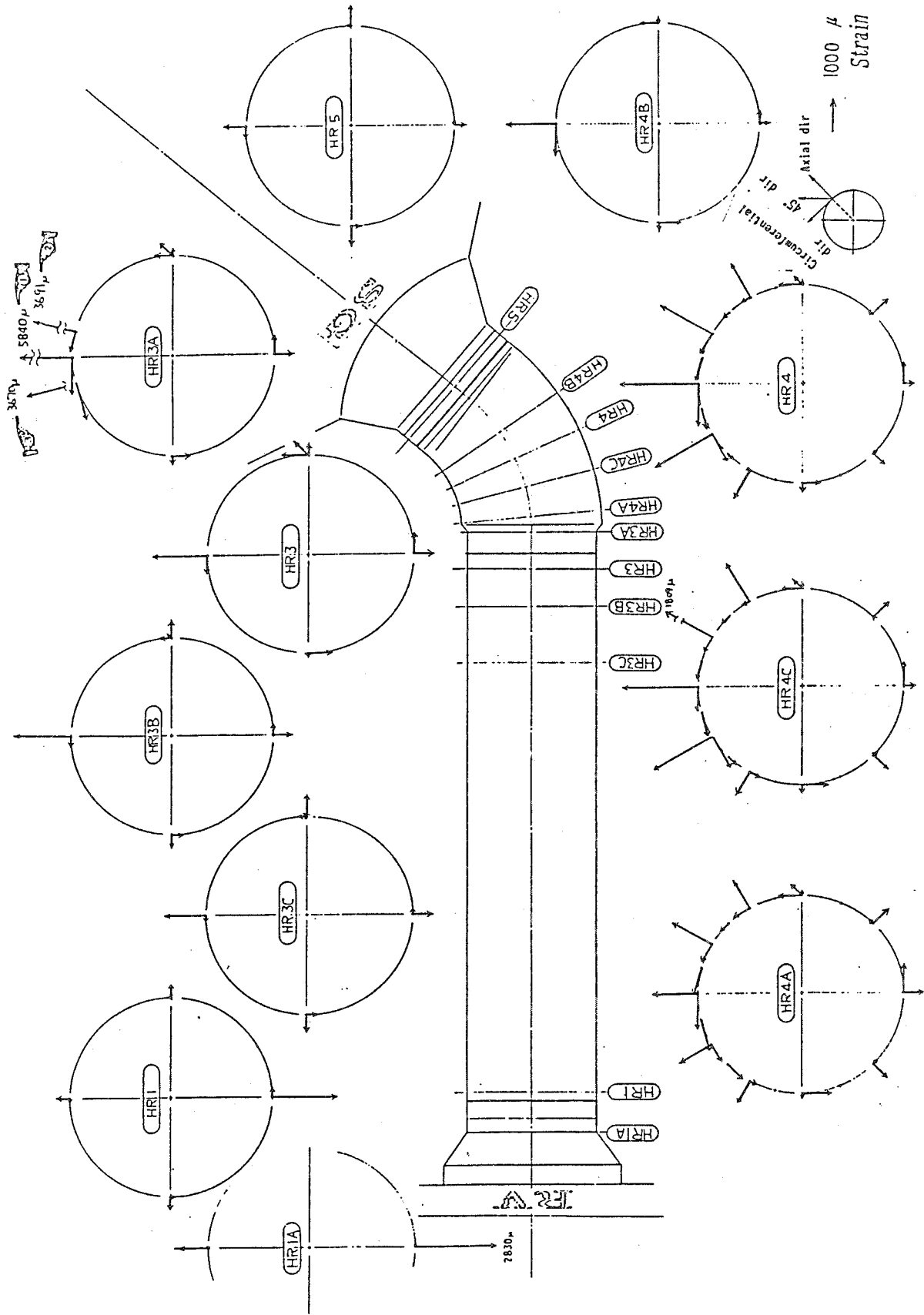
Figure D.8 (1)   Maximum Response Distribution
(Strain of Hot Leg, Run 5 ; 0.2 MPR)
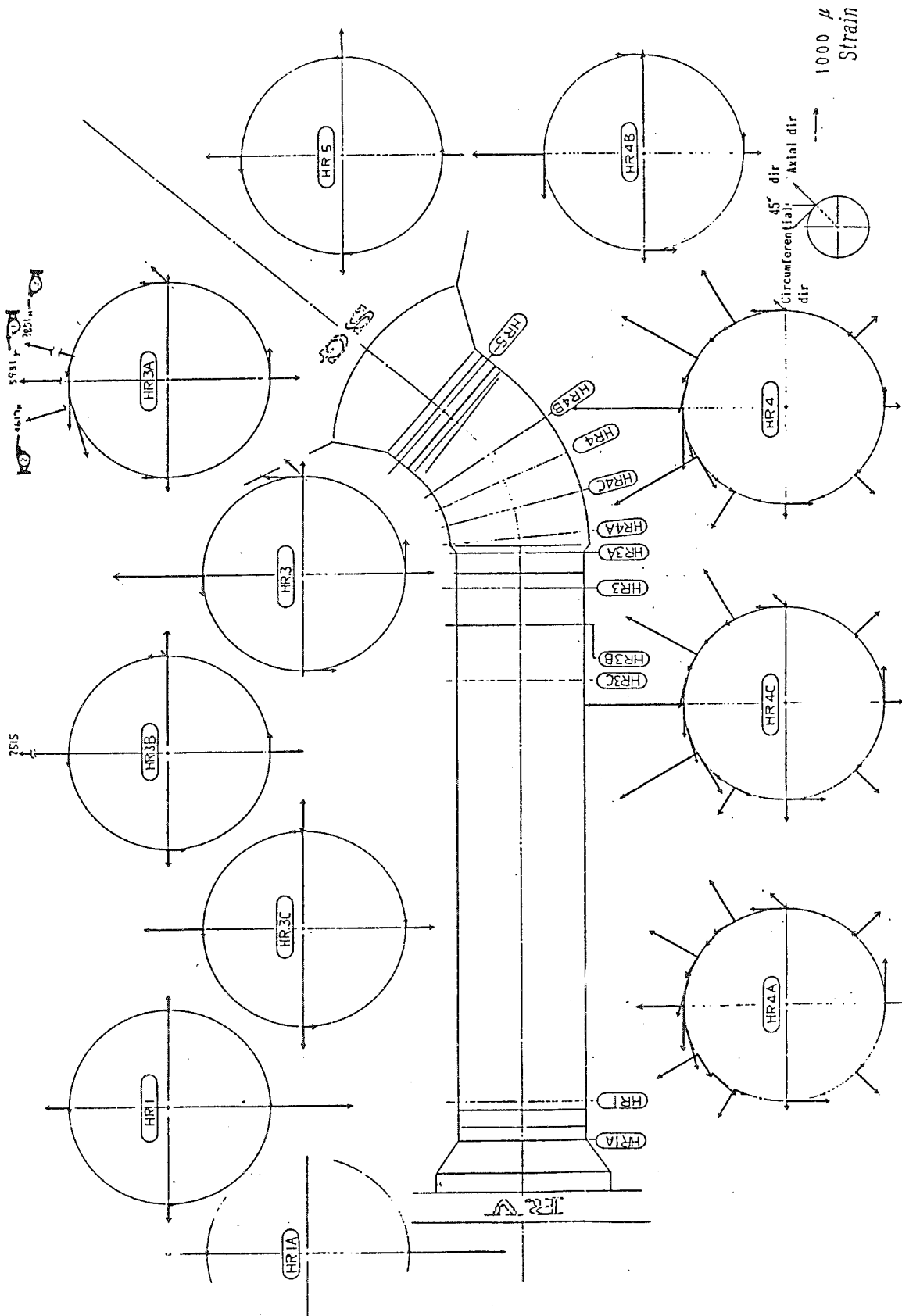
Figure D.8 (2)   Maximum Response Distribution
(Strain of Hot Leg, Run 8 ; 0.4 MPR)

(Direction of Excitation)

Truncated SG

DISP. $\circ\!\!-\!\!\!\!\xrightarrow{+20\,mm}$

STRN. $\circ\!\!-\!\!\!\!\xrightarrow{+5000\,\mu}$

+19.9 mm

5D9A (58X)

Hot Leg
+5840 μ

HR3A-BX

HR1-DX (135X)   : (153X)

+1819 μ

Figure D.9 (1)   Instantaneous Response Distribution
(Displacement of S/G and Strain of Hot Leg,
Run 5 ; 0.20 MPR)

(Direction of Excitation)

Truncated SG

DISP. ⊕ $\xrightarrow{+50\,mm}$

STRN. ○ $\xrightarrow{+10000\,\mu}$

+31.2 mm

SD9A(58X) →

Hot Leg
+5931μ

HR3A-BX

HRI-DX (135X) : (153X)

↔
+2394μ
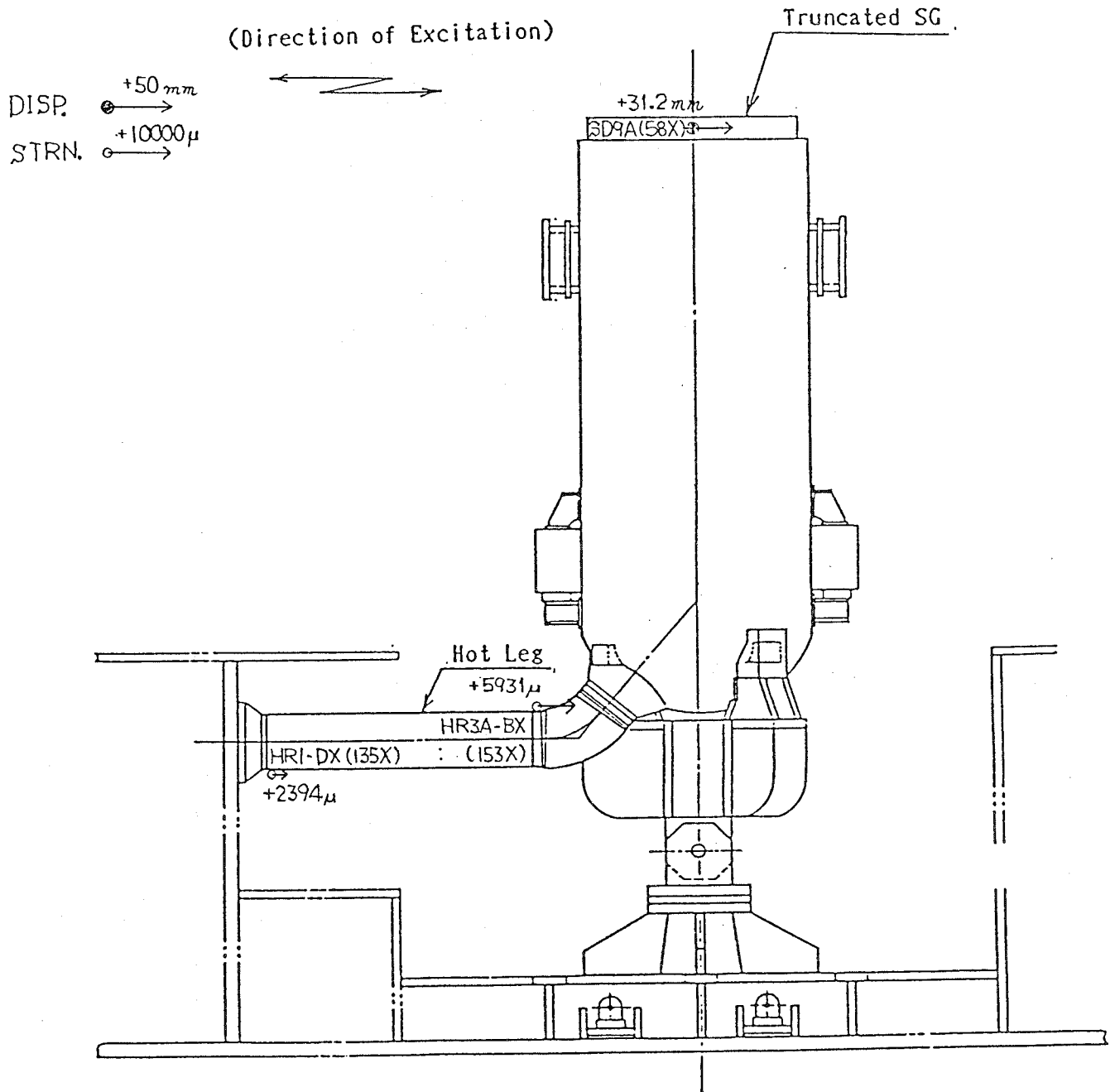
Figure D.9 (2)   Instantaneous Response Distribution
(Displacement of S/G and Strain of Hot Leg,
Run 8 ; 0.40 MPR)
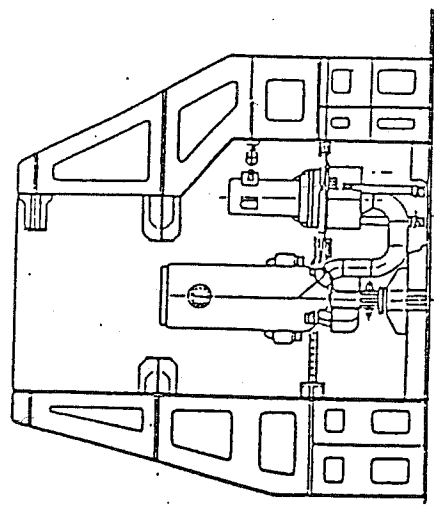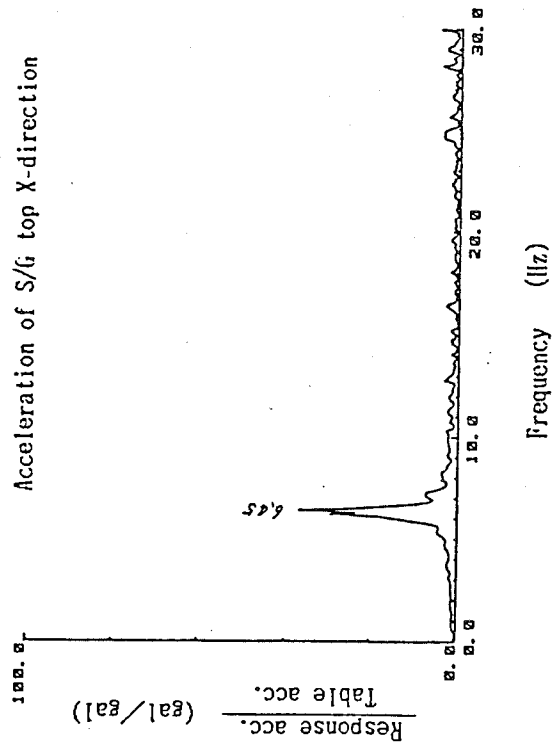
Figure D.10 (1) Transfer Function (Run 5 ; 0.2 MPR)

Figure D.10 (2) Transfer Function (Run 8 ; 0.4 MPR)

One cycle

A Segment

B Segment

C Segment

D Segment

Inertial force of S/G (TON)

Displacement of S/G Top
whole segment

Displacement of S/G Top
maximum one cycle
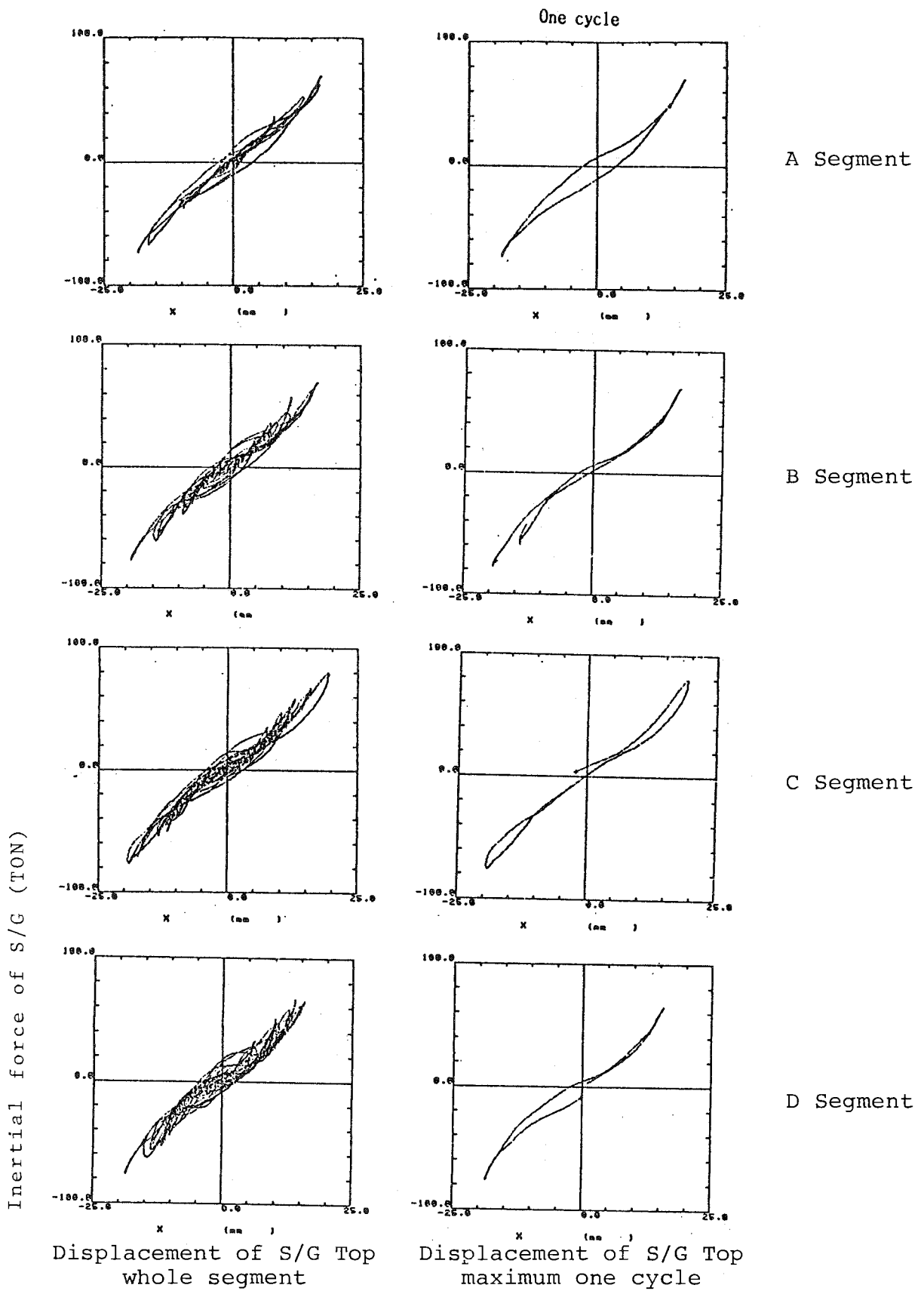
Figure D.11 (1)   Hysteresis Loop of Force and Displacement
of S/G (Run 5; 0.2 MPR)

Figure D.11 (2)   Hysteresis Loop of Force and Displacement
of S/G (Run 8 ; 0.4 MPR)

Figure D.12 (1)   Time History of Response
               (Run 5 ; 0.2 MPR)

Figure D.12 (2) Time History of Response
(Run 5 ; 0.2 MPR)

D-26

Strain of hot leg (HR3A-BX)
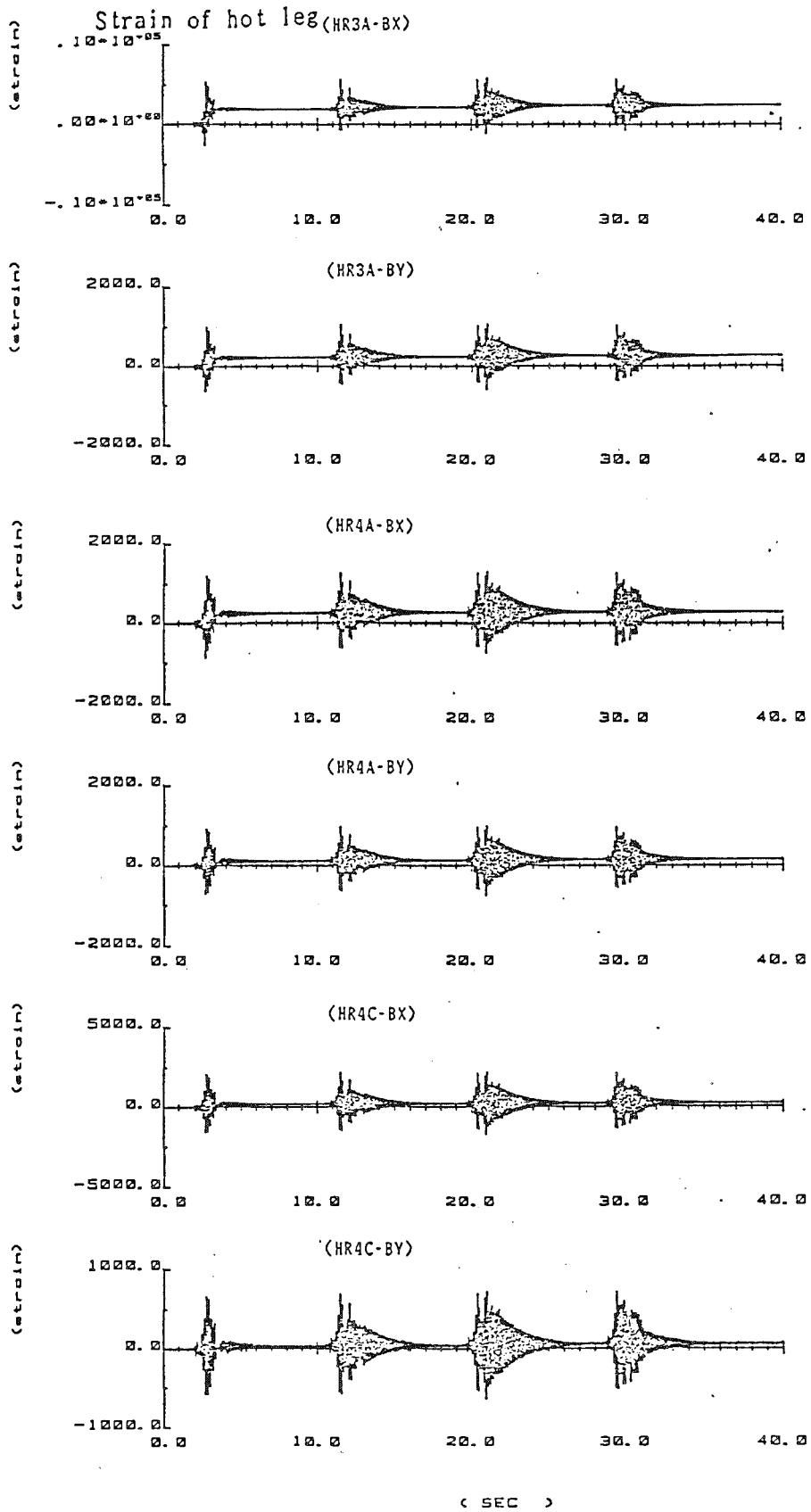
Figure D.12 (3)   Time History of Response
(Run 5 ; 0.2 MPR)

D-27
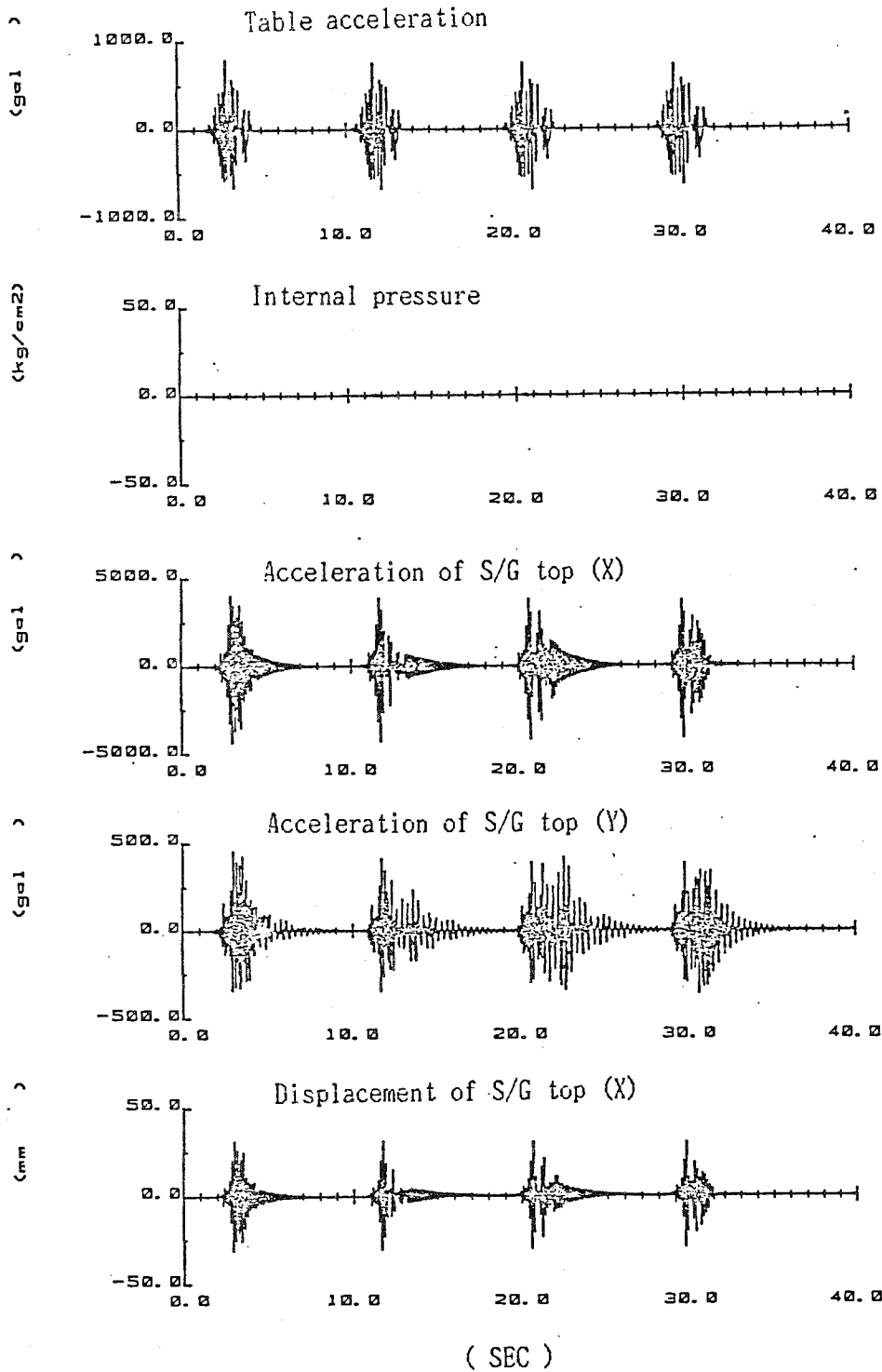
Figure D.12 (4)   Time History of Response
                  (Run 8 ; 0.4 MPR)
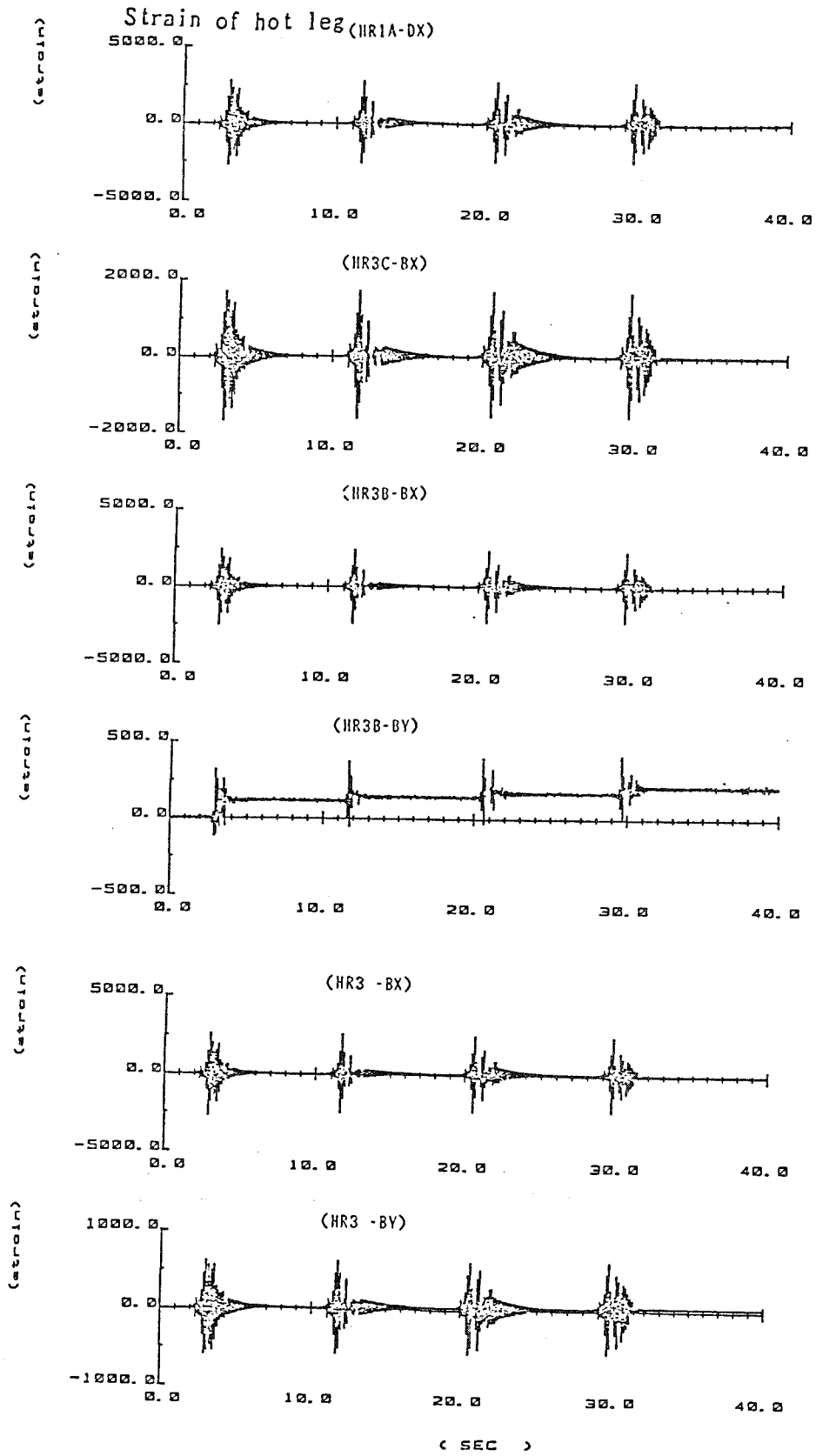
Figure D.12 (5)   Time History of Response
(Run 8 ; 0.4 MPR)

D-29

Strain of hot leg (HR3A-BX)
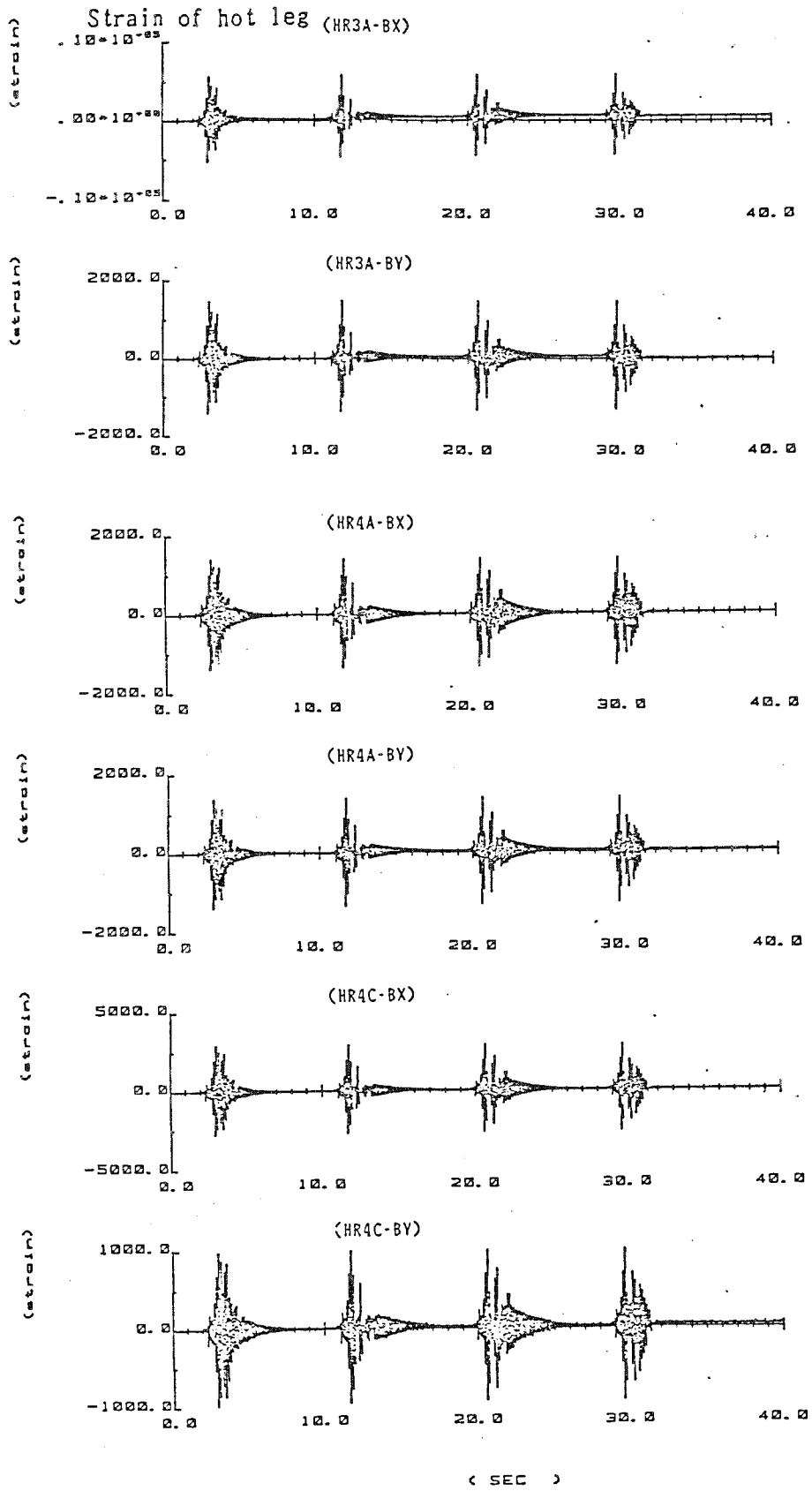
Figure D.12 (6)   Time History of Response
(Run 8 ; 0.4 MPR)
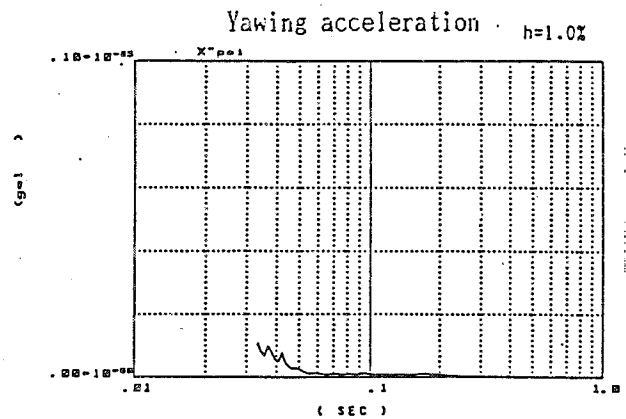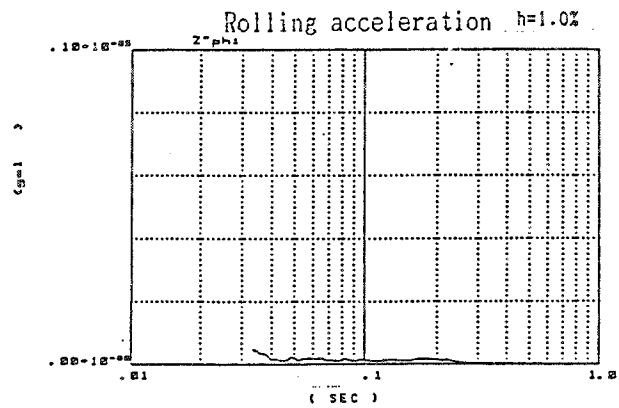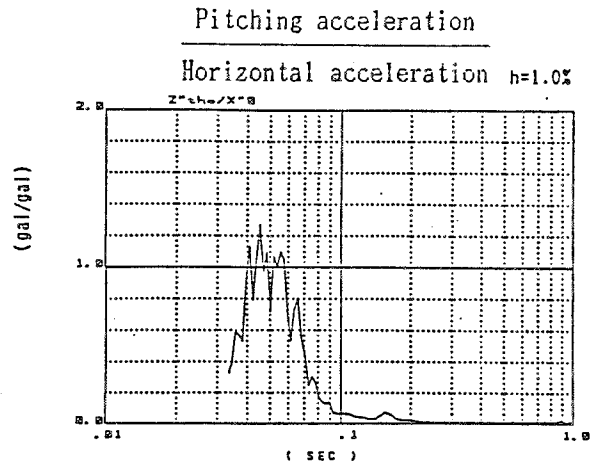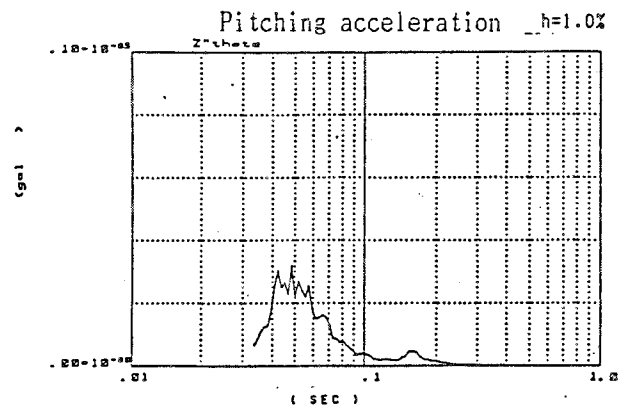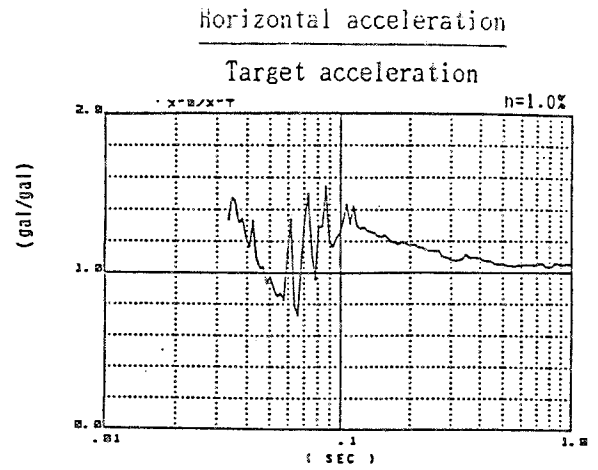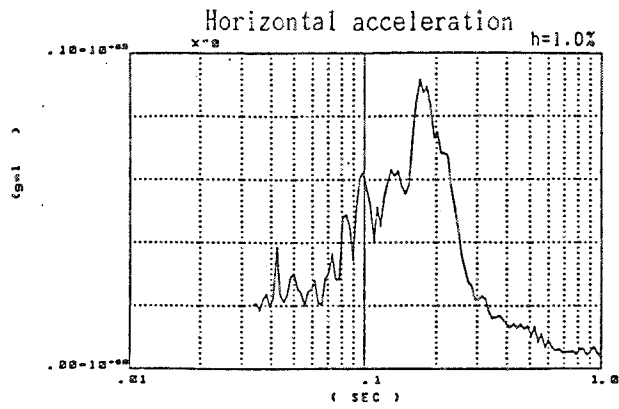
Figure D.13 (1)   Response Spectrum
                   (Run 8** ; Freq. shifted
                   0.4 MPR)
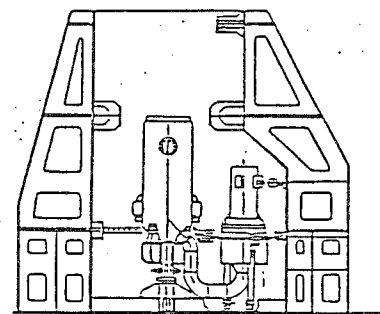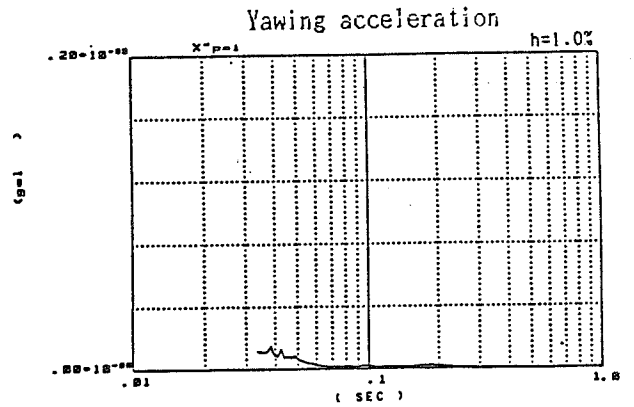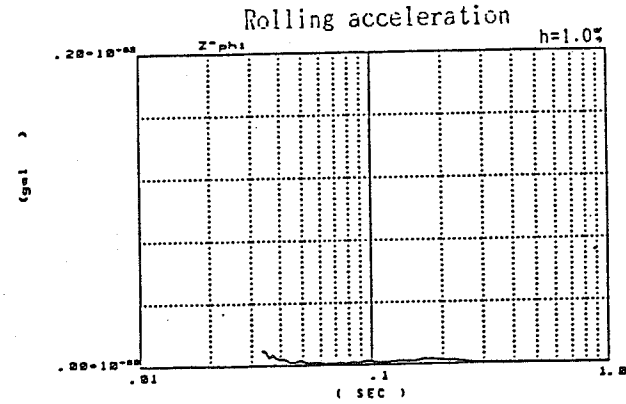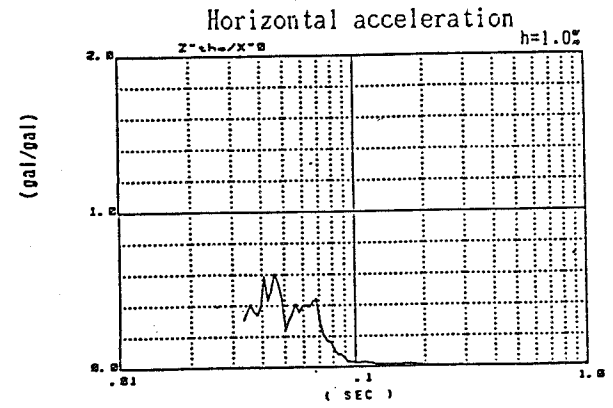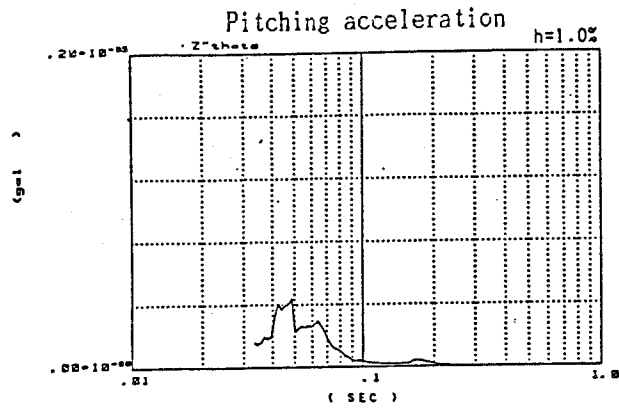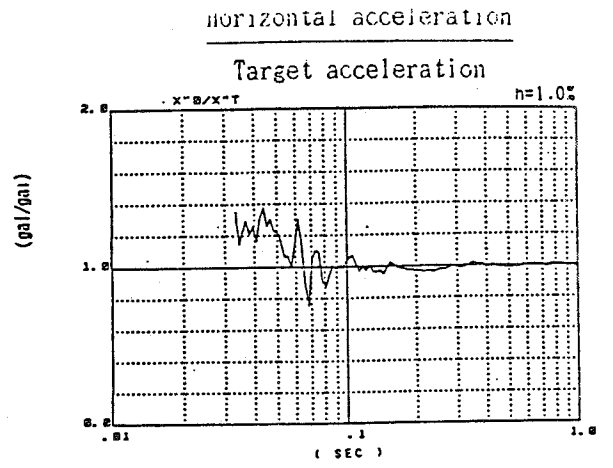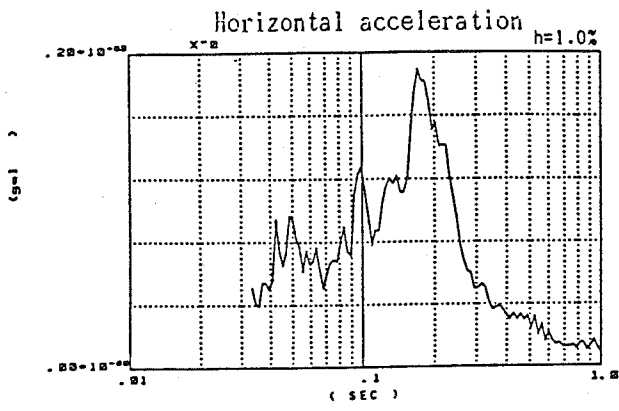
Figure D.13 (2)   Response Spectrum
(Run 11, 1.0 MPR, 2nd
Run)

Horizontal acceleration   h=1.0%

Target acceleration   h=1.0%

Pitching acceleration   h=1.0%

Pitching acceleration

Horizontal acceleration   h=1.0%

Rolling acceleration   h=1.0%

Yawing acceleration   h=1.0%
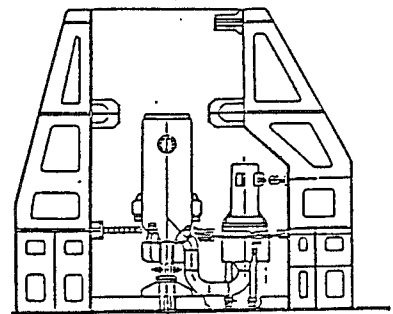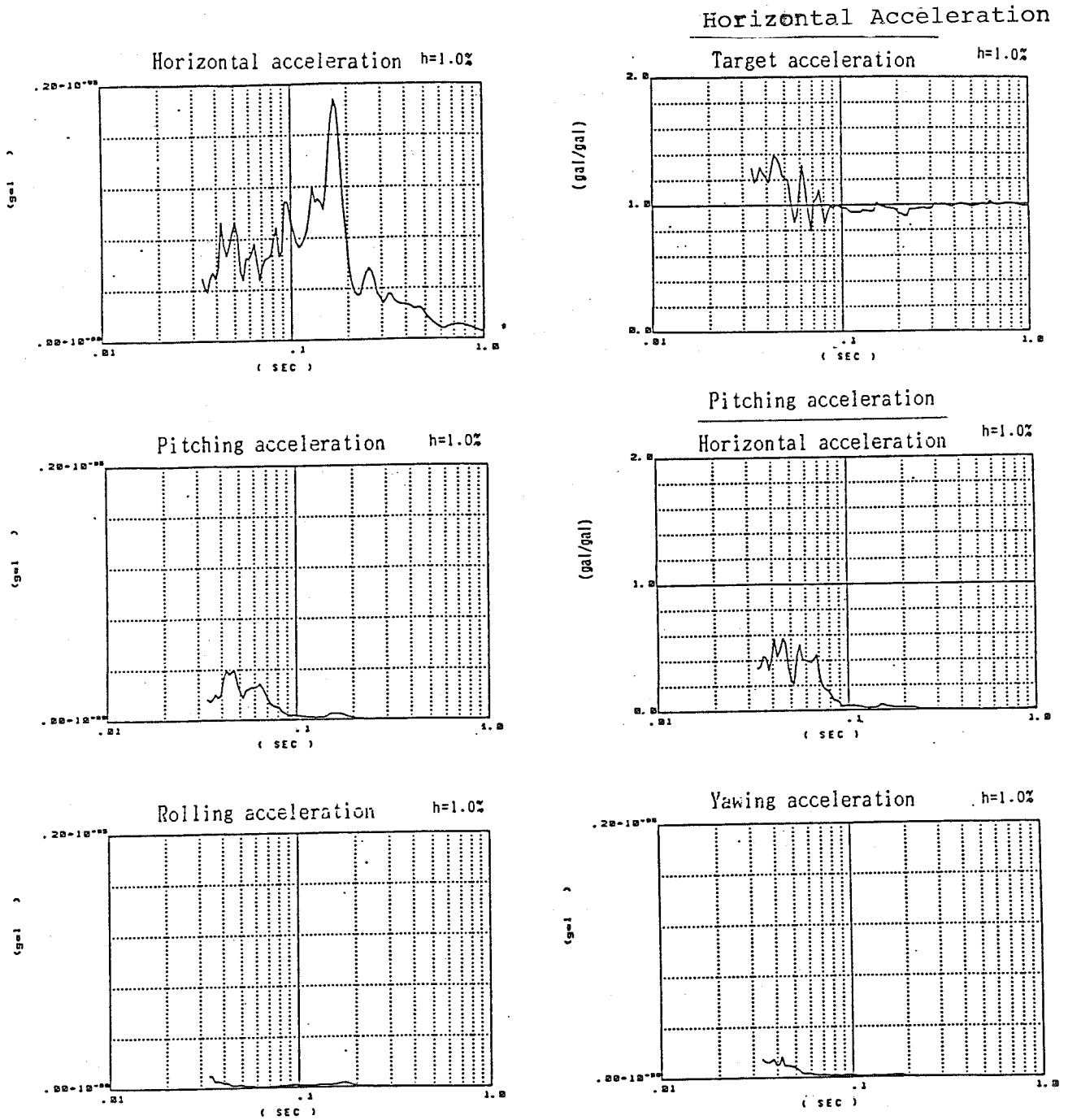
Figure D.13 (3)   Response Spectrum
(Run 14' ; 1.0 MPR, 5th Run)
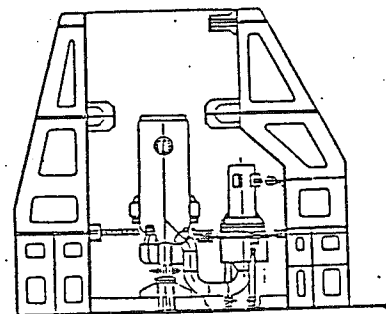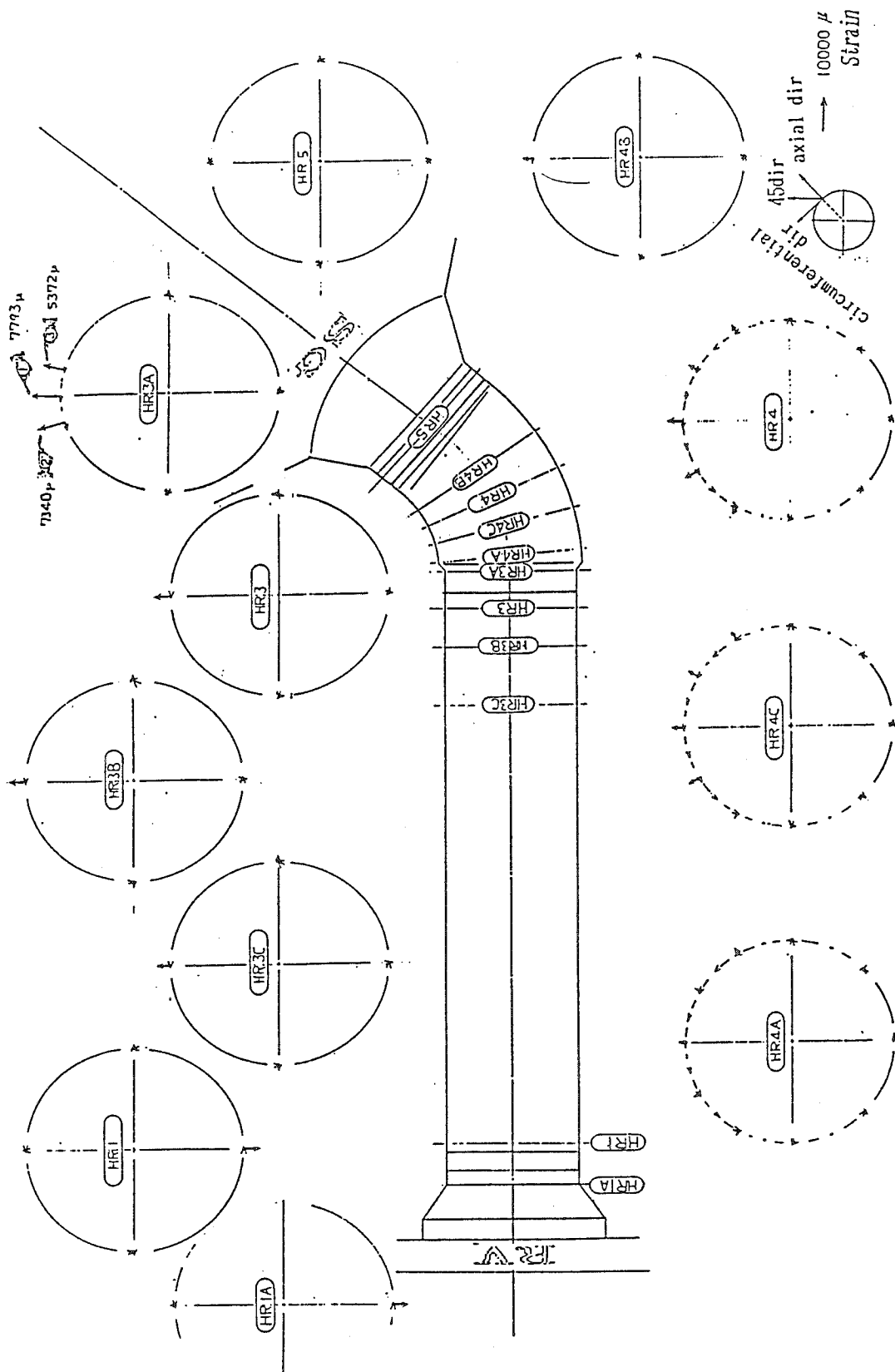
Figure D.14 (1) Maximum Response Distribution
(Strain of Hot Leg, Run 8**; Freq. shifted 0.4 MPR)
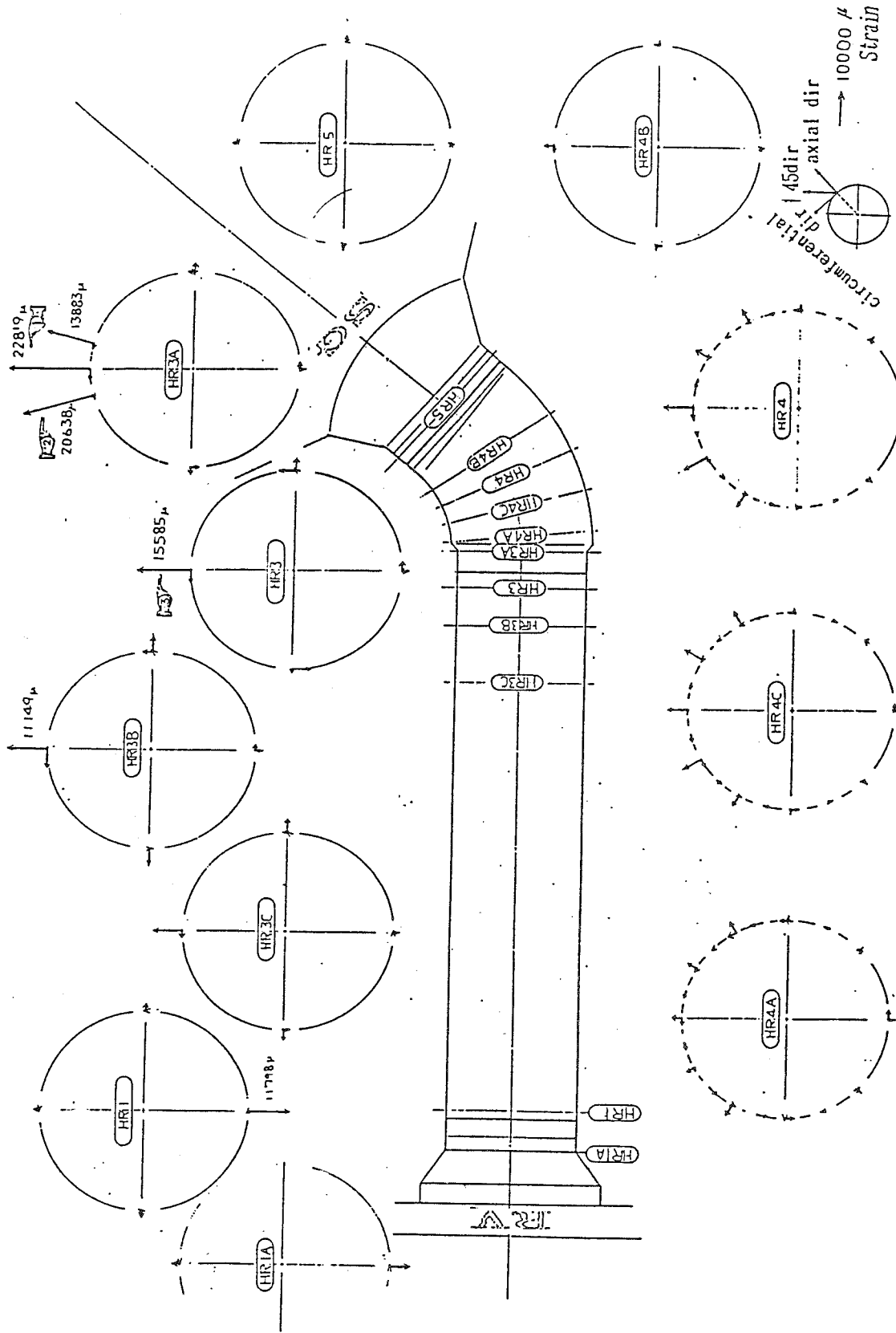
Figure D.14 (2)   Maximum Response Distribution
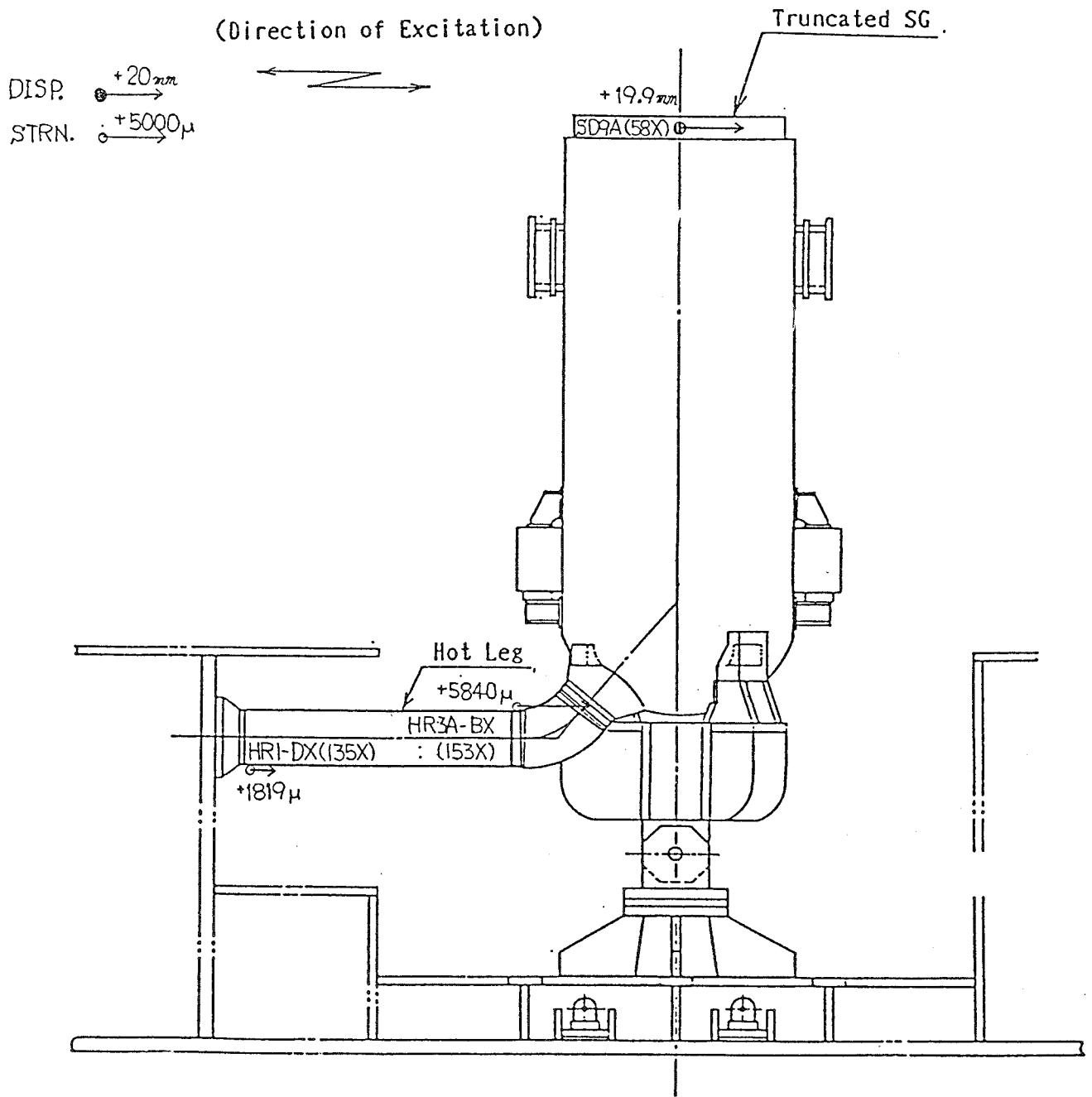(Strain of Hot Leg, Run 11 ; 1.0 MPR, 2nd Run)

D-35

Figure D.14 (3)   Maximum Response Distribution
(Strain of Hot Leg, Run 14' ; 1.0 MPR, 5th Run)

(Direction of Excitation)

Truncated SG

Disp $+50_{mm}$

STRN $+5000_{\mu}$

-38.9

SD9A
(58x)

Hot Leg

-7792.6

HR3A-BX
(153x)

HR1-DX (135x)

-3489.4
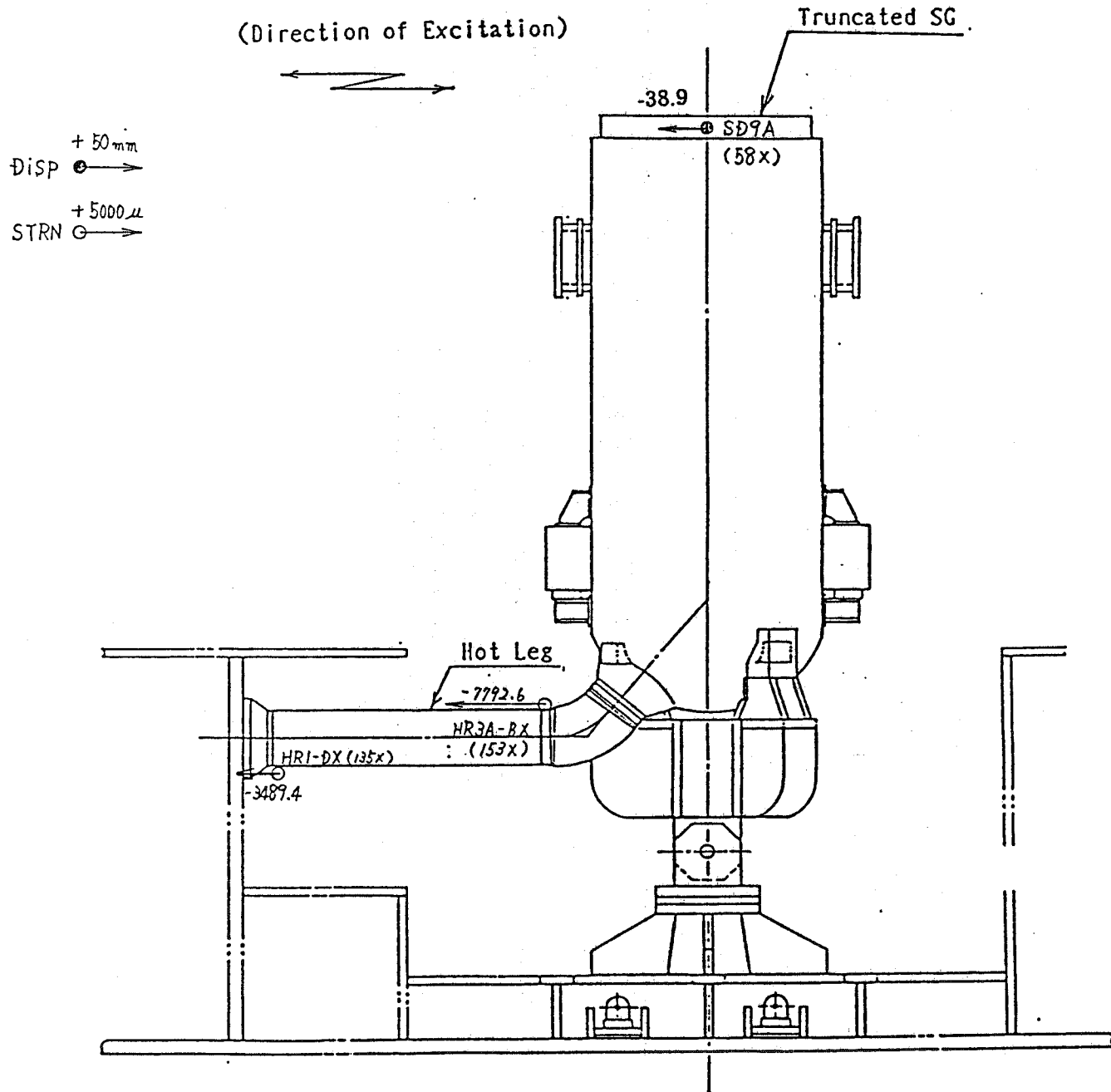
Figure D.15 (1) Instantaneous Response Distribution
(Displacement of S/G and Strain of Hot Leg,
Run 8** ; 0.4 MPR)

(Direction of Excitation)

Truncated SG

DISP $\circ\!\!\longrightarrow$ $+100_{m \cdot m}$

STRN $\circ\!\!\longrightarrow$ $+20000\mu$

-80.2

$\longleftarrow \circ$ SD 9A
(58X)

Hot Leg
-22819.1

HR3A-BX
(153X)

HR1-DX (135X)

-11744.7
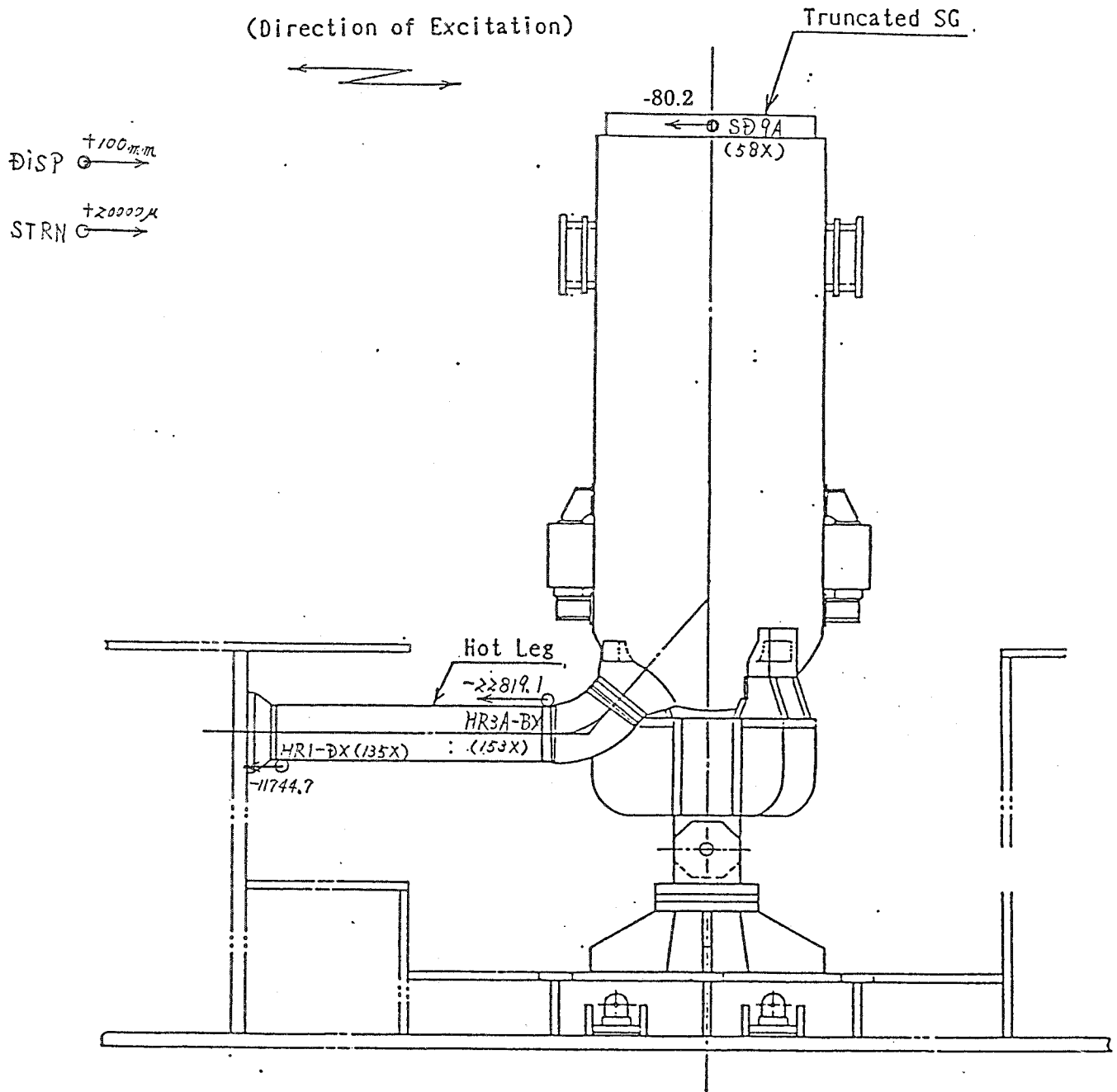
Figure D.15 (2)   Instantaneous Response Distribution
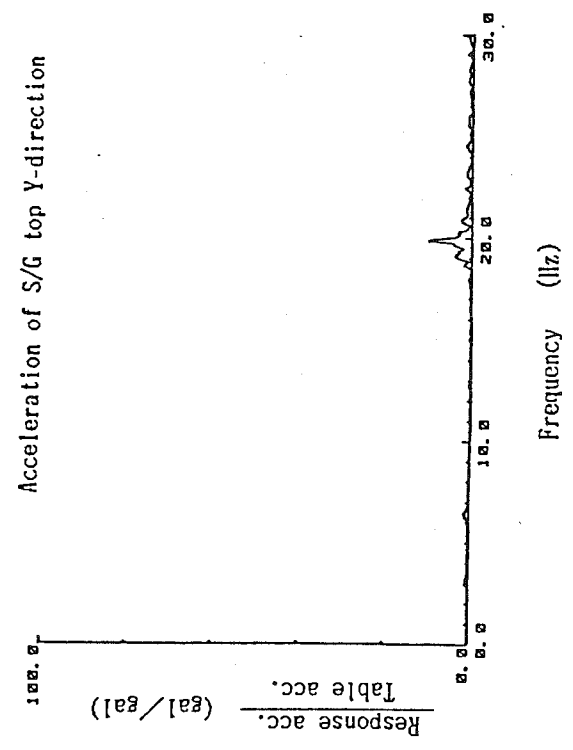(Displacement of S/G and Strain of Hot Leg,
Run 11 ; 1.0 MPR)

D-38
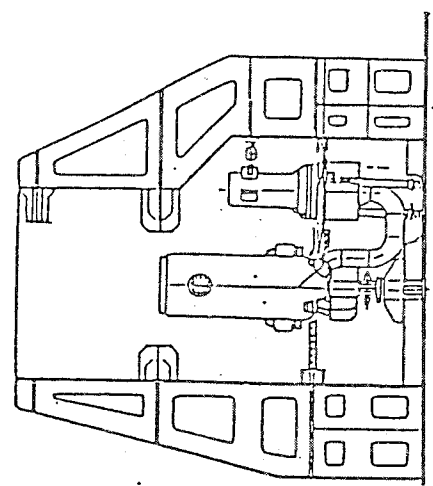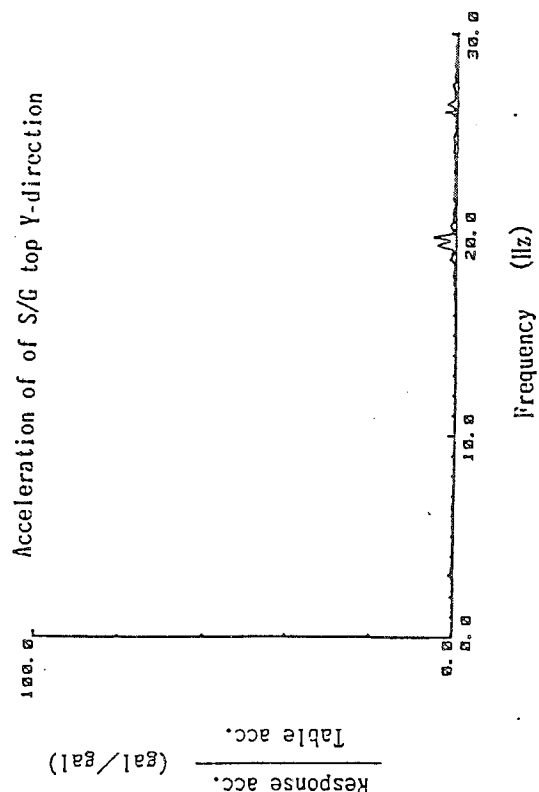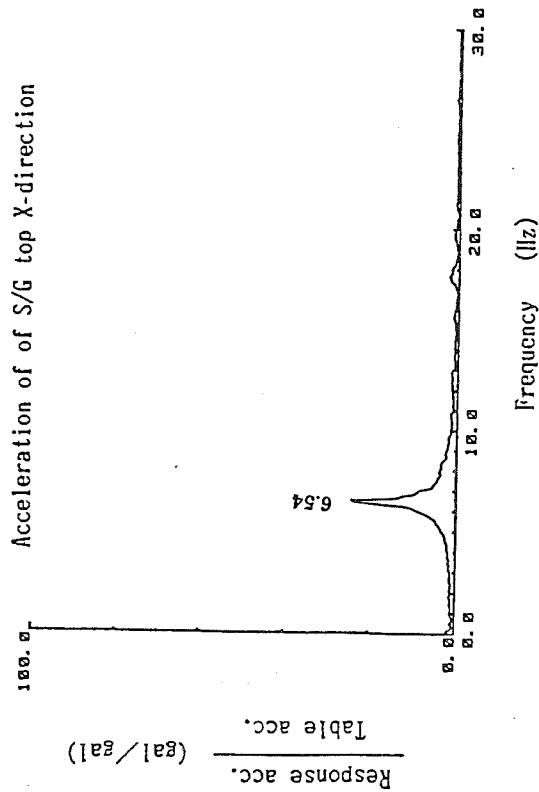
Figure D.16 (1) Transfer Function (Run 8 ; Freq. Shifted 0.4 MPR)
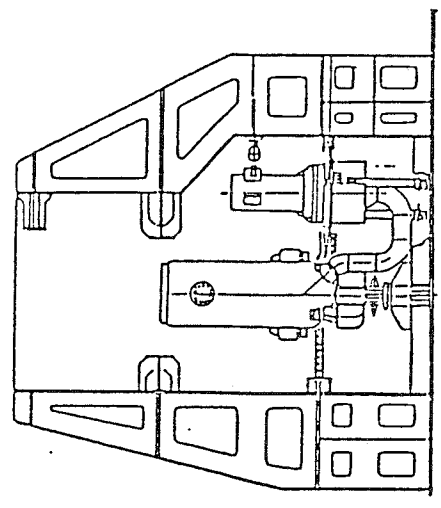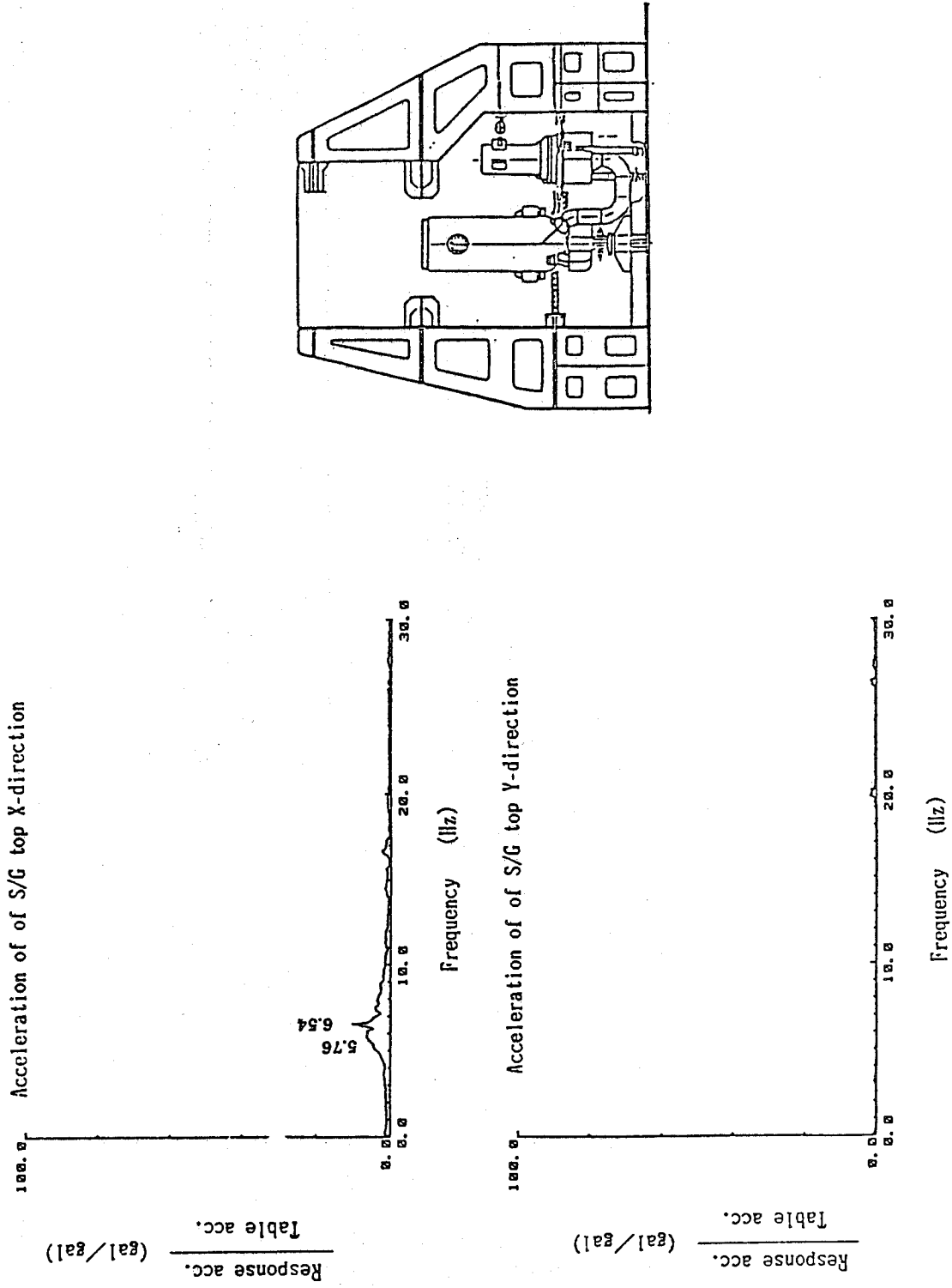
Figure D.16 (2) Transfer Function (Run 11 ; 1.0 MPR, 2nd Run)
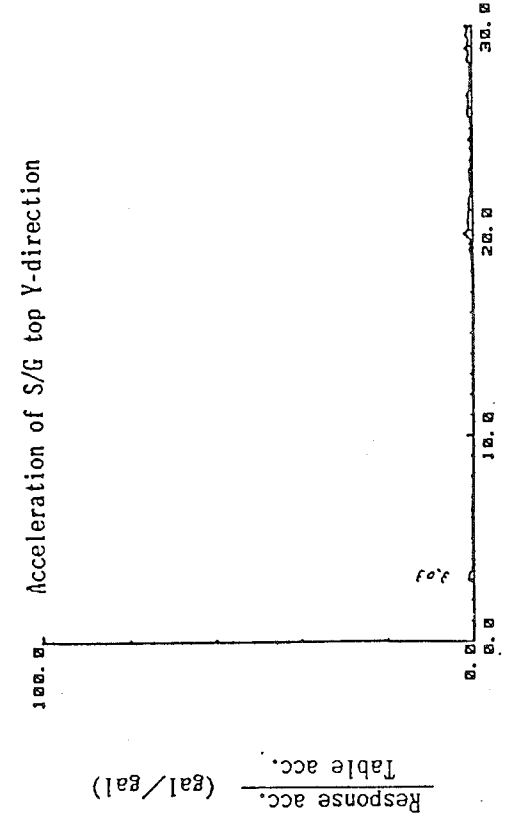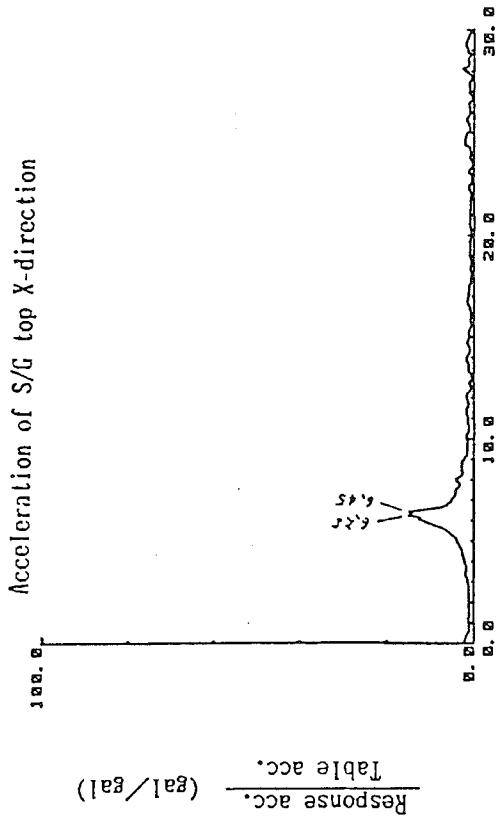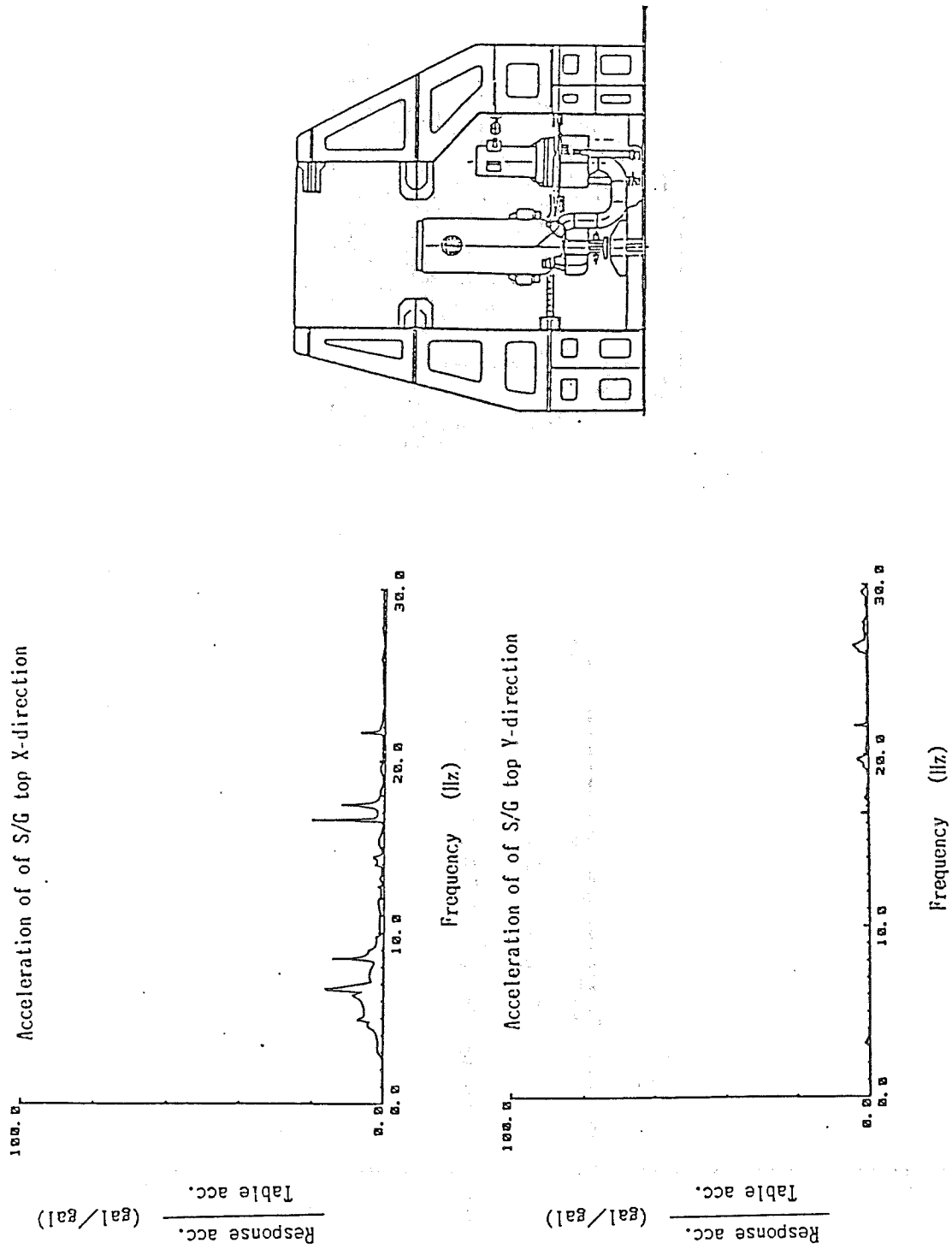
Figure D.16 (3) Transfer Function (Run 14 ; 1.0 MPR, 5th Run)

A Segment

B Segment

C Segment

D Segment

Inertial force of S/G (TON)

Inartial force of S/G (Ton)

Displacement of S/G Top
whole segment

Displacement of S/G Top
maximum one cycle
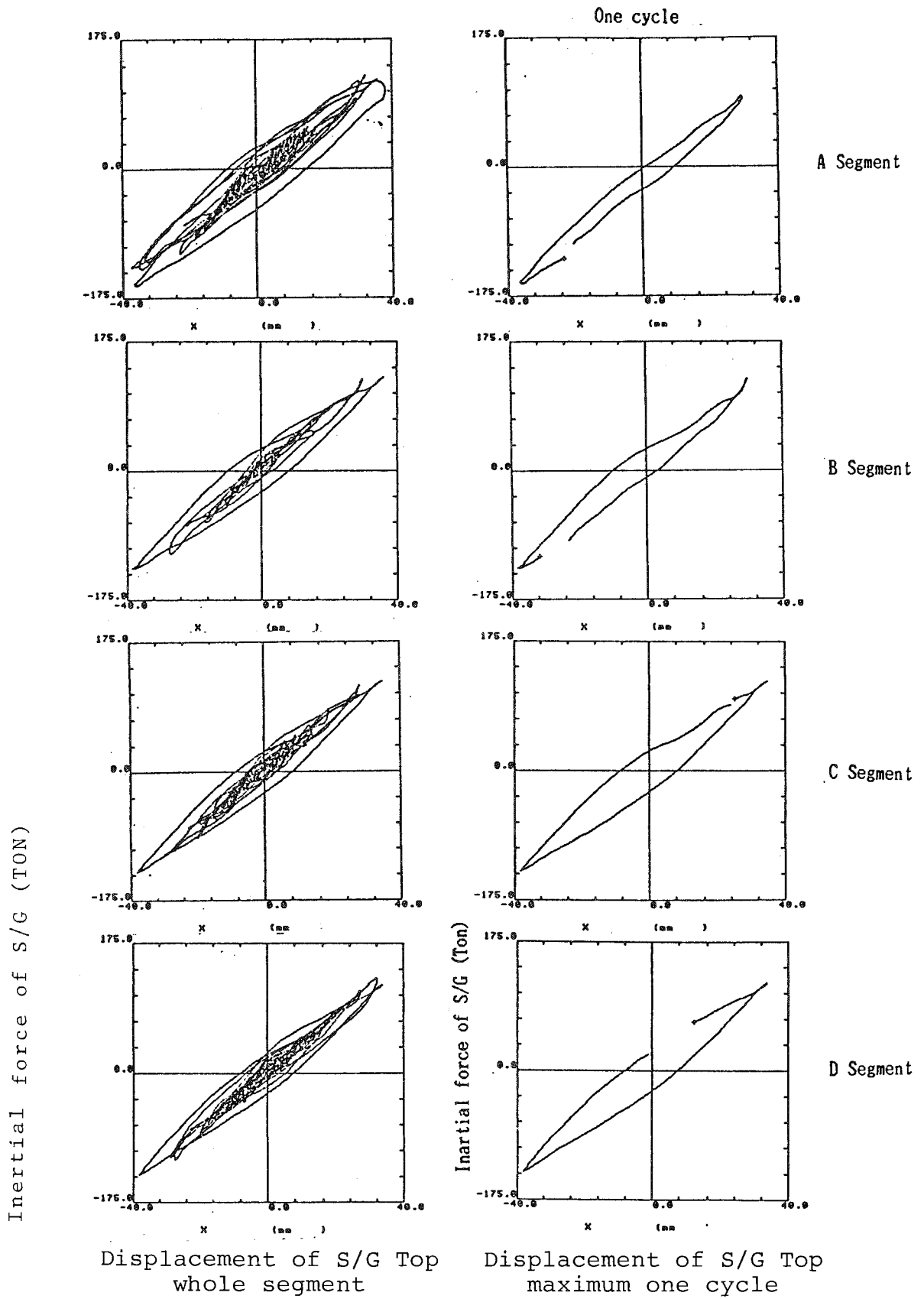
Figure D.17 (1)   Hysteresis Loop of Force and Displacement
of S/G (Run 8**; Freq. Shifted 0.4 MPR)

One cycle

A Segment

B Segment

ʟ Segment

D Segment

Inertial force of S/G (TON)

Displacement of S/G Top
whole segment

Displacement of S/G Top
maximum one cycle
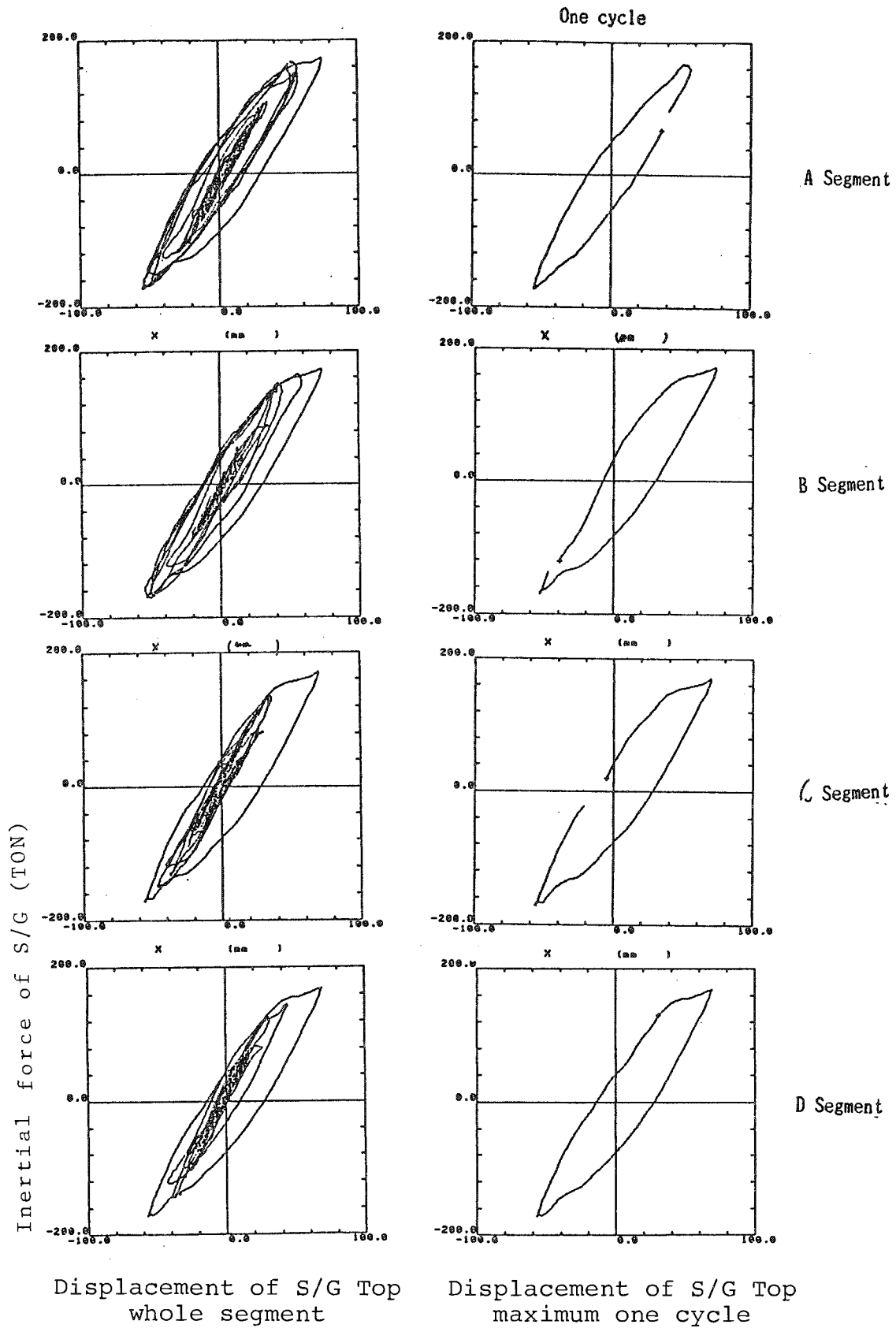
Figure D.17 (2)   Hysteresis Loop of Force and Displacement
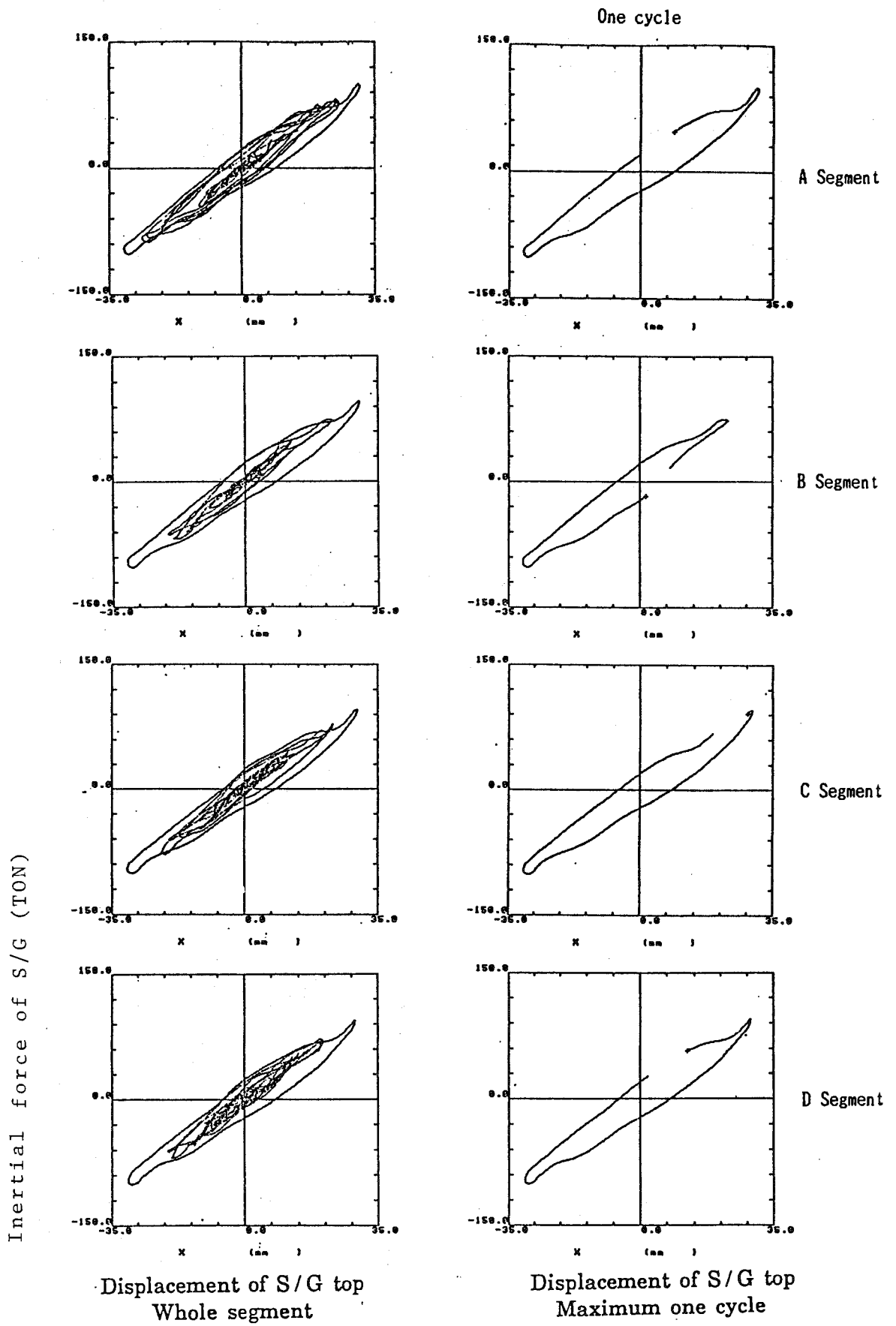of S/G (Run 11; 1.0 MPR, 2nd Run)
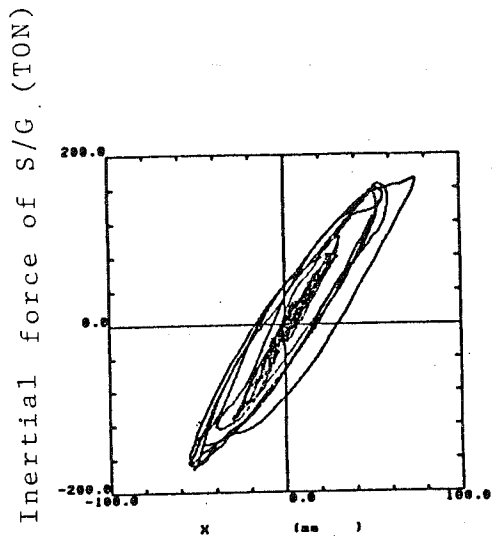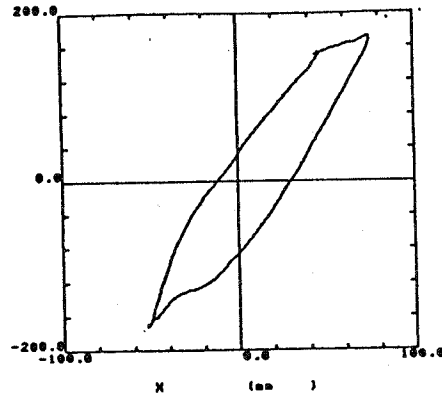
Figure D.17 (3)   Hysteresis Loop of Force and Displacement of S/G
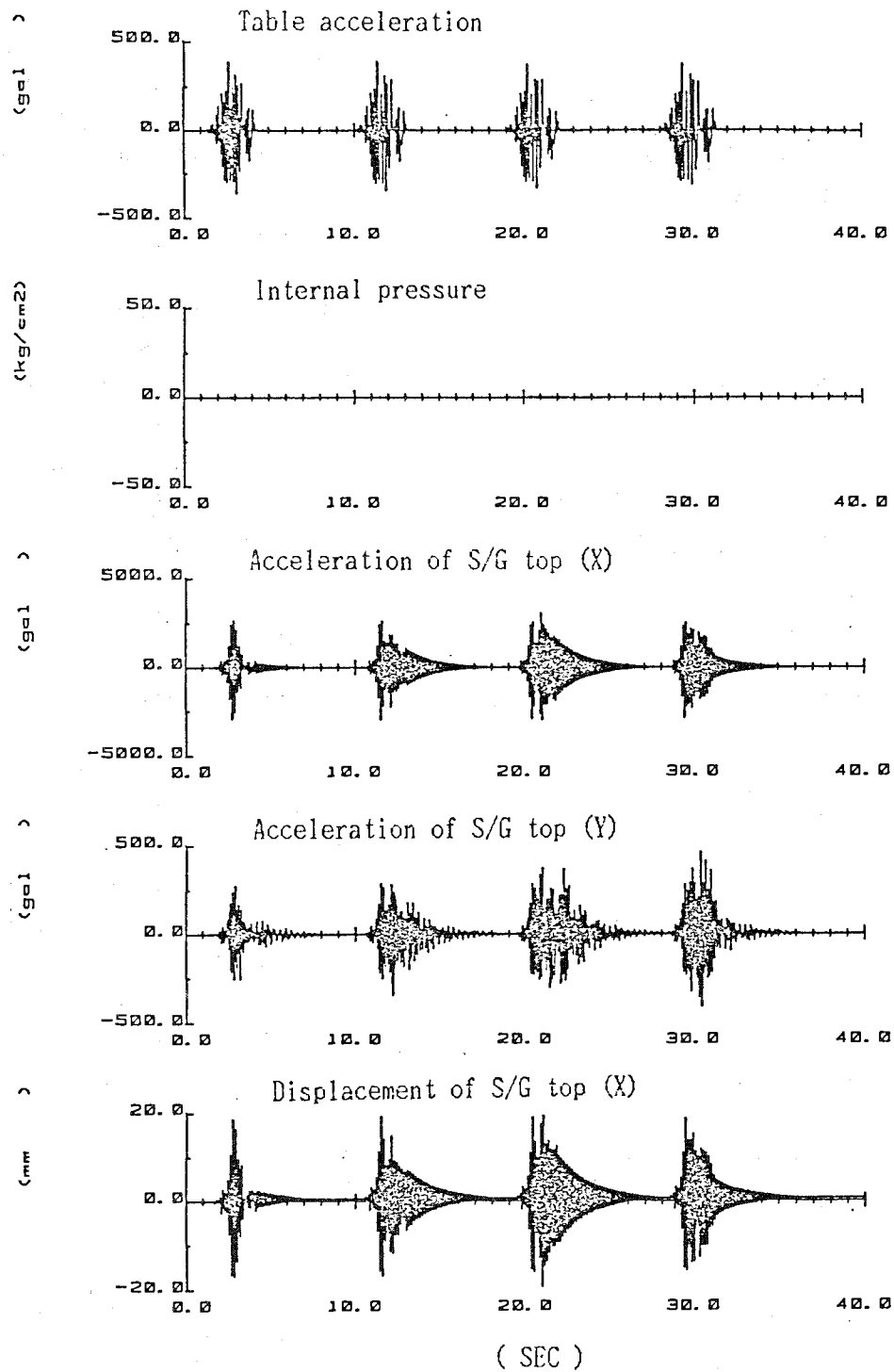   (Run 14' ; 1.0 MPR, 5th Run)
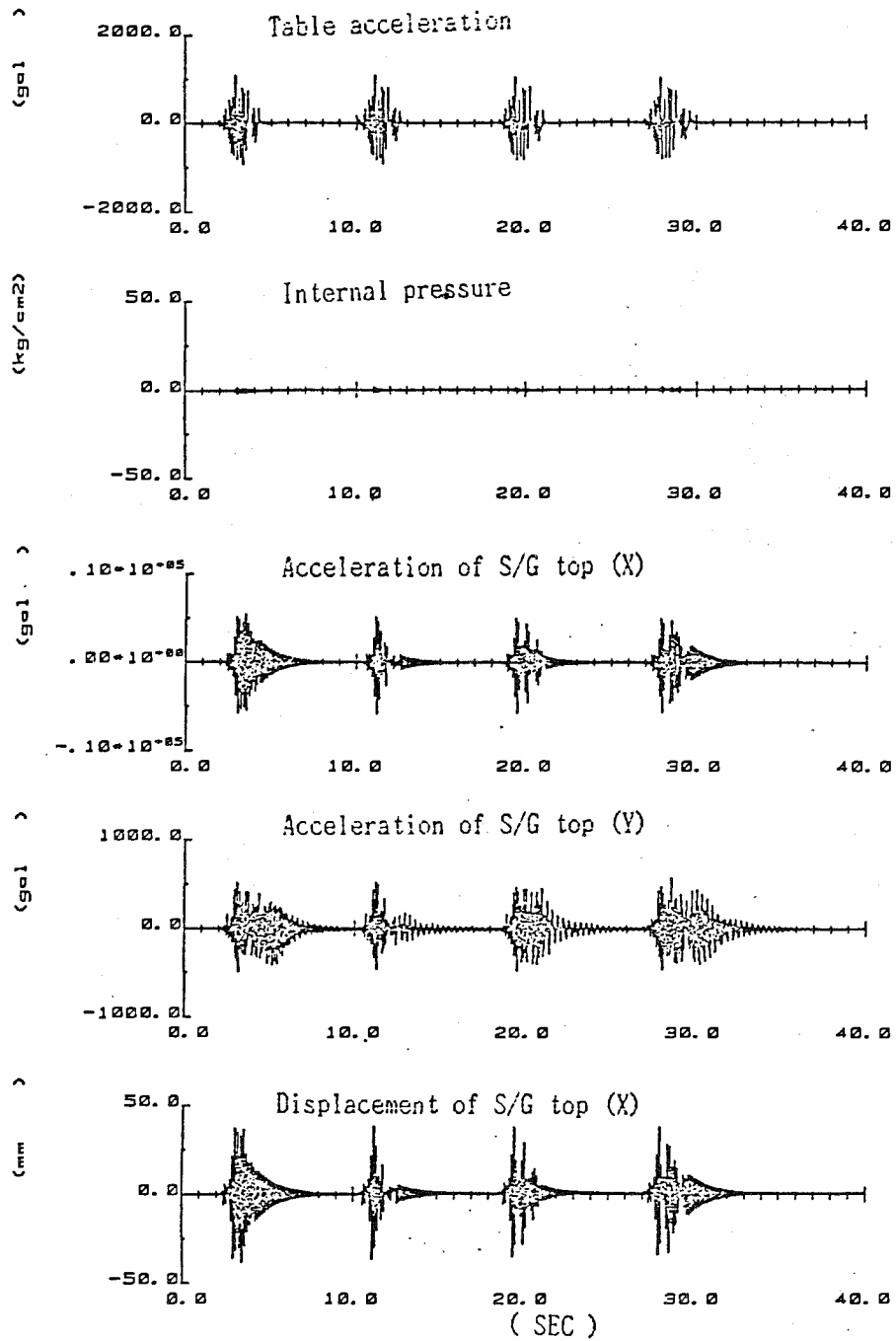
Figure D.18 (1)   Time History of Response
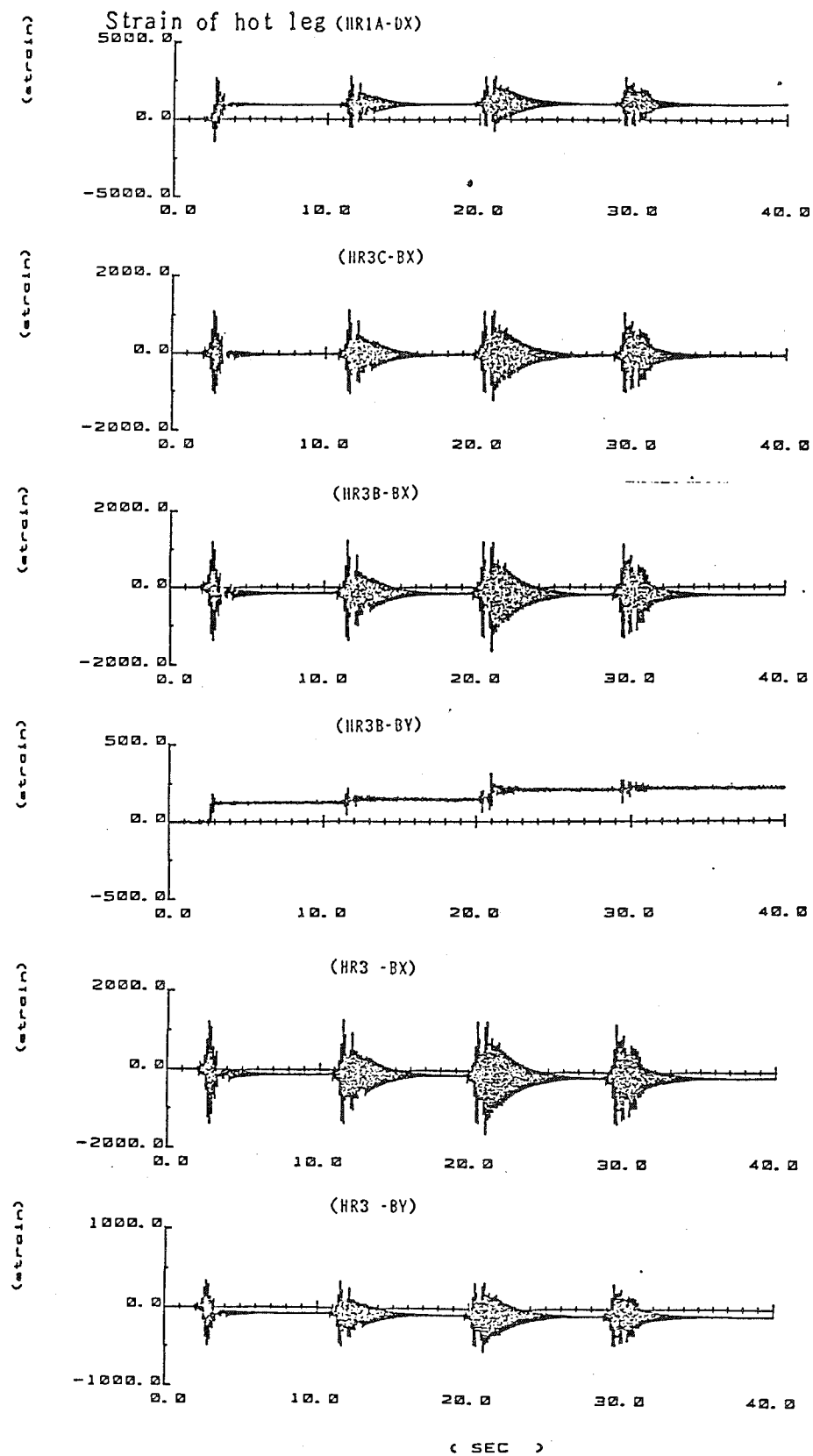   (Run 8** ; Freq. Shifted 0.4 MPR)
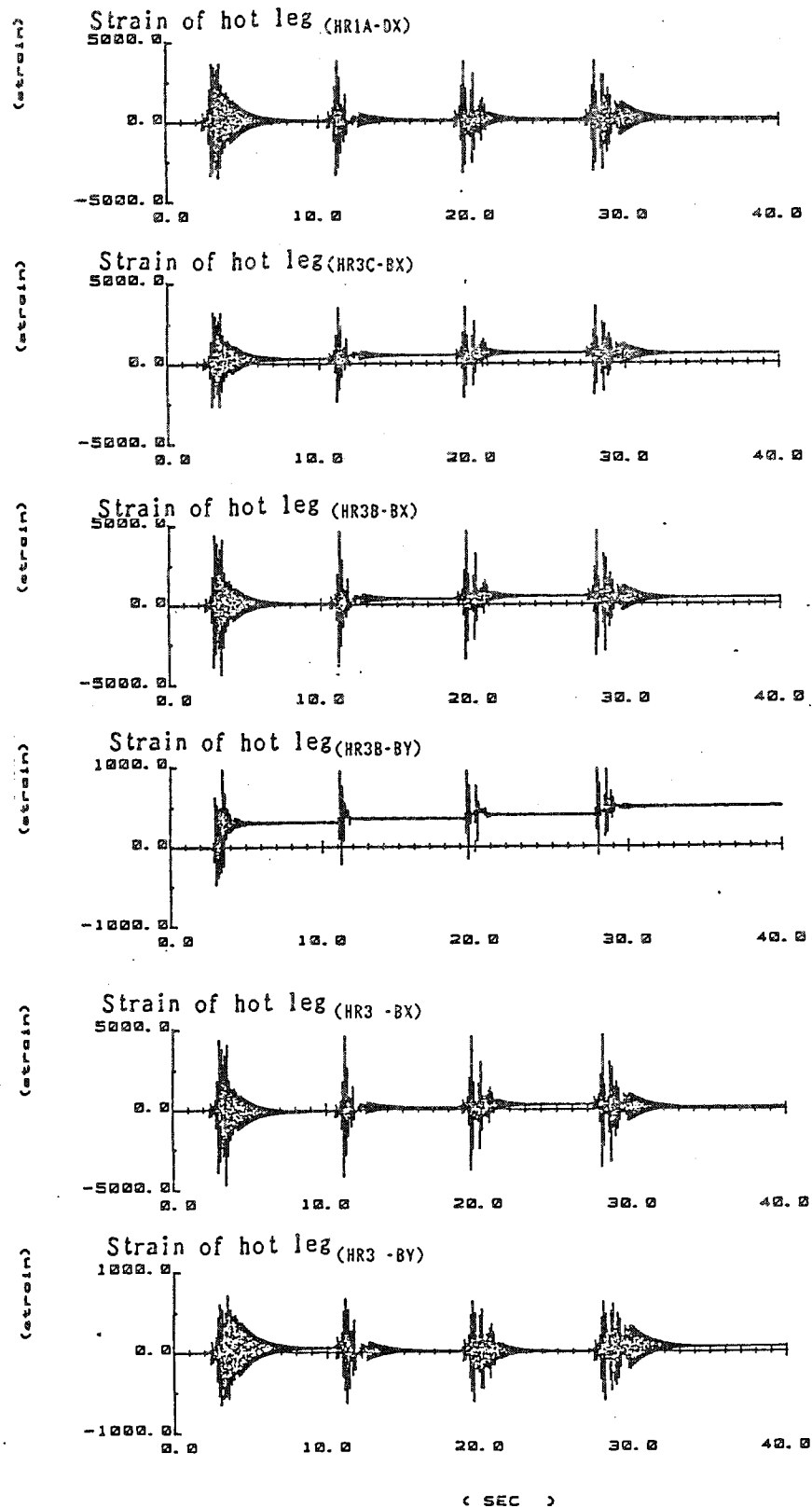
Figure D.18 (2)   Time History of Response
(Run 8**; Freq. Shifted 0.4 MPR)

D-46
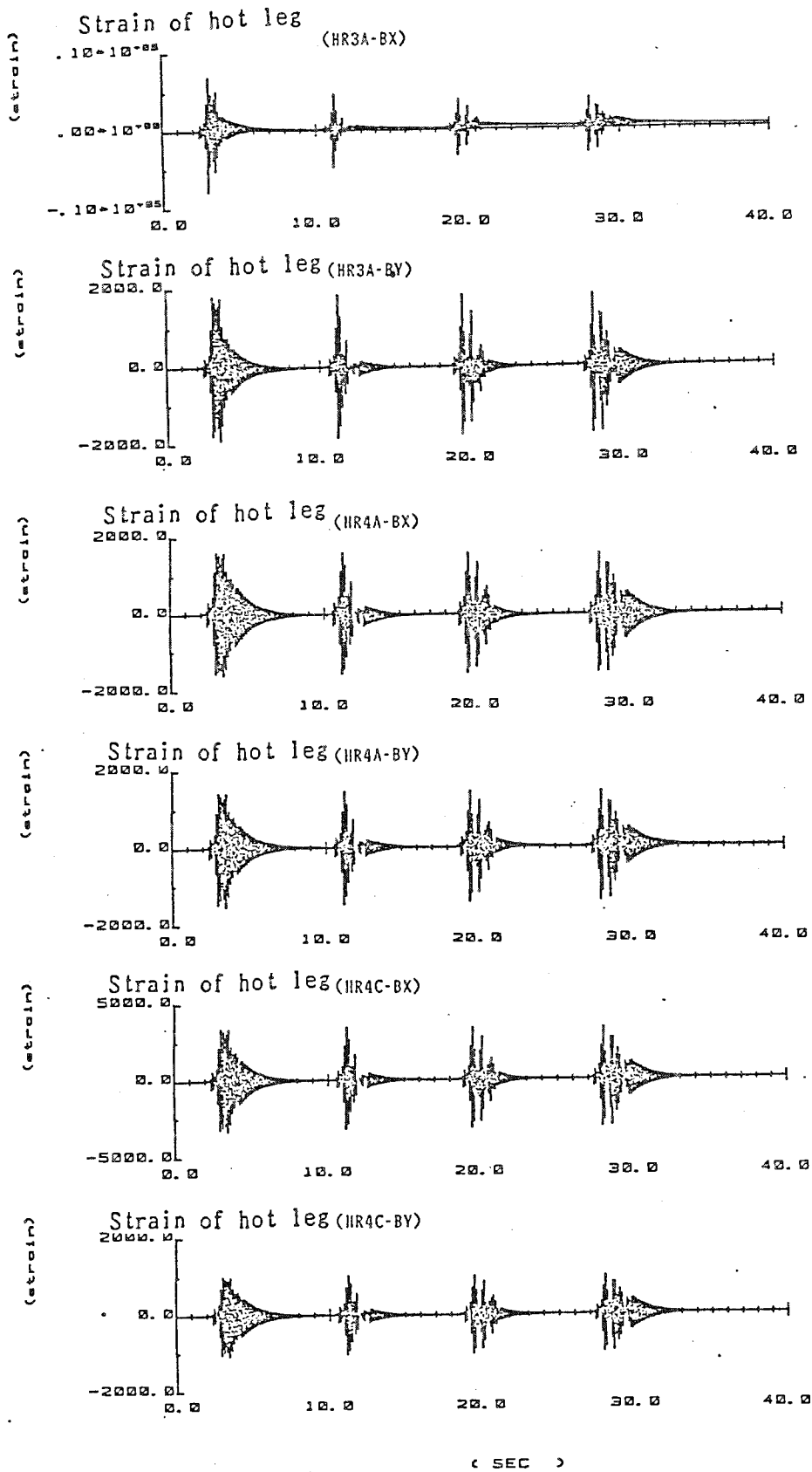
Figure D.18 (3)　Time History of Response
(Run 8** ; Freq. Shifted 0.4 MPR)

D-47
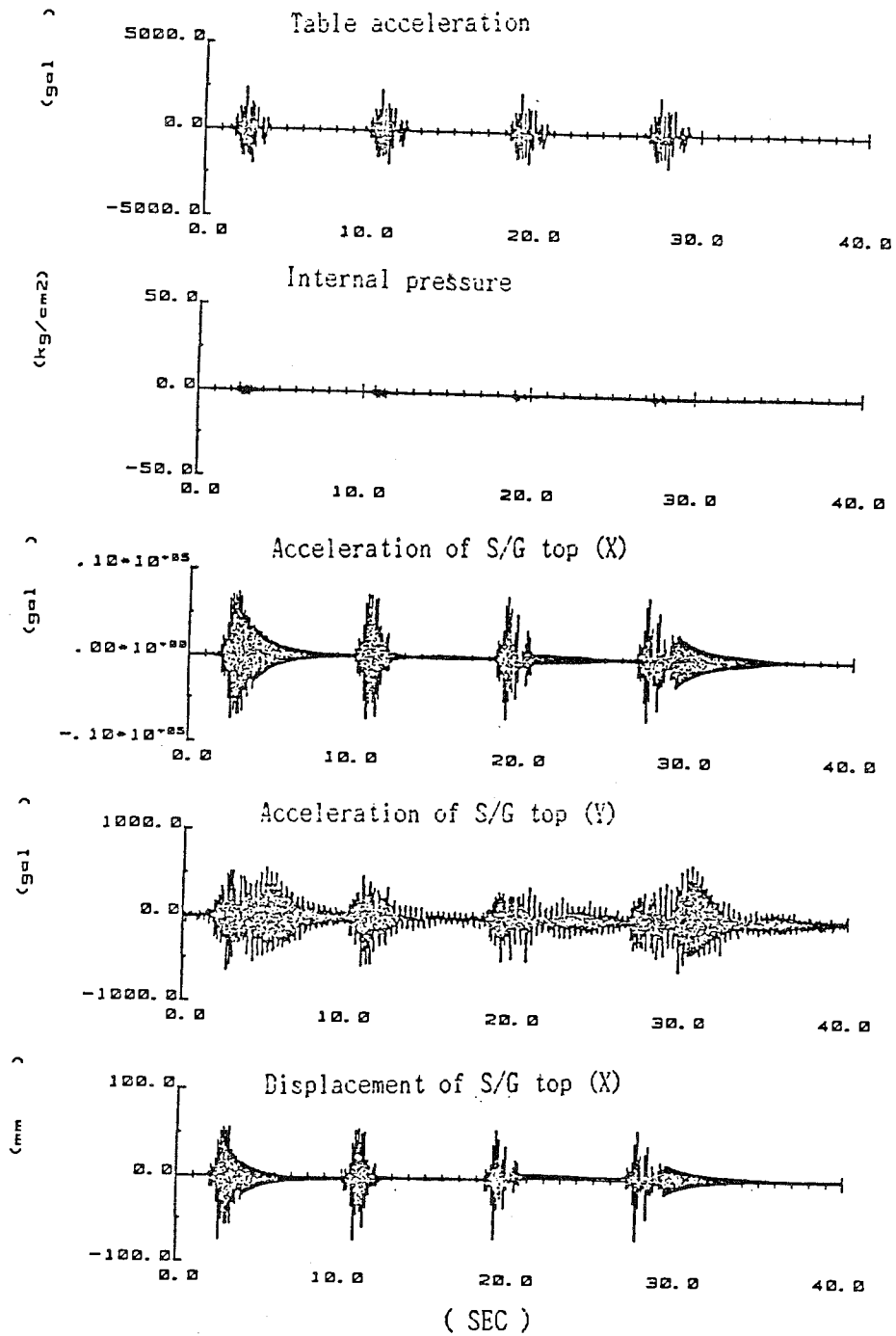
Figure D.18 (4) Time History of Response
(Run 8** ; Freq. Shifted 0.4 MPR)

Figure D.18 (5)   Time History of Response
(Run 11 ; 1.0 MPR, 2nd Run)

D-49
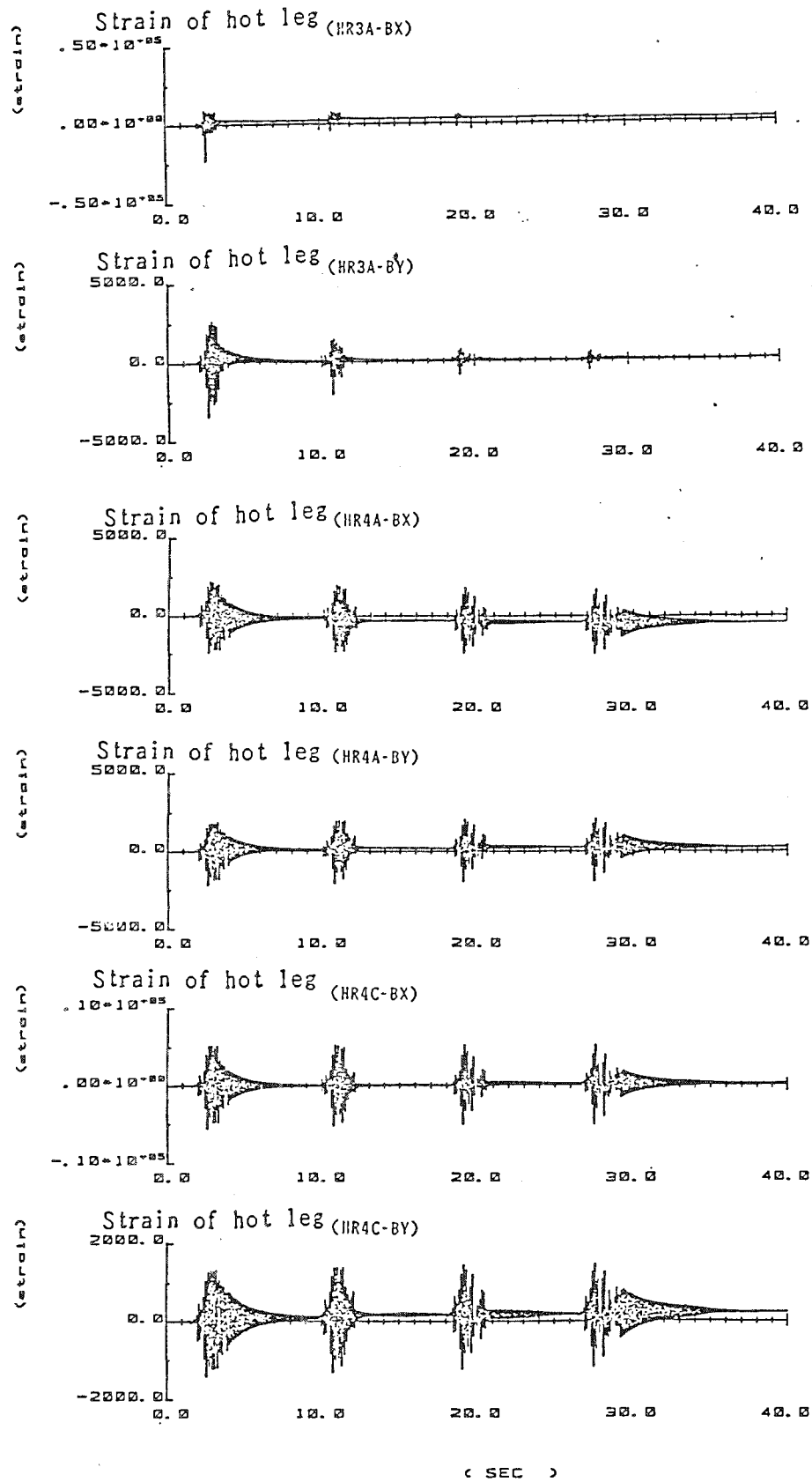
Figure D.18 (6)   Time History of Response
(Run 11 ; 1.0 MPR, 2nd Run)
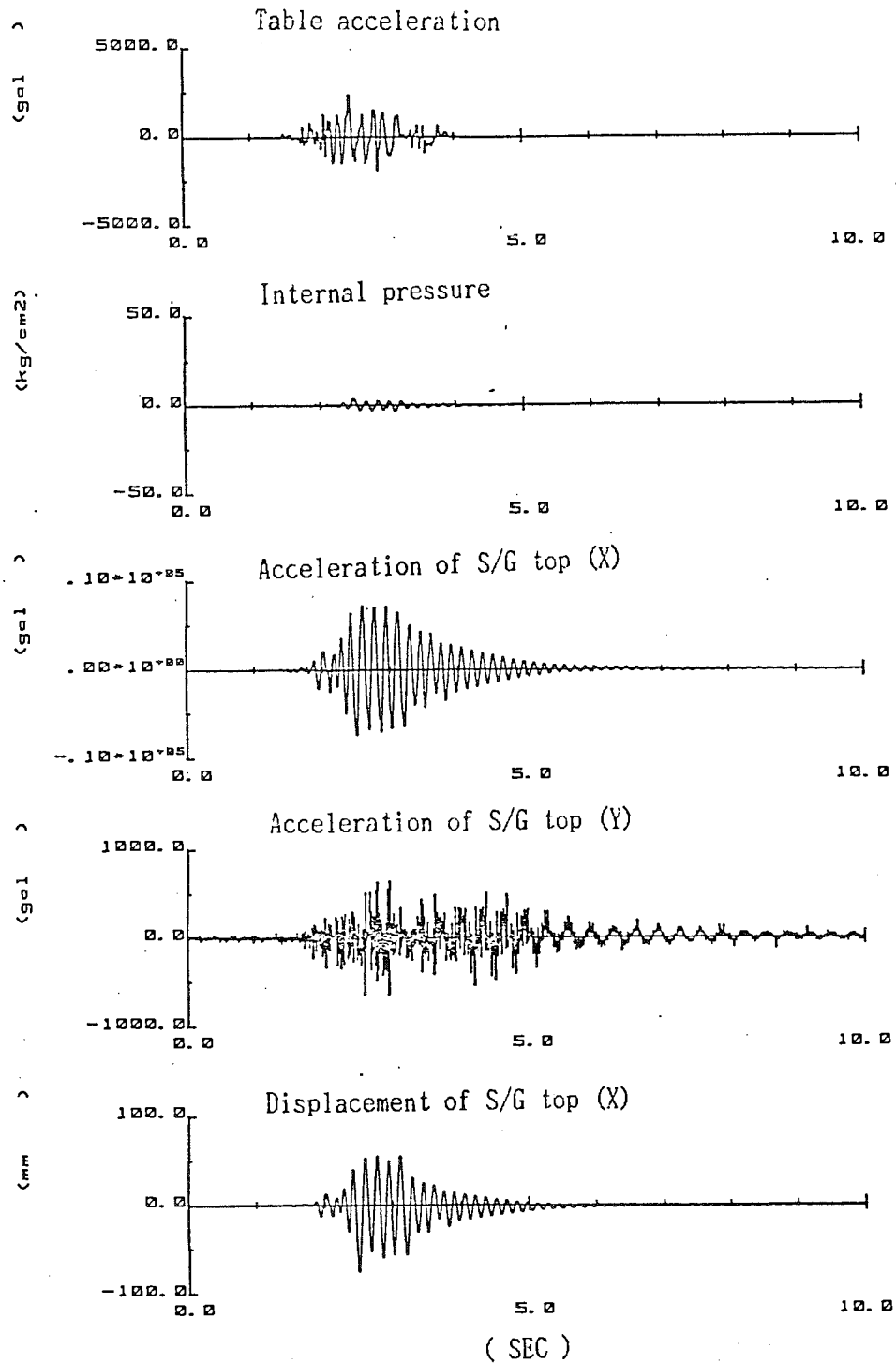
Figure D.18 (7)   Time History of Response
(Run 14' ; 1.0 MPR, 5th Run)
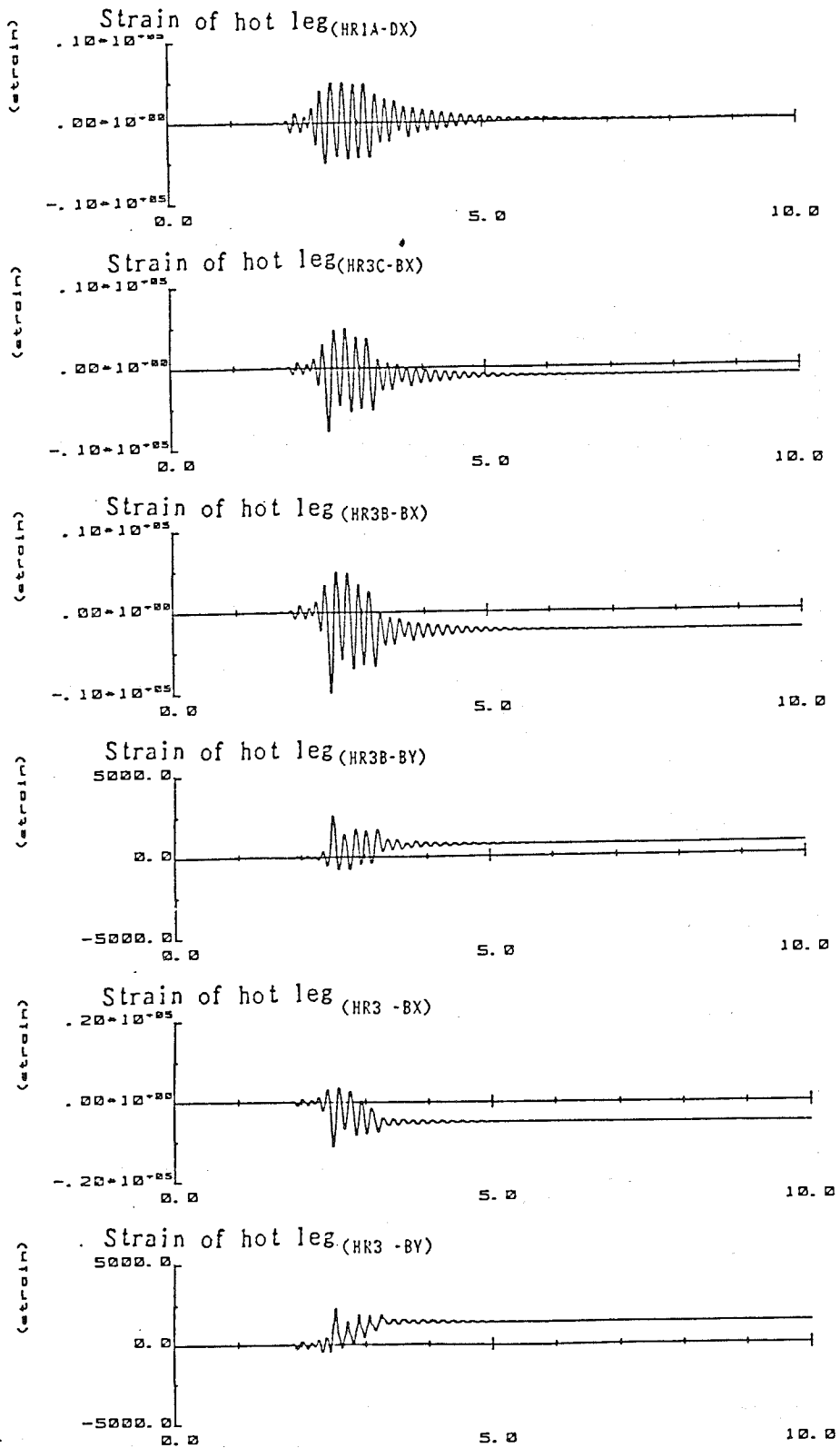
Figure D.18 (8)   Time History of Response
                   (Run 14' ; 1.0 MPR, 5th Run)
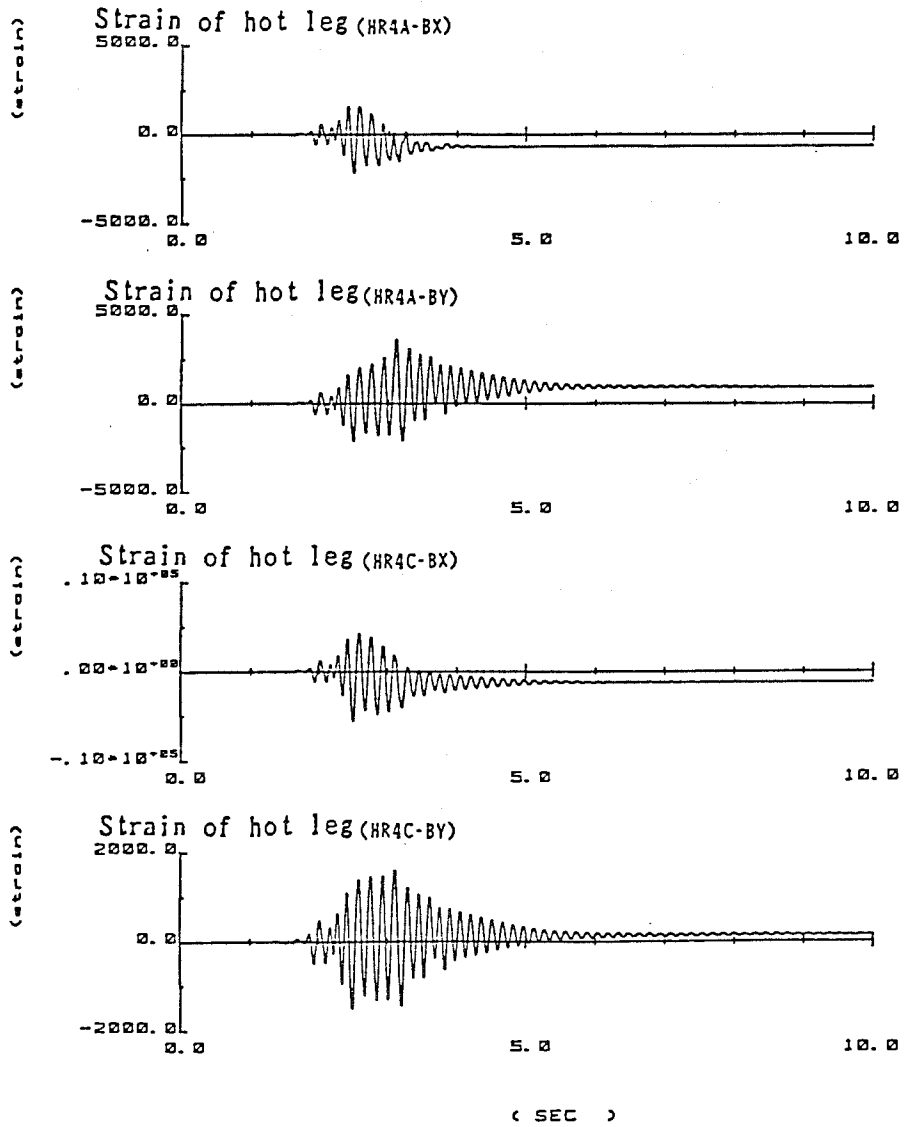
Figure D.18 (9)   Time History of Response
                  (Run 14' ; 1.0 MPR, 5th Run)
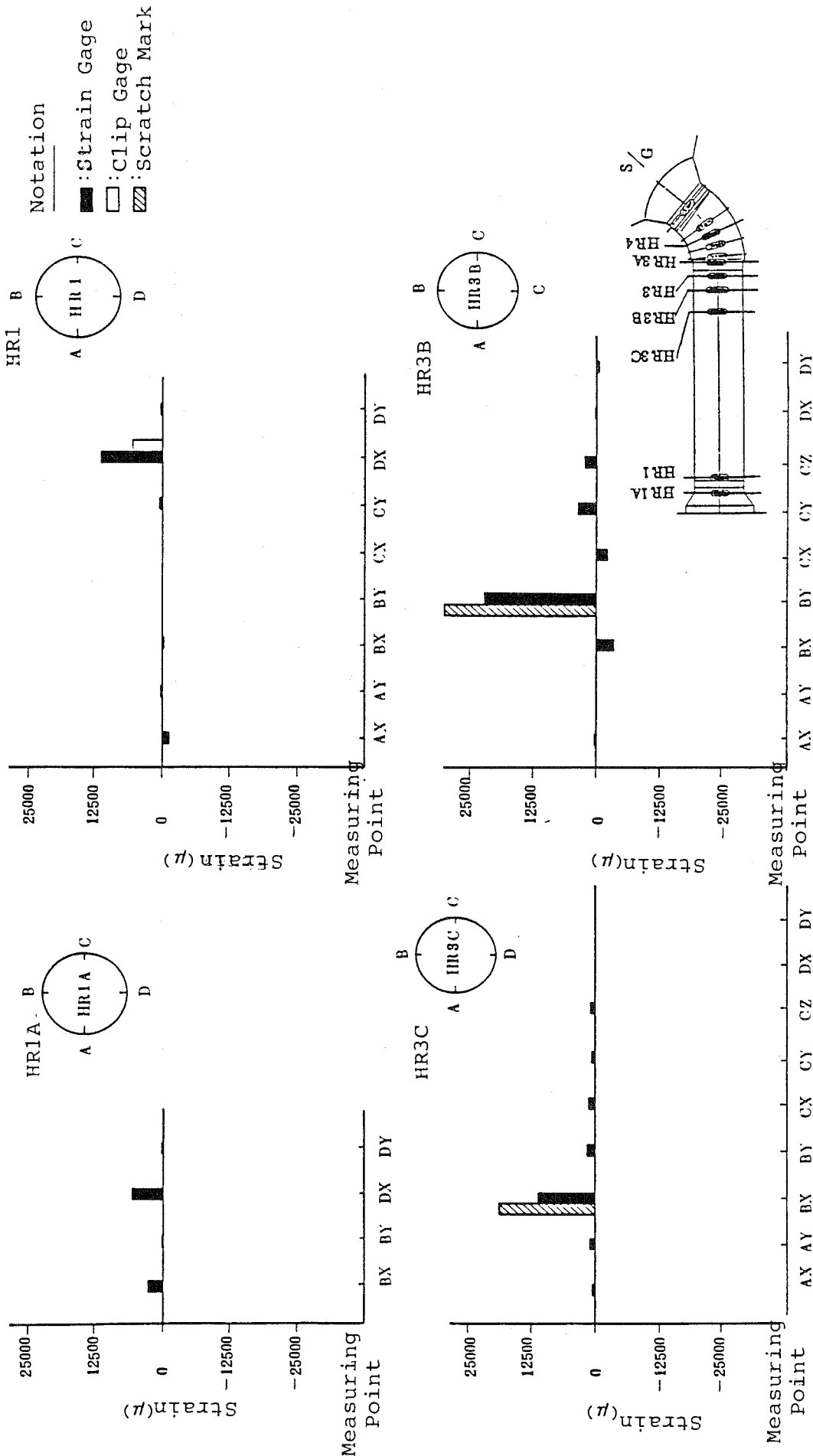
Figure D.19 (1)　Cumulative Strain in Hot Leg Pipe
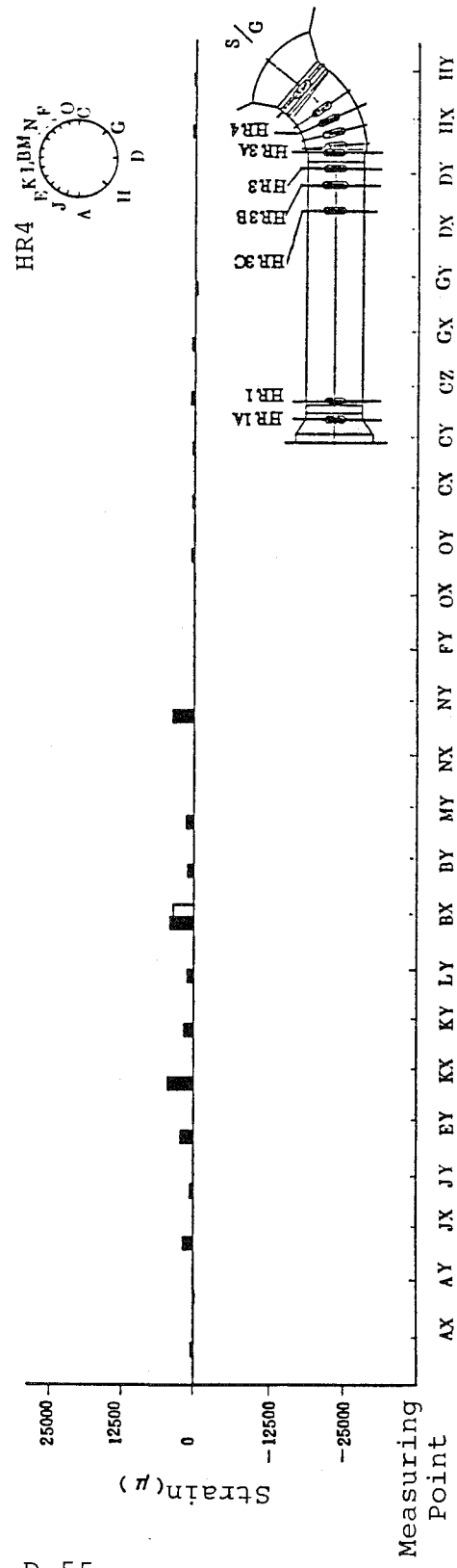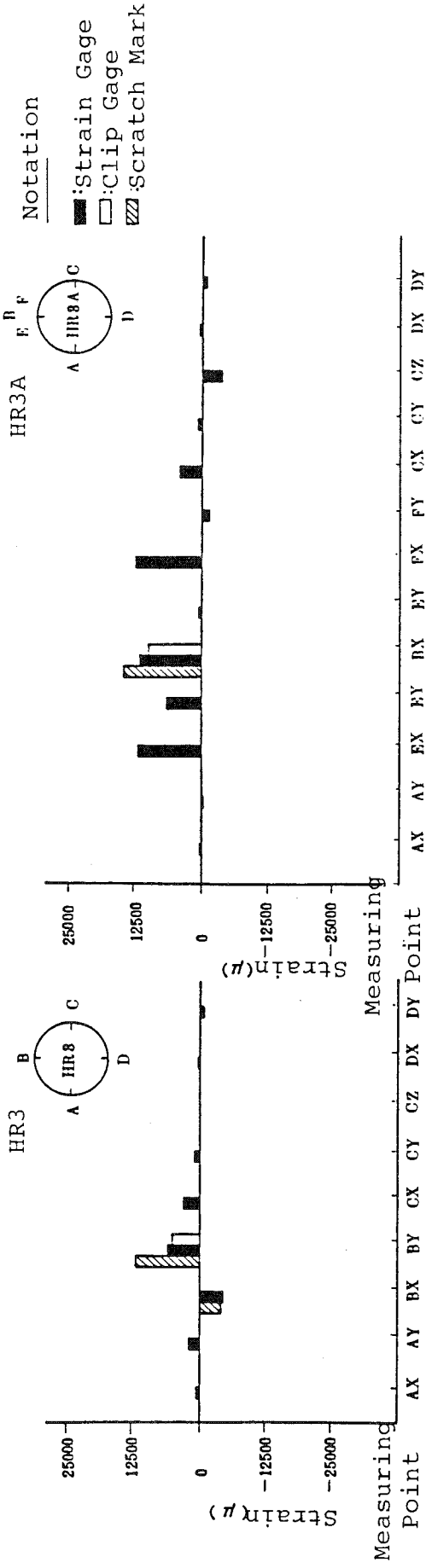
Figure D.19 (2) Cumulative Strain in Hot Leg Pipe
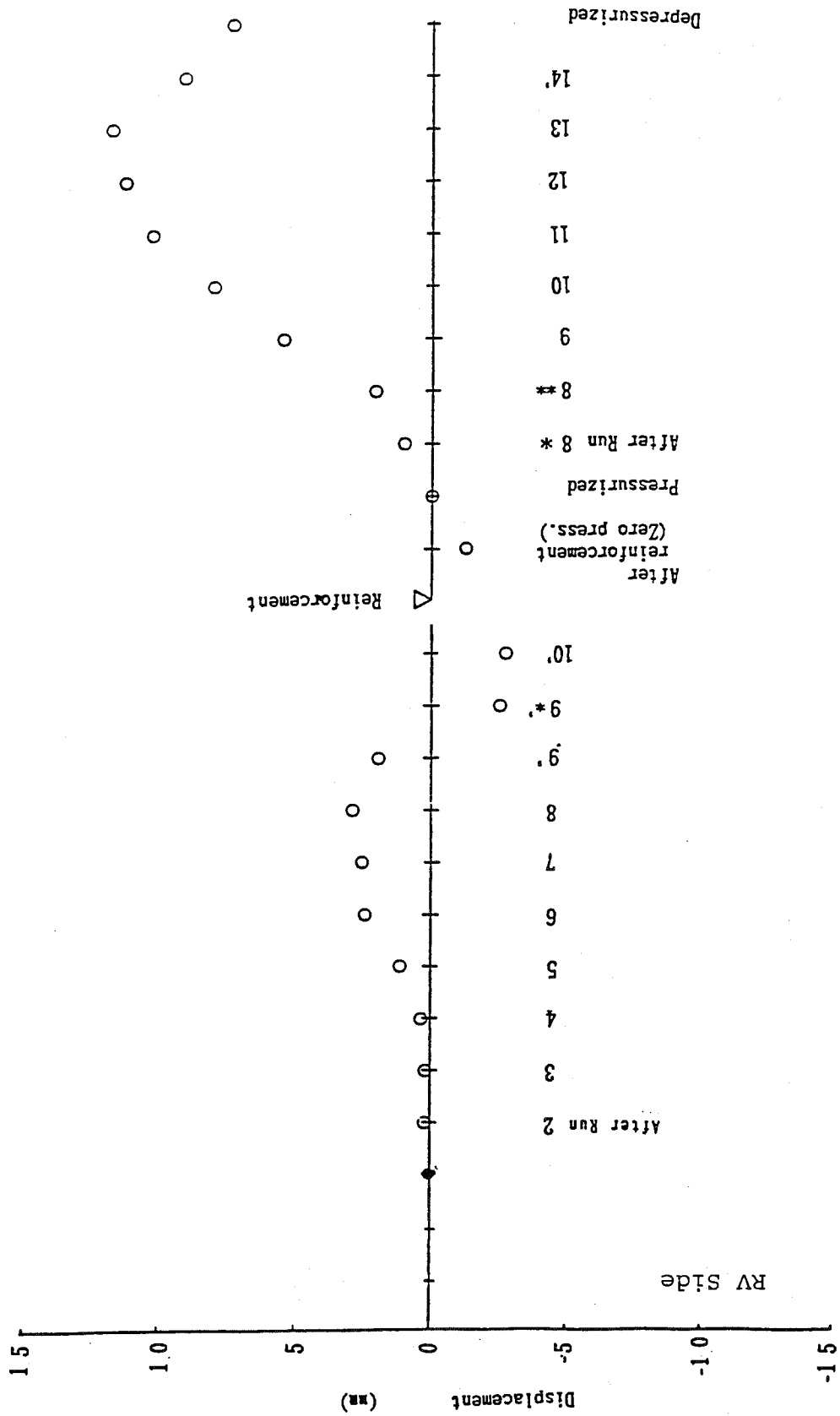
Figure D.20 (1) Cumulative Displacement of SG X-direction
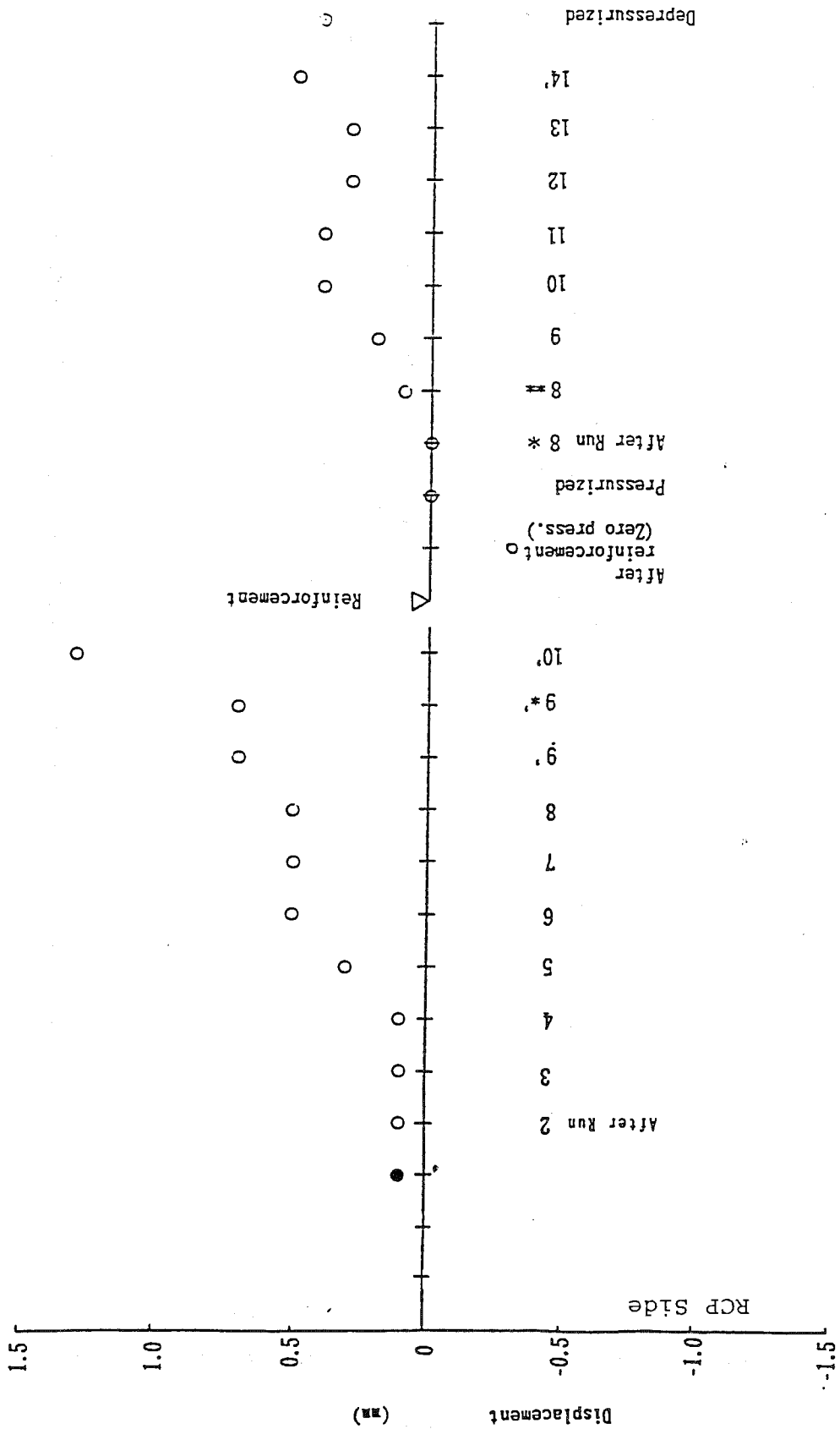
Figure D.20 (2) Cumulative Displacement of SG Y-direction

D-57

Appendix E

Details of the Reinforcement of the Test Model

During the latter half of HLVT run, the following reinforcements have been made on the S/G supports.

Additional plates (8 pieces)

S/G Support Pad Reinforcement

Direction of Excitation

Additional Plates
(each 2 pieces)

S/G Support Flange Rinforcement

E-2
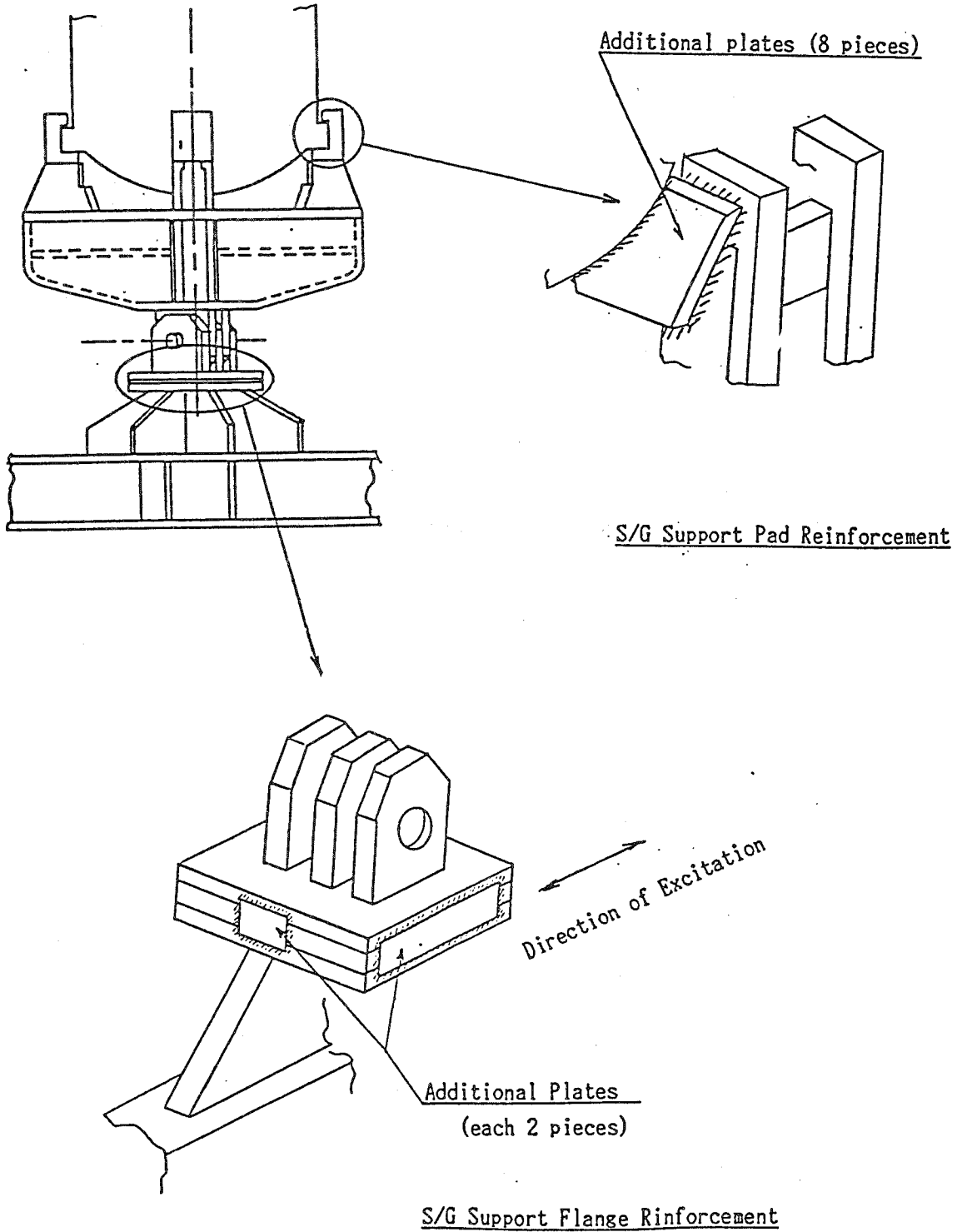
Appendix F

Summary of Inspection Results

Table F.1

Measurement location / Measurement time	① Dimension between center of installed RCP and R/V nozzle	② Dimension between center of installed RCP and R/V nozzle	④ Dimension between weld CL of cross-over leg horizontal straight run	⑤ Dimension between weld CL of hot leg S/G side straight run and installed S/G center	⑥ Dimension between weld CL of hot leg straight run	⑦ Dimension of R/V outlet nozzle
Design value	1180.4	2688.4	411.3	1006.5	1552.5	236
After modification	Not measured	Not measured	408.5	Not measured	1548	236
After reinforcement of S/G support	Not measured	Not measured	Not measured	Not measured	Not measured	Not measured
After completion of HLVT	Not measured	Not measured	409	Not measured	1548	236
Reference figure	Fig. F-2					Fig. F-2

F-2

Table F.2

Measurement location / Measurement time	㉑ X dimension between 90° side wall and SGM1	㉒ Y dimension between standard line and SGM1	㉓ SGM1 EL.	㉔ X dimension between 90° side bracket and SGM2	㉕ Y dimension between 180° side wall and SGM2	㉖ SGM2 EL.
Design value	1800	126	2865 (Set value)	826	2075	2865 (Set value)
After modification	1797	117.5	2865	819.5	2090	2865
After reinforcement of S/G support	1798	119.5	2866	820.5	2088.5	2865
After completion of HLVT	1795	119.5	2864.5	817	2089.5	2865.5
Reference figure	Fig. F-2	Fig. F-2	Fig. F-3	Fig. F-2	Fig. F-2	Fig. F-3

F-3

Table F.3

Measurement location / Measurement time	㉗ X dimension between 90° side bracket and SGM3	㉘ Y dimension between 180° side wall and SGM3	㉙ SGM3 EL.	㉚ X dimension between 270° side wall and SGM4	㉛ Y dimension between 180° side wall and SGM4	㉜ SGM4 EL.
Design value	1800	1101	2865 (Set value)	826	2075	2865 (Set value)
After modification	1797	1104	2865	814.5	2079	2865
After reinforcement of S/G support	1797.5	1103	2864	814	2077	2864
After completion of HLVT	1794.5	1102.5	2864	816.5	2078	2863.5
Reference figure	Fig. F-2	Fig. F-2	Fig. F-3	Fig. F-2	Fig. F-2	Fig. F-3

F-4

Table F.4

Measurement location / Measurement time	④① X dimension between 90° side wall and PM-1	④② X dimension between 0° side displacement sensor bracket and PM-1	④③ PM-1 EL.	④④ Y dimension between 90° side displacement sensor bracket and PM-2	④⑤ Y dimension between 0° side wall and PM-2	④⑥ PM-2 EL.
Design value	1891 (Set value)	336 (Set value)	EL. 2480 (On pump flange)	388 (Set value)	1302	EL. 2480 (On pump flange)
After modification	1891	336	2479.5	388	1297.5	2480
After reinforcement of S/G support	1892.5	338	2481.5	389	1298	2481.5
After completion of HLVT	1891.5	337	2482	388	1298	2482.5
Reference figure	Fig. F-2	Fig. F-2	Fig. F-3	Fig. F-2	Fig. F-2	Fig. F-3

Table F.5

Measurement location / Measurement time	X dimension between 90° side wall and PM-3 ㊼	Y dimension between standard line and PM-3 ㊽	PM-3' EL. ㊾	X dimension between 270° side wall and PM-4 ㊿	Y dimension between 0° side wall and PM-4 �51	PM-4 EL. 52
Design value	1979	65	EL. 1363 (Set value)	986	1302	EL. 2480 (On pump flange)
After modification	1970.5	65	1363	990	1302	2479.5
After reinforcement of S/G support	1972.5	64	1364	989	1303	2481.5
After completion of HLVT	1971	64.5	1365	989.5	1302.5	2482
Reference figure	Fig. F-2	Fig. F-2	Fig. F-3	Fig. F-2	Fig. F-2	Fig. F-3

Table F.6

Measurement location ⟍ Measurement time	SG-T-1	SG-T-2			P-T
	S/G top EL.	S/G top EL.			RCP top EL.
Design value	5870	5870			EL. 4312
After modification	5869	5869			4312
After reinforcement of S/G support	5870	5867			4313.5
After completion of HLVT	5870	5869			4314.5
Reference figure	Fig. F-5	Fig. F-5			Fig. F-3

Table F.7

Measurement location / Measurement time	⑥1 X dimension between 90° side wall and [BM-1]	⑥2 Y dimension between 180° side wall and [BM-1]	⑥3 [BM-1] EL.	⑥4 X dimension between 270° side wall and [BM-2]	⑥5 Y dimension between 180° side wall and [BM-2]	⑥6 [BM-2] EL.
Design value	1600	2075	EL. 1170	2595	2075.5	EL. 1170
After modification	1601	2074	1172	2594	2073	1172
After reinforcement of S/G support	1601.5	2074.5	1172	Not measured	Not measured	Not measured
After completion of HLVT	1600.5	2074	1171	2595	2073	1171
Reference figure	Fig. F-4	←——→			←——→	Fig. F-4

Table F.8

Measurement location / Measurement time	(67) X dimension between 90° side wall and BPM-1	(68) Y dimension between standard line and BPM-1	(69) 0° side prolongation of pin	(70) BPM-1 EL.	(71) X dimension between 90° side wall and BPM-2	(72) Y dimension between 180° side wall and BPM-2
Design value	1800	100	76	EL. 1170	1800	1815
After modification	1803	95	80	1172	1805	1814
After reinforcement of S/G support	1803.5	95	80	1172	1804.5	1814
After completion of HLVT	1804.5	94.5	80	1170	1804.5	1815.5
Reference figure	Fig. F-4	←	→			Fig. F-4

Table F.9

Measurement location / Measurement time	⑦③ 180° side prolongation of pin	⑦④ BPM-2 EL.	⑧① X dimension between 90° side wall and SGBM-1	⑧② Y dimension between 0° side wall and SGBM-1	⑧③ SGBM-1 EL.
Design value	76	EL. 1170	1007.5	2075	EL. 6060
After modification	71	1172	1004	2066	6074
After reinforcement of S/G support	71	1171	1006	2068	6074.5
After completion of HLVT	71	1170.5	997	2068.5	6074.5
Reference figure	Fig. F-4	Fig. F-4	Fig. F-5	↕	Fig. F-5

Table F.10

Measurement location / Measurement time	X dimension between 270° side wall and SGBM-2 (84)	Y dimension between 0° side wall and SGBM-2 (85)	SGBM-2 EL. (86)	Y dimension between 180° side wall and SGBM-1 (87)	Y dimension between 180° side wall and SGBM-2 (88)
Design value	1007.5	2075	EL. 6060	2075	2075
After modification	994	2075	6073	2084	2075
After reinforcement of S/G support	991	2077	6072.5	2082.5	2073.5
After completion of HLVT	999.5	2078	6074	2081.5	2071.5
Reference figure	Fig. F-5	⟵⟶		⟵⟶	Fig. F-5

F-11

Table F.11

Measurement location / Measurement time	S/G (Plummet bob Upper side 0°,180° direction EL. 5600 / 90°,270° direction EL. 5550)				RCP (Plummet bob Upper side EL. 4250)			
	0°	90°	180°	270°	0°	90°	180°	270°
Set value	EL. 5600 Span 1550	EL. 5550 Span 1500	EL. 5600 Span 1550	EL. 5550 Span 1500	EL. 4250 Span 1250	EL. 4250 Span 1250	EL. 4250 Span 1250	EL. 4250 Span 1250
After modification	Upper 0 Lower −2	Upper 0 Lower −1	Upper 0 Lower +2.5	Upper 0 Lower +1.5	Upper 0 Lower +1	Upper 0 Lower +2	Upper 0 Lower −3	Upper 0 Lower −3
After reinforcement of S/G support	Not measured	← →	← →	Not measured	Upper 0 Lower +1	Upper 0 Lower +2.5	Upper 0 Lower −2.5	Upper 0 Lower −3.5
After completion of HLVT	Upper 0 Lower 0	Upper 0 Lower +0.5	Upper 0 Lower +2	Upper 0 Lower −1	Upper 0 Lower +2	Upper 0 Lower +3	Upper 0 Lower −2	Upper 0 Lower −3
Reference figure	Fig. F-3	← →	← →					Fig. F-3

Table F.12 Time and Item of Measurement

	Time of measurement	Item of measurement
Location marked with ○	Before and after HLVT only	Diameter Circumference
Location marked with ◎	Before and after each Run from 8 excluding Run 8∗ and Run 8∗∗ ※	Diameter Circumference
Location marked with ◎∗	Before and after each Run from 8 excluding Run 8∗ and Run 8∗∗	Diameter

※ Note ; Location、 Ⓒ'₁ was measured from Run 10.

Table F.13 Result of Pipe Dimensional Measurement (1/4)

Measurement location		Ⓐ₁	Ⓐ	Ⓐ₂	Ⓑ	Ⓒ₁'	Ⓒ₁	Ⓒ	Ⓒ₂	Ⓔ'	Ⓕ'	Ⓖ'
		R / V side weld joint			Horizontal straight pipe	Elbow weld joint of straight pipe side				50° elbow	50° elbow	50° elbow
Design value	Outer diameter	ø352.8			ø352.0		ø352.8			ø373.6	ø370.5	ø303.4
	Circumferential length	1100.4			1100.4		1100.4			1173.7	1109.1	1204.5
After modification	Outer diameter ⓐ	351.32	351.10	353.05	353.23	Not measured	352.04	351.05	351.66	372.00	376.95	301.65
	Outer diameter ⓑ	350.35	350.51	353.49	353.27		353.10	351.61	351.95	373.46	376.72	301.72
	Circumferential length	1107.5	1100.5	1115	1114		1114	1109	1111	1173	1109	1204
Run 0	Outer diameter ⓐ	Not measured		353.10	353.27	Not measured	352.79	Not measured		371.92	377.13	301.63
	Outer diameter ⓑ			353.61	353.30		353.21			372.55	376.72	301.63
	Circumferential length			1114	1114		1113			1173	1109	1204
Run 9'	Outer diameter ⓐ			353.16	353.35		352.05			371.07	376.64	301.62
	Outer diameter ⓑ			353.64	353.20		353.32			373.63	377.12	301.60
	Circumferential length			1114	1114		1114			—	—	—
Run 9''	Outer diameter ⓐ			353.19	353.30	Not measured	353.00			372.04	376.61	301.67
	Outer diameter ⓑ			353.63	353.18		353.23			373.10	377.14	301.64
	Circumferential length			1114	1114		1114			—	—	—
Run 10'	Outer diameter ⓐ			353.29	353.42		353.41			372.11	376.67	301.73
	Outer diameter ⓑ			353.73	353.31		353.44			373.47	377.16	301.65
	Circumferential length			1116	1115		1116			—	—	—
Run 9	Outer diameter ⓐ	Not measured		353.87	353.00		353.76	Not measured		372.20	376.60	301.76
	Outer diameter ⓑ			353.07	353.49		353.70			373.51	377.05	301.25
	Circumferential length			1116	1115		1117			1175	1109	1205
Run 10	Outer diameter ⓐ			353.52	353.35	354.92	354.50			372.22	376.62	301.02
	Outer diameter ⓑ			354.16	353.00	355.35	354.15			373.47	376.94	301.12
	Circumferential length			1116	1115	1122	1121			—	—	—
Run 11	Outer diameter ⓐ			353.65	353.37	355.39	354.95			372.45	376.73	301.03
	Outer diameter ⓑ			354.29	353.90	356.03	354.63			373.45	377.11	301.24
	Circumferential length			1116	1115	1124	Not measured			—	—	—
Run 12	Outer diameter ⓐ			353.60	353.37	355.74	355.34			372.37	376.00	301.95
	Outer diameter ⓑ			354.37	353.99	356.26	354.06			373.40	376.70	301.22
	Circumferential length			1117	1116	1124	Not measured			—	—	—
Run 13	Outer diameter ⓐ			353.56	353.34	356.03	355.50			372.20	376.09	301.96
	Outer diameter ⓑ			354.26	353.01	356.30	354.94			373.30	377.07	301.47
	Circumferential length			1117	1116	1126	Not measured			—	—	—
Run 14'	Outer diameter ⓐ			353.77	353.73	356.65	356.24			372.62	376.95	302.00
	Outer diameter ⓑ			354.34	353.78	356.22	354.50			373.40	376.00	300.90
	Circumferential length			1110	1117	1126.5	Not measured			—	—	—
After completion of HLVT	Outer diameter ⓐ	351.37	351.29	353.77	353.73	356.65	356.24	352.84	353.60	372.62	376.95	302.00
	Outer diameter ⓑ	350.43	350.51	354.54	353.70	356.22	354.50	351.44	352.94	373.40	376.00	300.90
	Circumferential length	1107	1100	1110	1117	1125.5	1122	1113	1112	1175	1109	1205
Reference Figure		F-8										F-8

F-14

Table F.13 Result of Pipe Dimensional Measurement (2/4)

Measurement time	Measurement location	H' (50° elbow)	(I_1)	I	(I_2)	(J_1)	J	(J_2)	K (40° elbow)	(K_1)	L' (40° elbow)
			Elbow weld joint of S/G side			40° elbow weld joint of S/G side					
Design value	Outer diameter	⌀300.3	⌀377.2			⌀377.2				⌀393.2	
	Circumferential length	1219.9	1105.0			1105.0				1235.3	
After modification	Outer diameter (a)	306.09	376.10	376.21	376.70	376.52	376.26	375.31	309.00	309.60	309.07
	Outer diameter (b)	300.25	376.46	376.05	376.45	376.09	375.00	375.55	392.90	394.30	393.72
	Circumferential length	1220	1104	1105	Not measured	1106.5	1105	1103	1234	1235	1235.5
Run 8	Outer diameter (a)	306.96							309.02	309.56	309.90
	Outer diameter (b)	300.20							393.37	394.40	393.69
	Circumferential length	1221							1236	1236	—
Run 9'	Outer diameter (a)	306.81							309.12	309.49	309.34
	Outer diameter (b)	300.36							393.37	394.20	393.69
	Circumferential length	1220							1236	1235.5	—
Run 9''	Outer diameter (a)	306.84							309.05	309.53	309.42
	Outer diameter (b)	300.19							393.26	394.30	393.70
	Circumferential length	1220	Not measured			Not measured			1235	1234	—
Run 10'	Outer diameter (a)	306.00							309.02	309.53	309.41
	Outer diameter (b)	300.33							393.29	394.41	393.46
	Circumferential length	1221							1234	1233	—
Run 9	Outer diameter (a)	300.64							300.97	309.43	309.45
	Outer diameter (b)	300.00							393.24	394.05	393.53
	Circumferential length	Not measured							1233	1235	—
Run 10	Outer diameter (a)	300.60							309.22	309.47	309.45
	Outer diameter (b)	300.17							393.24	394.35	393.54
	Circumferential length	1224							1233	1236	—
Run 11	Outer diameter (a)	300.91							300.66	309.52	309.39
	Outer diameter (b)	300.25							393.31	394.33	393.54
	Circumferential length	1224							1235	1236	—
Run 12	Outer diameter (a)	300.75							300.93	309.51	309.51
	Outer diameter (b)	300.18							393.33	394.53	393.62
	Circumferential length	1225							1234	1235	—
Run 13	Outer diameter (a)	300.75							309.00	309.52	309.59
	Outer diameter (b)	300.23							393.24	394.40	393.63
	Circumferential length	1224							1233	1235	—
Run 14'	Outer diameter (a)	300.99							300.90	309.45	309.50
	Outer diameter (b)	300.11							393.20	394.30	393.63
	Circumferential length	1225							1235	1235	—
After completion of HLVT	Outer diameter (a)	300.99	376.41	376.39	376.50	376.50	376.09	375.18	300.90	309.45	309.50
	Outer diameter (b)	300.11	376.50	376.60	376.31	375.99	375.81	375.56	393.20	394.30	393.63
	Circumferential length	1225	1105	1105	1105	1106	1106	1104	1235	1235	1235
Reference Figure		F-8	F-8			F-9			F-9		F-9

F-15

Table F.13 Result of Pipe Dimensional Measurement (3/4)

Measurement location			M₁	M	M₂	P₁	P	P₂	O'	O₁	O	O₂
			Vertical straight pipe weld joint of S/G side			Horizontal straight pipe weld joint of RCP side			RCP side 90° elbow		90° elbow weld joint of RCP side	
Design value	Outer diameter		⌀377.2			⌀377.2			⌀393.2		⌀377.2	
	Circumferential length		1105.0			1105.0			1235.3		1105.0	
After modification	Outer diameter	@a	373.21	374.13	377.02	375.77	375.06	376.10	392.02	394.14	376.56	377.23
		@b	373.70	374.08	378.15	375.24	375.27	375.61	391.59	392.01	378.23	379.32
	Circumferential length		1170	1101	1191	1105	1105	1106	1235.5	1235.5	1109.5	1191
Run 8	Outer diameter	@a			377.80				392.45	394.21		
		@b			378.20				391.97	392.26		
	Circumferential length				1192				1236	1236		
Run 9'	Outer diameter	@a			377.02				391.90	394.22		
		@b			378.19				391.01	392.27		
	Circumferential length				1192				1236	1236		
Run 9"	Outer diameter	@a			377.01				391.07	394.13		
		@b			378.14				391.69	392.02		
	Circumferential length				1192				1237	1237		
Run 10'	Outer diameter	@a			377.02				391.07	394.22		
		@b			378.09				391.24	391.78		
	Circumferential length				1191		Not measured		1235	1236		Not measured
Run 9	Outer diameter	@a			377.02							
		@b	Not measured		378.16				Not measured			
	Circumferential length				1193							
Run 10	Outer diameter	@a			377.81				391.03	394.39		
		@b			378.14				391.77	392.00		
	Circumferential length				1193				1236	1236		
Run 11	Outer diameter	@a			377.02				391.07	394.33		
		@b			378.09				391.69	392.19		
	Circumferential length				1193				1237	1237		
Run 12	Outer diameter	@a			377.83				391.98	394.17		
		@b			378.13				391.04	392.06		
	Circumferential length				1192				1236	1237		
Run 13	Outer diameter	@a			377.87				391.90	394.45		
		@b			378.19				391.75	391.94		
	Circumferential length				1193				1237	1237		
Run 14'	Outer diameter	@a			377.03				391.95	394.30		
		@b			378.20				391.71	392.14		
	Circumferential length				1193				1236	1236		
After completion of HLVT	Outer diameter	@a	373.20	373.05	377.03	375.72	375.75	375.94	391.95	394.30	376.49	377.06
		@b	373.90	373.93	378.20	Not measured	Not measured	Not measured	391.71	392.14	378.31	379.57
	Circumferential length		1170.5	1179	1193	1105	1105	1105	1236	1236	1190	1193
Reference Figure			F-9									F-9

F-16

Table F.13 Result of Pipe Dimensional Measurement (4/4)

Measurement time	Measurement location	(r₁)	(r₂)	(T₁)	(T)	(T₂)	(U₁)	(U)	(U₂)
		Straight pipe weld joint of RCP side		22° elbow weld joint of RCP side			22° elbow weld joint of R/V side		
Design value	Outer diameter	ø334.4		ø334.4			ø340.0		
	Circumferential length	1050.5		1050.5			1068.1		
After modification	Outer diameter ⓐ	333.69	333.15	333.52	333.06	334.23	339.92	339.66	338.83
	Outer diameter ⓑ	332.10	332.71	333.30	332.91	333.67	339.31	339.24	337.96
	Circumferential length	1052	1052	Not measured	1051.5	1053.5	1072	1072	1069
Run 8	Outer diameter ⓐ								
	Outer diameter ⓑ								
	Circumferential length								
Run 9'	Outer diameter ⓐ								
	Outer diameter ⓑ								
	Circumferential length								
Run 9''	Outer diameter ⓐ								
	Outer diameter ⓑ								
	Circumferential length				Not measured				
Run 10'	Outer diameter ⓐ								
	Outer diameter ⓑ								
	Circumferential length								
Run 9	Outer diameter ⓐ								
	Outer diameter ⓑ								
	Circumferential length								
Run 10	Outer diameter ⓐ								
	Outer diameter ⓑ								
	Circumferential length								
Run 11	Outer diameter ⓐ								
	Outer diameter ⓑ								
	Circumferential length								
Run 12	Outer diameter ⓐ								
	Outer diameter ⓑ								
	Circumferential length								
Run 13	Outer diameter ⓐ								
	Outer diameter ⓑ								
	Circumferential length								
Run 14'	Outer diameter ⓐ								
	Outer diameter ⓑ								
	Circumferential length								
After completion of HLVT	Outer diameter ⓐ	333.66	333.16	333.51	333.06	334.09	339.09	339.68	330.77
	Outer diameter ⓑ	332.21	332.47	333.55	333.07	333.51	339.20	339.21	337.02
	Circumferential length	1052	1051	1051.5	1051.5	1053	1072	1071.5	1060
Reference Figure		F-10							F-10

Table F.14 Result of Pipe Dimensional Measurement (Additional Bulging Portion) (1/2)

Measurement location	Ⓐ	Ⓧ₁	Ⓧ₂	Ⓧ₃	Ⓧ₄	Ⓧ₅	Ⓧ₆	○	○	○	·	○
Design value — Outer diameter	R/V side of hot leg straight pipe (No. Initial value on XI) ø352.8											
Design value — Circumferential length	1108.4											
After completion of HLVT — Outer diameter ⓐ	351.29	353.15	353.96	354.01	353.03	353.77	353.51					
After completion of HLVT — Outer diameter ⓑ	350.51	353.55	354.63	354.57	354.20	353.96	353.27					
After completion of HLVT — Circumferential length	1108	1117	1116.5	1118	1117	1116	1116					
Reference Figure	F-11						F-11					

Table F.14 Result of Pipe Dimensional Measurement (Additional Bulging Portion) (2/2)

Measurement location	Ⓨ₁	Ⓨ₂	Ⓨ₃	Ⓨ₄	Ⓑ'	Ⓨ₅	Ⓨ₆	Ⓨ₇	Ⓒ₁'	Ⓒ₁	Ⓒ
Design value — Outer diameter	S/G side of hot leg straight pipe (No. Initial value on Y₁ and C₁') ø352.8										
Design value — Circumferential length	1108.4										
After completion of HLVT — Outer diameter ⓐ	353.15	353.19	353.28	353.53	353.73	354.29	355.07	356.10	356.65	356.24	352.04
After completion of HLVT — Outer diameter ⓑ	353.74	353.04	353.79	353.78	353.78	353.95	354.45	355.65	356.22	354.50	351.44
After completion of HLVT — Circumferential length	1115	1115	1116	1116	1117	1118.5	1119	1124	1126.5	1122	1113
Reference Figure	F-11										F-11

F-18
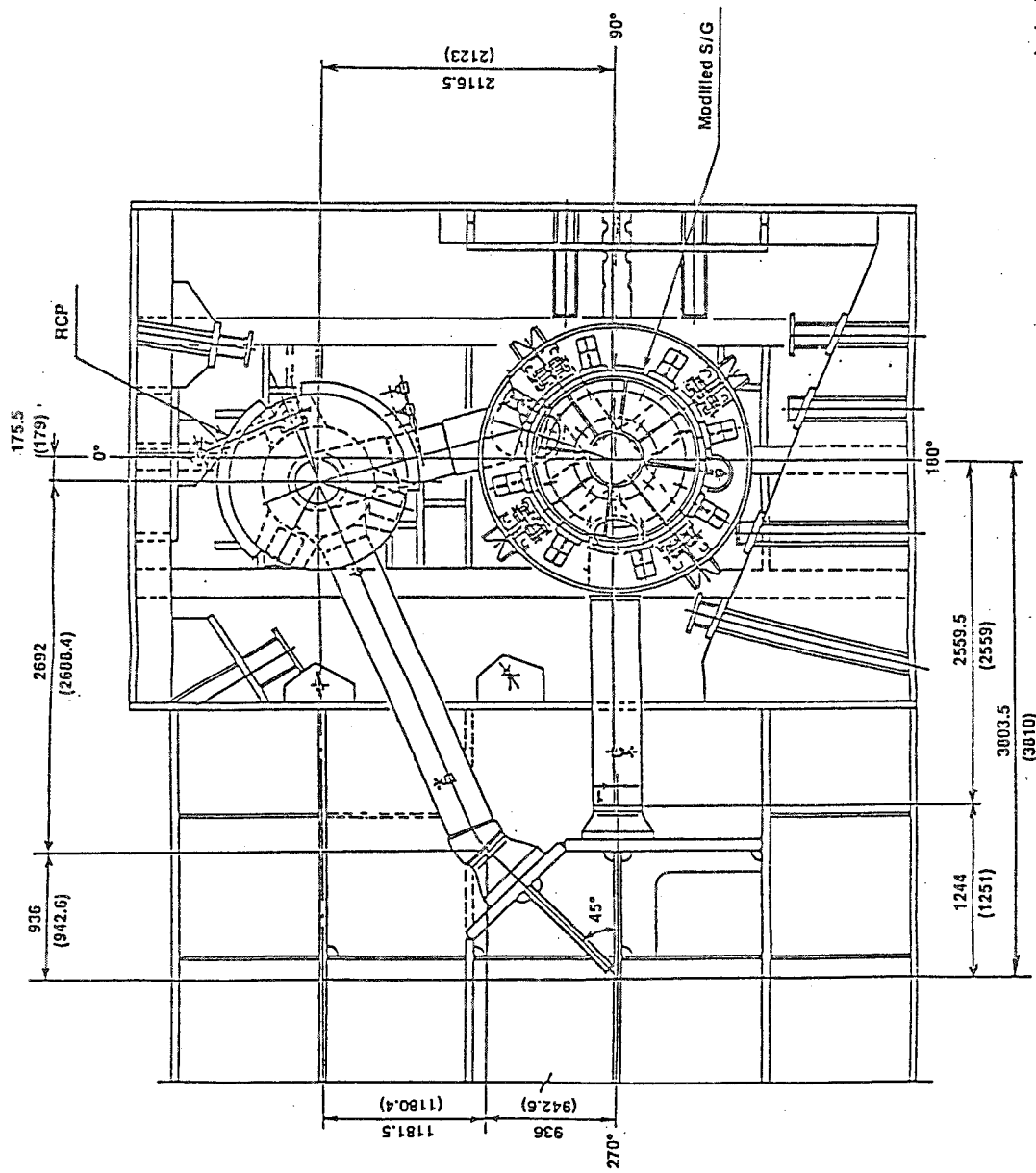
In ( ) :
dimension of design

(After Modification
After Reinforcement of S/G Support
After Completion of HLVT)

Figure F.1 As-Built Test Model Location of HLVT

Figure F.2

Figure F.3

F-21

Figure F.4 Measurement Location of Modified S/G Vertical Support

F-22
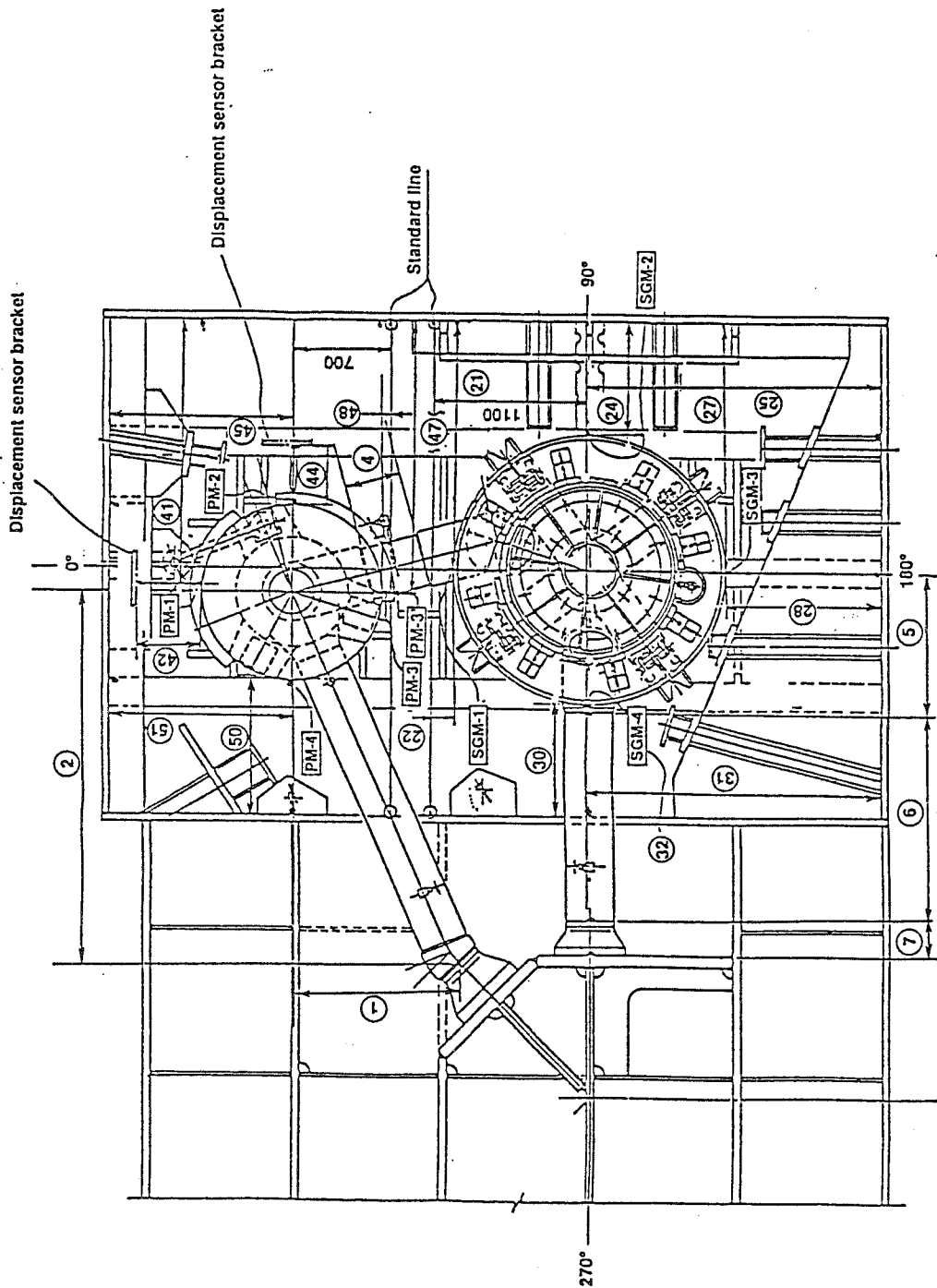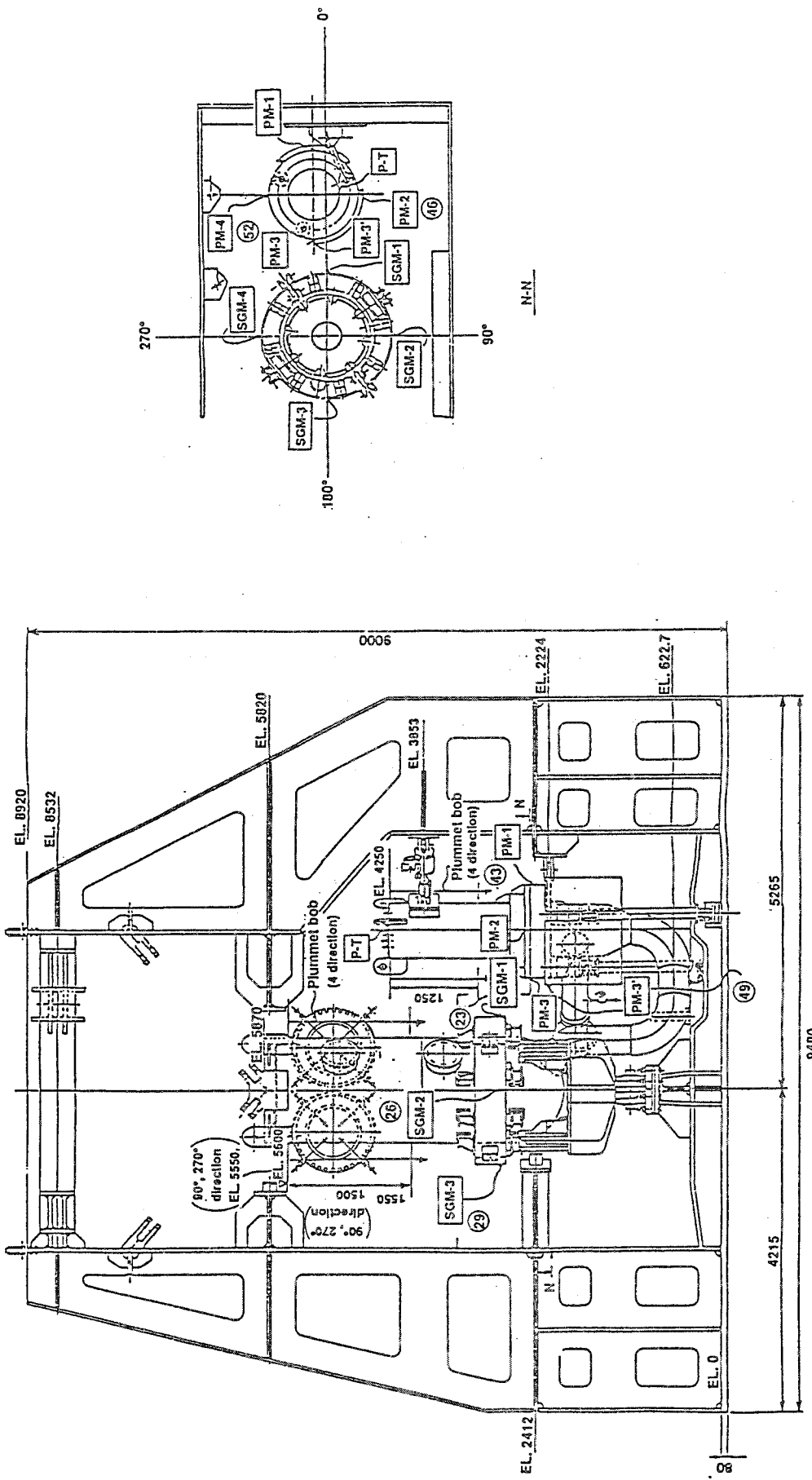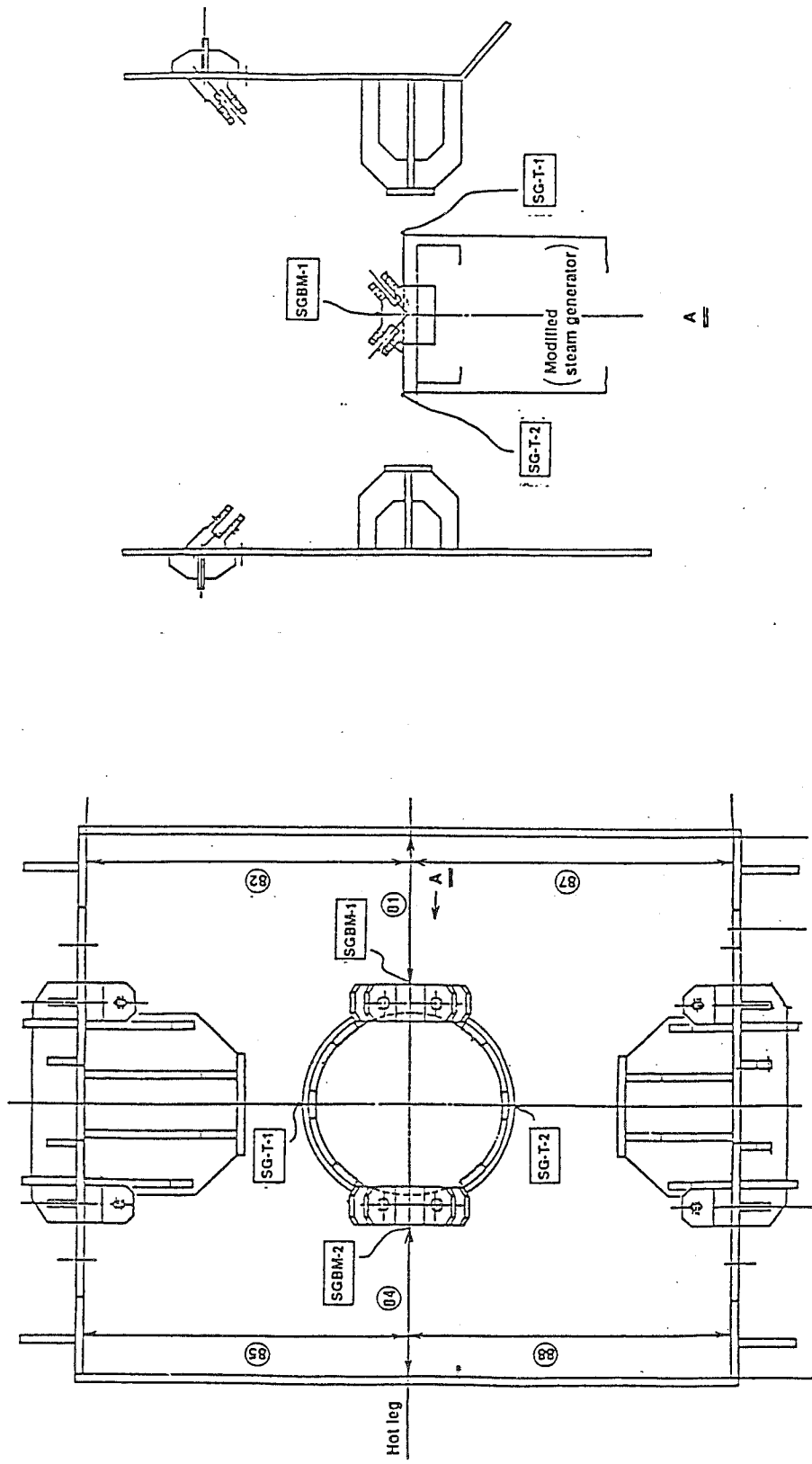
Figure F.5   Measurement Location of Tie Rod Brackets
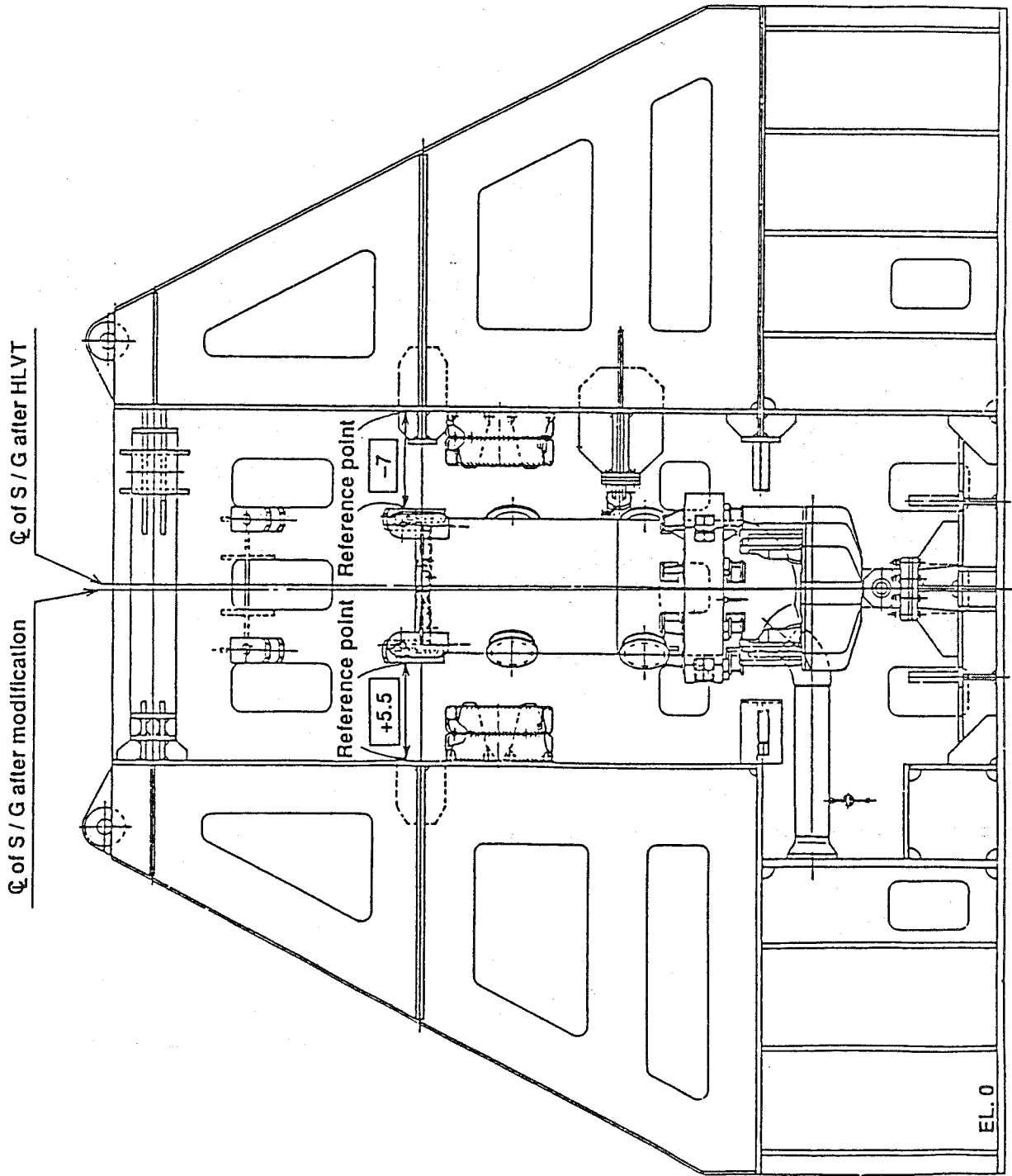
Figure F.6 The Inclination of S/G After HLVT (X-Direction)

Ç of S / G after HLVT

Ç of S / G after modification

Reference point

Reference point

Reference point

−7

+5.5

EL. 0
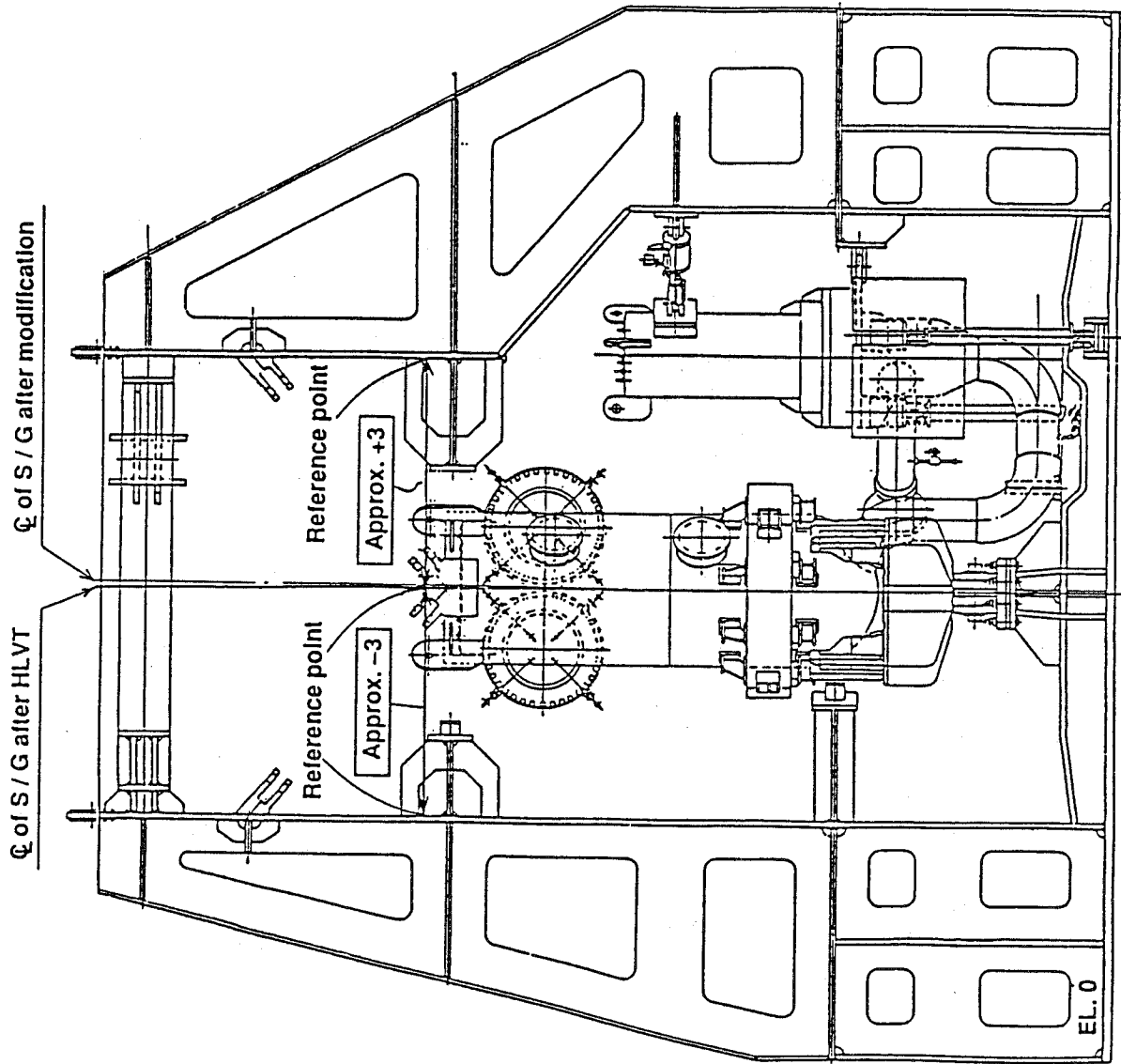
Figure F.7 The Inclination of S/G After HLVT (Y-Direction)

Ç of S / G after modification

Reference point

Approx. +3

Ç of S / G after HLVT

Reference point

Approx. -3

EL. 0

Figure F.8 · Hot Leg

Section view is seen from S/G side

F-26

Section view is seen from RCP side

Figure F. 9 Cross-Over Leg

F-27
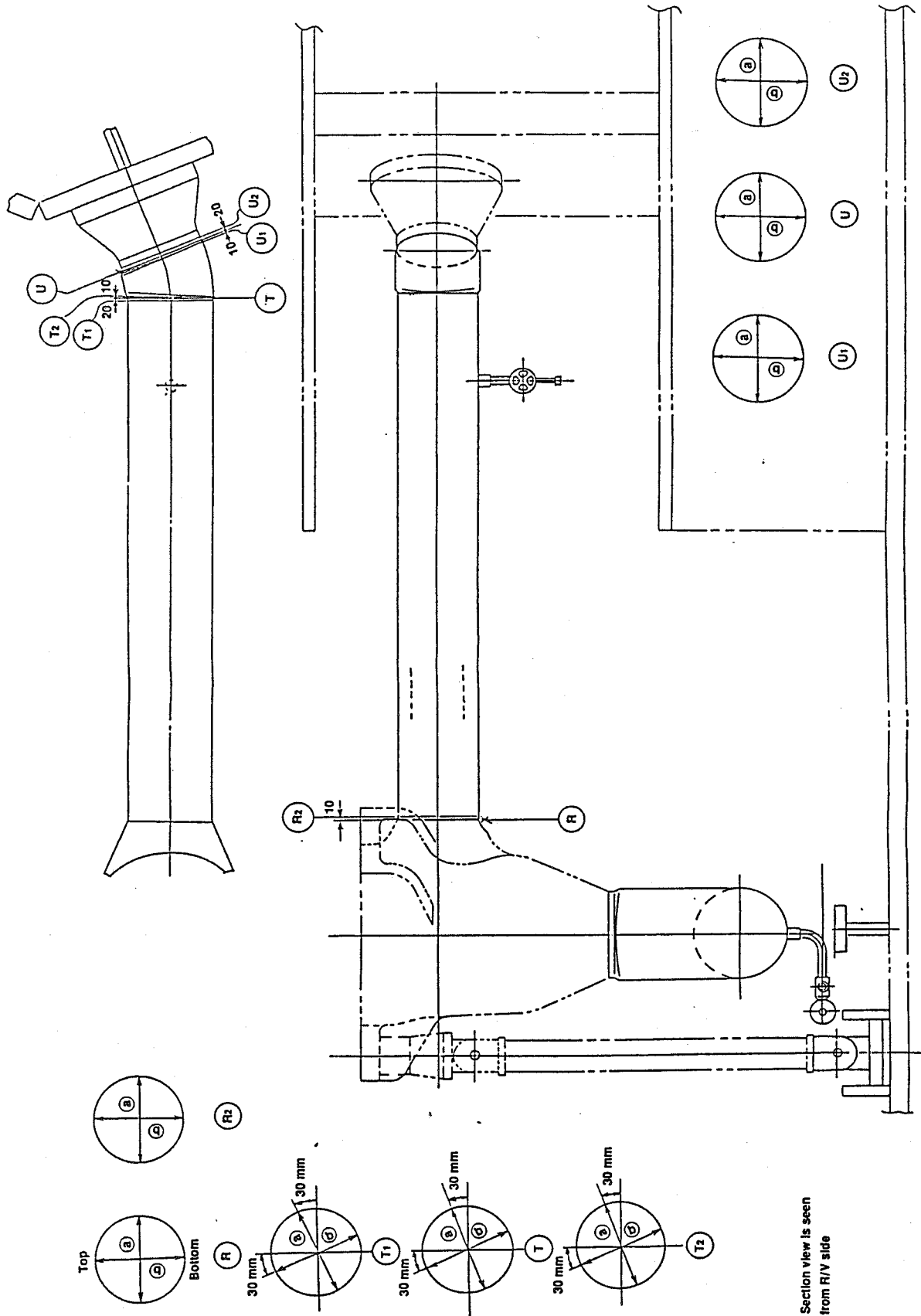
Figure F.10 Cold Leg

Section view is seen
from R/V side

F-28
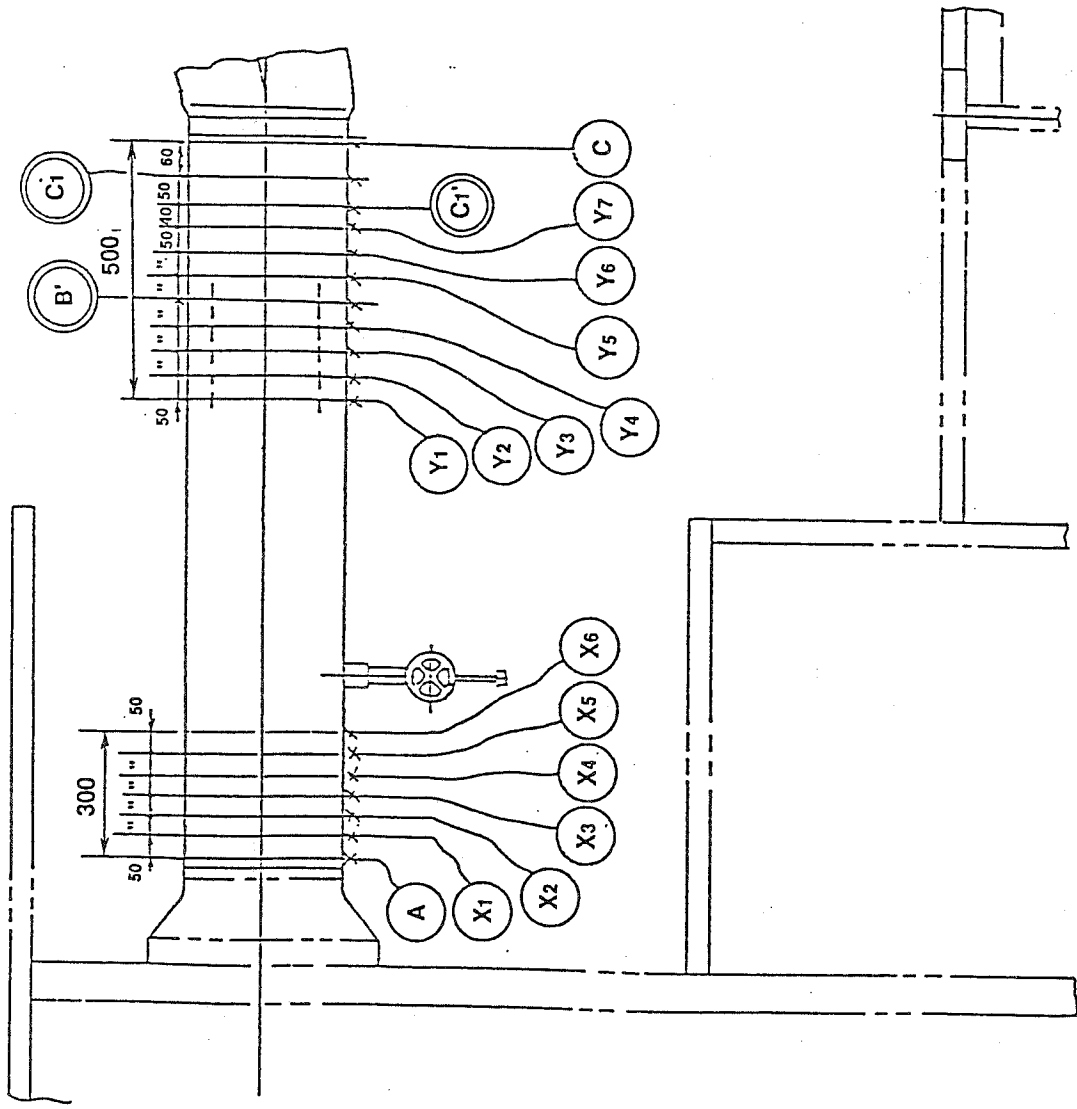
Figure F.11 Measurement Location of Bulging Portion of Hot Leg
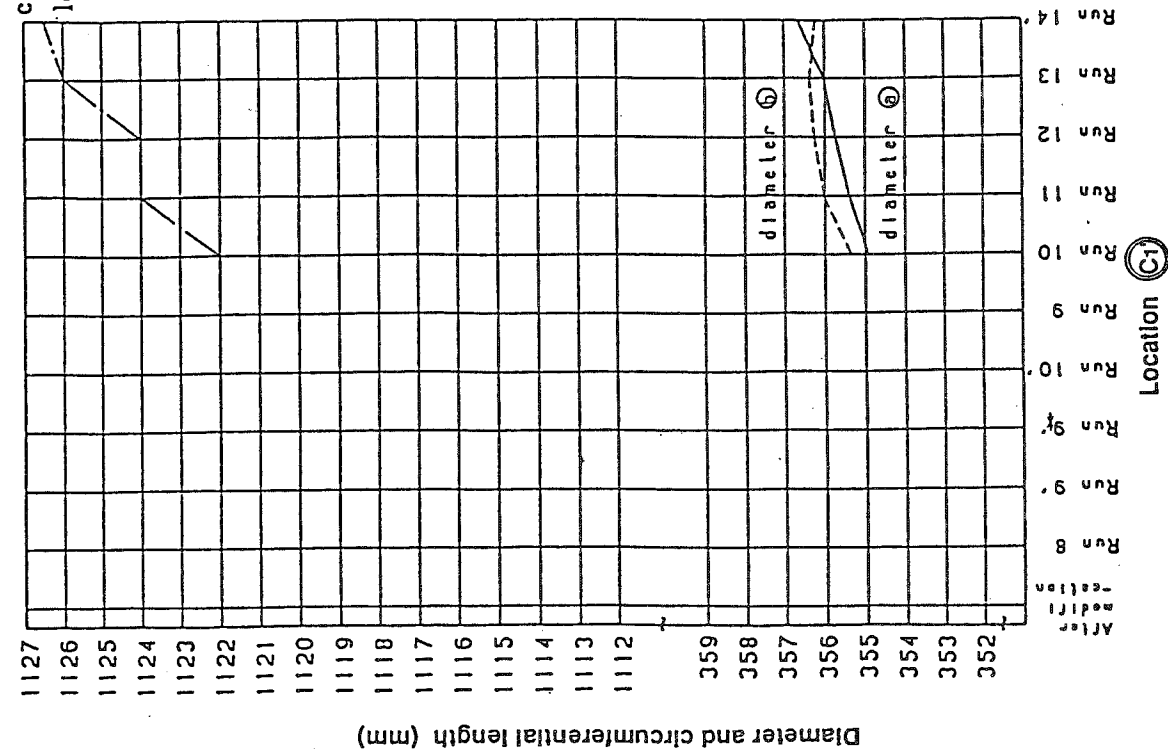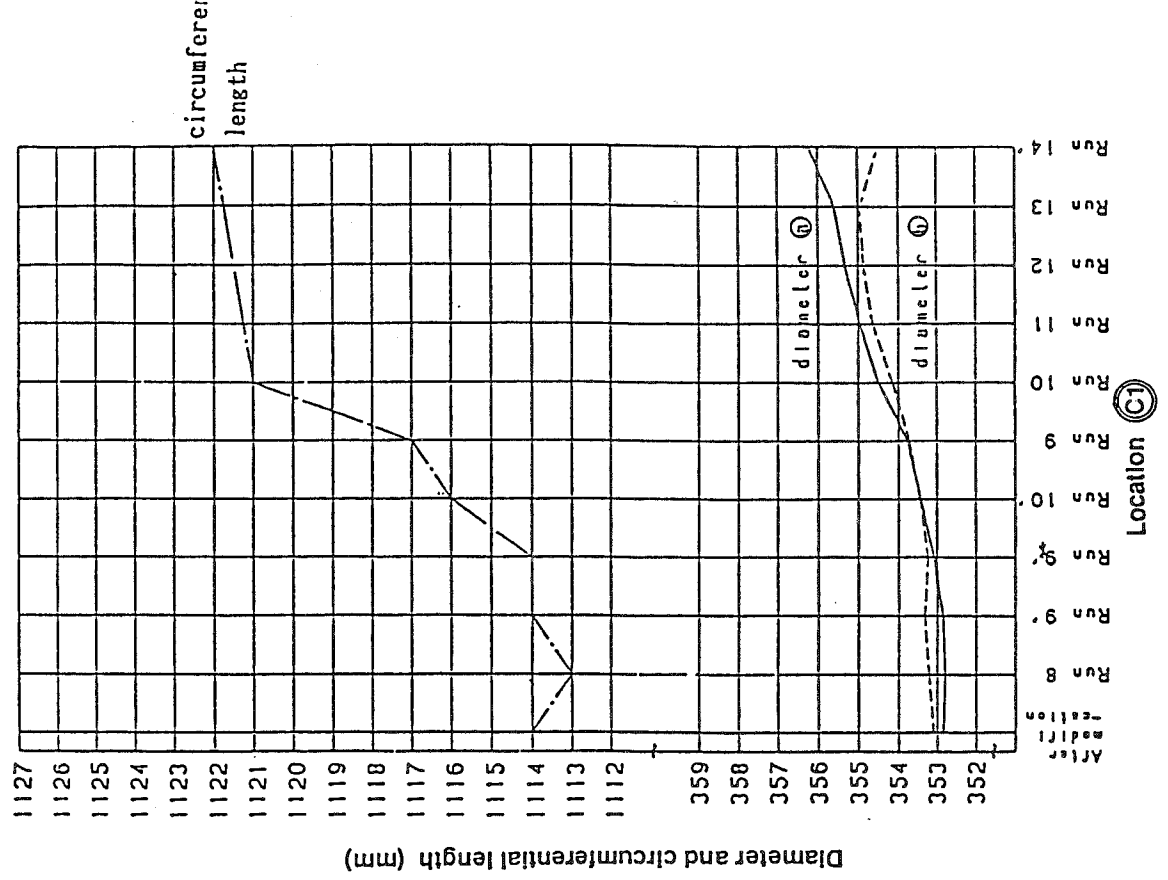
Figure F.12 History of Dimensional Change at Bulging Portion of Pipe

Figure F.13 Dimensional Change of Hot Leg
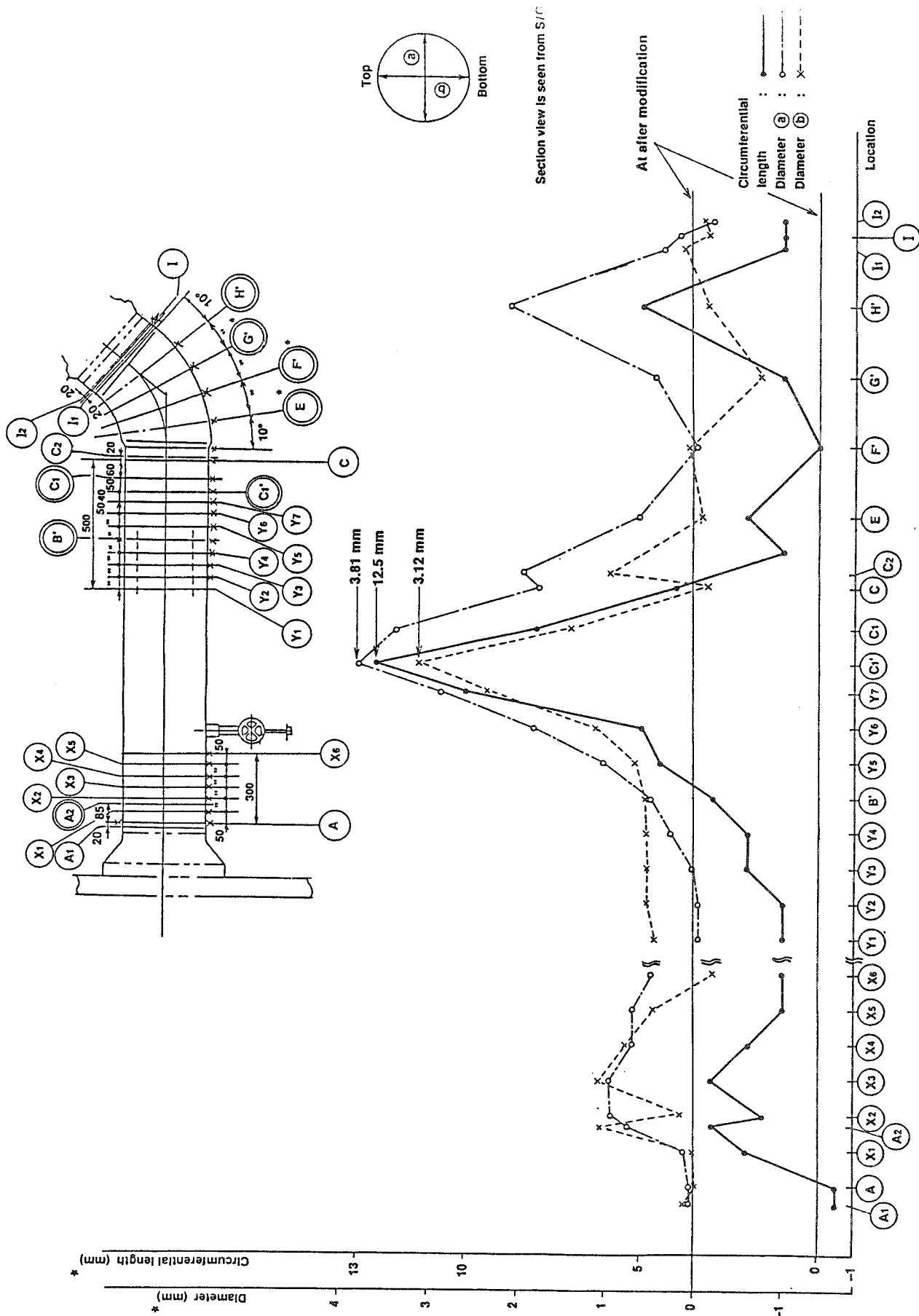
* : (After HLVT) − (After Modification)

F−31
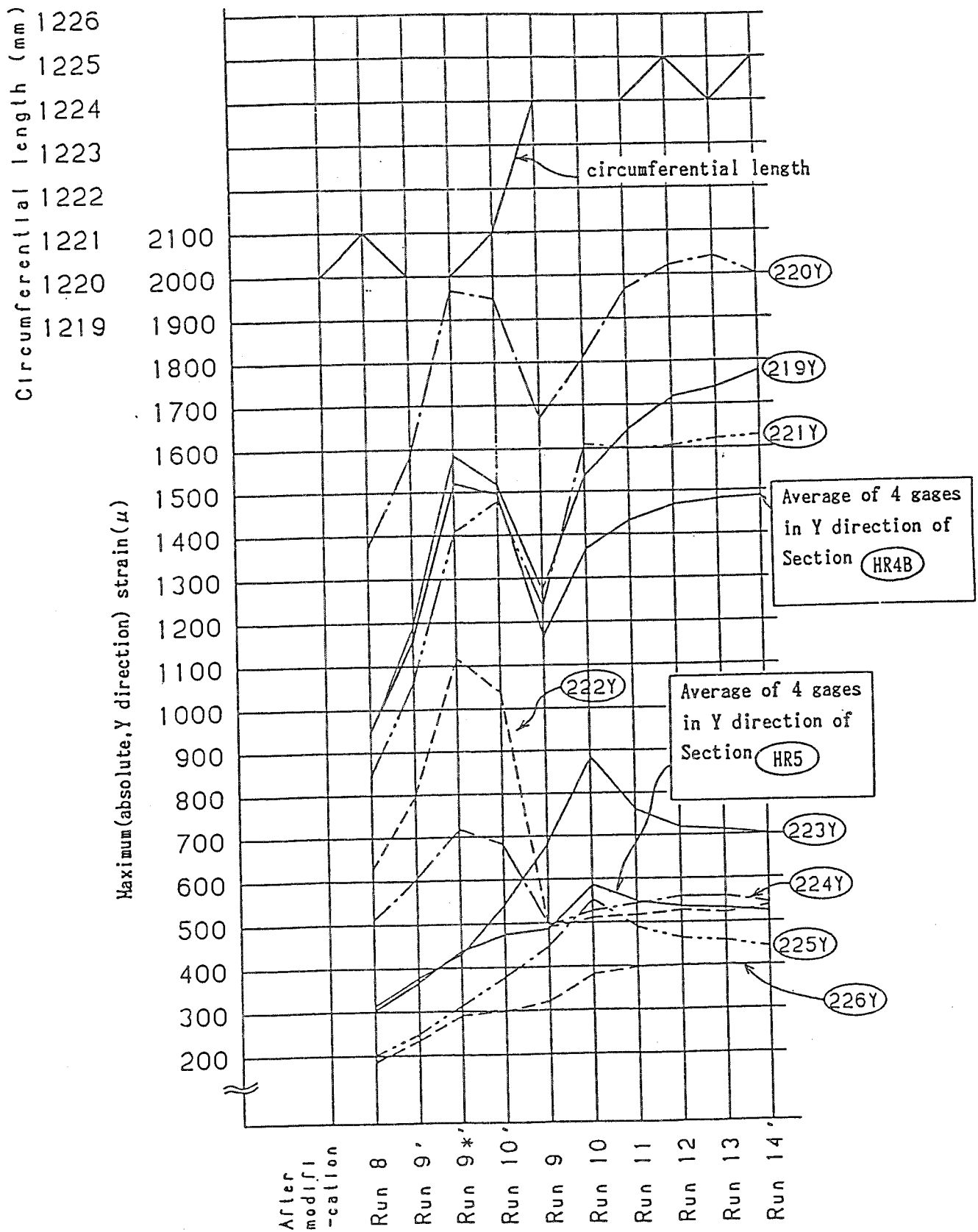
Figure F.14   Strains Adjacent to Location of H' and Circumferential Length of H'

F-32

Appendix G

Estimation of Member Force in Piping

Forces and moments in the piping are estimated using measured strains according to the following procedures.

Location of strain gages are considered as shown in Figure G.1

1. Axial force ; F_x

Axial stress of each measuring point.

$$\sigma_x^{0^\circ} = \frac{E}{1-v^2} \quad (\varepsilon_a^{0^\circ} + v \varepsilon_c^{0^\circ})$$

$$\sigma_x^{90^\circ} = \frac{E}{1-v^2} \quad (\varepsilon_a^{90^\circ} + v \varepsilon_c^{90^\circ})$$

$$\sigma_x^{180^\circ} = \frac{E}{1-v^2} \quad (\varepsilon_a^{180^\circ} + v \varepsilon_c^{180^\circ})$$

$$\sigma_x^{270^\circ} = \frac{E}{1-v^2} \quad (\varepsilon_a^{270^\circ} + v \varepsilon_c^{270^\circ})$$

$$F_x = \frac{1}{4} \quad (\sigma_x^{0^\circ} + \sigma_x^{90^\circ} + \sigma_x^{180^\circ} + \sigma_x^{270^\circ}) \cdot A$$

Where,

E ; Young's moduls ($= 1.99 \times 10^4 \ kg/mm^2$)

v ; Poisson's ratio ($= 0.3$)

A ; Cross sectional area of the pipe at measuring point

2. Shear force : F_y and F_z

Shear stress τ_{ac} is evaluated from the shear strain γ_{ac} at each measuring point and they are everaged in the measuring cross section.

i) F_y

$$\gamma_{ac}^{90°} = 2\varepsilon_b^{90°} - (\varepsilon_a^{90°} + \varepsilon_c^{90°})$$

$$\gamma_{ac}^{270°} = 2\varepsilon_b^{270°} - (\varepsilon_a^{270°} + \varepsilon_c^{270°})$$

Cancel strain component due to the tortional torque.

$$\gamma_{ac}^{y} = \frac{1}{2} \ (\gamma_{ac}^{90°} + \gamma_{ac}^{270°})$$

$$\therefore \quad \tau_{ac}^{y} = K \cdot G \cdot \gamma_{ac}^{y}$$

Thus,

$$\boxed{F_y = \tau_{ac}^{y} A = K \cdot G \cdot A \cdot \gamma_{ac}^{y}}$$

Where, G ; Shear moduls ($=E/2(1+v)$)

KA ; Effective shear area

m ; ratio of outer and inner diameter
($=$out$/$in)

$$K = \frac{6(1+v)(1+m^2)^2}{(7+6v)(1+m^2)^2 + (20+12v)m^2}$$

$$\gamma_{ac}^{0°} = 2\varepsilon_b^{0°} - (\varepsilon_a^{0°} + \varepsilon_c^{0°})$$

$$\gamma_{ac}^{180°} = 2\varepsilon_b^{180°} - (\varepsilon_a^{180°} + \varepsilon_c^{180°})$$

$$\gamma_{ac}^{y} = \frac{1}{2} \ (\gamma_{ac}^{0°} + \gamma_{ac}^{180°})$$

Thus,

$$F_z = K \cdot G \cdot A \cdot \gamma_{ac}^z$$

3. Bending moment ; M_y and M_z

i) M_y

$$\sigma_x^{90°} = \frac{E}{1-v^2} \quad (\varepsilon_a^{90°} + v\,\varepsilon_c^{90°})$$

$$\sigma_x^{270°} = \frac{E}{1-v^2} \quad (\varepsilon_a^{270°} + v\,\varepsilon_c^{270°})$$

Cancel stress component due to the axial force.

$$\sigma_M^{M_y} = \frac{1}{2} \quad (\sigma_x^{90°} - \sigma_x^{270°})$$

Thus,

$$M_y = \sigma_M^{M_y} \cdot Z$$

Where, Z : Section moduls

ii) M_z

$$\sigma_x^{0°} = \frac{E}{1-v^2} \quad (\varepsilon_a^{0°} + v\,\varepsilon_c^{0°})$$

$$\sigma_x^{180°} = \frac{E}{1-v^2} \quad (\varepsilon_a^{180°} + v\,\varepsilon_c^{180°})$$

Cancel stress component due to the axial force.

$$\sigma_M^{M_z} = \frac{1}{2} \quad (\sigma_x^{0°} - \sigma_x^{180°})$$
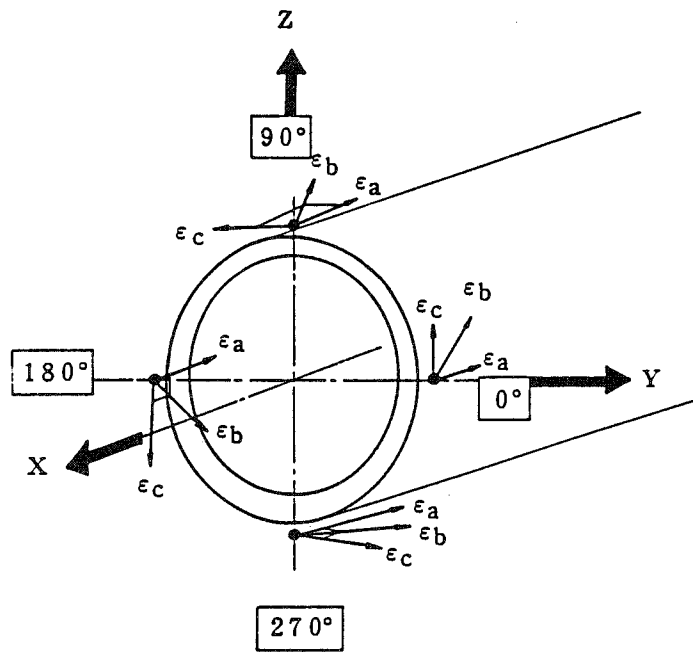
Figure G.1 Location of Strain Gage

Appendix H

Strain Concentration at Crack Location

Appendix H Strain Concentration at Crack Location

The stress distribution in the vicinity of the crack and the strain gage closest to the crack is calculated by use of a static finite element model. The relation between the measured stress and the stress at the crack location is then evaluated.

(1) Stress Concentration Factor in Elastic Range

Figure H.1 shows the finite element model used for the stress calculation. The axial axi-symmetric, two dimensional solid element of the ABAQUS code was employed, and a static tensile load was applied to the left side boundary of the model. Figure H.2 shows the maximum principle stress distribution in the vicinity of the crack and the strain measuring point.

When the crack location is considered to coincide with the maximum stress location, the magnification (K) of the stress at the crack location to the gage location becomes;

$$K = \frac{\text{stress at crack location}}{\text{average stress in the gage length}} = \frac{401 \ [kg/mm^2]}{341 \ [kg/mm^2]} = 1.2$$

thus, the stress at the strain measurement location should be multiplied by K =1.2 for the fatigue damage assessment at the cracked location.

(2) Strain Concentration Factor in Plastic Range

Figure H.3 illustrates the three stress-strain points, A, B and C as follows:

A: Stress conditions without any stress concentration
B: Stress concentration assuming elasticity
C; Actual stress concentration

also, the following ratios are defined

$k_t = \sigma_b/\sigma_c$ (elastic stress concentration factor)
$k_\sigma = \sigma_c/\sigma_a$, $k_\epsilon = \epsilon_c/\epsilon_a$

Then, according to Neuber, the following relationship can be assumed,

$$k_t^2 = k_\sigma \cdot k_\epsilon$$

Using the above ralationship, a strain concentration factor of k_ϵ = 1.35 is obtained as illustrated in Figure H.4 (k_t = 1.2).
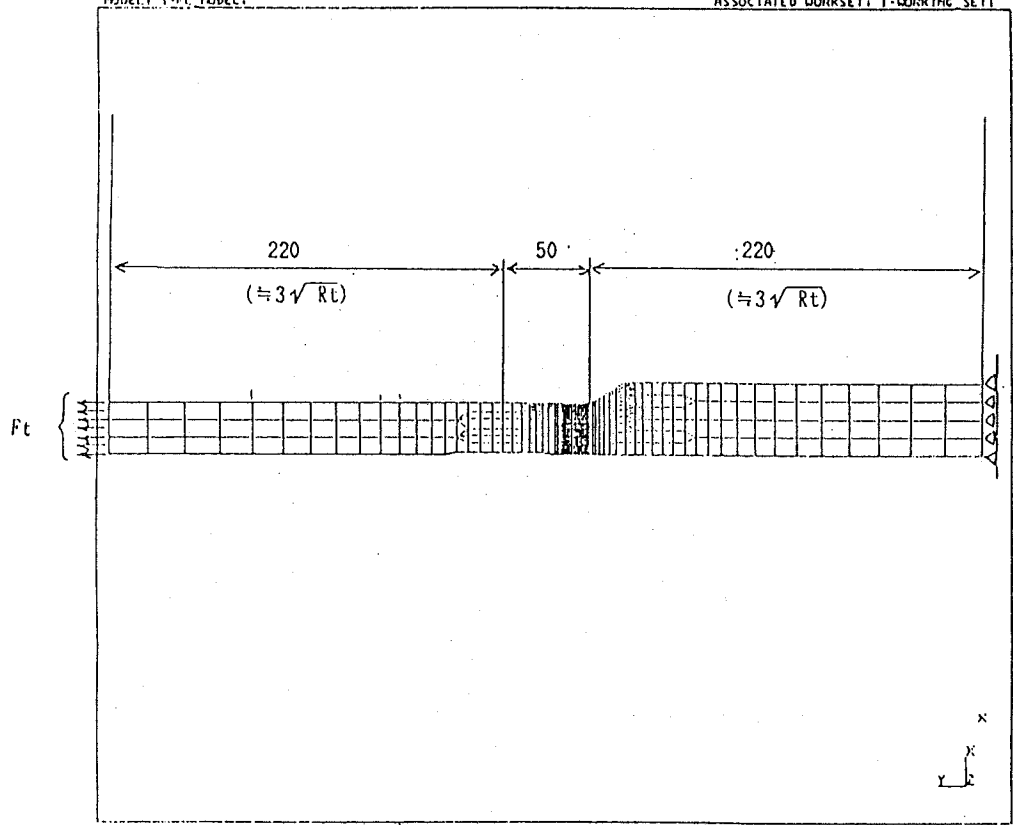
220

50

:220

$(\fallingdotseq 3\sqrt{Rt})$

$(\fallingdotseq 3\sqrt{Rt})$

Ft

X

Figure H.1 (1) FEM Model

H-3
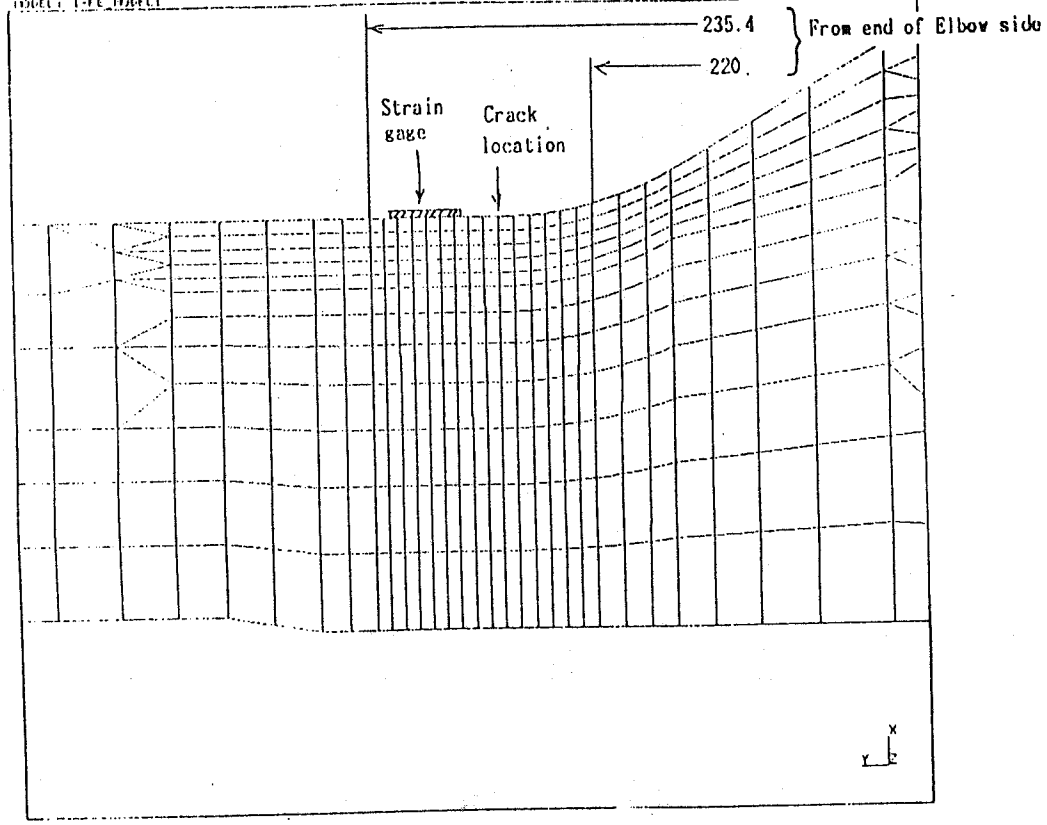
Figure H.1 (2) FEM Model (detail near crack location)

PLOT OF FUNCTION(S) - CURRENT
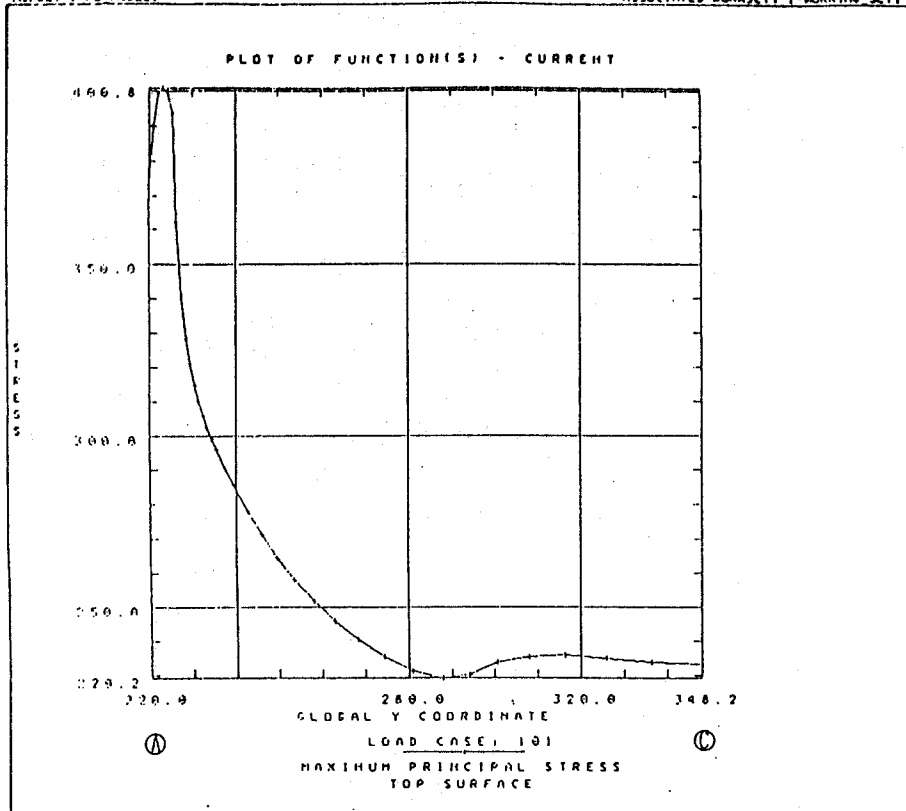
Figure H.2 (1) Stress Distribution

PLOT OF FUNCTION(S) - CURRENT
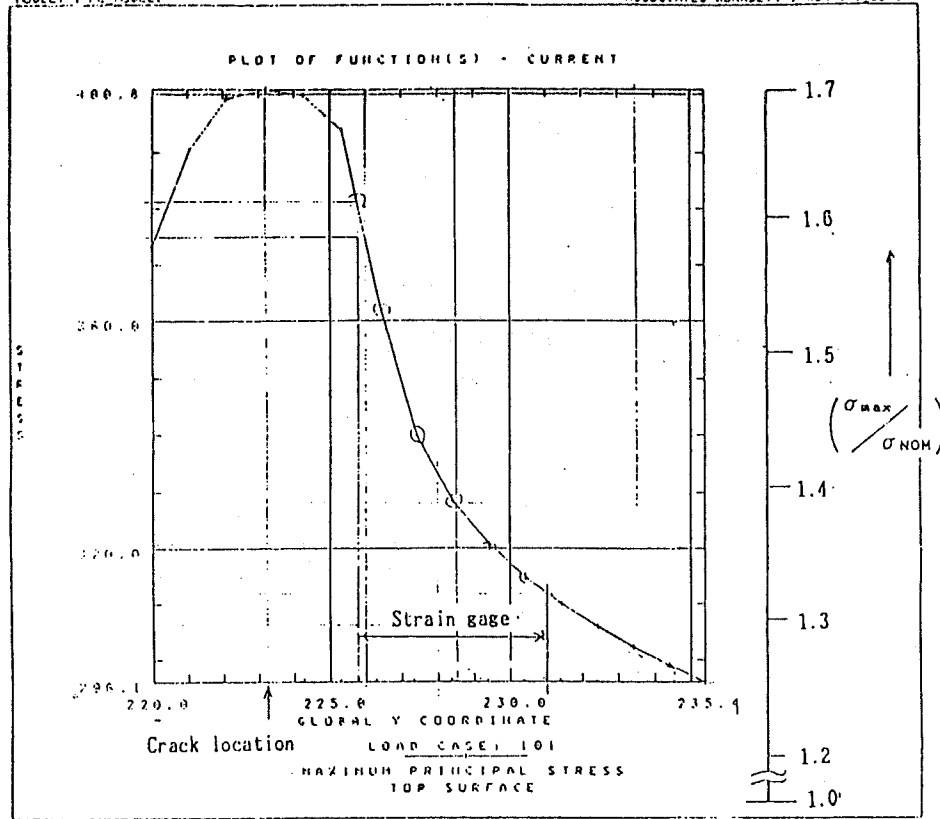
Figure H.2 (2) Stress Distribution Near Crack
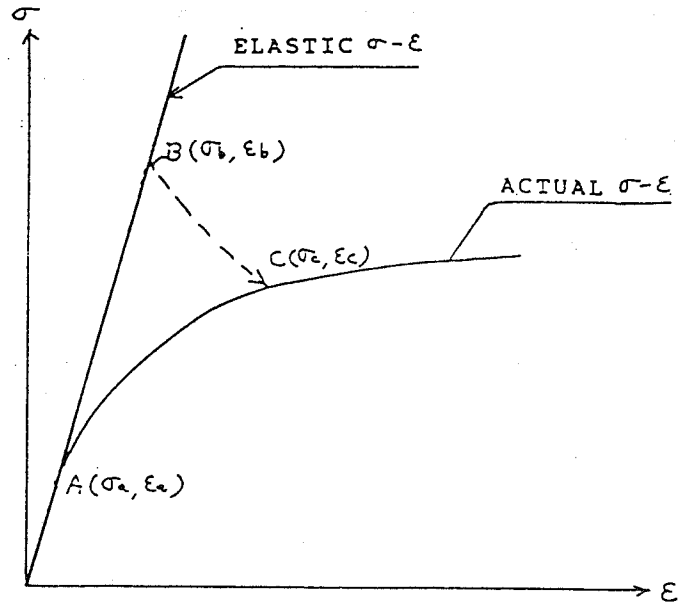
Figure H.3   Illustration of Neuber's Rule
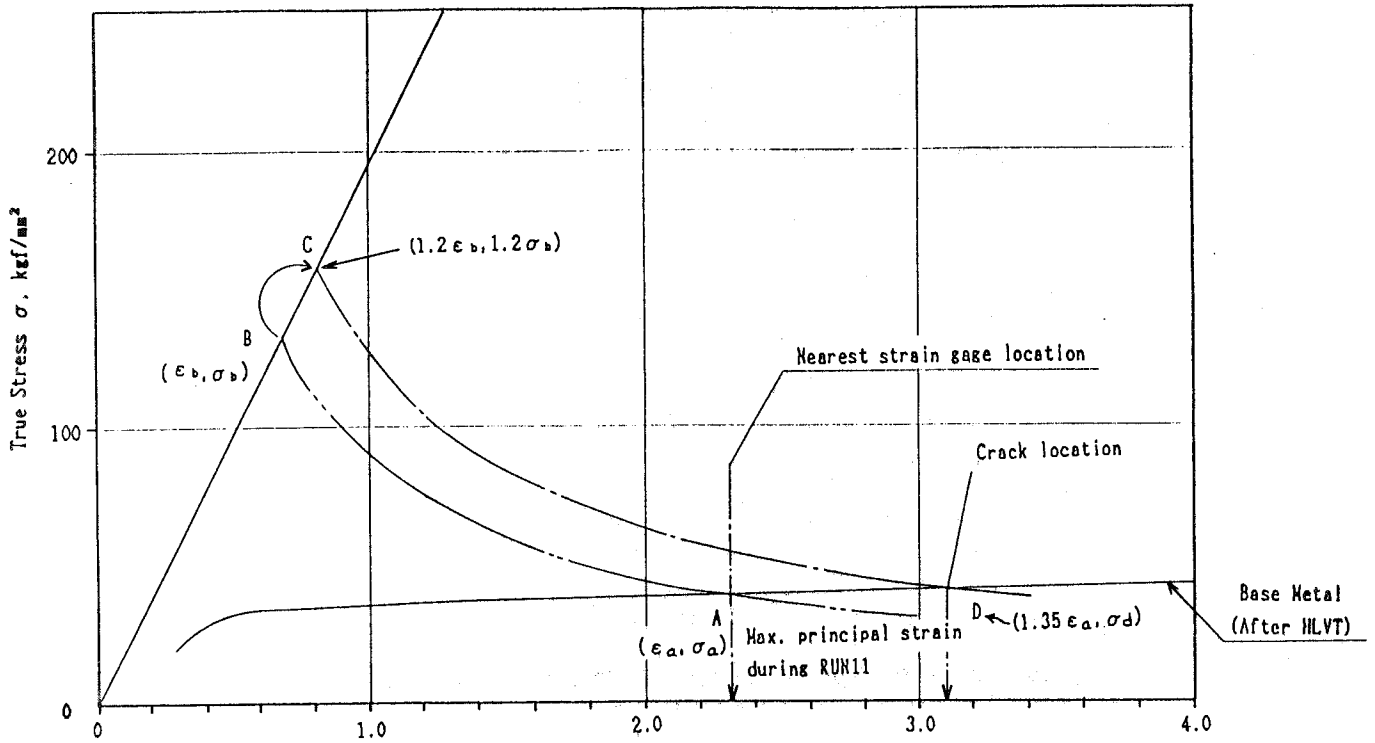
Figure H.4 Estimation of Strain Concentration Factor

Appendix I

Back-up Procedures for Damaged Strain Gages

Appendix I   Back-up Procedures for Damaged Strain Gages

1.   Introduction

Strain gages at cross section HR3A failed due to the large cyclic strain and/or the crack initiation under the gage base. As these are very important for estimating the cumulative fatigue damage factor of the piping, estimation procedures for strain signals of these damaged gages using neighboring gage signals are discussed.

2.   Backup Procedures

Backup procedures of the measuring point HR3A-BX (Channel 153X) and HR2A-EX,EY (Channel 144X,Y) are discussed. The following backup procedures are considered:

   a.   For HR3A-BX, the following two types of backup procedures are tried:

      i.   Evaluate average of the ratio of maximum values (HR3A-EX/HR3A-BX, Channel 144X/153X) in some plastic runs, and the product of this ratio to the measured maximum value of HR3A-EX is considered as the estimated maximum response of HR3A-BX.

      ii. Evaluate average of the ratio of maximum values (HR2A-FX/HR3A-BX, Channel 149X/153X), and the product of this ratio to the measured maximum value HR3A-FX is considered as the estimated maximum response of HR3A-BX.

   b.   For HR3A-FX and HR3A-EY, the following procedure is considered: Evaluate average of the ratio of maximum values (HR3A-EX/HR3A-FX, Channel 144X/149X), and the product of this ratio to the measured maximum value of HR3A-FX is considered as the estimated maximum response of HR3A-EX. The same procedure is also applied to the Y direction data.

3.   Estimated Response

Estimated maximum responses of HR3A-BX, HR3A-EX and EY are shown in Table I.1.   In Table I.1, available measured maximum values are compared with corresponding estimated values and it is found that estimation errors are about 10% or less for these test cases. Thus, it is concluded that the proposed backup procedures are acceptable for practical use.

Table I.1 Estimation of Maximum Response

Run (MPR)	HR3A-EX (144X) Measured	HR3A-EX (144X) Estimate	HR3A-EY (144Y) Measured	HR3A-EY (144Y) Estimate	HR3A-FX (149X) Measured	HR3A-BX (153X) Measured	HR3A-BX (153X) Est(*2)	HR3A-BX (153X) Est(*3)
8* (0.4)	6835	6562 (-4.0%)	2287	2342 (+2.4%)	4654	8325	7792 (-6.4%)	7539 (-9.4)
8** (0.4)	7340	7575 (+3.2%)	2521	2556 (+1.4%)	5372	7792	8367 (+13.8%)	8703 (+11.7%)
9 (0.75)	10479	11250 (+7.4%)	3867	3711 (-4.0%)	7979	failed	11946 (NA)	12926 (NA)
10 (1.0)	failed	13312 (NA)	failed	3955 (NA)	9441	failed	NA (NA)	15294 (NA)
11 (1.0)	20638	19575 (+5.4%)	failed	5583 (NA)	13883	22819	23527 (+3.1%)	22491 (-1.4%)

Note *1) Percentage in parenthesis denotes the estimation error

*2) Estimated from measured value of HR3A-EX (Ch 144X)

*3) Estimated from measured value of HR3A-FX (Ch 149X)

Appendix J

Correction of S/G Top Displacement

Appendix J   Correction of S/G Top Displacement

Wire type displacement sensors were employed to measure the displacements at the S/G top (SD9A, SD9B, and SD10). As shown in Figures J.1 and J.2, measured displacement signals are affected by the cross-talk components (i.e., interaction of X and Y direction movements) due to the finite length of the wire. The correction procedure for this error and results are discussed below.

1.   Correction Procedure

As shown in Figure J.2, measured displacement x and y are related to the actual displacement x and y as follows.

$$(l_x + x)^2 + y^2 = (l_x + \bar{x})^2$$

$$(l_y + y)^2 + x^2 = (l_y + \bar{y})^2$$

where,

lx, ly : length of wire $\quad \begin{cases} l_x = l_y = 127mm \ for \ Run \ 1 \sim 4 \\ l_x = l_y = 191mm \ for \ Run \ 5 \sim 14' \end{cases}$

Thus, x and y are evaluated as follows.

$$x = \{ -A + \sqrt{A^2 - 4B} \} / \left\{ 1 + \left(\frac{l_x}{l_y} \right)^2 \right\}$$

$$y = \frac{l_x}{l_y} x + \bar{y} - \frac{l_x}{l_y} \bar{x} + \frac{(\bar{y}^2 - \bar{x}^2)}{2l_y}$$

where,

$$A = l_x - \left(\frac{l_x}{l_y} \right)^2 \bar{x} + \frac{l_x}{l_y} \bar{y} + \frac{l_x}{2l_y^2} (\bar{y}^2 - \bar{x}^2)$$

$$B = \left[-l_x \bar{x} - \frac{\bar{x}^2}{2} + \left\{ \frac{l_x}{l_y} \bar{x} - \bar{y} - (\bar{y}^2 - \bar{x}^2)/2l_y \right\}^2 / 2 \right] \left\{ 1 + \left(\frac{l_x}{l_y} \right)^2 \right\} / 2$$

2. Results of Correction

Correction results for the maximum response of SD9A and SD10 for typical test cases are shown in Table J.1. It is found that the effect of the Y-direction movement on the X-direction data is small. On the other hand, the effect of the X-movement on the Y-direction data is rather large and the actual displacement in the Y-direction is larger than the measured value.

Data shown in Figure 5.6 (2) and 5.9 (2) in the report are already corrected by the above mentioned procedure.

Table J.1 Correction of S/G Top Displacement

(mm)

Measuring Point		RUN 4 (0.1 MPR)	RUN 8** (0.4 MPR)	RUN 11 (1.0 MPR)
SD9A (58X)	Original	- 10.6	- 38.7	- 75.6
	Corrected	- 10.6	- 38.9	- 80.2
SD9B (59X)	Original	- 10.7	- 37.4	- 73.3
	Corrected	- 10.7	- 37.6	- 77.9
SD10 (60Y)	Original	- 0.3	- 3.6	- 13.1
	Corrected	- 0.7	- 7.7	- 32.7
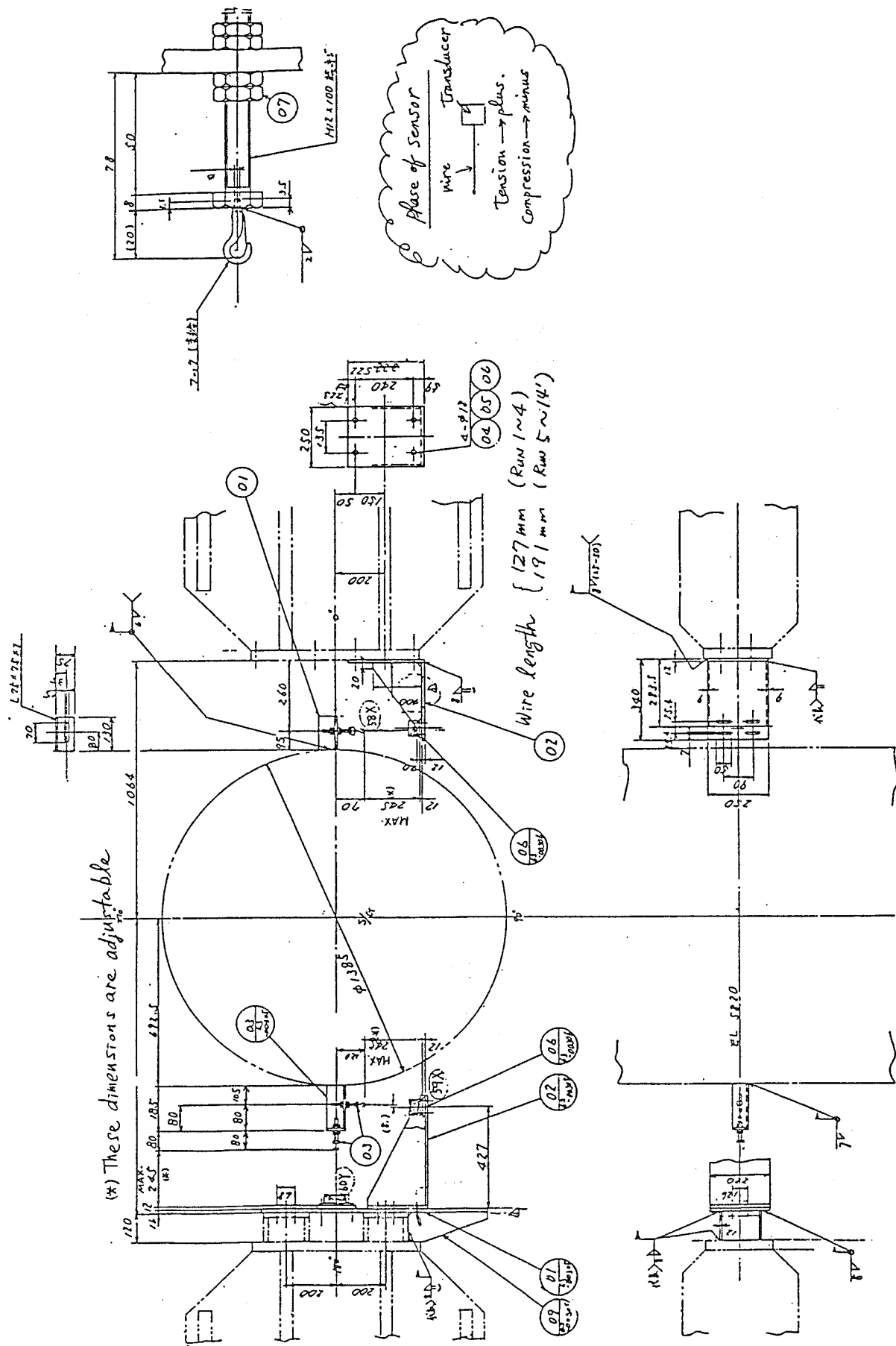
Figure J.1 Mounting Method of Transducer
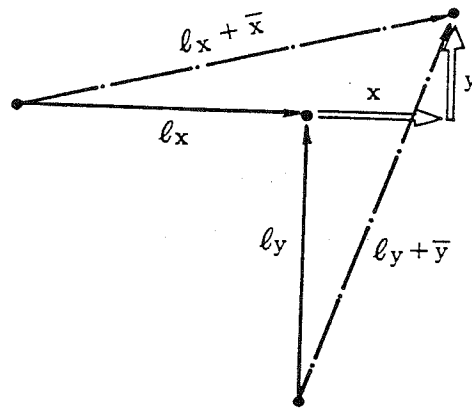
Figure J.2   Measured Displacement and Actual Displacement

Appendix K

Summary of Post-Test Examination Results

As received from TADOTSU

○ Visual inspection

○ PT at inner surface of weld joint

○ Measurement of circumferential length

○ Measurement of diameters

○ Measurement of thickness
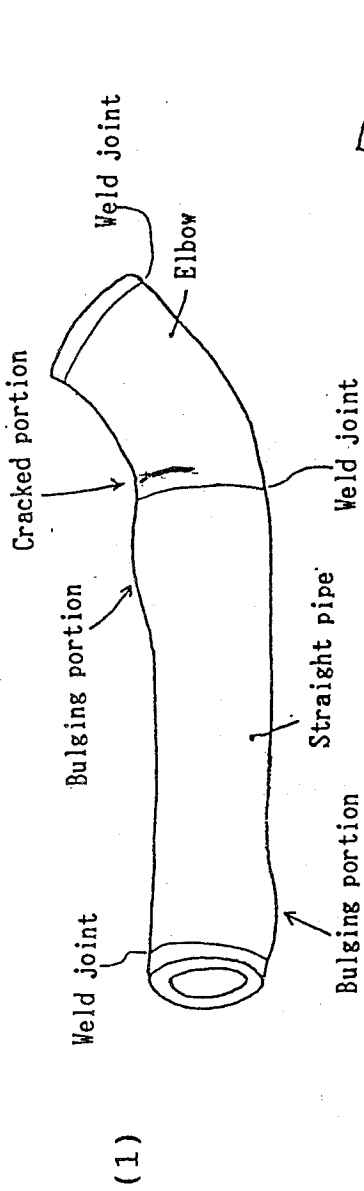
Transverse section cutting
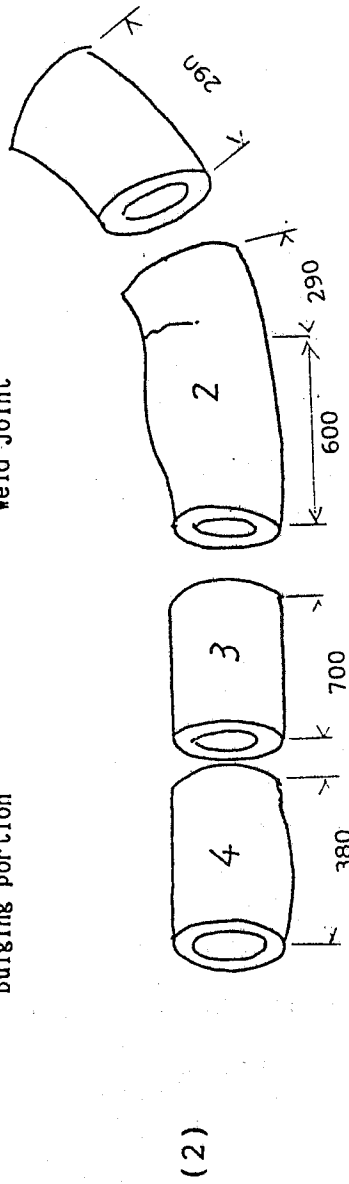
Longitudinal section splitting

○ PT of inner surface

○ Measurement of crack depth on inner surface

○ Measurement of thickness along longitudinal section
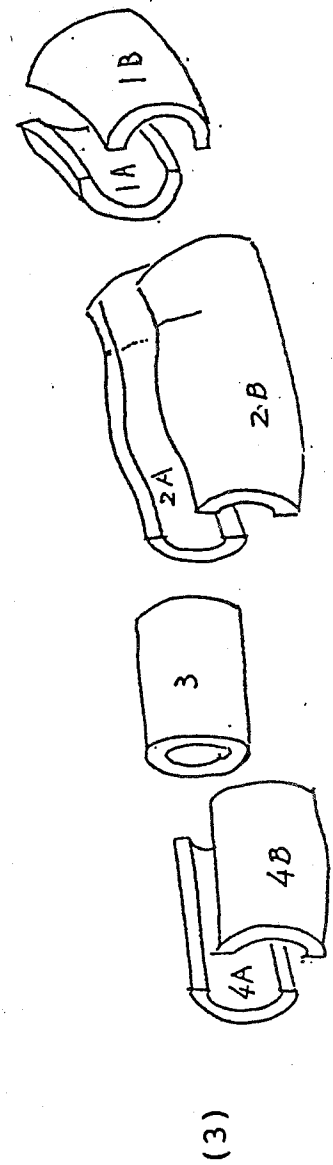
Figure K.i (1) Cutting Process (1/3)
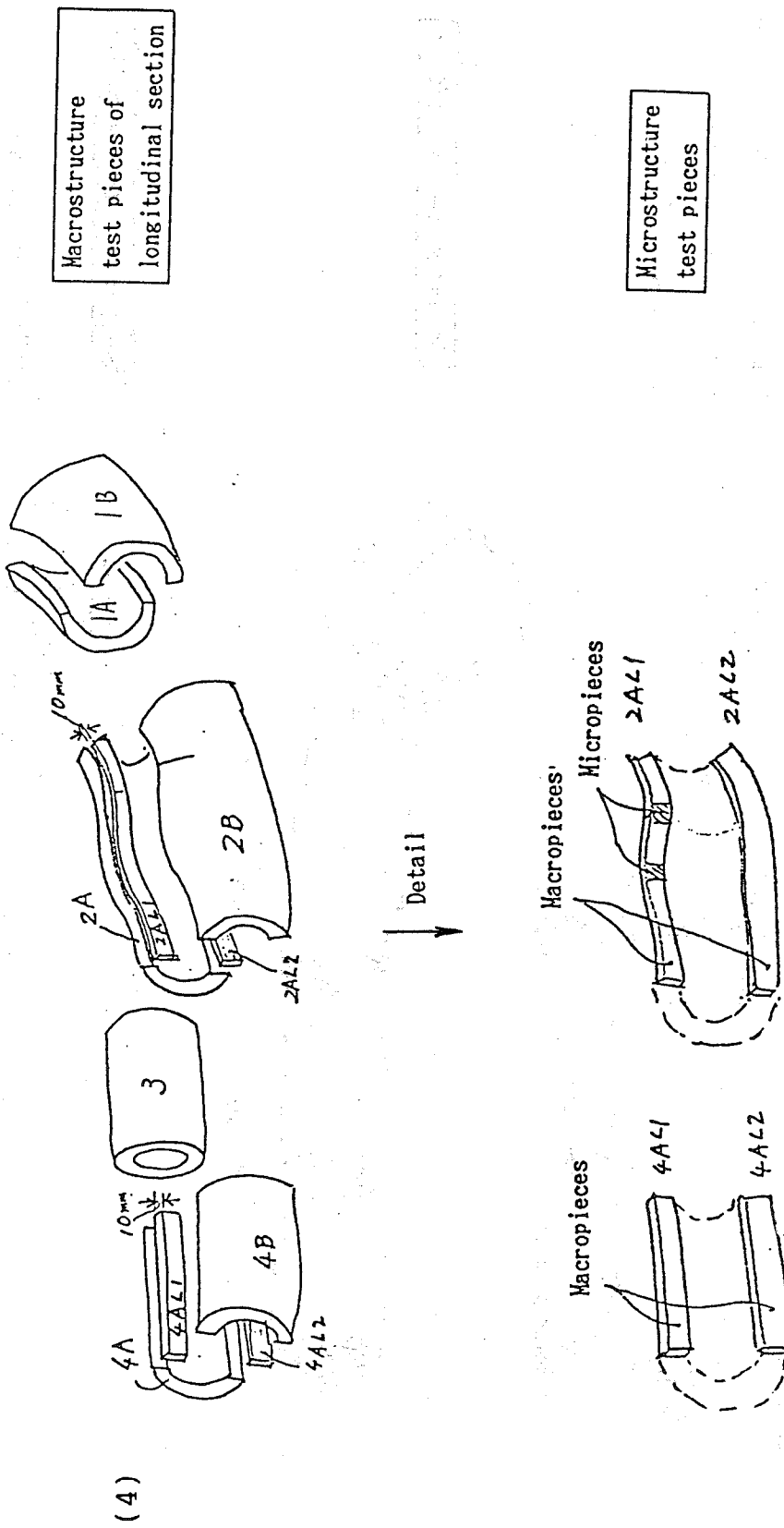
Figure K.1 (2) Cutting Process (2/3)

Figure K.1 (3) Cutting Process (3/3)

Transverse section cutting

o Measurement of thickness along transverse section

Macrostructure test pieces of transverse section

(I) Longitudinal section cutting

(II) Observation

(III) Tensile test pieces

(IV) Low cycle fatigue and crack growth rate test pieces

(5)

Send to US

Detail

(IV): Fatigue crack growth rate test pieces

(IV) Low cycle fatigue test pieces

(II) Fractograph pieces

Cracked portion

(I) Cutting line

(III) Tensile test pieces

Bulging portion

(I) Cutting line

Cutting line

K-4

(1) Tensile

(2) Low cycle fatigue

(Thickness 12.5mm)
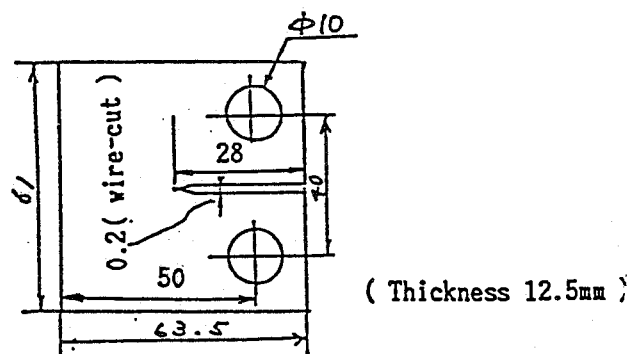
(3) Fatigue crack growth rate

Figure K.2   Specimen Dimensions
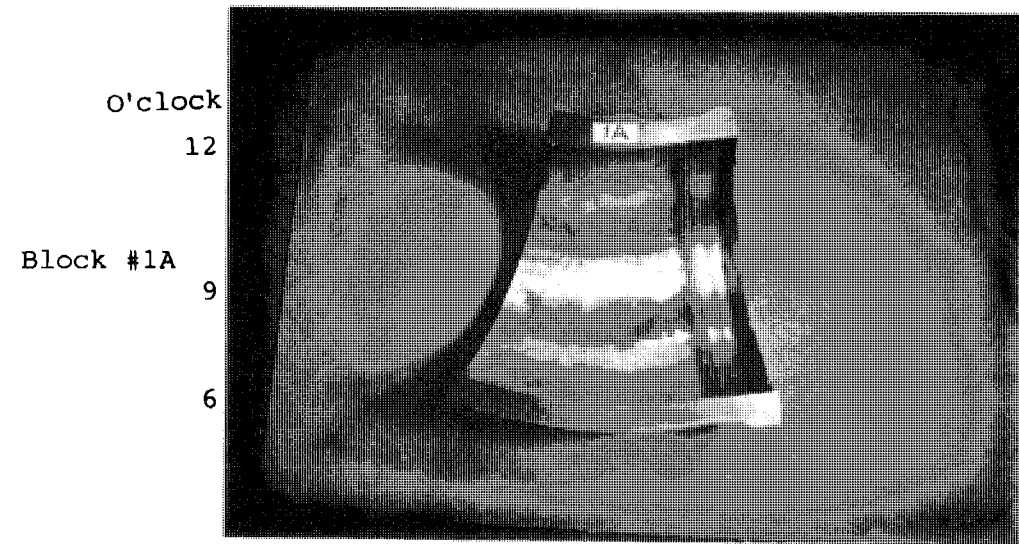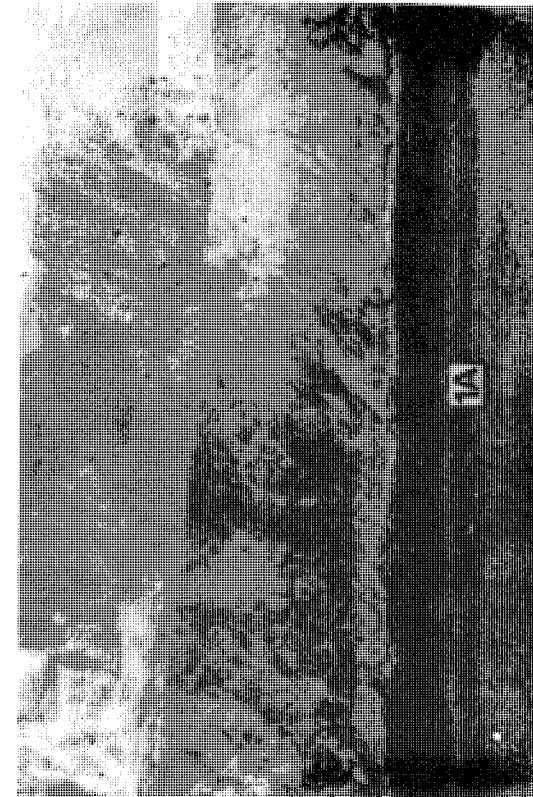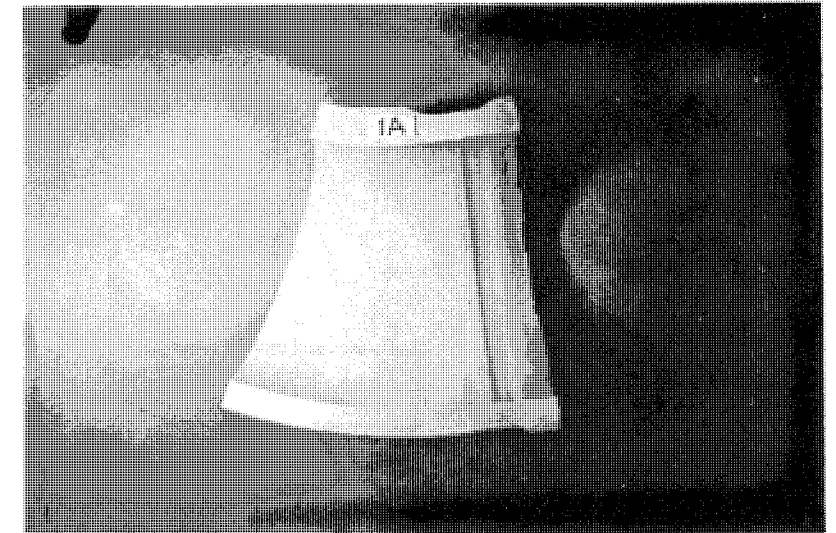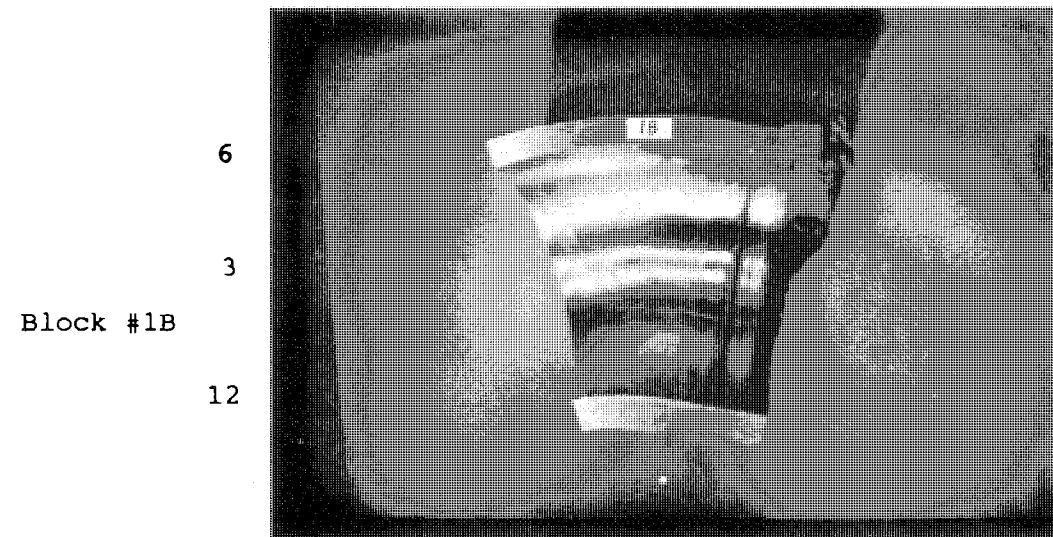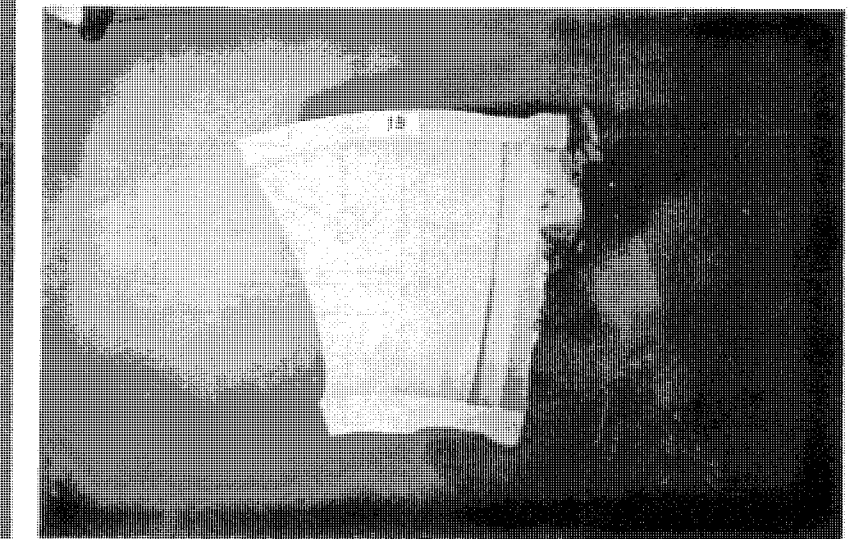
Figure K.3 Inner Surface of Blocks #1A and #1B

Before PT

After PT

12 O'clock

9 3

6

Cracks

Block #2A

O'clock

12

9

6
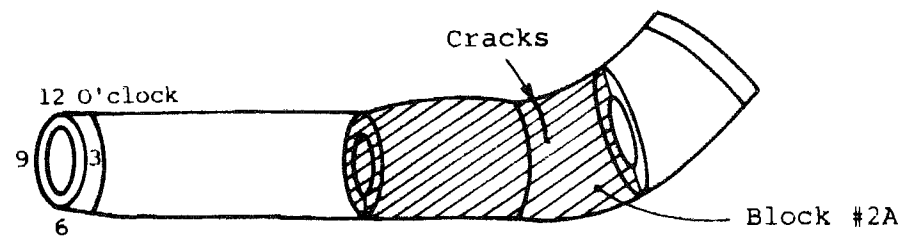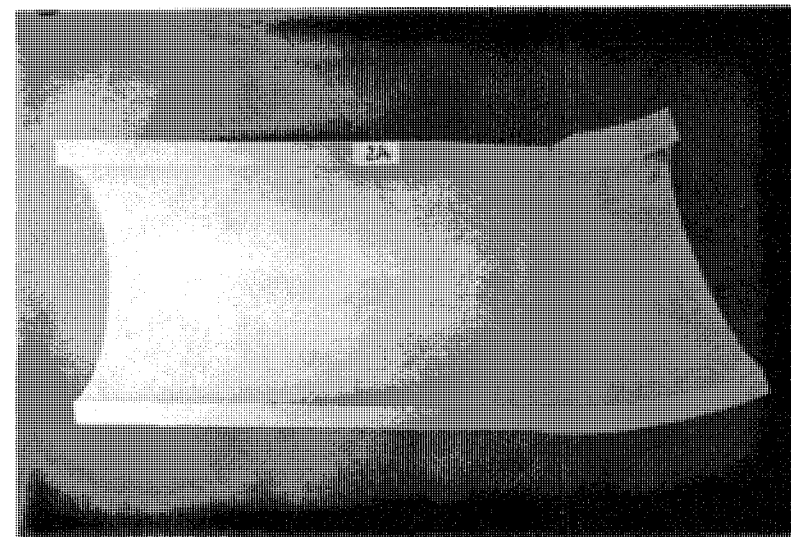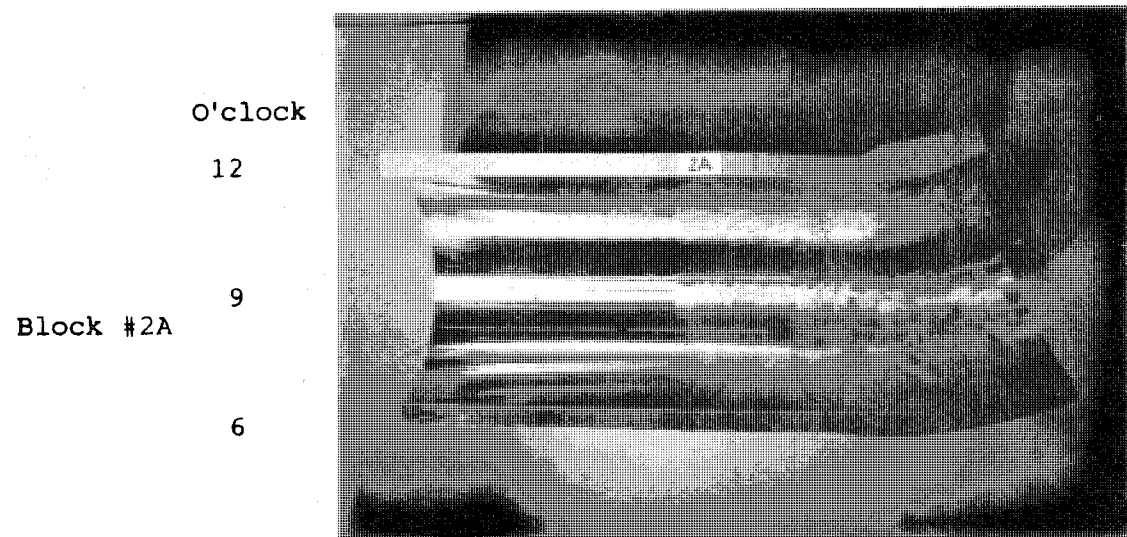
Block #2A

(1)

(3)

Close-up ⇓ Close-up

Close-up ⇓

Sketch

Dominant Crack

12 O'clock ➡

11 O'clock ➡

2A

2A

35

4*

3* 6*

5*

68
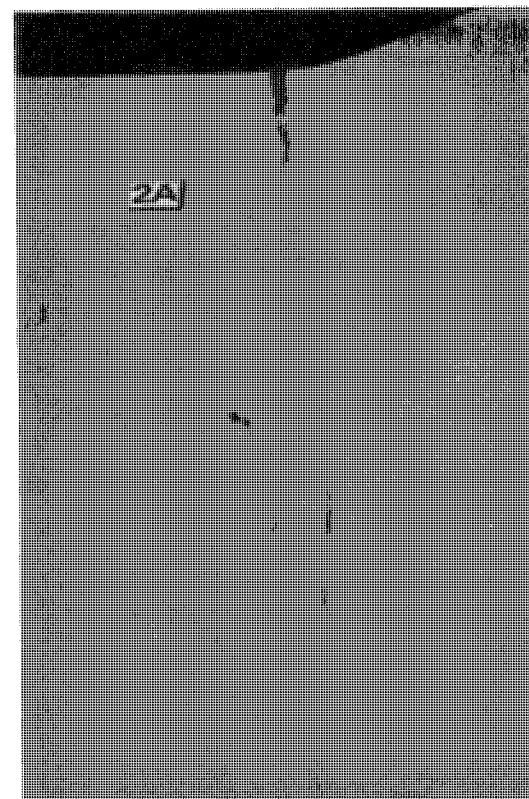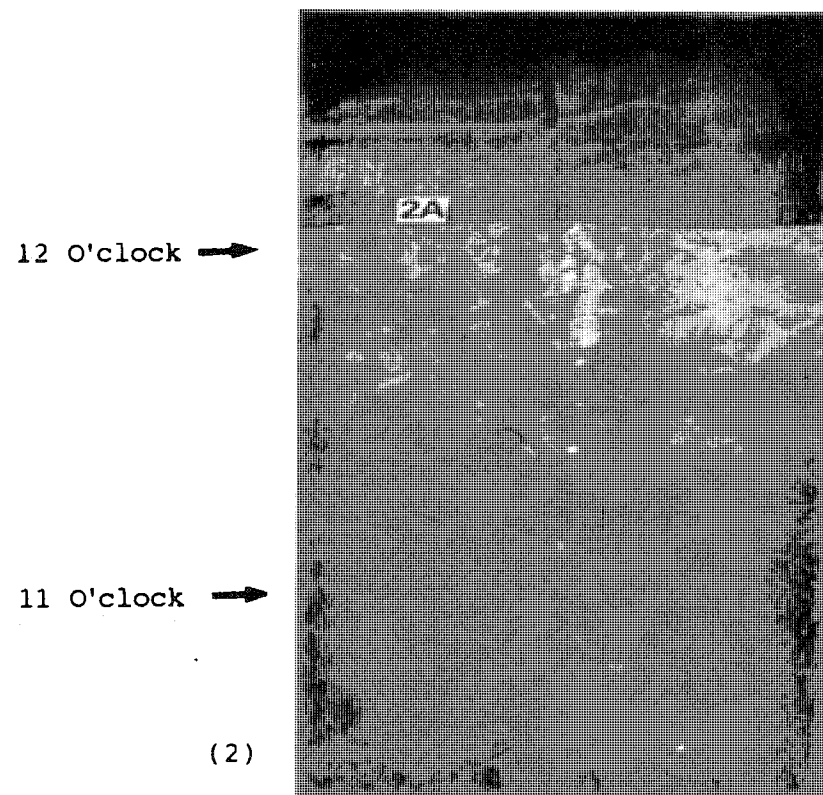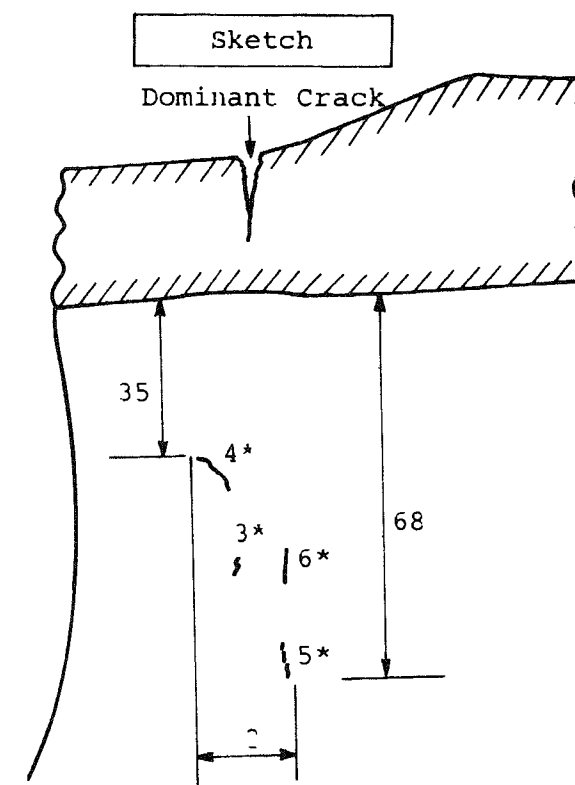
(2)   × 1   (4)   1

* : Crack length

Figure K.4   Inner Surface of Block #2A

Cracks

Block #2B

Before PT

O'clock

6

Block #2B   3

12

(1)

Close-up ⇓

(3)

After PT

(2)   × 2
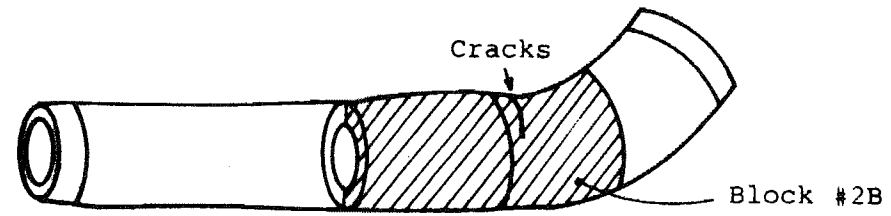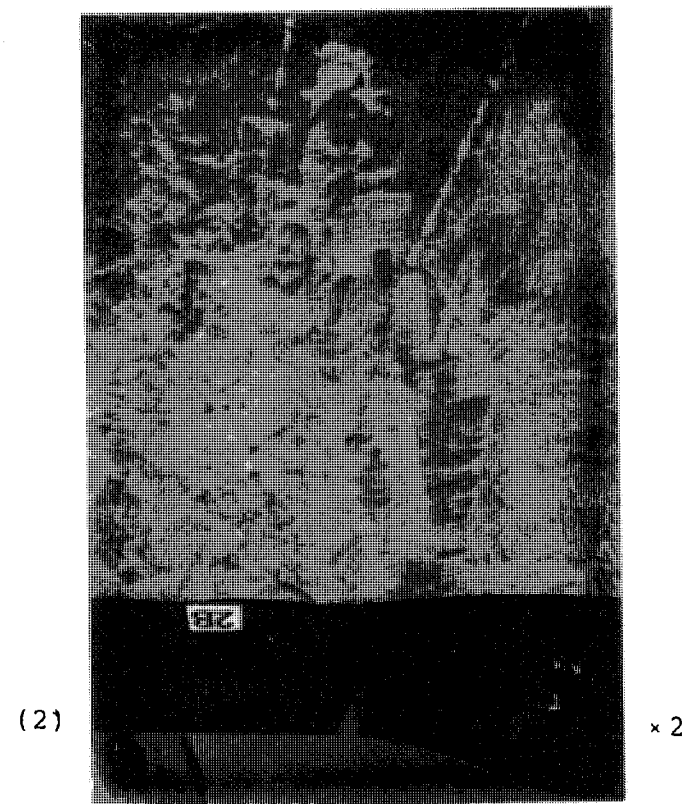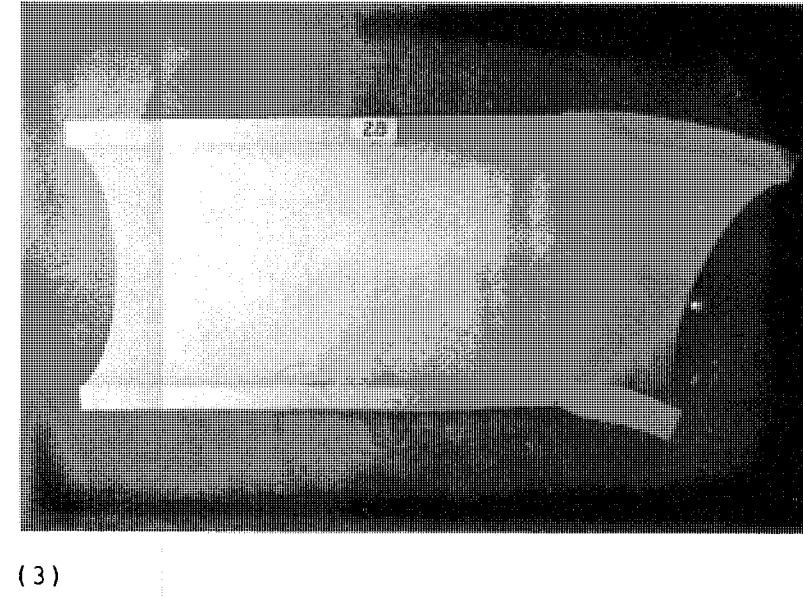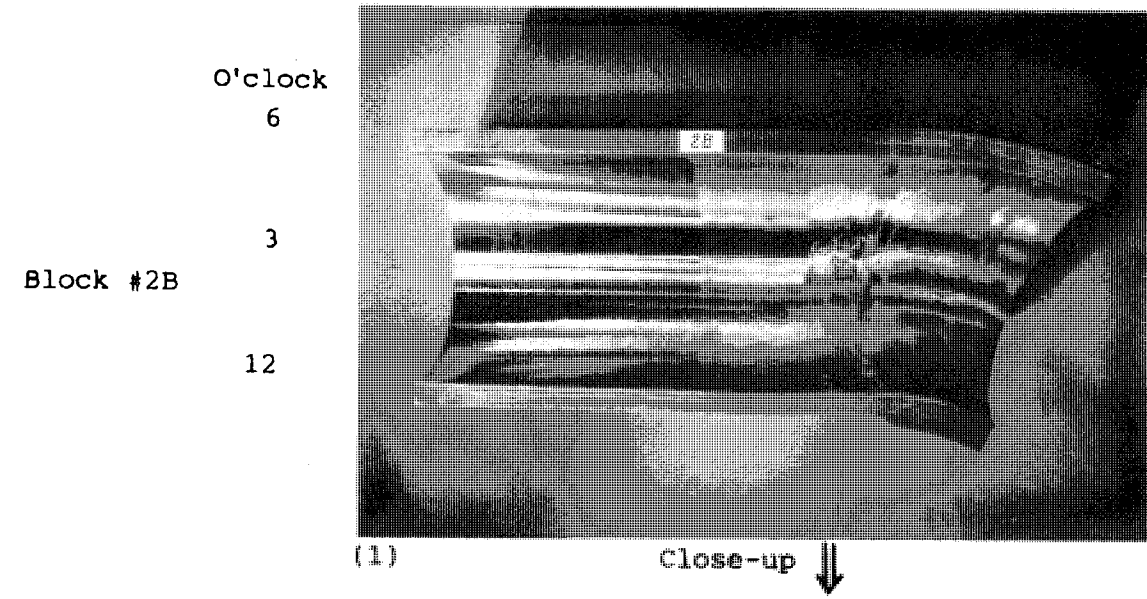
Figure K.5   Inner Surface of Block #2B
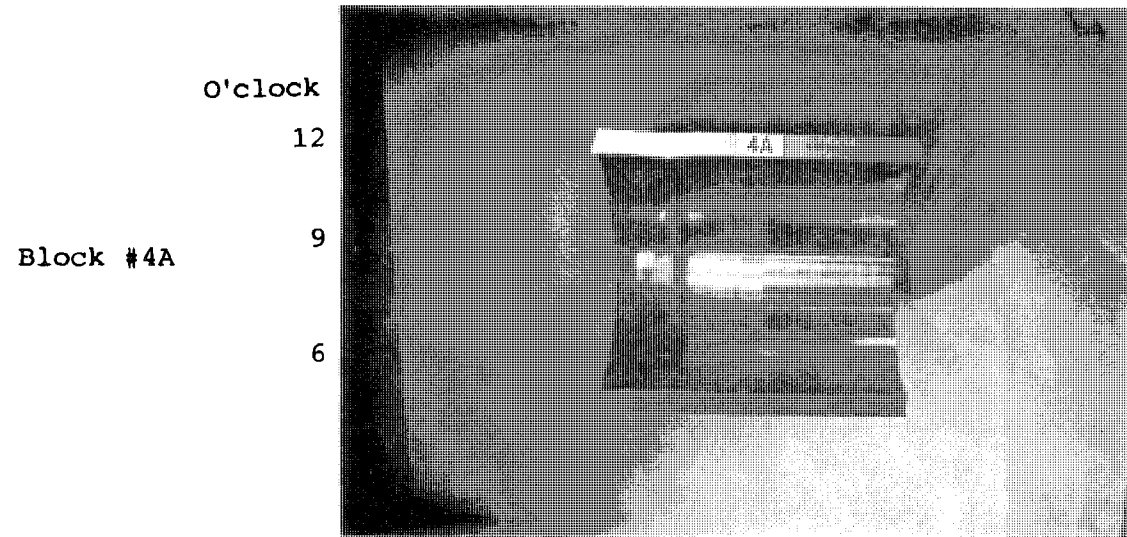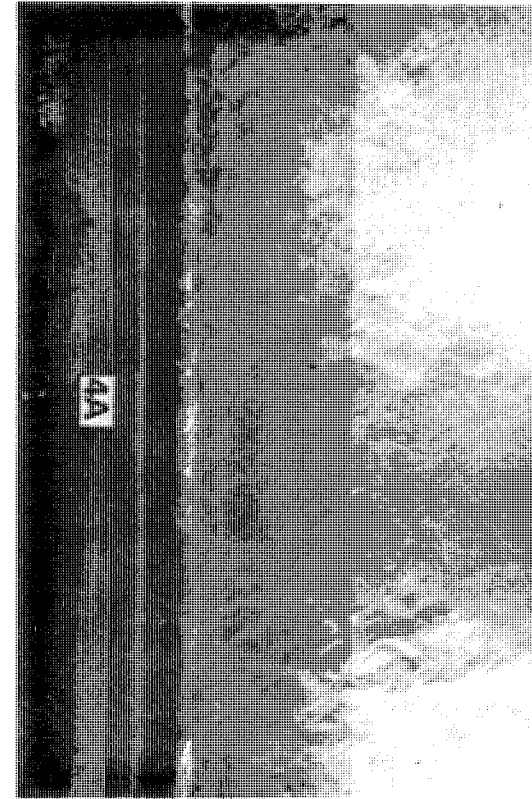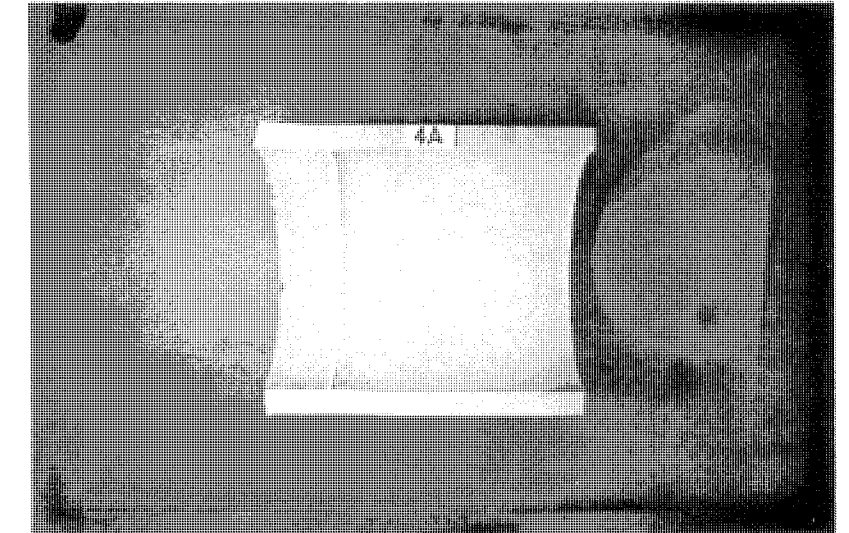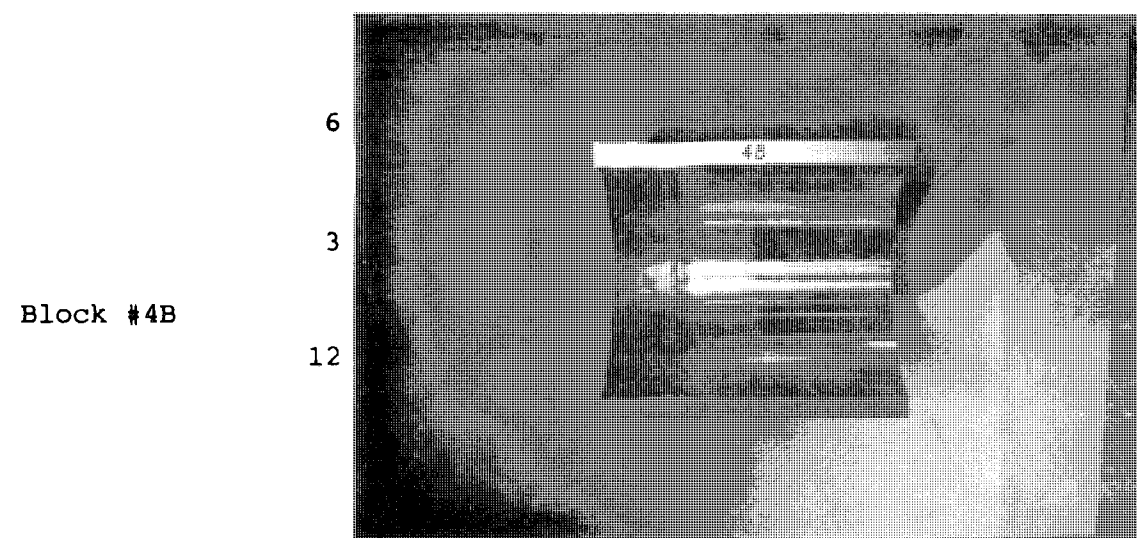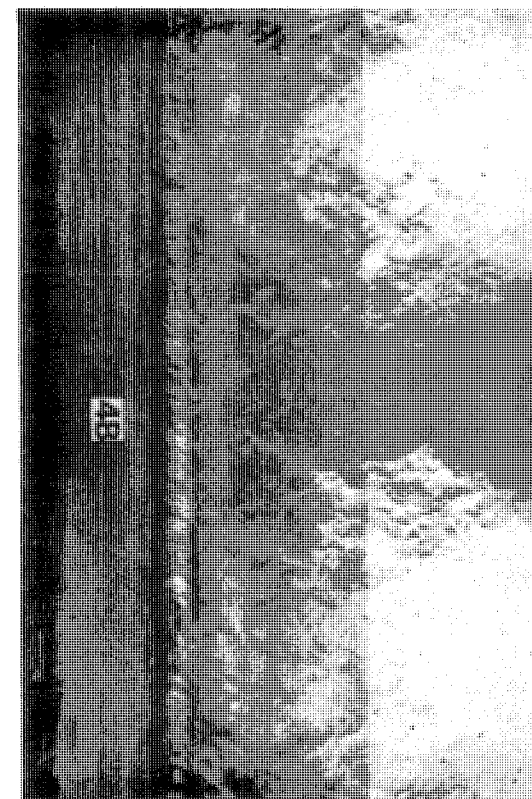
Figure K.6 Inner Surface of Blocks #4A and #4B

Weld joints
Cracks

Inner Surface, Near Weld

Before PT

After PT

O'clock

Block #4A

O'clock
12
9
6

(1)

Close-up

(5)

Block #4B

6
3
12

(3)

Close-up

(6)
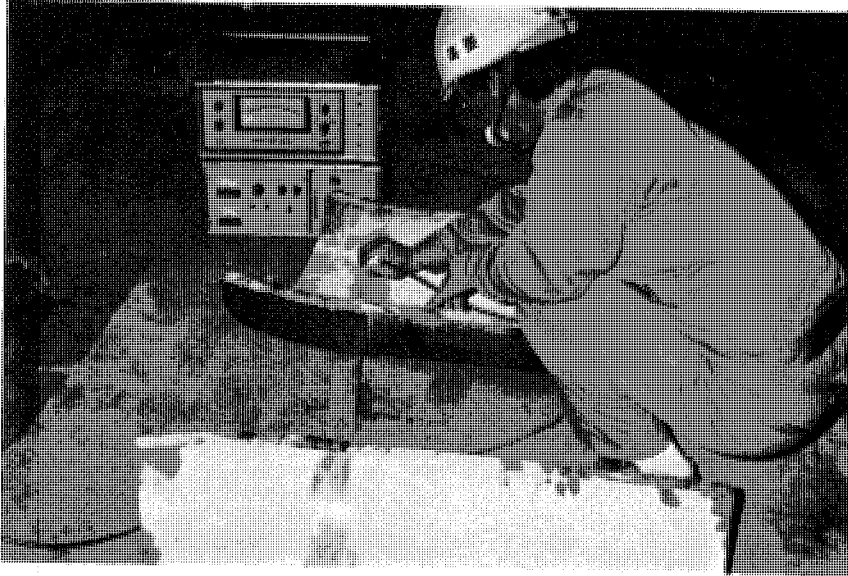
Maker : MHI

Name : Crack depth meter

Accuracy : ±10%

(1) Crack Depth Measurement

Dominant crack

(Outer surface)

(Inner surface)

Block #2A

$4^{\ell} \times 3^{d}$

$3^{\ell} \times 3^{d}$

$6^{\ell} \times 2.5^{d}$

$5^{\ell} \times 1^{d}$

d : depth (mm)

ℓ : length (")

(2) Crack Dimensions
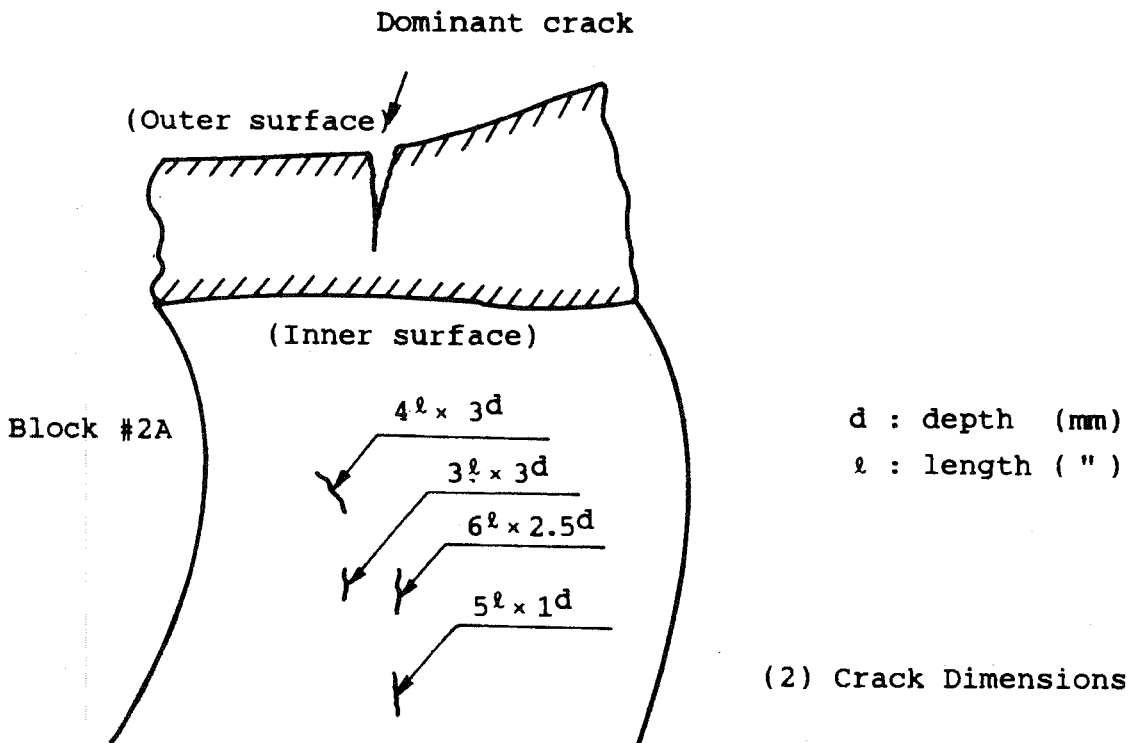
Figure K.7 Depth of Small Cracks on the Inner Surface
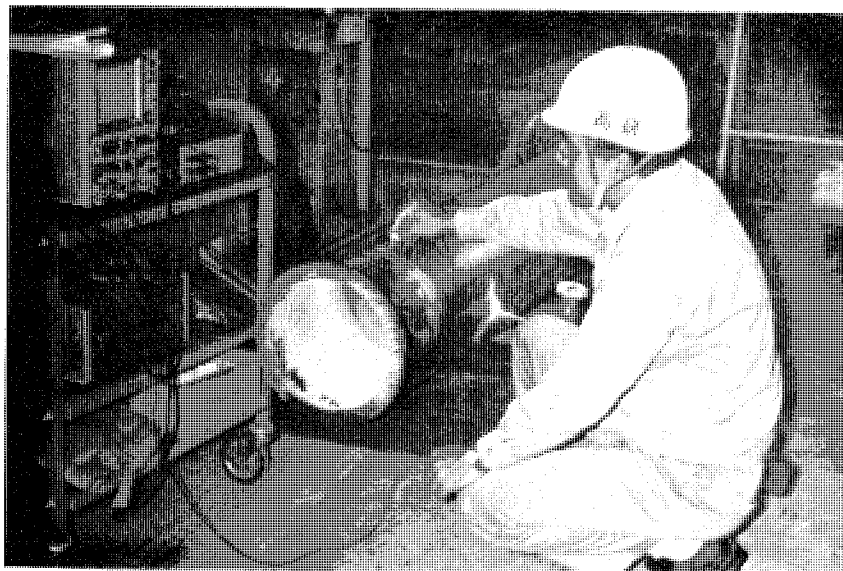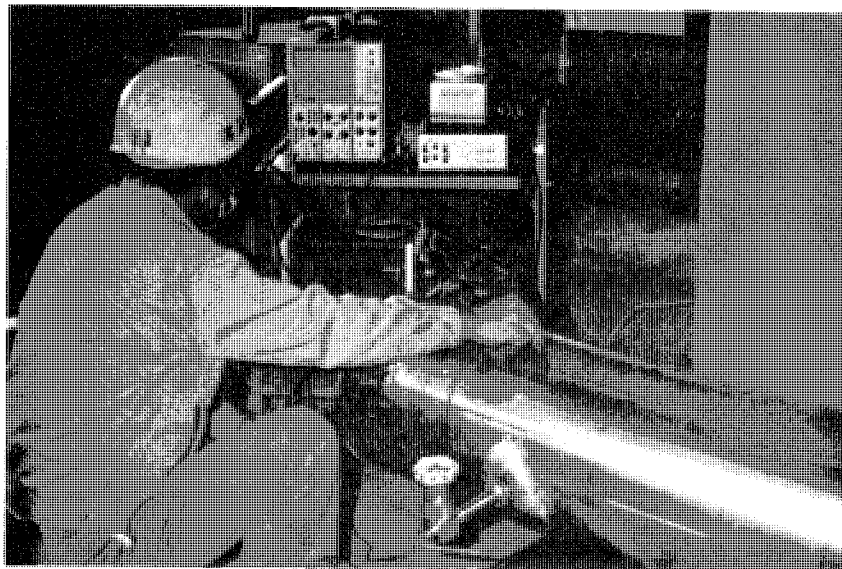
Instrument

Manufacturer : Sonick

Name : UT Detector MK-3

Accuracy : ±0.05mm

(1) Measurement

Figure K.8 (1)   Thickness of the Test Pipe (1/5)

K-11
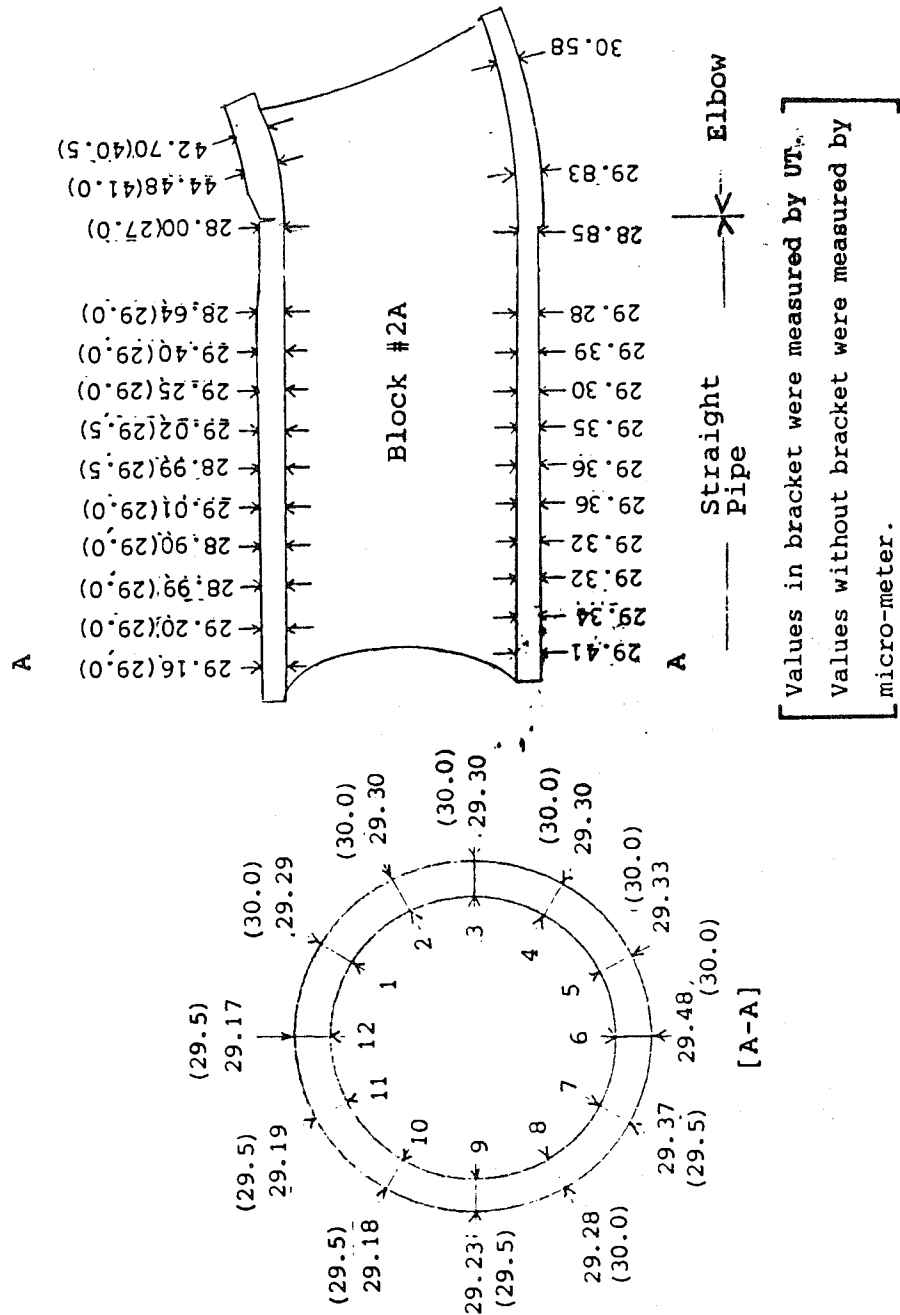
(1) Block #2A

Figure K.8 (2) Thickness of the Test Pipe (2/5)
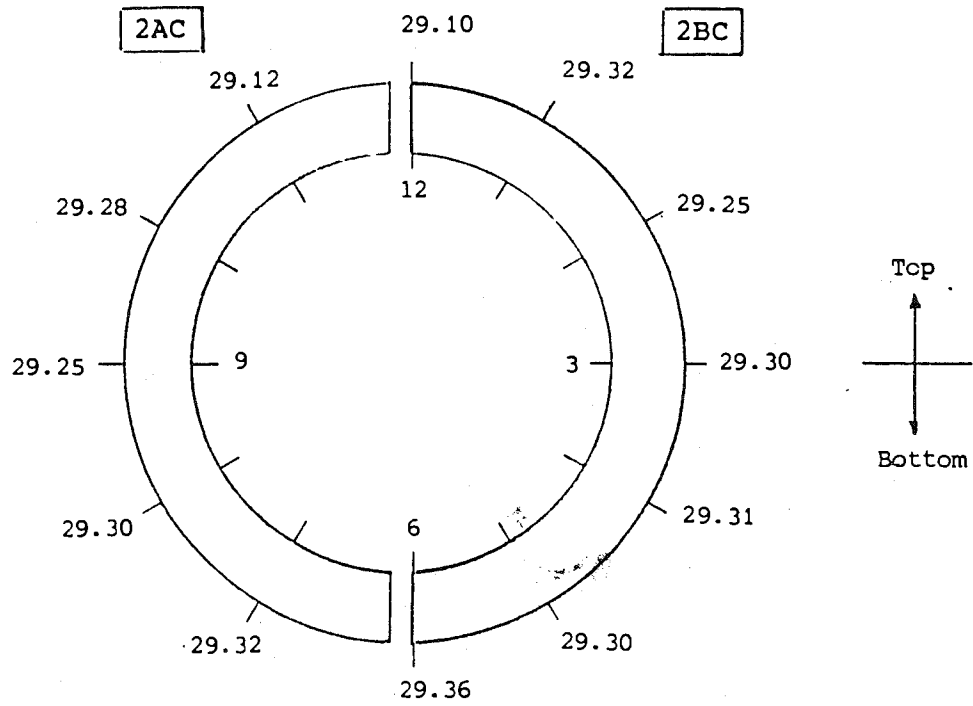
(2) Typical cross-section of top bulging region
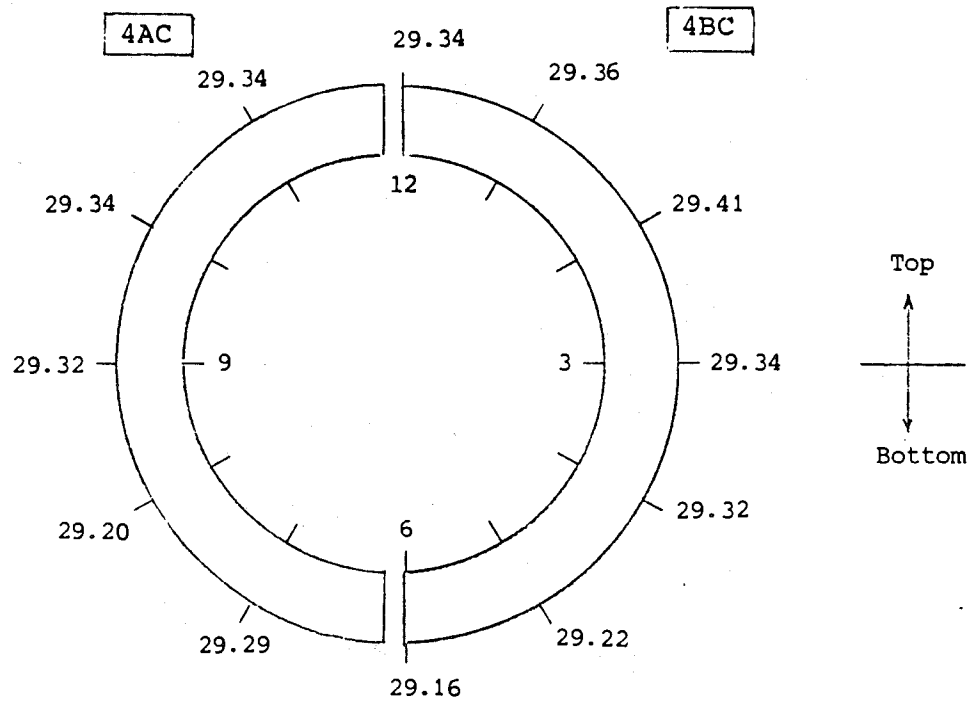
(3) Typical cross-section of bottom bulging region

Figure K.8 (3)   Thickness of the Test Pipe (3/5)

Figure K.8 (4) Thickness of the Test Pipe (4/5)
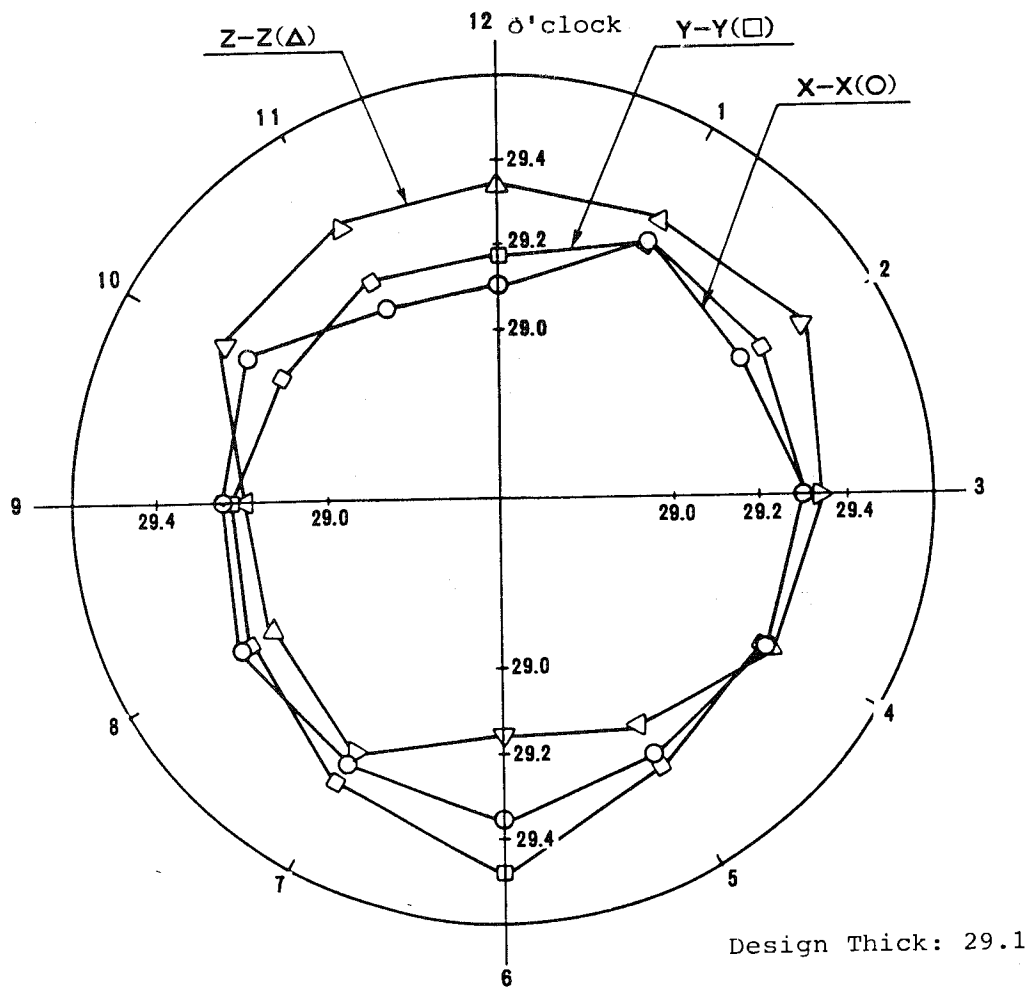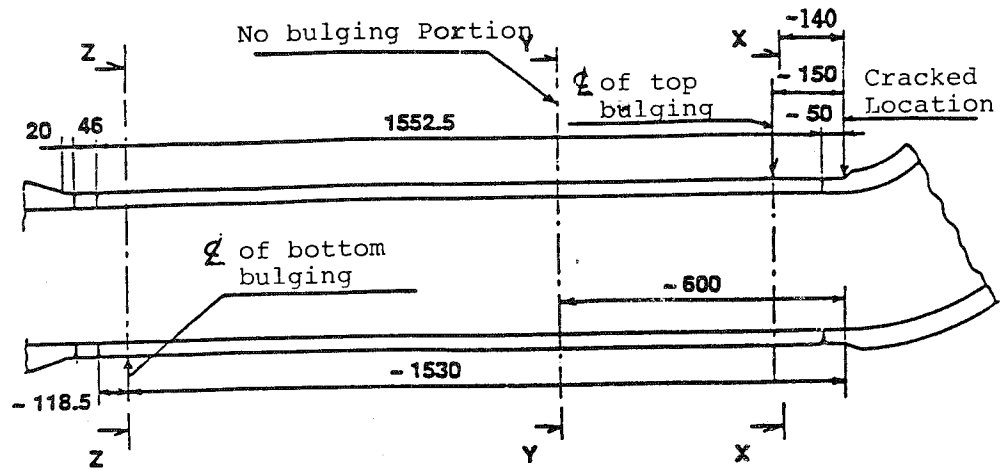
NOTE: Measured by Micrometer
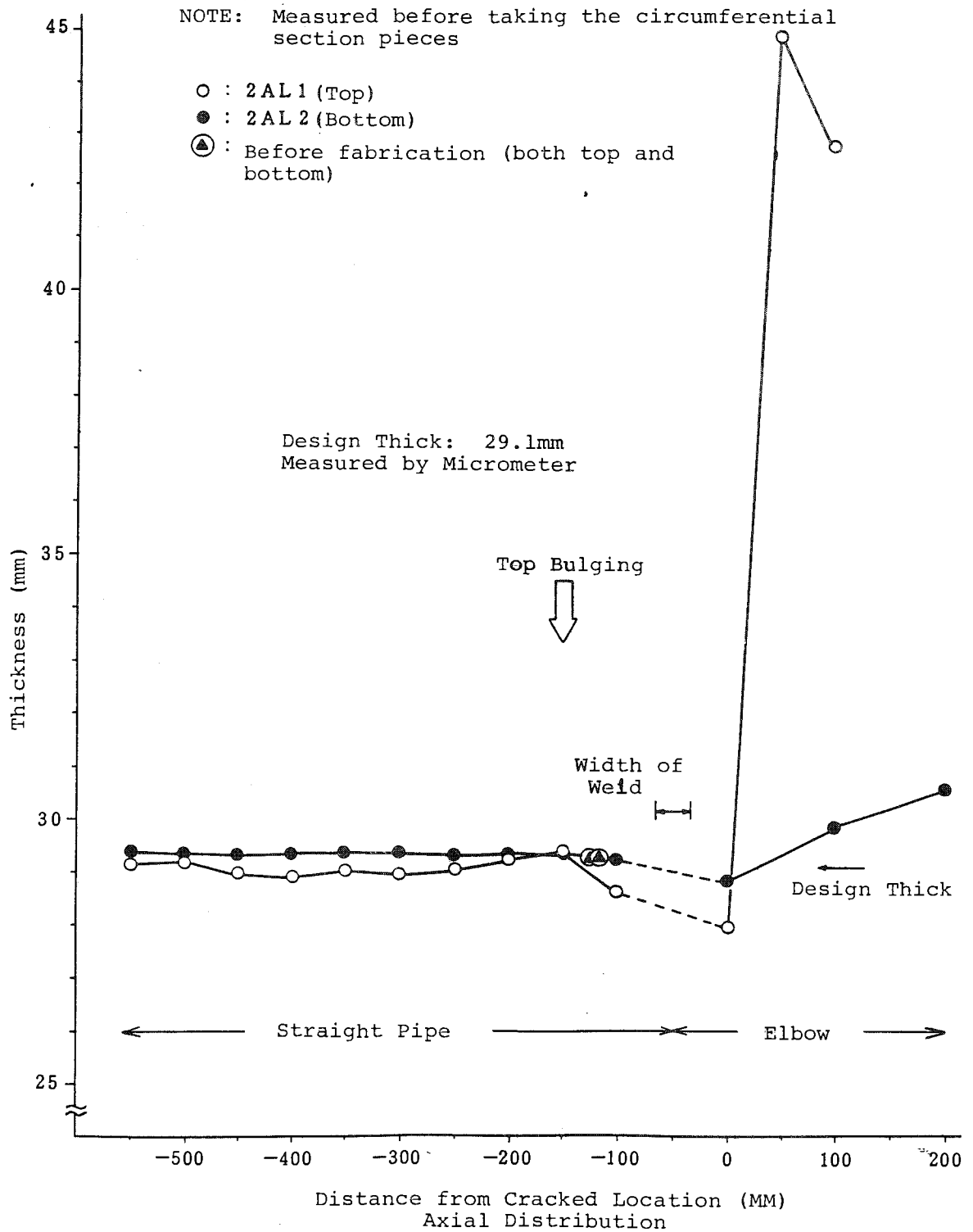
Figure K.8 (5) Thickness of the Test Pipe (5/5)

K-15
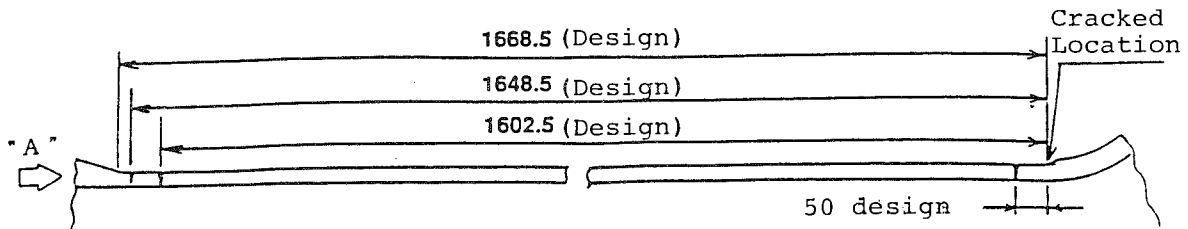
Figure K.9   Distribution of Diameter and Circumferential
Length

[Observation]

Bulging

Close-up

×0.14

×1
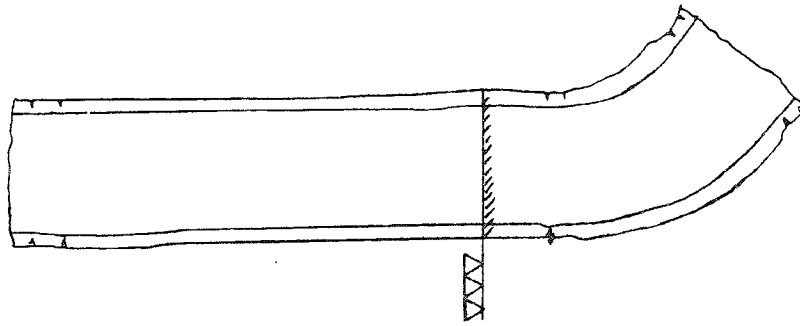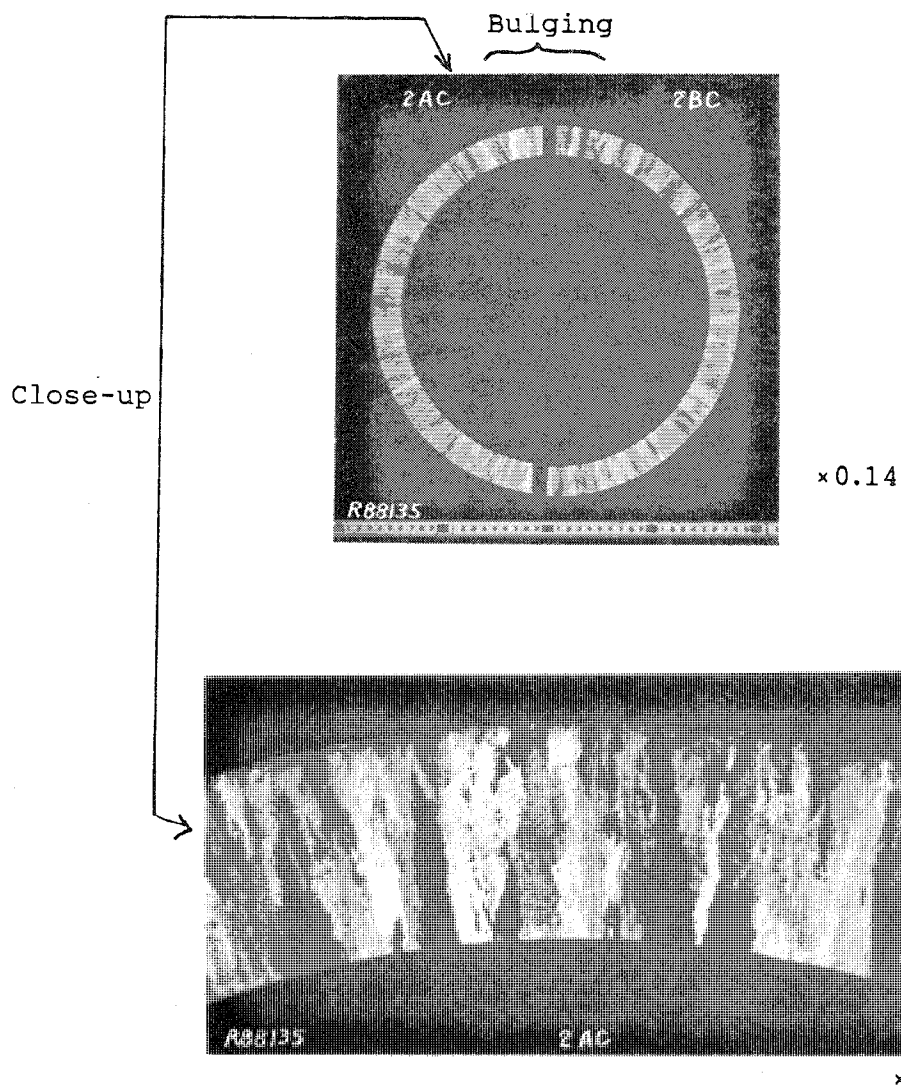
Figure K.10   Macrostructure of Blocks #2A and #2B Cross Section
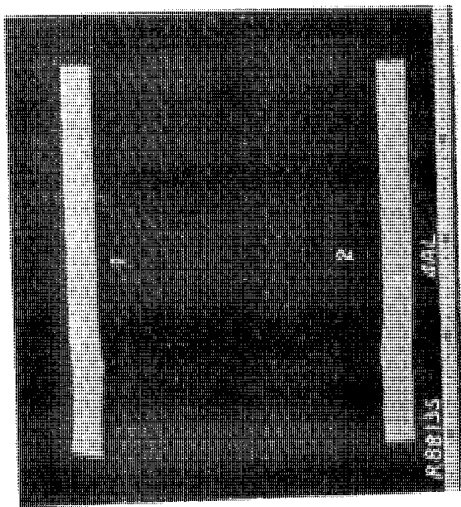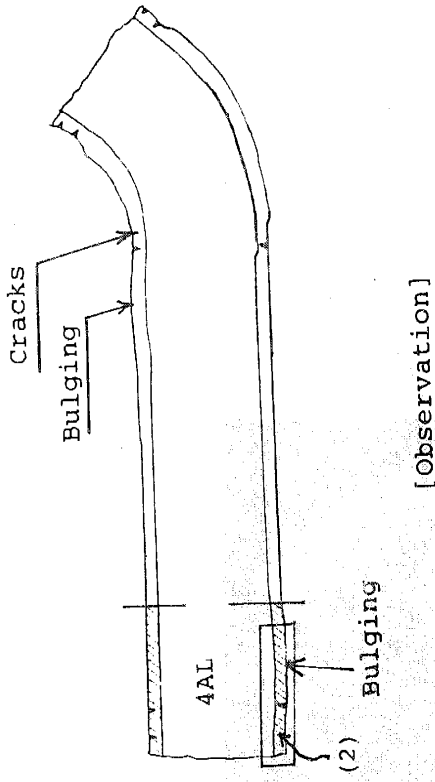
Figure K.11 Macrostructure of Block #4A Longitudinal Section

K-18

[Observation]

(1) Bulging × 0.14

Close-up

(2) ×1
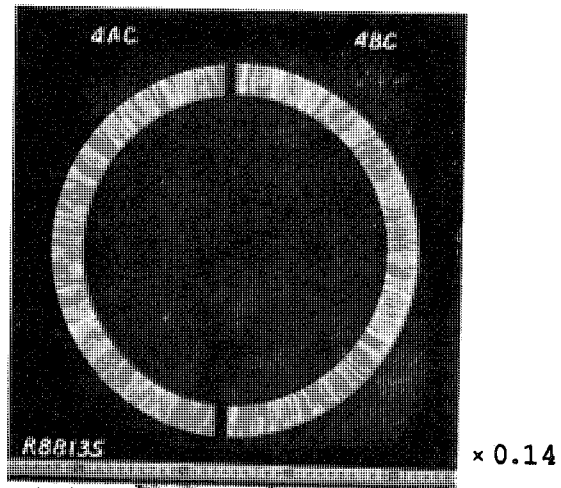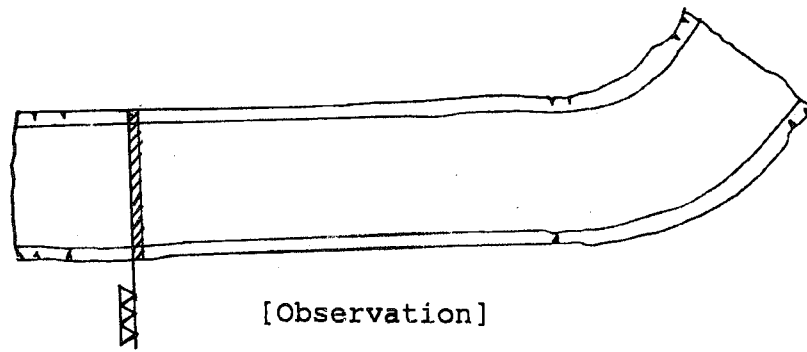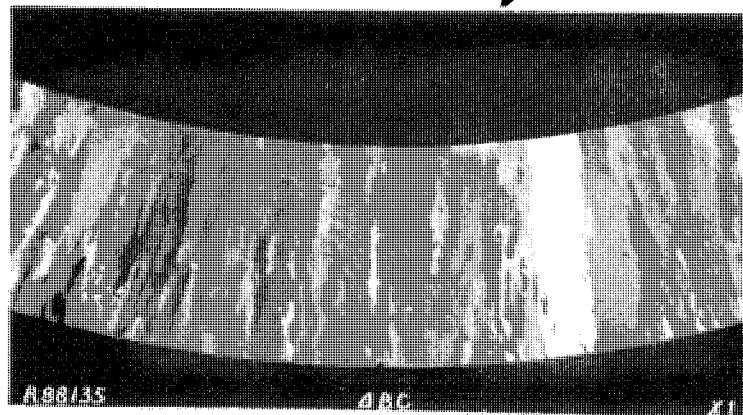
Figure K.12   Macrostructure of Blocks #4A and #4B Cross Section

Block #2AL1

ⓑ origin

Close-up

R88135 2AL1-1-b X500

R88135 2AL1-1-b X100

ⓐ origin

R88135 2AL1-1-a X100

Close-up

R88135 2AL1-1-a X500

Close-up of a crack

Outer surface

R88135 2AL1-1 X5

inner surface

ⓓ middle

R88135 2AL1-1-d X500

Close-up

R88135 2AL1-1-d X100

ⓔ crack tip

R88135 2AL1-1-e X500

Close-up

R88135 2AL1-1-e X100

ⓕ inner surface

R88135 2AL1-1-f X500

ose-up

R88135 2AL1-1-f X100

ⓒ general

R88135 2AL1-1-C X100

Close-up

R88135 2AL1-1-C X500

Figure K.13 Microstructure of Cracked Region (Sample No. 2AL1-1)
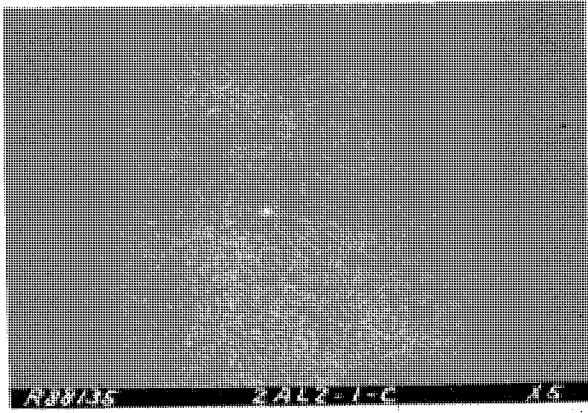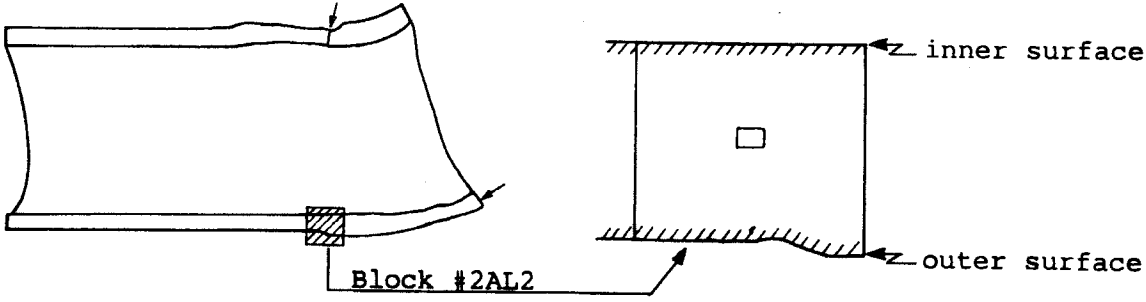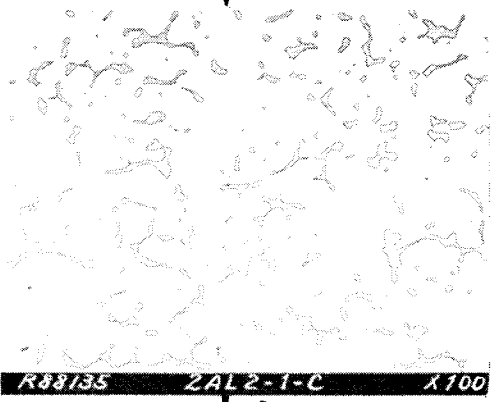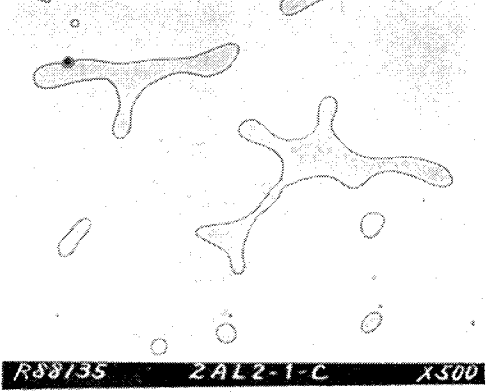
K-20

Figure K.14 Microstructure of Undamaged Region (Sample No. 2AL2-1)
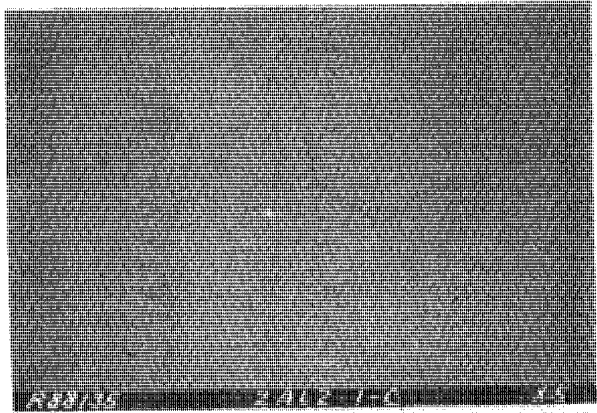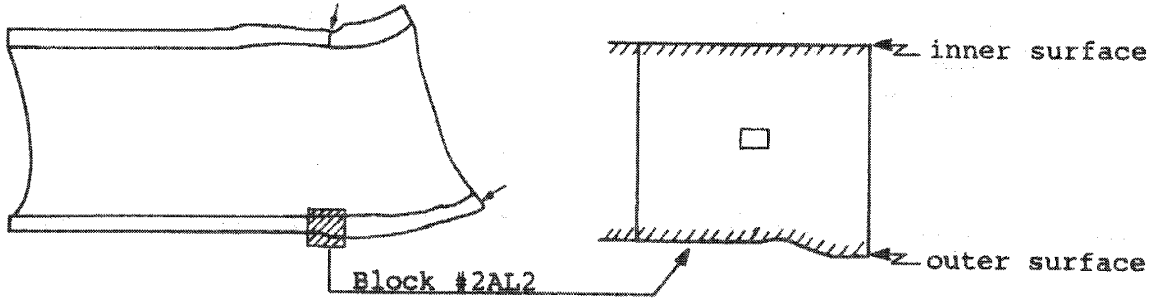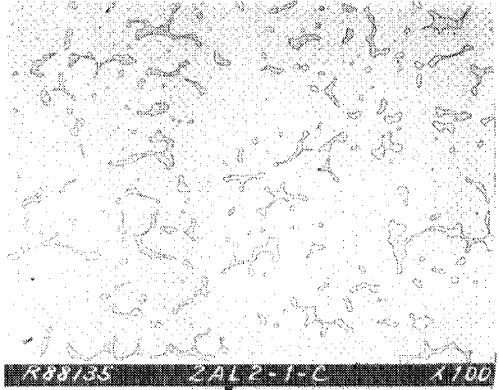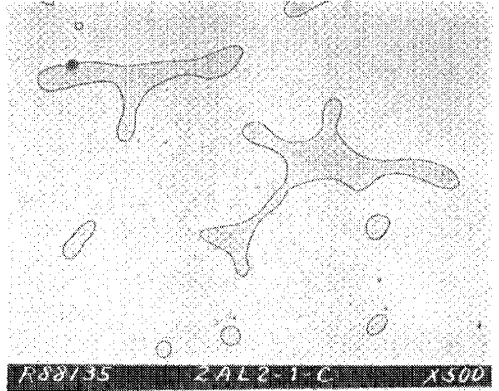
Figure K.14 Microstructure of Undamaged Region (Sample No. 2AL2-1)
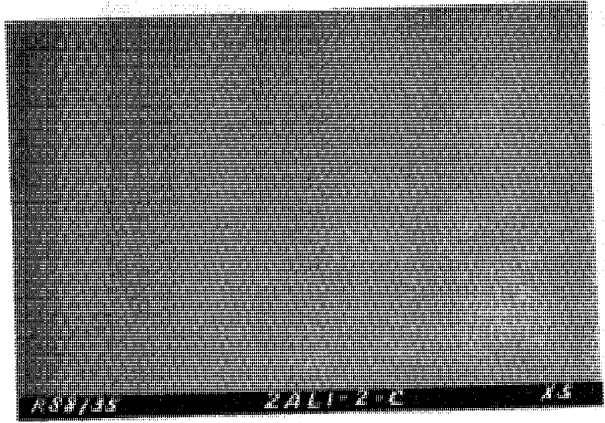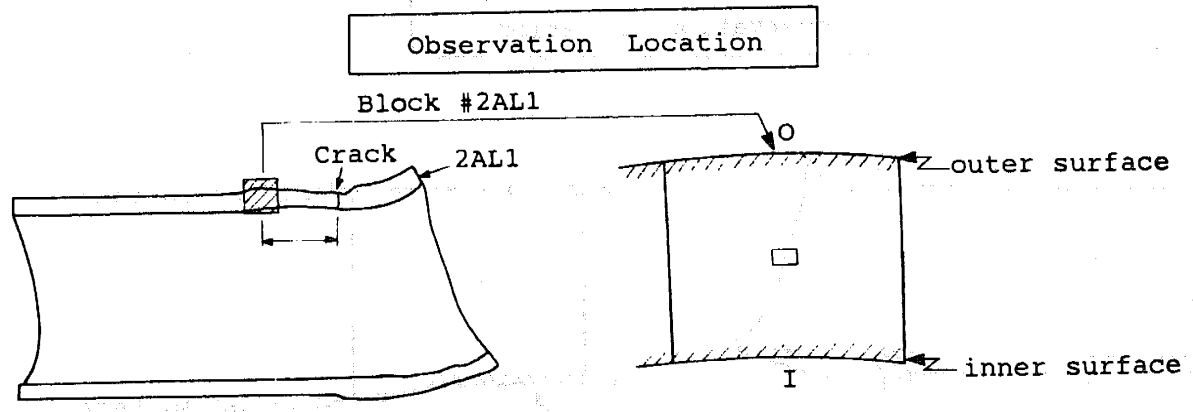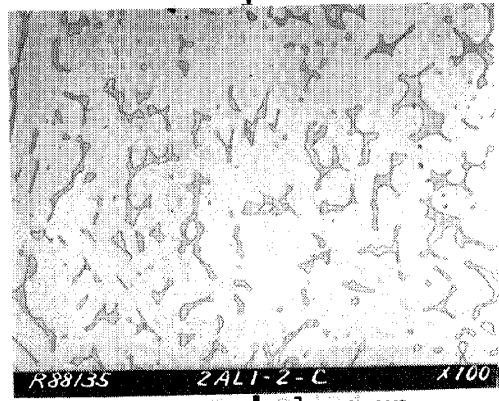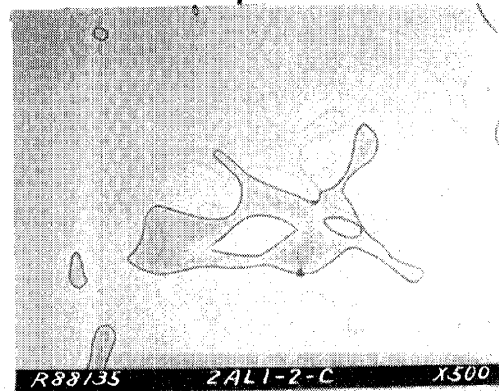
Figure K.15   Microstructure of Bulged Region (Sample No.   2AL1-2)
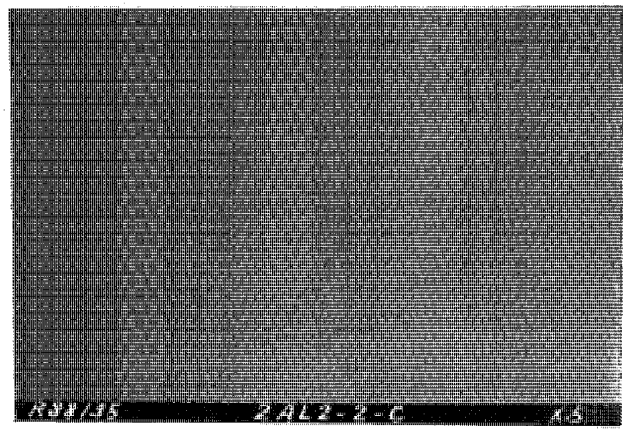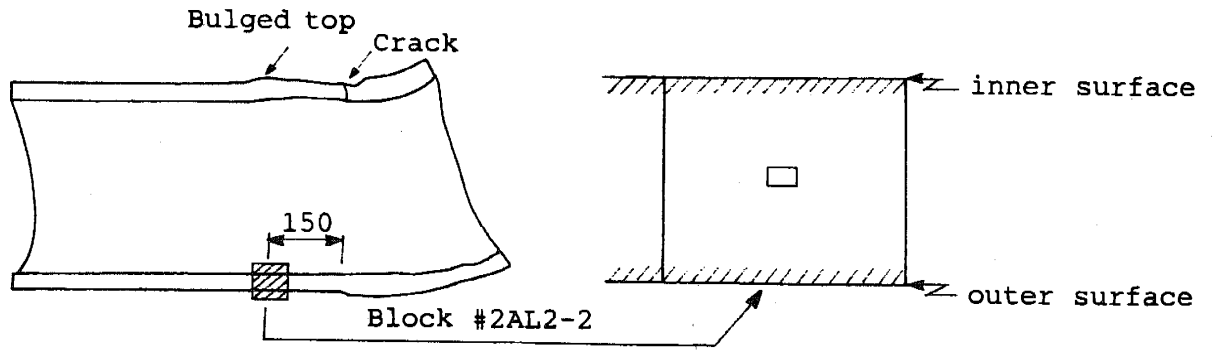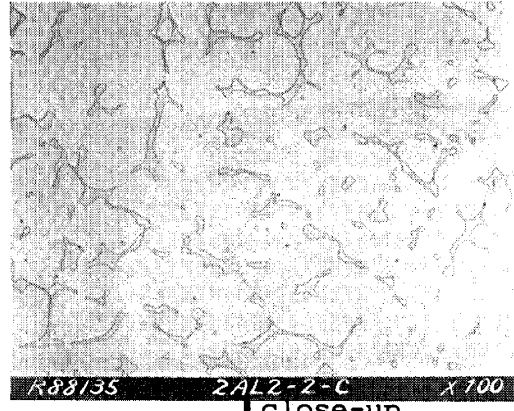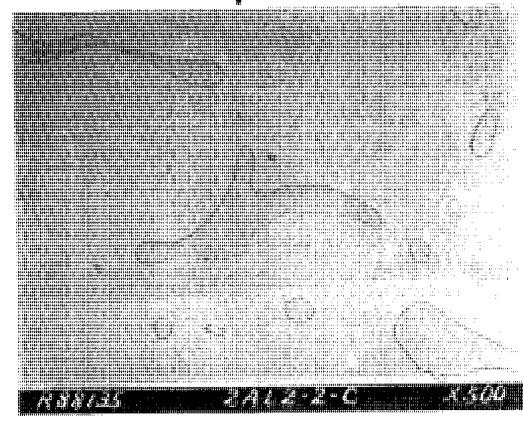
Figure K.16   Microstructure of Undamage Region (Sample No.   2AL2-2)
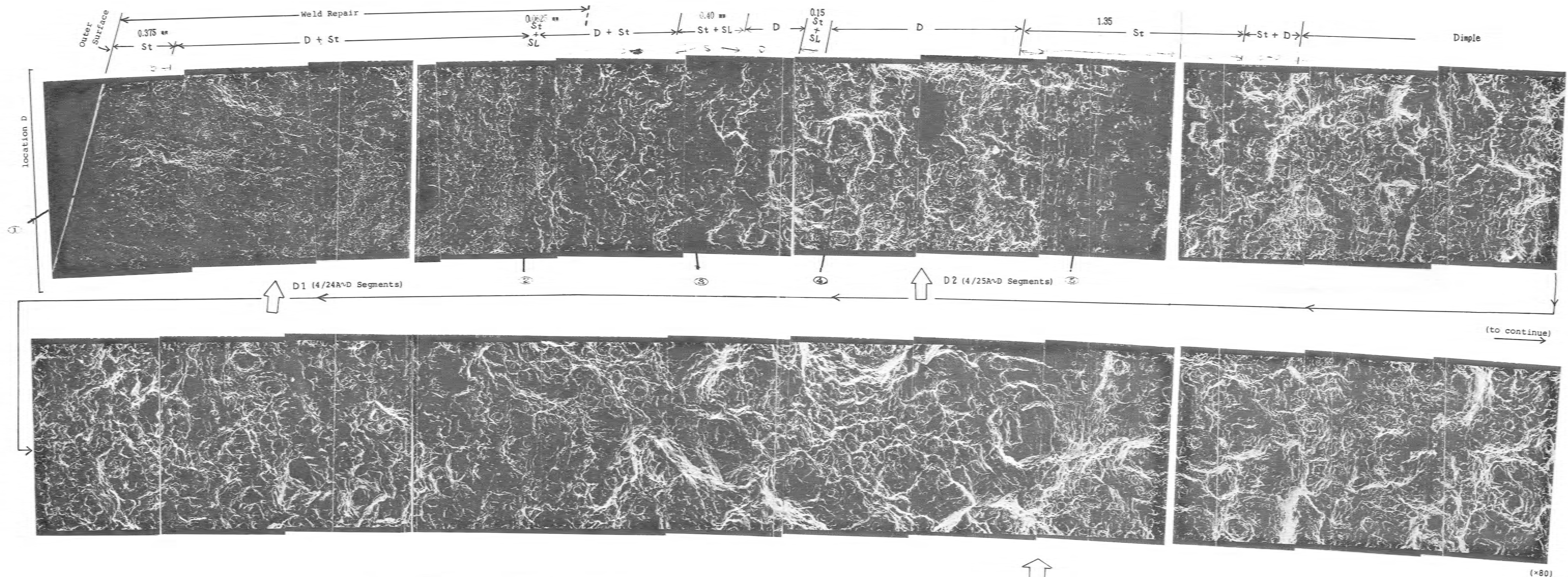
Figure K.17 (1) Observation by SEM (1/3)
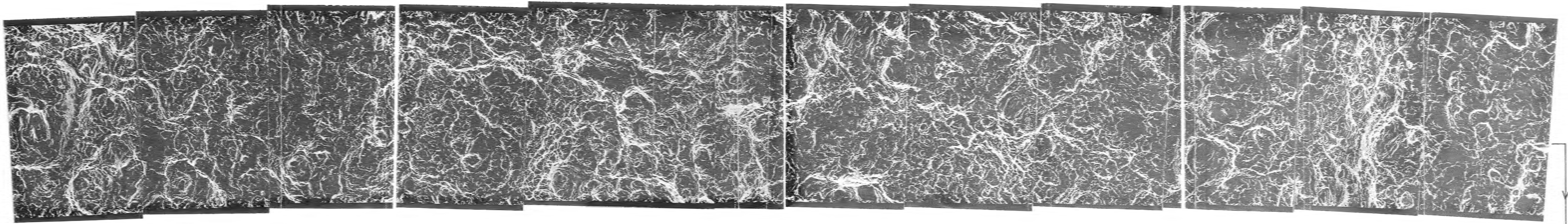
Outer Surface

location D

Weld Repair

0.375 mm
St

D + St

0.65 mm
St
+
SL

D + St

0.40 mm
St + SL

D

0.15
St
+
SL

D

1.35
St

St + D

Dimple

D1 (4/24A~D Segments)

D 2 (4/25A~D Segments)

D 3 (4/26A~D Segments)

(to continue)

(×80)

K-24

St : Striation
SL : Deformation Slip
D : Dimple

• ①~⑧ : Observed in more detail.
• D 1~D 3 : Crack Depth measured at site.

(Continued)
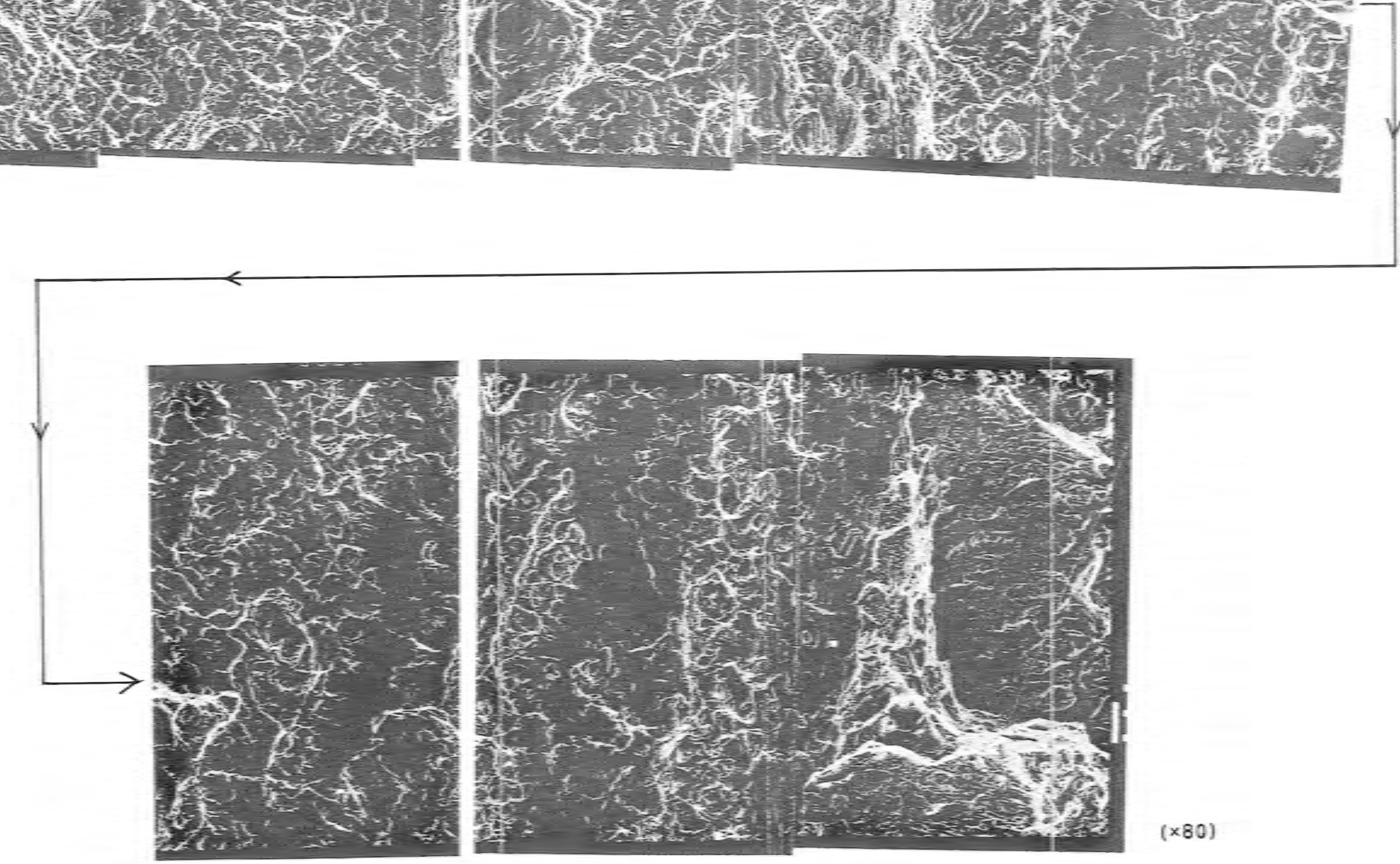
Figure K.17 (2)   Observation by SEM (2/3)

(×80)

Forced Open Area

Crack Front

Surface
Mode ⟹ St   St + SL   St + SL   St + SL
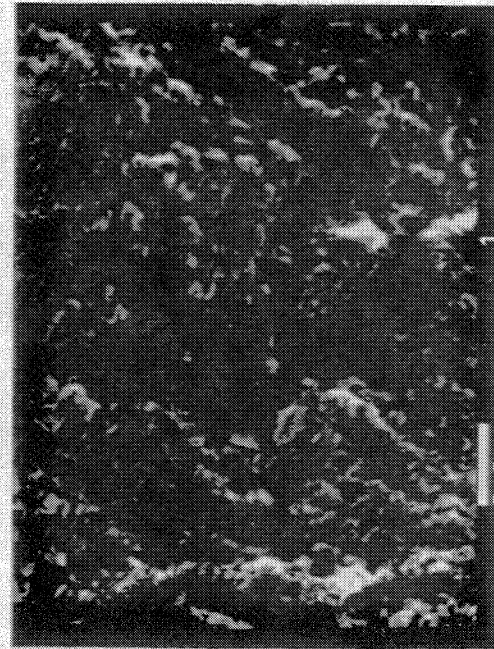
(×1200)

(×1200)

(×1200)

(×1200)

① $\Delta\ell = 0.375$, $t = 0.1$
$\Delta S = 2.5 \sim 5.8 \times 10^{-3}$
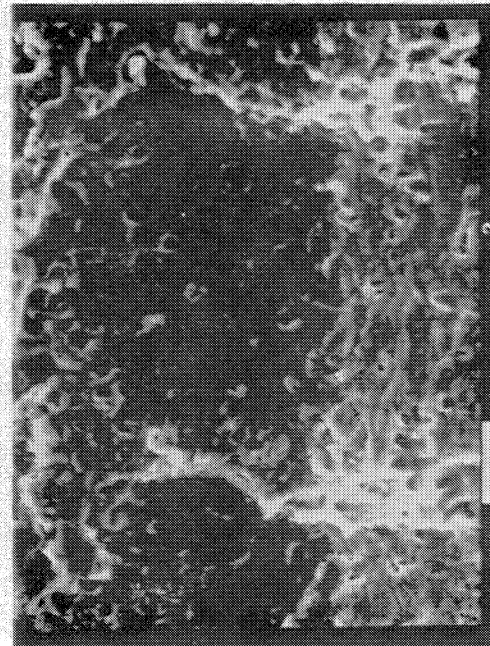
② $\Delta\ell = 0.0625$, $t = 2.7$
$\Delta S = 4.6 \sim 5.8 \times 10^{-2}$
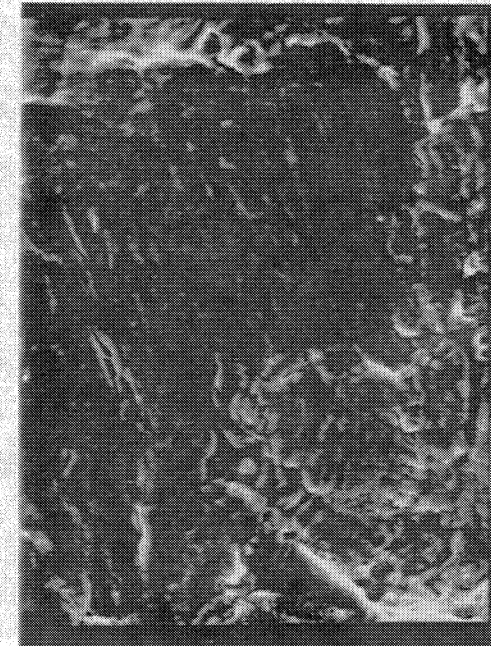
③ $\Delta\ell = 0.40$, $t = 3.7$
$\Delta S = 2.5 \sim 4.2 \times 10^{-2}$

④ $\Delta\ell = 0.15$, $t = 4.6$
$\Delta S = 3.75 \sim 5.2 \times 10^{-2}$
(Continued)

| St : Striation |
| SL : Slip |
| $\Delta\ell$: Interval of Characteristics (mm) |
| t : Distance from D (mm) |
| ΔS : Striation Pitch (mm) |

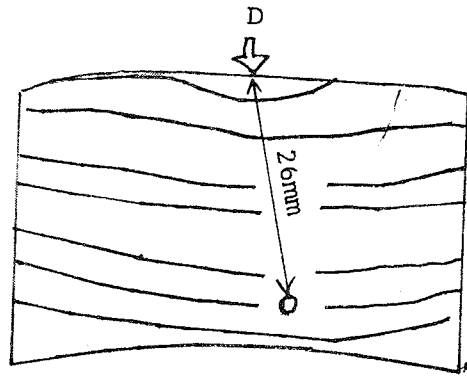| Estimation |
| --- |
| $N_1 = \dfrac{0.375}{2.5 \sim 5.8 \times 10^{-3}} = 150 \sim 65$ |
| $N_2 = \dfrac{0.0625}{4.6 \sim 5.8 \times 10^{-2}} = 2 \sim 1$ |
| $N_3 = \dfrac{0.40}{2.5 \sim 4.2 \times 10^{-2}} = 16 \sim 10$ |
| $N_4 = \dfrac{0.15}{3.75 \sim 5.2 \times 10^{-2}} = 4 \sim 3$ |
| $N_5 = \dfrac{0.13}{2.6 \sim 3.3 \times 10^{-3}} = 520 \sim 409$ |
| $\Sigma N = 692 \sim 483$ 回 |

St

(×1200)

⑤ $\Delta\ell = 0.13$, $t = 6.1$
$\Delta S = 2.6 \sim 3.3 \times 10^{-3}$

Figure K.17 (3) Observation by SEM (3/3)

K-26

[Observation Location]
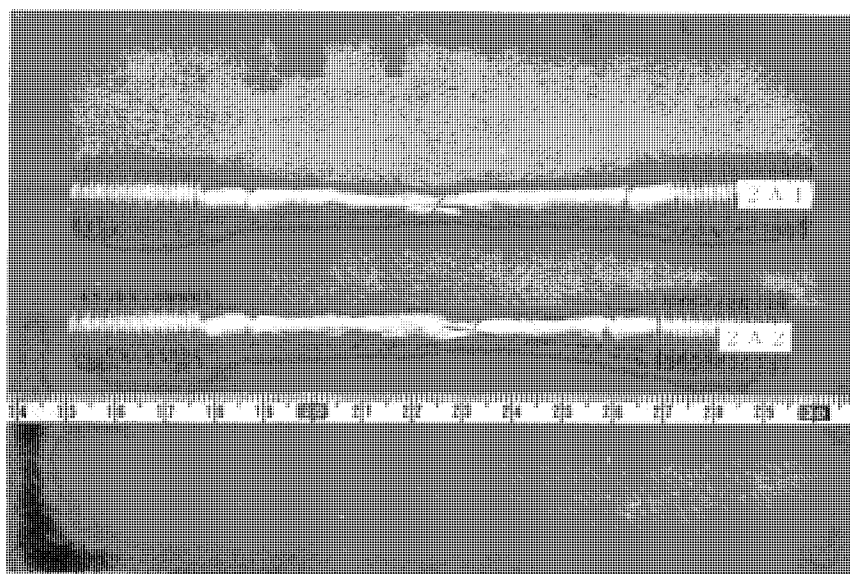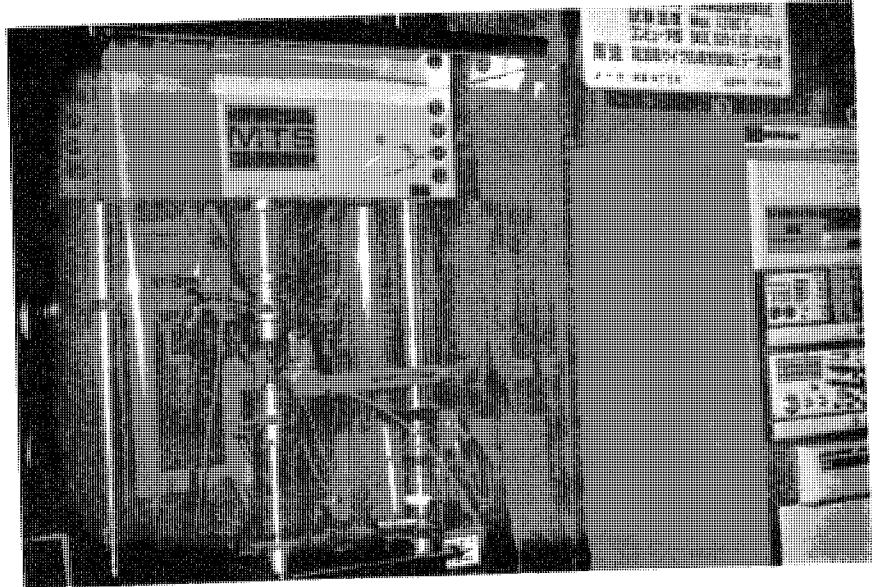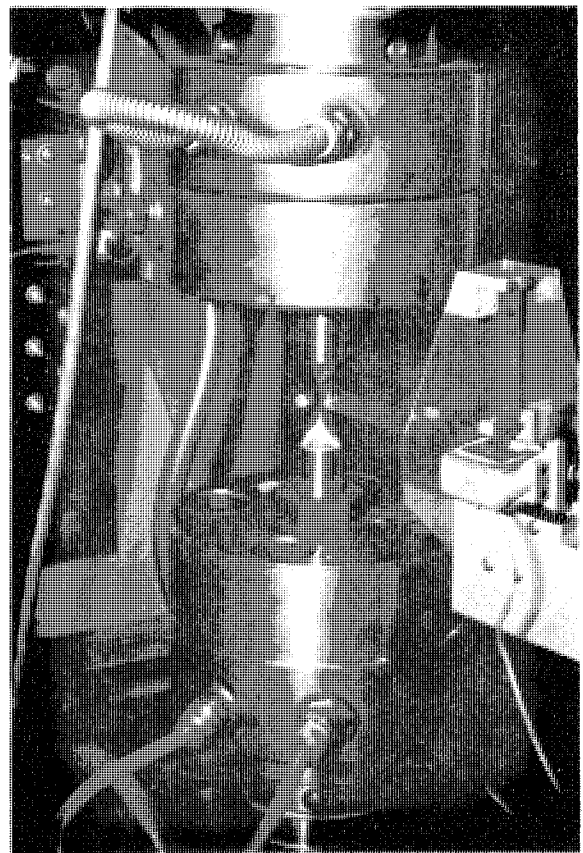
D

26mm

Close-up

Figure K.18 Observation of Beachmark

Figure K.19 Hardness Distribution

Location		Range	Average
2AL1	Pipe	HV162 ~ 235	186
	Elbow	HV172 ~ 238	194
2AL2	Pipe	HV141 ~ 182	156
	Elbow	HV176 ~ 264	198
Weld Joint		HV178 ~ 242	215
Crack area		HV201 ~ 314	270

K-28

Figure K.20   Specimens after Test

Close-up

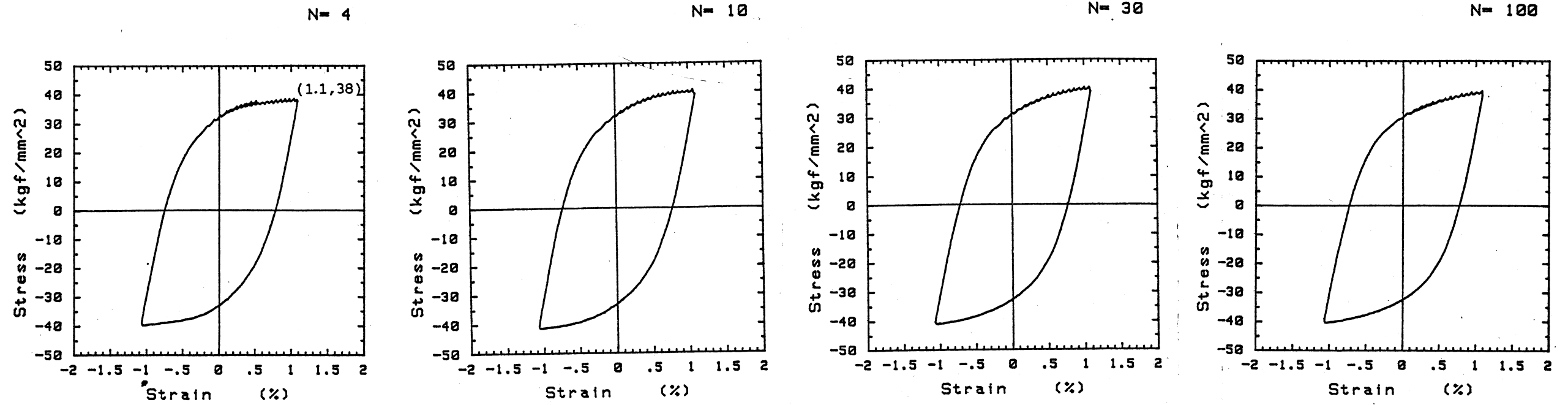Manufacturer : MTS

Accuracy : 1.2% of F.S.

Figure K.21 Low Cycle Fatigue Test
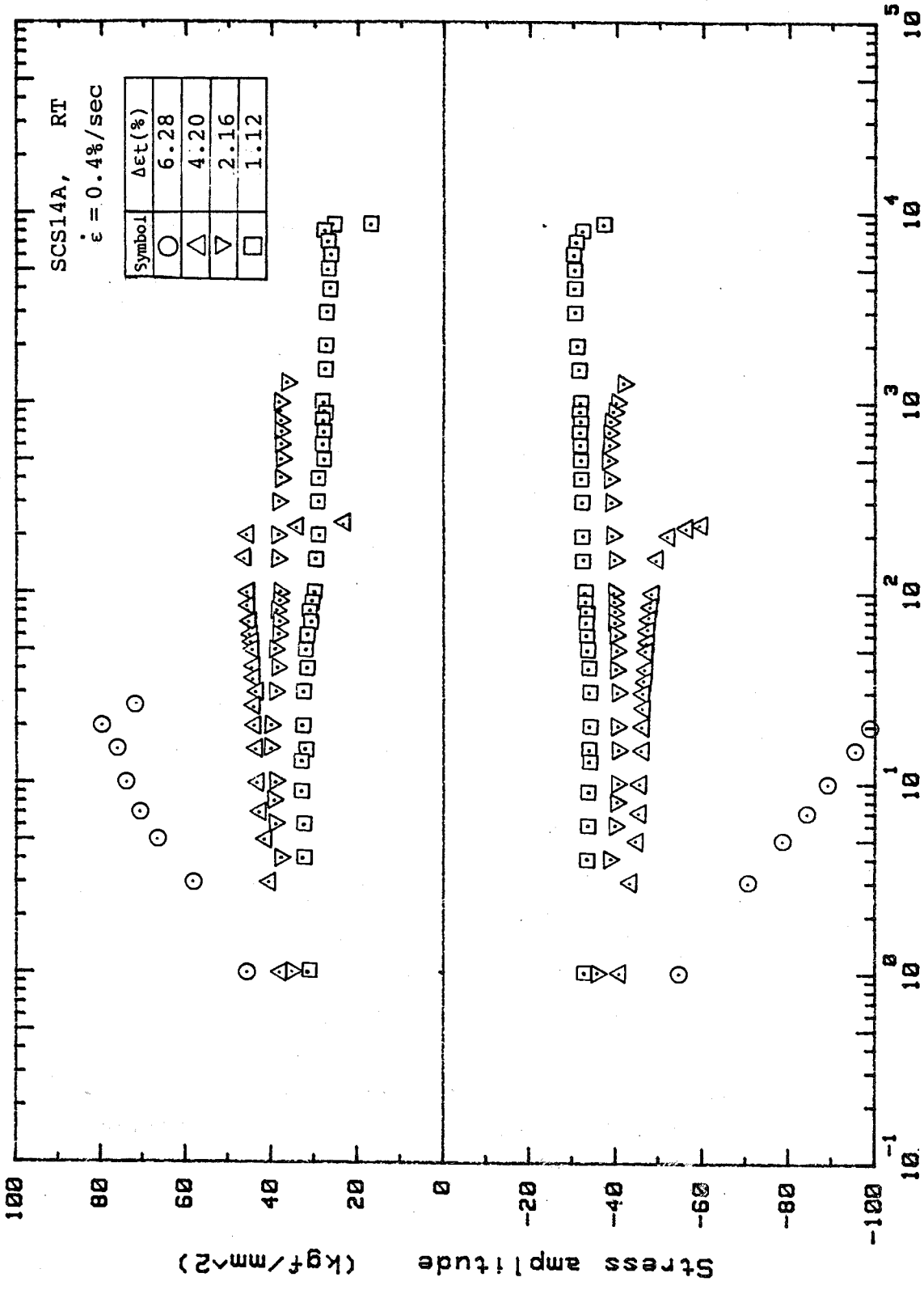
Figure K.22 Stress During Test
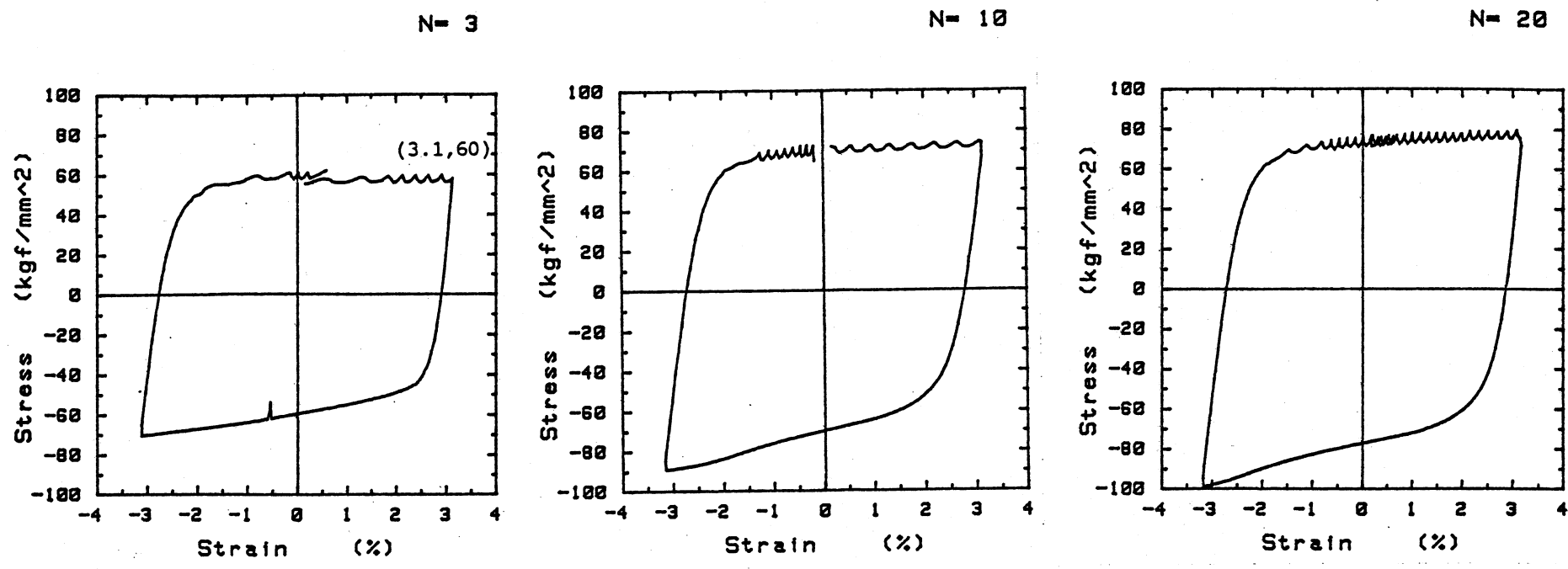
(1) TP NO.4 ($\Delta\varepsilon_t = 6.28\%$, $N_f=25$)

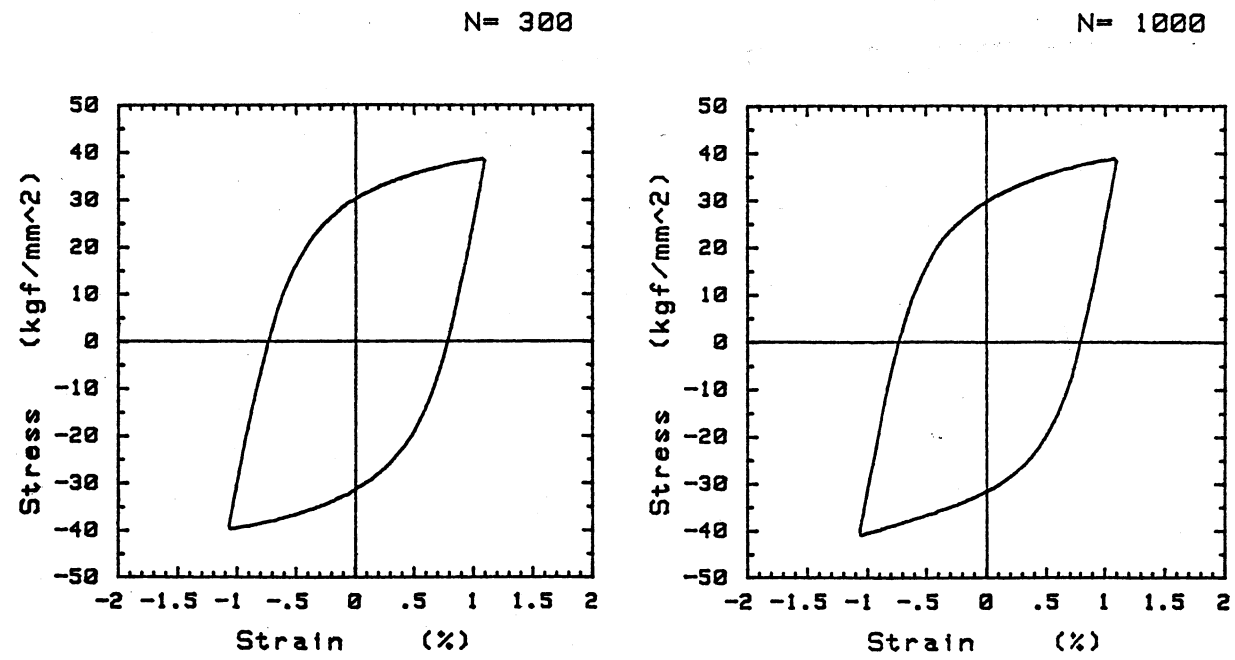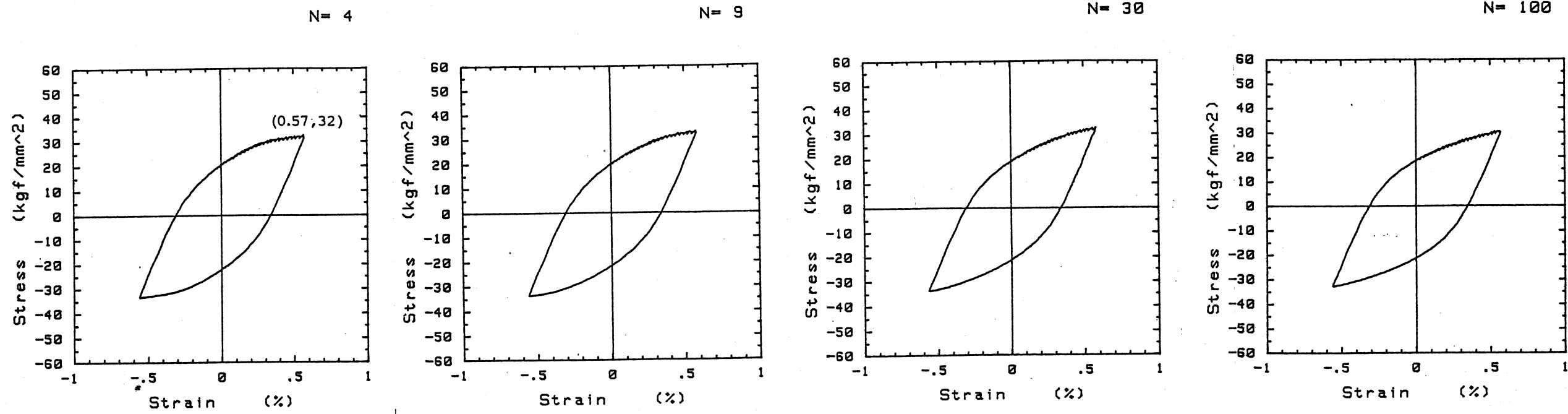(2) TP NO.3 ($\Delta\varepsilon_t = 4.20\%$, $N_f=220$)

Figure K.23 (1)   Examples of Hysteresis Loops (1/3)
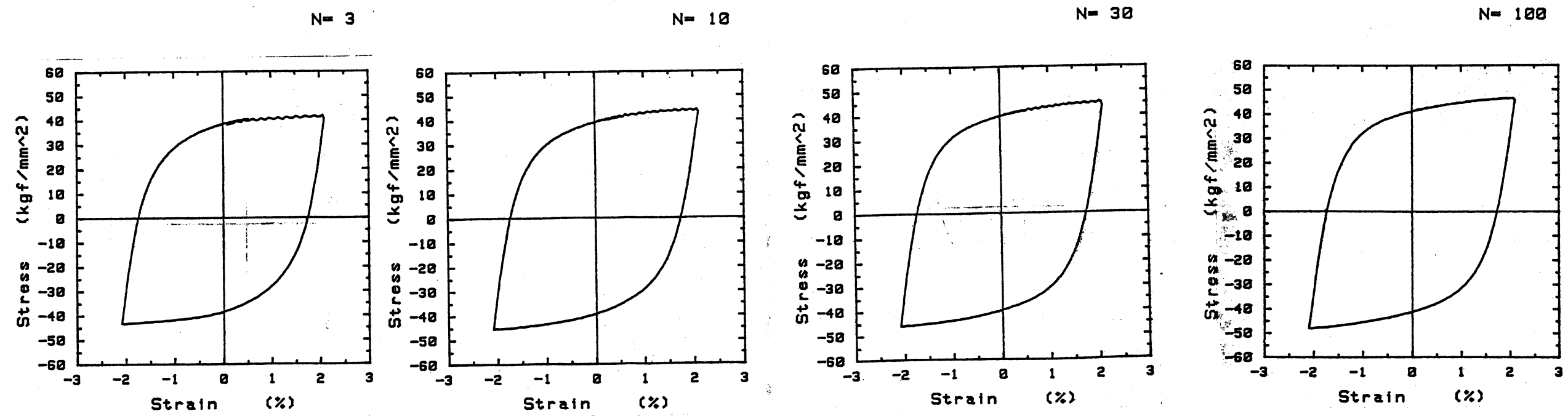
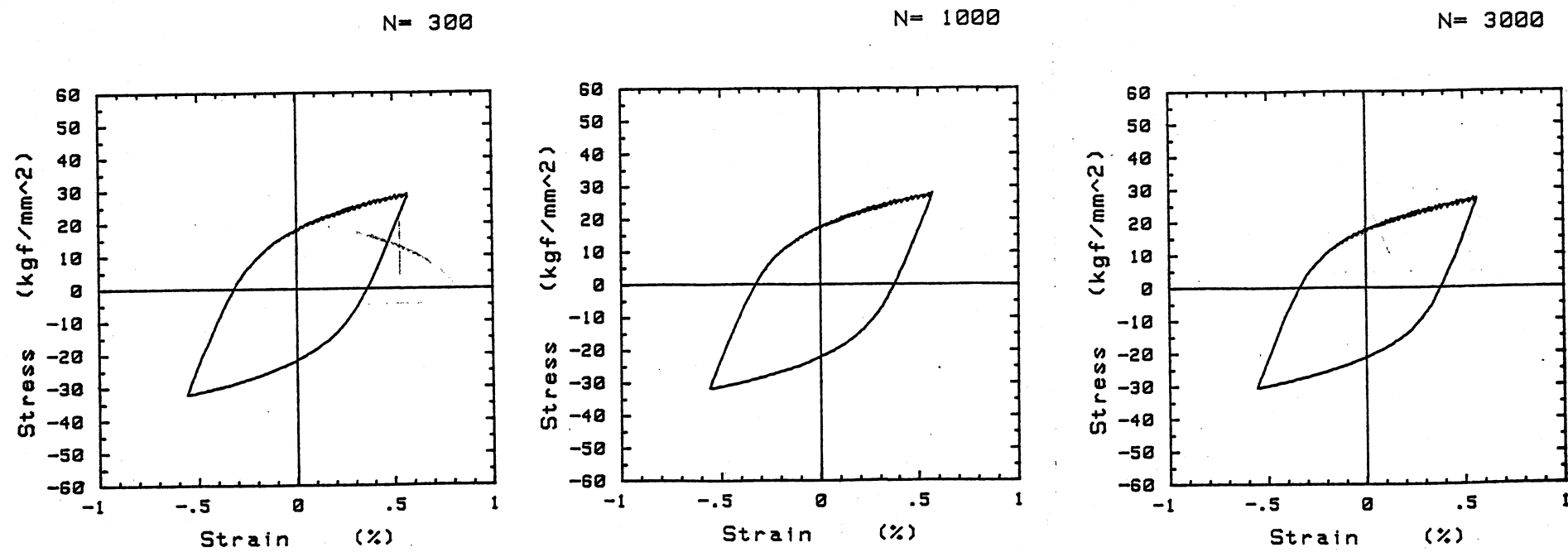(3) TP NO.2 ($\Delta\varepsilon_t = 2.16\%$, $N_f = 1270$)

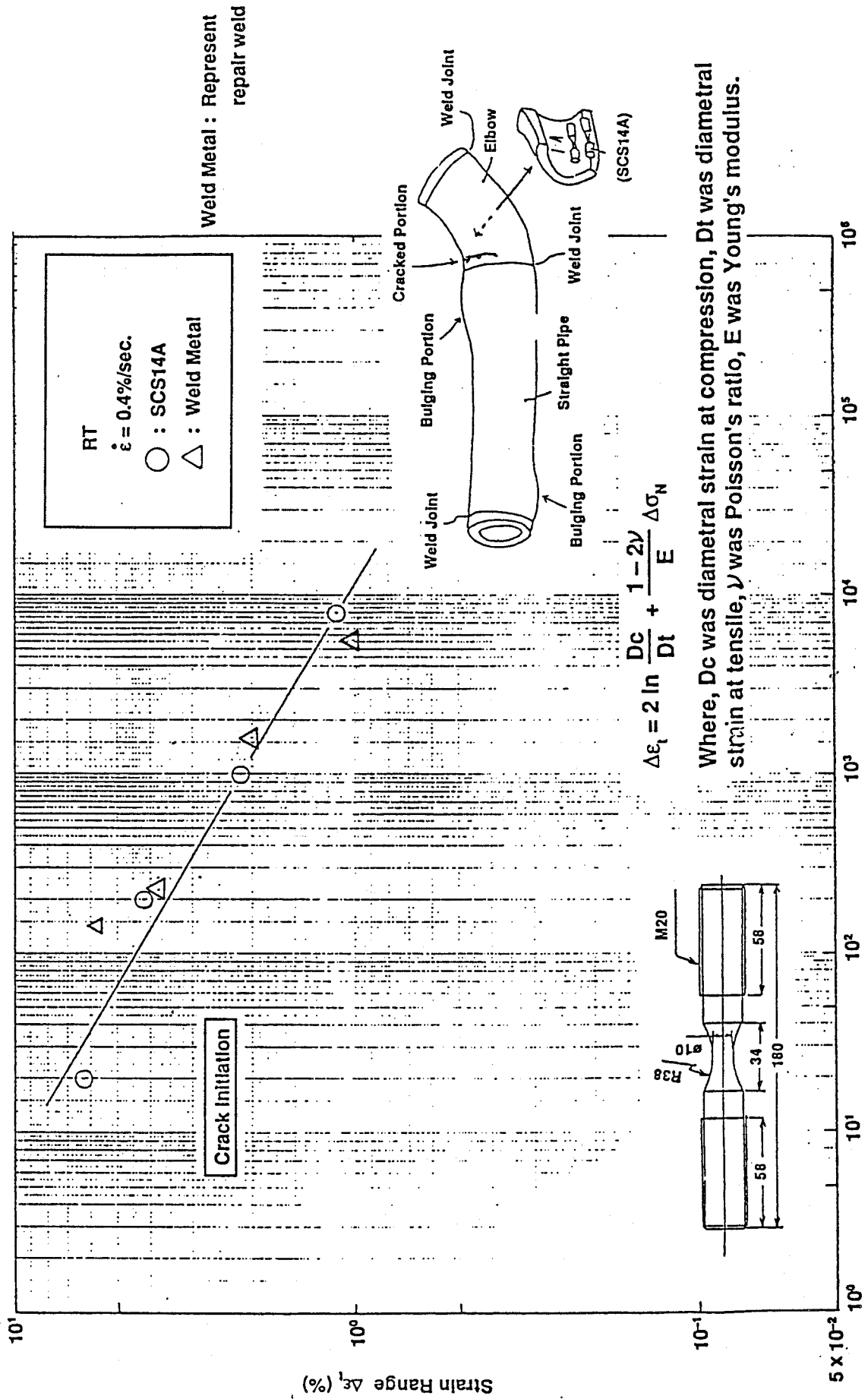Figure K.23 (2) Examples of Hysteresis Loops (2/3)

N= 4   N= 9   N= 30   N= 100

(4)   TP NO.1 ($\Delta\varepsilon_t = 1.12$, $N_f = 8642$)

N= 300   N= 1000   N= 3000

Figure K.23 (3)   Examples of Hysteresis Loops (3/3)

Figure K.24 (1)   Low Cycle Fatigue Strength (1/2)

Where, Dc was diametral strain at compression, Dt was diametral strain at tensile, ν was Poisson's ratio, E was Young's modulus.

$$\Delta\varepsilon_t = 2\ln\frac{Dc}{Dt} + \frac{1-2\nu}{E}\Delta\sigma_N$$

Weld Metal : Represent repair weld

Where, Dc was diametral strain at compression, Dt was diametral strain at tensile, ν was Poisson's ratio, E was Young's modulus.

$$\Delta\varepsilon_t = 2\ln\frac{Dc}{Dt} + \frac{1-2\nu}{E}\Delta\sigma_N$$

Figure K.24 (2)　Low Cycle Fatigue Strength (2/2)

○ : Literatures

(1) K. Tokimasa, etal., No.100 Symposium, The iron and Steel Insutitute of Japan, April, 1981.

(2) K. Iida, FRC Subcommittee, Japan Welldng Society

    1) FRC-79, February, 1981

    2) FRC-80, March, 1982

    3) FRC-81, January, 1983
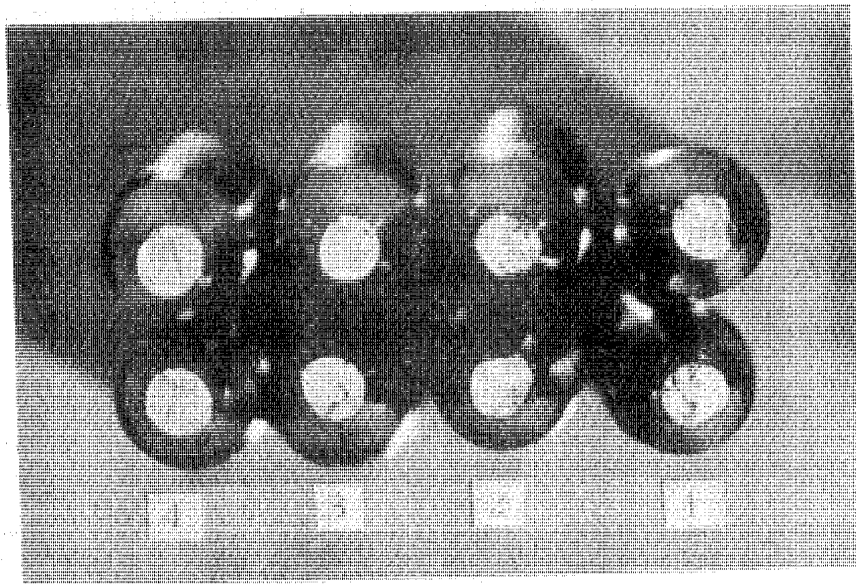

$$\varepsilon_{ta} = \frac{\varepsilon_t}{2}$$

Current Data
● Base Metal
▲ Weld Metal

ASME Best Fit Curve

ASME Design Fatigue Curve

Strain Amplitude ε_{ta} (%)

Number of Cycles to Failure Nf (Cycles)
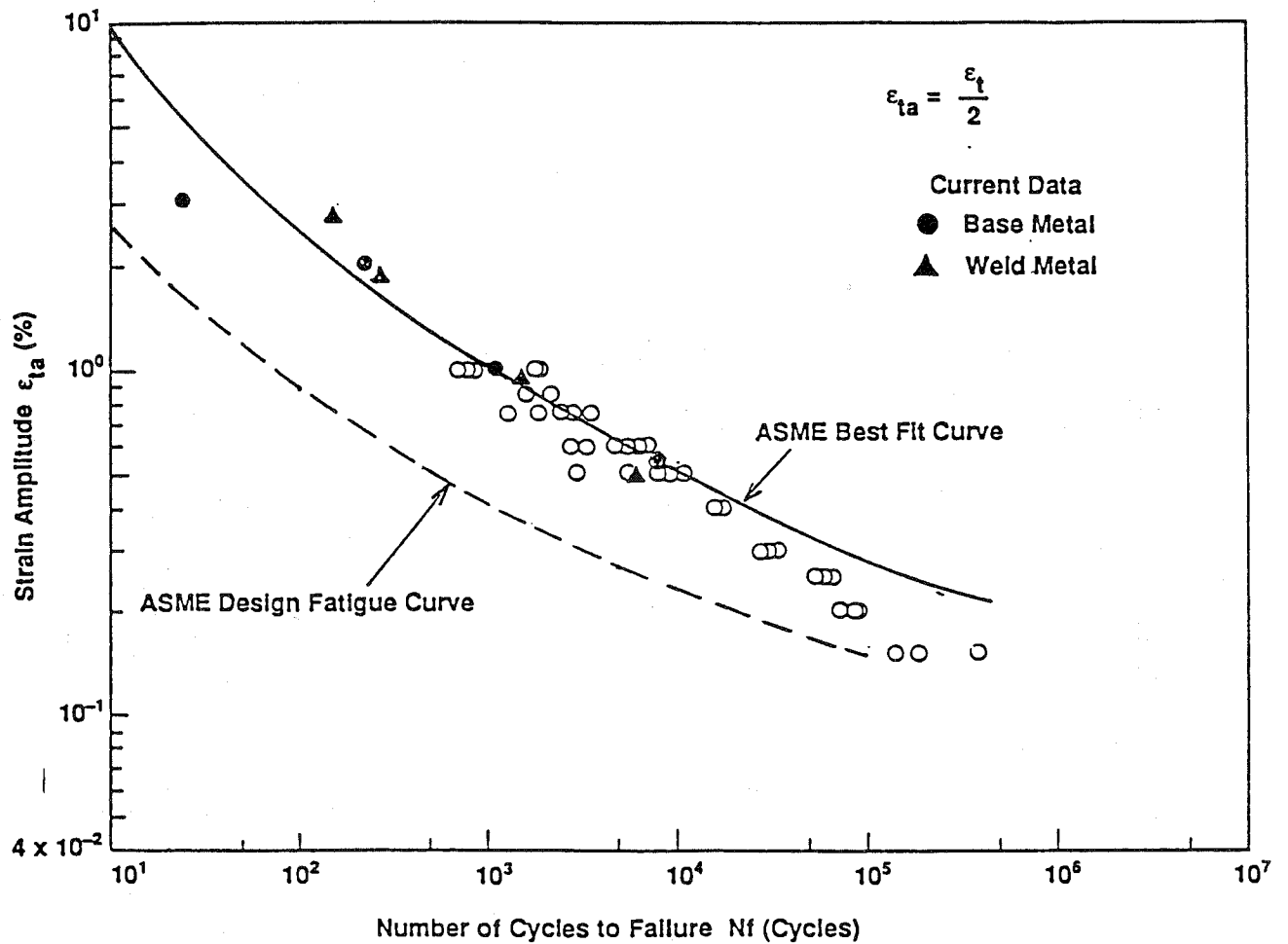
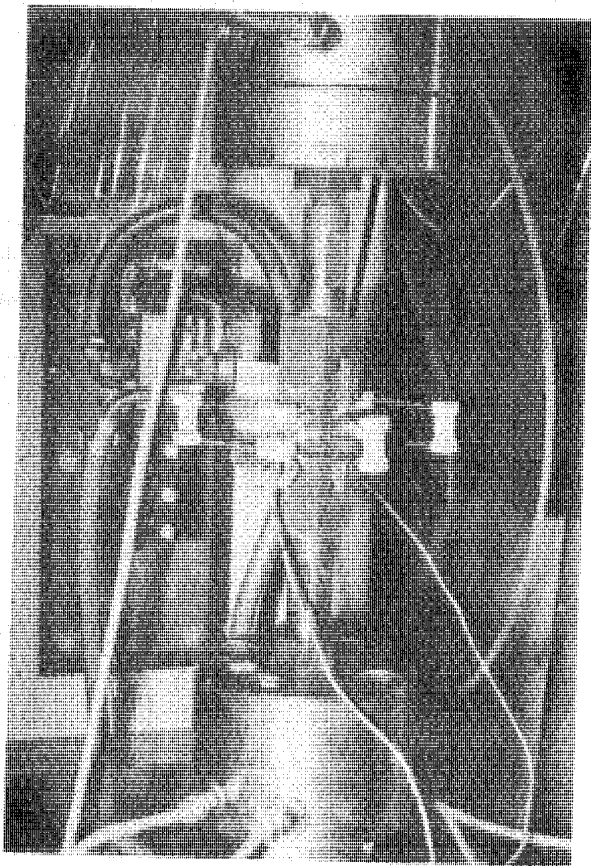Figure K.25   Comparison with Conventional Fatigue Data
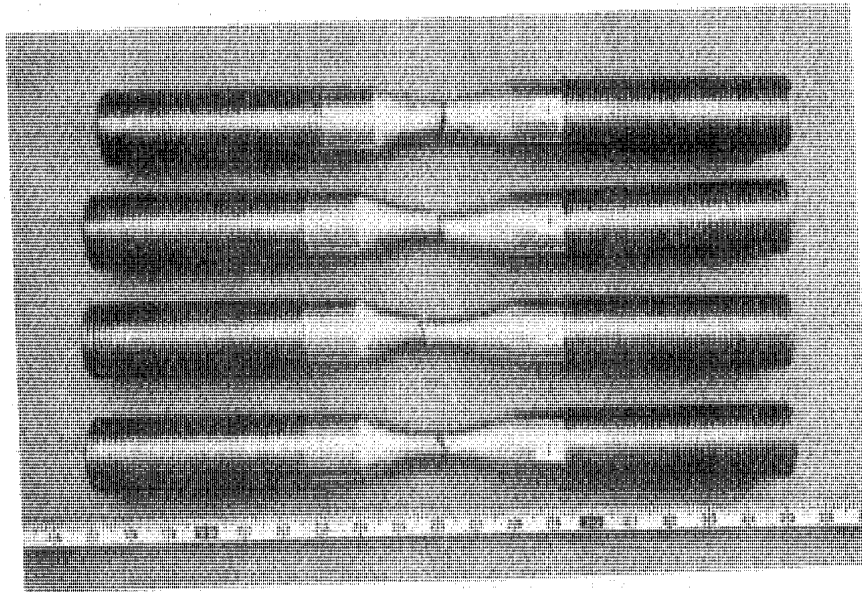
(1) Side

(2) Fracture surface

Figure K.26 Specimens after Test
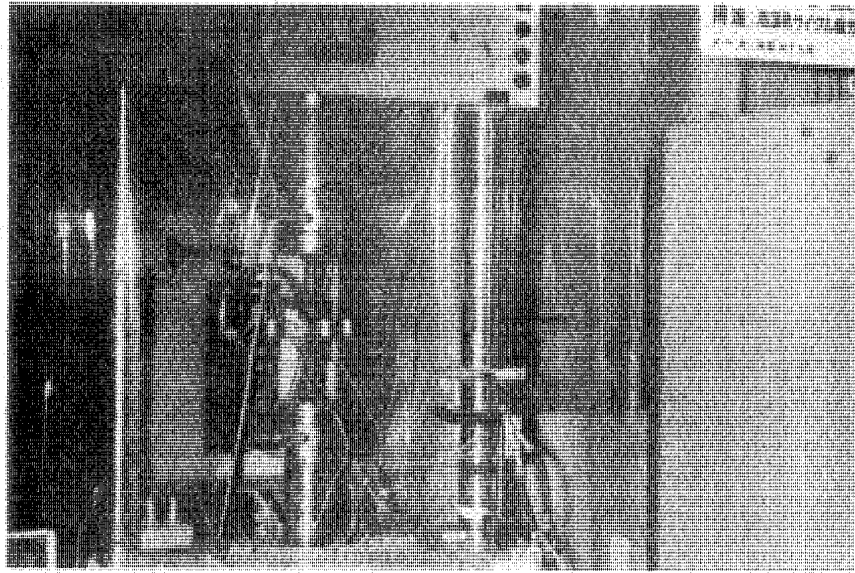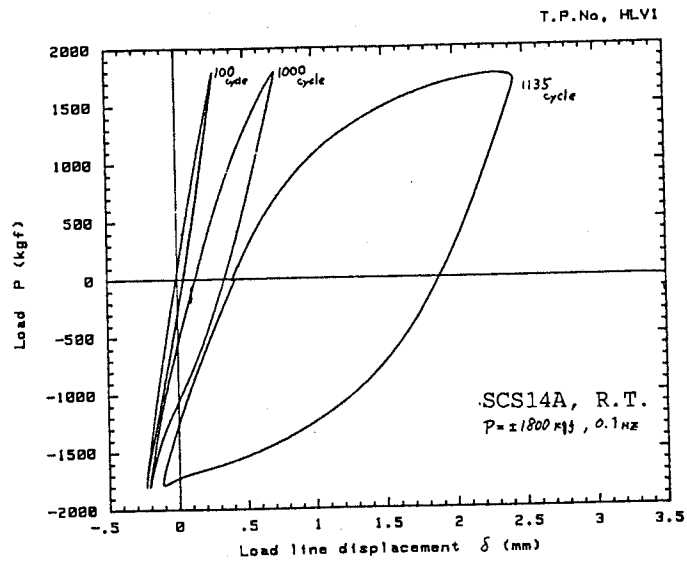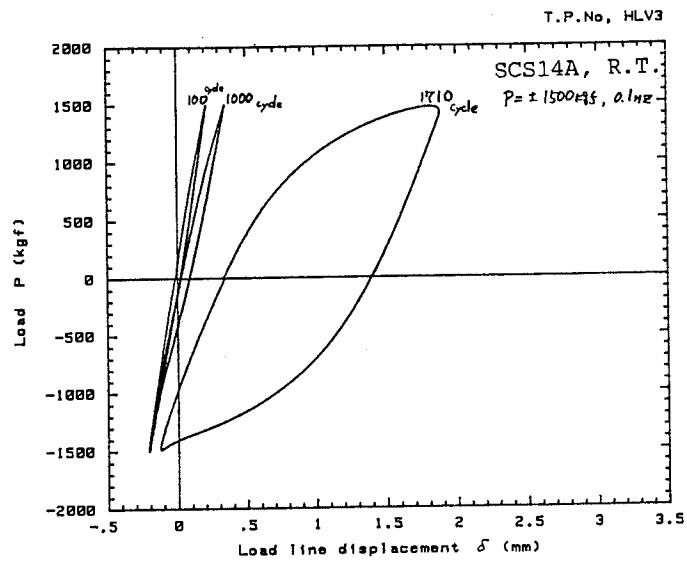
Close-up

Manufacturer : MTS

Accuracy : 1%/F.S.

Figure K.27 Fatigue Crack Growth Rate Test
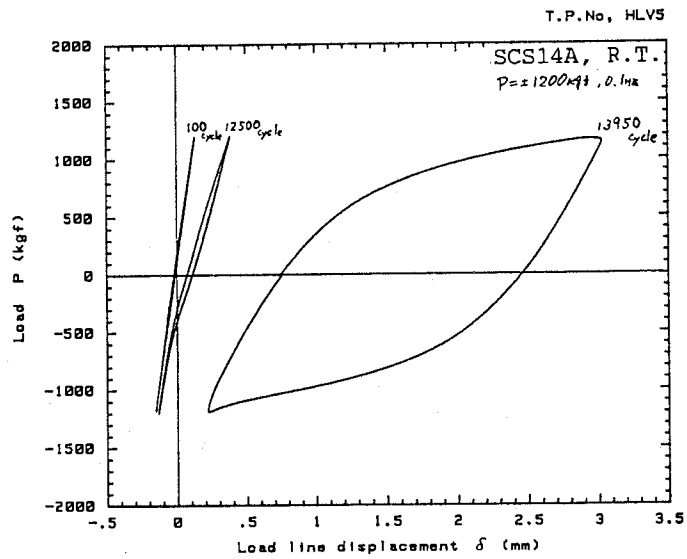
(1) TP : HLV1

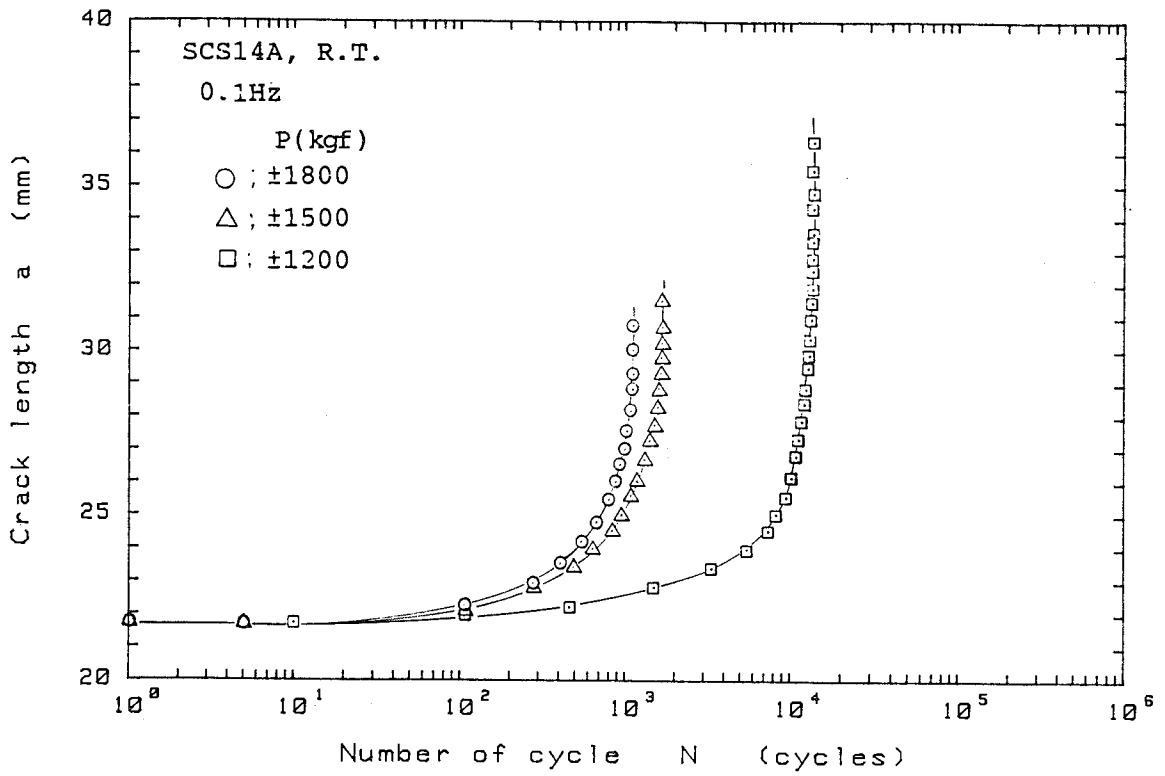(2) TP : HLV3

(3) TP : HLV5

Figure K.28   Examples of P- δ Curve
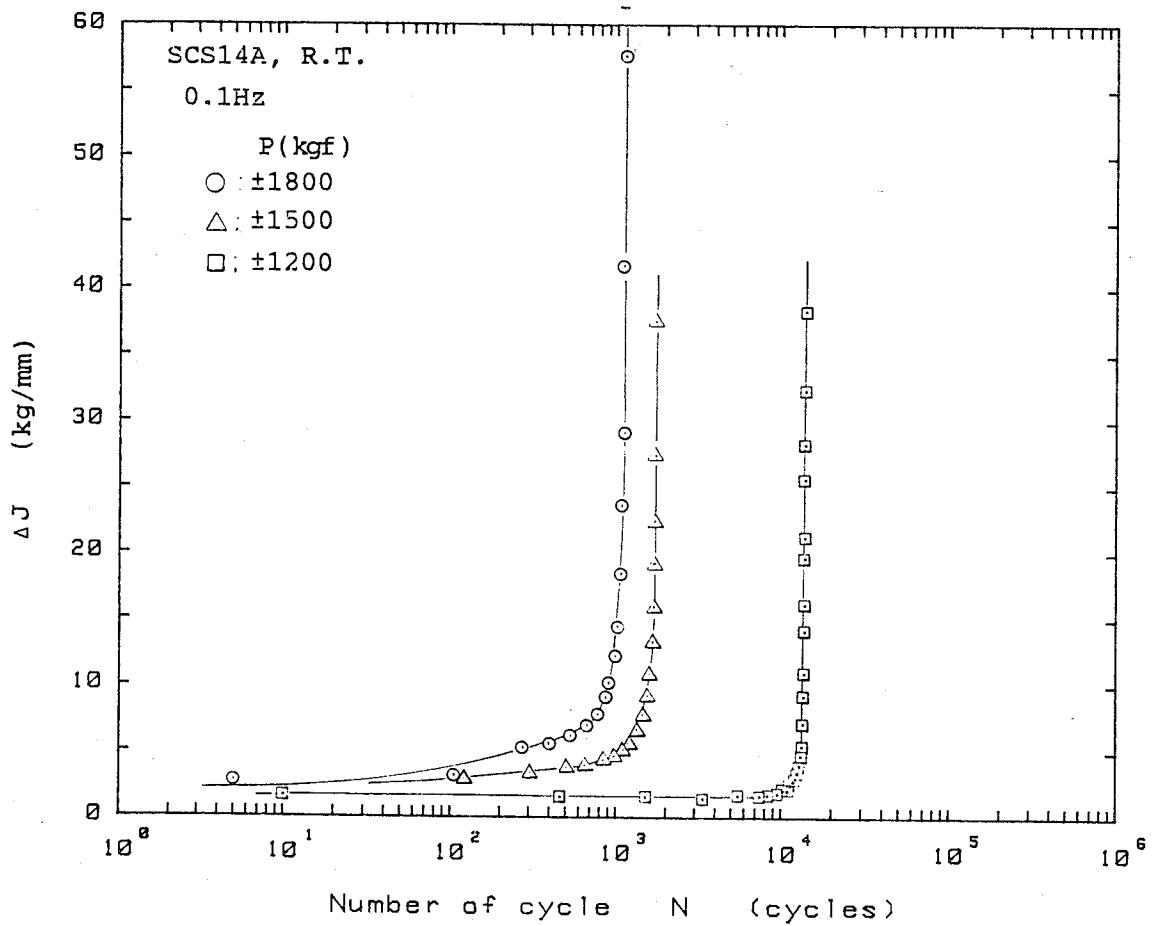
K-40

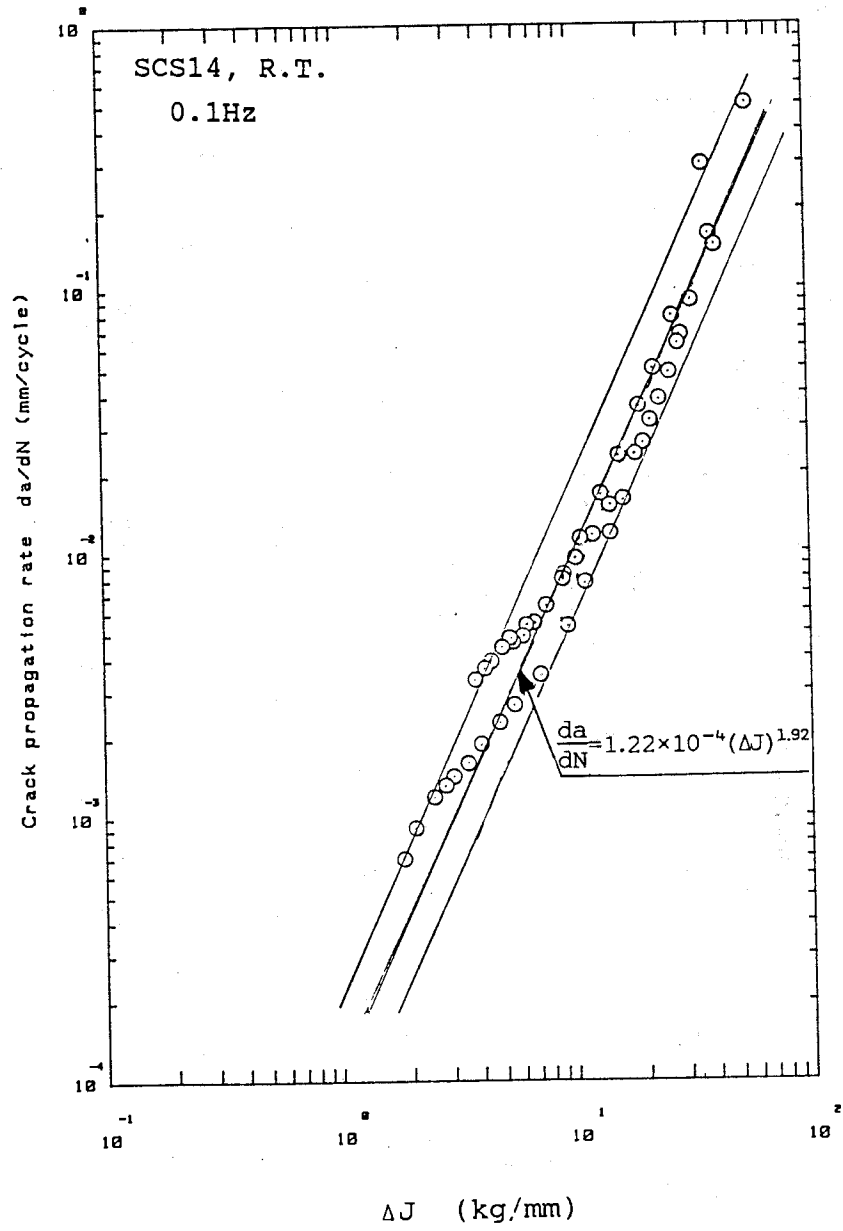**Fig. K-29 a-N Curves**

Figure K.30 Δ J-N Curves

K-41

Figure K.31 (1) Fatigue Crack Growth Rate (1/2)

$$\dot{\Delta J} = \frac{2A}{Bb} \cdot \frac{1+\eta}{1+\eta^2} \rightarrow \Delta K = \sqrt{\frac{E\Delta J}{1-\nu^2}}$$

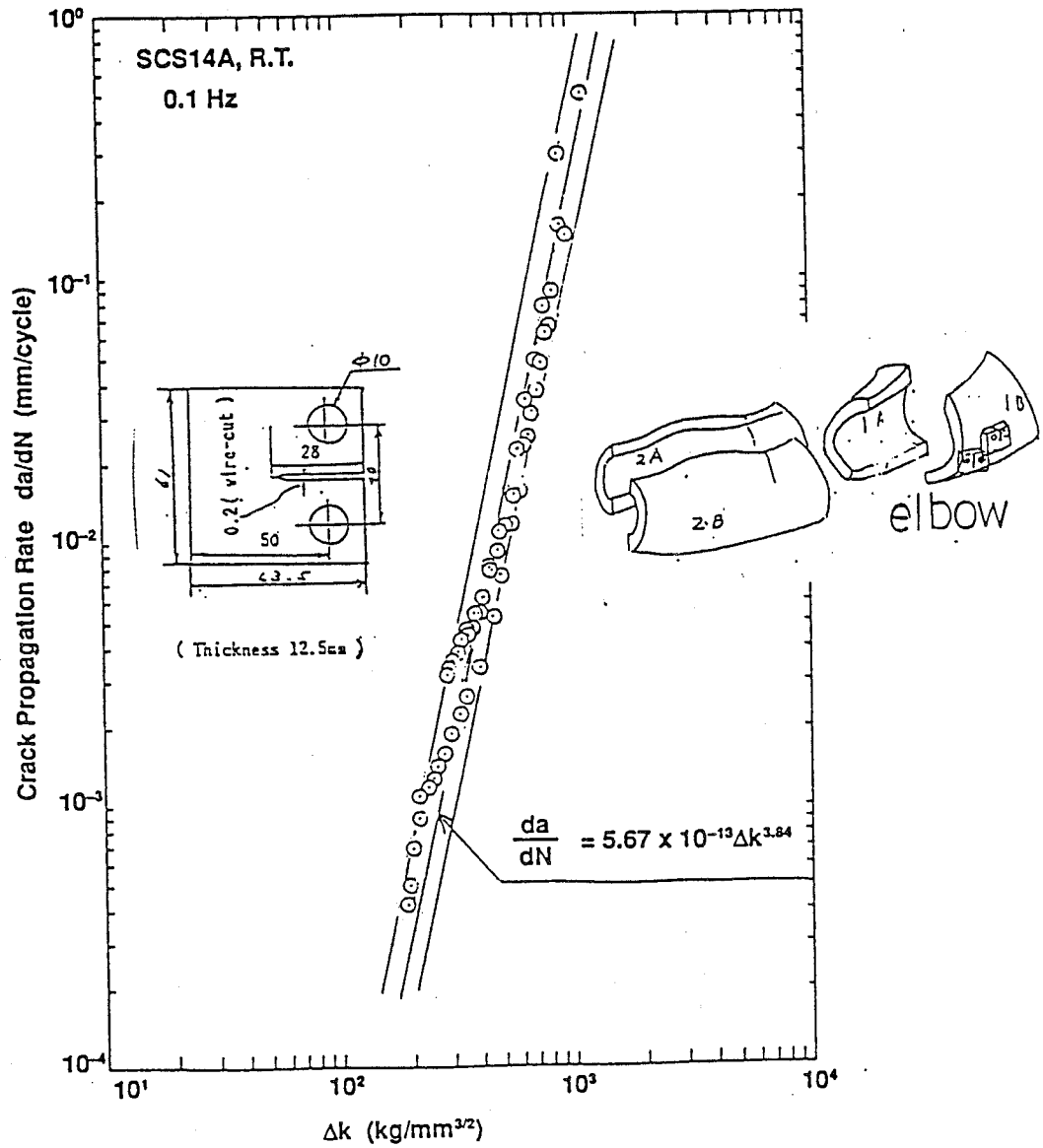where, A was Applied energy, B was Thickness, b was ligament length, η was shape factor.
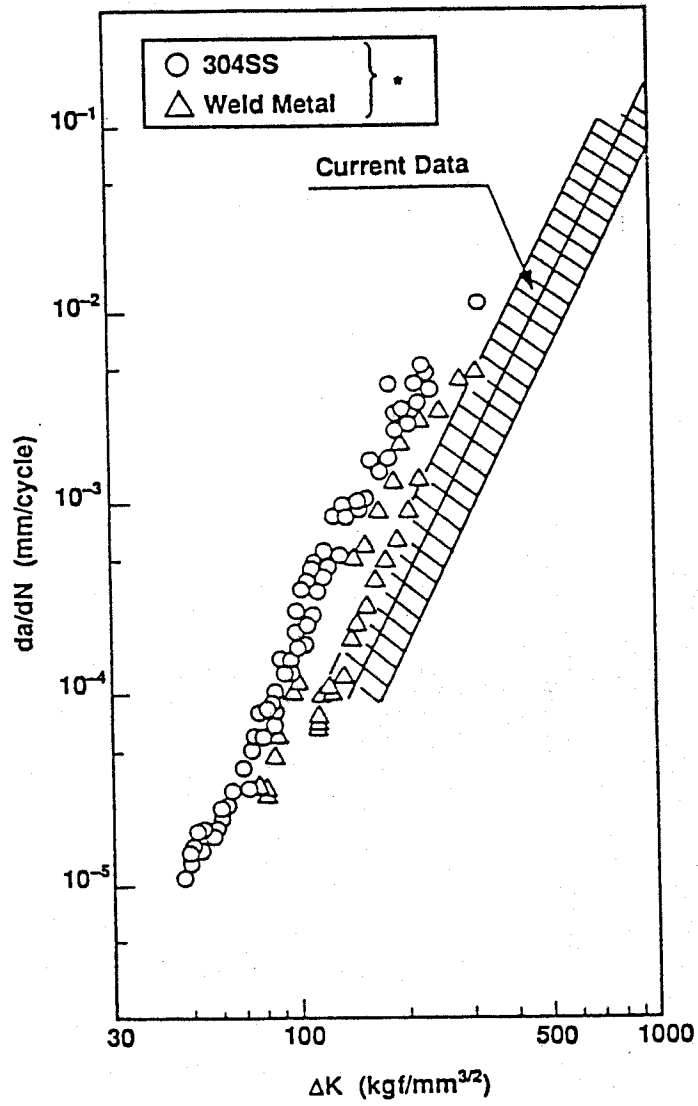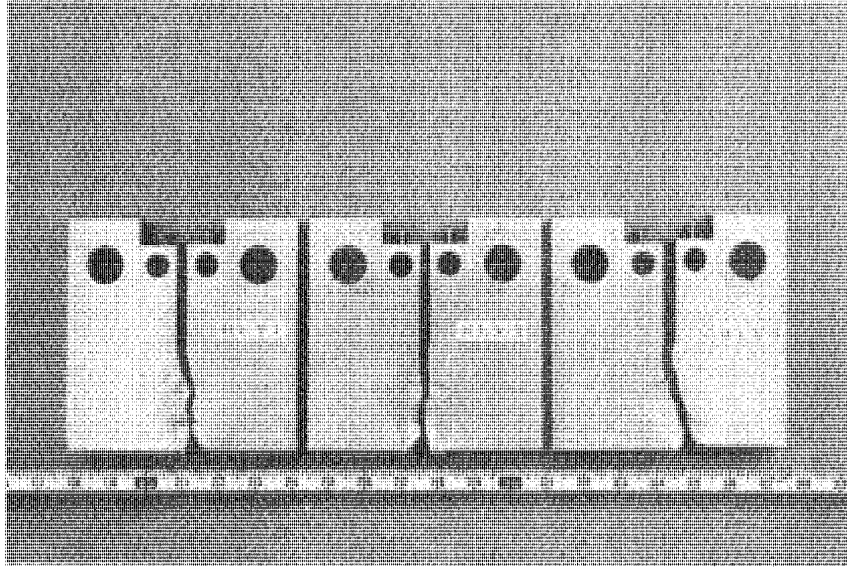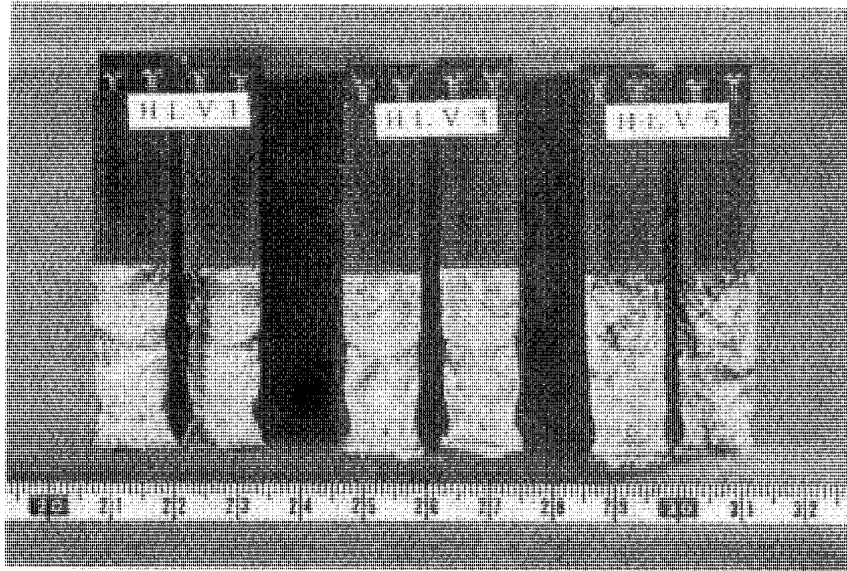

Figure K.31 (2)   Fatigue Crack Growth Rate (2/2)

Figure K.32   Comparison with Conventional Data

(1) Side

(2) Fracture surface

Figure K.33　Specimens after Test

2. TITLE AND SUBTITLE

The High Level Vibration Test Program

Final Report

3. DATE REPORT PUBLISHED

MONTH	YEAR
May	1991

4. FIN OR GRANT NUMBER
   FIN A-3288

5. AUTHOR(S)

Y.J. Park, J.R. Curreri, and C.H. Hofmayer

6. TYPE OF REPORT

Technical

7. PERIOD COVERED *(Inclusive Dates)*

8. PERFORMING ORGANIZATION — NAME AND ADDRESS *(If NRC, provide Division, Office or Region, U.S. Nuclear Regulatory Commission, and mailing address; if contractor, provide name and mailing address.)*

Division of Engineering
Office of Nuclear Regulatory Research
U.S. Nuclear Regulatory Commission
Washington, DC 20555

9. SPONSORING ORGANIZATION — NAME AND ADDRESS *(If NRC, type "Same as above"; if contractor, provide NRC Division, Office or Region, U.S. Nuclear Regulatory Commission, and mailing address.)*

Brookhaven National Laboratory
Upton, NY 11973

10. SUPPLEMENTARY NOTES

11. ABSTRACT *(200 words or less)*

As part of a cooperative study between the United States and Japan, the U.S. Nuclear Regulatory Commission (USNRC) and the Ministry of International Trade and Industry (MITI) of Japan agreed to perform a test program that would subject a large scale piping model to significant plastic strains under excitation conditions greater than the design condition for nuclear power plants. The objective was to compare the results of the tests with state-of-the-art analyses. Comparisons were done at different excitation levels from elastic to elastic-plastic to levels where cracking was induced in the test model. The vibration tests and post-test examination were carried out in Japan by the Nuclear Power Engineering Test Center (NUPEC). Input motion development and pre- and post-test analysis were carried out in the United States at the Brookhaven National Laboratory (BNL) and the Electric Power Research Institute (EPRI).

This report describes the results of the cooperative studies performed both in Japan and the United States.

12. KEY WORDS/DESCRIPTORS *(List words or phrases that will assist researchers in locating the report.)*

Nuclear Power Plants--Pipes; Pipes--Performance Testing; Pipes--Seismic Effects; PWR Type Reactors--Pipes; Primary Coolant Circuits--Performance Testing; Mechanical Vibrations; Scale Models; Test Facilities; Earthquakes; International Cooperation; Japan; Modifications; Simulation; Strains; Cracks; USA

13. AVAILABILITY STATEMENT

unlimited

14. SECURITY CLASSIFICATION

(This Page)

unclassified

(This Report)

unclassified

15. NUMBER OF PAGES

16. PRICE

NRC FORM 335 (2-89)

UNITED STATES
NUCLEAR REGULATORY COMMISSION
WASHINGTON, D.C. 20555

———

OFFICIAL BUSINESS
PENALTY FOR PRIVATE USE, $300